CRANFIELD INSTITUTE OF TECHNOLOGY

SCHOOL OF MECHANICAL ENGINEERING

Ph.D THESIS

Academic Year 1989-90

J.M. BELLIA

Aerodynamic Measurements on a Small HAWT Rotor in Axial and Yawed Flow

Supervisors: R.L. Hales & Professor J.B. Moss

July 1990

ABSTRACT

Current wind turbine performance codes are not yet able to predict the rotor aerodynamic behaviour with sufficient certainty. This has led to both the over-design of blades and to operational restrictions in certain wind conditions.

Essentially the problem is one of aerodynamic stall. Steady 3-dimensional stall can occur near the blade root in high wind conditions and may produce more power than predicted. Dynamic stall can also be expected due to the effects of yawed operation, turbulence, tower shadow and the earth's boundary layer.

The main aim of this work is to provide a coherent set of measured aerodynamic data accounting for both axial/non-axial flow and stall in high winds. These measurements are designed to highlight the effects of both steady and dynamic stall on the rotor aerodynamic performance. In addition, the data will enable current performance prediction codes to be developed and validated.

A completely new turbine has been designed and built at Cranfield to make aerodynamic measurements using pressure transducers. The design has been dominated by the requirements of accommodating the transducer signal processing equipment and allowing variation of many of the rotor parameters. Three commercial glass fibre blades were installed and performance curves measured on a conventional field site at a height of 11.5m for three rotor speed settings. These measurements show the turbine to give adequate power performance.

A mobile trailer has been used to tow the turbine at a height of 4m along the Cranfield runways. Mobile testing facilitates an accelerated test schedule and allows aerodynamic data to be acquired under controlled wind conditions. A fully instrumented blade, fitted with

forty transducers, has been tested under these circumstances and produced a large database of pressure measurements covering operation in winds up to 25 m/s and yaw angles between -45° and +55°.

Analysis of the data has shown it to be of good quality and allowed some of the effects of yaw and stall to be identified. The use of the data base for performance prediction code validation has also been established.

C O N T E N T S

LIST OF TABLES

LIST OF PLATES

LIST OF FIGURES

CHAPTER 1

INTRODUCTION

1.0 Summary

The technical feasibility of electricity generation from the wind is becoming more widely accepted [1.1], [1.2]. There is still, however, a great deal of uncertainty whether large scale wind energy derived electricity is viable on economic grounds.

One currently active area of research is aimed at improving the understanding of the air flow through the wind turbine rotor so that the aerodynamic behaviour can be enhanced. This may lead to simpler, lighter and cheaper wind turbines and make wind energy more economically acceptable.

The deficiencies in the aerodynamic prediction codes currently used by wind turbine designers are described. These clearly show the need for improvements in HAWT rotor flow modelling.

Current research in wind turbine prediction codes would significantly benefit from a comprehensive range of aerodynamic measurements. These would enable the aerodynamic phenomena unique to wind turbine rotors to be correctly modelled and assist greatly in code validation.

One of the main aims of this work is to provide such a set of measured aerodynamic data accounting for both axial/non-axial flow and stall in high winds.

The effects of yaw, steady three-dimensional stall and dynamic stall may then be determined directly from the data base and allow them to be included in the prediction models. The data base then also forms the means of validating such codes by comparison with the enhanced predictions.

1.1 Wind Energy

The potential use of wind energy for the large scale generation of electricity has now been under investigation for over 15 years. The oil

price shocks of 1973 and 1979/80 redirected energy policies world-wide. Indigenous renewable energy sources, such as wind energy, took on a new importance and diversity of supply became a key issue. Many industrialised nations initiated research and development programmes and encouraged the greater exploitation of wind energy (see [1.1] and [1.2]). In particular local legislation and tax credits in California initiated a massive and hasty wind turbine building program between 1981 and 1987 [1.3] resulting in the grid connection of almost 17000 machines. The Californian experience has served to highlight the important technology areas in which improvements are required and has provided a better understanding of many of the technical and economic difficulties in harnessing the wind. With the resulting gradual increase in confidence there is now a much greater commitment to wind energy; current EEC policy states that wind energy should be producing 5% of EEC electricity requirements by 2010, saving the community 26 million tons of oil per annum. In a recent EEC report [1.4] the Directorate General for Energy (DG XVII) concluded that if manufacturers could achieve mass production and a 30% reduction in investment costs then cost effective electricity could be produced in most European countries.

The U.K. has one of the best wind resources in Europe. Studies performed for the Department of Energy estimate that there are wind turbine sites (land-based and offshore) capable of producing 185 TWh/annum. (The U.K.'s current total electricity generation from nuclear, oil, gas and coal stations is approximately 240 TWh/annum [1.5]). Realistic estimates for wind energy penetration into the grid, however, vary widely, from less than 1% up to over 20%. In a recent speech made in the House of Lords, Baroness Hooper announced that amendments to the forthcoming Electricity Bill would obligate the Public Electricity Supply Licensees to acquire a certain amount of their electricity from non-fossil fuel sources; the target being to have 600 MW of generating capacity installed in the U.K. by 2000. This capacity may be met by generating stations driven by wind, solar, geothermal, tidal and bio-fuels (including refuse and landfill gas) but not by nuclear power. The initial wind energy contribution will be dominated by the three wind parks which the CEGB is currently establishing. Two of these will probably consist of 25 horizontal axis wind turbines (HAWT's) spread over 3 to 4 km^2 with each wind park capable of producing a total of about 8 MW [1.6].

The technical feasibility for the production of a proportion of the U.K. electricity requirement is now widely accepted. The economic feasibility, however, is far from certain. The cost of wind energy derived electricity is presently estimated to lie between 2.1 p/kWh [1.7] and 3.4 p/kWh [1.8] although forecasts for offshore wind energy are much poorer at over 7 p/kWh. The onshore based wind energy generation costs compare favourably with those of generation from coal (at about 3 p/kWh - [1.9]) and nuclear power (currently estimated at costing up to 9 p/kWh - [1.9]). Current wind energy research is ultimately aimed at improving the economics of wind powered electricity generation by producing designs for simpler, cheaper and more reliable wind turbines which are therefore capable of producing cheaper electricity.

Within the last few years another factor in the energy policies of the developed world has become much more important. This is the global warming now taking place due to the production of carbon dioxide from conventional electricity generation methods. An extra 3 billion tons of CO_2 are entering the atmosphere every year [1.10] and steps to reduce these emissions will only force the conventional generation costs up. This will not only make wind energy more economically competitive but will also provide further incentives to use forms of energy which do not contribute significantly to the production of CO_2.

The work described in this thesis has been funded by the Commission of the European Communities. Its R & D programme (D.G. XII) aims to "decrease the cost of wind derived electricity via concomitant improvements in the cost, performance and lifetime of wind turbines" [1.11]. One area identified by the Commission as deserving of a better understanding is that of the rotor aerodynamic behaviour. The U.K. Department of Energy has also identified the need for better aerodynamic design codes for wind turbines and has initiated its own experimental and computational research programs. The presently accepted 'gaps' in the understanding of HAWT aerodynamics are discussed below.

1.2 HAWT Aerodynamic Design Requirements

Most of the present day research activity in wind energy is aimed at improving the economic viability of harnessing the resource. The cost of electricity is shown by Lindley [1.5] to be most sensitive to site mean windspeed, wind turbine capital cost, availability and machine life. The

wind turbine rotor is crucial to the machines economic success since it has considerable influence over the last three of these parameters. It represents a significant proportion (usually around 20%) of the wind turbine capital cost and according to Lynette [1.3] has been responsible for 60% of lost production (during 1981-1987) in California. The life of a wind turbine is also expected to be dominated by the fatigue constraints of the rotor since this is the component which endures one of the severest load spectra. A better understanding of the aerodynamic processes which load the rotor could therefore lead to simpler and cheaper designs with reductions in capital cost and improvements in availability and lifetime. There are two key areas in the field of wind turbine aerodynamics in which designers currently hope to achieve this.

i) Increased confidence in load predictions.

Present day wind turbine design codes are not capable of calculating all of the rotor operating loads with sufficient accuracy. Figure 1.1, (taken from [1.12]), clearly shows the measured and predicted values of blade flapwise bending moment diverging at high wind speeds with a 19% under-prediction at 18 m/s. The associated power vs. windspeed graph (Figure 1.2) also shows the poor predictions made in high winds resulting in a 30% underestimate of the rotor power. This discrepancy between predicted and measured loads is of some importance in terms of static loads (although operation in high winds may not constitute the worst rotor design load case) but is of great significance in terms of the rotor fatigue life. This uncertainty in load prediction inevitably leads to the design of heavier and costlier blades than may really be necessary.

ii) Simpler control strategies.

Simpler wind turbine control strategies would also produce cheaper electricity through cheaper, more reliable wind turbine designs. The requirements of a HAWT control system include:-

a) starting the machine
b) governing the rotor rpm for electrical synchronisation
c) limiting the power developed in high winds
d) stopping the rotor (routine or emergency shutdowns)

The third of these requirements is usually the most problematic since economic pressures drive the design to be optimised for the most frequently occurring range of windspeeds. The potentially large amounts of power available in high winds must be limited.

Two schemes of power regulation have become established; stall regulation and pitch regulation, although both also usually rely on shutdown of the machine in excessively high winds. A comparative study of the two regulation modes has been carried out by the Wind Energy Group [1.12] on a machine that was originally designed and built to operate under pitch control. Under this mode of operation the pitch angle of the complete blade is continuously monitored and adjusted to control the power output of the wind turbine. This means that at low windspeeds the pitch is optimised to capture the most energy whilst at high windspeeds (at and above the rated windspeed) the pitch is set to limit the power to the rated value (see Figure 1.2). In the other mode of operation (with a different set of rotor blades on the machine) the pitch control mechanism was locked and the rotor operated under 'stall control'. This passive method of power control attempts to limit the power in high winds by the occurrence of stall on the rotor blades and has the obvious advantage of being very much simpler and cheaper to engineer. The obvious incentives, however, of the elimination of the pitch change mechanism, pitch bearings and pitch control system are tempered by several other factors. One of the main disadvantages of stall regulation is the reduced energy capture due to rounding of the power curve at the 'knee' (rated power). This is caused by the onset of stall and was estimated to account for an 18% loss of energy compared with a pitch controlled machine [1.12]. However, since the wind resource is free the reduced efficiency of a stall regulated rotor may, nevertheless, prove more cost effective.

Other potential problems with stall regulation include the requirement of a new aerodynamic braking system (previously provided by blade pitching) and the occurrence of higher mean blade loads. The power quality of stall controlled machines, however, may be improved over their pitch controlled counterparts although the evidence which suggests this is far from conclusive. On the whole, the stall control vs. pitch control issue is a very contentious one and only slowly will a preferred solution evolve. Clearly, from Figure 1.2 the present day prediction codes are not able to model the stalling behaviour of either pitch or stall regulated machines with any confidence and improved load

predictions would be of great commercial benefit to a wind turbine manufacturer.

Another means of passive power control which is currently receiving much attention is that of 'yaw control'. In this scheme the power is limited by turning (yawing) the machine away from the conventional axial flow condition so that the effective rotor disc area is reduced. An experiment performed by Anderson [1.13] showed that for small yaw angles (less than 15°) the reduction in power roughly follows a $\cos^3$ law. If yaw is to be used as a means of power regulation then much greater yaw angles will be required and will certainly result in the occurrence of 'dynamic stall' on the rotor blades. Investigations into this form of power regulation are underway because yaw is not accounted for adequately in any of the existing prediction codes. (Recent announcements from one of the Italian electricity generating companies have stated their intention to build a 60m diameter HAWT with yaw power regulation).

1.3 Current HAWT Aerodynamic Design Practice

Three types of prediction code are currently in widespread use. In ascending order of complexity (and solution cost) they are momentum theory (or actuator disc theory), blade element theory (or strip theory) and vortex-wake theory. Of the three, by far the most common is the blade element or strip theory calculation.

Assuming a uniform flow through a constant speed wind turbine rotor, the velocity diagrams at various radial stations can easily be determined from strip theory calculations such as the PROP code given by Hibbs and Radkey [1.14]. Due to the lower rotational component at the blade root the local angle of attack steadily increases from the tip to the hub. The strip theory calculations which produce these velocity vector relationships assume completely independent blade chordwise strips and involve iterative solution for the inflow factors. Enhancements to this basic problem include allowance for wind shear (the variation of windspeed with height above ground) and blade tip losses. It is aerodynamic models which include these various refinements which produce the 'predicted - measured' discrepancies described above, but which also represent the most cost effective formulation of the rotor flow. A review of the accuracy of current predictions using this method is given by Wilson et al [1.15].

None of the three types of code, however, are capable of accurately computing the power of the rotor in high wind speeds, when stall occurs on the blades. Present developments are concentrated in two main areas. Firstly, enhancement of the existing strip theory or vortex-wake calculations by inclusion of empirical extensions (usually accounting for stall) and secondly, development of a new generation of aerodynamic models based on 3-D panel methods. These more complex codes (which may include 2 or 3-D boundary layer calculations) are very much more expensive to use, are largely un-validated and are consequently not currently used by wind turbine designers. A more thorough understanding of the stalling process on a HAWT (which may be obtained by experiment) would serve both to validate the panel method codes and also provide better empirical stall models for inclusion in the widely used blade element and vortex-wake prediction codes.

1.4 Objectives

The main objective for this work is to provide a coherent set of measured aerodynamic data accounting for both axial/non-axial flow and stall in high winds. The steady and dynamic stall phenomena which would be expected to occur within such a data set are regarded as the key to current performance prediction code deficiencies. The measured aerodynamic data set is expected to provide opportunities for progress in two ways.

i) Determination of modification to 2-D aerofoil characteristics which might be caused by steady/dynamic stall.

Analysis of the database is expected to indicate the way in which the rotor blade aerofoil performance may be modified from the conventional 2-D data. Parametric trend studies performed on the entire data base are expected to indicate the overall nature of these modifications. A more comprehensive data analysis phase will then allow these phenomena to be more closely examined and will also serve to check on the quality of the data.

ii) Prediction code development and validation.

The modifications to 2-D behaviour which can be determined from the data are, in their own right, useful for prediction code development. An empirical stall model could be included within the code and may partly

resolve the prediction/measurement discrepancies. In addition, the data base itself will allow comparison with the results from enhanced prediction codes. The use of the data in validating the codes is thought to provide the quickest route to improved performance predictions.

CHAPTER 2

REVIEW OF HAWT AERODYNAMICS RESEARCH

2.0 Summary

The research currently underway to improve load prediction and produce simpler control strategies for wind turbines can broadly be divided into two categories. Firstly, the steady, three dimensional stall which occurs progressively from the blade root in high wind conditions is being investigated. The better understanding of this stalling process should improve load prediction for both stall and pitch controlled machines but is vital to the success of stall regulation as a means of power control.

The second area of work concerns all of the unsteady aerodynamic influences on load prediction, rotor control and, perhaps more importantly, fatigue life estimates. Yaw, turbulence and the stochastic nature of the wind all combine to produce a very unsteady flow environment for the wind turbine which will no doubt influence the steady three-dimensional stall behaviour discussed above. Dynamic stall may occur and its understanding will be especially important if future machines are to have successful power regulation by means of yaw. The current research in each of these areas is reviewed below.

2.1 Steady Stall Research

2.1.1 Theoretical work

With an entirely theoretical approach Klimas [2.1] has modelled spanwise flow in the attached flow over a wind turbine blade and has demonstrated that lift coefficients can be increased over their 2-D counterparts. The peak increases are seen to be of the order of 0.1 and occur only around Cl_{max}.

With a more elaborate approach Sorenson [2.2] uses a panel method coupled to a 3-D boundary layer calculation to predict the separation line along the aerofoil. His limiting surface streamlines show pronounced radial flow aft of the separation line which he predicts to occur about 10% of the chord length further back on the aerofoil as

compared to a 2-D calculation. Comparison of Sorenson's predictions with measurement for a 7.5 m Aerostar wind turbine blade (reported in [2.3]) show that power is overestimated for wind speeds above 10 m/s whilst 2-D strip theory predictions underestimate the power above 13 m/s. The shape of Sorenson's predicted power curve at stall, however, is improved and more closely agrees with measurements.

In a parametric study of the steady stalling process by Rawlinson- Smith [2.4] a vortex wake method was used to investigate the effects of a range of prescribed wake parameters. The results indicate that the wake assumptions are most important for high tip speed ratios and that in the high windspeed cases the predicted power is relatively insensitive to the wake parameters. The conclusion drawn from this is that the reason for poor power predictions in high winds must lie on the blade itself and is concerned with the prediction of blade section aerodynamic performance. More recently a more sophisticated model of the flow has been developed using a 3-D boundary layer code, a panel method for the outer flow and a free shear layer model to accommodate large areas of separated flow [2.4]. The code has been used to predict the performance of the WEG MS-2 and suggests that the blade section aerodynamic characteristics are modified from the expected 2-D wind tunnel behaviour. For all cases investigated the calculated angles of attack and lift coefficients for the outboard blade sections indicate a lower lift curve slope in the un-stalled region with a more delayed stall than the 2-D data suggests. The root section calculations show high angles of attack (up to 35°) with large separated flow areas but maintaining high lift coefficients. Comparisons with wind tunnel data are unfortunately not possible near the root (due to the high incidences) but nevertheless, the results suggest that the 3-D flow produces significant modification of the 2-D Cl vs α data.

2.1.2 Experimental work

Much experimental evidence is available which suggests that lift coefficients on a wind turbine blade are increased near the stall. By far the majority of this evidence ([2.5], [2.6], [2.7], [2.8], [2.9]) is based on experimental determination of the rotor power and its subsequent use in strip theory models of the flow to determine 2-D lift curves for the blade sections. These results then show either delayed stall (occurring at angles of attack higher than the 2-D static stall angle) and/or increased Cl_{max} at the stalling incidence. In a slightly

more elaborate experiment at Risø [2.10] blade bending moments were measured using strain gauges, at three locations along the blade length and, again using a strip theory model of the flow, were used to calculate '3-D' aerodynamic section characteristics. This method yielded estimates of Cl vs. α curves at various spanwise locations which were a requirement of the measured bending moment distributions. The latest results [2.11] show that lift coefficients well above the static 2-D Cl_{max} were required near the blade root and that slightly decreased values of 2-D lift curve slope and Cl_{max} were necessary towards the tip. The effects of Reynolds number in the 3-D case were tentatively stated to be the same as those in the 2-D case. It should be noted, however, that the results were very sensitive to small errors in the strain gauge measurements and should therefore be treated with some caution.

None of the experiments above, however, are able to specify the actual aerodynamic parameters at the blade. (i.e. angle of attack, incident velocity, lift and drag). They all use strip theory to translate measured rotor parameters into a conventional 2-dimensional Cl vs. α relationship. This may be a serious deficiency since 2-D strip theory may never be able to adequately describe the rotor flow as stall is approached. Its fundamental assumption of independently acting strips is brought into question by the possibility of radially induced velocities. These may well occur due to centrifugal effects and/or spanwise pressure gradients. Clearly the present day description of the process is inadequate and there is, as yet, insufficient experimental evidence to identify the three dimensional effects which are no doubt important.

2.1.3 Other effects

In a recent review paper, Hales [2.12] illustrates the complexities of the 3-dimensional stalling process. The effects of Reynolds number, free stream turbulence and surface roughness are all identified as influencing boundary layer growth and hence determining the stall characteristics of an aerofoil. Moreover, experimental evidence is given in which complex 3-D stall cells are shown to occur in essentially 2-D wind tunnel tests. Consequently, the influence of spanwise effects in the inherently complex 3-dimensional flow of a wind turbine are possibly considerable.

On a purely theoretical basis Musial [2.13] has demonstrated the importance of Reynolds number in rotor power calculations. Using only a

strip theory model of the flow (i.e. essentially 2-D) the contrast between the use of high and low Reynolds number aerofoil data is dramatic with large (typically 0.1) reductions in performance coefficient for the low Reynolds number data, especially at off design tip speed ratios. This effect can only become more complex when one considers the spanwise variation of Reynolds number which typically has a maximum to minimum ratio of about 2:1. Typical wind turbine Reynolds numbers are certainly in the low range and comparatively little 2-D aerofoil testing has been performed [2.14].

The effects of free stream turbulence and surface roughness on wind turbine blade steady stall are even less well understood but they are both important. One obvious effect of turbulence is its destabilising effect on the laminar boundary layer giving early transition and consequently increased Cl_{max}, especially at low Reynolds numbers (see Miley, [2.14]. Whether the experimentally noted increases in Cl_{max} could be partly caused by atmospheric turbulence is a matter for debate. Miley suggests that this could not be the case due to the large discrepancy in typical size between the boundary layer and atmospheric turbulence, the only effect being the resultant angle of attack changes caused by large turbulent eddies. The effect of turbulence intensity on Cl_{max}, however, is quite clearly shown by experiments performed by Barrack [2.15] and McKeough [2.16]. These show that for increasing turbulence intensity (up to 10%) the value of Cl_{max} for a range of aerofoils increases significantly and in some cases by as much as 50% over the zero turbulence value.

According to Miley [2.14] the effects of surface roughness counter those of turbulence with increases in roughness tending to give lower values of Cl_{max}. Roughness effects are also more critical at lower Reynolds numbers and operational experience in California [2.17] has shown that a wind turbines continuous operation in the earths relatively dirty boundary layer causes significant performance degradation due to leading edge dirt accumulation.

2.1.4 Pressure/load measurements

Recently, more ambitious wind turbine aerodynamics experiments have been performed in which the section properties are measured directly in the form of pressure distributions or loads. Current work at FFA in Sweden [2.18] on a 5m diameter turbine involves the measurement of steady

distributions with the pressures being averaged over many rotor revolutions. With the steady inflow obtainable in a wind tunnel the results, which are currently being analysed, should help to identify the changes in aerofoil characteristics which occur as steady stall approaches. No information about dynamic stall can be obtained. The Swedish work, however, does highlight one of the main difficulties of wind tunnel testing; tunnel blockage. Even with a tunnel cross-sectional area of 192 m^2 the blockage ratio achieved was in excess of 10%. Uncorrected power coefficient data shows peak Cp's approaching the Betz limit so the quality of the results will depend greatly on the accuracy of the tunnel blockage corrections used.

Experimenters at the University of Southampton [2.19] have adopted a rather different approach. In an attempt to test a small machine at Reynolds numbers approaching those of a full scale HAWT the wind turbine built for these tests runs at nominally 2200 rpm. The wind tunnel speeds of up to 30 m/s give minimum tip speed ratios of about 4 for the 1m diameter machine. Early results show that the root section lift coefficients are sometimes higher than would be predicted by blade element theory, but not higher than the 2-dimensional C_{Lmax} for this section. The measured pressure distributions, however, indicate some surprising effects with a large suction peak occurring on the blade pressure surface over the inboard 40% of the blade span. They attribute this to a separation vortex shed by the almost circular root sections of the blade.

In a similar wind tunnel experiment at Imperial College of Science and Technology [2.20] measurements of both 2-dimensional and 3-dimensional aerofoil section characteristics have been made. Running a 2.7m diameter machine in the tunnel settling chamber (with a high blockage ratio of approximately 70%) has produced steady pressure distribution measurements for the 3-dimensional wind-turbine rotor configuration. These results have been compared with measurements made on the same untwisted, untapered blade in conventional wind tunnel aerofoil tests. They conclude that the effects of rotation lead to both delayed stall (the 2-D C_{Lmax} being reached at higher incidence) and in some instances higher values of C_{Lmax} than in the 2-D case.

All the experiments discussed above use slow data acquisition systems with data being averaged over many rotor revolutions at the time of measurement. As a result of this, dynamic changes in the pressure

distributions cannot be recorded. This is in contrast to the work described here and also to that performed by NASA [2.21], SERI [2.22] and Risø [2.23]. In both of the American research projects surface pressures on the blades of full size operating wind turbines (91m and 10m diameter respectively) have been recorded many times during each rotor revolution. Information about the unsteady behaviour of the aerofoils is therefore available and analysis of the data is in progress.

~Initial results from NASA have shown that for the 65% span measurement location;-

i) Fully attached flow exists for low windspeeds.

ii) The flow separates and reattaches every revolution due to the tower effects in medium windspeeds.

iii) With increasing windspeed the proportion of the rotor revolution with separated flow increases until the flow is unattached for the whole rev.

iv) Suction peak pressure coefficients on the wind turbine appear to reach values higher than those for the same aerofoil measured in a wind tunnel irrespective of angle of attack.

The SERI work has so far produced the following results;-

i) At low angles of attack (low windspeeds) the pressure distributions on the rotating aerofoil agree well with those from 2-D wind tunnel tests on the same aerofoil.

ii) Even in moderate winds the pressure distributions indicate that there are relatively large dynamic changes in angle of attack.

For both experiments a vast amount of data is obtained in a comparatively short time and much work in the data analysis is still to be done.

This is also true of the recent work at Risø [2.23]. In this experiment local aerodynamic forces are measured directly using blade sections which are supported on load cells. Three such sections provide lift and drag forces and moments at 37% span, 68% span and at the blade tip. A

five hole probe is also used to measure the local flow velocity about one chord length ahead of the blade. Combining the load and velocity information allows the Cl vs. α relationship at each station to be determined. Tests have been carried out in both axial and yawed flow and also with the wind turbine stationary (yawed at 90° with the instrumented blade pointing vertically upwards). Early results have produced the following conclusions;-

i) Comparisons between the rotating and non-rotating measurements show no clear rotational influences on the aerofoil characteristics below the stall.

ii) Beyond stall the normal force coefficients seem to increase.

iii) Evidence of stall hysteresis in yawed operation (see 2.2.1).

2.1.5 Flow visualisation tests

A further technique for identifying the steady stalling process is flow visualisation. Many methods have been used including smoke, oil and blade tufts and a broad range of results have been obtained. In a comparative study of three types of HAWT performed by Eggleston and Starcher [2.24] completely different flow patterns existed over basically similar machines. They concluded that there were significant deviations from the flows that would have been assumed in applying 2-D aerofoil data in a strip theory model.

Evidence of delayed separation (which may contribute to increased lift coefficients) was found on a Danwin 22m diameter machine in tests carried out by Risø [2.25]. Flow visualisation estimates of the separated region were smaller than calculated (i.e. delayed separation) and this coincided with blade flap loads which were larger than anticipated. Quite the reverse was found by Savino and Nyland [2.26]. They suggest that separation occurs 10 to 20 percent of the chord length earlier (toward the leading edge) than would be expected on a non-rotating blade.

On one issue, however, many of the flow visualisation experiments seem to agree. This is the existence of spanwise flow (radially outward) on the blade. Savino and Nyland found evidence for its existence only in the separated region with the fully attached flow being chordwise. In

another experiment [2.24] evidence of spanwise flow ahead of the separation line in the attached flow region was also found.

The Risø experiment using wool tufts also showed a very strong influence of blade azimuth position on the separated flow area. [2.25]. This serves to remind us that the steady three dimensional stall phenomena is only part of the wind turbine rotor flow problem. In reality the flow will be unsteady.

2.2 Dynamic Stall

Dynamic stall is sure to occur on wind turbine rotor blades. The combination of wind shear, atmospheric turbulence, tower shadow and operation in yaw produce the unsteadiness in local blade angle of attack which can cause dynamic stall.

A great deal of dynamic stall research has been carried out in the helicopter field and the process is well illustrated by Figure 2.1, reproduced here from [2.27] and [2.28]. From a recent review paper by Carr [2.29] it is clear that many experiments have shown the dependence of dynamic stall effects on the aerofoil motion characteristics (i.e. pitch amplitude, pitch rate and reduced frequency). The application of this data to wind turbines, however, is difficult, since as stated by Courtney [2.30] much of the stalling wind turbine blade may be experiencing incidence variations which lie well outside the limits for helicopter dynamic stall models or measured data bases.

Little work, however, has been done in either the helicopter or wind turbine fields regarding the effects of Reynolds number or turbulence on dynamic stall. Both these factors have been shown earlier to influence considerably conventional 2-D stall and should therefore be expected to continue their influence to some extent under dynamic and 3-D conditions.

Recent research into the factors which may influence dynamic stall are now reviewed in turn.

2.2.1 Yaw

Courtney ([2.30], Figures 5a to 5c) clearly shows the strip theory estimates of the variation of minimum and maximum angle of incidence

along a Vestas 15 wind turbine blade operating in 8, 14 and 20 m/s winds and at 20° and 40° of yaw misalignment. The case for yaw as a potential source of dynamic stall is graphically shown by the 20° yaw, 14 m/s windspeed case which is an operating condition that would be relatively frequently encountered. Under these conditions strip theory estimates show that near the blade root the angle of incidence oscillates between about 20° and 40° during every rotor revolution. Even if these strip theory results are qualitative rather than quantitative the principle is clear that large incidence variations due to yaw are likely to occur.

Many experiments have been performed examining the effects of yaw on rotor responses such as power, cyclic blade loads or yaw torque. The main body of work was performed in the early 1980's on the MOD-0 100 kW experimental wind turbine ([2.31],[2.32],[2.33],[2.34],[2.35], [2.36]). Tests were performed to examine the variations of rotor power and blade loads with yaw and also the response of the rotor when allowed to yaw freely. Remembering that the machine has a downwind, two bladed, teetered rotor, the results indicated that rotor power approximately followed a $\cos^3$ relationship up to yaw angles of about 30°. Beyond this less power was produced than would have been predicted by the law. Mean blade loads were not seen to increase with yaw angle, although this is thought to be due to the teetered hub; teeter excursions in yawed operation were larger. Another significant result was that the yaw response was not symmetric, i.e. positive and negative yaw gave different teeter responses. The free yaw tests showed that the nacelle stabilised at -45° to -55° yaw and that this was independant of wind speed in the range tested (only 5-9 m/s). This large angle is thought to be due to the large nacelle tilt (8.5°).

Some of the NASA findings have been confirmed by Anderson [2.37]. He also shows good agreement with the $\cos^3$ theory during experiments on a 3m diameter downwind turbine. The theory, however, does not predict well above yaw angles of 15° and, contrary to the NASA result, the power produced then exceeds the predicted values.

The asymmetry between positive and negative yaw responses has also been shown by ECN [2.38] and by early work at Risø ([2.39] and [2.40]). In both these cases the results are for a turbine mounted upwind of the tower. Asymmetry of yaw response has consequently been seen on both upwind and downwind (NASA Mod-0) machines.

More recent work in the United States has been performed by Hansen [2.41]. A comprehensive yaw dynamics model for HAWTS is being developed and validated using data provided by SERI and U.S. Windpower. The code is capable of predicting yaw tracking behaviour but as yet underestimates the magnitude of both yaw torque and blade flap moments. The work has shown the importance of dynamic stall on the mean yaw moment; once stall hysteresis was included in the code the mean levels of yaw moment were increased and agreed more closely with measurements. Also of major significance is any mass imbalance in the rotor. This was shown to be the largest single source of cyclic yaw loads for the SERI rotor with its centre of gravity just 0.02% of the rotor diameter from the rotational axis. For the free yaw cases considered all three results indicate that the behaviour is strongly influenced by horizontal wind shear which loads the left and right halves of the rotor unevenly and produces a yaw torque. This is seen in the data from both SERI and US Windpower and also in preliminary results from work at Oregon State University (see [2.42]).

All the above have been concerned with the rotor response to yaw with little regard to the underlying aerodynamic phenomena caused by yaw. Work in this area is being performed by the same researchers who are currently able to measure unsteady aerodynamic forces. Namely NASA, SERI, Risø and FFA. The analysis of data from both Risø and SERI is still underway and only preliminary results are available. The latest results from Risø [2.23] indicate significant stall hysteresis during operation at 40° yaw and are very similar to those given by SERI [2.22]. In both cases a great deal more analysis needs to be performed to draw conclusions from the data. Results from FFA are not yet available due to the more complex tunnel blockage correction required for a yawed wind turbine.

2.2.2 Turbulence

The atmospheric turbulence which affects the rotor blade aerodynamics can broadly be divided into two. Large scale turbulence which produces gross changes in angle of attack is more easily considered in terms of temporal and spatial variations of the inlet wind conditions, such as veering and gusting. On the other hand, smaller scale turbulence which is of the order of the boundary layer thickness will affect the local aerodynamic behaviour due to its influence on transition. The latter effect has been discussed in 2.1.3 in its steady stall context. Little

work has been performed showing the effects of this type of turbulence on the dynamic stall behaviour of wind turbine or helicopter blades.

The nature and effects of larger scale turbulence have been investigated. Connell [2.43] describes the atmospheric processes which produce this turbulence and goes on to explain the difference between fixed-point wind measurements and rotationally sampled wind measurements. The dramatic increase in the higher frequency content of the rotationally sampled wind indicates that the wind turbine actually sees much more unsteady inlet wind conditions than would be expected from upstream wind measurements. This is theoretically accounted for by Sundar [2.44] who shows that the transfer of energy from low frequency to the rotational frequency and its harmonics is caused by the spatial variation of the turbulence across the rotor disc and that the effect becomes more significant for larger rotors. Sundar describes the wind input with a Davenport model and using simple blade element theory is able to estimate the effects of spatial and temporal wind turbulence on rotor power.

All of the work reviewed deals with the variations of power and wind conditions on a frequency basis and formulates some form of response function, again in terms of frequency. The random nature of the wind means that this is a sensible formulation of the problem. It also means, however, that no work could be found in which the effects of the large scale turbulence are accounted for directly in the local aerodynamic calculations. Any influence which this large scale turbulence may have on dynamic stall is therefore presently unknown.

2.2.3 Tower shadow and windshear

The effects of tower shadow have been illustrated by flow visualisation tests at Risø [2.25]. Video pictures have been obtained showing the movements of wool tufts on a 22m diameter rotor (mounted upwind of the tower). The area of flow separation in winds of 14 m/s is a strong function of blade azimuth with periodic separation and reattachment as the blade passes in front of the tower. The observed chordwise movements of the separation points are usually greater than those predicted by Eppler code calculations.

The effects for a downwind rotor have been shown to be even more severe [2.35]. Mean flapwise loads seemed to be unaffected when experiments

were performed with a 38m diameter rotor mounted upwind and then downwind of a lattice tower. Cyclic loads, however, were much increased for the downwind case due to the flow disturbance from the tower. The works of Snyder and Wentz [2.45] and of Powles [2.46] both support these observations with measurements of the wakes downstream of wind turbine towers. The velocity deficit, compared to freestream, is accompanied by both random fluctuations and low frequency periodic vibrations due to shed vortices which give rise to increased cyclic loads.

The effects of wind shear are usually incorporated into most forms of prediction code using a simple height power law. If the real wind does indeed conform to this form of relationship the effects on the rotor aerodynamics will be small for all but the largest wind turbines. Smith [2.47] questions the validity of the law when applied to most wind turbine sites which are usually chosen because of some degree of natural wind concentration (e.g. a smooth hill). Examples are given in which the law is not obeyed, with cases of the same windspeed being noted at 16m and 60m above the ground but with slightly lower velocities in-between. One conclusion may be that wind shear as a separate issue need not be considered as long as the effects of spatial turbulence are accounted for. For large machines, however, the effects of wind shear become more important. The pressure measurements made by NASA [2.21] on a 91m diameter Mod-2 wind turbine show the variation of tangential force coefficient during a rotor revolution. (The coefficients were found from the pressure distribution with dynamic head equal to the rotational velocity component only). In moderate winds with zero yaw angle and attached flow at all blade azimuths the coefficient was seen to increase to its maximum value as the blade approached top-dead-centre and reduce to its minimum at bottom-dead-centre. NASA believe this to be due to the wind shear at the site.

2.3 Definition of the Present Experiment

As referred to earlier, many researchers are experimentally investigating the aerodynamics of horizontal axis wind turbines. The experiment reported in this thesis was designed to complement other work and involves some novel techniques not used elsewhere. From the outset the experiment was intended to allow investigation of the unsteady effects by using high frequency response transducers and sampling the available data streams many times per rotor revolution. This is in contrast to the work carried out by the FFA in Sweden [2.18], the work

of Southampton University [2.19] and the work carried out by Imperial College [2.20] all of which are aimed solely at the 'steady stall' problem. The experiment performed here is therefore very much more comparable to those performed by NASA [2.21] and SERI [2.22] where unsteady measurements are taken which allow the 'within rev' aerodynamic processes to be investigated. The most novel feature of this experiment which distinguishes it from the two American experiments is the use of mobile testing in addition to the more conventional tests carried out on a fixed tower.

The Cranfield experiment is essentially a field experiment (performed in the open air like those of NASA and SERI) but with many of the benefits of a wind tunnel experiment. The stochastic nature of the wind makes field testing a difficult exercise. High windspeeds are rarely experienced and when they do occur the experiment must be fully operational to take full advantage. In addition the unsteady inlet wind conditions (with turbulence, gusting and veering) cannot be controlled and make understanding the rotor response all the more difficult. For the mobile test facility at Cranfield the inlet wind conditions are much more controllable since testing during calm periods (which are more frequent than very windy ones) allows the wind speed to be chosen. (The towing speed of the facility allows windspeeds up to 25 m/s to be simulated.) Perhaps more importantly it also means that the effects of gusting and veering can be eradicated (allowing tests at fixed, known yaw angles) and that the inlet turbulence levels can be very much reduced. (Testing on windier days in the long term will allow a range of inlet turbulence conditions to be investigated.) The main compromise which is inevitable for mobile testing to be possible is that of wind turbine size. The NASA and SERI experiments use turbines of 91m and 10m respectively whereas the Cranfield experiment uses a 3m diameter wind turbine. Special consideration must therefore be paid to the possible effects of scale (Reynolds number). These considerations led to the following specification for the four major components of the experiment;-

i) Transducers

Inlet wind conditions measured using quick response anemometers (distance constant = 300 mm) and located at two upwind locations giving some spatial information.

Load cells measuring rotor and yaw torques and allowing for operation in both fixed and free yaw.

Quick response pressure transducers mounted in a blade giving dynamic pressure distribution information.

ii) Wind turbine

Design of wind turbine allows variation of operational parameters. Rotor speed, blade pitch, and turbine body angle can be adjusted. Tilt angle and cone angle are fixed at zero.

A NACA 4415 blade aerofoil section is used. This is well behaved at low Reynolds numbers (down to 100,000).

iii) Data acquisition system

High speed digital data acquisition system for data of high temporal resolution.

All relevant channels sampled many times every rotor revolution with analogue to digital conversion of measurements for later calibration and analysis on digital computer.

iv) Method

Tests on both conventional field site and controlled velocity testing on Cranfield runway to produce wind tunnel conditions.

CHAPTER 3

WIND TURBINE DESIGN, CONSTRUCTION AND COMMISSIONING

3.0 SUMMARY

A commercially available wind turbine capable of accommodating the experiment could not be found so the decision to scratch build a machine was taken. The design was based on "PROP" code type performance predictions and included provision for operation at various blade incidences and at a range of rotor speeds. Systems for the measurement of rotor speed and torque, yaw speed and torque and, of course, blade surface pressures were also included.

An induction motor, rated at 7.5 kW was chosen to absorb the rotor power via a high torque drive belt. Interchangeable pulleys allowed the rotor speed to be varied over a 2:1 range. A pneumatic disc brake system was used to stop the rotor under both normal and emergency conditions.

Electrical signals were transferred to/from the rotating frame of reference to the stationary one via a commercially available 28-way slip ring assembly. A purpose built pneumatic slip ring was used to transfer the blade reference pressure to/from the rotor.

Several commissioning tests were performed on various sub-assemblies and on the completed wind turbine. Once operational, three tail vane configurations were explored and resulted in a satisfactory method of yaw control.

The design parameters for the completed wind turbine are given in Table 3.1

3.1 Wind Turbine Design Specification

Consideration of the experiment to be undertaken was of paramount importance in choosing a wind turbine appropriate for the testing. Commercially available turbines with rotor diameters of up to about 5m were examined for their suitability. If the necessary modifications could be made quite easily then the purchase of such a machine would save a considerable amount of work. Unfortunately, no such wind turbine

could be found, the main inadequacies being insufficient space for the electronics required (both on and off the rotor) and lack of provision for control or variation of the rotor parameters.

The decision to build a wind turbine from scratch was therefore taken. This would obviously require much effort and time both in terms of design and construction but would allow a great deal of flexibility to be inherently designed into the machine (e.g. variable pitch, speed, etc.) The design specification of the required wind turbine can be summarised as follows;-

. Rotor diameter up to 5m
. Variable pitch (not necessarily during operation)
. Variable speed (not necessarily continuously variable)
. Systems for measurement of rotor torque and yaw torque
. System for the measurement of rotor speed
. Free yaw and fixed yaw operation capabilities
. Systems for measurement of blade surface pressures
. Maximum weight of 250 kg. (due to tower strength)

With a general machine specification decided, work on design of the wind turbine commenced. Perhaps the most important decision regarding a scratch-built machine concerns the choice of the rotor blades. It was considered important to use a blade which met the following criteria;-

i) The blades should be commercially available. The rotor would most likely consist of three blades and therefore, allowing for at least one instrumented blade, more than four blades would be required. It was decided that the in-house fabrication of these blades would be impractical and that an outside contractor would be required. In addition, although this generic research is primarily aimed at issues important for large machines, it was considered important to use commercially available blades since the aerodynamic problems are none-the-less important for small machines in their own right.

ii) The blades should be constructed in such a way so as to facilitate later instrumented versions.

iii) The blades should have an aerofoil section which is well behaved at the low Reynolds numbers of normal wind turbine operation. For a

machine in the 3 to 5 m diameter range typical (75% span) Reynolds numbers lie between 0.4 and 0.8 million.

iv) The blades should be as stiff as possible in an attempt to uncouple any unsteady aerodynamic effects from the blade structural dynamic characteristics.

Blades from Bergey Windpower Inc., Marlec Engineering Co., Energy Services Ltd. and Hawker Siddeley Power Plant Ltd. were considered. The decision taken was to use blades manufactured by Marlec Engineering Company, because they were the only ones which met all the above criteria and the manufacturer was only 1 hours drive from Cranfield.

Three 1.377 m length blades form a 2.854 m diameter rotor rated by Marlec at approximately 1 kW. The blades use a standard NACA 4415 aerodynamic section which is well behaved at low Reynolds numbers (see [3.1]). The glass reinforced polyester construction gives relatively stiff blades. Resonance tests on plain, uninstrumented blades showed that the first flapping frequency was at approximately 15 Hz which is between two and three times the rotational speed range used here.

3.2 Preliminary Design Study

With the chosen blade and the wind turbine specification completed a performance prediction exercise was undertaken. This would provide estimates of the loads which the design should withstand and subsequently allow the demarcation of 'testing window' boundaries. A performance prediction code for propellers and wind turbines [1.14] was used to predict the rotor response in wind speeds from 1 to 30 m/s and running at tip speed ratios in the range 1 to 8. These limits were chosen such that the testing window to be mapped out would definitely be included. Within these ranges, values of rotor torque, thrust and power were calculated and plotted for blade setting angles between 2° and 14°. (Since the blade aerofoil section is set at nominally 8° to its root fixing this resulted in $\Delta\beta$ values between -6° and +6°). To assist in choosing a suitable testing window, plots of rotational speed (r.p.m.) and Reynolds number (based on the local chord and velocity at the 75%R spanwise station) were also produced. It must be remembered that prediction codes such as that used here are unable to correctly determine the rotor response when either steady or dynamic stall may be

present. Consequently the results of this exercise should be used with caution.

Examination of the resulting plots (Figs. 3.1 and 3.2) led to an assessment of the most important factors, these being blade design maximum r.p.m., size and type of motor (determining maximum generated power and torque), maximum allowable rotor thrust and the strategy to be adopted for rotor speed control. The chosen test window boundaries (shown in Figure 3.2) provided the following design parameters. (They cannot all occur simultaneously).

Maximum allowable rotor power	15000 W
Maximum allowable rotor speed	800 r.p.m.
Maximum allowable rotor thrust	4500 N
Maximum allowable rotor torque	350 Nm

Since stall is seen as one of the key factors in HAWT aerodynamics, the test window was then examined to check if the correct conditions for stall were included. To determine the possibility of stall on the blade, the predicted effective angle of incidence was examined along the blade under all conditions. If this angle of attack was greater than +15° then this section was deemed to have stalled. The results of this analysis showed that for steady flow stall starts to occur on the blade as the tip speed ratio drops below about five with the entire blade in stall by tip speed ratios of about one.

It was therefore concluded that the design specification above would produce a wind turbine capable of producing the aerodynamic effects which are of interest. Unsteady effects were not considered and it therefore should be remembered that the dynamic loads on the wind turbine could be greater than those given in the specification.

3.3 Detailed Mechanical Design

Figure 3.3 shows the general layout of the wind turbine which was designed to meet the required specifications. All of the important machine parameters are given in Table 3.1. The front compartment of the turbine houses the heavy-duty electrical/mechanical systems; the separate rear compartment houses the delicate signal processing electronic circuitry. Each of the main features will be considered in turn.

3.3.1 The Motor

Once this design concept had been adopted the induction motor and drive system were sized to cope with the range of speeds, torques and powers indicated by the design study. The resulting drive system was based on a high torque drive belt, 50 mm in width with teeth of semicircular cross-section. The maximum power this belt will transmit is about 30 kW. A 144 tooth pulley is fixed to the main rotor shaft but any one of five pulleys can be fitted to the motor shaft to give nominal rotor speeds of 333, 395, 458, 583 and 667 r.p.m. The motor is used in conjunction with a star/delta starter which reduces the starting torque and currents to one third of their running values providing relatively gentle starting. During operation the actual rotor speed does vary slightly from the nominal values given above due to the slip characteristics of an induction motor. Under very light wind conditions with no aerodynamic torque being produced the slip is just positive to overcome the mechanical/electrical losses and the rotor will run at one of the above nominal speeds to maintain the motor at just below synchronous speed. As the wind speed increases the aerodynamic torque produced accelerates the rotor to give a super-synchronous speed at the motor and hence negative slip. Under these conditions the motor is running under generator action and electrical power is being fed back to the supply. The distance between the two shafts changes for each different pulley so the motor support bracket is held within a vertical track. This enables the belt tension to be set for each new rotor speed.

3.3.2 The Brake

A customised pneumatic disc brake system is fitted to the rotor shaft to ensure gentle and fail-safe braking (see Figure 3.3). A 250mm diameter disc is keyed onto the main shaft with the brake calliper mounted on an adjacent bracket. The calliper and actuator system, manufactured by Twiflex, is a gas released/spring applied unit capable of producing a braking force of 5700 N and consequently a maximum braking torque of 542 Nm. Nitrogen is supplied to the brake actuator at between 5 and 7 bar via an electrically operated solenoid valve. A large spring which supplies the pad braking force is compressed by the gas and the pads are therefore pulled clear of the disc. Application of the brake while the rotor is running is achieved by switching off the supply to the solenoid valve (which also electrically disconnects the motor). This removes the gas pressure from the brake allowing the compressed spring to extend and

press the pads firmly against the disc. The system is also fail-safe since if either the gas supply or the electrical supply to the solenoid valve are lost the brake is automatically applied.

3.3.3 Main shaft and hub

The blades are attached to the main rotor shaft via a pair of 'Y' plates which clamp the three blade roots as shown in Figure 3.3. Blade pitch changes are effected by replacing the parallel sided packers with wedges and replacing all of the M12 bolts with thinner M10's. The main shaft is a 50mm O.D., 31.75mm I.D. steel tube running in two main bearings. The forward bearing takes only side loads whilst the rear is capable of taking thrust as well as side loads. Just behind the rear bearing, in the rear section of the wind turbine the main shaft is split into two and rejoined with a flexible coupling. This prevents excessive loads being transmitted to the rear of the machine where the slip rings may be damaged. Most of the rear shaft is used for the rotating electronics and is described below.

3.3.4 The rotor blades

Blades for the wind turbine were chosen at an early stage of the turbine design. Aside from all of the more usual constraints upon the choice (such as size, aerodynamic section, weight, cost etc.) the suitability of the blade for subsequent instrumented versions had to be evaluated. This was imperative since any instrumented blade (equipped with pressure transducers) should be as near identical as possible to any other, non-instrumented blades on the rotor.

The MARLEC blades chosen for the turbine are made of glass-fibre reinforced polyester around a foam core former (see Figure 4.6) with the manufacturing process utilising a pair of moulds - one for foam core production and the other for polyester resin injection to the final blade shape. These materials and construction method were thought to provide some scope for the inclusion of pressure transducers.

3.3.5 Rotor speed optical disc

A thin aluminium disc machined with 128 equi-spaced radial slots is fitted directly behind the rotor shaft pulley in order to measure rotor speed. A pair of optical switches are mounted such that the slots are

registered as the rotor turns. This system is located in the front of the machine so that the speed signal accurately represents the rotor speed without the flexible coupling interposed.

3.3.6 Accelerometer

A small piezo-electric accelerometer is mounted on a bracket attached to the rotor shaft front bearing. The sensitive axis of the device can be rotated and the signal is sampled by the data acquisition system. There are, however, two other functions for the accelerometer signal. Firstly, it is used for rotor balancing as described in 3.5.1 and secondly it is continuously monitored by the wind turbine control system (see 3.4.2) for application of the brakes in the event of increased vibration levels.

3.3.7 Slip rings

A 28 channel electrical slip ring is mounted at the very rear of the machine. The unit was obtained from D.J.Mouldings and featured silver rings and silver/graphite brushes with typical resistances of 10 mΩ. A 28 way unit was chosen since a total requirement of 21 separate channels could be foreseen whilst space for a 28 way unit could be utilised at little extra cost.

A second slip ring assembly is mounted just forward of the half moon plate. This pneumatic slip ring is a custom designed and built unit required to transfer the pressure transducer system reference pressure from the rotating to the stationary frame. The reference pressure pipe within the rotor shaft is bent through a right-angle and brought through the shaft wall. A pair of oil seals (lubricated with graphite impregnated grease) sit either side of the reference pipe which is brazed into the main shaft and is carefully machined flush with the shaft surface. This arrangement means that there will be no appreciable flow across the interface and that the reference pressure will be faithfully transferred.

3.3.8 Yaw bearing

The yaw bearing used was salvaged from a similar sized wind turbine. A pair of needle roller bearings sandwich the tower based plate around the main yaw cylinder which is fitted to the wind turbine base. A small

modification was added to the bearing to allow the measurement of yaw torque. This is obviously not meaningful when the machine operates in free yaw so a system had to be devised in which the yaw bearing was locked causing all yaw loads to pass through a load cell. This is achieved when a locking collar is tightened against the main yaw cylinder, restraining the wind turbine in yaw (fixed yaw mode) and enabling both positive and negative yaw torques to be measured.

When the wind turbine was at an advanced stage of construction the machine was rolled back and forth over a steel pipe in order to locate the for/aft position of the centre of gravity. The yaw bearing was then bolted to the turbine in this position.

A later modification to the yaw system was the addition of a yaw direction sensor producing a signal of wind turbine yaw position relative to the tower in either free or fixed yaw mode. This was done by mounting a servo- potentiometer (capable of unlimited rotation) on the yaw axis and restraining its spindle (via a flexible coupling to account for any eccentricity) in the tower frame of reference.

No yaw slip rings are fitted to the machine. All of the electrical, electronic and pneumatic systems which cross the yaw bearing do so via a pair of cable/pipe bundles which allow only $\pm 270°$ of rotation from the home position. Continuous yaw rotation, and hence unattended operation is therefore unwise.

3.3.9 Cowlings

Two large sheets of 22 s.w.g. aluminium are used to cover the front and rear compartments of the wind turbine. The forward cover is fitted first (with its motor cooling slits and bubble to clear the brake) followed by the plain rear cover. Each of these are screwed into position trapping a small bead of silicon rubber grease to give a waterproof seal. The nose fairings for the machine were also fabricated from aluminium with separate sections forward and aft of the rotor plane. The in-house capability to produce double curvature in sheet metal did not exist so a two frustrum spinner was made. This bolts directly on to the front 'Y' plate allowing sufficient space for all of the transducer wiring to pass into the main shaft. Three 120° arc sections then bolt over the rear 'Y' plate between each blade.

3.3.10 Tail vane

The wind turbine tail vane design was not finalised until operating experience of the machine had been obtained. Two different designs were tried, the first being salvaged from a similar sized wind turbine and illustrated in Figure 3.4(a). During operation in winds up to about 10 m/s this configuration performed adequately but in stronger winds yaw oscillations tended to develop with the machine hunting about the mean wind direction. (The most serious occurrence of this resulted in the wind turbine yawing through 180° and running, unattended, in propeller mode for almost an hour.) It was suggested that more aerodynamic damping would suppress these yaw excursions and could be achieved by fitting a larger vane. This was attempted with the second design shown in Figure 3.4(b). This vane provided greater area but unfortunately no greater damping in operation. The reason for this was thought to be that the larger vane sat in both the rotor and nacelle wakes and would have had to extend very much further downstream to provide sufficient yaw torques. At this stage the situation was re-examined and a third solution was attempted. For this some mechanical damping was introduced at the yaw bearing by slightly tightening up the yaw lock collar, without locking it completely. This resulted in successful operation in all wind regimes even with neither of the above described tail vanes fitted! (see Plate 3). The slab sides of the wind turbine, themselves act as a yaw vane since there is a greater area behind the yaw bearing than in front of it.

3.3.11 Test and transport frame

A large iron frame was designed and built to provide a convenient work-bench for test of the machine (with rotor running) whilst indoors during commissioning. With the machine firmly bolted to this frame a second lifting frame could be attached allowing the whole assembly to be lifted, rotated on to its back and lowered onto four castors. In this mode the frame enables the machine to be moved and easily aligned with both the field test site and mobile trailer tower assemblies.

3.4 Detailed Electrical Design

3.4.1 The Motor

In the front section of the turbine lies a 3 phase induction

motor/generator. Early in the design process the choice between an a.c. or d.c. drive system had to be made. Based on the initial design study outlined in section 3.2 desirable ranges for rotor speed/power and wind turbine weight were identified. It quickly became clear that a d.c. motor/generator of sufficient electrical power rating would weigh in excess of 90 kg. This would represent too great a proportion of the 250 kg. design target weight and consequently the use of a d.c. motor in the wind turbine was rejected. An a.c. induction motor weighs approximately half that of an equivalently rated d.c. machine and in addition the transient nature of controlled velocity testing suggested that the overload capability of an induction motor could be exploited. Hence the choice of a 3-phase a.c. induction motor rated at only 7.5 kW (weighing 49 kg), with the capability of generating 15 kW for periods of less than one minute. The pull-out torque of this motor/generator is always higher than the 15 kW power limit.

Amongst the drawbacks of the a.c. machine, however, are its starting and speed regulation characteristics. Controlling the speed of an induction motor by using an inverter drive would have produced an extremely versatile system but it was found to be impracticable due to the large regenerative capacity required. (The inverter drive would have to absorb considerable amounts of power when the wind turbine was generating in high wind speeds.) The decision was therefore made to use the induction machine in combination with a belt and pulley drive system. This would not allow a continuously variable rotor speed but would give a 2:1 range of rotor speeds in discrete steps.

3.4.2 Rotor control

The wind turbine electrical system is shown in Figure 3.5. The fundamental principle, on which the system is based is that the three phase supply, wind turbine motor/generator and dummy load are all connected in a star configuration. This arrangement allows the supply power always to be positive (i.e. not generating back into the grid or diesel generator) for all wind conditions. When the wind turbine is operating at large output powers the dummy load is adjusted to absorb all of this power and a little more (from the supply). At low wind turbine power outputs, the size of the dummy load can be reduced and even removed completely when the wind turbine is absorbing power. Under all power conditions the wind turbine rotor speed remains nominally constant and allows fixed speed rotor measurements.

Two other systems are contained within the control box. The power measurement system (described in 4.3) and the brake control system. Signals from a pair of micro-switches mounted on the brake actuator convey the brake state to the main control board. If the brake is 'on' the interlock to the star/delta starter prevents the rotor being started. The starter can only be armed when the 'brake off' micro-switch is closed confirming that the pads are well clear of the rotor brake disc. In this way it is impossible to start the rotor with the brake applied.

The brake control board also shuts down the wind turbine if any of the safety trip criteria are met. Comparator circuits continuously monitor the rotor speed, torque and vibration levels. If any of these parameters exceed pre-set limits the control board automatically de-energises the motor and applies the brake. The safety limits set into the system are 800 r.p.m., 350 Nm torque and about 0.4 g accelerations.

3.5 Commissioning

During construction of the wind turbine all of the separate systems were tested as thoroughly as possible in an attempt to reveal any design problems before the machine was in operation. Without blades or the rear shaft fitted the motor was run continuously for several hours to identify any overheating problems and was cycled through hundreds of stop/start operations to test the star/delta and braking systems.

Rotor deceleration rates (with blades fitted) were thought to be too severe so an exhaust reservoir was added to the braking system. This has the same internal volume as the actuator and therefore allows the actuator pressure to halve as soon as the solenoid is de-energised. (At a pressure of approximately 3 bar the pads are just touching the disc). The reservoir bleed causes the brake system pressure to then drop slowly. This arrangement causes the rotor to be quickly but gently braked to a standstill.

The slotted disc speed measurement system was commissioned and tests on the electrical and pneumatic slip rings were carried out. The electrical slip rings were easily tested by simply shorting a pair of channels together on the rotor and examining the effect of the two slip ring interfaces on a d.c. voltage. The noise levels introduced by the slip

rings (when running at 333 r.p.m.) are better than expected at about 6mΩ.

The pneumatic slip ring was also tested to assess its performance. With the rotating tube plugged at its rotor blade end, pressure was applied to the stationary pipe with an air pump and measured with a water manometer. With a pressure of approximately 500mm of water applied, readings were taken every few minutes and these showed that the leakage rate was negligible. This is obviously not a sufficiently adequate test by itself since the slip ring was not rotating. However, repeating the above test with the rotor running yielded less encouraging results, since the pressure readings increased with time indicating heating of the trapped air within the measurement system. Careful consideration of this revealed that it is not as serious a problem as might at first be imagined since when in use the stationary end of the pipe is left open to atmosphere. In this situation, even if heating of the air in the slip ring area occurs, the pressure transmitted to the transducer reference ports is not different from that had no heating occurred. Any local air temperature rise causes a change of air density which will cause a small volume flow of air from the reference pressure pipe. (The testing procedure adopted for the experimental runs minimises the time for which the rotor is running and hence further reduces any air heating effects).

Calibrations for all the fitted measurement systems were performed at this stage and are described in Chapter 6. Amongst the last of the commissioning operations was that of rotor balance.

3.5.1 Rotor balancing

Balancing of the wind turbine main shaft is essential for smooth rotor running. The balancing operations carried out were those of static balance both in the rotor plane and in the drive pulley plane. (see Figure 3.3) These two planes represent the main contributors to the shaft imbalance due to the rotor torque load cell system and any mass distribution differences between one rotor blade and another. Balancing was performed with the main shaft running (usually at 333 r.p.m.) but this does not constitute dynamic balancing since only one plane of the shaft was balanced at a time. Firstly without blades or 'Y' plates fitted to the shaft the main pulley/rotor torque system was balanced using an iterative method until the magnitude of the imbalance was at

the limits of the systems detection. With the rotor blades fitted the rotor plane was then balanced in the same way and to the same degree. It should be noted that each time a different blade was fitted in the rotor (e.g. PIB or FIB) the balancing operation was repeated.

Balancing was simply accomplished using the output of the accelerometer mounted at the rotor shaft front bearing. Its response was amplified, heavily filtered and displayed on an oscilloscope together with the Top Dead Centre rotor pulses. Examination of the responses with various combinations of added test weights enabled the calculation of the required balance weights.

CHAPTER 4

INSTRUMENTATION

4.0 Summary

The choice of experimental parameters to be measured (see Chapter 2) was based on a detailed review of the experimental objectives. The most important measurements are those of local surface pressures on one of the rotor blades. These data should be acquired at a high enough rate to enable unsteady aerodynamic events to be analysed and therefore the pressure transducers used should be fast acting. Earlier work at Cranfield [4.1] had identified the most suitable transducer for wind turbine aerodynamics, although further work is described in Appendices I and II. The transducers and their signal processing requirements are discussed in 4.8.

As an indication of whole rotor response both the rotor torque and yaw torque of the wind turbine were chosen to be measured. Both of these signals are produced using load cells mounted in the respective load paths and are sampled quickly to obtain information on torque variations during a rotor rev. These systems are discussed in 4.4.

An accelerometer mounted at the front rotor bearing and a servo potentiometer measuring yaw position also produce information about the wind turbine rotor response and are described in 4.6 and 4.7 respectively.

Measurements of the inflow to the rotor disc are obviously also very important so that the input - response relationship can be investigated. Detailed wind speed and direction movements are therefore required to complement the detailed blade pressure measurements. The anemometry system used to sample the inflow is described in 4.1.

Measurements of electrical power were made in addition to the direct measurement of rotor torque. With all the instrumentation operational the two data streams could be cross referenced and if one should subsequently fail determination of rotor power would still be possible. These electrical measurements are described in 4.5.

The values of air temperature and barometric pressure at the time of the test are also measured to enable determination of the air density and viscosity. These are described in 4.2 and 4.3 respectively..

4.1 The Anemometry

Assessments of the wind turbine rotor flowfield which may be obtained from the blade mounted pressure transducers are of limited use without a detailed picture of the incoming flowfield. The parameters which are of interest include the wind speed and direction and both spatial and temporal variations of each. Good temporal resolution is achieved by using fast-responding anemometers (short distance constant) and sampling the signal at relatively high frequency (more than 700 Hz). Good spatial resolution of the data at the measurement station is achievable but would imply many anemometers and would therefore be expensive and difficult to implement. The compromise arrangement used is shown in Figure 4.1.

Measurements of both wind speed and direction are made at two locations in the incoming streamtube. Each measurement stream has good temporal resolution since anemometers with a short distance constant are used and some information about the spatial variation of the wind is achieved by using measuring points which are separated by a distance equal to one rotor diameter.

The anemometers chosen for the task are low inertia, unidirectional rotors manufactured by Lowne Instruments. An ordinary cup anemometer and wind vane are also used to give an indication of overall inflow conditions.

4.1.1 The anemometers and windvane

Information on the temporal and spatial variation of the wind is provided by four Lowne anemometers, which were developed by the Ecological Physics Research Group at Cranfield and consist of low inertia horizontal-axis rotors made up of eight mica vanes set at 45° to the plane of rotation. This arrangement allows the rotor to respond quickly to a change in the inflow velocity giving a short aerodynamic distance constant of approximately 300 mm. [4.2]. The rotor is shrouded so that only the component of velocity perpendicular to the plane of rotation is measured. The work described in [4.2] indicates that the

anemometer demonstrates a good cosine response to flow direction. The central hub of the anemometer contains a light emitting diode and sensor arrangement such that a pulse train is produced when the rotor turns. The nominal calibration for the anemometers is one pulse for every 25.0 mm of air flowing through the rotor although a small non-linear correction is also required.

Clearly, a single Lowne anemometer is only capable of measuring one component of wind speed. Hence a pair of anemometers, mounted orthogonally are used to provide data about both the wind speed and its direction in the horizontal plane. Any vertical components of wind speed, however, cannot be measured with this arrangement. Two pairs of anemometers are used in this study in order to give two independent measurements of the horizontal wind vector. The pairs are centred at the edges of the projected wind turbine rotor disc upwind of the turbine.
The cup anemometer and windvane used are capable of providing information about the general inflow conditions. This is useful to know at the time of testing so that data can be collected at a range of windspeeds. It also provides a useful sorting parameter for later data file analysis.

The cup anemometer used was a Vector Instruments A100R with a three cup rotor head. This type of instrument is known as a switching anemometer since it contains a mercury switch which is operated once per rotor head revolution. The aerodynamic calibration for the rotor head is given by the manufacturer as 48.7 r.p.m. per m/s of wind speed and the distance constant is approximately 5 metres. This shows why this type of anemometer is unsuitable for use in place of the Lowne but is adequate for the purpose of general wind speed measurements.

The wind vane used was a Vector Instruments W200P potentiometer type vane. It consists of a circularly wound resistor and a wiper, making electrical contact, which is connected to a vane which accurately aligns itself with the local flow. With 5 volts applied across the resistor the wiper voltage varies linearly with direction. Like the cup anemometer, however, the vane also has a distance constant since a step change in flow direction takes some time to be registered. Its value for the vane used here is approximately 5 m.

The complete inflow measurement station (Figure 4.1) was identical for both the field tests of the partially instrumented rotor (not reported

in this thesis) and the mobile tests of the fully instrumented rotor. The only difference between the two testing configurations was in the distance between the anemometer tower and the wind turbine:- this distance had to be reduced for the mobile testing from approximately three rotor diameters (9.2m) for the field tests, to approximately two diameters (6.3m).

4.1.2 Signal processing

The cup anemometer and the four Lowne anemometers produce pulse train outputs which need to be converted from the frequency domain into analogue voltages for compatibility with the data acquisition system. This process is done, for each of the anemometers, by a 'phase lock loop' integrated circuit which produces a steady analogue voltage for a fixed frequency pulse input.

The phase lock loop circuits used are tuned to accommodate different frequency ranges. For the Lowne anemometers this range is approximately 100-1000 Hz and for the cup anemometer is 2-20 Hz. The circuit is easily calibrated by applying a known frequency square-wave (from a signal generator) and measuring the circuit output voltage. Typical calibrations are shown in Figures 6.1 and 6.2 showing that the circuit response is slightly non-linear. Unfortunately this could not be eradicated necessitating greater effort in the data analysis than had been anticipated. Aliassing problems are avoided since the phase lock loop circuit acts like a low pass filter.

If a step change in frequency occurs the analogue output takes some time to achieve a new steady value which is approached asymptotically. This effect gives rise to another 'distance constant' which is a function of the electronics only. The magnitude of this effect was evaluated using two signal generators to represent the varying output from a single Lowne head. By modulating the output frequency of one signal generator with the output from the second, a third signal is produced which is made up of a square wave whose frequency varies sinusoidally between two extremes. The analogue output from the Lowne circuit was then seen to vary between these limits which fell short of those values which would be obtained under steady inputs of the minimum and maximum frequency. Estimates of this shortfall were made over a range of modulation frequencies and resulted in the data shown in Figure 4.2. The equivalent windspeed rates of change are given for each modulation

frequency (based on the nominal anemometer aerodynamic calibration) and these clearly show that the electronic distance constant is not important for rates of change of windspeed less than 7 m/s^2 where the circuit response is -3dB down.

No signal processing is required for the wind vane since its output (wiper) voltage must be within the 0 - 5 volt range and this is suitable for direct input to the multiplexing and digitising circuitry of the data acquisition system.

4.2 Air Temperature Measurements

Estimates of the ambient air temperature (and pressure) are required in order to determine the air density and viscosity from the ideal gas law [4.3] and Sutherlands law [4.4], given below.

$$\rho = 1.225 * \frac{15.0 + 273.15}{T} * \frac{p}{101330.0}$$

$$\mu = 17.161E\text{-}6 * \frac{T}{273.15} * \frac{(1.0 + 110.4/273.15)}{(1.0 + 110.4/T)}$$

where ρ is density (kg/m^3), p is barometric pressure (Pascals), T is the temperature (°K) and μ is the viscosity (kg/m/s).

Measurements of the air temperature and barometric pressure at the time of each test then allow all of the data to be standardised and compared more easily.

An automatic temperature mesurement system was designed and built to simplify the running of the experiment and to enable consistently reliable results to be obtained. The sensor used by the system is an inexpensive temperature sensitive transistor which was chosen with the aim of measuring the air temperature to within 1 °C. The device is laser calibrated to produce 1 μA per °K and was mounted in a small metal pipe. A cable from the sensor connects the device with a signal processing board mounted in the control box (see 3.4.2).

Measurement of this output voltage was not possible within the main analogue to digital conversion system (see 5.2) since there were no channels available. Consequently the crude analogue-to-digital converters within the BBC micro were used instead. The 8 bit accuracy of this device was improved to 10 bits using an averaging technique. The A-D conversion is performed 64 times and the standard deviation of the resulting average is therefore reduced. Further errors can arise because of the poor stability of the voltage reference used within the BBC micro. This was overcome by taking measurements of three voltages, each 64 times over. The first of them was the local ground voltage, the second was the actual temperature signal itself and the third was a very stable voltage produced by a voltage reference device (giving 1.26860 volts over large temperature ranges). Using the digitised levels given by the 0 V and 1.26860 V signals as a continuously updated calibration of the analogue to digital converter itself, the temperature signal could be digitised with much greater certainty.

The resulting voltage could then be converted into a temperature in °C using a temperature calibration for the circuit. This was obtained by monitoring the ambient temperature with a digital thermocouple thermometer. The calibration results were then used to determine the sensitivity and offset coefficients given in the following equation.

$$\text{Temp } (°C) = (100.36 * \text{Voltage}) - 26.1$$

These coefficients were then incorporated within the data acquisition control software (see 5.4.3) and hence made available the automatic inclusion of ambient air temperature in the saved run data files. Using the calibration information it was estimated that any temperature measurement should be within 0.5°C of the true value.

4.3 Barometric Pressure Measurements

In order to achieve accurate and automatic measurements of the barometric pressure, a proprietary barometer was purchased. The specification for the Druck DPI140 digital barometer quotes accuracies of $\pm$15 Pa on absolute pressure measurements between 80000 and 115000 Pa. This is not quite as accurate as measurements from a typical (new) Fortin barometer which are usually quoted as accurate to $\pm$10 Pa. The Druck device, however, allows automatically acquired measurements to be integrated directly into the data acquisition system via its RS232

serial communication output. With this connected to the BBC micro computer which controls data acquisition a measurement of barometric pressure is provided by the digital barometer every 0.4 seconds and can be automatically saved in the run data files.

4.4 The Load Cells

The instrumentation includes two load cells for the measurement of rotor torque and yaw torque. Both these cells are Maywood Instruments U-4000 series 'Z' section devices and comprise a strain-gauged load-carrying element fitted with temperature compensation. Both load cells are capable of taking tensile and compressive loads and are used in a similar manner so that the required torques are registered.

4.4.1 Rotor torque load cell

The maximum rotor torque expected is 350Nm so a load cell with a 250kgf full scale load was chosen (the mounting radius is 0.1494m). The cell has a '1.5 times rated' overload capacity (without damage) allowing transient torques as high as 550Nm. (The most important of these transients for consideration is the rotor starting torque, which, with a star/delta starter fitted to the motor, is less than 180Nm.) The load cell mounted in position can be seen in Figure 4.3 . The rotor shaft pulley is not keyed onto the shaft but is mounted on a pair of bearings which potentially allow it to rotate freely. The load cell, however, mounted between a pulley spoke and the driving arm (which is keyed onto the rotor shaft) prevents this rotation and consequently all the shaft torque is transmitted through it (ignoring the friction load of the pulley on the shaft). This is the case whether the shaft torque is positive or negative, i.e. the motor under generator or motor action. The load cell is held in the load path by rose bearings, one fitted at each end, and ensuring only axial loads are transmitted. This does allow the load cell to rotate slightly about the load path axis so this movement is prevented by small aluminium fingers lightly resting on the load cell body. The power supply/signal cable from the cell passes straight into a small hole in the main shaft and into the signal processing package at the rear of the machine.

4.4.2 Yaw torque load cell

Yaw torque is measured using the same principle for measurement of rotor torque. An assessment of the maximum yaw torque expected was very much more difficult to perform than for the rotor torque system. Consequently a review of previous experimental yaw torque measurements was undertaken [4.5], [4.6] and [1.13]. After extracting the relevant information from each of these reports the maximum value of the non-dimensional yaw moment coefficient (usually referred to as C_x) was calculated and then applied to the Cranfield rotor. This produced a range of estimates of maximum yaw torque between 182Nm (C_x max = 0.10, [4.5]) and 330Nm (C_x max = 0.18, [4.6]) both calculated for a windspeed of 25m/s. The work of Anderson et al [1.13] gave a maximum torque of 218Nm under the same conditions, from experimental work on a 3m diameter rotor and was therefore assumed to be more representative of the Cranfield machine. The chosen load cell has a 100kgf full scale rating giving a maximum yaw torque capability of 113Nm (operating at a 0.115m radius). The overload capability of 1.5 times rated will allow torques up to 170Nm to be recorded without permanent damage to the cell.

4.4.3 Signal processing

The load cells are both powered by a 10 V dc source which is synthesised in the wind turbine and is referenced to the 3 V pressure transducer excitation voltage for a high degree of voltage stability. The load cell sensitivity is quoted at nominally 27 mV output at full rated load with linearity and hysteresis errors of 0.03% full scale output. The low level outputs are each fed into a high precision instrumentation amplifier where the gains of each channel are chosen so that the output voltage is between +5.0 and -5.0V for the range of expected input torques. This relationship is slightly confused by the interposition of the data transmission system which has its own gain of 2 and provision for offsetting the transmitted voltage by up to -2.5 Volts. This offset is set to zero for the yaw torque signal because the parameter should vary equally about zero Nm. The rotor torque offset, however is set to -2.5 Volts since positive rotor torques (generator action) are greater than negative ones. (The maximum negative rotor torque of interest is that produced by the wind turbine in 0 m/s winds.) These offsets can be seen in the calibration plots given in Figures 6.4 and 6.5. The calibrations were obtained by digitising the signals produced under

application of a known torque (introduced by means of a torque arm with various masses hung onto it).

Anti-aliassing filters are not used in the signal processing of either of the torque signals. This is no doubt acceptable for the yaw torque which should contain little energy at frequencies above the low harmonics of the rotor (i.e. 1p, 3p or at the most 11, 33 Hz). Since the torque signals are sampled at between 700 and 1400 Hz only frequencies above 350 Hz could be aliassed. For the rotor torque signal, however, the maximum frequency which could be expected to be present in the signal is that associated with the belt teeth (800 to 1600 Hz). Careful examination of the rotor torque signal on an oscilloscope indicated that 100 Hz (twice the frequency of motor excitation) appeared to be by far the highest component in the signal and consequently aliassing problems were not expected.

4.5 The Power Measurements

The wind turbine motor/control system was described in 3.4.2 and can be seen in Figure 3.4. Electrical power measurements were thought necessary in addition to the mechanical power measurements (rotor torque) for many reasons. Firstly , the use of two independent methods for determining the rotor power was thought to be sensible because the measurand is so important and the in-built redundancy in the data acquisition system would help to ensure that an accurate assessment of rotor power was always available. In addition the relationship between the electrical power and the mechanical power is nonetheless important. Variations of an induction machine's efficiency with speed mean a small increase in mechanical power could produce large increases in electrical power. This is especially important for this system where the motor/generator must sustain electrical powers greater than its rated value for short periods of time. Hence measurement of at least the motor electrical power was deemed to be necessary for wind turbine control purposes.

Due to the star electrical configuration used (Figure 3.4) measurements of power must be taken in two 'arms' of the star to completely determine the electrical status of the system. The difference between the power measurements made in the grid (or diesel generator) supply arm and the wind turbine arm would clearly represent the power in the dummy load. It was decided at an early stage in the system design that measurements in only one phase would be sufficient since electrical balance should be

maintained under all circumstances. Consequently there are two points in the system where the electrical power needs to be measured. Typical phasor diagrams at these points are shown in Figure 4.3 and indicate the relationship between the real, reactive and apparent powers in each of the star branches. Only two of these need be evaluated to completely specify the electrical condition. Since the real power is perhaps the most important parameter as far as the wind turbine is concerned this was chosen as one of the measurements. The apparent power was chosen as the other measured parameter since it is the next easiest to determine.

4.5.1 Signal processing

At each of the measurement points one of the phase conductors is wound in a single loop through a toroidal current transformer. (As can be seen in Figure 3.4 the complete measurement system is electrically isolated from the actual measurement points for safety reasons.) The induced currents in the transformer are electronically conditioned into an a.c. voltage, Vi, which is proportional to the current flowing in the phase conductor and is also exactly in phase with it. A second transformer, this time wired across a pair of phases is used to produce a small a.c. voltage proportional to the line voltage (i.e. the voltage difference between the phases). This signal, known as Vv, is scaled to be approximately +4.15 V a.c. (r.m.s.) for a line voltage of 415 V (r.m.s.). This voltage measurement is only necessary at one of the measurement points since it will be nominally the same at all points in the star system. The two a.c. voltages, Vv and Vi, are then fed into an electronic circuit which contains a 'multiplier'. This device forms the dot product of the voltage and current vectors (Vv and Vi) and consequently produces a d.c. output voltage proportional to real power (i.e. the in phase components of the line voltage and line current). This d.c. analogue voltage is fed directly to the analogue-to-digital converter so that , once calibrated, the real power at the measurement point is known.

The two a.c. voltages, Vv and Vi, are also used to determine the apparent power. Each of them also passes through a rectifier circuit to produce a d.c. voltage proportional to its a.c. counterpart. These are both then fed to the analogue-to-digital converter system so that at each measurement point the r.m.s. current and line voltage can be determined. The apparent power is found as the product of these two

parameters since the total current has been measured, and no account of its phase relationship with the voltage has been made.

Using these five measurements (two of real power, two of r.m.s. current and only one of r.m.s. line voltage) the complete phasor diagram can be identified for two points in the star system. The difference between the two diagrams represents the power in the dummy load. Since the power in the dummy load is certain to be entirely real with no reactive component a useful check on the accuracy of the measurements is possible - the reactive power calculated at each of the measurement points should be the same.

4.6 The Accelerometer

A piezo accelerometer is mounted in the front section of the wind turbine. It is sensitive to accelerations in one axis only and its output signal is used for both control of the wind turbine (emergency shutdown due to excessive imbalance in the rotor) and for monitoring the turbine body accelerations during data acquisition (especially important during mobile testing). Unfortunately, these two requirements impose conflicting requirements for the disposition of the sensitive axis (at right angles to the rotor axis in the former case and aligned with the rotor axis in the latter). During early mobile testing it was decided to adopt the more cautious approach and monitor the rotor balance. This configuration would allow trailer roll and wind turbine yaw accelerations to be monitored but would not determine trailer pitching motions.

A third application for the device was during initial rotor balancing. Whenever the turbine rotor blades were removed and replaced the accelerometer was used, together with the slotted disk signal, to accurately balance the rotor.

4.7 The Body Angle Sensor

A servo potentiometer with the capacity for unlimited rotation was mounted beneath the yaw bearing of the wind turbine, on the yawing axis. Its spindle was connected to the tower frame of reference via a flexible coupling to account for any eccentricity. The potentiometer was excited with +5 and 0 Volts and the wiper signal sent to the data-acquisition system.

4.8 The Pressure Transducers

Previous work carried out by Oram [4.1] used pressure transducers to measure the unsteady aerodynamic behaviour of a 6m vertical-axis wind turbine. Several different types of transducer were extensively tested to determine their suitability for the task. Both absolute and differential sensors were studied and the effects of temperature and strain were investigated. The Sensym SPX50D differential transducer was chosen because of its insensitivity to strain effects and its repeatable pressure and temperature characteristics. The device is very bulky when compared with its miniaturised competitors. Because of this and the lack of any attempt at temperature compensation the transducers are very cheap, costing about £10 each.

Problems encountered with the SPX50D in Oram's work were examined to determine whether they could be overcome more easily in the context of this work. Two such problems were identified. Firstly, the metal/plastic housing of the transducer did not allow simple connection of the required pressure ducts, the problem being overcome in the earlier work by using custom made fittings held on to the transducer ports by sponge tape. The introduction of a new 'easy-connect' package for the whole SPX range meant that the leakage problems of the earlier work could be avoided. The new SPX50DN actually contains an (old) SPX50D but housed in a plastic package providing a pair of connection pipes suitable for plastic tubing. The tests described in Appendix I determined that the newly packaged transducer performed as well as the old one.

The second problem noted was that of the low resonant frequency of the transducer/duct system. Due to the higher rotational speed of a 3m diameter HAWT this problem has greater consequences for this work than in that for the VAWT. Work carried out to improve this is described in Appendix II.

4.8.1 The Sensym SPX50DN

With regard to the work described above, the SPX50DN differential pressure transducer manufactured by SENSYM was chosen for this experiment. This type of transducer is a piezo-resistive device which senses fluid pressure by the deflection of a silicon diaphragm. Resistors etched in the diaphragm are connected to form a full four arm bridge so that when the transducer is powered up it transforms the

diaphragm shear stresses due to pressure into an electrical output. The four arm resistances are not usually identical, either in absolute value or in temperature coefficient. The former results in a significant zero pressure offset (an electrical output for zero applied pressure) and the latter causes a shift of this offset with changes of temperature. The sensitivity of the transducer is nominally 1.2 mV/kPa although another inherent temperature effect causes a 0.23 % reduction of this value for each °C increase in temperature.

Clearly with such a device, temperature compensation is essential to measure pressures with sufficient confidence. The work of Oram showed that this compensation could successfully be carried out in the data analysis software at the calibration stage rather than electronically in the hardware, as is more customary. This is achieved by monitoring the transducer 'temperature' as well as its pressure output so that the correct zero pressure offset and sensitivity can be chosen for the device at the time of calibration. This technique has also been adopted for this work.

4.8.2 Signal processing

The pressure transducer signal processing circuit used in this work is very different to that used by Oram [4.1]. It was designed by Mr. B.R. Moffitt of the Electronics group within the School of Mechanical Engineering at Cranfield, so that the circuit could more easily deal with the large zero pressure offsets which are characteristic of this type of pressure transducer. The circuit associated with just one transducer is shown in Figure 4.4 and shows that two output signals are produced. The first of these outputs, V_o, is an analogue d.c. voltage which varies with the applied differential pressure, Δp. The second, V_i, is a function of the current drawn by the transducer and therefore correlates well with its ambient temperature.

The pressure transducer, shown on the left of Figure 4.4, is excited by $\pm$3.0 V stabilised power supply rails. No 'bus bars' were used in this work so four conductors were required between each transducer and its signal processing. The transducer output pair, which (for no applied Δp) would typically carry a 12 mV zero pressure offset signal, was connected directly into a very high accuracy instrumentation amplifier (Burr Brown INA104). The gain applied to the incoming signal is determined by the value of the resistor R_g according to the equation;-

$$\text{Gain} = 1 + (40000/R_g) \qquad (R_g \text{ in } \Omega)$$

Consequently for a gain of 501 (typical), a high stability 80 ohm resistor would be used, its 15 p.p.m./°C temperature coefficient ensuring that the gain changes negligibly even over a wide range of operating temperatures. If no account were taken of the offset, the amplifier output would be a voltage of about 6.0 V (assuming the typical 12 mV transducer zero pressure offset) and would therefore be outside the ±5.0 V analogue-to-digital conversion range. The other discrete components associated with the INA104 are provided to shift the output voltage by +5.0 to -7.0 Volts so that the 6.0 V zero pressure output could be offset to lie anywhere in the range -1.0 to +11.0 V. This facility allowed much higher gains than would otherwise have been possible and enabled each channel to be adjusted to suit the individual characteristics of its pressure transducer.

In the example discussed above the output would most likely be set to -1.0 V (using -7.0 Volts of offset) and this would be the single-ended signal which would reach the SHC5320 Sample/Hold chip. This chip, as its name suggest, operates in one of two modes. In sample (or track) mode the chip is 'invisible' to the signal with the input signal simply reproduced at the output. The 'hold' mode causes the output to be disconnected from the input and held at the last value of the input for a certain time. In this mode the input signal can vary wildly and yet have no effect on the output signal which has been 'stored' in both internal and external capacitors. The output voltage does decay, however, due to discharge of the capacitors although the 'droop' rate is very small if the held signal is examined relatively quickly. The 'track/hold' bus, which the chip also has access to, determines which of the two modes the chip will be in at any time. The use of such a device enables many channels of data to be 'frozen' at the same instant and then allows a short time for each of the channels to be digitised in turn. With forty pressure transducer channels this results in a 'snapshot' of the pressure distributions and avoids any time-skew errors due to the finite time required for analogue to digital conversions. The output of the sample/hold chip is sent to the multiplexer chips which are described in 5.1.

The second data stream to be produced by the transducer is the 'temperature' signal derived from the current drawn by the device. As the temperature increases the SPX50DN bridge resistance also increases

and so more current is demanded. This is sensed by a second instrumentation amplifier (OP07) which has to supply the current and so produces an output which varies with transducer temperature. The gain of this signal is determined by the value of the resistor R_t (see Figure 4.4) for which a value of 3000 Ω was found most suitable. This gives a downward shift of about 0.7 V in the output for a 30°C rise in temperature. The room temperature output level is set by the relative values of the offset setting resistor R_a and the bridge resistance R_b and can be found from the following equation:-

$$V_i = \frac{+3.0*R_t}{R_b} + \frac{-3.0*R_t}{R_a}$$

where R_t is 3000 Ω for all channels. The value of R_a is matched closely to that of R_b so that the room temperature value of V_i is about 0 Volts. Highly temperature stable resistors (15 p.p.m./°C) are used for R_a and R_t so that V_i is not susceptible to drift due to temperature changes in the circuitry.

With approximately 0.023 V/°C sensitivity the V_i signal is capable of determining the temperature to within 0.1°C (the 12 bit resolution of the analogue-to-digital converter is 0.0024 V). This, however, is not the aim of this signal; more important is the fact that the zero pressure offset and sensitivity of the pressure transducer may vary by up to 0.0105 V/°C and 0.002 V/°C respectively (based on a nominal gain of 700 and the pressure transducer specification). Consequently, these parameters may be specified sufficiently accurately with the above sensitivity of the V_i signal to temperature.

4.9 Instrumented Blades

The instrumented blades used for the rotor were based upon standard 1.42m Marlec blades. Three non-instrumented blades were used for the initial wind turbine tests and it is helpful to describe the production processes involved in producing these standard blades in order to understand the manufacture of the instrumented blades. Refer to Figure 4.6 throughout.

4.9.1 Marlec blade manufacture

Firstly, a foam core former is fabricated in a purpose built mould. The mould is split into two halves, in approximately the core's spanwise chordal plane. Both mould sections are carefully polished to aid later removal of the finished core and are bolted together. A marine plywood root block is placed into the root section of the mould and finally the end cover is bolted in place. This completely seals the mould with the exception of an injection hole near the blade core tip. The polyurethane foam is injected by a special machine which mixes two liquid chemicals just before being squirted into the mould. The reaction between the two components in the presence of a catalyst produces Freon which causes a great increase in volume to completely fill the mould with foam. The injection hole is plugged and the mould allowed to stand for 35 minutes to cure completely. After this time the core, complete with its now integral plywood root block is removed from the mould and cleaned of any flashing. The foam core is then placed in a drilling jig which allows accurate drilling of the five blade root mounting holes. These then have split metal inserts pressed in which provide for load transfer between the blade and its mounting via 1/2" bolts.

The core is now ready for laying up with glass fibre which will provide the finished blade with all of its strength. Uni-directional glass-fibre strips, 35 mm wide, are laid into the recesses in the foam core, starting at the root recess, passing completely around the root block and finishing at the root recess on the other blade surface. Ten strips are used in double thicknesses forming five overlapping bundles. The strips are usually stapled in place and the procedure is repeated with longer strips of glass from the next two sets of recesses (using only single thicknesses) producing a lay-up which increases greatly in strength towards the root. To give the blade overall strength a glass-fibre matting 'sock' is made to completely enclose the blade. Two types of glass are used, one being a 2 by 45° woven mat and the other a random network of very fine glass used to give a fine surface finish. This combination is laid around the leading edge of the foam core and over both upper and lower blade surfaces. The two thicknesses at the trailing edge are then sown together as close to the foam core as possible and the rest of the glass is trimmed away. The blade is now ready for the final stage of production - that of polyester resin injection. A second set of moulds which have the aerodynamic shape required for the blade are used for this process. Again the mould is

split along the blade spanwise chordal plane forming two mould halves. These are each finely polished and then bolted securely together (sandwiching a small bead of silicon rubber which helps to prevent resin leakage). The blade foam core/glass-fibre construction is then pushed firmly into the mould leaving the open ended glass fibre sock protruding. This is carefully trimmed and folded onto the butt end of the root block and stapled in position. A pair of steel pins are then hammered through holes in the mould positioned to coincide with a pair of blade bolt holes - this helps to centralise the foam core exactly within the mould. Once the mould end plate is bolted on (again with a silicone rubber gasket) the blade is ready for injecting.

The polyester used for the blade is a mixture of two resins producing a blade with the correct combination of properties. A 5:1 mix of hard and flexible resins are pre-mixed in the injection machine. A catalyst is swirled into the resins just as they are injected through the hole in the end plate of the mould. Fifteen 'shots' of resin are injected at about one minute intervals. After the 13th or 14th, resin is seen to ooze from a vent hole at the tip of the blade. When this appears to be free of air bubbles this hole is plugged and a final shot injected. The injection hole is then also quickly plugged and the resin left to cure. This takes about 3-4 hours and produces quite a lot of heat due to the exothermic polymer reaction. After curing the mould is unbolted and the blade is removed. Again, due to the ill-fitting mould halves there is a small thickness of flash all the way around the blade which is removed with a file. Once the three resin filled bolt holes in the root have been drilled out the blade is finished.

The Marlec blades made in this way are very cheap to manufacture (with mass produced versions expected to cost about £10 each) and they are perfectly adequate for their intended purpose. A wind turbine rotor made up of three of these blades is capable of producing 1kW (the rated power), running at several hundred r.p.m. and able to withstand windspeeds in excess of 25m/s. Hence, from the manufacturer's point of view they are a satisfactory solution to the blade problem. However, for the purposes of this experiment the finished blades have one major shortcoming. Surveys of the blade profiles show that the aerodynamic sections deviate from the NACA 4415 profiles which were intended and also that the sections vary slightly from blade to blade (see 4.9.4). This is due to small deformations of the glass reinforced polyester moulds which were produced for blade development only. The production

moulds will be of aluminium and will therefore improve both the accuracy of the aerofoil sections and the blade-to-blade disparities. Unfortunately the aluminium moulds were not available for this work.

4.9.2 Partially and Fully Instrumented Blades (PIB and FIB)

During the initial design stage of the instrumented blade it became clear that there were many unanswered questions concerning the construction techniques. The approach was definitely to be one of a 'sealed for life' blade in which the instrumentation was built in during blade fabrication and could only then be accessed by destroying the blade. Due to the finality of this method and the uncertainty regarding the constructional details it was thought prudent to split the problem into two stages, the first attempt being to construct a partially instrumented blade (PIB) with only eight pressure transducers installed. This would be followed by a fully instrumented blade (FIB) with the full complement of 40 transducers fitted. Eight transducers were chosen for the PIB because this represents the number whose signals can be processed on a single board (as described in 5.1).

The choice of spanwise location for the pressure transducer tappings and the number of tappings per location for the PIB was a difficult one. The concepts of steady stall and radial flow lead to the biasing of the chosen sections towards the root of the blade. On the other hand a 'control section' further outboard was also thought to be important and resulted in the selection of 75% span. This location is close to the point of maximum circulation along the blade and remote from the tip effects felt further outboard. The inboard sections were chosen as 25%, 35% and 45% span. The position of the wind turbine fairing at about 40% span, suggested that the local flow may be corrupted so the chosen sections were intended to straddle any such effects. At all of these four stations two transducers were chosen as the minimum which could produce some useful information about the local flow. The most obvious characteristic of pressure distributions around an aerofoil at incidence is the suction peak and the effects of steady and dynamic stall can be expected to modify its size and shape. Hence, in an attempt to obtain a qualitative feel for suction peak variation the two transducers per spanwise station were positioned at approximately 1% and 20% chord on the suction surface of the blade. The eight locations can be seen in Figure 4.7.

4.9.3 PIB Design and Construction

There was no doubt, during the PIB design phase, that the pressure transducer system had to be built into the blade during the normal 'Marlec' blade construction process. Retrospective fitting of the instrumentation into a finished blade was rendered unworkable due to the structural integrity of the resulting blade. It became clear that the pressure transducers would have to be fitted in the non-load- carrying foam core. Assuming this to be possible the next problem encountered would be the provision of the necessary 'plumbing' allowing the transducer to communicate with both the blade surface pressure and the required reference pressure. These problems were solved in the fashion illustrated in Figure 4.6. Each transducer was connected to the reference pressure system via silicon rubber tubing and also to a green nylon pipe with a blanked off end. This pipe had been manufactured from solid nylon cylinder, 3mm in diameter and 12 mm in length (in fact, previously a child's knitting needle). A 1 mm hole was drilled axially along a 10 mm length of rod leaving one open and one closed end. The open end was then connected to the active side of the pressure transducer, again by a short length (50 mm) of silicon rubber tubing. The reference pressure system, which branches to connect with the reference port of every transducer, ends in one or two pipes which are brought to the blade root. These allow the reference pressure (and calibration pressures) to be applied to every transducer via the gas slip ring and the reference pressure manifold within the blade. The manifold includes extra pipe connections to provide some redundancy in case pipe blockages occur. The blade root reference pipes are plugged at their ends during the foam and resin injection processes. The net result is a completely sealed system which is resistant to the ingress of foam or resin during later stages of blade production. All electrical connections (4 per transducer) are brought to the blade root where there is a connecting pin array.

Fitting the entire pressure transducer system into a completed foam core proved impossible because the foam material could not be machined without it crumbling. For this reason it was decided to install the system into the foam core mould and inject the core around it. In order to position the pressure tappings accurately, balsa wood profiles of the foam core section at the required station were made and the green nylon tubes were mounted on this.

The resulting structure (comprising of balsa wood sections, pressure transducers, green tapping positions, many lengths of silicon rubber connecting pipe, electrical connections and the root block with connecting pins) was laid into one half of the foam core mould and the mould sealed around it. The foam core was then injected and resulted in the entire pressure transducer system being 'sealed for life'. The core was then treated like any other with the glass fibre layers being added and the resin being injected in the blade shape mould. The only difference for the instrumented blades was in the use of un-pigmented resin which resulted in the glass fibre and resin curing to a completely transparent layer.

The final stage in producing an instrumented blade was the drilling of the tappings. With the blade mounted on a milling machine table a 1 mm diameter hole was drilled in such a way as to penetrate into the centre of the green nylon tubes (which were clearly visible within the blade) and also to be normal to the local blade surface. This was achieved by carefully adjusting the position of the blade for each drilling operation and resulted in all eight tappings succesfully being produced. Great care was taken to avoid swarf material from dropping back into the tapping and thereby preventing the transducer from registering the true blade surface pressure. Also, in order to monitor the success or failure of the drilling operation each transducer was powered up and its output monitored on a voltmeter. Due to the initially trapped air being heated by the transducer and raising the pressure the initial transducer output was high. At the moment of successfull penetration into the nylon tube this pressure was released and the transducer output would be seen to drop. From this point a further 1 mm of depth would be drilled to completely rupture the tube side wall and the tapping operation would have been a success.

4.9.4 FIB design and construction

Many lessons were learnt from the manufacture of the partially instrumented blade and the cautious, two-stage approach was thought to have been justified. The construction techniques used for the FIB were, on the whole identical except in as much as the increased scale (going from eight to forty transducers). Unfortunately insufficient data analysis of PIB results had been carried out by the time the FIB construction had to commence. Consequently, in the absence of any further information, the chosen fully instrumented stations were at 35%

and 75% span and were each composed of 19 tappings. (12 on the suction surface and 7 on the pressure surface). The remaining two tappings were put at the 1% suction surface chord locations of the 25% and 45% spanwise stations. It was felt that this may provide some useful comparisons with the PIB data. The forty locations can be seen in Figure 4.7 which also shows how the tapping locations are arranged at the two fully instrumented stations. The locations were carefully chosen to achieve the best chance of registering the pertinent pressure distribution features of the NACA 4415. Typical Cp distributions were studied [4.7] and the tappings distributed accordingly (loosely based on a linear spread over the $(x/c)^2$ function.) Precise determination of the location requirements (i.e. to better than 1% chord) were not thought necessary because of the uncertainty introduced by the manufacturing process. After manufacture, however, the positions of the finished tappings were measured, along with the blade geometric profiles at the instrumented stations.

The forty transducers were built onto a balsa wood frame in the same way as for the PIB. The completed structure took several weeks to build and can be seen in Plate. 1. The foam injection and final resin injection stages of blade manufacture were then carried out and resulted in the succesful fabrication of the blade structure.

Before the tappings were drilled the blade profile was checked using specially manufactured profile templates cut from 16 s.w.g. steel and hand finished to the NACA 4415 shape. The correspondance between the templates and the blade at both the fully instrumented stations were poor with the blade being too fat. This was attributed to the fact that the moulds used during blade manufacture had been deteriorating in strength with each blade produced due to the high pressures involved. This led to bulging of the mould and to an oversize blade despite the preventative measures taken (in the form of an outer restraining steel frame).

To overcome the problem, the surface of the finished blade was scraped down to approach a true NACA 44XX shape. New templates were made for a 15.5% thick aerofoil shape at the 35% station and a 16.5% thick at the 75% station. The change in thickness to chord ratio was required in order not to remove too much of the load carrying parts of the blade and resulted in the use of slightly unconventional blade profiles. The final results are given in Table 4.1 and can be seen in Figure 4.8. This

shows the measured profiles at the 35% and 75% span locations (after the tappings were drilled) compared to the true NACA profiles.

The tappings were drilled in the same way as for the PIB with each tapping perpendicular to the local blade surface and directed at the centre of the visible green nylon tubes. Every tapping was a success except for one. The unsuccesful location was that near to the trailing edge at the 35% span suction surface (see Table 4.1). This pressure transducer therefore has its sensing port registering air trapped in the duct whilst its other port correctly sees the calibration/ reference pressure. It can therefore be used to monitor some fluctuations in the reference pressure system and consequently is known as PREF (see Figure 4.5).

CHAPTER 5

DATA ACQUISITION AND TRANSFER

5.0 Summary

The data acquisition system which brings together the information from all of the transducers is described here and can be seen in Figures 5.1 and 5.2. Two types of data stream can be identified - those which are derived on the rotor and those derived off the rotor. Section 5.1 deals with the former which includes all of the blade mounted pressure transducers and also the rotor torque signal. The remaining (off rotor) signals include the anemometry channels, the electrical measurements and the yaw/acceleration measurements. These are all processed (and multiplexed) in a purpose built piece of hardware known as 'BOB' (Board 0 Box). The five boards in BOB each perform a separate task and are described in 5.2.

At the heart of the data acquisition system lies the Cambridge Electronic Design 1401 which performs the essential task of analogue-to-digital (A-D) conversion. Specially written machine code controls the A-D conversion process and allows the acquisition and storage of one million samples in under 20 seconds. The wind turbine experiment application of the CED 1401 is described in 5.3.

A BBC micro-computer is used to control the data acquisition performed by the CED 1401. To do this a considerable amount of software has been written to provide easy data acquisition (both run and calibration data) and hardware system debugging. These BBC micro programs are described in 5.4.

5.1 The "On Rotor" Data Streams

The signal processing electronics required for each pressure transducer is shown in Figure 4.4 and has been discussed in 4.4.2. The SPX50DN pressure transducer is shown on the left and is excited by $\pm$3.0 V stabilised power supply rails. As discussed previously two output signals are produced by each transducer. A pressure output (V_o) and a 'temperature' output (V_i) which is derived by monitoring the current drawn by the device. The circuit was constructed, tested and found to

behave satisfactorily when connected to a dummy bridge. A suitable printed circuit board layout was arranged and a single prototype signal processing channel was again tested using a dummy bridge. Once the layout had been refined the circuit layout shown in Figure 5.3 was designed and five of these boards were manufactured. Known as Boards 1, 2, 3, 4 and 5 they are mounted on the wind turbine rotor each having the capability of processing and multiplexing the output signals from eight transducers.

All five boards are mounted radially in the wind turbine instrumentation package which rotates with the rotor. Connection to the in-blade pressure transducers is achieved via eight cables per board which emerge from the hollow main shaft and are fitted with 'Lemo' connectors. These plug into the board mounted sockets (allowing easy transducer/channel swapping) and are retained mechanically to avoid working loose under the rotational and vibrational loadings. The Lemo connectors used are very high quality with large surface area gold plated electrical interfaces and hence should not prove problematic under the conditions of use.

For each board, the eight pressure signals and eight temperature signals are routed from the channels to the multiplexer chip at one end of the board. This chip is fitted after all of the signals have been checked and any erroneous ones corrected. (Problems have been found due to 'dry joints'). The chips are expensive to replace and easily ruined by over-voltage conditions.

One corner of the board is devoted to power supply conditioning where a carefully designed circuit ensures very little drift of the rail voltages and consequently repeatable results. Each board also has a 25 pin Canon 'D' connector 'hard wired' to it. This connects with a socket in the rear bulkhead of the instrumentation package to allow power supply rails, multiplexed data, multiplexer address and track/hold signal lines to pass on/off the board. The bulkhead mounted sockets are all interconnected by a loom on the outside of the instrumentation package which relays all these signals to the end mounted electrical slip ring so that connections off the rotor are achieved.

5.1.1 Transducer gain selection

The amplification factor (gain) of each of the pressure signals is set by the value of the gain setting resistor, R_g (see 4.4.2). The value of

gain required for each channel was obviously dependent upon the location of that particular pressure transducer tapping (e.g. was it sensing the suction peak or the pressure surface trailing edge) and also upon the characteristics of the transducer (its zero pressure offset and sensitivity). A comprehensive method for the choice of gain was developed and is described below.

An experiment to evaluate the approximate sensitivity of each transducer was carried out using a 3 V power supply, voltmeter, manometer and air pump. An amplifier was also used to increase the size of the measured signals but was not fitted with offset facilities. For each transducer in turn, both the zero pressure output voltage and the output under approximately 500 mm water pressure were noted. Both these results were then corrected to remove effects of amplifier gain and produced 'raw' values of transducer zero pressure offset (in mV) and sensitivity (mV/Pa) (see Table 5.1). The next problem was that of deciding which transducers would behave best in the signal processing system and which worst. To obtain a suitable ranking it was not sensible to simply rank them based on sensitivity alone since the effects of zero pressure offset would then be ignored. This is important because the maximum gain which could be accommodated for a given transducer (which would determine the final sensitivity) would be influenced by the zero pressure output which is also amplified and varies considerably from transducer to transducer. The system by which the sensors were ranked is shown in Table 5.2 which is the output from a suitable spreadsheet package. For each of the labelled transducers the zero pressure offset and sensitivity were entered from the results of the experiment described above. The 'Max gain - no room' column is then calculated as the value of gain required to amplify the zero pressure output alone to the full scale 10 volt level. This entry shows that higher gains are possible for sensors exhibiting smaller zero pressure offsets. The total sensitivity column is than found from the product of the maximum allowable gain and the transducers inherent sensitivity. This yields a value (in V/Pa) which does account for the variability of both zero pressure offset and sensitivity and enables them to be ranked more sensibly.

The next problem (encountered during FIB construction) was that of how to use this ranking system to allocate each transducer to a particular blade tapping location. A policy was adopted by which the most sensitive transducer would be used in the position where the pressure measurement

would be smallest. This meant that the expected values of pressure at the forty chosen tapping locations (see 4.5.4) would also need to be ranked so that a 'one for one' relationship between tapping and transducer could be identified. A typical pressure distribution for the NACA 4415 aerofoil was obtained [4.7] and allowed an approximate range of pressure coefficient (Cp) values to be allocated to each tapping location based on its chordwise position. For a given rotational speed (chosen as 458 r.p.m.) the dynamic head appropriate to each of the spanwise stations then allowed the Cp values to be converted into true pressures (in Pascals). Once these expected pressure ranges were ranked the two lists were matched and transducers allocated to each tapping.

The choice of gain for each pressure transducer channel was then made possible using the layout seen in Table 5.3. The spreadsheet system used was found to be ideal for this process due to the ease with which various combinations of parameters could be investigated. For the 3S00 tapping shown in the example the expected maximum and minimum pressures and pressure range were entered as determined from above. The sensitivity required from the signal processing system was then determined as that which would produce a 9 V output for the expected pressure range. Given the actual transducer sensitivity, the gain required was found, but in most cases this value was not achievable. This is due to the size of the output voltage produced by just the zero pressure offset, even with the maximum amount of output 'back-off' (-7V). An initial guess at the value of the gain resistor would then produce estimates of the output (with full back-off) and could be adjusted until a suitable value of around 0 to 2 volts was achieved. The back-off chosen could then be adjusted and would sometimes allow further increases in gain. For the finally determined values of back-off and gain resistor the output voltages at both the maximum and minimum pressures are given together with that for zero pressure differential.

A similar decision was required regarding the temperature signal gain from each transducer. This was also set by a resistor (3KΩ for all channels) which gave a downward shift of approximately 0.7 V in the temperature output for a 30°C rise in temperature. The 'room' temperature output of each channel was set by the value of the offset setting resistor (R_a in Figure 4.4) which was individually chosen for each transducer. The choice was very much easier to make than for the pressure signal (above) and was simply a value of nominally the same or lower resistance than the pressure transducer bridge resistance

(measured between the +3 V and 0 V pins). This meant that the room temperature output for all channels usually lay in the range 0 to +1 V allowing easy and quick signal checks.

5.1.2 Setting up of boards 1 to 5

Boards 1 to 5 (which rotate on the wind turbine) each process the pressure and temperature signals from eight transducers so that in total forty sensors can be monitored at a time. Each channel/transducer pair was connected using the Lemo plug and socket system and 'set up' for the individual characteristics of that transducer. This consisted of adjusting the zero pressure offset to the value given by the gain choice spreadsheet (see Table 5.3) and installing the appropriate gain resistor. After all channels has been debugged, checks could be made on every channel using the 'QLOOK' program (described in 5.4.1), typical results from which are shown in Figure 5.4.

5.1.3 The rotor torque

This signal is also produced on the rotor and its amplification is therefore carried out in the rotating signal processing package with that of the pressure transducers. This avoids transferring a low level signal across the slip ring. As described in 4.2.1 the load cell mounted in the rotor drive produces an output ($\pm$27 mV full scale) which is proportional to rotor torque. This signal is amplified using an INA104 instrumentation amplifier as used for the pressure transducers but without the provision for offset adjustment. A gain resistor of 169Ω is used so that the final gain is 238 and the full scale output is approximately $\pm$6.4 V. The zero torque output voltage on the rotor is nominally 0 V but after data transmission (which involves a gain of 2) and the data receiving offset (set to -2.5 V) the zero torque voltage seen at the CED 1401 is -2.5 Volts. Consequently 365 Nm of driving torque and 123 Nm of braking torque can be measured. The components required for this channel are mounted on a small board which in turn is mounted onto a steel chassis plate. This plate has the same dimensions as boards 1 to 5 and is mounted as the sixth board in the rotating package. Room for any future on-rotor signal processing expansion is provided and the mass (and c.g.) of the board is kept as close to that of the other boards to avoid balance problems. No sample/hold facility is provided for the rotor torque signal.

5.2 The "Off Rotor" Data Streams

The data streams which are not multiplexed on the wind turbine rotor are those which themselves originate off the rotor (with the exception of the rotor torque signal). The initial performance measurement phase (described in Chapter 7) was a very important stage in the development of both the wind turbine and the instrumentation and it was at that stage that the channels to be digitised on Bank 0 were determined. For this purpose the 'Board 0 Box' (known throughout this work as 'BOB') was designed to process and multiplex the 16 signals destined for Bank 0 of the CED 1401. It also performs other vital functions including shaping and control of the 'events' to trigger actions in the CED 1401, anemometer signal processing and data transmission between the wind turbine and the CED 1401. The schematic diagram shown in Figure 5.5 shows how 'BOB' fits into the data acquisition system. Each of its functions are described separately in the following sections.

5.2.1 Event control

The CED 1401 'WNDML' command (which controls data-acquisition) is synchronised with blade azimuth position by two pulse trains produced by the rotor slotted disc/optical sensor (see 3.3.5). These signal trains are known as 'TDC' (Top-Dead-Centre) and 'TATS' (Two And Thirteen-Sixteenths degrees of azimuth) and occur once and 128 times per rotor revolution respectively. In this way the same amount of data is collected for every rotor revolution regardless of the rotor speed.

The command was originally written for data acquisition from a vertical-axis wind turbine [4.1] which had a maximum rotor speed of 120 r.p.m. Since the WNDML command is capable of digitising 49 channels in under 850μs the VAWT experiment was set up to take 256 sets of readings every complete rotor rev. (At this speed, 1/256th of a rev is moved in 1953μs so the command is easily fast enough). The command expects 256 'Event 1' pulses evenly spaced in time between each 'Event 0' pulse marking each rotor rev.

For this horizontal-axis experiment, however, the rotor speed may be as high as 666 r.p.m. and the WNDML command would not be capable of sampling data quickly enough since 1/256th of a rev is turned in 352μs. This problem could be overcome by re-writing the command and perhaps reducing the number of channels sampled so as to reduce the acquisition

time. This option is undesirable since as many transducers (and hence channels) as possible are required to adequately map the flow. An alternative solution, used here, is to reduce the azimuthal resolution, obtaining fewer than 256 sets of samples per rotor rev. Based on 128 sampling events per rev the existing WNDML command will run at rotor speeds up to 551 r.p.m. Even this sacrifice is insufficient to allow sampling at 666 r.p.m. and to accommodate this speed the rate must be further reduced to 64 sample sets per rev. This solution is the neatest since no changes to the CED 1401 command are actually necessary. This is achieved by suppressing any unrequired TDC pulses until 256 sampling positions have occurred (i.e. 2 or 4 rotor revolutions). In this way, with the wind turbine equipped with a 128 slotted disc (one of them being a TDC slot) if every other TDC pulse is suppressed the two pulse trains can be fed directly to the CED 1401 to log data at up to, say, 500 r.p.m. The CED 1401 will 'see' 256 Event 1 pulses (E1) for every Event 0 pulse (E0) and a complete data acquisition cycle is executed over 2 rotor revs with 128 sampling positions in each. In a similar manner, when the rotor speed is greater than 500 r.p.m. both the TATS and TDC pulses are 'divided down' in this way with every other TATS pulse and three out of every four TDC pulses being suppressed. In this mode a complete data acquisition cycle is executed over 4 rotor revs with 64 sampling positions in each rev. A timing diagram showing the interaction between all of the event pulse trains is shown in Figure 5.6. It is important to note that a CED 1401 sampling scan is initiated by each negative going edge of the E1 pulse train.

The E1 signal which is derived from the TATS pulse train is also required on the wind turbine rotor. This is because as well as initiating each of the azimuthal data sampling operations in the CED 1401 it is needed to freeze the analogue data which is being sampled. This is achieved by using the E1 pulse train to control the on rotor track/hold bus which communicates with all of the Sample/Hold chips. For each and every TATS pulse occurring a monostable circuit is fired which sets the track/hold bus into its hold state and freezes all 40 of the pressure transducer outputs. The CED 1401 is then able to sample all of the analogue values in turn, storing a digital 'snapshot' of the rotor pressures at one instant in time and avoiding any time-skewing of the data. After 900μs the monostable 'times out' and the track/hold bus reverts to its track state (The chips may be damaged if left in 'hold' mode for too long).

All of the data described in this thesis was acquired in the 'less than 500 r.p.m.' mode and with exactly the system described above. On analysing early results, however, it was noted that the time interval between successive azimuth slots (stored as an additional data stream by the CED 1401) was predictable but erratic (see Figure 5.7). In other words the slots cut in the disc were not very accurately machined so that, although the intervals were repeated each and every rev, there were some much longer and some much shorter than the nominal. Thus the 'instantaneous r.p.m.' apparently varied by about ±20 r.p.m. when the rotor was running steadily at nominally 333 r.p.m.

This set back was overcome for all of the fully instrumented blade data by the inclusion of a 'Phase Lock Loop' circuit in the Event 1 signal path. This circuit uses the same type of PLL chip that is used for the anemometer signal processing although in a slightly different way. The unevenly spaced 'TATS' pulses are input to the chip and emerge averaged out (in the frequency sense) so that the pulses occur at much more regular time intervals (see Figure 5.7). The time constant of the circuit is carefully chosen so that sufficient 'smoothing' occurs whilst maintaining a quick response to any real changes in rotor r.p.m. This can be seen in Figure 5.7 where the large peaks are suppressed to a much lower level and occur fractionally later.

5.2.2 Anemometer signal processing

This is also carried out in 'BOB' but has been fully described in 4.1.2

5.2.3 Data transmission

Another of the functions performed by 'BOB' is that of data transmission between the wind turbine and the CED 1401. This matter requires some attention because of the transmission distances involved; about 40 m for the field test site and 10 m for the mobile set-up. Figure 5.2 shows the passage of digital data from the CED 1401 to the rotor (to address the on-rotor multiplexers) and also of multiplexed analogue data from the rotor to the CED 1401. These two transmission tasks are described below.

Firstly the five analogue data transmission lines of pressure transducer data will be considered. The worst mode of operation is on the field test site when the distance of 40m should be considered as the design

case. The signals to be transmitted are very dynamic since they contain multiplexed data and could theoretically contain 10 V step changes (-5 V to +5 V) occurring every 50μs. Due to propagation delay and the signal rise time (caused by cable capacitance) there is a finite time between transmission and reception of the signal. To minimise the effects of this delay, and so maximise the settling time of the lines an actively driven transmission system was developed.

The system took the form of a data line driver circuit in the wind turbine and an associated receiver circuit in 'BOB'. The main features of the system are its ability to resist noise pickup due to the use of a twisted pair for transmission and by maintaining separate ground potentials at each end of the system by the use of optical isolation. As a by product of this arrangement the data transmission system has an effective gain of 2 so that a single ended pressure transducer output of 1.5 V is transmitted as +1.5 and -1.5 volts in the twisted pair and is received as a 3.0 V difference. Also in the receiving circuitry, the ability to offset the input voltage difference by up to -2.5 V is provided so that a 3 V input signal can be adjusted to lie anywhere between 0.5 and 3.0 Volts.

Digital data is also transmitted between the wind turbine and the CED 1401 (via 'BOB') so that the rotor multiplexers can be driven correctly from the CED 1401 and so that the TATS and TDC pulse trains arrive correctly at the CED 1401. The design requirements for both these purposes are similar to those described above since again the signals are very dynamic in nature. The circuit used for transmission and reception provide full isolation between source and destination and is based on only a single wire per signal (the susceptibility to corruption by noise being much less than for the analogue signals).

5.2.4 Bank 0 multiplexer - Board A

The output from this multiplexer is sent straight to the CED 1401 Bank 0 A-D converter input. Hence the sixteen signal channels shown in Table 5.4 must all arrive at the IH6116 multiplexer chip. All of the anemometer signal processing is also done within BOB so these signals are simply wired onto the correct multiplexer inputs. The five electrical power measurements made in the control box (grid power/current, turbine power/current and line voltage) are relayed to BOB via a cable connection between the two devices and hence appear at

the Bank 0 multiplexer. This leaves only five signals to be considered; the two torque measurements (rotor and yaw), the accelerometer output, the yaw position signal and the pressure transducer excitation voltage. All of these signals are sent from the wind turbine (but not on driven lines) and arrive in BOB at analogue receiver circuits which work equally well with driven or non driven signals. From here the signals are wired across to their respective Bank 0 multiplexer inputs.

5.3 The CED 1401

The Cambridge Electronic Design 1401 is an intelligent laboratory interface with its own micro-processor (65C02), a 64 kilobyte random access memory, a 2 megabyte mass RAM and comprehensive analogue and digital ports. A calendar clock with read-out to the nearest second is also provided and allows experimental records to be individually date-stamped. The data acquisition system used in this work was designed around this proprietary unit, as shown in Figure 5.2. The CED 1401 performs the essential task of analogue to digital conversion in the data flow. A total of 4096 different digital levels (12 bits) are available over the analogue voltage range of +5 to -5 volts. The CED 1401 is capable of digitising an input voltage in 12μs and therefore makes it possible to obtain dynamic data from a rotating wind turbine blade.

Figure 5.8 shows in more detail how the CED 1401 fits into the data-acquisition system. A total of 96 analogue signals are multiplexed down into 6 data streams, each carrying information on 16 channels. These 6 data 'banks' are fed directly into the CED 1401 where they are digitised. The CED 1401 controls which of the 16 channels in each bank is presented to its inputs by resetting the state of its digital outputs. This resets the address bus communicating with all the multiplexers and hence causes them to switch to the appropriate channel.

Data acquisition is controlled by a specially written assembly language program (called 'WNDML') which is stored on a ROM inside the CED 1401. When data acquisition is requested the program sets a repeating series of addresses at its digital outputs which is synchronised by the Event 0 and Event 1 inputs. Incoming analogue voltages are digitised and the results stored in RAM. The program has several different modes of

operation, the two most important ones being 'run data acquisition' (initiated by the 'WNDML,G' command) and 'calibration data acquisition' (performed by 'WNDML,C').

5.3.1 The WNDML,G command

The WNDML,G command controls run data acquisition and is written in such a way as to maximise the data acquisition rate of certain channels and to sample other channels less frequently. For this reason the 96 analogue data streams are divided into two types - 'fast' and 'slow' channels. This is so that signals which are not expected to change quickly (such as the pressure transducer 'temperature' signals) are sampled at a much slower rate than those, like the pressure signals, which are known to be more dynamic.

Data sampling is synchronised to the wind turbine rotation by two pulse trains produced by the rotor and sent to the CED 1401. The first of these is a top-dead-centre pulse known as E0 which is fed to the EVENT 0 input of the CED 1401 and normally occurs once every 2 rotor revs! (see 5.2.1). The second pulse train, sent to EVENT 1, usually consists of 128 pulses equally spaced around one revolution of the rotor and is known as E1.

The division of 'fast' channels (sampled 256 times per 2 rotor revs) and 'slow' channels (sampled once per 2 rotor revs) is shown in Table 5.4. There are 48 fast analogue data channels sampled 256 times between successive E0 pulses. The 48 slow channels are sampled only once per E0 pulse. A 49th fast channel is created by storing the time interval between each pair of successive E1 pulses (in units of 2μs) so that rotor r.p.m. can be determined accurately. The absolute time of the start of each data acquisition cycle (measured in seconds from the start of data acquisition) is stored also and constitutes an extra slow channel. Hence there are 49 different slow channels and 49 different fast channels.

Each digitised voltage is stored as a pair of bytes (in the order low byte, high byte) forming a 16 bit number. The 'twos complement' representation of the byte pair will lie in the range -32768 to +32767 representing voltages in the range -5.0 V to +5.0 V. The bottom four bits of the 16 bit value are always set to zero so that the resolution of the A-D conversion is actually only 12 bits. This represents a

possible quantisation error of up to 2.44 mV, this figure being the size of each of the 4096 digital levels available across the 10.0 V analogue range.

The command is written so that there is one slow channel sampled with each group of 49 fast channels at each of the 256 sampling points per cycle. This is equivalent to 50 'fast' channels per E1 and hence the data for each cycle will occupy 50*256*2 = 25,600 bytes. There is space for the data from 81 data acquisition cycles to be stored in the 2 Mbyte mass RAM.

5.3.2 The WNDML,C command

This command controls the acquisition of calibration data and produces very much less data than the run data acquisition command. Upon issuing the command all 96 of the analogue input channels are scanned many times and the digitisation results stored in CED 1401 memory. The calibration scans are performed at about 80 scans per second (i.e. they are not synchronised by the E0 or E1 event signals). The number of scans is prescribed by the user and will therefore determine the time taken to acquire all of the data. Every calibration performed during this work used 80 scans (taking about 1 second) so that changes in the applied calibration parameter over this time would be negligible. The results of the digitisation scans are stored in a 576 byte block of memory and contain the mean, maximum and minimum values for all 96 channels. Calibrations are performed by applying an independently measured parameter to one or several of the transducers and then sending the WNDML,C command to the CED 1401. Only that data relating to the calibrated channel(s) is then defined although all of the 576 byte block is stored.

5.4 Data Acquisition and Transfer Software

The CED 1401 "WNDML" command is a fast and powerful piece of machine code capable of order locked data acquisition, calibration data acquisition and data transfer to the host computer. The data transfer routines were designed for use over a serial link (RS232) between the CED 1401 and the BBC micro and are therefore very slow. The parallel bus data transfer achieved in this experiment is much quicker and renders the WNDML command data transfer routines redundant. A number of BASIC

programs were written for the BBC micro to provide the user with easy, menu driven data acquisition, data transfer and initial data checking.

Once calibration or run data has been stored on floppy discs or winchester (and checked) the data transfer process is not complete since analysis on the BBC micro would be impracticable. Hence, data is transferred from winchester (or floppies) to the Cranfield VAX cluster and usually archived onto magnetic tape. This transfer is achieved using 'Kermit' software which was specially designed and written by University of Lancaster for data translation between mainframes and micros. During early tests with Kermit its limitations became clear and the consequences for fast data transfers were apparent. Careful organisation of the file transfer system allowed these restrictions to be alleviated and resulted in the following scheme.

The data pertaining to each 'run' (calibration run or wind turbine data logging run) is recognised by a three integer run identifier such as '193'. Two types of file are recognised by the Kermit system; ascii (or text) files and binary (hex) files and so each run identifier has two files associated with it. The text file (e.g. 'T.193') contains ascii data whilst the data file ('D.193') contains the actual run data in the form of hex bytes. Data and text files can thus be transferred separately to the VAX cluster producing readable text files and untranslated data files for subsequent analysis. The calibration and data run identifier numbers form a single sequence so that there is no duplication of run identifiers. Each pair of files, therefore, represents the data and text information for either a calibration or an experimental run. The most important of the programs will now be briefly considered in turn.

5.4.1 Program "QLOOK"

With 96 multiplexed analogue data streams arriving at the CED 1401 there is a fair chance that a single channel which develops a fault could go undetected for some time. This could render any run or calibration data collected useless and must therefore be avoided. The BBC micro program "QLOOK" goes a long way to ensure that any faults are detected quickly so that remedial action can be taken; a block diagram is shown in Figure 5.9.

The program simultaneously displays the status of 16 of the 96 channels (i.e. one bank). After the BBC micro has been initialised for graphics work, the bank required is requested of the user and the calibrate command is issued to the CED 1401 ; "WNDML,C,80,0;". This causes the CED 1401 to scan all 96 channels 80 times over, storing the mean, maximum and minimum values found on each channel. A set of axes are displayed on the screen and when the CED 1401 is ready the 576 bytes of calibration data (pertaining to all 96 channels) are transferred to the BBC micro. The relevant data for the chosen bank is extracted from BBC memory and bars are plotted on the axes representing the magnitude of each of the channel output signals (see Figure 5.4). The bars actually show two levels indicating the maximum and minimum values obtained during the 1 second scan with the mean value printed to the nearest mV above it. In this way a quick check of the 16 channels can be made by visually scanning the pattern produced by the 16 bars; the correct patterns being quickly learnt. Any channels which are showing large ranges or are offscale altogether are immediately evident whilst more detailed checking can be made by reference to the printed mean value.

5.4.2 Program "C/34"

This program controls acquisition of all of the calibration data and is menu driven for ease of use. A simplified block diagram is given in Figure 5.10. After the run identifier, build number, map number etc. have been entered (in the initiate module) the main menu is displayed. Here any filing system commands may be entered without interrupting program execution. The other two menu options control the two stages involved in acquiring and storing the calibration data. The conclude option can only be performed after some calibration data has been acquired in the calibrate option.

This calibrate option controls the use of the "WNDML,C,80,..." command which is used to scan all 96 analogue input channels for one second and store mean, maximum and minimum data in CED 1401 memory. To identify which channel(s) is/are being calibrated a 'type' letter is requested from the user. For each calibration 'spot' taken, all 96*3*2 = 576 bytes are saved. Only some of this data is relevant, its position in the data block being identified by the 'type' letter and the Map Number.

The calibration data scans can be made in either of two modes; an interactive mode in which scans are initiated manually by the operator

or an automatic mode in which scans are made at regular time intervals without the operator necessarily present. The mode of operation is determined by the operators response to the programs next request for user input;- "Enter the number of repeats (Zero gives 'One-Shot')". Entering zero results in the use of the more usual manual mode and the display of a sub-menu with three options;- Input, Execute and Exit (i.e. back to the main menu)

The Input phase demands from the user the value of the 'applied parameter'. For example, if the calibration type letter entered earlier, were 'A' (an anemometer calibration) then the message 'Enter the applied frequency in Hz.' would appear and the appropriate value should be entered. Further requests for the input of Beaufort weather descriptors, barometric pressure and ambient air temperature may then appear depending upon the relevance of each to the type of calibration and whether they are automatically being monitored by the BBC micro. Choice of the Execute option immediately activates the "WNDML,C" calibration command in the CED 1401. After the scans have been made the data is transferred to the BBC micro's memory ready to be saved on floppy disc or winchester.

Once both these options have been exercised (in either order) the text and data are stored together in a temporary file. They will have to be separated later to satisfy the requirements of Kermit as discussed earlier. The two phases, Input and Execute can be repeated in pairs as many times as required up to a maximum defined by the disc filing system in use ;- 29 or 60 times for DFS and 47 times for ADFS. A set of calibration 'spots' will be built up as the applied parameter is varied over some expected range. Once sufficient spots have been acquired (resulting in several small calibration files stored on disc) the exit option is chosen and control returns to the main menu. Here, further calibrations of the same or of a different type letter may be obtained by re-entering the 'calibrate' option. If this is not required the conclude option should be chosen. This takes all of the calibration spot files (with the current run identifier number) and re-organises the data. All of the text data is stored in a single file called T.xxx and all of the calibration scan data is written to a file called D.xxx, where xxx stands for the run identifier entered earlier. The stored files are then ready for checking or transfer to the VAX system using Kermit and execution of the calibration program is complete.

5.4.3 Program "H/10/22"

The "WNDML,G" command which actually acquires the experimental data is initiated from within the program H/10/22, which again runs on the BBC micro-computer. This code is designed to allow the user menu driven control over the actions of the CED 1401. A simplified block diagram is given in Figure 5.11 which indicates the four main modes of program operation. The first operation mode is the default one should no other option be chosen. This is the status mode in which various parameters are continuously displayed and frequently updated in the lower half of the display screen. These parameters include the status of the WNDML command, the current windspeed and the currently selected 'Good Wind' criterion (see below).

Two modes of data acquisition are available. The first is an automatic logging mode in which data is acquired regardless of the current wind conditions. This is achieved by setting the windspeed window limits to -30 and +30 m/s, a window which is bound to include the current windspeed. After the WNDML command has been 'armed' with the "WNDML,G,80;" instruction the 'Good Wind' criterion is tested. If the current windspeed lies within the window then data logging should commence. This is achieved by 'setting' the enable/disable bit of the CED 1401 digital input port (using one of the BBC micro user port lines configured for output). Once the bit is set, data acquisition commences as can be seen by the 'Revs in MRAM' indicator which should steadily increase. (NB. Each rev in mass RAM contains the data relating to either two or four real wind turbine rotor revolutions - see 5.2.1). Half way through the data acquisition cycle, other run parameters are determined including approximate r.p.m., ambient air temperature and barometric pressure (if the relevant equipments are connected).

The approximate r.p.m. is determined by sending the 'TATS' signal directly into one of the BBC user port lines (configured for input). The time interval between pulses is measured by a fast piece of machine code so that the nominal r.p.m. can automatically be entered into the text file. The measurement of ambient air temperature is achieved with the equipment described in 4.2. The output is digitised by the BBC micro's own A-D converters giving the temperature in °C. Finally the barometric pressure measurement made by a DRUCK DPI140 digital barometer may be received at the BBC micro's RS232 port for direct inclusion in the data run text file. In order to correctly control the data logging functions

of the CED 1401 described above the BBC micro must be fed with the windspeed signal from one of the anemometers. The cup anemometer signal, having been processed in 'BOB' (see 4.1.2) is split into two and sent, both to the Bank 0 multiplexer and the BBC micro's own A-D converters. With crude calibration coefficients stored in BBC memory, the program has the power to implement the 'Good Wind' criterion with an accuracy of about ±0.5 m/s. (Any errors involved in this system only affect the "log/don't log" decision and have no bearing on the final data analysis.)

The second of the data acquisition modes operates in exactly the same way except that the user is required to enter the minimum and maximum windspeed values defining the window. Again, after the WNDML command has been armed the "Good Wind" criterion is tested. If the current windspeed does not lie within the window the system waits with the CED 1401 enable bit unset and hence preventing data acquisition. Only when the criterion is met does the enable bit automatically become set and data acquisition commence.

After data has been logged and the CED 1401 mass RAM is full the fourth and final mode of operation can be entered; that of text file compilation and data downloading. The destination of the data is entered in the form of a 'W' for the winchester or 'F' for the floppy disc drives. According to the response the correct filing system is initiated and the text file entry commences. Those pieces of information about the run which have not been acquired automatically are then requested of the user for inclusion in the run text file. When the text file is complete it is saved onto the appropriate storage device and the main data transfer program is 'chained'. (i.e. automatically loaded and ran by the previous program). The correct program according to the storage medium is then executed, G/10/10 for data transfer to winchester and F/10/10 for transfer to floppy discs.

5.4.4 Program "G/10/10"

Data transfer from the CED 1401 mass RAM to the winchester hard disc is accomplished with the BBC BASIC program G/10/10. The entire 2 Mbyte RAM (arranged as 32 banks of 64 Kbytes each) is accessed in 16 Kbyte blocks, transferred to BBC memory and then written onto the hard disc. To accommodate the data 'en route' a 16 Kbyte block of BBC memory must be kept available. This is not possible if a large BASIC program (such as

H/10/22) is loaded and running, since the program itself occupies memory. For this reason the data transfer programs (G/10/10 or F/10/10) are 'chained' from the data acquisition program so that only the smaller transfer program is in memory during the transfers. Smaller blocks of data could have been transferred but the complete process would then have taken a great deal longer.

Speed of transfer is of paramount importance since in previous experiments [5.2] the 40 minutes required to download the mass RAM constituted a major delay during a data acquisition exercise. This potential delay is equally important to this experiment (in both the mobile and field test modes) because when the weather conditions are favourable as much data as possible should be acquired. Several coding alternatives for transferring the basic 16 Kbyte block of data were timed so that the quickest method could be determined. The chosen scheme transferred the data in less than 2 seconds and hence allowed the entire mass RAM to be downloaded by 128 repeats of this code in under 4 minutes.

5.4.5 Program "OFFSCALES"

The 30 Mbyte winchester used for this experiment was only capable of storing the data from 13 data acquisition runs (i.e. 26 Mbytes) due to the space taken up by these programs and other utilities. The transfer of these 26 Mbytes onto the VAX cluster is very time consuming. It is therefore desirable to know in advance of the transfer whether a particular run contains useful data or corrupted data, due, perhaps to an instrumentation fault. This requirement is fulfilled by the BBC BASIC program "OFFSCALES" which can scan through all 13 of the data files looking for any occurrences of the hex bytes '7F' or '80' in the 'high' byte positions. If they are found to occur in the file this indicates that the +5.0 V or -5.0 V 'endstops' of the CED 1401 A-D converters have (almost) been reached and consequently the data may not be sensible. The program output details the number of times that offscale values occurred for each of the 96 channels and hence provides a useful indication of how good or bad the data is. The decision to delete or keep each run can then be taken and further data acquisition runs may then be possible. When all 13 of the runs stored seem to contain sensible data the 'uploading' process must commence.

5.4.6 "KERMIT" Software

The 'full' winchester, once removed from the data acquisition system, is installed at another BBC micro computer. This machine is connected to a Cranfield 'Ethernet' terminal server via its RS423 port and is therefore capable of serial communication with the VAX cluster. The transfer of information between the two is controlled by 'Kermit' software installed on both the BBC micro and the VAX. As previously described, the text and data files are sent to the VAX separately using different Kermit 'settings'. Due to the fact that the link is a serial one, the transfer process is rather slow ;- 10 Kbytes per minute even at 19200 baud. All of the text files are transferred within a few minutes but the data files require about 135 minutes each! This process represents the bottleneck in the data acquisition/transfer system. All attempts to improve the transfer rate were frustrated due to the use of the BBC micro as the source machine.

CHAPTER 6

CALIBRATION PROCESSING AND ERROR ANALYSIS

6.0 Summary

Calibration information for all data streams are required so that the raw voltages stored by the data acquisition system during an experimental run can be converted into the appropriate engineering units. This calibration process is described here.

The acquisition of the calibration data is outlined in Section 6.1, each type of channel having its unique method for application of the calibration parameter. The calibration data files produced are then transferred onto the VAX cluster and processed as described in Section 6.2 to find the calibration coefficients. Application of these calibrations to the raw test data is then discussed in Section 6.3.

The resulting EXP files contain only calibrated data (in engineering units) and are the basis for all subsequent data analysis. Any given measurement in an EXP file should be considered as an estimate of the measurand. The possible errors which could be expected are assessed for each type of channel in Section 6.4 so that the levels of confidence which should be attributed to the data streams can be determined.

6.1 Calibration Data Acquisition

Calibration data for every transducer is obtained as a series of calibration spots acquired under conditions of known transducer input. The applied parameter is independently measured as accurately as possible at the time of the calibration spot. The digitised transducer output voltage for the spot then allows a relationship between transducer output voltage and applied parameter to be determined. Each type of transducer has its own particular requirements for the acquisition of calibration data. Each of them are dealt with in the following sections.

6.1.1 The Anemometry Channels

6.1.1.1 The anemometer calibrations

All the anemometers used in this experiment produce pulse train outputs. The frequency of this pulse train can be used to determine the applied windspeed by reference to the manufacturer's aerodynamic calibration for the device. In other words, the manufacturer's quoted calibration (in m/s per Hz) can be assumed implicitly and the calibration required here is simply that of the conversion from pulse train frequency (Hz) to analogue voltage (V) as produced by the anemometer signal processing circuitry. From this pair of calibrations the true calibration for each anemometer can be determined (i.e. the relationship between windspeed (m/s) and output voltage (V)). This approach also simplifies the calibration process since the applied parameter is not a measured windspeed (which would be difficult to produce and measure accurately) but a pulse train of a measured frequency. This is very much easier to produce and measure with any proprietry signal generator. One weakness of this method, however, is the reliance upon the manufacturers aerodynamic calibration.

All five anemometer channels were calibrated using a signal generator to simulate the square wave pulses from the anemometer. The applied parameter was entered in terms of frequency (Hz) so that the calibrations (see Figures 6.1 and 6.2) relate frequency with output voltage and leave the manufacturer's calibration to be applied later. The four Lowne anemometer channels were calibrated for frequencies between 100 and 1150 Hz which are approximately equivalent to windspeeds in the range 2 to 28 m/s. The cup anemometer was calibrated over a much lower range of frequencies (3 to 26 Hz) corresponding to a windspeed range of about 4 to 32 m/s. It can be seen that both Lowne and cup anemometer calibrations are slightly non-linear and are therefore treated slightly differently from other channels when the calibration coefficients are calculated.

In order to convert an analogue voltage given by the data acquisition system into an estimate of the windspeed the anemometer manufacturer's aerodynamic calibrations are required. For the Lowne anemometers the aerodynamic calibration used was that given by Hobbs [4.2] which was determined by the National Maritime Institute (formerly N.P.L.). For the

Lowne anemometers (fitted with mica vane rotors) the calibration equation which best fits the measured data is:-

$$Vr = 0.02430 * n + 0.0994$$

where Vr is the Lowne indicated windspeed in m/s and n is the pulse frequency in Hz, for wind speeds up to 8 m/s. Hobbs indicates that over this range the error between Vr and the true windspeed is always less than 0.0141 m/s. Calibrations of the mica-vaned Lowne anemometers have never been performed above 8 m/s so the above equation could lead to significant errors for higher windspeeds. A series of calibration experiments have recently been undertaken by the National Engineering Laboratory to check that extrapolation of the equation is satisfactory. In the absence of these results, however, the above relationship has been assumed throughout this work.

Hobbs also reviewed the effect of yaw angle on the Lowne anemometer response: comparison of the measured response with an estimate based on the product of the axial-flow (unyawed) response and the cosine of the yaw angle revealed discrepancies of less than 2% for yaw angles less than 70%. Variations from one Lowne anemometer to another are estimated by Hobbs to be small so that the calibrations for two identical anemometer heads should agree to better than 1%.

For the cup anemometer the calibration given by the manufacturer (48 r.p.m. per m/s) was determined by referencing the response to a standard anemometer which had previously been calibrated at N.P.L. The calibration for this particular cup anemometer has, more recently been independently determined at the National Engineering Laboratories who have quoted a value of 49.98 r.p.m. per m/s.

For both Lowne and cup anemometers, a further correction is applied to account for mechanical non-linearities. For the cup anemometer this information is the manufacturer's supplied correction table to be applied after the basic calibration. For the Lowne anemometers, the error is much smaller, but the information from the NMI calibrations is applied.

6.1.1.2 The wind vane calibration

The wind vane calibration was carried out by aligning the vane in each

of eight major directions at 45° to each other (using a clinometer with the anemometer tower lowered) and digitising the output voltage at each. A different calibration was required for the field test site (N.I. and P.I. data) and the mobile trailer experiments (F.I. data). A typical calibration is shown in Figure 6.3. At the field test site the zero degrees direction was the direction such that the anemometer tower was directly upwind of the wind turbine, whilst on the trailer the origin was taken as the trailer forward direction. In either case, in order to derive a linear calibration line for the data, without any discontinuities, all spots with outputs above a certain value have an offset angle applied. In the case shown in Figure 6.3 all spots with outputs above 2.0 V have 360° added to the applied parameter. The result is a linear calibration relationship which produces directions in the range 270° to 490°.

6.1.2 The Load Cell Calibrations

Both the rotor torque and yaw torque load cells were calibrated by applying known torques with the respective shaft locked. In this way, all of the applied torque passed through the load cell (ignoring the small errors due to friction). The calibrations were done in the laboratory with the turbine mounted on its test/transport frame.

For the rotor torque load cell calibration, the rotor shaft was jammed against the wind turbine body using a purpose made plate. A steel arm was then bolted to the rotor hub 'Y' plate (with blades removed) so that its top edge was horizontal and on a rotor radius. Various weights could then be hung from the arm at a number of different moment arms so that a large range of torques could be applied. This method was found to be most satisfactory but unfortuneately could not be used to calibrate the yaw torque load cell. This was because it was impossible to rotate the entire wind turbine from its usual orientation so that the yaw axis was horizontal. Consequently the yaw load cell calibration was performed with a rope pulling horizontally and attached to a fixed object via a spring balance. By adjusting the load in the rope various yaw torques could be applied. This method was not considered to be as accurate as that for the rotor torque calibration.

Whilst the calibrations were performed the applied load was converted into a torque by multiplying by the moment arm and the applied torque was entered into the computer as the applied parameter. This means that

the calibration data relates rotor and yaw torque directly to the analogue output voltage digitised at the CED 1401. The resulting rotor torque calibration (Figure 6.4) was linear and hysteresis errors due to 'load increasing' and 'load decreasing' calibrations were negligible. The yaw torque calibration (see Figure 6.5) also showed negligible hysteresis errors but indicated a significant 'dead band' at around zero yaw torque, when the load cell goes from tension to compression. This is thought to be due to the relatively worn yaw bearing which required considerable movement before the slack was taken up and torques transferred.

6.1.3 The power measurement calibrations

All five of these signals were calibrated by applying independantly measured electrical parameters and digitising the circuit outputs. Line voltage calibrations were performed at 0 V and 415 V by temporarily rewiring the channel input. The response shown in Figure 6.6 resulted.

Both the current and power calibrations were rather more complicated because of the requirement for the calibration data over a range of phase angles. These conditions were produced using the circuit shown in Figure 6.7 which allows various combinations of purely resistive and purely capacitive load. Using the independant measurements of resistive current and capacitive current, simple calculations produced an estimate of the r.m.s. current seen by the two current sensors. Variation of the number and size of both resistors and capacitors allowed several calibration spots to be acquired (see Figures 6.8 and 6.9). In the same way the real power measurement circuitry was calibrated by finding the product of the resistive current and the line voltage. Capacitive loading, however, was also introduced so that the absence of its effect on the real power measurement could be verified (see Figure 6.8).

6.1.4 The accelerometer calibrations

The accelerometer used in the experiment was not calibrated because of the difficulty in producing an accurately determinable applied acceleration. (Being of the piezo-resistive type, simply inverting the sensitive axis of the device would not produce $\pm$1g). The nominal calibration given by the manufacturer was therefore assumed implicitly.

A further complication is created due to the low pass filter which is present in the accelerometer signal conditioning. This avoids aliasing by removing much of the high frequency content of the signal but it also means that the amplifier gain (used to boost the quoted sensitivity of 50 mV/g to more measurable levels) varies with frequency and a single calibration factor is impossible to determine. However, circuit calculations showed that for frequencies around 5 Hz (the fundamental rotor frequency) the gain was approximately 250. It was therefore decided to use this value to calculate calibration coefficients which would then be used over all measured frequencies.

For these reasons the acceleration results presented here should be used to locate major acceleration events and for inter-run comparisons rather than for the exact numerical determination of the levels of vibration.

6.1.5 The body angle sensor calibrations

The body angle sensor was calibrated by turning the wind turbine into a number of measured angular positions and digitising the potentiometer output in the usual way. After checking that the triangular tower top yaw plate was equilateral (all angles were 60° ± 0.2°) the turbine was positioned at a number of body yaw angles by referencing the body to the tower with a large flat plate of metal. Calibration spots were acquired at 30° intervals between -90° and +90° with each position done twice, approached in both the clockwise and anticlockwise directions. The resulting spots can be seen in Figure 6.10 and indicate a linear relationship with body angle with a small hysteresis uncertainty caused by slop in the yaw bearing.

6.1.6 The pressure transducer calibrations

The use of low cost pressure transducers (with no in-built temperature compensation) for the measurement of aerodynamic pressures has been demonstrated by Oram [4.1]. The requirement was obviously therefore to build up an extensive data base of calibrations covering a broad range of ambient temperatures, sufficient to allow the determination of (linear) calibration parameters for any transducer temperature (as indicated by its drawn current) that may occur during an experimental run. A typical set of calibrations for a single pressure transducer, showing the magnitude of temperature drift, is given in Figure 6.11. The procedure followed has been to use the calibration data base, for

each transducer separately, to determine its sensitivity and offset as a (non-linear) function of its 'temperature'. The method (to be described in detail in Section 6.2) is to generate a multi-parameter curve fit (over as much of the calibration data base as possible) of the measured applied pressure as a (linear) function of the transducer's output signal (V_o) and a (non-linear) function of its drawn current (V_i).

During the earlier part of the experiment, a two-stage approach was adopted to try to cut down on the number of calibrations done, by isolating the temperature effect. Frequent pressure calibrations were done during the testing period (at the "temperature of the day"), but additionally, zero-pressure calibrations were done automatically over many hours (usually overnight and therefore over large temperature ranges). But it was later realised that unlimited replication of the zero-pressure calibrations merely had the effect of weighting the curve-fit at the bottom of the "pressure-ramp", and that there was no real substitute for a complete pressure calibration at the conditions appropriate to the experimental runs. Nonetheless both calibration procedures are described in the following sub-sections.

6.1.6.1 Pressure calibrations

These calibrations were performed by applying a known pressure to all of the tranducers and digitizing all of the analogue output voltages.

The V_i temperature signal is used to determine the correct sensitivity and offset for each particular transducer. At a fixed temperature, the transducer response is linear and the measured pressure can be determined easily using the values of sensitivity (slope) and zero pressure offset (intercept). The response to temperature, however, is non-linear as can be seen in Figure 6.12 which only gives data relating to zero applied pressure. The transducer sensitivity is much less affected by temperature changes than is the zero pressure offset (see Figure 6.11).

The "pressure ramp" type of calibration is therefore at more or less constant temperature (although this is not assumed) and follows one of the lines indicated in Figure 6.11. A typical calibration exercise would take about an hour and consist of around 20 calibration spots.

After the transducers and data acquisition system had been checked for satisfactory operation (by using the 'QLOOK' program) the calibration software was loaded and prepared for a pressure calibration. Using a small air pump, a pressure or suction was applied to the reference pressure pipe which communicates with all of the pressure transducers. A pressure in the range -3000 to +8000 Pa would be applied and 'sealed in' using a valve, the value then being determined from a high accuracy Nutem manometer. The data-acquisition system would then be instructed to digitize all channels and thereby capture all of the calibration data.

Repeating this process over a range of applied pressures soon built up a series of calibration spots for all of the transducers. The manometer used was equipped with an eye piece and vernier arrangement for accurate measurements of the liquid column height. The resolution of 0.1 mm is equivalent to approximately 1 Pa pressure since water was used as the working fluid. Careful attention was paid to the stability of the liquid height since any gradual falls of the pressure could indicate a leak in the reference pressure system. These effects were minimised anyway, by systematically performing each calibration spot in the same way. First the pressure/suction was applied, followed by alignment of the eyepiece with the water column meniscus. Then, before this level was read the data acquisition system was triggered and only then was the manometer vernier read and entered into the computer. To further improve the accuracy of the calibration data, the ambient temperature was also recorded and used to correct the water column height for density changes.

6.1.6.2 "Temperature" calibrations

As previously stated, pressure calibrations acquired on various days (and consequently over a range of temperatures) would provide temperature calibration information for the transducers. However, since the temperature effects on transducer zero pressure offset are much greater than those on sensitivity, it was thought prudent to calibrate at fixed pressures over large temperature ranges.

The provision of a fixed calibration pressure (non-zero) which is insensitive to changes in temperature was investigated and found to be very difficult to achieve at the required level of accuracy. Consequently zero differential pressure (i.e. atmospheric pressure) was chosen as the reference pressure value for all temperature calibrations.

With the calibration software running and the temperature calibration option chosen the computer would automatically obtain a set of calibration data at pre-determined time intervals. The reference pressure system would be left unconnected and the software would assume a zero differential applied pressure. By choosing a dozen repeat calibrations at a time interval of one hour or more, calibrations could be obtained through the night and consequently over a wide temperature range.

Typical calibration data acquired for a single pressure transducer is shown in Figure 6.11. All spots are shown, whether they are derived from pressure type calibrations or temperature calibrations, although most of the spots at zero differential pressure are from "temperature" type calibrations. Figure 6.12 illustrates the temperature effects in the absence of any applied pressure. Each zero pressure calibration spot is shown with the pressure signal V_o plotted against the temperature signal V_i. This plot clearly shows the non-linear temperature effects on the transducer zero pressure output and comparison with the previous figure shows how important it is to choose the correct zero pressure offset to obtain an accurate estimate of the pressure. (The pressure sensitivity of the transducer can be seen to be mostly independant of the temperature effects).

6.2 Calibration Data Processing

6.2.1 The calibration process

Calibration data for every transducer in the data acquisition system (with the exception of the accelerometer) is acquired under control of the BBC micro program C/34 (as described in Chapter 5). In each case a series of calibration spots are acquired under conditions of known transducer input. This applied parameter is independently measured as accurately as possible at the time of the calibration spot and is noted in the calibration text file; the corresponding data file contains the digitised transducer output voltage for the spot. A relationship between transducer output voltage and applied parameter can therefore be determined by associating these two files. This is the essence of the calibration process and, in exactly the same way as for experimental run data, the calibration data acquired on the BBC micro system is transferred to the Cranfield VAX cluster using KERMIT software.

Once on the VAX, the calibration data must be processed to determine the calibration relationship for each transducer channel. As previously indicated, a curve fit is generated for the transducer channel as a function of the output voltage (and 'temperature' in the case of pressure transducers). But before this is done, the ensemble of calibration spots must be viewed, and any offscale or outlying spots rejected. The first stage of the calibration processing is therefore to assemble the relevant spots into a (SET) file, to view this data, and to edit the file as necessary. The second stage is then to generate a curve fit to the calibration spots in a valid SET file. All this is done using the software described in the following sections. The end result of this processing is a file of calibration coefficients used in converting a raw run data file into a calibrated run (EXP) file.

6.2.2 RotACAP library

The 'RotACAP' subroutine library has been developed in order to examine experimental wind turbine rotor aerodynamics data. Over 160 'building block' subroutines can be called from various FORTRAN programs and allow raw data (as transferred from the CED 1401 via Kermit) to be calibrated into engineering units, analysed and the results presented in a usable format.

The RotACAP library can be split into two distinct parts. The first part, "Callib", contains all of the subroutines which enable calibration data to be manipulated and applied to produce an 'EXP' file in which all data is in specified engineering units. This file forms the basis for all analysis work which is performed using other subroutines called from the second part of the RotACAP library "Explib", to be described later.

6.2.3 GEN PLOT and TRAN PLOT Programs

Raw calibration data and text files, once transferred onto the VAX cluster are initially processed using the programs GEN_PLOT and TRAN_PLOT. For each of the programs, the raw calibration spots are taken as input, and a SET file and plot are produced as output. The TRAN_PLOT program is used exclusively to deal with the pressure transducer calibrations which involve 'temperature' and excitation voltage in addition to the output signal. The GEN_PLOT program is used for the other (general) data streams. In most respects, the programs are similar, so only the TRAN_PLOT program is described here.

The TRAN_PLOT program is run for each of the pressure transducers in turn. Each one has a four character 'item code' which is indicative of it's blade location (e.g. "7S40" - 75% blade span Suction surface 40% chord). When the TRAN_PLOT program is run the transducer channel is specified by it's item code, and a SET file created (e.g. 7S40.SET;5). The input loop begins by entering the run identifier for the raw calibration data and textfiles. By referring to the MAP file (see Table 5.4), the data acquisition channel is determined, and the output voltages (mean, maximum and minimum) for this transducer can be located for the 'spot' in the calibration data file. For each calibration spot a single line is written out to the SET file on which is written the source of the data, the value of the applied parameter (obtained from the raw text file), the d.c. voltages as digitized by the CED 1401 (for both the pressure and temperature channels) and much other information. The transducer output voltages are adjusted for fluctuations of the excitation voltage compared to the nominal value, so that individual calibration spots are comparable. Under the control of the user, each spot within one or many calibration data files is dealt with in this way to build up a large file of many data points. In addition, spots may be incorporated (copied directly) from previous SET files. A plot of the applied parameter versus the digitized voltage is also produced so that any outliers can be identified. The rogue spots, if any, can then be deleted by simply editing the completed SET file so that the final version contains only valid calibration data.

To repeat this process for all transducers would be very tedious. But because the same pressure was applied (via the reference pressure manifold) to each of the transducers simultaneously, the transducer SET files essentially show the individual response to the same sequence of calibration pressures. TRAN_PLOT therefore makes it possible to 'clone' a complete transducer SET file from that of a 'parent' transducer. Each line of the 'parent' SET file is copied, but its output voltages replaced with the appropriate voltages from the raw calibration data file.

The cloning procedure is only available within the TRAN_PLOT program and not within GEN_PLOT. Only sixteen channels (those of Bank 0) are dealt with by the latter program and many of these require different treatment. The principle of SET file and plot creation is the same, however, and all of the calibration plots shown in Figures 6.1 to 6.10 were created using GEN_PLOT.

6.2.4 GEN FIT and TRAN FIT Programs

Once a valid SET file and satisfactory plot have been produced the GEN_FIT program (for all Bank 0 channels) or TRAN_FIT program (for all pressure transducers) is used. These programs use curve fitting routines to determine the best calibration coefficients to fit the SET file data.

The TRAN_FIT program uses a non-linear least squares technique to evaluate the best calibration coefficients for each of the pressure transducers. It is assumed that the transducer response is linear in V_o (the pressure signal) with coefficients which are dependent (though not necessarily linearly dependent) on V_i; in mathematical terms the following functional relationship is assumed for pressure:-

$$p = c + m * V_o$$

where the "offset" is given by

$$c = x_1 + x_2 V_i + x_3 V_i^2$$

and the "sensitivity" by

$$m = x_4 + x_5 V_i$$

(Actually, linear transformations are applied to the measured quantities p, V_o, V_i, so that the parameters used in the numerical procedure lie in the range [-1, +1].) The orders of polynomials chosen to represent the offset and sensitivity are an acceptable compromise between the need to achieve accuracy but avoid spurious wobbles. A double-precision Gauss-Newton algorithm (NAG routine E04GEF) is used to find the minimum of the sum of squares of un-weighted residual pressures, for an unconstrained vector of unknown coefficients (x_1, x_2, x_3, x_4, x_5). A discussion of the magnitude of residuals obtained is given in Section 6.4.

For the Bank 0 channels there is no associated 'temperature' channel, so the program GEN_FIT effectively determines the best (constant) values of offset and sensitivity. In the case of the Lowne and cup anemometers, however, the linear fit is inadequate and would result in errors of up to 1 m/s due to the slightly non-linear frequency to voltage response. Consequently extra calibration coefficients are calculated which

represent the correction which should be applied to the best linear fit to the data. This correction is a non-linear function of the apparent windspeed (given by the linear calibration) and is found using a fourth order Chebyshev polynomial (NAG routine E02ADF).

All GEN_FIT and TRAN_FIT runs work through the input SET file and produce an output (CAL) file of calibration coefficients (e.g. 7S40.CAL;2). A typical CAL file contains only the channel and map information and the calibration coefficients in double precision format. An additional print file contains the curve fit residuals and highlights any poorly fitting calibration data which may indicate the need for splitting the SET file into two or more separate SET files according to build number changes. The residual information is also used to help in quantifying the accuracy of the calibration as outlined in Section 6.4.

6.2.5 SUPER.CAL File

Once a satisfactory set of CAL files has been produced for all active channels, the calibration data processing is nearly complete. The final stage consists of combining all of the required CAL files (each one containing the calibration coefficients for a different data stream) into a single SUPER.CAL file.

As previously mentioned, the practice was followed of incrementing the build number whenever a modification (no matter how trivial) was made to the instrumentation, during the measurement campaign. Generally, these changes had no effect on the majority of transducers, but on a small number of occasions, a modification or repair required a re-calibration of one or other of the transducers. To accommodate such minor changes, the test campaign was divided into two or three periods, each one covered by its own set of calibration coefficients (SUPER.CAL).

6.3 Application of Calibrations to Raw Data

6.3.1 Initial data checking

Once a group of run data files have been transferred from the Winchester to the VAX cluster (via KERMIT) they are appraised using a Fortran program called OFFSCALES. This performs a more comprehensive statistical analysis of the data than the BBC micro version of the program which is only used to determine if each run is worthy of transferring. The

analysis is carried out on raw voltage outputs, so it is performed before the calibration exercise described below. All data streams are scanned for a count of the number of 'offscales' (± 5 volts). A 'fast' data stream (20480 samples per run) is flagged if it is 'flat' (a small range); a 'slow' data stream (80 samples per run) is flagged if its range is large.

Once a data file has been vetted in this way it is ready for the application of calibrations, to convert it from a series of voltage measurements into engineering units (an EXP file).

6.3.2 FORM EXP Program

This is the program which, as its name suggests, actually builds the EXP files. For a given raw data and text file pair the appropriate SUPER.CAL file is chosen; it is likely to contain coefficients based on calibration runs from both just before and just after the data run. The FORM_EXP program processes the raw data file, taking one data acquisition cycle (see Chapter 5) at a time. For each pressure transducer, the 'temperature' (V_i) and common excitation voltage for each cycle are used to evaluate the sensitivity and offset, which are then applied to the 256 samples in the cycle. Warnings may be issued at many stages, if for instance calibrations are being used beyond their range of validity. A correction is made for the centrifugal effect of rotation on the reference pressure. The other fast and slow channels (of Bank 0) are also converted to engineering units and stored in the EXP file, together with all of the information from the run text file.

The EXP file forms the basis for all subsequent analysis, which is performed using subroutines from the "Explib" part of the RotACAP subroutine library to be described in Chapter 9. It is a direct-access binary file, with record length equal to the number of samples per revolution for each fast data stream (generally 128 for this HAWT experiment). Handler routines are used to write the data to file, and to recover information from the file - this simplifies the development of the data analysis application programs. The million samples of data acquired per run, converts to something approaching 4 Mbytes per EXP file.

6.4 Errors and Accuracy

Every measurement made by the instrumentation has an uncertainty associated with it and this is assessed here, following the procedures suggested by Hayward [6.1]. Definitions of the terms used in the following analyses are essential to their understanding and are therefore reproduced from Hayward's work.

i) The difference between the value of a measurement (after all calibrations, corrections etc. have been applied) and the true value is the Error.

ii) The total uncertainty of a measurement is the range within which the true value is likely to lie at a stated level of probability. (Here the level of probablility used is 95% throughout.)

iii) The total uncertainty is made up of the random uncertainty and the systematic uncertainty. The half range random uncertainty, R, represents the scatter of measurements about the measurement mean and is quoted such that 95% of the measurements lie $\pm$R from the mean.

iv) The half range systematic uncertainty, S, represents the maximum difference between the mean value (of a very large number of measurements) and the true value of a measurement at a 95% confidence level.

v) The repeatability of a measuring instrument is the half-range random uncertainty of a typical measurement made by the instrument under specified conditions.

vi) The accuracy of an instrument is the quadrature sum of its repeatability and its half range systematic uncertainty. i.e.

$$\sqrt{(\text{Repeatability})^2 + (\text{Half-range systematic uncertainty})^2}$$

6.4.1 Determination of Accuracy

There are many possible sources of error in the measurement system. Two approaches are available in trying to determine the final accuracy of each of the measurements. Firstly, the possible errors introduced at

every stage of the chain of data acquisition can be estimated from first principles using detailed specification information for the transducers, the amplifiers, slip rings, multiplexers etc. This approach is difficult to implement and may not be sufficiently accurate in itself.

The second approach, which is preferred, involves a consideration of both ends of the measurement chain, and comparison of the 'true' input and the estimate of it made by the measuring system. This approach is described by Hayward and is likely to provide a better indication of measurement accuracy. It does, however, require more information, usually obtained from extensive calibrations.

Each of the types of data stream used in this experiment will be considered in turn and an assesment of the accuracy of each will be attempted. Where sufficient calibration data exists the second approach described above will be adopted. Otherwise a subjective assessment of the accuracy based on the experimenter's observations will be given.

6.4.2 Wind measurement accuracy

An assessment of the accuracy of the anemometry channels is, perhaps, the most difficult since for the cup and Lowne anemometer signals there are several stages in going from the local airflow to the estimate of windspeed in the EXP file.

6.4.2.1 Anemometers

For both Lowne and cup anemometers the digitised channel voltage is first converted into an apparent windspeed (using linear calibration coefficients) and then adjusted to account for the non-linear response of the signal processing equipment (with non-linear calibration coefficients). The windspeed estimate is then further corrected by the manufacturer's own calibration data which accounts for mechanical non-linearities in the anemometer response to wind speed. The accuracy of the first two of these steps can be investigated here but they are unlikely to involve significant error. The accuracy of the third step (involving 'manufacturers' aerodynamic calibrations of the anemometers) may well contribute to larger errors but they are much more difficult to assess.

For the first two steps in converting an anemometer signal into a windspeed estimate the calibration data itself can be used to determine the accuracy of the calibration coefficients. Since all calibrations were performed with the applied parameter of frequency (Hz) and not of windspeed (m/s), again, the conversion factor (or nominal anemometer aerodynamic calibration) will have to be taken from the manufacturer, implicitly.

The worst residual for the four Lowne anemometer calibrations is 0.8 Hz which means that the final fit to the data produces maximum errors of 0.02 m/s. Coincidentally, this is also the approximate size of the possible error due to the finite quantisation levels available at digitisation (i.e. 2.44 mV ≡ 0.8 Hz ≡ 0.02 m/s). The integrity of the calibration source (a signal generator) was also investigated and was not found to produce any significant error. Consequently both systematic and random errors in the calibration process performed here are expected to be very small and should not account for more than 0.05 m/s error.

For the cup anemometer calibration the worst residuals are of the order 0.02 Hz (equivalent to errors of only 0.025 m/s) whilst quantisation errors are approximately 0.022 m/s. As for the Lowne anemometers above, the errors due to the calibration fit and quantisation step are therefore expected to be negligible.

Neither of these error estimates, however, accounts for any systematic errors in the manufacturer's nominal aerodynamic calibration factor nor any errors in the mechanical non-linearity corrections. These quoted corrections are of the order 0.1 m/s for the Lowne anemometers, and 0.1 m/s for the cup anemometer operating up to 10 m/s. Above this speed the cup anemometer correction steadily increases to a value of 0.82 m/s at 25 m/s. Verification of the manufacturer's calibration constants and non-linear corrections is clearly most important for the validity of the experiment. This has been done for the cup anemometer and resulted in the data given in Table 6.1. The windspeed estimates given by the cup calibration used throughout this work are compared with those which would be given by the recent NEL calibration. Above 10 m/s the accuracy of the manufacturers calibration used here is never more than 2.5% below the NEL value with better windspeed estimates at higher windspeeds. Corroboration of the Lowne calibration coefficients is being undertaken by NEL.

6.4.2.2 Wind vane

The accuracy of the wind vane measurements can be determined more easily than that of the anemometers. Firstly the approximate calibration gives a quantisation uncertainty of about 0.18° so the random error should be at least this value. The residuals of the curve fit are encouraging since they show that on average, the linear fit applied to the calibration data produces errors of about 0.4°, the largest value being 0.8°. This tends to suggest that the calibration technique (using a clinometer to set the windvane in each required direction, with anemometer tower lowered) was better than had been expected, with acceptable random errors. The systematic error, however, is much more difficult to quantify in this case. For both the field and mobile test configurations the calibration was performed with the anemometer tower lowered. This means that any offsets caused by uneven rotation about the tower hinges could not be accounted for and bias errors of a few degrees might be introduced. On examination the hinges and geometry of the mobile tower system were not thought to be able to introduce significant errors for all mobile test data. For the tests at the field test site, however, such an assessment was not possible due to the size of the tower. In either case the errors are not expected to be greater than a few degrees, with the mobile system significantly better than that of the field test system.

6.4.3 Torque measurement accuracy

The resolution of each of the torque signals (i.e. the torques represented by the 12 bit digitisation step of about 2.4 mV) are 0.12 Nm for both rotor and yaw torque channels. The rotor torque calibration shown in Figure 6.4 indicates very little hysteresis (for loading/unloading cycles) and a linear response to torque. This is reflected in the curve fit residuals which indicate that the fit to the calibration data is never more than 1 Nm in error. This figure would perhaps indicate the random uncertainty attributable to this channel but does not account for any systematic error inherent in the calibration. The use of laboratory weights for the calibration is thought to have minimised any systematic error to a value comparable to the random error. (Taking the 94.16 Nm calibration spot, a 1Nm bias error would be caused by a 70g error in the mass or a 14 mm error in the moment arm.) Proper evaluation of the random uncertainty which should be attributed to an individual measurement is possible only if many calibrations were

performed. This was not practicable in this case and only two calibrations of the rotor torque channel and one calibration of the yaw torque channel were performed. The two rotor torque calibrations, however, did give encouraging results. They are both plotted in Figure 6.4 and show that the eleven months of operation between them had little effect. Despite the limited calibration data available it seems reasonable to assume that the measurements of rotor torque are accurate to within a few Nm at a 95% confidence level.

For the yaw torque calibration (see Figure 6.5) the residuals also indicate errors in the fit up to 1 Nm. Bias errors, however, are likely to be larger due to the less satisfactory calibration procedure. Unfortunately, only one calibration was ever performed so an accurate assessment of the uncertainty is impossible. However, given that the yaw torque load cell and signal processing used are the same type as for the rotor torque, comparable random errors would be expected. Increased values of systematic uncertainty are sure to exist due to the zero torque dead band (see section 5.1.2) which is estimated to be $\pm$10 Nm in size. Therefore a subjective estimate of the yaw torque measurement accuracy would be given by:-

$$\text{Accuracy} = \sqrt{1^2 + 10^2} \simeq 10 \text{ Nm}$$

and can be seen to be dominated by the systematic uncertainty.

6.4.4 The Power Measurement Accuracy

The five channels associated with the electrical power measurements are made up of two real power channels, two r.m.s. current channels and the line voltage channel. Each of these were calibrated only once as described in Section 6.1.3. The calibration residuals can be used to make estimates of the random errors.

For the real power measurement channels the largest residual is about 30 Watts whilst the quantisation errors are of the order of 4 Watts. Random errors can thus be estimated to be no larger than 30 Watts although nothing can be said about systematic errors. The r.m.s. current channels indicate maximum residuals of 0.1 Amps with quantisation errors equivalent to only 0.01 Amps. Again no estimate of systematic errors can be made but the random errors are likely to be of the order of 0.1 Amps. Finally for the line voltage measurements the quantisation errors are

equivalent to about 0.25 Volts with residuals (based on only four calibration spots) of the order of 1 Volt.

6.4.5 The accelerometer accuracy

Since no calibration data for this channel was acquired an assessment of accuracy is impossible. Any estimate would be unreasonable since the low pass filter present in the signal processing circuits means that the gain is a function of frequency. The quantisation uncertainty of approximately 0.002 m/s^2 is negligible compared to the other potential sources of uncertainty.

6.4.6 The body yaw angle sensor accuracy

The largest source of uncertainty in the body angle measurements is that produced by the hysteresis shown in the calibration (Figure 6.10). This is estimated to be in the order of $\pm 1.3°$ and is very much greater than any quantisation errors (0.17°). The residuals indicate that the error between the fit and the calibration data itself is dominated by the hysteresis and therefore gives confidence in assuming that the applied angles were accurate to better than 0.5° and that the potentiometer is adequately linear with rotation.

6.4.7 Pressure measurement accuracy

As stated above the accuracy will be estimated from assessments of the systematic uncertainty and random uncertainty at the 95% confidence levels. The assessment of systematic uncertainty in the pressure transducer measurements relies on a special calibration run performed using a more accurate method of determining the applied pressure and on the analysis method described by Hayward [6.1]. The Druck digital barometer (described in Chapter 4) was connected to monitor the reference pressure line through which the calibration pressure is applied during run numbers 180 and 181. As well as the usual measurement of pressure obtained from the Nutem manometer (which is usually used to determine the calibration coefficients as described in Section 6.1.6) an independent measurement was recorded from the barometer to an accuracy of $\pm$ 15 Pa (as quoted by the manufacturer's specification).

A pressure of approximately 1700 Pa was applied and removed nine times and the results digitised for a total of 37 transducers in the usual

way. The measured values of pressure (Pi) at each calibration spot were compared with the much more accurate Druck measurement (Pc) and used to determine the percentage discrepancy (d) for each transducer from:-

$$\frac{Pc}{Pi} = 1 + \frac{d}{100}$$

The discrepancies for each of the pressure transducers were aggregated to determine their mean (md) and standard deviation (sd). The systematic uncertainty (Si) for the pressure transducer measurements is then given by:-

$$Si = md + 2.05*sd$$

where 2.05 is Student's t for a batch of 37. This exercise was repeated nine times to account for each of the calibration spots performed. The nine values of Si produced varied between 0.729 % and 1.731 % with a mean value of 1.222 % (see Table 6.2). This is therefore the estimate of systematic uncertainty inherent in the pressure measurement system assuming that the Druck measurements are true. Since the value is positive it can be seen from the above equations that the SPX50DN system tends to underestimate the true pressure by about 21 Pa (1.222 %). This may be a pessimistic assessment of the pressure transducer measurement accuracy because the Druck digital barometer measurements may not be exactly true. Since the average discrepency between the Druck instrument and pressure transducer measurements is only 21 Pa, it is possible that the differences are dominated by Druck instrument errors (given by the manufacturer as $\pm$15Pa). Conversely, however, the exact reverse is also possible if the Druck instrument is underestimating the true pressure by the maximum possible 15 Pa. Therefore, the conclusion must be made that the systematic uncertainty in the pressure measurements lies between 6 and 36 Pa.

The random uncertainty or repeatability can also be determined from the calibration residuals. The method used [6.1] involves calculation of the pair repeatability for two identical instruments, or in this case two pressure transducer channels. For two chosen channels the difference between the measurements (Pi_1-Pi_2) can be determined. (The measurements which result from the calculated calibration coefficients must be used and not those which are used to determine the coefficients). Repeating this for 20 calibration spots enables mean and standard deviation values

of Pi_1-Pi_2 to be determined. The pair repeatability R_{12} is then found by multiplying by the appropriate value of Student's t for the batch. This entire process is then repeated at least three times to give a number of estimates of the pair repeatability R_{12} which are only accepted if the ratio between the highest and the lowest is less then 2. The assumption is then made that repeatability of each of the channels is the same and that there is no difference between the pressures seen by the transducers at the time of calibration. The repeatability for each of the two channels is then given by:-

$$R_1 = R_2 = R_{12} / \sqrt{2}$$

This process can obviously be repeated 741 times for all pair combinations of 39 pressure transducer channels, and could involve every calibration spot performed during the FIB experiment. This is not practicable however, and it was therefore carried out for only 15 pairs and only using the data from calibration Runs 155 to 182. For each pair of transducers 60 calibration spots were compared in groups of twenty spots at a time. The three resulting values of pair repeatability were then accepted or rejected as described above and the average value for the fifteen pair combinations was found (see Table 6.3).

The results show little scatter and are therefore sufficient to conclude that the mean pair repeatability is 10.2 Pa. Using the above equation then gives an estimate for the repeatability of each of the pressure transducer channels of about 7 Pa.

The accuracy for a typical pressure transducer channel is then given by the quadrature combination of the systematic and random uncertainties. Assuming the worst case for the value of systematic uncertainty (36 Pa) this results in an accuracy of approximately ±37 Pa dominated by the systematic uncertainty. By assuming the best value of systematic uncertainty (6 Pa) the resulting accuracy is approximately ± 10 Pa. It can therefore be assumed that the pressure measurement accuracy lies between ±10 and ±37 Pa.

The results presented in later Chapters deal exclusively with pressure coefficients rather than in terms of true pressure. The above pressure measurement accuracies should therefore be stated in dimensionless form for each of the two spanwise stations which have approximate dynamic heads of 200 Pa (35%R) and 900 Pa (75%R). Consequently, for the inner

station the pressure measurement accuracy lies between ±0.05 and ±0.185 Cp and for the outer station, between ±0.011 and ±0.041 Cp.

CHAPTER 7

PERFORMANCE OF THE NON-INSTRUMENTED ROTOR

7.0 Summary

Performance data for the newly built wind turbine was acquired during the machine commissioning phase whilst fitted with non-instrumented blades. Currently recommended practices for the acquisition and analysis of wind turbine performance data were examined, all measurements here being in the form of 'one minute averages' of wind speed and rotor mechanical power.

Only part of the complete instrumentation and data acquisition systems which have been described in Chapters 4 and 5 were used here. The differences between the two systems are described in 7.3.

Data was acquired between February and May of 1988 resulting in nearly 5000 one minute average data records. These were transferred from floppy disc to the Cranfield VAX cluster system and analysed using a purpose written Fortran program called 'Perform'.

Much useful turbine operating experience was obtained and the machine performance was found to be satisfactory but slightly below that given by a typical prediction code.

Reynolds number effects appear to be negligible over the rotor speed range tested but the effects of wind direction were more significant. This was thought to be caused by the asymmetric anemometer support geometry.

7.1 HAWT Performance Evaluation

A review of the literature on the subject of wind turbine performance evaluation revealed a host of different techniques for both the data acquisition and data analysis. [4.3], [7.2], [7.3], [7.4], [7.5]. In an attempt to regularise this situation the International Energy Agency produced a set of guidelines [4.3] for the complete assessment of a wind turbine's performance. These guidelines are shortly to be superseded by a European standard which is, as yet unpublished (see [7.1]). In

consequence the IEA guidelines have been adhered to as closely as possible but, as with most other work on this subject, certain departures from them have been inevitable and justification that these have little effect on the final results must be given.

The most common short cut to a reasonable set of performance data is in the choice of an averaging time which is less than 10 minutes. The work of Stacey [7.2] addresses this problem directly by acquiring data based on a data averaging time of 30 seconds but analysing it based on times of 30 seconds, 1 minute, 2 minutes, 5 minutes and 10 minutes by further averaging of the same initial data-base. The results show very little change in the mean Cp–λ relationship although the standard deviation does increase with the shorter averaging times, especially at high tip speed ratios. Hausfield [7.3] also reaches this conclusion showing that the standard deviation of the power is doubled as the averaging time is reduced from one minute to 2 seconds, but increased by a factor of only 1.25 when it is reduced from 5 minutes to 1 minute. Both Hausfield and Christensen [7.4] indicate few problems with reduced averaging times for small wind turbines and in consequence the 1 minute averaging time has been chosen for this work.

There are many ways in which the data could be analysed and displayed with no clear standard for either. The method of bins is one of the most favoured methods for further data averaging. This is essential for any progress in the analysis as is demonstrated by the 'scatter plot' given in Figure 7.5. This includes every valid 'one minute average' data spot acquired during the entire performance measurement phase. The amount of scatter in these results is typical of that found in other work (see [7.5]).

7.2 Performance Test Facility

The wind turbine described in Chapter 3 (see Table 3.1) was initially installed at a site within the SME "Test Area" (shown in Figures 7.1, 7.2 and Plate 3). The surrounding terrain is quite favourable for wind turbine performance testing, with an excellent fetch from the prevailing wind direction (South–West) and no large obstructions to the North or South. The East and South–East approaches to the site are not as good, although all of the closest buildings are set in cuttings and therefore well below the wind turbine.

The wind turbine tower was of modular construction and was capable of being raised and lowered using a hand operated winch. With the tower lowered the wind turbine could be transferred from its test/transport frame onto its tower top mounting plate. All cables and pipes between the ground based data acquisition system and the wind turbine were attached to the tower with a loop across the yaw bearing allowing for ±270° of continuous rotation from the 'home' (South-West) position. The cables from the turbine and anemometer tower fed into a manhole near the base of the wind turbine tower. From here they were routed through a pair of underground pipes running the 20m to the control room (Test House 17). All the data cables were sent down one pipe and all mains/power cables down the other pipe which entered the control room in an adjacent corner. In this way the two sets of cables were kept as far apart from each other as possible. The data acquisition system and the wind turbine control system were laid out and connected in the control room and allowed for complete operation of the system from 'indoors'. A window in the control room allowed the turbine to be viewed during operation.

With the tower erect the hub height of the turbine was approximately 11.5 m. (The hedge which crossed the South-West approach to the turbine was estimated to be 2-3 m high). The anemometer tower was sited 9.2 m from the wind turbine tower (see Figure 7.2) in approximately the prevailing wind direction (i.e. South-West from the wind turbine tower), with the Vector cup and wind vane at wind turbine hub height. The wind direction measurement convention is also given in Figure 7.2.

7.3 Data Acquisition

Wind turbine performance data was obtained during an early phase of machine development because there are comparatively few data streams required to obtain an assessment of the wind turbine rotor behaviour. The only signals needed are those of rotor power (speed and torque) and wind speed and direction. Hence this work could be carried out with completely non-instrumented rotor blades. The instrumentation used to make these measurements is the same as that used for the later work and has already been described in Chapter 4. Only those aspects which differ from those previously discussed are given here.

For the performance measurements, the only data streams required from the data acquisition system are those obtained from Bank 0 of the CED

1401 analogue-to-digital converter. As shown in Table 5.4, these signals include yaw and rotor torques, all the electrical parameters (line voltage, currents and powers), all the anemometer outputs and the wind vane output.

The data streams connected to Banks 1,2,3,4 and 5 of the CED 1401 are those from pressure transducers. Since plain, non-instrumented blades were used for the performance measurements these channels were left unconnected. Hence, while the pressure transducer systems were being developed and built the turbine was allowed to run, obtaining performance data and also allowing checking and debugging of the Bank 0 signals.

The sixteen channels of Bank 0 data are averaged over one minute periods and then stored. Fortunately the averaging requirement is within the capabilities of the calibration command, 'WNDML,C', written in machine code and stored within the CED 1401 (see 5.3.2). This simplifies considerably the BBC written software for acquiring the data since the averaging does not take place within the BBC micro itself. Instead, time averaged data is transferred from the 1401 to the BBC where, if relevant, it is saved on floppy disc. This scheme also has the benefit of keeping the amount of stored data to a minimum.

One potential problem, however concerns the data acquisition rate of the WNDML,C command which is 87 Hz per channel and cannot be adjusted. Consequently each one minute average value is formed from 5150 samples and the potential exists for aliassing of information above 43.5 Hz. For most data streams this is not serious but it may become important for more dynamic signals such as that from the rotor torque load cell. However, as stated in [7.6], aliassing will only have the ability to affect the standard deviation of the data within the averaging period and will have little consequence for the mean values.

The data was acquired under the control of a BBC micro computer program called 'BANK0'. A block diagram of some of this program is shown in Figure 7.3. It is a menu driven program but only the data logging option is of interest here. (The other options provide Disc Filing System support during program execution and program development routines which assisted in debugging the program and all the associated hardware).

At the heart of the program lies the data acquisition loop. The CED 1401 contains a calendar clock and first this is read to determine the date. The file into which the performance data will be written is opened with its name made up from the day and month (e.g. "20/APR", "17/MAY"). The 1401 is then instructed to begin assembling one-minute averaged data. This is done with the calibrate command in the form WNDML,C,5150,0; .

The calibrate command is used here in a way it was not intended for but nevertheless works very well in this application. The command causes the 1401 to sample all channels in a series of 5150 separate scans each of which takes between 11 and 12 milliseconds. Each channels' mean, maximum and minimum values are stored in CED 1401 memory (each as a pair of bytes) and taking up a total of 576 bytes.

Whilst the CED 1401 is performing the calibration scans the BBC micro is used to obtain other relevant data. Firstly the outside air temperature is calculated using the BBC's own A-D converters (see 4.2). Secondly the barometric pressure is read from the DRUCK Digital Barometer via the BBC's RS423 port (see 4.3). Next the wind turbine rotor speed is estimated by finding the time taken for 128 rotor revolutions. This operation has to be performed by fast assembly language code running in the BBC micro because the 1401 does not store this data whilst executing its calibrate command. (Event 1 pulses from the wind turbine slotted disc system are applied to the BBC user port B for this purpose - see 5.2.1.)

The CED 1401 clock is then read again to give the one-minute average data record a time stamp which is relevant to about the middle of the one minute period. For convenience the last one minute averaged data record is displayed on the screen at this point and remains on the screen until the next record can be displayed - about one minute later.

When the CED 1401 has finally completed its 'calibration' scans this is detected by the BBC micro and the 576 byte data block is transferred to BBC memory. Since the data relates to all 96 of the 1401 channels much of it is undefined and therefore can be discarded. Only those bytes concerning the mean values on Bank 0 channels are stored on floppy disc. Even the maximum and minimum values for Bank 0 are not retained so that the size of the data files can be kept to a minimum. The data is stored in a 64 byte record which also contains the BBC acquired values for

rotor rpm, barometric pressure, outside air temperature, the time and any notes which the user had entered.

The data acquisition loop is then repeated over and over again producing large data files containing hundreds of 'one minute average' 64 byte records.

7.4 Data Transfer and Analysis

The performance data described here was acquired during the commissioning phase of the wind turbine and consequently some major changes took place over this period. By far the most significant of these were the three yaw control configurations tried which are likely to affect the turbine performance and can therefore be used to divide the data collected into three groups. Data at three rotational speeds was also collected and this forms the second major variable parameter in the data base. The nine different combinations are shown in Table 7.1. This indicates the data files which fall into the 5 categories which were actually tested, each of which is identified as a subset of Build 1; Builds 1A, 1B, 1C, 1D and 1E.

The entire performance data-base was transferred from floppy disc to the Cranfield Vax cluster system using a standard transfer package Kermit. Nearly 5000 sets of 'one minute average' data records were transferred forming a data-base of approximately 300 Kbytes. The performance data file format is completely different from that produced by the instrumented blade measurements and is consequently unsuitable for analysis by the 'RotaCAP' subroutine library (see 6.2.2). A purpose written Fortran program called 'Perform' was developed which is capable of reading data-base records (containing both hex and ascii data), calculating and manipulating bin average values and outputting the results in the form of tables and plots. A flow chart of the program is given in Figure 7.4 which shows how each 'one minute average' data spot is processed.

'Perform' was written to produce several types of output. Plots of power vs. windspeed can be produced and in addition two types of non-dimensional versions can be catered for (Cp vs. λ and Cp/λ^3 vs. $1/\lambda$). For each type of plot raw unbinned data can be plotted ('scatter plots') which show each one minute average data spot. Binned data can also be plotted in terms of the bin mean value with vertical bars

indicating the bin standard deviation. In addition to the plotted output, tables of both the unbinned and binned data can be produced. It was also thought useful to be able to compare the measured data with a typical strip theory performance prediction. Consequently the results from an analysis using the PROP code [1.14] were built into the 'Perform' program for inclusion on many of the plots.

Different versions of the program provided the opportunity to investigate the effects of changing the binned parameter, the bin width and of averaging time.

7.5 Results and Discussion

7.5.1 Data overview

The scatter plot of Figure 7.5 displays every valid one-minute average data spot acquired during the performance testing. Each spot shows the average power coefficient and tip speed ratio over a one minute period. Plotting these non-dimensional quantities allows the entire data base to be shown together so that trends in the data can be identified. The 'Perform' program allows plots like this to be created with spot colour determined by one of four criteria;-

1) Yaw configuration
2) Run r.p.m. (nominal)
3) Yaw torque
4) Wind direction

By plotting these four scatter plots the effects of each of the parameters can be inferred from the groups and patterns of colour. In Figure 7.5 (using criteria 2 above) the three displayed colours indicate data taken at nominally 333, 395 and 458 r.p.m. The plot appears to show that the 458 r.p.m. data set exhibits less scatter than either the 333 or the 395 r.p.m. data sets. Referring to the tabulated data also produced by the program, the statistics given in Table 7.2 were extracted to form the average standard deviation of power coefficient. It can be seen that similar numbers of data spots are involved and yet the C_p standard deviation for the 458 r.p.m. data is considerably lower than that for the 333 and 395 r.p.m. data.

The first potential explanation of the reduced scatter for the 458 r.p.m. data is the use of different yaw configurations during testing. (see Table 7.1). Referring to Figure 7.6 indicates that this is unlikely because all of the 395 r.p.m. data (Build 1E) was taken with the same yaw configuration as most of the 458 r.p.m. data (Build 1D ; very little Build 1C data was acquired). Another explanation for the reduced scatter in the 458 r.p.m. data must therefore be sought.

Figure 7.7 shows the data plotted using the yaw torque criteria. The five colours represent five equal width yaw torque bins ranging between the maximum and minimum torques. No clear link between this and the yaw configuration plot (Figure 7.6) can be made. Additionally, the reason for the difference between the 458 r.p.m. data and the rest is not evident.

The clue to the reduction in scatter for the 458 data is given by Figure 7.8 which uses criteria 4. In this plot the average wind direction during the one minute period is used to determine the spot colour. Five bins of wind direction between -135° and +135° are set up and indicate that most of the data from the central bin may coincide with the data at 458 r.p.m. In other words the plot suggests that the data acquired with the wind passing directly over the anemometer tower and then into the wind turbine was mostly 458 r.p.m. data and perhaps explains the reduced data scatter.

In order to confirm this hypothesis a modification to the program was made so that the entire data base could be binned with respect to two parameters at once. Essentially this then enabled the effects seen on the colour scatter plots to be quantified. Each tip speed ratio bin was also divided into five wind direction bins so that every data spot was placed into one of the 125 available bins (25 tip speed ratio bins times 5 direction bins). The resulting grid of binned data is shown in Table 7.3 and indicates that, below tip speed ratios of 8.0, a total of 1306 spots of data were binned.

The five resulting Cp-λ curves (one for each set of direction bins) are shown in Figure 7.9. The data from direction bins [-67.5 to -22.5] and [22.5 to 67.5] provide the highest power coefficients over almost the entire tip speed ratio range. The bin mean Cp maxima are 0.388 and 0.398 respectively (see Table 7.3) and represent some of the highest mean power coefficients calculated. In the [-22.5 to 22.5] direction bin

which spans the zero direction condition (anemometer directly upwind of the wind turbine) the maximum bin mean Cp is only 0.342 and is consistently the lowest curve up to tip speed ratios of 8. The intermediate curves represent the data from the [-135 to -67.5] and [67.5 to 135] direction bins and indicate that the changing Cp-λ relationship appears to be symmetrical about the zero wind direction.

Possible explanations of this phenomenon have been examined and resulted in two main hypotheses. Firstly the cup windspeed measured at the anemometer will be most well correlated to the windspeed at the wind turbine for the zero wind direction. In cases where the wind direction is, for example, 90° the cup windspeed measurements will obviously be less well correlated with the windspeed seen by the rotor and therefore also the rotor power. One would, however, expect the correlation to be lowest at $\pm$90° and highest at 0°. The results found here do exhibit this characteristic as shown by Table 7.3. The change in power coefficient standard deviation from one direction bin to the next (for a given tip speed ratio) shows the minimum value for the zero direction case. The actual mean Cp value, however, should not be affected by this since for all non-zero directions the cup is as likely to see a higher windspeed than that relevant to the rotor as it is a lower one. Local terrain effects could cause variations of the bin mean Cp but are not expected to be symmetrical as indicated by the data.

The second hypothesis to explain these effects is that concerning the local aerodynamic flow through the cup anemometer. Cup windspeed measurements have been shown to be susceptible to the cup anemometer support geometry [7.7] and can account for significant errors in estimates of windspeed. This is very significant for power coefficient calculations which depend upon the cube of the windspeed. Given that the local aerodynamic flow through the cup anemometer is dependant upon the wind direction (due to the fixed direction of the support boom) it can be shown that the above noted changes in power coefficient could be caused by only a 5% change in the cup sensitivity.

7.5.2 Binned data analysis results

Further versions of the program were used to perform data binning in slightly different ways. In addition to the tip speed ratio bins of 0.5 width, a second version used bins of wind speed with a width of 1 m/s. Both programs produced tabulated results and also the same three kinds

of plot. Figures 7.10, 7.11 and 7.12 show the relative merits of the different types. Plotting Cp vs. λ (Figure 7.10) highlights the differences between measured and predicted power at high tip speed ratios where such differences are relatively unimportant. The differences at low tip speed ratio, however, are disguised despite the fact that they are of much greater significance. Conversely, a plot of Cp/λ^3 vs. $1/\lambda$ (Figure 7.11) shows a less distorted non-dimensional relationship and indicates that the predicted-measured discrepancies increase with $1/\lambda$ (or windspeed). This type of plot should be preferred over that given in Figure 7.12 (power vs. windspeed) since data from different rotor speeds can be plotted together to form a single curve. Of the two types of non-dimensional plot the Cp vs. λ plot is usually used despite its shortcomings. In the plots shown here the Cp-λ plot is used most frequently because it tends to spread the data out and enables the scatter to be more easily appraised.

Another, perhaps obvious result, is that plots of Cp vs. λ are best produced by data binned with respect to λ whilst plots of power vs. windspeed and Cp/λ^3 vs. $1/\lambda$ are best defined by the same raw data binned with respect to windspeed. This is clearly shown by the standard deviation bars given on the Cp-λ plots of Figures 7.10 (λ bins) and 7.13 (windspeed bins) and infers that Figures 7.10, 7.14 and 7.15 are the more accurate since the binned parameter is used as the abscissa.

In another version of the performance program the effect of averaging time was investigated. The code was rearranged so that sets of ten contiguous one minute average data spots were taken together to form a single ten minute average. No clear differences were found between the two types of analyses although the reduced size of the ten minute average data set did not allow rigorous statistical comparisons.

7.5.2.1 Comparison with theory

Figure 7.10 shows the discrepancy between the measured data and the performance calculated by the strip theory code due to Hibbs and Radkey [1.14]. The maximum Cp indicated by the data analysis is approximately 0.37 at a tip speed ratio of about 5. The strip theory prediction, however, gives a maximum Cp of 0.43 at the same tip speed ratio. The scatter in the data is quite considerable as can be seen by the ± 1 standard deviation bars. The prediction is always more than one standard deviation higher than the data. The data is generally thought to be of

good quality although at tip speed ratios less than 4 there is a lack of data with bin mean tip speed ratios exceeding the bin centre value. Consequently at low tip speed ratios the calculated power coefficients are likely to underestimate the true values.

The most obvious reason for the measured/predicted discrepancy is the effect of the blockage created by the wind turbine body (see Plate 3) which geometrically accounts for 4% of the rotor swept area. Estimating the aerodynamic effect to be up to twice this means that the blockage could account for something like an 8% loss in power coefficient. The minimum difference between measured and predicted Cp, however, is about 19% (occuring at Cp max) and hence may not be completely accounted for by the blockage. It can therefore be concluded that there is also some element of over-estimation present in the PROP code power predictions.

7.5.2.2 Effect of r.p.m. on rotor power

Figures 7.12 and 7.15 show the entire data base binned with respect to either windspeed or tip speed ratio, as appropriate. The effects of rotor speed on the wind turbine performance can be investigated by splitting the data base into its rotor speed sub-divisions and running the analysis code on the three separate data sets. Space does not permit the presentation of all of the resulting plots since their differences from Figures 7.12 and 7.15 are relatively minor. Some conclusions about the effects of rotor speed, however, can be drawn from the tabulated data reproduced here in Table 7.4.

Firstly, the effect of rotor speed on power is as would be expected. The power curve at low windspeeds shifts downwards by about 150 Watts in going from 333 to 395 r.p.m. and then by a further 190 Watts at 458 r.p.m. This low windspeed power difference is slowly eroded as the wind speed increases until, by 12 m/s, all three rotor speeds produce about the same amount of power (approximately 2.5 kW). Unfortunately, windspeeds greater than 13 m/s are not available in the 395 and 458 r.p.m. data sets so the trend could not be followed any further. The predicted curves at each rotor speed did, however, indicate that the power produced at 458 r.p.m. was the same as that produced by the 333 r.p.m. case at about 11 m/s and that by 14 m/s the higher rotational speed would result in almost 1 kW of extra power over the 333 r.p.m. case. It should be remembered, however, that the prediction nowhere

indicates the onset of stall (see Figure 7.15 which indicates the predicted power for a rotor speed of 400 r.p.m.).

In the case of the 333 r.p.m. data set, where data was acquired up to 18 m/s, gentle stall of the rotor is apparent. (See Figure 7.15, which is made up of only 333 r.p.m. data above 12 m/s.) The rotor is still not fully stalled by this windspeed although the deviation from the prediction increases quickly. The pressure measurements discussed later should help to identify the cause of this behaviour.

7.5.2.3 Effect of r.p.m. on rotor power coefficient

The Cp–λ plots also indicate that the performance of the machine is best at the middle rotor speed tested. The data given in Table 7.4 shows that the maximum power coefficients produced are 0.3720, 0.3880 and 0.3437 for rotor speeds of 333, 395 and 458 r.p.m. respectively. It is unfair to say that this is conclusive since the data indicates that the maximum power coefficient may not have been reached for the 458 r.p.m. case.

The slightly improved performance at 395 r.p.m. may be explained in several ways. Firstly, the different yaw configurations (see Table 7.1) used during testing would certainly affect the turbines ability to extract the optimum amount of the winds kinetic energy. It is possible that the damped yaw characteristic of the turbine during the acquisition of all of the 395 r.p.m. data enabled the machine to track the mean wind more accurately and consequently slightly improved the performance.

A further possibility is that the small changes in efficiency are Reynolds number effects. This is possible if the performance of the NACA 4415 aerofoil is relatively insensitive to Reynolds number in the range 0.3 to 0.5 million. According to both Ostowari et al [7.8] and Saliveros [3.1] the performance of the aerofoil can both improve and degrade with increasing Reynolds number depending upon the angle of attack although the effects are small.

It must, however, be concluded that the effects seen here are not sufficiently conclusive to support any of these arguments. The effects of wind direction demonstrated above are also contained within this data. They have been shown to cause changes in power coefficient which are themselves greater than the possible effects on Cp due to r.p.m.

Without further systematic testing the true cause of these small effects cannot really be determined.

7.6 Conclusions

i) As a result of the initial performance measurement program the newly designed and built wind turbine has been shown to perform satisfactorily. The mechanical and electrical design of the machine were found to be good with few in service problems encountered.

ii) The Marlec blades used appear to behave well and produce their rated power (1kW) in winds of 10 m/s (allowing for modest mechanical to electrical power conversion losses). The rotor shows signs of stall regulation (4.5 kW of mechanical power are produced at windspeeds of 18 m/s) but to limit the power to only 1 kW an active (yaw?) regulation system would be required.

iii) The main difficulty encountered during operation was in arriving at a suitable method of yaw control. After trying three tail vane configurations a suitable system using mechanical damping was found. In this mode the yaw behaviour of the turbine was benign.

iv) Performance curves were measured at three different rotor speeds and for three yaw configurations although these parameters were not investigated systematically. Tests with a rotor speed of 395 r.p.m. produced marginally the best performance although all measurements indicated lower power coefficients than those given by the prediction. The data base was sufficiently populated only in the lower windspeed range giving less certain results for winds higher than 14 m/s.

v) Reynolds number effects appear to be negligible over the rotor speed range tested but the effects of wind direction were more significant. This was thought to be caused by the asymmetric anemometer support geometry.

vi) Extending the data base, especially at high wind speeds and with the finalised yaw control method would be useful and allow comparisons with the pressure measurements over a wider range of windspeeds.

vii) The decision to discard the minimum and maximum values recorded during each one minute average period (see 7.3) does not allow any wind turbulence information to be inferred. Any further tests should produce larger data base records and hence allow this information to be saved and exploited.

CHAPTER 8

FULLY INSTRUMENTED BLADE TESTING

8.0 Summary

After completion of the performance measurements described in the previous Chapter, the wind turbine was fitted with the partially instrumented blade and prototype pressure transducer signal processing circuits. Data from the eight pressure transducers was then acquired at the conventional field test site with the turbine in its free yaw mode. The analysis of these measurements is not reported in this thesis.

The controlled velocity tests described in this Chapter were performed with the fully-instrumented blade and the complete data acquisition system as described in Chapters 4 and 5. The results are discussed in the following Chapters and future comparison with the field site data (PIB) is expected to highlight the effects of turbulence.

The mobile facility used for the testing is briefly described in 8.1 and the data acquisition and preliminary analysis procedures used are discussed in 8.2 and 8.3 respectively.

8.1 The Mobile Test Facility

In order to carry out controlled velocity experiments the mobile test facility shown in Figure 8.1 and Plate 4 was developed. The facility consists of a fabricated trailer towed by a powerful car and its design, construction and commissioning, discussed below, are fully reported in [8.1].

8.1.1 Design, construction and commissioning of the car-trailer system

The 4.2 litre tow car was capable of pulling the experiment along the runways of Cranfield airport at speeds up to 25 m/s. The anemometry system discussed in 4.1 and shown in Figure 4.1 was mounted on a braced aluminium frame. This bolted directly onto a standard car roof rack fitted to the tow vehicle and, with the rear mounting bolts removed

allowed the whole assembly to be lowered for access to the instrumentation.

The trailer structure was fabricated from hollow section steel tubing, welded together to form a very stiff space frame. The front and rear suspension units from a large British estate car were bolted directly into the frame to form a heavy rolling chassis. The original springs were changed for stiffer ones to improve the ride quality but the conventional braking system was retained and connected to its own hydraulic supply independent of that of the tow car.

The trailer was joined to the car towing hitch via a drawbar which provided for both trailer steering and braking. The trailer front suspension unit retained its steering gear which was controlled by the drawbar angle via an adjustable crank. This allowed the ratio between the drawbar angle and trailer front wheel steer angle to be varied. A 1:1 ratio had been found best for manoeuvering the system whilst the 1:3 position provided better directional stability during straight line runway testing. An overrun system within the drawbar actuated the trailer braking system such that no more than 50% of the total braking effort could be applied at the trailer wheels.

A guyed tower of the same type as that used for the performance tests (see 7.2) was bolted to the trailer. A pivoting base allowed the tower to be raised and lowered by a hand operated winch. Once lowered the tower top then projected from the rear edge of the trailer so that the wind turbine could be transferred to or from its test/transport frame. Three other major components were installed in the trailer. A bottle of nitrogen gas fitted with a regulator was carried within the trailer frame to supply the wind turbine braking system. A 7.5 kW diesel powered generating set was installed between the trailer front suspension and the wind turbine tower. Power for both the operation and control of the wind turbine and to supply the data acquisition system were derived from this. Finally a "dummy" electrical load consisting of several 1 kW electric fire elements was positioned near the rear of the trailer.

The commissioning tests carried out on the car/trailer systems were designed to ensure that the required controlled velocity tests could be carried out both safely and satisfactorily and are more fully described in [8.1]. Indoor tests were performed to determine the lateral force

required to roll the trailer over and also to derive a satisfactory method for assessing the guy-rope tension (pre-load). The first runway tests were carried out with 280 kg of concrete fitted in a frame at the tower top to represent the wind turbine mass. Further tests simulated the effects of rotor drag by the addition of a large wooden board which could be set to represent the rotor thrust in both axial and yawed flow. These runway tests demonstrated that the performance of the car/trailer system met the design specifications for acceleration, maximum speed, braking and steering. They also showed that the pitch and roll stability of the trailer were satisfactory but emphasised the importance of using the smoothest of the three Cranfield airport runways.

To complete the commissioning of the mobile system, flow visualisation tests were performed to determine the nature of the air flow over the car and trailer. Coloured smoke was released automatically from the anemometer tower and showed that the extent of the flow distortion caused by the car was well below the turbine rotor disc.

8.1.2 Installation of the turbine and data acquisition system

The fully tested car/trailer system was completed in March 1989. The turbine and its associated data acquisition equipment were then installed and commissioned. With the trailer tower lowered, (concrete removed) the wind turbine was transferred from its test/transport frame and bolted to the tower. The six electrical cables which connect the turbine to the data acquisition system were then attached to the tower (allowing for turbine yaw) passed along the trailer drawbar and into the car boot via a pair of cut-outs. Cables from the anemometers were brought down the anemometer tower and also passed into the car boot. The CED 1401 and 'BOB' (see Chapter 5) were then secured in the boot and the relevant connections made. The turbine control box and the BBC micro computer for data acquisition control were installed in the rear of the car in place of the rear seats. Holes in the rear bulkhead allowed cables to connect these with the equipment in the boot and also with the turbine on the trailer. All cables connecting the car and trailer were fitted with plugs and sockets in the car boot so that the car and trailer could be easily separated.

One of the 3-phase socket connectors in the boot was the mains feed to both the turbine control box and the entire data acquisition system. During mobile operation this would be connected to the output from the

diesel generator but for the lengthy task of system commissioning, a connection to the local grid was made. This meant that the debugging phase, which was carried out within the School of Mechanical Engineering hangar, could be performed without operating the diesel.

With the entire mobile testing facility brought together for the first time numerous systems were found to be not working correctly or not working at all. Careful checking and rectification slowly brought the whole system to repeatable operation with the majority of the time spent in ensuring the correct operation of each of the forty pressure transducer signal processing circuits. In contrast, all of those systems which had previously been commissioned for the performance measurements (see Chapter 7) were found to work satisfactorily almost immediately.

One of the main tools used in checking out the data acquisition system was the QLOOK program (see 5.4.1) which enabled the analogue outputs from one of the CED 1401 banks to be displayed on the monitor. By the time that all 96 channels were functioning correctly the voltages expected on each one had become familiar so that any channels which then developed a fault were easily identified.

The final step in commissioning the data acquisition system involved acquiring a 'run' of data. With the entire system inside the SME hangar and powered from the mains, the wind turbine was motored up to speed and the data acquisition control code, H/10/22 (see 5.4.3) was initiated. Once the data acquisition process was complete the data was copied onto the winchester disk in the usual way and then transferred to the VAX cluster system. Here the OFFSCALES code was used to determine the statistical spread of voltage data on each channel so that these results could be compared with those from QLOOK. The comparison indicated that (with some allowance for the rotational effects) the data acquisition system appeared to be working satisfactorily.

The final hurdle to be overcome was in repeating this test with the entire system powered from the diesel generator instead of the grid. The autonomous operation of the experiment had been expected to be problematic because the entire electrical system would float with respect to ground. No difficulties were encountered, however, with the only noticeable difference between the test data acquired under grid power and that acquired under diesel power being the rotor r.p.m. The

nominal rotor speed under diesel power was about 340 r.p.m. whilst when connected to the grid a slightly slower speed (333 r.p.m.) was recorded. This was assumed to be caused by the diesel generator frequency being slightly greater than 50 Hz but was not seen to adversely affect the turbine control or data acquisition systems in any way. With the one exception of the rotor speed the spread of data found during the diesel power run was very similar to that from the grid powered run with all channels appearing to behave satisfactorily.

8.1.3 Preliminary testing

One of the last difficulties to be encountered whilst setting up the experiment was that of the source of the pressure transducer reference pressure. The philosophy used in previous work [4.1] and in earlier tests with the partially instrumented blade was to utilise local static pressure (i.e. atmospheric pressure) as the reference pressure and this was found to work well. The end of the pipe feeding the reference pressure system would be left open and clear from draughts. In this way, local atmospheric pressure could be sensed and applied to all of the transducer reference ports simultaneously.

For the mobile system, however, sensing atmospheric pressure was rather more difficult due to the motion of the entire system. Several options were considered including trailing the end of the reference pipe in the flow, attaching the end of the pipe to a wind vane arrangement or allowing the pipe to open out to atmosphere in the centre of a large flat plate over which the flow could be expected to be tangential. None of these were expected to be adequate so a system utilising a standard pitot-static probe was adopted. This was mounted on the car borne anemometer tower pointing upstream in the undisturbed flow above the main cross bar (see Plate 4). Tests to determine if the pressure sensed in such a way would be adequate were deemed essential mainly because of the directional sensitivity of such devices and hence these were among the first tests to be carried out on the runway.

A total of six runway tests were carried out; data at 3 windspeeds (7, 13 and 18 m/s) was collected using two methods for sensing the reference pressure. The use of pressure transducer signals themselves for measuring the reference pressure was thought to be unwise even with the rotor stationary and the FI blade cover on. It was therefore decided to carry the DRUCK DPI-140 digital barometer in the car so that a separate

assessment of the reference pressure could be made. The DRUCK was installed so that its sensing port was joined into the reference pressure pipe which connects with all the transducers in the FI blade. The open end of the reference pressure system was lead up the anemometer tower and fed from a standard pitot-static probe conforming to BS1042 [8.2].

Referring to the British Standard and to Dean [8.3], it became apparent that using the pitot pressure sensing port instead of the static pressure port may result in less corruption of the sensed pressure by yaw and pitch errors. If this had been the case the one dynamic head difference between the pitot pressure and the static pressure would have had to be subtracted from every pressure transducer measurement. The results, however, from the six runway tests, three using the static reference pressure and three using the pitot pressure, showed only small differences so further use of the pitot pressure port was ruled out. For the three static reference pressure tests the maximum difference between any two DRUCK readings was 25 Pa. This occurred during the 18 m/s run which naturally utilised more runway length than the other tests. This is significant because the slight slope of the runway (the same runway was used exclusively for all the tests reported here), has been estimated to account for a 21 Pa variation in atmospheric pressure from one end to the other due to a 2.249 m height difference [8.4]. Consequently, the static pressure sensed by the pitot probe was deemed a satisfactory source for the reference pressure and was used for all tests reported in this thesis.

8.2 Data Acquisition

The main body of the FIB testing took place between April and August of 1989. During this time data was acquired on just four days on which the weather conditions were satisfactory. The requirements of calm winds, no precipitation, the runways being available and the mobile experiment being fully operational were difficult to satisfy together. In order to get the most out of the resultant limited testing time it was felt necessary to adhere to strict operational procedures. These ensured that the data acquired would be of the highest quality and that safety of the personnel would not be compromised. A check-list detailing all of the required procedures was drawn up (based on experience acquired during the initial pitot-static probe tests) and was followed carefully

throughout each day's testing. The typical test procedure is described below.

8.2.1 Testing procedure

When all other conditions required for testing were met, the state of the transducers and data acquisition system would first be ascertained using the QLOOK code. All electrical warm-up drift problems were avoided by keeping the entire system continuously powered up (supplied from the mains and with the exception of the wind turbine motor/generator). Once all channels were seen to be operating normally a pressure transducer calibration exercise (see 6.1.6) would be carried out. Only a few calibration spots would be acquired but any later problems with calibrating that days data would have been avoided by using the calibration data acquired on the same day.

Finally the anemometers would be plugged into their sockets and aligned into their $\pm$ 45° positions using a purpose made jig. Once correct operation had been checked using QLOOK, the anemometer tower was raised and secured. A comprehensive safety check would then be made of the car and trailer, special attention being paid to the tyres, brakes, tow hitch, draw bar and the turbine tower guys. Once this was complete the data acquisition system would be shut down and the connection to the grid supply removed. The supply cable to the system would then be plugged into the output from the diesel generator although this would not be started until testing was to commence on the runway. The intervening time during which the electronics is allowed to cool was kept as short as possible.

The mobile system would then be driven out of the hanger and, with permission from the airfield control tower, 'taxied' to the appropriate runway threshold. Using 2-way radio contact the mobile testing facility would then be granted permission to turn onto the runway and proceed with tests over a previously arranged stretch of the three Cranfield runways. Once on the runway threshold the diesel generator would be started, the data acquisition system powered up and the trailer steering ratio moved to its 1:3 setting.

The parameters required for the particular run in question would then be set (see Table 8.1), the two variables being windspeed and yaw angle. The wind speed measured by the cup anemometer is indicated to the car

driver rather than the cars ground speed. The analogue signal produced (see 4.1.2) is fed from the data acquisition system and sent to a meter which is in the driver's line of sight. The centre zero position of this meter can be adjusted to occur at a range of voltages using a multi turn potentiometer fitted with a counter. The windspeed vs. potentiometer counter relationship given in Table 8.1 is used as a demanded windspeed setting so that the driver simply has to accelerate or decelerate such that the meter needle is held at its centre zero. The wind turbine body angle was then also set using the values given in Table 8.1 and the measured value given by QLOOK. The yaw lock would be tightened when the turbine body had been turned to give the required reading.

A final check using QLOOK would then be carried out to ensure the entire data acquisition system was still operating correctly. The data acquisition code H/10/22 would then be loaded into the BBC micro before shutting down the Winchester hard disk. (This type of device is renowned for being intolerant of vibration; every time the mobile system was moved, including during testing, the Winchester heads would be parked and the disk drive turned off.)

The final tasks to be performed before attempting the data acquisition were starting the wind turbine rotor and setting the dummy load required. This was always done in this order so that the diesel generator was not expected to start the turbine motor (its most onerous task) while also supplying appreciable dummy loads. Once the rotor was up to full speed, sufficient dummy load would be introduced to ensure that during the run the load on the diesel generator would remain positive. In practice, due to the inefficiency of the turbine motor in generation mode, an extra 3 kW of load were required for only those runs over 15 m/s.

With the turbine running at its nominal speed and both the driver and experimentalist strapped into their seats, the car/trailer system would be accelerated along the runway until the demanded wind speed had been reached. At this point the data-acquisition process would be started by choosing the automatic logging option on the menu. If runway length permitted the required speed would be held until the data acquisition was complete; the data logger has space for 160 revolutions of data which takes approximately 28 seconds to acquire at the nominal 340 r.p.m. rotor speed. For the faster windspeed tests (over 20 m/s)

braking was sometimes necessary during the last few seconds of data acquisition.

With the mobile facility stationary once more the rotor was braked to a standstill and any dummy load disconnected. After noting the natural wind direction and speed (given on the menu screen) tha data transfer option is chosen and the text information for the run (including the natural wind conditions) is entered. The Winchester disk is then powered up and transfer of the 2 Mbyte CED 1401 memory commences. This takes approximately four minutes during which time any parameter changes required for the next run can be started. The acquisition process can then be repeated up to thirteen times before the Winchester disk becomes full.

8.3 Data Transfer and Preliminary Processing

The data stored on the Winchester hard disk, including both calibration and run data would then be transferred to the VAX cluster system using the Kermit transfer package. The calibration data would be added to the pool of data previously acquired. The run data, however, would be analysed immediately with the VAX OFFSCALES code. Statistics about the spread of data for each of the 96 channels would be printed out and appraised. Unhealthy runs of data (of which there were few) could immediately be identified and any further processing on these files would be abandoned. The well behaved data files can then be converted into EXP files which contain data in engineering units. The SUPER_CAL and FORM_EXP concepts described in 6.2 and 6.3 convert each raw data file into real calibrated values in the EXP file. With such large files it was usually necessary to archive both the raw data files and the calibrated EXP files to magnetic tape. The database held on tape grew to 64 Mbytes of raw data and 87 Mbytes of calibrated EXP data.

CHAPTER 9

OVERVIEW OF THE FIB DATA

9.0 Summary

The large data base of calibrated mobile test run data presents a significant data analysis challenge. The approach used in attempting to select the best data from the data base is outlined in 9.1 and resulted in the choice of 76 sub-runs over which the wind input and rotor response were considered steady. Analysis of the sub-run data is accomplished using four main analysis codes, WINDY, ROTOR, PROFILES and FORCES, which deal separately with selected data streams. These Fortran application codes are described in 9.2.

An overview of the data is presented in 9.3 using heavily averaged data, usually one data spot per sub-run. Together with a brief look at the frequency domain behaviour of the rotor (9.4), this forms a general outline of the data available for further, more detailed analysis.

9.1 Data Analysis Approach

Over the period of April to August 1989 the wind turbine, fitted with the fully instrumented blade, was tested on the mobile facility following the procedures described in the previous Chapter. During the entire testing phase, the blades were set at the "design" pitch of six degrees (nominal), and the drive train set up with the 32-tooth pulley to provide a (nominal) rotational speed of 333 r.p.m, as described in Chapter 3. In this configuration, a total of 23 useful experimental runs were taken according to a test schedule which covered a range of windspeeds up to 25 m/s and fixed yaw angles within $\pm$ 45 degrees. Each run consisted of almost one million samples of data, over the time of 160 revolutions (around 28 seconds) with exactly 128 time "slots" per revolution. The analysis of this data forms the subject of this and the following Chapters.

The objective of "controlled velocity" testing is to provide steady conditions, with a low level of free-stream turbulence, much akin to those in the wind tunnel. The philosophy behind the analysis was therefore to examine the data streams for stationarity, and to use

averaging methods where appropriate to obtain a description of the rotor's underlying periodic response to the essentially steady inlet conditions. Judgements about the stationarity of the data were based (qualitatively rather than quantitatively) on a preliminary examination of the anemometer signals and the rotor power.

As described previously (Chapters 5 and 6), the data analysis was carried out on the central computing facility at Cranfield (a large VAX cluster). Calibrations were applied "once and for all" to each raw experimental run to produce a single, 4MByte, direct-access, binary-format file for each run (given the file type .EXP). To ease the job of writing analysis programs, a large FORTRAN subroutine library (the EXPLIB half of RotaCAP) was built up, including "handlers" to recover the data streams, and various routines to process, summarise, print and plot the data. In this context, it proved expedient to develop a number of specific analysis programs, each "application" program passing through the data file to carry out a single analysis task; this appeared to be more appropriate than trying to incorporate a "complete" analysis in just one program. The four most important analysis programs are described in the next Section.

Complete time histories of wind speed and mechanical rotor power for a typical experimental run (160 rotor revolutions) are shown in Figures 9.4 and 9.5 respectively. It can be seen from this example that any given experimental run, taken as a whole, cannot be considered stationary, although it is apparent that "instantaneous" rotor power correlates well with "instantaneous" wind speed. This non statatationarity is primarily caused by the sudden, light breezes which tend to appear under the calm-wind, fine-weather conditions necessary for controlled velocity testing. As can be seen from Figure 9.2, the fluctuating cross-wind component is of the same magnitude as the variations in longitudinal component of air speed, indicating the presence of a certain amount of "natural" wind on an otherwise calm day. In addition, to some extent the variability of wind speed also arose from unsteadiness of the car speed during the tests. With so much drag associated with the rotor, the response of car speed to applied pressure on the accelerator pedal did not show the same sensitivity characteristics as would be expected on an unladen vehicle; this aspect of driver skills did improve, however, as testing progressed.

In view of this lack of stationarity in the 160-rev records, it was decided to analyse the data in selected blocks of 40 revs each; this record length was sufficient for the averaged wind input over the period to be well related to the averaged rotor response, yet not so long as to exclude a large part of the data base on the grounds of being unacceptably variable. For the purposes of this analysis, a preliminary examination of the continuous signals for windspeed, wind-direction and rotor power was made. On the basis of these basic data streams, the run was divided into a number of sub-runs over which the conditions could be considered particularly steady. (The criteria for this judgement were not formally quantified.) For some runs, only one such sub-run was considered to be of adequate standard; for other runs, up to four sub-runs (without overlap) were extracted. To enable fair comparisons between sub-runs, they were all chosen to have the same length of 40 revs, representing about 7 seconds of continuous operation. The data presented in this Chapter, based on ensemble averaging over these sub-runs, therefore represents the periodic response of the rotor in steady flow conditions. Statistical measures of data scatter over each sub-run were used to assess just how steady conditions were.

Each sub-run is thus identified by three digits for the run number (160 to 202), analysis version 2 (previous releases of data were for development purposes only), with the particular sub-run being identified by the rev-range or a letter (A,B ...). All measurement streams are analysed over each sub-run separately. The test matrix of sub-runs (76 in all) is shown in Table 9.1, showing wind speed classified in steps of 4 m/s and yaw angle in steps of 15 degrees. With the sub-runs analysed separately, the Table indicates wind speeds up to 23.5 m/s (that is to say, tip speed ratios down to 2.1) and yaw angles from -43 to +56 degrees. The table should be compared with Table 8.1 which gives the intended windspeed and yaw angle for each test run; the differences being mainly caused by natural (cross) winds.

The complete analysis of the data base of sub-runs was then carried out, using the four programs described below (including a re-analysis of the anemometer and rotor power data streams).

9.2 Primary Analysis Codes

The four most important analysis programs were written to provide summaries of certain groups of signals. The wind input to the rotor is

analysed using the WINDY program whilst all of the off-rotor signals (such as rotor power, yaw torque etc.) are dealt with by the ROTOR program. The pressure transducer measurements are examined by the other two main analysis codes; PROFILES dealing with pressure coefficient distributions and FORCES with time histories of the integrated forces. All of these programs were written to process a nominated rev-range within a single, nominated experimental run (.EXP file), generating both graphical and printed output. In general terms, time histories over the rev-range are presented graphically, to give an immediate impression of a large amount of data. Since there is a limited number of EXP files which could be held on-line simultaneously, some kind of statistical summary must be derived for the groups of signals in each EXP file. Hence, a "catalogue" is built up as each sub-run analysis is done and various cross-comparisons can be made (called "parametric trends") after the principal analysis is complete. Thus each of the analysis codes also generates "catalogue files", one for each sub-run, in printable format, but suitable for input to the parametric trends analysis.

In general, two types of statistical summaries were saved in the catalogue file for each data stream under consideration. Firstly, the "run-average" was calculated as the mean of the complete data stream (within the nominated rev-range). The standard deviation, maximum and minimum of this "instantaneous signal" were also saved to provide a summary of the total variability of the data stream. Secondly, the "rev-average" was calculated as the mean of the 128 samples for a single revolution, counted from the "Event 0" trigger from the slotted disc. Over a run or sub-run the standard deviation, maximum and minimum of this "filtered signal" provide a summary of the rev-to-rev variability of the data stream. Both these types of statistics are used in the programs described in this Section. In addition, the "azimuth-average" for an azimuth 'slot' may be calculated as the mean of the samples occurring at that azimuth in each rev of the run; a complete revolution of (128) azimuth-averages then forms a "typical-rev", which may be displayed graphically, together with an indication of the variation about this typical time history. Programs which generate "typical-revs" for the integrated forces and pressure profiles will be introduced later.

9.2.1 Program WINDY

This application code provides a summary of the wind speed and direction

data derived from the anemometer tower. The cup anemometer and wind vane streams (both SLOW) are "doubled-up" to provide one sample per rotor rev, then becoming equivalent to "rev-average" streams. The pairs of Lowne anemometer streams (all four FAST) are resolved into longitudinal and cross-wind components, that is to say in line with the car-trailer axis and anemometer crossbar respectively (see Figure 9.1). Time histories of the four Lowne derived data streams are plotted, as typically shown in Figure 9.2.

Two pairs of fast-response anemometers were specified for the experiment to give an indication of the wind variation across the rotor disc; first the data from the two sides is "summed" to give a composite picture of the wind input, then "differenced" to indicate spatial correlation. Weighting the left and right Lowne pairs according to which is most relevant to the turbine, the point on the anemometer crossbar is found which is directly upwind of the turbine (Figure 9.1). Using this mean-wind direction for the sub-run, the composite mean-wind data stream (W) is derived, together with the composite mean-lateral data stream (X) which has a mean of zero over the sub-run; the time histories of these two composite data streams are plotted, as shown in Figure 9.3. Rev-average streams are then obtained from W and X, and combined to give rev-average resultant wind speed and direction for the Lowne anemometers; these are compared graphically (Figure 9.4) to the cup anemometer and wind vane data streams. Even in this particular example, the discrepancy between the Lownes and the cup/vane instruments is striking, and will be addressed in 9.3.

The spatial correlation between the left and right Lowne anemometer pairs is evaluated, considering both longitudinal and both cross-wind components in turn. All auto- and cross- correlation and -spectra analyses of the W and X data streams are also evaluated. (The code which performs these calculations is discussed in 9.4.)

9.2.2 Program ROTOR

This application code provides a summary of the off-rotor data streams. For the rotor torque signal, the first four revs within the nominated rev-range are plotted (Figure 9.5) to show in detail the within-rev fluctuations due to the four-pole electric motor. The complete rev-range is plotted for the rev-averaged (smoothed) rotor torque. The rev-averaged mechanical power is derived from this using the

rev-averaged rotational speed. The electrical power (a SLOW stream "doubled-up") is shown alongside (Figure 9.5), and a rev-to-rev correlation for the mechanical and electrical power is evaluated. Time histories for the yaw torque and turbine body acceleration are shown in Figure 9.6. The turbine body angle is rev-averaged and plotted, together with the rev-averaged yaw angle derived from the SLOW wind vane signal "doubled-up". (The sign convention for yaw angle for this turbine is such that a positive yaw is to starboard). Summary statistics for all the data streams considered are written to a catalogue file.

9.2.3 Program PROFILES

This application code calculates the azimuth-averaged pressure coefficient profiles at specified azimuths for each of the two main measurement stations. The four cardinal azimuths (0° = horizontal rising, 90° = top-dead-centre, 180° = horizontal falling, 270° = bottom-dead-centre) have been specified, and plotted on the same graph for both the 35%R and 75%R measurement stations (Figures 9.7 and 9.8 respectively). The dynamic head used to calculate the pressure coefficients is simply based on the vector sum of the local rotational speed and the windspeed derived from the cup anemometer; the induced velocity is effectively taken as zero and any yaw angle is ignored, so that the same dynamic pressure is used at each azimuth. Consequently the stagnation pressure is not, in general, indicated by a pressure coefficient of +1. on the plots, the measured pressures are joined by straight lines between the tapping positions; no smoothing is done.

The same local flow vector triangle is used to evaluate a geometric angle of attack which is displayed on the plot along with the dynamic head. The run-averaged values of rotational speed, body angle, cup anemometer windspeed, wind vane direction, and derived yaw angle are also displayed; the displayed tip speed ratio is calculated as the run-averaged tip speed divided by the run-averaged wind speed. The integrated normal force, chordwise force and pitching moment at each azimuth are also calculated (using an integration technique described below) and are written to the catalogue file, though only the normal forces are displayed on the plot. Angle of attack "indicators", such as suction peak Cp and stagnation point position are also recorded in the catalogue file.

9.2.4 Program FORCES

This application code provides time histories of the integrated forces at each of the measurement stations over the nominated rev-range. Data streams are derived for the normal force, chordwise (tangential) force, nose-up pitching moment (about the trailing edge), and stagnation pressure (which is here taken to be the maximum indicated pressure without interpolation). The forces are evaluated using an integration subroutine which uses the chordwise and thickwise pressure tapping positions to calculate a set of integration coefficients. The blade forces can then be found as the linear combination of the measured pressures in the ratios given by the coefficients. The only difficulty presented by this formulation is in the value of pressure assumed at the aerofoil trailing edge where no tapping exists. This pressure is therefore set to lie half way between the measurements given by the most rearward suction and pressure surface transducers. The integration subroutine was tested using dummy data (unit pressure on suction surface, pressure surface, forward facing surface or rearwards facing surface) to ascertain its accuracy in estimating the forces and the pitching moment. The test results showed that the code could correctly estimate the sign and magnitude of each of the test forces and indicated that the pitching moment was best calculated about the aerofoil trailing edge.

For a more appropriate test of the accuracy of the subroutine, however, the normal and tangential forces for one measured pressure distribution were evaluated by 'counting squares'. The discrepancy between the integration subroutine results and the counted area was found to be about 3% for both the normal and chordwise forces. The pitching moment was also evaluated by hand calculation using the pressure distribution and this also agreed to within 3% of the value given by the integration subroutine.

The rev-averaged time histories of normal force, tangential force, pitching moment and "stagnation pressure" are plotted, as shown in Figures 9.9 and 9.10 for the 35%R and 75%R stations respectively; without the smoothing inherent in these plots, the within-rev fluctuations tend to obscure the rev-to-rev trends in the data.

It should be remembered that integration of pressure measurements to form chordwise forces cannot account for the effects of skin friction.

9.3 Data Overview

Before detailed discussions of the results from the four main analysis codes, it would be most appropriate to take a broad overview of the experimental data, by examining the mean levels of rotor response against tip speed ratio and yaw angle. Obviously, features of the unsteady aerodynamic response (significant when the turbine is yawed) will be eliminated; but the influence of the main aerodynamic parameters on rotor power and loads will be elucidated. These cross-comparisons of sub-run statistics, called "parametric trends", will be discussed here. The data "overview" is then completed by a frequency domain analysis of some of the more important data streams before a more detailed look at the data in the following Chapters.

9.3.1 Wind speed and direction

The plot of Lowne anemometer wind speed versus cup anemometer wind speed shown in Figure 9.11 is typical of the output from a "parametric trends" analysis. Pairs of run-averaged data are extracted from the "catalogue" files and plotted, one point for each 40-rev sub-run, the plotting symbol used being chosen according to the value of a third run-averaged value (referred to as "Z" on the plot) which is the wind vane angle in this case. The correlation between Lowne anemometer wind speed and cup anemometer wind speed is acceptably linear, especially for winds of less than 16 m/s. But the striking result is the slope of the correlation, which indicates that the run-averaged composite wind speed derived from the two pairs of Lowne anemometers is about 15% greater than that indicated by the cup anemometer. Taken in conjunction with the NEL cup anemometer calibration (see 6.1.1), this suggests that the calibration of the Lowne anemometers is in error. As described earlier the mica-vaned rotors for the Lowne anemometer heads have only been calibrated up to 8 m/s, and it could be that some aeroelastic distortion of the fragile vanes causes the Lowne rotor to overspeed at higher wind speeds.

Unfortunately, the plot of lowne anemometer wind direction versus wind vane direction shown in Figure 9.12 adds to the confusion. This correlation is again acceptably linear (except for some of the low windspeed data) but with the Lowne anemometers tending to indicate the wind direction further round to the right. There is an error of approximately three degrees in the Lownes anemometer direction when the

wind vane indicates axial flow, but this is not incompatible with the uncertainty in setting up the Lowne heads at ±45 degrees to the longitudinal. Since high confidence is attached to the wind vane calibration, the response of the Lowne heads must again be suspected, the indications being that the Lowne anemometer response does not drop away according to the cosine of its yaw angle, and may even be asymmetric. What is certain, however, is that these discrepancies are serious and highlight the urgent need for full, independent (NEL) calibrations (including the yaw response) of the Lowne anemometers.

In the absence of this information, however, the data from the Lowne anemometers will not be used in the following analysis, which relies solely on the wind data from the cup anemometer and wind vane.

The Lowne data, however, has been used to assess the turbulence levels encountered during mobile testing. Values of around 5% were typical; very much lower then those which pertain in the atmosphere.

9.3.2 Rotor power in axial flow

Measured rotor power versus wind speed is shown in Figure 9.13, with the wind speed non-dimensionalised by the tip speed and the power by a factor proportional to the cube of the tip speed. This method of presentation is useful in that it preserves the familiar shape of a "power versus wind speed" curve, yet it removes the unwanted effects of air density and rotor speed differences. The un-yawed data (actually, up to ±7.5 degrees yaw) from the controlled velocity tests, is compared to the one minute averaged data from the non-instrumented blade tests in free-yaw at the same nominal rotational speed (333 r.p.m.) on the field test site (see Chapter 7). The correspondance is close, the vertical lines indicating the bin standard deviation for the field test data. The discrepancy is zero at $1/\lambda = 0.2$ with the apparent field test performance less at higher wind speeds and slightly more at lower wind speeds, when compared to the equivalent mobile test performance. Two reasons could be suggested to account for this. Firstly the free yaw tests on the field test site must inevitably involve some tracking error over the one minute averaging period; this yaw error would tend to produce less power than might be expected for purely axial flow, especially at higher wind speeds. And secondly there is the rotor stall effect at higher winds which tends to reduce the energy capture in fluctuating winds. For a stalling rotor in a field test, fluctuations

of wind speed above the mean (for the averaging period) tend to recover less additonal energy than the deficit caused by a similar wind speed fluctuation below the mean. This conclusion is valid whenever the power versus wind speed characteristic has a negative second derivative, if the "ideal" characteristic is treated in a quasi-steady fashion. The opposite conclusion could be drawn at lower wind speeds where the performance characteristic has a positive second derivative, and the power follows something like a "wind speed cubed" law. Unfortunately, no record was kept of the wind speed fluctuations over the one minute averaging periods of the field test (see Chapter 7), so it does not seem possible to simulate this power loss effect using the mobile test performance as "ideal". None-the-less, the performance comparison does not suggest any reason to doubt the validity of this form of mobile testing for aerodynamics measurements.

9.3.3 Rotor power in yawed flow

The complete set of FIB data, including all the yawed sub-runs, is shown in Figure 9.14, where the plotting symbol is determined by yaw angle. At first glance it might appear that the machine shows good stall regulation with a flat-topped performance characteristic; but it should be observed that in fact there are no unyawed sub-runs at more than 20 m/s, ($1/\lambda$ = 0.38) and according to the plotting symbols the very high speed runs are yawed by around 15 or 30 degrees. In reality, it was concluded from the field testing that the turbine does not appear to have well-limited power in high winds. It is apparent however, that power limiting does occur for the turbine set in yaw. Sketching in the performance curves at fixed yaw angles of 30 and 45 degrees does suggest a similar gradient to the unyawed characteristic, but reducing quickly to zero for wind speeds over 20 m/s.

The same data is replotted in Figure 9.15, this time versus yaw angle with plotting symbol determined by wind speed. The sharp reduction in power with increasing yaw angle is now quite apparent at the higher wind speeds. It is also clear that the power response to yaw is asymmetric at the higher wind speeds and that for wind speeds of around 14, 18 and 22 m/s the power appears to be rather insensitive to the first 20 degrees of positive yaw (although this may be because of the width of the z value wind speed bins). This plot also indicates a number of gaps in the data base, pointing out the need for additional runs at medium and high windspeeds and negative yaw angles.

Cross-comparisons show that electrical power correlates well with mechanical power, (as demonstrated in Figure 9.16) being essentially linear for mechanical powers above 1kW.

9.3.4 Angle of attack indicators

Since no direct measurement of incidence was made on the blade, a number of different methods have been explored to derive "indicators" of angle of attack from the pressure transducer measurements. Such an indicator should show a positive trend with wind speed, just as the "true" incidence would, and that the blade element forces should be well-correlated with it, showing clearly-defined ranges of "attached flow" and "stalled flow". The obvious choice of stagnation (attachment) point position was investigated, but proved to be disappointing. With only 19 tappings at each of the main measurement stations, and with very little space within one chord (especially at 75%R), it was not possible to achieve sufficient resolution at the leading edge for the determination of both suction peak and stagnation point. Since accurate determination of the suction peak is important to the accuracy of the integrated blade element forces, the coverage of pressure tappings at the leading edge was biased towards the suction surface at the expense of the pressure surface. "Stagnation position" has therefore been defined as the location of the tapping indicating the maximum pressure. Results, however, have shown that during a revolution in yaw (when the stagnation point would be expected to cycle back and forth smoothly) the indicator "sticks" at one tapping location before "jumping" on to the next. Various methods to interpolate the stagnation point position were tried but were not considered satisfactory.

A number of other "alpha indicators" have been investigated including the values of adverse pressure gradient and suction peak pressure coefficient. The latter method (as used by the RAE [9.1]) has been found to be the most promising. It is defined here as the minimum indicated pressure non-dimensionalised by the 'geometric' dynamic head defined in 9.2.3. Labelled as "suction peak alpha" and azimuth-averaged for the 75%R measurement station at top-dead-centre (90° azimuth), it is shown in Figure 9.17, cross plotted with wind speed. (Strictly speaking, the wind speed should be non-dimensionalised by tip speed but the variation in rotational speed from run to run is small.) The correlation has the same appearance as that of mechanical power versus windspeed shown in Figure 9.14. Looking closely at the higher wind

speeds, however, it appears that the suction peaks in the unyawed cases (at around 19 m/s) have dropped to the level of those at around 45 degrees yaw, but the suction peaks at around 15 and 30 degrees of yaw maintain their linear trend with wind speed. It should be noted that the top dead centre blade is advancing into the wind for positive yaw, which, for this azimuth, would normally be associated with reduced angle of attack and increased dynamic head.

When derived for the inner blade station, the suction peak alpha indicator at 90° azimuth shows (Figure 9.18) much greater "angles of attack" than at the outer station, as would be expected with a lower effective speed ratio. What is noticeable is that around windspeeds of 20 m/s the high yaw runs (around 45 degrees) have much higher suctions relative to the general trend, but that the runs at around 15 degrees yaw have the same level of suction as at the outer station, in contrast to the general trend.

It must be remembered however, that at both spanwise stations the dynamic head used in calculating the "suction peak" Cp is simply the value given by the tip speed ratio (see 9.2.3) with no account for yaw angle and, as will be seen later, this can distort the results for non-axial flow.

Notwithstanding this, these plots show (in so far as suction peak is valid as an angle of attack indicator) that indicative levels of blade element incidence are certainly influenced by wind speed (tip speed ratio) and spanwise station.

9.3.5 Chordwise force versus wind speed

The trend of run-averaged integrated chordwise (tangential) force at 75%R against wind speed is shown in Figure 9.19; the plot has not been non-dimensionalised. The mean level of chordwise force is plotted here, even though some oscillation is to be expected with azimuth for the yawed runs. The broadly similar appearance to the plot of rotor power (Figure 9.14) would tend to endorse the view that the rotor's power generation originates principally from the stations with peak circulation. (It is not strictly accurate to associate measured chordwise force with "driving force", for two reasons: firstly the chord line is not exactly in-plane, with a nominal pitch setting of six degrees; and secondly no surface-friction drag is accounted for in the

pressure transducer measurements.) One difference indicated, however, is that the mean chordwise force with around 15 degrees yaw continues a linear trend with wind speed beyond 20 m/s whereas the mean chordwise force with around 30 degrees yaw follows the flat-topped trend.

The azimuth-averaged chordwise (tangential) force at this measurement station is shown in Figures 9.20 to 9.23 for the four cardinal azimuths starting at top-dead-centre. Looking at the unyawed runs at a speed of around 19 m/s, in each of these plots, it can be seen that the chordwise force at 75%R is more or less constant with azimuth, as would be expected. The sub-runs with around 15 degrees yaw at around 20 m/s exhibit loss of driving force at 270° azimuth (bottom dead centre) and 360° azimuth. But the sub-runs with around 30 degrees yaw at 22 m/s and above show loss of driving force over the bottom half rev, with almost total loss (zero driving force) at bottom dead centre. Comparing this with the trends of run-averaged chordwise force in Figure 9.19 and the whole rotor power in Figure 9.14, it appears that the loss in rotor performance at speeds of 22 m/s and above caused by yawing to around 30 degrees can be accounted for by the total loss of driving force at 75%R around bottom dead centre. In addition the continued linear trend in driving force at around 20 m/s caused by yawing to about 15 degrees is accounted for by the more constant levels of driving force at the 75%R station. Consequently the loss of rotor power at speeds of 20 m/s caused by yawing to around 15 degrees is not caused by the 75%R station. Presumably the region of severe separation responsible for power regulation does not extend as far as the 75%R station for the 20 m/s, +15 degree yaw cases, but reaches this span when the rotor reaches the 22 m/s cases at 30 degrees yaw.

The overall trends of the azimuth-averaged chordwise (tangential) force at the inner measurement station, shown in Figures 9.24 to 9.27, are less satisfactory. Looking at the unyawed runs for the "attached rotor" case of around 10 m/s, it can be seen that there is loss of driving force at bottom dead centre. For the "stalled rotor" case of around 19 m/s, these unyawed runs indicate a significant increase in driving force at bottom dead centre, but a collapse in driving force at 360° azimuth. Variations of chordwise force at 35%R with azimuth are quite erratic for the unyawed runs, with much reduced driving force at 360° azimuth. The problems with the pressure measurements at the 35%R station over the bottom half rev are thought to be associated with flow distortions caused by the turbine body. This flow distortion is not a simple matter

of "tower blockage", but involves flow accelerations either side of bottom dead centre. When the turbine is yawed, especially to the large angles investigated in this experiment, the region of flow distortion can be expected to shift relative to the 270° aximuth; for positive yaw angles, the 360° azimuth represents the leeward side of the turbine body, as well as being the azimuth where the cross flow component is radially outwards along the blade span.

The point should therefore be made here, that the data derived from the 35%R measurement station at bottom dead centre (270° azimuth) is unreliable, and the data at 180° and 360° azimuth should be used with caution.

9.3.6 Chordwise force versus "angle of attack"

Cross-comparisons of the azimuth-averaged chordwise (tangential) force with the suction peak alpha indicator are shown in Figures 9.28 to 9.31 at the 75%R station for each of the cardinal azimuths. Only the versions with plotting symbols determined by wind speed are presented here since those versions which indicate the yaw angle show that the relationships are broadly insensitive to yaw. Looking at Figure 9.28 for the 90° azimuth (top dead centre), it is immediately apparent that the correlation has now collapsed onto a single linear curve. From the low incidence runs at around 6 m/s to the highest incidence runs at around 22 m/s, driving force bears the same relation to this alpha indicator, more or less irrespective of yaw angle. In addition the four figures indicate exactly the same relationship between suction peak alpha and chordwise force. This is a very desirable characteristic for a measure of angle of attack, although it may have been expected for this indicator since both the tangential force and the suction peak alpha value are calculated from the same pressure distribution. (In other words they are both associated with the leading edge of the aerofoil.) However, there are many rotor conditions (of windspeed, yaw angle and blade azimuth) which can produce the same instantaneous angle of attack at the blade. The relationship between tangential force and suction peak alpha appears insensitive to these parameters and, perhaps more importantly, appears to be independent of local spanwise flow.

The second plot (Figure 9.29) for 180° azimuth is again well correlated as a single curve, but a non-linearity has been introduced for the high speed runs. These runs, which also happen to be yawed by around 15 or

30 degrees, are skewed by higher than expected values of suction peak Cp given the level of chordwise force. Figure 9.30 for 270° azimuth exhibits rather more scatter (perhaps some kind of "tower effect" at bottom dead centre); for both this and the next plot for 360° azimuth, the non-linearity appears more extensive. The use of a constant dynamic head in the suction peak calculation, irrespective of yaw angle, may be the source of this high speed non-linearity.

The correlation of azimuth-averaged chordwise force with the suction peak alpha indicator, at the 35%R station for 90° azimuth, is shown in Figure 9.32. As with the outer station at top dead centre, the correlation has collapsed onto a single linear curve, but with some very high incidences for the four sub-runs extracted from run 202 (of Table 9.1), previously seen in Figure 9.18. The plots at the 35%R station for the other cardinal azimuths (not presented here), also show fair correlations, thus reinforcing the adequacy of the suction peak alpha indicator, even for a distorted flow.

9.3.7 Effective blade length

A single cross-comparison is presented in this section, which combines the integrated chordwise forces derived from both the main measurement stations. The effective blade length has been defined as follows. First the run-averaged chordwise forces were calculated for the 35%R and 75%R measurement stations. Then a spanwise distribution of driving force was presumed, based on the linear extrapolation of these two forces (N/m). (In fact, the chordwise forces were projected onto the rotor plane, and the normal forces also included. But still no account was taken of the surface-friction drag.) On the assumption that this spanwise distribution applied over the full 100% of the blade radius, a rotor torque was calculated for three blades. The effective blade length, plotted in Figure 9.33 versus wind speed, was obtained by dividing this by the measured rotor torque. Regarded as the proportion of blade actively contributing to the rotor power, this derived statistic tends, at higher wind speeds, towards a value of about 85%, which appears reasonable. At lower wind speeds below 12 m/s, the effective blade length falls away to zero, suggesting perhaps the invalidity of the assumption of a linear spanwise distribution of driving force over this range of tip speed ratios.

9.3.8 Normal force versus wind speed

The trend of run-averaged normal force at 75%R against wind speed is shown in Figure 9.34, which may be compared to the equivalent plot for chordwise force in Figure 9.19. For normal force the trend is broadly linear at low wind speeds. Sketching in the trends for the individual yaw settings, it would appear that the unyawed runs have some kind of stalling effect at around 15 m/s, in contrast to the positive yaw settings (15, 30 and 45 degrees) which exhibit a much gentler non-linearity at higher wind speeds. Considering the unyawed runs at around 7 m/s, it also seems that there is no "linear range" for the unyawed runs below 15 m/s.

The same data is plotted again in Figure 9.35, versus yaw angle, with plotting symbol determined by wind speed. The asymmetry with respect to yaw angle, as noted previously in the context of chordwise force, is apparent with increasing wind speed. Also, there is possibly a linear trend versus wind speed of the point (yaw setting) of peak "rotor load": 0 degrees at 6 m/s, +5 degrees yaw at 10 m/s, 10 degrees yaw at 14 m/s and 15 degrees yaw at 18 m/s. The peculiar stalling characteristic noted above for the unyawed runs, appears to be associated with the downturn of normal force with "negative" yaws for wind speeds around 18 m/s.

The trends of azimuth-averaged normal force at 75%R against wind speed are shown in Figures 9.36 to 9.39 for the four cardinal azimuths. Looking at the first of these Figures for 90° azimuth (top dead centre), the stalling effect with increasing wind speed seems to occur progressively later with increasing positive yaw angle. For 180° azimuth (Figure 9.37) the stalling is not progressive with increasing yaw, but indicating around 15 degrees yaw for the "latest" stalling effect with increasing wind speed. The next plot for 270° azimuth shows a very large scatter of response, though broadly in line with yaw angle for increasing wind speed. This scatter is much greater than that seen previously (Figure 9.22) for the chordwise force at bottom dead centre. The scatter of normal force at 360° azimuth (Figure 9.39) is somewhat reduced, though still rather larger when compared to the initial picture (Figure 9.36) for top dead centre.

The trend of run-averaged normal force @ 35%R against wind speed is given in Figure 9.40 which may be compared with the plot for the 75%R

station given in Figure 9.34. The trend is linear with wind speed but shows none of the axial flow stalling effect seen further outboard. The normal force at the 35%R station appears not to show any stalling characteristics with increasing yaw either. Slightly reduced slopes and a shift towards lower values are seen, however, with increasing positive or negative yaw.

The trend for azimuth-averaged normal force at the inner measurement station against wind speed for top-dead-centre, as shown in Figure 9.41, is linear and fairly well correlated, in fact more closely correlated than the outer station at this azimuth (Figure 9.36). In addition the magnitudes of normal force are only slightly less than the values found at top-dead-centre for the 75% spanwise station and do not show the stall delaying phenomena produced by positive yaw further outboard. Assuming that the section incidence at the 35%R station in high winds is beyond the static stall angle, the data suggests that the normal force may become dominated by drag rather than lift loads.

9.3.9 Normal force versus "angle of attack"

Four plots are presented next (Figures 9.42 to 9.45) which show the trends of azimuth-averaged normal force at 75%R against the suction peak alpha indicator, for the four cardinal azimuths. Only the graphs where the plotting symbol is determined by yaw angle are presented here, though there is interest in those versions where wind speed is indicated. Taking in the general impression of all four graphs, it is striking that for the two horizontal azimuths (Figures 9.43 and 9.45) the trend has collapsed onto a single curve with no discernable yaw angle effect, whereas for the two vertical azimuths (Figures 9.42 and 9.44) it does not. In addition, all of the horizontal blade data and the vertical blade data under axial flow conditions lies on exactly the same curve relating normal force with suction peak alpha. At top-dead-centre, however, the runs exhibit progressively more normal force with increasing positive yaw angle, and at bottom-dead-centre, progressively less normal force with increasing yaw.

It has been noted earlier, that the relationship between 75%R chordwise force and the suction peak alpha indicator collapsed onto a single curve for each of the four cardinal azimuths. This is clearly not the case here, for the normal force with the blades vertical and the rotor in yaw. The use of a misleading value of dynamic head in the calculation

of suction peak Cp is a possible cause but then would bring into question the consistent correlations found for the tangential force. Another possible explanation may be the presence of dynamic stall which can produce very large suction peaks as the angle of incidence increases through the static stall angle and may alter the relationship between suction peak alpha and normal force. For positive yaw cases this might occur at the 270° (bottom-dead-centre) blade azimuth (Figure 9.44) when a given value of normal force might be produced at higher suction peak alpha indicators than would be expected. The opposite would be true at top-dead-centre (Figure 9.42) and the data is therefore consistent with this hypothesis. The effects of dynamic stall on the tangential force may be much less significant (due to the large changes in both lift and drag during a dynamic stall event) and this again is consistent with the data.

Again, the alpha indicator appears to remain consistent under conditions of spanwise flow (blade horizontal).

A further caution should be warned at this stage against the uncritical use of leading edge suction peak as an indicator of angle of attack. The collapse of suction peak pressures indicated in Figure 9.44 for some of the runs at approximately +30° yaw should obviously not be interpreted as a reduction of incidence at bottom-dead-centre! Two-dimensional wind tunnel data would indicate that the use of suction peak as an alpha indicator breaks down beyond the linear, attached flow range.

The correlation of azimuth-averaged normal force at 35%R against the suction peak alpha indicator is unsatisfactory, even at top-dead-centre.

9.3.10 Yaw torque

The final trend to be examined, in this overview of the experimental data, concerns the yaw torque response against yaw angle and wind speed. Yaw torque (about the rotor plane vertical centre line) is the result of an imbalance of thrust forces on the two sides of the rotor disc, which may be approached via the blade element normal force variation with azimuth. What is measured here is the total yaw torque about the yaw bearing, including a possible (restoring) torque contributed by the wind turbine body, acting as a kind of tail vane at large yaw angles. With

this in mind, it may be difficult to establish the link between yaw torque and blade element normal forces, without knowing the contribution of the turbine body.

The cross-comparison of run-averaged yaw torque against run-averaged yaw angle is plotted in Figure 9.46, with plotting symbols determined by wind speed. The conventions adopted here are that both yaw angle and yaw torque are positive to starboard (the turbine rotates clockwise looking down wind); the negative trend at the graph origin would therefore indicate a stable yaw characteristic. The possibility is apparent, however, that for windspeeds around 10 m/s for instance, a yaw angle of about 60 degrees (positive or negative) would cause the turbine to turn around completely. This is in keeping with the observed yaw behaviour during the field testing.

A series of comparisons were made to determine any correlation between turbine body vibration and either yaw angle or yaw torque (or the variability of these); no such correlation was found however.

9.4 Frequency Domain Analysis

A spectral analysis of some of the data base has also been carried out. This enables the inter-relationships between certain data streams to be identified and also serves as a check on certain aspects of the experimental apparatus.

The analysis is based on the G13CXX series of NAG subroutines which allow the auto-correlations and auto-spectra to be calculated for a single data stream and the cross-correlations and the cross-spectra to be found for a pair of data streams. The NAG subroutines utilise the lag window technique (for spectral smoothing) based upon the work of Jenkins [9.2]. (Spectra are given in arbitrary units.)

In order to gain confidence in the use of the routines and the choice of input parameters, test cases given by Jenkins were run and allowed the present application to be "fine-tuned". The subroutines are interfaced with the EXP file database in a FORTRAN program called FREQ which has been used to perform several analyses, some of which are discussed below.

9.4.1 Rotor torque and yaw torque

The auto-correlations and auto-spectra for both rotor and yaw torque measured during a 14 m/s, axial flow run, are shown in Figure 9.47. The rotor torque signal is dominated by energy at approximately 5.5, 13, 26 and 34 Hz. (The three curves represent the calculated frequency response and positive and negative 95% confidence limits.) The rotor speed of about 340 r.p.m. is responsible for the 5.5 Hz peak (1p) and probably also the 34 Hz peak (6p). The peaks at both 13 and 26 Hz are both produced by the 4 pole electric motor which, for all mobile tests ran at nominally 1530 r.p.m. due to the slightly raised frequency of electrical excitation (51 Hz).

The yaw torque frequency spectrum shows that most energy is present at about 2.5 Hz and probably represents the resonant frequency for the machine rotating about its yaw axis whilst attached to the relatively 'soft' mobile tower system. The frequencies associated with the rotor and motor shafts are also present but to a lesser degree.

9.4.2 W component of windspeed with 75%R station tangential force

Auto-correlations and auto-spectra of the W component of windspeed and the 75% span tangential force are given for two experimental runs in Figures 9.48 and 9.49. The first of these figures is for a 14 m/s, axial flow run and shows that the tangential force is dominated by peaks at 1p, 2p, 3p, 4p and to a lesser extent 5p and 6p. The auto-correlation and auto-spectrum for the wind data stream indicate that very little energy has been measured at frequencies above a few Hz. This may be due to the aerodynamic and electronic distance constants inherent in the anemometry systems and may explain why attempts to determine the "time of flight" for flow to pass from the anemometers to the rotor using the cross correlation were unsuccessful. Figure 9.47 shows the same information for a yawed flow case (+40°) at 14 m/s and indicates that energy in the tangential force signal has been shifted to lower frequencies due to the yaw.

9.4.3 Turbine Body Vibration and Yaw Torque

The parametric trend analysis did not reveal any systematic correlation between the turbine body vibration measured by the accelerometer and the levels of yaw torque or yaw angle. An examination of the signals in the

frequency domain revealed that the body vibration frequency spectrum contains peaks at about 2.5, 5.5 and 13 Hz but is dominated by energy at about 9 Hz (see Figure 9.50). As discussed earlier, the yaw torque signal is dominated by energy at 2.5 Hz, also contains the 1p component but does not indicate a peak at 9 Hz (Figure 9.47).

The cross spectral density function between the two signals is determined from the real (cospectrum) and imaginary (quadspectrum) and shows (Figure 9.50) that the coupling between the two occurs at mainly 2.5, 5.5 and 9 Hz. The value of the cross-correlation coefficient, however, is low and therefore indicates that the coupling is not strong.

9.4.4 Gas Slip Ring Integrity

The reference pressure which is applied to the reference port of all pressure transducers is passed onto the rotor via a gas slip ring (see Chapter 3). Oscillations in this reference pressure system which might be caused by the slip ring are capable of corrupting the pressure measurements and therefore this situation should be avoided. An indication that the slip ring used was well behaved is given in Figure 9.51 which gives the auto-correlations and auto-spectra for the raw pressure signals from two transducers. The top pair of graphs are for the 75% station, leading edge transducer, 7S01, whilst the bottom pair give the response for the PREF transducer which is connected only to the reference pressure system, its other port being blocked. The results clearly show the 1p, 2p, 3p etc., peaks present for the 7S01 transducer and their absence for the PREF channel. This strongly suggests that systematic reference pressure oscillations due to the rotation did not occur.

9.5 Conclusions

Several conclusions regarding the data base can be drawn from the initial overview.

(i) The calibration data presently available for the Lowne anemometers gives over estimates of the windspeed and the cosine response of the devices is suspect (Figures 9.11 and 9.12). The cup anemometer calibration, however, has been verified by the National Engineering Laboratory and this is therefore used in the analyses given in the following Chapters.

ii) The agreement between the instantaneous power-windspeed measurements made during the mobile tests and those obtained from conventional field tests is good and therefore confirms the validity of controlled velocity testing (Figure 9.13). The slight differences between the two responses is in keeping with expectation and illustrates the potential errors in predicting instantaneous power from conventional one-minute-average binned data.

iii) The power limiting (stall regulation) capabilities of the rotor are enhanced by yaw. A gentler stall characteristic which occurs at higher windspeeds is demonstrated by the rotor in positive yaw (Figure 9.14). At high windspeeds a flat topped yaw response is indicated (constant power over a 10° to 20° yaw range) with significant yaw asymmetry (Figure 9.15).

iv) The use of stagnation point position as a measure of section angle of attack is unsatisfactory due to the low pressure tapping density and the best measure of alpha available from the pressure measurements is the value of suction peak pressure coefficient. However, the analogy breaks down beyond the linear, attached flow range.

v) The suction peak alpha indicator is a non-dimensional pressure coefficient which has an embedded assumption of the value of dynamic head (q). The value given by the quadrature sum of the rotational speed and the wind speed has been used here and may give rise to potentially misleading results for yawed flow cases.

vi) The variation of tangential force with windspeed suggests that the behaviour of the rotor is driven by the outboard sections of the blade rather than the inboard sections (Figure 9.19). In addition, the stall regulation characteristics for the rotor in positive yaw are produced by reductions in driving force over the bottom-half revolution where section incidence is increased and stall is likely to occur. The region of separation appears to spread outboard as the windspeed and yaw angle are increased (Figures 9.20 to 9.23).

vii) The pressure measurements at the 35%R station are likely to be unreliable around the bottom-dead-centre azimuth due to the turbine nacelle blockage. The influence of the blockage may affect a larger range of azimuths in yawed flow conditions. (Figures 9.24 to 9.27.)

viii) Acceptably linear relationships exist between tangential (chordwise) force and suction peak 'alpha' for both the 35%R and 75%R spanwise positions, although the results for the inner measurement station are less well behaved. (Figures 9.28 to 9.32). The effects of yaw are small.

ix) The effective blade length calculations indicate that the calculated values of tangential force (integrated up pressure measurements) broadly tally with the independently measured rotor torque and give confidence in the integration procedure. The deterioration of the correlation with decreasing windspeed probably indicates that the assumed linear distribution of in-plane force becomes more unrealistic on a lightly loaded rotor. However, for windspeeds greater than 12 m/s the results suggest that the instrumented stations (35%R and 75%R) do represent typical inboard and outboard blade stations(Figure 9.33).

x) The variation of normal force with windspeed again illustrates the yaw asymmetry and at the 75%R station generally shows a delayed stall for yawed flow cases as compared to axial flow cases (Figures 9.34 to 9.39). Stall does not appear to occur at the 35% spanwise station as would be expected for the high windspeed runs (Figures 9.40 to 9.41). This may be due to the fact that at high incidences the normal force can become dominated by drag rather than lift.

xi) For the 75%R station the variation of normal force with suction peak alpha indicator appears more non-linear and collapses onto a single curve (irrespective of yaw angle) only for the two horizontal blade azimuths (Figures 9.42 to 9.45). Spanwise flow, therefore, does not appear to disturb this alpha indicator. The spreading of the data in families of yaw curves for the vertical blade azimuths may be associated with dynamic stall. The results for the 35%R station give no clear trends.

xii) The frequency domain analyses (Figures 9.47 to 9.51) have illustrated modest coupling between rotor torque, yaw torque and turbine body accelerations. Attempts at the derivation of time-of-flight were unsuccessful but a shift of energy in the aerodynamic response of the rotor to lower frequencies with yaw has been demonstrated. The satisfactory operation of the pneumatic slip ring has also been shown.

CHAPTER 10

PRESSURE DISTRIBUTION ANALYSIS

10.1 Introduction

Following the general appraisal of the entire data-base, a more detailed analysis of some of the data is described in this Chapter. The key to more fully understanding the rotor behaviour lies in the pressure measurements so the Profiles analysis of these data streams is more fully discussed here.

10.1 Interpretation of the Profiles Plots

The Profiles application code, as previously discussed, presents the pressure coefficient distributions around the rotor blade at the 35%R and 75%R instrumented stations. In both cases the pressure profiles are given for the four cardinal blade azimuths, i.e. horizontal blade rising (0° azimuth), top-dead-centre (90°), horizontal blade descending (180°) and bottom-dead-centre (270°). For each profile the tapping pressure coefficient data is plotted and the points are joined with straight lines. Since no smoothing is done the resulting shapes are sometimes unfamiliar.

Each pressure coefficient distribution is found from the pressures measured at the same blade azimuth position over the forty contiguous rotor revolutions which form the sub-run. The dynamic head (q) used to non-dimensionalise the average pressure distrubutions is found from the quadrature sum of the mean cup anemometer windspeed and mean rotational speed, both evaluated over the same rev range. No account is made for azimuth and yaw (see Figure 10.1a).

Using this value of dynamic head, has many implications for the resulting pressure coefficient distributions. The effects of induced velocities and yaw have both been excluded so that comparing and interpreting the data is simplified intentionally. However, the absence of these effects must be borne in mind since the implications for the non-dimensional representation of the data can be significant. The absence of induced effects (which can be estimated from strip theory) are considered in Figures 10.2 to 10.5. The first two figures give (for

the two instrumented stations respectively) the blade incidence given by a strip theory prediction (solid line) and that given by purely geometric considerations (i.e. α_g in Figure 10.1). It can be concluded that the induced effects will be more important at the 35% span and at the higher tip speed ratios. The effects of induced velocities on the local dynamic head (see Figures 10.4 and 10.5) are much smaller than the effects on angle of attack and their absence is therefore less important.

The effects of yaw, however, are certain to affect both the local angle of incidence and the dynamic head, especially for large yaw angles. These effects also vary with blade azimuth and therefore must be considered when comparing the four cardinal pressure coefficient distributions found on a single Profiles plot. The yaw effect can be qualitatively estimated (purely geometrically) for any windspeed, yaw angle and blade azimuth by:

$$q_{gy} = \tfrac{1}{2}\rho \left[(\omega r + \sin\theta . V_\infty . \sin\psi)^2 + (V_\infty . \cos\psi)^2\right]$$

$$\alpha_{gy} = \tan^{-1}\left[\frac{V_\infty \cos\psi}{\omega r + \sin\theta\, V_\infty \sin\psi}\right] - \beta$$

where θ is the azimuth angle, ψ is the yaw angle and the other symbols are as indicated in Figure 10.1.

For positive yaw this leads to the maximum incidence occurring when the dynamic head is at its minimum (i.e. at bottom-dead-centre). Conversely the minimum angle of attack occurs at top-dead-centre where the dynamic head is at its maximum value. The vector diagrams for the two horizontal blade positions (rising and falling) are identical (with opposite sense spanwise flows) but neither the angle of attack nor the dynamic head have the values which would have prevailed had the yaw been ignored (see Figure 10.1b).

By way of example, for a modest (20°) yaw angle, operation in a 16 m/s wind gives rise to variations in "angle of attack" between 13° and 19° and variations in dynamic head between 800 and 1300 Pa, both for the 75% span location. At the 35% station the corresponding oscillations are between 26° and 44° angle of attack and between 230 and 475 Pa dynamic

head. It is clear, therefore, that excluding the (geometric) effect of the yaw angle can produce misleading pressure coefficients due mainly to the large azimuthal variation in dynamic head. The approach used here, however, is to be preferred over the more complex (but not necessarily more accurate) approach in which yaw (azimuth) and/or induced effects are accounted for since it enables comparisons to be made more fairly. The pressure coefficient plots must therefore be interpreted with care. It should be noted, however, that the general shape of the pressure coefficient distribution retains its value as an indication of true angle of attack despite the distortions introduced by the use of a constant dynamic head.

10.2 Review of the Profiles Plots

The Profiles code (see 9.2.3) and the Contours code were used to analyse the data for each of the 76 sub-runs in turn (see Table 9.1). The second of these codes is an extension of the Profiles code and (using the same value of dynamic head) presents a "typical" revolution of pressure coefficient data by displaying the azimuth averaged pressure distributions for every other measurement slot (i.e. 64 of the 128 sampling positions). To reduce the number of plots to be studied in detail, the mean wind speed and yaw angle during each sub-run were examined and the sub-runs shown in Table 10.1 were chosen such that any trends due to the effects of yaw and windspeed would be correctly represented. The issues which are raised by the resulting matrix of plots are discussed below; first for the 75% span location where the angle of attack is lower and then for the 35% span location.

10.3 Pressure Coefficient Distributions at the 75% Span Station

10.3.1 Axial flow cases

The pressure coefficient distributions given in the lower halves of Figures 10.6 to 10.13 show that, for the 75% spanwise station, the effects of blade azimuth are minimal. The flow over the aerofoil is steady at all azimuths over the entire windspeed range (7 to 18 m/s) with the angle of attack increasing with windspeed. Referring to the predicted incidence angles (Figure 10.3) gives some indication of the strip theory estimates of section incidence with induced velocity effects included. A subjective comparison between the measured pressure coefficient profiles and those given by Riegels [4.7] and Saliveros et

al [3.1] (for the angle of attack indicated by strip theory) is encouraging; the shapes of the measured pressure distributions broadly corresponding with those given by the wind tunnel tests.

The heights of the suction peaks also compare well with the wind tunnel data although account must be made for the likelihood that the peak is not actually registered by a tapping. This is best illustrated by Figure 10.9 which suggests that the true suction peak is much 'greater' than -3.0 (i.e. more negative). This is borne out by Saliveros et al [3.1] which indicates the suction peak C_p for approximately this incidence to be about -4.0. The value of dynamic head used in converting the pressure measurements into coefficients could also be brought into question. However, again accounting for the low tapping density, all the plots show that the estimate of dynamic head is plausible.

The highest windspeed case (18 m/s, - Figure 10.9) indicates that a steady trailing edge separation may be occurring at about the 60% chord location and this is confirmed in Figure 10.13.

10.3.2 Yawed flow cases

As discussed earlier, one of the effects of yaw will be the cyclic variations in both dynamic head and, perhaps more importantly, angle of attack. For the positive yaw cases (to which this measurement program has been biased) this means reduced angles of attack and increased dynamic head at the top-dead-centre blade azimuth. These effects can be seen in the data for yawed cases and are discussed in the next sections.

10.3.2.1 Yawed flow cases at 10 m/s

The effects of yaw are illustrated by considering Figures 10.14, 10.7 and 10.15 (Profiles) and 10.16, 10.11 and 10.17 (Contours). These two sets of figures represent runs at -43°, -5° (nominally axial) and +56° of yaw all at about 10 m/s windspeed. Firstly, it should be noted that the pressure surface transducer at 43% chord (75% span) is clearly not responding to the pressure at the aerofoil surface and it should therefore be ignored. It is clear from the two yawed cases that blade azimuth gives rise to significant changes in both angle of attack (indicated by the profile shapes) and dynamic head (indicated by the 'stagnation' pressure coefficient). For the large negative yaw angle

(Figure 10.12) the lowest angle of incidence is seen at bottom-dead-centre and the local dynamic head is obviously larger than the 957 Pa value used. The highest angle of attack is clearly indicated by the top-dead-centre azimuth where the chordwise location of peak suction is furthest forward and the 'stagnation' point is furthest back. Examining the case given in Figure 10.13 (large positive yaw angle) the situation is reversed with respect to azimuth with minimum incidence occurring at top-dead-centre and maximum incidence at bottom-dead-centre. This is entirely in keeping with geometric expectations given in Figure 10.1.

Referring to Figures 10.16 and 10.17 shows that the angle of attack and dynamic head variations are approximately simusoidal in nature and that the cardinal points do represent the approximate azimuthal location of the incidence maxima and minima.

10.3.2.2 Yawed flow cases at 14 m/s

Figures 10.18 to 10.23 present the aerodynamic responses at approximately 14 m/s windspeed at yaw angles of -15°, +20° and +43°. (The axial flow case at this windspeed is given in Figures 10.8 and 10.12.) The angle of attack and dynamic head variations seen at the lower windspeeds are again evident but another feature is also apparent. Referring to Figure 10.20 (+43° yaw) a 'double suction peak' is noticed where, after the initial (partly registered) peak the flow is again seen to accelerate before entering the pressure recovery region. This occurs most noticeably for the horizontal rising and falling blades and is therefore probably associated with a small range of incidence angles. This phenomenon is also seen for other windspeeds and yaw angles (which give similar angles of attack) and is not caused by the averaging process used to create the profiles since it is also evident in 'instantaneous' (un-averaged) pictures of the measured data (see Figures 10.36 and 10.39). Similar irregularities are also seen at the 35%R instrumented station (see Figure 10.19) and are therefore probably not caused by local imperfections in the blade aerofoil section (shown in Figure 4.8). The most plausible explanation of these phenomena is that they represent laminar separation bubbles which are typical of the NACA 4415 aerofoil (see [3.1], [4.7]). The occurrence of these separation bubbles in other sub-runs is consistent with the earlier observation that they are associated with a relatively narrow range of incidence angles which occur at higher yaw angles as the windspeed increases from

14 m/s. Figures 10.21 to 10.23 show again that the flow changes caused by azimuth are gentle and predominantly sinusoidal.

10.3.2.3 Yawed flow cases at 18 m/s

The pressure coefficient distributions for the 75%R station at approximately 18 m/s are given in Figures 10.24 to 10.29. These plots give results for yaw angles of +28°, +42° and +53° (no negative yaw cases are available) and can be compared with Figures 10.9 and 10.13 which give the axial flow case at nominally the same windspeed.

The Profiles plots (Figures 10.24 to 10.26) indicate large azimuthal variations in both angle of attack and dynamic head as would be expected. The case shown at a yaw angle of +28° (Figure 10.24) shows a maximum in angle of attack at bottom-dead-centre and suggests that trailing edge separation and reattachment may be occurring every revolution. This is corroborated by unaveraged data for a single rev (Figure 10.36) and also in Figure 10.27 which, upon careful examination, indicates that, on average, separation occurs first, just after the blade passes its horizontal descending azimuth. The separation point then moves forward to about 50% chord before reattachment occurs between bottom-dead-centre and the horizontal rising blade azimuth. This should be contrasted with the axial flow case (Figure 10.9) which indicates a steady separation at about the 60% chord location.

Figures 10.25 and 10.26 show the response at larger yaw angles; 42° and 53° respectively. These indicate that the extent of the trailing edge separation diminishes with increasing yaw angle; fully attached flow having been re-established for all azimuth positions at +53° yaw.
The reason for this is apparent when the conditions for maximum angle of attack are investigated. On a purely geometric basis (induced effects ignored) the yaw angle for maximum incidence (at bottom-dead- centre) is found by setting the differential of the previously given expression for α_{gy} to zero. This results in the expression:

$$\psi = \sin^{-1}\left(\frac{V_\infty}{\omega r}\right)$$

Hence, the conditions for maximum bottom-dead-centre incidence are produced when the windspeed and local chord speed are in the appropriate ratio. Given a windspeed of 18 m/s and a local chord speed of

approximately 38 m/s the expression yields a yaw angle of 28°. In other words at yaw angles of 28° the maximum (bottom-dead-centre) angle of attack seen at this tip speed ratio will be achieved. This then broadly explains the reduction in the size of separation (i.e. angle of attack) as the yaw angle is increased beyond +28°.

10.3.2.4 Yawed flow cases at 22 m/s

Figures 10.30 and 10.31 give the aerodynamic response for cases at 20.8 m/s with +9° yaw and 23.5 m/s with +25° yaw. For the lower yaw angle case the responses at top-dead-centre and descending blade are similar to each other as are the responses at bottom-dead-centre and rising blade. This behaviour is also to be seen in Figure 10.24 (18.6 m/s with +28° yaw) and suggests that the dynamic head variations may lag behind those given by the geometric model with maximum q (for positive yaw) occurring after top-dead- centre. Separation appears to be consistently occurring at about the 50% chord section and this is confirmed by both the typical revolution contours shown in Figure 10.32 and the unaveraged data for a single rev given in Figure 10.43. When both the yaw angle and windspeed are increased the consistently cyclic behaviour given in Figure 10.33 is obtained. Here the separation point moves forward during the blade descending arc and results in suction peak collapse and stall during every rotor revolution. (The un-averaged data in Figure 10.44 confirms this.) As the blade passes the bottom-dead-centre position the suction peak begins to re-establish itself and promote predominantly attached flow once again. Figure 10.44 also indicates that the suction peak collapse may form part of a dynamic stall event, with possibly a vortex shed down the chord indicated by large anomalous pressure spikes in the contour plot.

10.4 Pressure Coefficient Distributions at the 35% Span Station

The pressure measurements at the 35%R station are expected to be quite different from those at 75%R. In addition to the higher angles of attack the turbine nacelle blockage effects will undoubtedly perturb the flow around the blade bottom-dead-centre position. On a purely geometric basis the arc swept by the blade whilst any part of the 35% span station is directly in front of the nacelle is about 76°. The aerodynamic influence of the nacelle is therefore expected to persist over at least a 90° arc and for yawed cases would be asymmetrically disposed about bottom-dead-centre.

10.4.1 Axial flow cases

Figures 10.6 to 10.13 also give the response of the 35%R station in nominally axial flows of 7, 10, 14 and 18 m/s. In each case the mean angle of attack is seen to be greater than that at 75% span but the changes during one revlution are much greater, due in part to the larger variations in both angle of attack and dynamic head (which is, here, assumed constant) and also partly because of the nacelle blockage. Figures 10.10 to 10.13 show that the blockage effect manifests itself gently up to 10 m/s with a localised angle of attack reduction centred on the bottom-dead-centre blade azimuth.

Above 14 m/s, however, the suction surface flow appears to be much more 'unsteady' and the blockage effects seem to affect the entire revolution; in fact the pressure distributions appear steadiest around bottom-dead-centre. The reason for this becomes clear when the instantaneous pressure distributions used to form the average are examined individually. Figure 10.34 shows two such pressure profiles which are snapshots of the 35% span response at top-dead-centre for two contiguous rotor revs of an 18 m/s, axial flow run. This clearly shows that averaging could be misleading in as much as two distinct flow conditions are being smeared together. For some top-dead-centre snapshots a very large suction peak (Cp = -6) is followed by separation at about the 10-20% chord position. At the same azimuth on other revs the suction peak is missing and the flow is separated over the entire aerofoil. The effect of averaging this 'blade stall instability' leads to the "unsteadiness" in Figures 10.8, 10.9, 10.12 and 10.13 which is therefore unrepresentative of either of the true flow states. The same conclusion can be reached by examining the standard deviation of the pressure values at each tapping. These become much larger when flow conditions from one rev to the next are inconsistent. For the bottom-dead-centre blade azimuth the angle of incidence is clearly reduced (as at lower windspeeds) which leads to the same attached flow condition in every revolution and hence a more realistic averaged pressure coefficient distribution.

With the above reservations noted, the average 35% span response in higher windspeeds can be deduced. Examining the average suction peak height as it changes during a rotor revolution (see Figure 10.13) gives some indication of angle of attack trends despite the smearing due to averaging. This can also be validated by comparing the typical

revolution contours with contours giving instantaneous (measured) data as given in Figure 10.35 for a single un-averaged revolution of the same sub-run. This figure indicates fully separated flow at the rising blade azimuth and large suction peaks followed by separation for the top-dead-centre azimuth (see also Figure 10.34). Clearly, the apparent steady increase in incidence between these two azimuths which is indicated by Figure 10.13 is only a shift in emphasis between the two flow states (stall instability) which are being averaged together. In reality the angle of incidence is probably changing only very slightly (due to small yaw or tilt angles) but this is sufficient for the flow to flip between the two unstable states. Superimposed upon this effect, two other peaks in angle of attack can be seen in Figure 10.13 and 10.35. These are probably due to local accelerations which occur either side of the nacelle as the flow attempts to squeeze past it.

10.4.2 Yawed flow cases

10.4.2.1 Yawed flow cases at 10 m/s

Figures 10.14, 10.7 and 10.15 give the cardinal point pressure coefficient distributions at nominally 10 m/s whilst Figures 10.16, 10.11 and 10.17 give the complete typical revs. The yaw angles represented are -43°, -5° (nominally axial) and +56°. The distributions suggest that the flow conditions are repeatable from rev to rev and that no averaging problems should have arisen as with the higher windspeed axial flow cases. The large yaw angle cases (see Figures 10.16 and 10.17) show that an approximately sinusoidal variation in angle of attack is being superimposed upon the once per rev reduction in incidence due to the nacelle blockage. This is best identified by the leading edge pressure coefficient shown on the suction surface plot and can be seen to move to earlier blade azimuths for positive yaw and later for negative yaw as would be expected.

10.4.2.2. Yawed flow cases at 14 m/s

Figures 10.18 to 10.23 give the aerodynamic response at approximately 14 m/s for yaw angles of -15°, +20° and +43°; the axial flow case for this windspeed is given in Figures 10.8 and 10.12. Clearly, for the -15° yaw, axial flow and +20° yaw cases (Figures 10.21, 10.12 and 10.22) the apparent unsteadiness may again be caused by averaging. For the +43° yaw case, however, (Figure 10.23) the distribution appears more stable

and the standard deviations for each pressure tapping become smaller. This typical revolution of pressure distributions is therefore more likely to accurately depict the true flow and infers that the unsteady flowfield has become a stabilising influence on the aerofoil behaviour. The nature of the flows are better represented by the plots in Figures 10.36, 10.37, 10.38 and 10.39 which give one rev of instantaneous (un-averaged data) for the one axial and three yawed cases.

In every case, where the averaged contours indicate some unsteadiness, the single revolution of measured data is seen to depict very unsteady flow. This unsteady flow does not suggest any coherant aerodynamic process; the flow appears to be chaotic, random and mostly separated on the suction surface whilst remaining well behaved on the pressure surface. For the -15° yaw case (Figure 10.36) the unsteady flow occurs over the entire upper arc of blade azimuths (0 to 180°) with the flow becoming well behaved and attached over the lower arc. (From geometric calculations the 'incidence' for this case is 42° at top-dead-centre and 36° for both rising and descending blade.) In the axial flow case (Figure 10.37) the extent of the well behaved flow is much reduced and occurs only very close to the bottom-dead-centre position. The picture at +20° yaw (Figure 10.38) is similar to the negative yaw case but with the azimuths for maximum and minimum incidences reversed and consequently unsteady flow at all blade azimuths. (The increase in bottom-dead-centre angle of attack due to yaw appears to cancel out the effects of blockage.) The single rev of data given in Figure 10.39 (yaw = +43°) indicates that the averaging performed to give the typical rev (Figure 10.23) is probably satisfactory. A large increase in incidence occurs while the blade passes from 90° to 225° azimuth where a sudden stall results in loss of the suction peak and propagation of a low pressure region down the chord (between bottom-dead-centre and rise azimuths). This could be the passage of a vortex shed by a dynamic stall event.

The presence of this dynamic but repeatable behaviour at 43° yaw and unsteady flows for lower yaw angle cases at the same windspeed can partly be explained by the purely geometric incidence model described earlier. It can easily be shown that for a given windspeed, as the yaw angle increases (positively from zero), the average angle of incidence over the 0-180° azimuth arc of the rotor rev reduces, whilst the bottom-dead-centre incidence increases. For the case in Figure 10.39 the mean incidence has reduced sufficiently to allow attached flow

during most of the rotor rev and the behaviour at bottom-dead-centre has been modified (decreased angle of attack) due to the nacelle blockage. At the lower yaw angle of +20° (Figure 10.38) the higher mean incidence gives rise to unsteady flow at all blade azimuths.

10.4.2.3. Yawed flow cases at 18 m/s

The typical revolution contours for the 18 m/s cases at yaw angles of +28, +42 and +53° yaw are given in Figures 10.27, 10.28 and 10.29. These demonstrate the same phenomenon as observed in the 14 m/s runs where increasing yaw angle has a stabilising effect on the flow probably due to the reduction in mean angle of attack. The higher windspeed, however, produces even lower pressure coefficients with an even more abrupt stall (see Figure 10.28). The instantaneous data given in Figures 10.40, 10.41 and 10.42 again validates the averaging procedure.

10.4.2.4 Yawed flow cases at 22 m/s

Figures 10.30 and 10.31 give the 35% span section response for run cases at 20.8 m/s with +9° yaw and 23.5 m/s with +25° yaw. The lower yaw angle case suggests fully separated flow for the rising and perhaps the descending blade also, with reattachment at bottom-dead- centre. The typical revolution contours (Figure 10.32) confirm this but also show considerable unsteadiness, due perhaps to the averaging of blade stalling pressure distributions as stated earlier. This is indeed the case as indicated by the unaveraged data for a single rotor revolution given in Figure 10.43 which shows the suction surface flow to be very unstable. The typical revolution contours in Figure 10.32 should therefore be regarded more cautiously since they represent the average behaviour of the aerofoil which in reality is in a very unsteady flow environment.

At the higher yaw angle and windspeed, however, the flow behaviour is slightly improved, although still quite unsteady (Figure 10.44). There is an apparently consistent leading edge suction peak development for the rising/top-dead-centre blade with collapse occurring as the blade descends (Figure 10.33). An unusual suction peak at the 50% chord also seems to develop close to the bottom-dead- centre position (see Figures 10.33 and 10.44) but this is almost certainly due to nacelle blockage effects.

10.5 Conclusions

The detailed look at the pressure coefficient distributions leads to the following conclusions.

i) The use of a constant dynamic head (Figure 10.1a) is a useful starting point for pressure distribution analysis because of the common basis for comparisons due to the absence of the effects of yaw and induced velocities.

ii) The enhanced geometric model of local flow vector (Figure 10.1b) is qualitatively obeyed by the measurements. Examination of the cardinal azimuth pressure distributions highlights the flow behaviour at the minima and maxima of both angle of attack and dynamic head. For axial flow the comparisons with strip theory infer that the induced effects on dynamic head are less important than the effects on angle of attack. Confidence in assuming this to also be the case for non-axial flow is gained by the apparent "stagnation" pressures given by the Profiles plots for yawed cases which are consistent with the model used. The enhanced geometric model (which accounts for yaw) may therefore yield realistic values of dynamic head for non-dimensionalising blade forces (although a certain amount of lag has been noted - 10.3.2.4) but is expected to produce less plausible values of angles of attack.

iii) The pressure distributions look similar to those obtained for NACA 44XX series aerofoils in wind tunnel tests giving confidence in the accuracy of the achieved aerofoil sections.

iv) The flows at the two measurement stations are very different for many reasons. The angles of attack seen at the 35%R station are obviously higher than those at 75%R but the effects due to blade azimuth vary due to the extent of the nacelle blockage. Up to 10 m/s the 35%R blockage effects appear well behaved, the flow becoming more unstable above windspeeds of 14 m/s. There is also evidence for flow acceleration either side of the bottom-dead-centre azimuth and the shifting of these effects with yaw angle. The behaviour of the 35%R section at top-dead-centre,

however, appears to be entirely unaffected by the blockage. For the 75%R station blockage effects are not seen and the flow is well behaved at all windspeeds.

v) Evidence that laminar separation bubbles occur at both blade stations over a narrow range of incidence angles has been observed.

vi) The effects of averaging the data can be misleading when the flow is not steady. The instability of the flow pattern close to blade stall (in both axial and yawed flow) can lead to the smearing together of two distinct flow conditions. Examination of the instantaneous data or the pressure measurement standard deviations is then required.

vii) The 75% spanwise station in 18 m/s axial flow approaches the section stalling incidence with separated flow aft of the 60% chord location. In 20.8 m/s flow (nominally axial) the trailing edge separation point moves forward to approximately 50% chord and the effects of azimuth are minimal.

viii) At modest positive yaw angles and high windspeeds the 75%R station can reach the stalling incidence and give rise to cyclic trailing edge separation close to the bottom dead centre azimuth. The occurrence of suction peak collapse and perhaps vortex progression down the chord indicate that dynamic stall may be taking place.

ix) The flow at the 35%R spanwise station can become chaotic and mostly separated on the suction surface whilst remaining well behaved on the pressure surface. Stall instability also creates averaging problems at this spanwise location and evidence that dynamic stall exists here has been noted.

x) Over certain ranges, increases in yaw angle can reduce the mean local incidence and promote more attached rather than more separated flow.

CHAPTER 11

ESTIMATION OF AEROFOIL SECTION COEFFICIENTS

11.0 Introduction

A further analysis phase using the Parametric Trend approach (discussed in Chapter 9) is appropriate in the light of the detailed look at the Profiles plots in Chapter 10.

Various methods for combining the measured data and strip-theory predictions [1.14] are examined so that fair comparisons can be made. Attempts at calculating the aerofoil angle of attack from the measured suction peak height were unsuccessful but useful comparisons between cardinal azimuth measured data and strip theory are made in terms of tip-speed ratio (or the geometric inflow angle).

Using the most valid form of data presentation the variation of force coefficients during a typical rotor revolution are examined so that the behaviour between the cardinal points can be determined. These may show both stall hysteresis and dynamic stall but analysis of the instantaneous (un-averaged) data is required to verify the presence of the latter.

11.1 Angle of Attack Estimation

Ambitious attempts were made at deducing the aerofoil section properties from the available data despite the difficulties involved. A comparison between the measured aerofoil section behaviour and 2-dimensional wind tunnel data could support the growing body of evidence for modification of C_L vs α curves on rotating wind turbine blades ([2.4] to [2.11]).

It has been shown that the most sensitive angle of attack "indicator" which has been measured is the suction peak height (defined in terms of the minimum indicated pressure on the aerofoil). Using 2-dimensional wind tunnel data [3.1] for a NACA 4415 aerofoil at low Reynolds number, a quadratic relationship between angle of attack and suction peak height was determined (see Figure 11.1). The measured normal and tangential force coefficients (sub-run averages) were then plotted against "true" angle of attack using the mean suction peak height to determine an

estimate of the incidence on the rotating blade. The validity of this approach may be questioned due to the numerous differences between the wind tunnel data (which is essentially 2-dimensional and steady) and the measured wind turbine data (which is 3-dimensional, at two different spanwise stations (and hence Reynolds numbers) and for aerofoil sections which have slightly higher thickness to chord ratios).

Despite these misgivings one of the best resulting plots is shown in Figure 11.2. This gives the normal force coefficient at the 75%R station for the measured (axial flow) wind turbine data (symbols) and two sets of wind-tunnel data; the Hunt data [11.1] used in the strip theory prediction given throughout this work (solid line) and the Saliveros data [3.1] which is responsible for the suction peak-alpha relationship. As would be expected, the correlation is poor due, in part, to the insensitivity of suction peak height to incidence at low angles of attack. (The incidence relationship has been extrapolated.) This is compounded by the suction peak moving rearwards on the aerofoil at low incidence, into a region of lower tapping density. Over a narrow range of incidences, however, the correlation indicates that the measured normal force coefficients may lie beneath the 2-dimensional wind tunnel data (for the same "angle of attack") which is in agreement with the power performance of the machine (see Chapter 7).

11.2 Force Coefficient Variation with Tip Speed Ratio in Axial Flow

In an attempt to achieve a more valid comparison between the measured aerofoil characteristics and the wind tunnel data assumed in the strip theory predictions, an alternative approach was adopted. The unsatisfactory attempt at deriving a true angle of attack from the measured data is avoided by calculating the geometric angle ϕ_g (see Figure 10.1a) implicit in the PROP code predictions [1.14].

Figures 11.3 to 11.6 show normal and chordwise force coefficients at both the measurement stations plotted against tip speed ratio. (ϕ_g and λ are, to some extent, interchangeable since they are both simple functions of the rotational and wind speeds.) The data shown is for axial flow cases only (yaw angle $< \pm 10°$) and is plotted with the predicted coefficients given by strip theory (for the same value of λ or ϕ_g). For the 35%R spanwise station the normal force coefficients are in quite good agreement with strip theory although there is no obvious kink in the measured data. (Caused in the predictions by the value of C_N

becoming dominated by drag loads rather than lift loads). At high tip speed ratios (low ϕ_g) the measured data falls consistently below the predictions whilst at higher windspeeds the data straddles the line. The reason for this can be seen clearly by the four measurement spots which lie at a tip speed ratio of approximately 2.8. Since the symbols denote the azimuth, it is evident that the variation in the value of dynamic head (even at small yaw angles due to the nacelle blockage) is sufficient to spread the data out considerably.

This is also demonstrated in Figure 11.4 which gives the 35%R chordwise force coefficients, clearly showing the predicted stall characteristics at tip speed ratios of about 4. The measurements suggest a less steep rise in C_T (with decreasing λ) and indicates stall (at only some azimuth positions) for tip speed ratios below about 3. It should be pointed out here, that the strip theory prediction includes the effect of skin friction drag whereas the measurements do not. The value of C_{DO} included in the predictions is 0.014 (C_{DO} must include the contribution from skin friction) and removing its contribution to C_T would therefore shift the solid line up by only a small amount.

The similar plots for the 75%R station are given in Figures 11.5 and 11.6 and overall, the strip theory prediction and measurements agree far better at this spanwise station. The measured normal force coefficients tend to lie below the prediction for low tip speed ratios whilst the tangential force coefficients agree much better (even after accounting for C_{DO}). The lowest tip speed ratio data seems to lie away from the rest of the data in both plots and perhaps, this is because this run represents the largest yaw angle (+9.3°) shown on the plot. Consequently, the effects of even modest yaw on the dynamic head and angle of incidence may be significant even at the 75%R spanwise station.

11.3 Force Coefficient Variation with Inflow Angle in Axial Flow

The plots given in Figures 11.7 to 11.10 go some way towards removing these yaw effects, by non-dimensionalising the measured blade forces by a dynamic head which, on a purely geometric basis, accounts for yaw (see Figure 10.1b). Hence measurements taken at different blade azimuth positions are divided by slightly different values of dynamic head for nominally axial flow cases. The values of "stagnation Cp" observed in the Profiles plots give confidence that this geometric approximation is reasonable, especially for the 75%R measurement station. Any induced

effects have also been ignored but these are expected to be small (see Figures 10.3 and 10.4). The validity of the dynamic head calculation, however, is less certain for the 35%R station, especially close to the bottom dead centre position.

The results for the 35%R station (Figures 11.7 and 11.8) bear this out since considerable scatter (in the azimuth sense) is still present. (The data has now been plotted against geometric angle ϕ_{gy} rather than tip speed ratio). The normal force coefficients given in Figure 11.7 indicate that all of the data lies below the strip-theory curve below the predicted stall. Excluding the data at bottom-dead-centre, which is known to be unreliable, all of the remaining data at the other three azimuthal positions lies above the strip theory prediction and maintains a linear trend over the entire range of angles of attack. For the tangential force coefficients (Figure 11.8) a similar picture is produced when the 270° azimuth data is ignored. The measured data now follows the prediction well up to a value of ϕ_{gy} of 30°. Beyond this the measurements suggest a reduction in slope and a later stall about 10° after the predicted stall. Taken together these two plots might suggest that stall is delayed at the 35%R station and that the lift-curve slope may be lower (compared to wind tunnel data). In addition, the maximum normal force coefficients calculated exceed the predicted values by about 20% in the stalled aerofoil region; maximum tangential force coefficients agree better with the prediction.

For the 75% span plots (Figures 11.9 and 11.10) the non-dimensionalisation is likely to be more accurate and the results are more interesting. The trends observed earlier still persist, in that the measured normal force coefficients tend to appear below the strip theory prediction whilst the tangential force coefficients agree better. For C_N (Figure 11.9) agreement is good up to ϕ_{gy} of about 16°, beyond which the slope of the measured data reduces and indicates stall with a lower C_{Nmax} than predicted. The correlation for C_T (Figure 11.10) is very much better, even after allowing for skin friction. Since the outer blade stations are more responsible for rotor power than the root sections it seems sensible to conclude that the under performance of the turbine in high winds (when compared with strip theory predictions - see Chapter 7) is dominated by lower values of normal force over the outer blade span rather than tangential force.

11.4 Force Coefficient Variation with Inflow Angle in Yawed Flow

For yawed flow any assumptions regarding induced effects are more unreasonable and the uncertainties in the geometric model for dynamic head and inflow angle (q_{gy} and ϕ_{gy}) become greater. Nevertheless, the same "parametric trend" approach as above was used to analyse the data from all axial flow and positive yaw sub-runs by splitting the data into the 15° wide yaw bins seen in Table 9.1. The results (some of which are given in Figures 11.11 to 11.16) have been produced using a modified version of the analysis which reads from special catalogues files. These contain the azimuth averaged forces at each of the 128 measurement slots and hence make up a typical rev. Plotting this data allows the progress of the force coefficients between the cardinal azimuths to be investigated. The dynamic head used is given by q_{gy} as before, but with one modification. Evidence had been noted where the values of q_{gy} used in certain high windspeed, high yaw angle sub-runs were actually less than pressures measured on the aerofoil, clearly indicating the inadequacy of the geometric model in some instances. As a result Figures 11.11 to 11.16 have been produced on the basis that the force coefficients are calculated using either the value of q_{gy} or the measured "stagnation" pressure; whichever is the greatest. It is important to note, however, that no adjustments to the data given in Figures 11.7 to 11.10 were made and that the q_{gy} calculation for all the axial flow cases is entirely consistent with the data.

Examining Figures 11.11 to 11.14 in more detail reveals some of the effects of yaw and blade azimuth. Figures 11.11 and 11.12 give the normal and tangential force coefficients for the 75%R station at a nominal yaw angle of +15°. The low windspeed data (low ϕ_{gy}) shows very few azimuth effects with significant hysteresis loops developing as the inflow angle increases. For a given value of ϕ_{gy} the maximum force coefficients are generally obtained for azimuths between 90° and 180°, these maxima forming a locus well above the strip theory prediction for C_T and perhaps indicating delayed stall for C_N. It is important to remember that the same dynamic head array has been used in both these figures and this gives confidence in the accuracy of the calculation for the aerofoil close to bottom-dead-centre. Significant stall in C_T is noted which is entirely absent in the normal force coefficient data and, as previously observed, this is caused by the normal force becoming dominated by the drag of the stalled aerofoil.

The same data for nominally +30° yaw is given in Figures 11.13 and 11.14. The hysteresis loops have now enlarged and the response at low windspeeds is also cyclic. The stall seen earlier in the tangential force coefficient is again indicated (at approximately the same value of ϕ_{gy}) but the normal force response is less well behaved with some crossing of the hysteresis loop to form a figure of eight, perhaps indicating dynamic stall. Again, however, the dynamic head value assumed in both plots appears reasonable even though for much of the data between 180° and 270° the measured stagnation pressure substitution has taken place.

Figures 11.15 and 11.16 give the normal and tangential force coefficients for the 35%R station at a nominal yaw angle of +45°. The data over the lower half-rev should be ignored although the values indicated at both 180° and 360° azimuth are thought to be reasonable. Very large hysteresis loops are indicated with, in some cases, a factor of 5 between C_T values at 180° and 360° and a factor of 1.6 between C_N values. Comparison of these plots with those produced using q_{gy} alone (not shown here) indicate that the sudden changes in slope at C_N = 1.4 and ϕ_{gy} = 25° are caused by the changeover from q_{gy} to measured stagnation pressure. This switching of data streams occurred less obviously at the 75%R station suggesting that the results at 35%R should be treated more cautiously.

In all the examples, however, it is interesting to note that the hysteresis loops of both C_N and C_T are executed in a clockwise sense whether the data is above or below the predicted stall. This infers that C_L also behaves in the same way and contradicts existing experimental evidence [2.27] that suggests that below stall the hysteresis should occur in an anticlockwise direction.

11.5 Dynamic Analysis

In order to determine if there is evidence of dynamic stall within the data base, examination of the instantaneous (un-averaged) data is required. Inevitably, this approach requires the manipulation and presentation of large amounts of data so this section restricts itself to the detailed analysis of just 2 of the 76 sub-runs in which the conditions for dynamic stall should exist. Hence the analysis is by no means complete.

11.5.1 Dynamic Stall

The unsteady aerodynamic process of dynamic stall is to be expected on the wind turbine rotor under certain conditions. One of the most important parameters which defines the conditions for it to occur is the reduced frequency, k. Ignoring induced effects, and assuming the local section velocity to be the quadrature sum of the local rotational speed and windspeed, the values of k at the two spanwise stations, can be calculated. For the controlled velocity tests described in this thesis the rotor speed was nominally 340 r.p.m. throughout and therefore the range of k values at the two instrumented stations is relatively narrow. Hence, at the 35%R station the reduced frequency will normally lie in the range 0.12 to 0.18 whilst further outboard at the 75%R station its value should lie between 0.05 and 0.07.

The aerodynamic response of an aerofoil operating at a range of reduced frequencies has been illustrated by Carr et al [2.28]. The force and moment characteristics shown in Figure 2.1 indicate the hysteresis for a reduced frequency of 0.05 which is typical of the 75%R station. The hysteresis loops at the 35%R station can be expected to be larger since k is larger and the mean level and range of angles of attack are also larger. Hence dynamic stall can be expected to occur at both spanwise stations when the incidence time history (governed by windspeed and yaw angle) oscillates about the aerofoil static stall angle.

Experimental evidence ([2.27], [2.28], [2.29]) suggests that there are several aerodynamic characteristics which are associated with dynamic stall. These include sudden collapse of the suction peak accompanied by increases in the normal force coefficient (and $dC_N/d\alpha$) for increasing angle of attack. Large negatively damped pitching moment events and vortex passage down the aerofoil chord are also typical of dynamic stall and it is therefore these main features which should be observed in the data to conclude that dynamic stall has occurred.

The analysis of the aerofoil behaviour during an entire sub-run is performed using a purpose written FORTRAN application program called DY_STALL. This code produces several plots of which Figures 11.17 and 11.18 are typical. These figures attempt to show the dynamic response of the aerofoil during a 40 rev sub-run. Figure 11.17 uses the geometric angle of attack (α_{gy}) based on the sub-run average windspeed, rotational speed and yaw angle. Consequently the geometric alpha time

history repeats itself every rev (being a function of azimuth also) and appears as a single curve in the figure. The normal force coefficient, tangential (chordwise) force coefficient and pitching moment coefficient (now shifted to be about the quarter chord) are all plotted against this repeating, basically sinusoidal alpha variation. The non-dimensionalisation has been performed using the value of geometric dynamic head (q_{gy}) as given in 10.1. It too is based upon the sub-run mean values of windspeed, rotational speed and yaw angle and therefore, like α_{gy}, it also repeats every rotor rev. The data from the entire 40-rev sub-run is plotted in this way as a continuous line and typically produces the pictures shown in Figure 11.17. The azimuth-average of each data stream (see 9.2) is also evaluated and superimposed upon the dynamic response to give the variation during the typical rotor revolution.

Figure 11.18 gives four similar plots but using the value of suction peak pressure coefficient as an angle of attack indicator rather than α_{gy}. The "alpha" time history is no longer a repeating series and therefore does not constrain the data to lie within the maximum-minimum geometric range as before. The coefficient data, however, is the same as before, being non-dimensionalised by a repeating series of dynamic head (q_{gy}). These two types of plots will be used in an attempt to illustrate some of the aerofoils dynamic behaviour.

11.5.2 75%R span response for a high windspeed, positive yaw

Figures 11.17 and 11.18 give the response at the 75%R station for sub-run 200A (18 m/s at +53° yaw). The calculated geometric incidence range (Figure 11.17) is approximately 6° to 19° and, therefore, allowing for induced effects, this sub-run may produce the conditions for dynamic stall. The departure of the α_{gy} variation from a true sinusoid is well illustrated here, showing a wide trough and a sharp narrow peak in the incidence time history. The suction peak Cp variation given in Figure 11.18 indicates, for some revs, a sudden loss and then recovery of the leading edge suction at about the bottom dead centre azimuth. This is the location of maximum incidence and may therefore represent a dynamic stall event.

In order to further investigate this effect the rev range over which the large suction peak collapses were obtained, was identified and the code ran again over this reduced range of revs. These results are shown in

Figures 11.19 and 11.20 and provide a clearer picture of the events. Figure 11.19 (geometric incidence) shows that there are large drops in all three of the coefficients just after the bottom-dead-centre azimuth. These are indicated even for the tangential force coefficient although they are moderated when the suction peak alpha indicator is used (Figure 11.20). This suggests that the inherent link between suction peak and tangential force is strong enough to disguise any unsteady aerodynamic effects which may exist in the data. Examining the normal force coefficient response (Figure 11.20) indicates maximum values greater than 1.3 to occur just before bottom-dead-centre. After dropping to about 1.18 this level is maintained through the suction peak collapse before falling back via a "recovery loop" where both the suction peak Cp and C_N remain relatively constant for a time. This is caused by attached flow re-establishing itself on the aerofoil as the angle of attack reduces on the ascending blade pass.

Sudden pitching moment events are usually a good indicator of the presence of dynamic stall. Figure 11.20 shows that the pitching moment is entirely linear with the suction peak alpha indicator for the descending blade half-rev (from top-dead-centre to bottom-dead-centre). Just after bottom-dead-centre, however, moment-stall appears to occur as sudden large negative going pitching moments are produced. The pitching moment then increases (becomes less negative) as the "recovery loop" is entered before the rising blade azimuth. Further indications that these dynamic events are caused by dynamic stall are obtained by comparing the maximum normal and tangential force coefficients calculated here with those given by the 'steady' analysis given in section 11.3. Consideration of Figures 11.9, 11.10, 11.19 and 11.20 shows that the dynamic values of both normal and tangential force overshoot the steady axial flow values.

The instantaneous pressure distribution contours during a single rev which exhibits the suction peak collapse (rev 44) are given in Figure 11.21. The lower half of this figure, for the 75%R station, clearly shows the collapse in suction peak just after the bottom-dead-centre blade azimuth. In addition, on careful examination, a low pressure region can be seen to progress down the aerofoil indicating the propagation of a vortex. Taken together, all of the characteristics indicated in this sub-run, confirm that dynamic stall events are taking place.

11.5.3 35%R span response for a low windspeed, negative yaw case

The dynamic response of the 35%R station is here examined for a negative yaw case so that the maximum angle of attack is attained for the top-dead-centre azimuth, thereby excluding the influence of the nacelle blockage. The geometric incidence for the 35%R station during sub-run 187B (10.7 m/s at -43% yaw) has been calculated to vary between 11° and 30°. Assuming that the axial flow induced effects of Figure 10.2 apply, this results in an effective incidence time history ranging from around 0° at bottom-dead-centre to 19° at top-dead-centre. This is clearly borne out by Figure 11.22 which shows large suction peaks and their collapse for the upper half rev and apparently very little nacelle blockage effect in the lower half rev. Evidence for dynamic stall may also be present.

The normal force coefficient variation indicates a hysteresis loop to occur during the upper half-rev blade azimuth. C_N steadily increases as the blade rises from bottom-dead-centre and continues to rise slightly even after the suction peak has collapsed. After top-dead-centre, fully attached flow re-establishes itself and the normal force coefficient returns to the linear part of the curve. These events produce an anti-clockwise going loop in C_N which is in the opposite sense to the previous evidence for dynamic stall seen in Figure 11.20. Experimental evidence [2.28] suggests that for a sinusoidal variation in angle of attack (see Figure 2.1) the suction peak does collapse (point f or g) before the occurrence of maximum lift or drag (point h). This is consistent with an anticlockwise going hysteresis loop as indicated in Figure 11.22. Comparison of these results with those given in Figures 11.7 and 11.8 indicates that the steady levels of C_N are not exceeded by the instantaneous data. The dynamic response of C_T, however, appears to considerably overshoot the steady state data given in Figure 11.8.

Further indications that dynamic stall is taking place are given in Figure 11.23 which shows that at the 35%R station the sudden suction peak collapse is followed by suction spikes further down the aerofoil. Steady propagation of a vortex along the chord is not apparent here, but unsteady effects are certainly indicated. This evidence then suggests that dynamic stall also occurs at the inner measurement station.

11.6 Nacelle Blockage Effects

The DY_STALL code also forms a useful tool in assessing the magnitude of the nacelle blockage for the 35%R station. The azimuthal suction peak pressure coefficient variations for two axial flow cases are given in Figure 11.24. The case at 14 m/s (sub-run 162) clearly shows the dramatic effect of the nacelle blockage as a periodic dip in suction peak which occurs on every rev. The influence extends between approximately 225° and 300° azimuth (i.e. centred slightly before bottom-dead-centre) and is consistent with the azimuth position of the aerofoil leading edge. High suction peaks are recorded for all other blade azimuths indicating generally high angles of attack but there is no discernable rev-to-rev repeatability other than near to bottom-dead-centre. The figure also gives the 35%R section response at 18 m/s. It is apparent that the blockage significantly disturbs the flow between 200° and 315° and that comparison with the lower windspeed axial flow case allows us to infer that the effects become more extensive with increasing windspeed.

On the assumption that the blockage is actually symmetrical about bottom-dead-centre the high windspeed case gives the extent of the blockage to be ±70° either side of bottom-dead-centre. Allowing for yaw suggests that at the 35%R span only the top half-rev of data should be relied upon.

11.7 Conclusions

i) Using the suction peak alpha indicator to quantitatively determine the aerofoil incidence from wind tunnel data is unsatisfactory. The range of incidences over which some correlation was obtained is very small and the link between the wind tunnel data and the rotor measurements is tenuous (Figure 11.2). Its use as a qualitative angle of attack indicator, however, has been validated earlier.

ii) More valid comparisons with strip theory are obtained by using a less sensitive measure of angle of attack such as tip-speed-ratio or the inflow angle. This then enables the aerofoil section characteristics to be compared with the predicted behaviour from strip-theory.

iii) In low windspeed, axial flow, the lift curve slope at the 35%R station appears to be reduced when compared to the strip theory prediction. In higher winds the normal force coefficient shows no signs of stall (continuing a linear trend with ϕ_{gy}) and reaching values higher than given by the prediction. The tangential force indicates stall to occur at higher incidences than predicted but maximum values are broadly unchanged (Figures 11.7 and 11.8).

iv) For the 75%R station in axial flow the normal force coefficient does indicate stall but this occurs at a lower C_{Nmax} than given by the prediction. The tangential force agreement is much better, suggesting that the discrepancy between the power predicted by strip theory and the measured performance (Chapter 7) stems from the lower normal force coefficients in the outer blade region (Figures 11.9 and 11.10).

v) For yawed flow significant force coefficient hysteresis is obtained. This may partly be due to the uncertainties in the value of dynamic head assumed (even after ensuring that the values used are consistent with the measurements).

vi) Plotting only the cases for a narrow range of yaw angles enables systematic trends with blade azimuth and yaw to be determined. For the 75%R station the averaged yawed flow hysteresis loops of tangential force lie above both the strip theory prediction and the axial flow data whilst the normal force values tend to lie below (Figures 11.11 to 11.14).

vii) At the 35%R station the averaged hysteresis loops are much larger but the uncertainty in the values of dynamic head used are also greater. Ignoring the results at bottom-dead-centre and using stagnation pressures measured on the blade still produces normal and tangential force coefficients which are much geater than the strip theory predictions (Figures 11.15, 11.16).

viii) All force coefficient hysteresis loops indicated are traversed in a clockwise sense irrespective of their disposition about the stall angle.

ix) For the 75%R station the ±53° yaw, 18 m/s windspeed case appears to produce dynamic stall at the aerofoil. Large excursions in the pitching moment coefficient occur just after the aerofoil reaches the bottom-dead-centre azimuth and are accompanied by sudden changes in the normal and tangential force coefficients which tend to exceed the "steady" values. A vortex appears to progress down the chord after the suction peak collapses (Figures 11.20 and 11.21).

x) For the 35%R station the -43° yaw, 10 m/s case also appears to give rise to dynamic stall. Again, large pitching moments are suddenly produced but the hysteresis loop seen in the normal force coefficient is in the opposite sense and the vortex progression down the aerofoil is not as obvious as at the 75%R station (Figures 11.22 and 11.23).

xi) Positive yaw cases give rise to maximum incidence near to bottom-dead-centre whilst negative yaw cases produce it at top-dead-centre. Consequently at the 35%R station the nacelle blockage effects would significantly modify any dynamic behaviour in positive yaw cases. These effects are much less important for negative yaw cases which exhibit low angles of attack over the region of nacelle influence.

xii) The azimuthal extent of the nacelle blockage at the 35%R station has been identified. The arc swept by the blade whilst any part of the aerofoil is affected is approximately 140° in size but becomes smaller for lower windspeed cases. The effects of yaw mean that the pressure data over the top half-rev only should be used at the 35%R station (Figure 11.24).

CHAPTER 12

OVERALL CONCLUSIONS

12.0 Introduction

Deficiencies in current wind turbine aerodynamic load prediction codes have been illustrated. Aerofoil section characteristics may be modified in the 3-dimensional, rotating environment of a wind turbine blade or the modelling assumptions may be invalid. This results in uncertainty in the predicted power for the stalling HAWT rotor in high winds. The experiment described in this thesis aims to more fully explain the behaviour of a wind turbine blade by acquiring aerodynamic measurements from the aerofoil accounting for both axial and yawed flow.

12.1 The Experiment

A complex experiment has been undertaken involving the measurement of aerofoil surface pressures, rotor and yaw torques and turbine body vibration on a purpose built wind turbine. The machine was successfully field tested at an early stage of development, and was found to operate satisfactorily. The Marlec blades fitted to the turbine easily produce the manufacturers rated output but show only slight stall regulation characteristics in high winds.

Controlled velocity tests have been carried out using a "fully-instrumented blade" incorporating forty SENSYM SPX50DN pressure transducers. The high risk blade construction approach was successful and resulted in thirty-nine aerofoil surface pressure measurement locations. All in-service problems with the pressure measurements have been due to temporary failures within the signal processing electronics and these have gradually been erradicated. Both the data-acquisition system and the chosen pressure transducer model worked well and the software temperature compensation approach [4.1] resulted in acceptable levels of pressure measurement accuracy.

Measurements of the rotor inlet flow have also been made using four Lowne anemometers, a cup anemometer and a wind vane. The instrumentation behaved well but difficulties with obtaining reliable calibrations for the Lowne anemometers have resulted in significant

discrepancies between the three independent measurements of wind speed and direction. Re-calibration of the existing data base will be possible after the results from an independent (NEL) calibration are known. The accuracy of the cup anemometer measurements has been determined and this device has been used in almost all of the analysis described here.

The experiment was mounted on a mobile trailer which was designed and built by the Automotive Studies Group at Cranfield and enabled controlled velocity tests on the airfield to be carried out. This form of testing was entirely successful and enabled 22 different operating conditions to be systematically and swiftly investigated. The main inadequancy of the testing approach was the implicit dependance upon the wind conditions. The requirement for light natural winds was especially difficult to meet because of the exposed nature of the airfield. However, infrequent occurrence of suitable conditions highlighted the importance of the fast data-transfer approach in which thirteen 'runs' could be acquired within a short time. Difficulties with the runway surface were not as severe as expected due to the exclusive use of a recently resurfaced section.

12.2 The Results

A large data-base of measurements has been obtained with the turbine operating over a range of windspeeds (5.4 to 23.5 m/s) and yaw angles (-43° to +56°). A total of just 12 minutes of real time data has been calibrated to form a 46 Mbyte data base. This presented a significant data analysis challenge which was tackled by using a large subroutine library containing purpose written data manipulation code. Several application codes have also been developed to perform the analysis with extensive use of graphical output so that a large amount of data can be quickly appraised. The analysis described earlier has been performed on the entire data base, although only a small fraction of the results are presented here. The analysis phase is by no means complete but some conclusions can be drawn from that so far carried out.

The two blade measurement stations at 35%R and 75%R give indications of the behaviour of typical inboard and outboard blade sections although the data at 35%R for the lower half-rev should be considered more cautiously.

The parametric trend approach described in Chapter 9 provided a useful overview of the entire data-base. Comparisons between the field test turbine performance and the controlled velocity test data have demonstrated the validity of this form of testing.

With the rotor operating in yaw the regulation characteristics of the turbine are enhanced. This regulation can be derived from complete loss of driving force over only a part of the rotor rev which then produces lower rev-average values of torque. (The loading spectrum for a yawed turbine will therefore be severe.) The power regulation characteristics of the yawed turbine have also been noted to be asymmetric about the axial flow condition.

The 'effective blade length' concept introduced in Chapter 9 has corroborated the independent measurement of rotor torque and indicates that the assumption of linearly distributed loading is reasonable in high winds.

The yaw torque developed by the rotor has not yet been separated from the torque measured by the yaw load cell. Measurements of the yaw loads caused by the turbine body alone are required before comparisons between asymmetric rotor loads and rotor yaw torque can be made. However, analysis of the measured yaw torque, which includes both contributions, have corroborated the field performance observations that yaw instability occurred when the yaw angle exceeded about $\pm 50°$. Some spectral analysis of the pressure data has been carried out and a shift of energy to lower frequencies has been noted to result from rotor yaw.

In axial flow the 35%R measurement station gives some evidence for delayed stall (reaching a higher $C_{N_{max}}$ than given in 2-D wind tunnel data) and also exhibits a lower lift curve slope than would be expected. The 75%R measurements also indicate lower values of $dC_N/d\alpha$ but suggest earlier stall at lower values of $C_{N_{max}}$ than expected. The comparisons with strip-theory predictions for rotor power clearly show that the rotor behaviour is more dominated by the 75%R blade section than the 35%R section and explains why the measured performance falls below that predicted in high winds.

For positive yaw cases evidence of force coefficient hysteresis has been seen at both spanwise stations. This result does depend upon the assumed variation of dynamic head (which appears reasonable) but results

in force coefficients which generally lie above the axial flow case at the 75%R span and values which lie both above and below the axial flow case at the 35%R span. (The latter result has excluded the data for the bottom-dead-centre azimuth.)

Over certain yaw ranges, increases in the yaw angle can produce lower mean angles of attack and hence less separated flow conditions. This is in keeping with the simple geometric model for the aerofoil incidence on a yawed rotor. This model has been used to derive simple approximations of both the incidence and dynamic head seen by the aerofoil sections and in general, is preferable to assuming fixed values of α and q given by the tip speed ratio alone. The geometric yaw model, however, can be misleading and was found to agree with measurements best at the 75%R station. Also the estimates of dynamic head were more plausible than the values given for incidence angle, presumably because induced effects are more significant for the latter.

The angle of attack seen at the aerofoil has been indicated by various characteristics of the pressure distributions. The estimation of both incidence and dynamic head from the position and magnitude of the stagnation pressure has so far been unsuccessful due to the low tapping density in this region of the aerofoil. (Work on extrapolating the pressure distribution measurements for better estimates of the stagnation position and pressure is currently underway and appears to provide significant enhancement on these data streams.) The height of the suction peak however, did provide a useful alpha indicator although attempts to fully calibrate the relationship were unsuccessful. Excellent corrolation was found to exist between chordwise force at 75%R and suction peak alpha and the relationship with normal force, although more non-linear, also proved to be well behaved. The suction peak C_p value was found to be relatively insensitive to yaw (and hence spanwise flow) but its calculation is dependant upon the assumed value of dynamic head. On the whole, this alpha indicator does appear to provide a good measure of the angle of attack seen at the blade.

Due to the controlled conditions under which the experimental data has been acquired, the analysis approach has relied heavily on ensemble averaging techniques. Comparison of the average pressure distributions with 'instantaneous' measurements indicates that this approach is satisfactory although the results need to be interpreted with care when the flow exhibits instability close to stall. In every case reference

to the standard deviations is deemed essential to ascertain the correct interpretation of the results.

For an investigation into unsteady aerodynamic effects use of un-averaged data is essential. A vast amount of data is therefore potentially available and the analysis given here has concerned a tiny fraction of this. Nevertheless, evidence for the occurrence of dynamic stall has been seen at both the spanwise measurement locations (not, however, under the same windspeed conditions) and this is characterised, mainly, by large sudden excursions in the derived pitching moment and normal force coefficients. Other evidence suggests that the rotor operation in yaw may be aerodynamically more stable than for the axial flow case due to the incidence forcing function. This suggests that the axial flow condition is just a special case (zero yaw angle) which gives rise to less well behaved flow than produced at moderate yaw angles. This is especially so for the 35%R station where yaw results in incidence time histories which do not exceed the (dynamic) stall angle.

Careful appraisal of the instantaneous pressure time histories at the 35%R station has also led to quantification of the extent ot the nacelle blockage effects. This has resulted in the decision to use only the upper half-rev of data in future analysis and also for a greater emphasis to be placed on testing at negative yaw angles.

12.3 Further Work

The data acquired to date represents a small proportion of that available given that the rotor r.p.m. and blade pitch could both also be varied in the existing experiment. There are, however, some aspects of the wind turbine which could be improved and would make further testing more valuable. The nacelle blockage effects for inner blade stations in the lower half-rev are seen to affect the measurements significantly and this problem could be most easily alleviated by fitting a larger diameter rotor. (The turbine was originally designed for rotors up to 5m.) This would also allow instrumented blades to achieve better pressure tapping resolution close to the aerofoil leading edge and result in improved estimates of stagnation pressure, suction peak height and angle of attack.

Further analysis could also be performed on the existing data-base and allow some of the qualitative conclusions drawn here to be quantified.

As mentioned earlier, work is in progress to obtain improved estimates of the stagnation position and pressure and this should lead to greater confidence in the values of force coefficients which are derived. The re-calibration of the data from the Lowne anemometers will also provide much more detailed pictures of the inlet wind conditions and allow the input-response relationship to be examined more closely. Improvements to the anemometer signal processing circuits are also in hand and should enable turbulence levels to be more accurately found. (Performing controlled velocity tests on days other than calm ones has been suggested in order to acquire data at a range of turbulence levels.)

The most promising use of the data-base however, is in the development and validation of modern performance prediction codes. This use of the data from this experiment has already been demonstrated [12.1] and the measurements are currently being considered by other European research groups.

REFERENCES

[1.1] NACFAIRE, H.L.E.
DIAMANTARES, K.
The European Communities Demonstration Programme for Wind Energy and the European Community Energy Policy.
Proceedings of the European Wind Energy Conference, Glasgow, Scotland. July 1989.

[1.2] ROGERS, L.J.
US Wind Energy Research Program
Proceedings of the European Wind Energy Conference, Glasgow, Scotland. July 1989.

[1.3] LYNETTE, R.
Status of the U.S. Wind Power Industry
Wind Energy Conversion 1988,
Proceedings of the 1988 Tenth BWEA Wind Energy Conference. London, U.K. March 1988

[1.4] HENDERSON, G.
CEC News, WINDirections, Volume VIII, No.4, Spring 1989. ISSN 0950 - 0642, p.16.

[1.5] LINDLEY, D
The Commercialisation of Wind Energy
Proceedings of the Euroforum - New Energies Congress Volume 2, 24-28 Oct. 1988, Saarbrucken, Germany.

[1.6] CEGB
CEGB Press Information
23 March 1988.

[1.7] BWEA
Wind Power for the U.K. (The Red Book)
Published by the British Wind Energy Association. February 1987.

[1.8] LINDLEY, D.
The Wind Turbine Industry - A Review
Proceedings of the Euroforum - New Energies Congress, Volume 1, 24-28 Oct. 1988, Saarbrucken, Germany.

[1.9] WYMAN, V.
Who will pay for nuclear folly?
The Engineer, 16 Nov 1989, pp.24-25

[1.10] LINDLEY, D
Opening Address at EWEC 1989
Proceedings of the European Wind Energy Conference, Glasgow, Scotland. July 1989.

[1.11] PALZ, W.
CARATTI, G.
SHOCK, R.
Wind Energy R&D in the European Community.
Proceedings of the European Wind Energy Conference, Glasgow, Scotland. July 1989.

[1.12] WEG Ltd.
The WEG MS-2 Stall-regulated rotor study, Wind Energy Group Ltd., WEG 25-4062 ETSU WN 5063

[1.13] ANDERSON, M.B.
MILBORROW, D.J.
ROSS, J.N.
Performance and Wake Measurements on a 3m Diameter HAWT. Proceedings of the 4th International Symposium on Wind Energy Systems. Stockholm, 1982.

[1.14] HIBBS, B.
RADKEY, R.L.
Calculating Rotor Performance with the revised 'PROP' computer code. Aerovironment Inc. Report PFN-13470W, 1983.

[1.15] WILSON, R.E.
WALKER, S.N.
WEBER, T.L.
HARTIN, J.R.
A Comparison of Mean Loads and Performance Predictions with Experimental Measurements for Horizontal Axis Wind Turbines. Eighth ASME Wind Energy Symposium, Houston, Texas, January 1989.

[2.1] KLIMAS
Three Dimensional Stall Effects. IEA R&D WECS, Joint Action on Aerodynamics of Wind Turbines, October 1986.

[2.2] SORENSON, J.N.
Three-level, viscous-inviscid Interaction Technique for the Prediction of Separated Flow Past Rotating Wing. AFM 86-03, Technical University of Denmark.

[2.3] SORENSON, J.N.
Some Physical and Numerical Aspects of Wind Turbine Aerodynamics, IEA R&D WECS, Joint Action on Aerodynamics of Wind Turbines, November, 1988.

[2.4] RAWLINSON-SMITH, R.
Progress in Aerodynamic Performance Prediction for the Stalling HAWT Rotor. U.K. Dept of Energy. Interim Report. E/5A/CON/5087/1642.

[2.5] MILBORROW, D.J.
ROSS, J.N.
Aerofoil Characteristics of Rotating Blades. IEA LS-WECS, 12th Meeting of Experts Copenhagen, October 1984.

[2.6] HIMMELSCAMP, H.
Profile Investigations on a Rotating Airscrew. Ph.D. Dissertation, Gottingen, 1945. Ministry of Aircraft Production, Völkenrode, Reports and Translations No. 832, VG 177, Sept. 1947; ARC 10856.

[2.7] MILBORROW, D.J.
Changes in Aerofoil Characteristics Due to Radial Flow on Rotating Blades. BWEA, 7th Annual Workshop, Oxford, 27-29 March, 1985.

[2.8] VITERNA, L.A.
JANETZKE, D.C.
Theoretical and Experimental Power from Large Horizontal Axis Wind Turbines.
Fifth Biennial US Wind Energy Conference and Workshop. Washington D.C. 1981.

[2.9] RASMUSSEN, F.
Aerodynamic Performance of a New LM 17.2m Rotor.
Risø-M-2467, Risø National Laboratory 4000 Roskilde, Denmark.

[2.10] RASMUSSEN, F.
PETERSEN, S.M.
LARSEN, G.
KRETZ, A.
ANDERSEN, D.
Investigations of Aerodynamics, Structural Dynamics and Fatigue on Danwin 180 kW.
Risø-M-2727, June 1988, Risø National Laboratory, DK-4000, Roskilde, Denmark.

[2.11] MADSEN, H.A.
RASMUSSEN, F.
Derivation of three-dimensional Airfoil Data on the Basis of Experiment and Theory.
IEA R&D WECS. Joint Action on Aerodynamics of Wind Turbines, November 1988.

[2.12] HALES, R.L.
Aerodynamic Research Requirements for Fixed Pitch Horizontal Axis Wind Turbines.
U.K. Department of Energy, Final Report E/5A/CON/5043/1337.

[2.13] MUSIAL, W.D.
CROMACK, D.E.
Influence on Reynolds Number on Performance Modelling of Horizontal Axis Wind Rotors.
Journal of Solar Energy Engineering, May 1988, Vol. 110.

[2.14] MILEY, S.J.
A Catalogue of Low Reynolds Number Airfoil Data for Wind Turbine Applications. Feb. 1982, Texas A&M University RFP-3387, UC-60.

[2.15] BARRACK, P.G.L.
The Effect of Free Stream Turbulence on the Stalling Characteristic of a Family of NACA 23000 Series Aerofoil Sections. MSc Thesis. Imperial College of Science and Technology, London, 1977.

[2.16] McKEOUGH, P.J.
Effects of Turbulence on Aerofoils at High Incidence. Ph.D. Thesis. University of London, Faculty of Engineering, 1976.

[2.17] HILL, D.C.
GARRAD, A.D.
Design of Aerofoils for Wind Turbine Use.
IEA R&D WECS, Joint Action on Aerodynamics of Wind Turbines, November 1988.

[2.18] RONSTEN, G.
DAHLBERG, J.
DEXIN, H.
MING, C.
Pressure Measurements on a 5.35m HAWT in CARDC 12*16m Wind Tunnel Compared to Theoretical Pressure Distributions.
European Wind Energy Conference and Exhibition, EWEC'89, Glasgow, Scotland. July 1989.

[2.19] BARNSLEY, M.J.
WELLICOME, J.F.
Design and Testing of a Horizontal Axis Wind Turbine Model for the Investigation of Stall Regulation Aerodynamics.
European Wind Energy Conference and Exhibition. EWEC'89, Glasgow, Scotland. July 1989.

[2.20] BROWN, C.J.
GRAHAM, J.M.R.
Investigation into the Effect of Turbine Rotation on the Maximum Lift Coefficient.
Imperial College of Science and Technology, Department of Aeronautics, December 1989.

[2.21] NYLAND, T.W.
Surface Pressure Measurements on the Blade of and Operating MOD-2 Wind Turbine With and Without Vortex Generators.
DOE/NASA/20320-72, NASA TM-89903.

[2.22] BUTTERFIELD, C.P.
Three Dimensional Airfoil Performance Measurements on a Rotating Wing.
European Wind Energy Conference and Exhibition. EWEC '89, Glasgow, Scotland. July 1989.

[2.23] MADSEN, H.A.
RASMUSSEN, F.
Measured Aerofoil Characteristics of Three Blade Segments on a 19m HAWT Rotor.
IEA R&D WECS.
Joint Action on Aerodynamics of Wind Turbines.
Harwell, England. November 1989.

[2.24] EGGLESTON, D.M.
STARCHER, K.
Comparative Study of the Aerodynamics of Several Wind Turbines Using Flow Visualisation.
Eighth ASME Wind Energy Symposium.
Houston, Texas. January 1989.

[2.25] PEDERSEN, T.F.
MADSEN, H.A.
Location of Flow Separation on an 11m Wind Turbine Blade by Means of Flow Visualisation and a Two Dimensional Aerofoil Code.
Wind Energy Conversion, Proceedings of the 1988 Tenth BWEA Wind Energy Conference, London, March, 1988.

[2.26] SAVINO, J.M.
NYLAND, T.W.
Wind Turbine Flow Visualisation Studies.
Seventh Bienniel US Wind Energy Conference.
San Francisco, August, 1985.

[2.27] McALISTER, K.W.
CARR, L.W.
McCROSKEY, W.J.
Dynamic Stall Experiments on the NACA 0012 Airfoil.
NASA TP-1100, 1978.

[2.28] CARR, L.W.
McALISTER, K.W.
McCROSKEY, W.J.
Analysis of the Development of Dynamic Stall Based on Oscillating Airfoil Experiments.
NASA TN D-8382, 1977.

[2.29] CARR, L.W.
Progress in Analysis and Prediction of Dynamic Stall. Journal of Aircraft. Vol.25, No. 1, January 1988.

[2.30] COURTNEY, M.S.
Dynamic Stall on Stall-Regulated Horizontal Axis Wind Turbines.
Risø Report on EFP-85 Project
Risø National Laboratory, DK-4000, Roskilde, Denmark.

[2.31] CORRIGAN, R.D.
VITERNA, L.A.
Free Yaw Performance of the MOD-O Large Horizontal Axis 100 kW Wind Turbine.
NASA CP 2230, Large HAWT's, Cleveland, July 1981.

[2.32] GLASGOW, J.C.
CORRIGAN, R.D.
MILLER, D.R.
The Effect of Yaw on Horizontal Axis Wind Turbine Loading and Performance.
DOE/NASA Report 20320-35.

[2.33] GLASGOW, J.C.
PFANNER, H.G.
WESTERKAMP, E.J.
The Response of a 38m Horizontal Axis Teetered Rotor to Yaw.
NASA CP2230, Large HAWT's, Cleveland, July 1981.

[2.34] GLASGOW, J.C.
CORRIGAN, R.D.
Results of Free Yaw Tests of the MOD-O 100 kW Wind Turbine.
U.S. Wind Workshop VI, Minneapolis/St. Paul. June 1983.

[2.35] GLASGOW, J.C.
MILLER, D.R.
CORRIGAN, R.D.
Comparison of Upwind and Downwind Rotor Operations of a DOE/NASA 100kW MOD-O Wind Turbine. (NASA TM-81744)
Wind Turbine Dynamics, Cleveland, February 1981.

[2.36] GLASGOW, J.C.
MILLER, D.R.
Teetered, Tip-controlled Rotor; Preliminary Test Results from MOD-O 100 kW Experimental Wind Turbine.
DOE/NASA/1028-80/26, NASA TM-81445.

[2.37] ANDERSON, M.
Horizontal Axis Wind Turbines in Yaw.
Fourth International Symposium on Wind Energy Systems.
Stockholm, September 1982.

[2.38] DIAMANTARAS, K.
Analysis of Data 25m HAT, ECN Under Yaw Misalignment.
ECN. FYS-WIND-84-36.

[2.39] RASMUSSEN, F.
PETERSEN, T.F.
Measurements and Calculations of Forces on the Blades of a Stall-Regulated HAWT.
Risø-M-2346, Risø National Laboratory, DK-4000, Roskilde, Denmark. June 1982.

[2.40] RASMUSSEN, F.
Measurements of Cyclic Loads on Vestas 55 kW Rotor.
IEA R&D WECS. Joint Action on Aerodynamics of Wind Turbines, October 1986.

[2.41] HANSEN, C.
CUI, X.
Precent Progress in the Prediction of Yaw Dynamics.
Eighth ASME Wind Energy Symposium. Houston, Texas, January 1989.

[2.42] WALDON, C.A.
Effects of Yaw Rate on the Fatigue Life of Horizontal Axis WECS.
Rockwell International, Wind Systems Programme. P.O. Box 464, Golden, Colorado.

[2.43] CONNELL, J.R.
A Primer of Turbulence at the Wind Turbine Rotor.
Solar Energy, Vol. 41, No. 3, 1988.

[2.44] SUNDAR, R.M.
SULLIVAN, J.P.
Performance of Wind Turbines in a Turbulent Atmosphere.
Solar Energy Vol. 31, No. 6, 1983.

[2.45] SNYDER, M.V.
WENTZ, W.H.
Dynamics of Wakes Downstream of Wind Turbine Towers.
Wind Energy Laboratory, Wichita State University, Wichita, Kansas.

[2.46] POWLES, S.R.J.
The Effects of Tower Shadow on the Dynamics of a Horizontal Axis Wind Turbine.
Wind Engineering, Vol.7, No.1. 1983.

[2.47] SMITH, D.R.
Optimum Rotor Diameter for Horizontal Axis Wind Turbines.
The Influence of Wind Shear Assumptions.
Wind Engineering. Vol.6. No.1, 1982.

[3.1] SALIVEROS E.
McD GALBRAITH R.A.
COTON F.N.
The low Reynolds Number performance of a NACA 4415 aerofoil. Wind Energy Conversion.
Proceedings of the 1988 Tenth BWEA Wind Energy Conference.
London 22-24 March 1988.

[4.1] ORAM, C.E.
Aerodynamic pressure measurements on a vertical axis wind turbine in a wind tunnel and atmosphere.
Ph.D. Thesis. School of Mechanical Engineering, Cranfield Institute of Technology, 1990.

[4.2] HOBBS, S.
Lowne Digital Anemometer Calibrations,
School of Industrial Science.
Ecological Physics Research Group,
Cranfield Institute of Technology.
October 1989.

[4.3] FRANDSEN, S
TRENKA, A.R.
PEDERSEN, B.M.
Recommended practices for Wind Turbine Testing.
1. Power performance testing
International Energy Agency, 1982.

[4.4] CHAPMAN, A.J.
Heat Transfer
McMillan, New York, 1960.

[4.5] PETERSEN, H.
Calculations on the DWT Wind Turbine, 29.3/3/3D, The Koldby Wind Turbine in Yaw.
BWEA6, Reading, March 1984.

[4.6] RASMUSSEN, F.
Aerodynamic forces acting on blades of stall-regulated windmills.
Risø National Laboratories,
Risø-M-2316, August 1981 (translated from the Danish).

[4.7] RIEGELS, F.W,
Aerofoil Sections.
Butterworth and Co. Ltd.
London, 1961.

[6.1] HAYWARD, A.T.J.
Repeatability and accuracy
Mechanical Engineering Publications Ltd. 1977.

[7.1] CURVERS, A.P.W.M.
PEDERSEN, T.F.
European wind turbine standard on performance determination.
Eighth ASME Wind Energy Symposium,
Houston, 1989

[7.2] STACEY, G.
MUSGROVE, P.J.
The performance of the Rutherford 6 m diameter vertical axis wind turbine, including the effects of various binning techniques and averaging periods.
BWEA 6, Reading, March 1984

[7.3] HAUSFIELD, T.E.
HANSEN, A.C.
A systematic approach to using the method of bins.
Sixth biennial Wind Energy Conference and Workshop,
Minneapolis, June 1983

[7.4] CHRISTENSEN, C.J.
DRAGT, J.B.
Accuracy of power curve measurements
Risø, Risø-M-2632, Nov 1986

[7.5] van BUSSEL, G.J.W
A comparison of open air performance measurements using different methods
Wind Energy Conversion.
Proceedings of the 1987 Ninth BWEA Wind Energy Conference, Edinburgh, April 1987.

[7.6] SPAG
Course notes - Basic Practical Signal Processing. Signal Processing and Applications Group, Cranfield Institute of Technology, 1987.

[7.7] HUNTER, R
The accuracy of cup anemometry.
European Wind Energy Conference
EWEC '89, 10-13 July, Glasgow, Scotland.

[7.8] OSTOWARI, C
NAIK, D.
Post stall wind tunnel data for NACA 44XX series airfoil sections
SERI/STR--217-2559, January 1985.

[8.1] HEALY, S.P.
HALES, R.L.
Development of a mobile facility for aerodynamic testing,
Volume 3 of 5, An Experimental Investigation of HAWT Aerodynamics in Natural Conditions.
Final Report for CEC DG XII Contract No. EN3W/0033/GB.

[8.2] BRITISH STANDARDS
B.S. 1042: PART 2A: 1973
Methods for the measurement of fluid Flow in pipes.
Part 2: Pitot tubes.

[8.3] DEAN, R.C.
Aerodynamic measurements gas turbine laboratory.
Massachusetts Institute of Technology, 1953.

[8.4] CRANFIELD INSTITUTE OF TECHNOLOGY
Drawing No. S/A/65.
Estates Department.

[9.1] BROTHERHOOD, P.
RILEY, M.J.
Flight experiments on aerodynamic features affecting helicopte blade design.
Vertica, Vol.2, 1978. pp27-42.

[9.2] JENKINS, G.M.
WATTS, D.G.
Spectral analysis and its applications.
San Francisco: Holden-Day, 1968.

[11.1] HUNT, A.
Two dimensional testing of the NACA 44XX series of aerofoils.
College of Aeronautics. Cranfield Institute of Technology, October 1979.

[12.1] RAWLINSON-SMITH, R.I.
HALES, R.L.
Computational study of stalled rotor performance.
BWEA 12, Norwich, 1990.

[AII.1]BERGH, H.
TIJDEMAN, H.
Theoretical and Experimental Results for the Dynamic Response of Pressure Measuring Systems.
Report NLR-TR F.238.

[AII.2]NYLAND, T.W.
ANDERSON, R.C.
Some Limitations on the Use of Damping in Short Probes.
NASA TN D-6526, October 1971.

[AII.3]SCHWEIKHARD, W.G.
Test Techniques, Instrumentation and Data Processing.
AGARD LS-72, DIstortion Induced Engine Stability, November 1974.

ACKNOWLEDGEMENTS

The assistance of many people has been sought throughout the execution of this project, and I am grateful to all who have helped and guided me.

In particular, Richard Hales, who initially proposed the work and consequently, without whom, the work may never have been started or finished.

Two of my peers at Cranfield have also given me great encouragement. In the early months Dr. Colin Oram instilled me with confidence and encouraged me to adopt his uncompromising approach to experimental work. Over the latter half of the project, Robert Rawlinson-Smith willingly provided invaluable help in interpreting the measurements and also in dealing with the Cranfield system!

My thanks go to Brian Moffitt, the electronics expert who is ultimately responsible for the high quality of the measurements and who was always there for help and support.

I am also grateful to Professor Barrie Moss, who willingly read the first drafts of much of this thesis and enabled me to complete it before I left Cranfield.

I must also thank Angela Walshe who has typed much of the later chapters and who had to endure my apparently never ending series of modifications.

Lastly, but by no means least, I must thank Chris, my wife, who saw me through this all and without whom it would never have been completed.

* * * * * * * *

APPENDIX I - Pressure Transducer Choice

AI.1 Introduction

In an attempt to further the work of Oram [4.1] six different transducer models were investigated. The device chosen for the earlier work was compared with five other transducers which has previously not been considered in an attempt to further improve the quality of the results or of finding a device which was easier to handle.

The following transducers were compared:-

(1) SX15AN High Impedance, 0-100 kPa absolute
(2) SX01DN High Impedence, 0-7 kPa differential
(3) SX05DN High Impedance, 0-35 kPa differential
(4) SPX50D Basic Package, 0-50 kPa differential
(5) SPX50DN Easy connect package, 0-50 kPa differential
(6) SPX100A Basic package, 0-100 kPa absolute

Two of the transducers tested were absolute devices measuring pressure with respect to a vacuum. The other four sensors tested were differential, producing an output proportional to the difference in pressure between two input ports. The use of an absolute device rather than a differential one for blade surface pressure measurements would have one major advantage in practice. This is the relaxation of the requirement for a reference pressure system on the rotor and hence no need of a pneumatic slip ring. In addition the use of an absolute pressure transducer for the measurement of barometric pressure (remote from the rotor) would relax the requirement for a dedicated barometer.

The four differential transducers tested fell into two groups. Two 'high impedence' devices (excited at 12.0 V) and two basic devices (excited at 3.0 V). It was thought that the two high impedence devices could improve the accuracy of pressure measurements due to their much larger pressure sensitivities.

AI.2 Experimental Work

The experiments carried out were designed to show the capabilities of these transducers in two areas. Firstly, their sensitivities to steady

temperatures and pressures were investigated, repeatability being of the utmost importance. Secondly, their dynamic characteristics were examined to see if their response under conditions of dynamic stall would be adequate. This aspect is described in Appendix II.

A total of seven experiments were performed to determine the steady-state behaviour of each transducer, all with the same experimental set-up shown in Figure AI.1a). The transducers were connected up in the same manner as for the tests performed by Oram [4.1] so that fair comparisons could be made. The experiments were of two types. Firstly the transducer outputs were recorded under conditions of varying temperature to determine how repeatable these outputs were. Secondly, a pressure calibration was performed, in which the transducer outputs under conditions of varying pressure (and constant temperature) were examined.

AI.2.1 Experiments 1 and 2

The first experiment was an attempt at evaluating the temperature characteristics of the transducers. However, the results from all transducers were found to be rather erratic, producing confused pictures of the temperature dependence of the transducer outputs. On careful examination it was suspected that the experimental technique was at fault. The environmental chamber in which the transducers were housed utilised a powerful fan system to circulate air over its heat exchangers and around the chamber. Despite attempts to isolate the transducers from these effects the results suggested corruption of the data from the fans electrical or pneumatic noise. Experiment 2 was then conducted to prove or disprove this theory. The temperature signal from one of the transducers was logged over several hours under varying conditions. First the chamber was left switched off to allow the system to settle. The chamber fan was then switched on without activating the chambers heat exchangers and finally some baffling material was added around the transducer. The results from this experiment proved conclusively that the chamber fans were responsible for a 0.15 mV shift in the output of the transducer tested. The conclusion was that all subsequent experiments would be conducted in a different way.

AI.2.2 Experiment 3

This experiment was performed to determine a better experimental procedure, avoiding the problems described above. The method adopted was as follows:-

i) The transducers are powered up and left to settle for a couple of hours.

ii) With the chamber off (room temperature), a set of measurements are taken.

iii) The chamber is turned on, a temperature of 1 or 2°C is demanded and the chamber is allowed to settle for an hour or so.

iv) The chamber is turned off and allowed to settle for a few minutes before taking a set of measurements.

v) During the next few hours measurements are taken at about half hourly intervals whilst the chamber temperature gradually drifts up to room temperature.

vi) The procedure is repeated for temperatures above room temperature by initially demanding a temperature of about 35°C.

AI.2.3 Experiments 4 and 6

These experiments were carried out as described above with the apparatus again as shown in Figure AI.1a). The results for transducer (5) only (the SPX50DN) are set out in Table AI.1 which also shows how the data is processed. To more faily compare data taken at different times of the day, the measured voltages are scaled to correct for the varying excitation voltage. The data is corrected to an excitation voltage of 12.000 V for transducers 1, 2 and 3 and 3.000 V for transducers 4, 5 and 6. The results for transducers 1 and 6 require a further correction for the effects of barometric pressure changes during the test. A Fortin barometer is read periodically during the tests and its value corrected to account for the mercury temperature. The data collected from the absolute transducers can then be corrected to a nominal barometric pressure of 760 mmHg so that data from different days may be compared. The results for all transducers are plotted in Figure AI.2.

AI.2.4 Experiments 5 and 7

These tests were performed to determine the response of each transducer to pressure changes. With the experiment still set up as shown in

Figure AI.1a), varying pressures were applied to each transducer's sensing port using a small air pump and were measured on a water manometer. The results were noted down quickly so that the complete test of about 10 applied pressures was completed in a short time. This meant that any dependence of the results on temperature could be excluded since it remained constant throughout. Again the results are corrected for power supply drift (and barometric pressure if necessary) and are given in Figure AI.3 for transducers (4) and (5), the SPX50D and SPX50DN.

AI.3 Results

The problems associated with the use of absolute pressure transducers are clearly illustrated by the results for transducers (1) and (6), the SX15AN and the SPX100A (see Figure AI.2). In their blade pressure measurement application, errors due to their hysteresis are greater than the typical pressures to which the required measurements should resolve. Consider a measurement of interest to be a pressure 30 Pa below atmospheric pressure (equivalent to 2% of a typical rotor dynamic head). If the barometric pressure is 100000 Pa then the transducer will be responding to a pressure of 99970 Pa. The transducer measurement, however, would lie in the range 99970 $\pm$ 99.97 Pa (the manufacturers quoted accuracy is 0.1% Full Scale) assuming that the only errors are those inherent in the transducer. Obviously this level of accuracy is equivalent to $\pm$ 7% of the typical dynamic head and is therefore unsatisfactory. The problem is further exacerbated, however, when considering the measurement of barometric pressure which is also required to find the true differential pressure at the aerofoil. Even if the barometric pressure can be measured to within 5 Pa (a typical Fortin Barometer can be read to within 0.05 mmHg or 6.67 Pa) the pressure drop required is the difference between two large numbers. It is therefore clear that the absolute devices considered here are not sufficiently accurate for the determination of barometric pressure or blade pressures. (The measurement of barometric pressure to the required accuracy was achieved with the purchase of a proprietry digital barometer (Druck DPI 140) which is described in Chapter 4).

Of the four differential transducers tested the results shown in Figure AI.2 indicate that the SPX50D and the SPX50DN are more capable of producing repeatable results than either of the other two transducers. Data taken during tests 4 and 6 (10 days apart) lie on a single curve

for transducers (4) and (5) whilst that for transducers (2) and (3) can easily be split into two distinct sets. To be fair, however, it should be noted that because of the different transducer excitation voltages the changes in V_i and V_o for transducers (2) and (3) are more than double those changes for transducers (4) and (5). Despite this, the uncertainty in the zero pressure offset for transducers (2) and (3) is of the order of 0.5% of its nominal value whereas for transducers (4) and (5) it is approximately 0.2%. With careful amplification of the signals from transducers (4) or (5), the SPX50D or SPX50DN, this benefit can still be realised at higher levels.

AI.4 Conclusions

It is clear from the above that the best transducers tested were the SPX50D and the SPX50DN. Their main advantage being much better repeatability than any of the other transducers (partly, but not entirely at the cost of lower sensitivity). Another important conclusion from these tests is that no significant differences between the responses of the two transducers could be found. In other words the easy connect package of the SPX50DN does not affect the performance of the sensing diaphragm and either the SPX50D or the SPX50DN transducer may be used. With this in mind the SPX50DN transducer was chosen for this work.

APPENDIX II - Pressure Transducer Frequency Response

AII.1 Introduction

The blade surface pressure measuring system described in Chapter 3 requires a duct to relay the aerodynamic pressure to the remote transducer. Due to restrictions of space within the blade and the density of tappings at the surface the minimum length of duct estimated to be practicle was 50 mm. In terms of the pressure transducer frequency response the duct length and diameter have been shown to be important parameters in work by Bergh and Tijdeman [AII.1]. They show both theoretically and experimentally how a sinusoidal pressure disturbance within a volume relates to pressure disturbances in the preceeding and next volumes when they are series connected by thin tubes. This is directly comparable with the instrumented blades used in this work where a surface tapping communicates with a transducer (which represents a sealed volume) via a thin tube.

AII.2 Theoretical Approach

NASA work [AII.2] develops the work of Bergh and Tijdeman and describes a FORTRAN program to calculate the amplitude and phase response for any series combination of tubes and volumes over a range of frequencies. A copy of the program was obtained and a series of runs were carried out to investigate the effects of varying the duct length and diameter for a single duct-volume system. The internal volume of the SPX50DN transducers was measured (approximately 15mm^3) and this value was used for all calculations. A typical result is given in Figure AII.1. The plot shows the variations of both amplitude ratio and phase with the applied frequency. At a frequency of 600 Hz the amplitude ratio (R) of 1.5 means that the pressure signal seen at a transducer would be 50% bigger than that applied at the duct opening. The plot also shows that at a certain frequency (dependent upon the configuration) a resonant peak occurs (R = Rmax) where further increases in frequency result in lower amplitude ratios. At even higher frequencies significant attenuation can occur and phase delays in the system become large.

In order to interpret these effects for the instrumented blades some knowledge of the maximum frequency of interest is desirable. This is very difficult to estimate with any certainty but will probably be the

frequency associated with the suction peak collapse during a dynamic stall event. It is suggested [4.1] that this frequency can be represented as having a period of 2 to 3% of that of the incidence function. Under the most pessimistic circumstances (operation in yaw at 666 r.p.m.) this frequency is approximately 555 Hz.

Assuming a 5% amplification factor to be acceptable at the maximum expected frequency, the configurations considered in the computer simulations can be assessed. The best practical combination of length and diameter were chosen as a length of 50 mm (the minimum due to space constraints) and a duct diameter of 1 mm. The calculated frequency response for this configuration is that shown in Figure AII.1. The diameter used may seem quite small in view of the fact that the resonance occurs at lower frequencies as the duct bore is reduced. However, the work of Schweikhard [AII.3] shows that there is little advantage in using a large diameter duct with smaller diameter sections along its length. Since the pressure transducer inlet duct is of 1 mm diameter and the tapping size chosen was 1 mm it is reasonable to adopt this same size for the connecting tube.

AII.3 Experimental Approach

In order to corroborate the computer predictions of the duct frequency response an experiment was set up to take measurements of the chosen configuration.

The experimental setup is shown in Figure AI.1b). A small loudspeaker is fitted to a brass plate using 'Blu-Tac' to produce an air-tight seal. Two SPX50D transducers are attached to the plate so that their input ports sense the loudspeaker output. One is fitted directly to the brass plate while the other is connected via a 50 mm length of 1 mm diameter silicone rubber pipe. When the loudspeaker is driven by a signal generator (set for sinusoidal output) the oscillating air movements are sensed by the transducers whose outputs are amplified and displayed on a digital storage oscilloscope. A series of results are noted as the excitation frequency is varied so that the effects due to the 50 mm length of duct can be identified.

After correcting for the slight difference in sensitivities between the two transducers, the ratio between the two outputs is calculated and represents the effects of resonance in the pipe. The experimental

results are also shown in Figure AII.1. (Attempts to measure the phase relationship between the two signals with this experimental setup were unsuccessful.)

AII.4 Results

The results show clearly that for excitation frequencies less than 200 Hz the target of 5% amplification has been achieved. Consequently, pressure measurements at 333 r.p.m. (which are estimated to involve frequencies up to 185 Hz) should be sufficiently accurate. For higher rotor speeds, however, this may not be the case. The data collected at 333 r.p.m., however, may be spectrally analysed and result in more acurate assessment of the maximum frequencies which actually results from this rotor speed. If they are much less than 185 Hz (as would be expected) then testing at the maximum speed of 666 r.p.m. may also prove to be sufficiently accurate.

TABLE 3.1 Specification for the Cranfield Aerodynamics Experiment Wind Turbine

The Turbine

Stall regulated	upwind rotor
Diameter	2.854 m
Number of blades	3
Rotational speeds (nominal)	333, 395, 458, 583 or 667 rpm
Rotational direction	clockwise, seen from upwind
Cone angle	0 degrees
Tilt angle	0 degrees
Rotor plane to yaw axis	0.6 m

The Blades

Manufacture	Marlec "3m diameter, 1kW"
Planform	Tapered, untwisted
Pitch setting (nominal)	6 degrees
Aerofoil section (nominal)	NACA 4415
Radius and pitch line	mid-chord line
Blade root 'cut out'	25% radius
Chord at 25% radius	0.225 m
Chord at tip	0.104 m
First flap frequency	15 Hz

Table 4.1(a) FIB Measured Profile at 35% Span

Pressure Surface

	Measurement Co-ordinate system			Chord Co-ordinate system		Non-Dimensional Co-ordinate system (Chord = 208.58)	
Point	Y	Z	X°	X′	Y′	X	Y
TE	0	101.765	-1.9E-2	208.58	0.597	1.0	2.86E-3
LE	208.58	101.727	208.561	0.0	0.0	0.0	0.0
3502P	203.485	108.229	Y°	5.0962	6.5011	2.44E-2	3.12E-2
3504P	200.415	109.55	101.765	8.1664	7.8215	3.92E-2	3.75E-2
3511P	186.815	111.785	Δ	21.7668	10.0540	0.10436	4.82E-2
3523P	160.675	112.078	-1.8E-4	47.9069	10.3423	0.22968	4.96E-2
3540P	125.685	111.328	Z bot	82.8967	9.5859	0.39743	4.6E-2
3563P	78.39	108.649	102.362	130.191	6.8983	0.62418	3.31E-2
3591P	21.79	104.978		186.791	3.2170	0.89553	1.54E-2

Suction Surface

	Measurement Co-ordinate system			Chord Co-ordinate system		Non-Dimensional Co-ordinate system (Chord = 208.58)	
Point	Y	Z	X°	X′	Y′	X	Y
TE	0	161.976	0.74938	208.582	0.0	1.0	0.0
LE	208.58	162.941	209.332	0.00	5.96E-8	0.0	2.9E-10
3500S	208.56	160.503		3.13E-2	-2.4379	1.5E-4	-1.2E-2
3502S	205.255	166.903	Y°	3.30663	3.97734	1.59E-2	1.91E-2
3504S	202.075	169.697	161.974	6.47367	6.78602	3.1E-2	3.25E-2
3508S	195.18	173.558		13.3507	10.6789	6.4E-2	5.12E-2
3514S	183.39	178.181	Δ	25.1192	15.3564	0.12043	7.36E-2
3522S	169.355	181.635	4.63E-3	39.1381	18.8753	0.18764	9.05E-2
3530S	152.85	183.718		55.6333	21.0346	0.26672	0.10085
3540S	130.99	184.887	Z Top	77.4876	22.3047	0.3715	0.10693
3550S	108.07	183.794	161.976	100.412	21.3178	0.4814	0.1022
3562S	80.35	180.492		128.147	18.1441	0.61437	8.7E-2
3575S	48.41	174.396		160.115	12.1959	0.76764	5.85E-2
3594S	16.115	165.913		192.449	3.8624	0.92265	1.85E-2

Table 4.1(b) FIB Measured Profile at 75% Span

Pressure Surface

Measurement Co-ordinate system			Chord Co-ordinate system			Non-Dimensional Co-ordinate system	
						Chord = 143.901	
Point	Y	Z	X°	X′	Y′	X	Y
TE	0	86.627	-1.0782	143.901	0.54596	1.0	3.79E-3
LE	143.89	84.836	142.823	0.0	-3E-8	0.0	-2E-10
7504P	137.305	90.83	Y°	6.6591	5.91158	4.63E-2	4.11E-2
7507P	132.795	91.694	86.6203	11.1795	6.71938	7.77E-2	4.67E-2
7510P	129.31	92.38		14.6728	7.36195	0.10196	5.12E-2
7519P	116.26	92.532	Δ	27.7236	7.35152	0.19266	5.11E-2
7541P	84.45	92.126	-1.2E-2	59.5261	6.54964	0.41366	4.55E-2
7565P	49.665	90.678	Z Bot	94.2904	4.66882	0.65524	3.24E-2
7588P	19.055	88.824	87.173	124.875	2.43399	0.86778	1.69E-2

Suction Surface

Measurement Co-ordinate system			Chord Co-ordinate system			Non-Dimensional Co-ordinate system	
						Chord = 143.846	
Point	Y	Z	X°	X′	Y′	X	Y
TE	0	149.975	1.81362	143.846	0.69845	1.0	4.86E-3
LE	143.835	151.714	145.659	0.0	-6E-8	0.0	-4E-10
7501S	143.575	153.264		0.24124	1.55303	1.68E-3	1.08E-2
7504S	139.185	158.394	Y°	4.56888	6.73574	3.18E-2	4.68E-2
7507S	134.97	160.782	149.964	8.75469	9.17454	6.09E-2	6.38E-2
7510S	129.585	163.093		14.1114	11.5505	9.81E-2	8.03E-2
7514S	123.345	165.1	Δ	20.3266	13.6328	0.14131	9.48E-2
7522S	111.655	167.259	1.21E-2	31.9897	15.933	0.22239	0.11076
7530S	99.955	168.402		43.675	17.2174	0.30362	0.11969
7540S	85.55	168.224	Z top	58.0811	17.2136	0.40377	0.11967
7550S	70.985	167.107	150.673	72.6585	16.2728	0.50511	0.11313
7562S	53.795	164.465		89.8792	13.8389	0.62483	9.62E-2
7575S	34.955	160.579		108.765	10.181	0.75612	7.08E-2
7591P	14.09	154.991		129.696	4.84575	0.90163	3.37E-2

Table 5.1 Transducer Ranking Experiment Results

Rg = 1370 Gain = 30.1971

Tran. I.D	Measured Zp o/p V	Measured Water Heights Left in	Right in	Measured o/p V	Tran. Zp o/p mV	Tran. sens. mV/kPa
Yellow1	0.377	12.7	7.3	0.579	12.4847	1.34411
Yellow2	0.592	14.7	9.1	0.762	19.6045	0.95057
Yellow3	0.349	14.9	9.4	0.533	11.5574	1.00768
Yellow4	0.406	15.5	10.3	0.677	13.445	1.39785
Yellow5	0.359	14.5	9	0.559	11.8886	1.13259
Yellow6	0.2866	14.4	9.1	0.499	9.49098	1.20282
Yellow7	0.359	14	8.5	0.568	11.8886	1.23616
Yellow8	0.469	14.9	9.9	0.636	15.5313	0.89614
Yellow9	0.591	15	9.5	0.74	19.5714	0.80934
White1	0.448	15	9.5	0.654	14.8359	1.11896
White2	0.437	14.5	9	0.628	14.4716	1.08163
White3	0.366	15	9.5	0.555	12.1204	1.02662
White4	0.383	15	9.5	0.562	12.6833	0.9723
White5	0.46	15	9.5	0.667	15.2333	1.12439
White6	0.245	15	9.5	0.483	8.11337	1.29278
White7	0.26	15	9.5	0.512	8.6101	1.36882
White8	0.368	15	9.5	0.557	12.1866	1.02662
White9	0.576	15	9.5	0.733	19.0747	0.8528
White10	0.483	15	9.5	0.726	15.9949	1.31994
White11	0.313	15	9.5	0.525	10.3652	1.15155
Gold Z	0.93	15.1	9.7	1.14	30.7977	1.12689
D	0.49	15	9.5	0.704	16.2267	1.16241
E	0.304	15	9.5	0.483	10.0672	0.9723
F	0.219	15	9.5	0.419	7.25236	1.08637
G	0.308	15	9.5	0.497	10.1997	1.02662
H	0.344	15	9.5	0.585	11.3918	1.30907
I	0.499	15	9.5	0.68	16.5248	0.98316
J	0.414	15	9.5	0.605	13.7099	1.03748
K	0.399	15	9.5	0.611	13.2132	1.15155
L	0.212	15	9.5	0.386	7.02055	0.94514
M	0.24	15	9.5	0.424	7.94779	0.99946
N	0.373	15	9.5	0.644	12.3522	1.47203
P	0.233	15	9.5	0.434	7.71598	1.0918
Q	0.379	15	9.5	0.548	12.5509	0.91798
R	0.278	15	9.5	0.491	9.20619	1.15698
S	0.464	15	9.5	0.699	15.3657	1.27648
T	0.324	15	9.5	0.504	10.7295	0.97773
U	0.379	15	9.5	0.571	12.5509	1.04291
V	0.348	15	9.5	0.562	11.5243	1.16241
W	0.524	15	9.5	0.734	17.3527	1.14068
X	0.72	15	9.5	0.926	23.8434	1.11896
Y	0.437	15	9.5	0.632	14.4716	1.05921
White Z	0.518	15	9.5	0.741	17.154	1.2113

Table 5.2 Transducer Ranking

Tran I.D.	Zero pressure o/p	Tran. sens.	MaxGain No Room	Total sens.	Rank
	mV	mV/kPa	mV/kPa		
Yellow1	12.4847	1.34411	800.984	1.07661	12
Yellow2	19.6045	0.95057	510.086	0.48487	39
Yellow3	11.5574	1.00768	865.246	0.87189	20
Yellow4	13.4450	1.39785	743.770	1.03968	14
Yellow5	11.8886	1.13259	841.144	0.95268	18
Yellow6	9.4910	1.20282	1053.63	1.26732	6
Yellow7	11.8886	1.23616	841.144	1.03979	13
Yellow8	15.5313	0.89614	643.861	0.57699	38
Yellow9	19.5714	0.80934	510.949	0.41353	42
White1	14.8359	1.11896	674.042	0.75422	29
White2	14.4716	1.08163	691.009	0.74741	30
White3	12.1204	1.02662	825.057	0.84702	22
White4	12.6833	0.97230	788.436	0.76659	27
White5	15.2333	1.12439	656.458	0.73811	31
White6	8.1134	1.29278	1232.53	1.59339	1
White7	8.6101	1.36882	1161.43	1.58979	2
White8	12.1866	1.02662	820.573	0.84241	23
White9	19.0747	0.85280	524.255	0.44708	41
White10	15.9949	1.31994	625.198	0.82522	26
White11	10.3652	1.15155	964.763	1.11097	11
Gold Z	30.7977	1.12689	324.700	0.36590	43
D	16.2267	1.16241	616.267	0.71636	34
E	10.0672	0.97230	993.325	0.96581	17
F	7.2524	1.08637	1378.86	1.49795	3
G	10.1997	1.02662	980.425	1.00652	16
H	11.3918	1.30907	877.822	1.14913	10
I	16.5248	0.98316	605.152	0.59496	37
J	13.7099	1.03748	729.398	0.75674	28
K	13.2132	1.15155	756.819	0.87151	21
L	7.0206	0.94514	1424.39	1.34625	5
M	7.9478	0.99946	1258.21	1.25753	7
N	12.3522	1.47203	809.573	1.19171	9
P	7.7160	1.09180	1296.01	1.41498	4
Q	12.5509	0.91798	796.757	0.73141	33
R	9.2062	1.15698	1086.23	1.25674	8
S	15.3657	1.27648	650.799	0.83073	25
T	10.7295	0.97773	932.009	0.91125	19
U	12.5509	1.04291	796.757	0.83095	24
V	11.5243	1.16241	867.732	1.00866	15
W	17.3527	1.14068	576.280	0.65735	36
X	23.8434	1.11896	419.404	0.46930	40
Y	14.4716	1.05921	691.009	0.73192	32
White Z	17.1540	1.21130	582.955	0.70613	35

Table 5.3 Pressure Transducer Gain Choice

	35% Station			Dynamic Head = 388.658		
	3S00	3S02	3S04	3S08	3S14	3S22
Cp=+1 (Pa)	388.658	388.658	388.658	388.658	388.658	388.658
Max -Cp	-6	-6	-5	-4	-3.2	-2.8
delta p (Pa)	2720.6	2720.6	2331.95	1943.29	1632.36	1476.9
Sen.req (mV/Pa)	0.91891	0.91891	1.07207	1.28648	1.53152	1.69274
Rank	20	19	18	17	16	14
Chosen Tran.	Yellow3	T	Yellow5	E	G	Yellow4
Z.P.o/p (mV)	11.56	10.73	11.89	10.07	10.2	13.45
Trn sen (mV/kPa)	1.01	0.98	1.13	0.97	1.03	1.4
Gain required	909.815	937.667	948.731	1326.27	1486.92	1209.1
Maxgain No hdrm	778.547	838.77	756.939	893.744	882.353	669.145
Rg (Ω) choice	61.9	59	61.9	51.1	51.1	64.9
Gain	647.204	678.966	647.204	783.779	783.779	617.333
Zpop-7 (V)	0.48167	0.28531	0.69525	0.89265	0.99454	1.30313
Backoff used	-7	-7	-7	-7	-7	-7
Zp o/p (V)	0.48167	0.28531	0.69525	0.89265	0.99454	1.30313
Cp+1 op (V)	0.22762	2.67E-2	0.41101	0.59717	0.68078	0.96722
Mx-Cpop (V)	2.00601	1.83695	2.11645	2.07459	1.99858	2.24366
Status	OK	OK	OK	OK	OK	OK

Table 5.4 FIB Transducer Map (version 3)

CED1401 Group Number	Sample Rate	CED1401 Bank 0	CED1401 Banks 1,2,3,4,5,
0	FAST	Lowne Anemometer 'RED'	40 pressure transducer pressure signals (V_o)
1	FAST	Lowne Anemometer 'GREEN'	
2	FAST	Lowne Anemometer 'BLUE'	
3	FAST	Lowne Anemometer 'YELLOW'	
4	FAST	Accelerometer	
5	FAST	Turbine Body Angle	
6	FAST	Turbine Yaw Torque	
7	FAST	Turbine Rotor Torque	
8	SLOW	Line Voltage	40 pressure transducer temperature signals (V_t)
9	SLOW	'Grid' r.m.s. current	
10	SLOW	'Grid' real power	
11	SLOW	Turbine r.m.s. current	
12	SLOW	Turbine real power	
13	SLOW	Pressure transducer system excitation voltage	
14	SLOW	Cup Anemometer	
15	SLOW	Wind Vane	

FAST sample rate = 256 times per data acquisition cycle

SLOW sample rate = 1 time per data acquisition cycle

Table 6.1 Comparison of Manufacture and NEL Cup Anemometer Calibrations

Measured pulse frequency	Windspeed estimate (manufacturers' calibration with mechanical non-linearity correction)	Windspeed estimate (NEL-calibration)	Percentage discrepancy
Hz	m/s	m/s	%
2	2.58	2.96	-12.8
4	5.05	5.36	- 5.8
6	7.50	7.77	- 3.5
8	9.93	10.17	- 2.4
10	12.34	12.57	- 1.8
12	14.74	14.97	- 1.5
14	17.14	17.37	- 1.3
16	19.55	19.77	- 1.1
18	21.94	22.17	- 1.04
20	24.40	24.57	- 0.7
22	26.68	26.97	- 1.1

Table 6.2 Systematic Uncertainty Analysis

Tran Item Code	System estimates of pressure from run:spot 180:04	180:06	181:02	181:04	181:06	181:08	181:10	181:12	181:14
7S91	1668.0	1590.0	1698.0	1760.0	1748.0	1735.0	1746.0	1665.0	1701.0
7S75	1670.0	1594.0	1695.0	1759.0	1746.0	1734.0	1744.0	1664.0	1698.0
7S62	1667.0	1589.0	1695.0	1757.0	1744.0	1734.0	1744.0	1664.0	1701.0
7S50	1662.0	1585.0	1693.0	1757.0	1745.0	1733.0	1742.0	1661.0	1699.0
7S40	1664.0	1587.0	1696.0	1757.0	1746.0	1734.0	1742.0	1663.0	1697.0
7S30	1663.0	1585.0	1690.0	1754.0	1740.0	1728.0	1739.0	1661.0	1694.0
7S14	1673.0	1596.0	1686.0	1749.0	1737.0	1726.0	1736.0	1654.0	1691.0
7S10	1660.0	1582.0	1697.0	1758.0	1748.0	1734.0	1743.0	1665.0	1695.0
7S07	1661.0	1583.0	1692.0	1754.0	1744.0	1729.0	1742.0	1663.0	1695.0
7S04	1661.0	1586.0	1691.0	1754.0	1742.0	1730.0	1741.0	1660.0	1697.0
7S01	1667.0	1587.0	1703.0	1765.0	1751.0	1741.0	1749.0	1670.0	1702.0
7P04	1655.0	1578.0	1696.0	1759.0	1744.0	1734.0	1743.0	1662.0	1698.0
7P07	1669.0	1593.0	1699.0	1762.0	1752.0	1738.0	1749.0	1671.0	1704.0
7P10	1664.0	1590.0	1689.0	1752.0	1740.0	1727.0	1738.0	1658.0	1693.0
7P19	1670.0	1592.0	1700.0	1763.0	1749.0	1737.0	1747.0	1668.0	1702.0
7P41	1671.0	1593.0	1699.0	1763.0	1749.0	1736.0	1747.0	1669.0	1701.0
7P65	1664.0	1586.0	1697.0	1761.0	1748.0	1734.0	1746.0	1668.0	1703.0
7P88	1669.0	1593.0	1699.0	1762.0	1749.0	1737.0	1747.0	1668.0	1701.0
3S75	1682.0	1604.0	1708.0	1772.0	1759.0	1747.0	1757.0	1678.0	1712.0
3S62	1677.0	1600.0	1703.0	1767.0	1753.0	1742.0	1750.0	1672.0	1707.0
3S50	1679.0	1600.0	1705.0	1770.0	1758.0	1744.0	1755.0	1673.0	1709.0
3S40	1680.0	1601.0	1709.0	1774.0	1761.0	1749.0	1758.0	1678.0	1714.0
3S30	1680.0	1600.0	1701.0	1767.0	1753.0	1742.0	1751.0	1673.0	1708.0
3S22	1680.0	1599.0	1706.0	1770.0	1757.0	1744.0	1752.0	1673.0	1708.0
3S14	1676.0	1600.0	1695.0	1761.0	1749.0	1738.0	1746.0	1666.0	1702.0
3S08	1665.0	1587.0	1700.0	1762.0	1749.0	1737.0	1747.0	1669.0	1703.0
3S04	1677.0	1602.0	1705.0	1769.0	1755.0	1742.0	1753.0	1674.0	1708.0
3S02	1666.0	1590.0	1697.0	1761.0	1748.0	1735.0	1745.0	1666.0	1701.0
3S00	1667.0	1589.0	1694.0	1759.0	1744.0	1733.0	1743.0	1665.0	1700.0
3P02	1673.0	1596.0	1702.0	1767.0	1754.0	1742.0	1750.0	1670.0	1706.0
3P04	1683.0	1606.0	1703.0	1766.0	1752.0	1741.0	1749.0	1672.0	1706.0
3P11	1680.0	1601.0	1706.0	1770.0	1757.0	1746.0	1755.0	1675.0	1711.0
3P23	1675.0	1598.0	1706.0	1769.0	1756.0	1743.0	1754.0	1673.0	1709.0
3P40	1679.0	1597.0	1701.0	1762.0	1751.0	1739.0	1749.0	1669.0	1707.0
3P91	1688.0	1611.0	1701.0	1765.0	1751.0	1740.0	1748.0	1670.0	1704.0
2S01	1677.0	1598.0	1702.0	1766.0	1752.0	1740.0	1751.0	1670.0	1706.0
4S01	1669.0	1591.0	1700.0	1764.0	1752.0	1737.0	1749.0	1668.0	1705.0
APPL	1684.0	1603.0	1700.0	1768.0	1759.0	1745.0	1757.0	1672.0	1718.0

Systematic uncertainty calculation

md	0.7735	0.5991	0.0662	0.3216	0.5417	0.4412	0.5608	0.2538	0.9026
sd	0.4672	0.4674	0.3234	0.3351	0.3214	0.3226	0.3000	0.3256	0.3272
Si	1.7314	1.5572	0.7293	1.0086	1.2005	1.1026	1.1758	0.9214	1.5733

Overall Mean systematic uncertainty = 1.222246

Table 6.3 Random Uncertainty Analysis

Mean of differences					Standard deviation of differences				
Spots 1-20	Spots 21-40	Spots 41-60	Spots 61-80	Spots 81-100	Spots 1-20	Spots 21-40	Spots 41-60	Spots 61-80	Spots 81-100
7S04 AND 7S07									
-0.15	1.55	-0.35	-1.60	3.05	4.81	6.52	6.19	4.47	6.49
7P04 AND 7S10									
-4.95	3.85	2.60	-0.15	-7.40	6.76	6.00	4.03	5.48	8.67
7S14 AND 4S01									
17.00	8.45	-0.50	-8.90	12.75	21.32	21.29	17.95	18.57	13.34
7S30 AND 7S40									
4.60	0.35	-1.80	-0.80	3.05	9.26	8.56	6.49	8.21	8.09
7P10 AND 7S50									
4.90	1.30	0.85	-1.60	1.60	4.17	5.76	4.41	4.03	5.00
3S02 AND 7S75									
-5.00	6.85	-0.30	-3.30	-2.00	13.29	4.90	7.02	5.76	6.06
7S91 AND 3S00									
-1.15	-5.15	1.05	1.60	2.20	7.74	4.51	4.15	3.61	4.73
3P23 AND 7P19									
2.80	2.15	2.85	0.40	0.50	11.64	10.29	4.56	8.34	6.20
7P88 AND 7P65									
-9.60	-9.90	2.85	2.80	3.75	20.50	8.73	3.20	9.11	14.70
7P41 AND 3S08									
5.10	-4.25	-0.60	4.85	1.10	19.00	6.78	3.80	6.62	4.98
3S62 AND 3S14									
1.60	1.55	-0.45	2.05	3.60	8.61	4.04	6.69	5.69	2.66
3P04 AND 3P91									
-0.20	0.65	-11.80	-1.65	3.95	14.58	12.14	9.58	10.02	2.09
3P40 AND 3S22									
-4.15	0.50	5.25	-7.70	-1.75	18.20	8.51	12.39	11.37	2.79
3S50 AND 3S40									
-3.75	0.75	0.25	-0.15	-0.95	9.09	8.81	9.32	7.44	2.09
3S30 AND 3S75									
0.55	-2.25	5.10	-4.25	-1.80	4.96	8.25	16.41	3.45	2.50

Pair repeatability = 10.24 ∴ Random uncertainty = $10.24/\sqrt{2}$ = 7.24

Table 7.1 Performance Data acquired during Feb–May 1988

Builds 1A, 1B, 1C, 1D, 1E showing date/filename

Yaw Control	ROTOR - SPEED 333 rpm		395 rpm		458 rpm		Total Spots
"WESCO" Tail Vane	1A	25/Feb 33 29/Feb 150 01/Mar 144 03/Mar 141 04/Mar 97					570
CIT Tail Vane	1B	11/Mar 366 15/Mar 18 18/Mar 276			1C	11/Apr 77	737
Yaw Brake Just On			1E	26/Apr 163 02/May 878 03/May 642	1D	14/Apr 487 18/Apr 428 20/Apr 489 21/Apr 447 23/Apr 181 24/Apr 174	3889
Total Spots		1230		1683		2283	5196

Table 7.2 Standard deviation of bin power coefficient

	333 r.p.m.		395 r.p.m.		458 r.p.m.	
TSR bin	Number of spots	Cp std. deviation	Number of spots	Cp std. deviation	Number of spots	Cp std. deviation
5.5	133	0.0508	18	0.0494	3	0.0061
6.0	111	0.0572	37	0.0434	14	0.0318
6.5	148	0.0452	48	0.0630	48	0.0277
7.0	95	0.0556	62	0.0615	56	0.0300
7.5	76	0.0711	74	0.0839	84	0.0287
8.0	56	0.0862	69	0.0800	97	0.0274
8.5	29	0.0903	70	0.0754	103	0.0309
9.0	29	0.0940	61	0.0879	103	0.0412
9.5	32	0.0875	60	0.0712	87	0.0427
10.0						
Total Spots	595		709		499	
Mean Cp standard deviation		0.0708		0.0686		0.0296

Table 7.3 Variation of Bin Power Coefficient with Wind Direction

Values given are number of spots
mean of power coefficient
standard deviation of power coefficient

TSR bins	Direction bins -135.0	-67.5	-22.5	22.5	67.5	135.0
3.0	0	0	8 0.2406 0.0203	0	0	
3.5	0	0	8 0.2923 0.0134	1 0.3184	26 0.3178 0.0253	
4.0	0	0	4 0.3415 0.0123	10 0.3792 0.0218	69 0.3410 0.0336	
4.5	1 0.3253	1 0.3768	8 0.3422 0.0204	55 0.3920 0.0309	70 0.3597 0.0377	
5.0	0	6 0.3880 0.0251	16 0.3346 0.0143	53 0.3980 0.0290	61 0.3583 0.0467	
5.5	11 0.3445 0.0511	17 0.3510 0.0443	27 0.3246 0.0223	52 0.3856 0.0442	45 0.3564 0.0565	
6.0	31 0.3342 0.0617	31 0.3503 0.0349	35 0.2965 0.0256	18 0.3897 0.0359	34 0.3296 0.0656	
6.5	62 0.3005 0.0502	35 0.3162 0.0616	72 0.2770 0.0275	12 0.3136 0.0362	38 0.2957 0.0592	
7.0	49 0.2821 0.0590	54 0.2713 0.0591	57 0.2420 0.0287	3 0.3099 0.0404	17 0.2622 0.0578	
7.5	39 0.2438 0.0733	71 0.2476 0.0833	79 0.2109 0.0270	4 0.2496 0.0373	16 0.2085 0.0964	
8.0						

Table 7.4 Variation of Bin Power Coefficient with Rotor Speed

	333 r.p.m.		395 r.p.m.		458 r.p.m.	
TSR bin	Number of spots	Mean Cp	Number of spots	Mean Cp	Number of spots	Mean Cp
4.0	83	0.3457	0		0	
4.5	133	0.3720	2	0.3511	0	
5.0	131	0.3711	6	0.3880	0	
5.5	133	0.3602	18	0.3551	3	0.3437
6.0	111	0.3281	37	0.3544	14	0.3057
6.5	148	0.2872	48	0.3226	48	0.2837
7.0	95	0.2649	62	0.2731	56	0.2458
7.5	76	0.2207	74	0.2490	84	0.2159
8.0	56	0.1993	69	0.2115	97	0.1646
8.5	29	0.1195	70	0.1687	103	0.1162
9.0	29	0.0590	61	0.0797	103	0.0657
9.5	32	-0.0027	60	0.0194	87	0.0479
10.0						
Total Spots	595		709		499	

Table 8.1 Test Schedule for Fully Instrumented Blade Testing

Nominal Rotor speed = 340 rpm Pitch setting = 6°

	Drivers	Yaw angle						
Windspeed	Pot setting	- 45°	-30°	-15°	0°	+15°	+30°	+45°
		Turbine body angle sensor voltage						
m/s		3.159	2.958	2.751	2.550	2.326	2.100	1.900
5	368				x	x		x
7.5	426				x		x	x
10	481	x	x	x	x	x	x	x
15	594			x	x		x	
20	708				x	x	x	
25	821				x	x		

Table 9.1 The Test Matrix of 40-rev Sub-runs

YAW (deg) / WIND (m/s)	Y -45 [-52.5,-37.5)	* -30 [-37.5,-22.5)	X -15 [-22.5,-7.5)	0 [-7.5,+7.5)	+15 [+7.5,+22.5)	+30 [+22.5,+37.5)	+45 [+37.5,+52.5)	+60 [+52.5,+67.5)
* 6 [4 , 8)		168.2D		163.2A B C	164.2A B C	170.2A B		
10 [8 , 12)	187.2A B C		167.2A B	161.2A B C 167.2C 160.2A 166.2A B		170.2C 169.2A B C 185.2A B C D	188.2D	186.2A B C D
14 [12 , 16)			168.2A B C	162.2A B C D	189.2A B C 192.2A	190.2D	188.2A B C	
18 [16 , 20)				165.2A B C D	201.2A 192.2B 190.2C	190.2A B 199.2A B C	191.2A B C 200.2B C	200.2A
22 [20 , 24)					201.2B C D 192.2C D	202.2A B C D		

Table 10.1 Sub-run CHOICE FOR PROFILES PLOT REVIEW
YAW ANGLE (see Table 9.1)

WIND SPEED								
	(168D)		163C	164A	170B		
187B		167A	167C/160A		169A	(188D)	186A
		168B	162A	192A/189A		188C	
			165B	192B	199C	191C	200A
				192C/201C	202D/202B		

Table AI.1 Typical Pressure Transducer Test Results

TRANSDUCER NO. 5 - SPX50DN

Expt. 4		MEASURED			V ex = 3.000 V	
Date	Time	V ex (V)	V o/p (mV)	V i (mV)	V o/p (mV)	V i (mV)
22:5:87	09:40	2.9690	16.242	63.471	16.4116	64.1337
	11:50	2.9717	15.476	64.679	15.6234	65.2949
	12:00	2.9716	15.492	64.651	15.6401	65.2689
	12:35	2.9718	15.582	64.549	15.7299	65.1615
	12:50	2.9715	15.650	64.452	15.8001	65.0702
	13:05	2.9716	15.663	64.433	15.8127	65.0488
	13:25	2.9716	15.688	64.403	15.8379	65.0185
	13:40	2.9715	15.721	64.355	15.8718	64.9722
	14:00	2.9718	15.782	64.287	15.9318	64.8970
	14:15	2.9714	15.860	64.170	16.0127	64.7876
	15:15	2.9720	15.925	64.085	16.0750	64.6888
	16:15	2.9720	15.988	63.993	16.1386	64.5959
	16:30	2.9721	16.056	63.890	16.2067	64.4898
	16:38	2.9720	16.086	63.834	16.2376	64.4354
	16:48	2.9718	16.103	63.796	16.2558	64.4014
	16:55	2.9720	16.156	63.717	16.3082	64.3173
	17:05	2.9717	16.212	63.631	16.3664	64.2370
	17:20	2.9719	16.257	63.555	16.4107	64.1559
	17:35	2.9719	16.265	63.530	16.4188	64.1307
26:5:87	09:20	2.9719	16.233	63.591	16.3865	64.1923
	11:35	2.9725	16.885	62.367	17.0412	62.9440
	11:50	2.9724	16.855	62.408	17.0115	62.9875
	12:20	2.9721	16.813	62.508	16.9708	63.0948
	13:00	2.9722	16.756	62.627	16.9127	63.2128
	13:40	2.9722	16.708	62.72	16.8643	63.3066
	14:10	2.9719	16.672	62.79	16.8296	63.3837
	15:30	2.9718	16.598	62.929	16.7555	63.5261
	15:50	2.9716	16.582	62.963	16.7405	63.5647
	16:30	2.9717	16.546	63.035	16.7036	63.6353
	17:05	2.9717	16.405	63.291	16.5612	63.8937
	17:25	2.9717	16.341	63.364	16.4966	63.9674
1:6:87	10:00	2.9718	16.237	63.544	16.3911	64.1470
	11:30	2.9718	15.547	64.578	15.6945	65.1908
	12:00	2.9717	15.623	64.475	15.7718	65.0890
	12:55	2.9716	15.733	64.335	15.8834	64.9499
	13:20	2.9717	15.784	64.262	15.9343	64.8740
	13:55	2.9717	15.817	64.217	15.9676	64.8285
	16:20	2.9717	15.975	63.983	16.1271	64.5923
	17:30	2.9717	16.017	63.921	16.1695	64.5297
2:6:87	08:55	2.9719	16.26	63.535	16.4137	64.1357
	10:50	2.9723	16.69	62.749	16.8455	63.3338
	11:55	2.9721	16.632	62.857	16.7881	63.4471
	13:10	2.9722	16.574	62.97	16.7290	63.5590
	14:45	2.9721	16.516	63.073	16.6710	63.6651
	15:45	2.9722	16.488	63.132	16.6422	63.7225
	17:20	2.9722	16.452	63.207	16.6059	63.7982

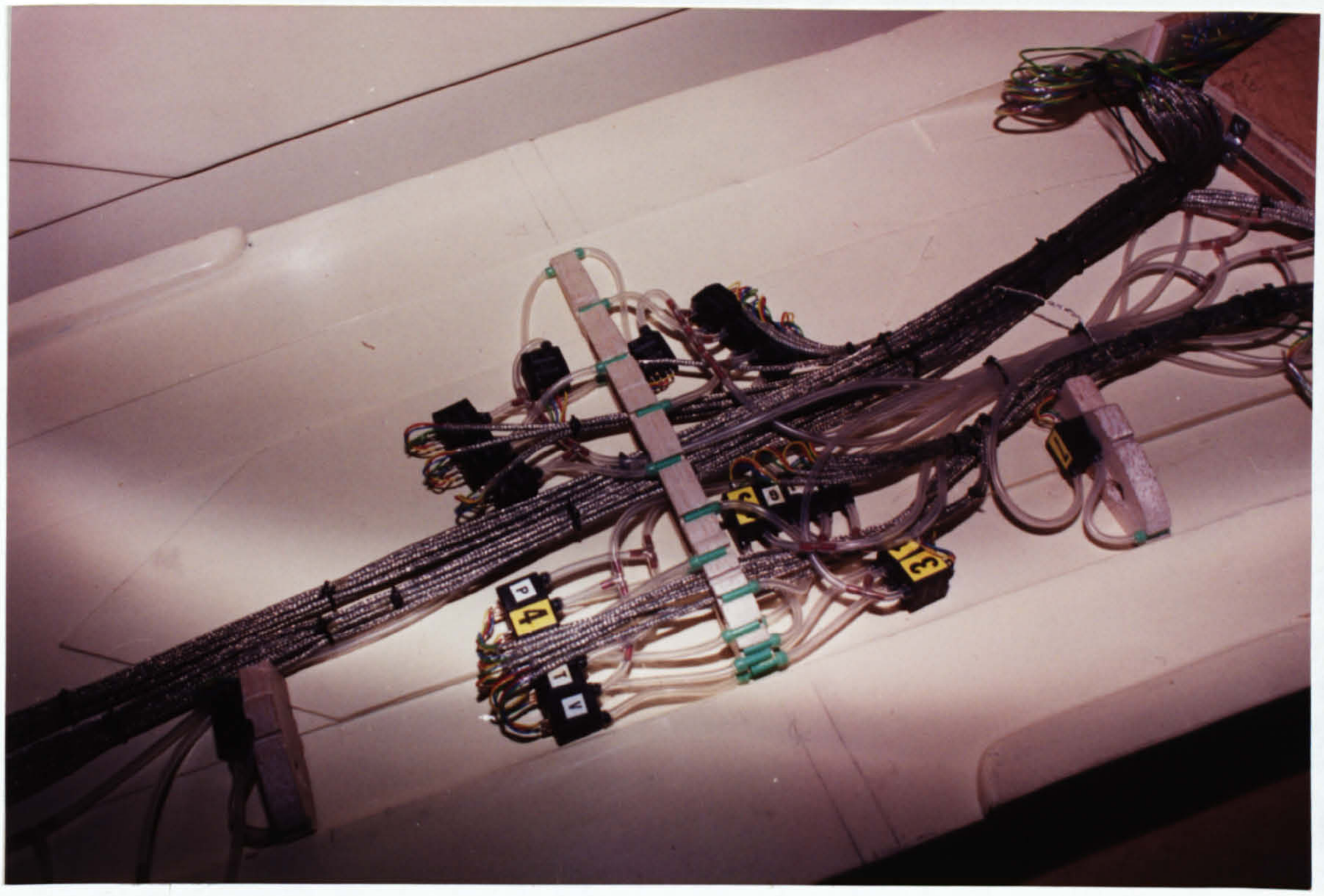

Plate 1 Construction of the Fully Instrumented Blade.

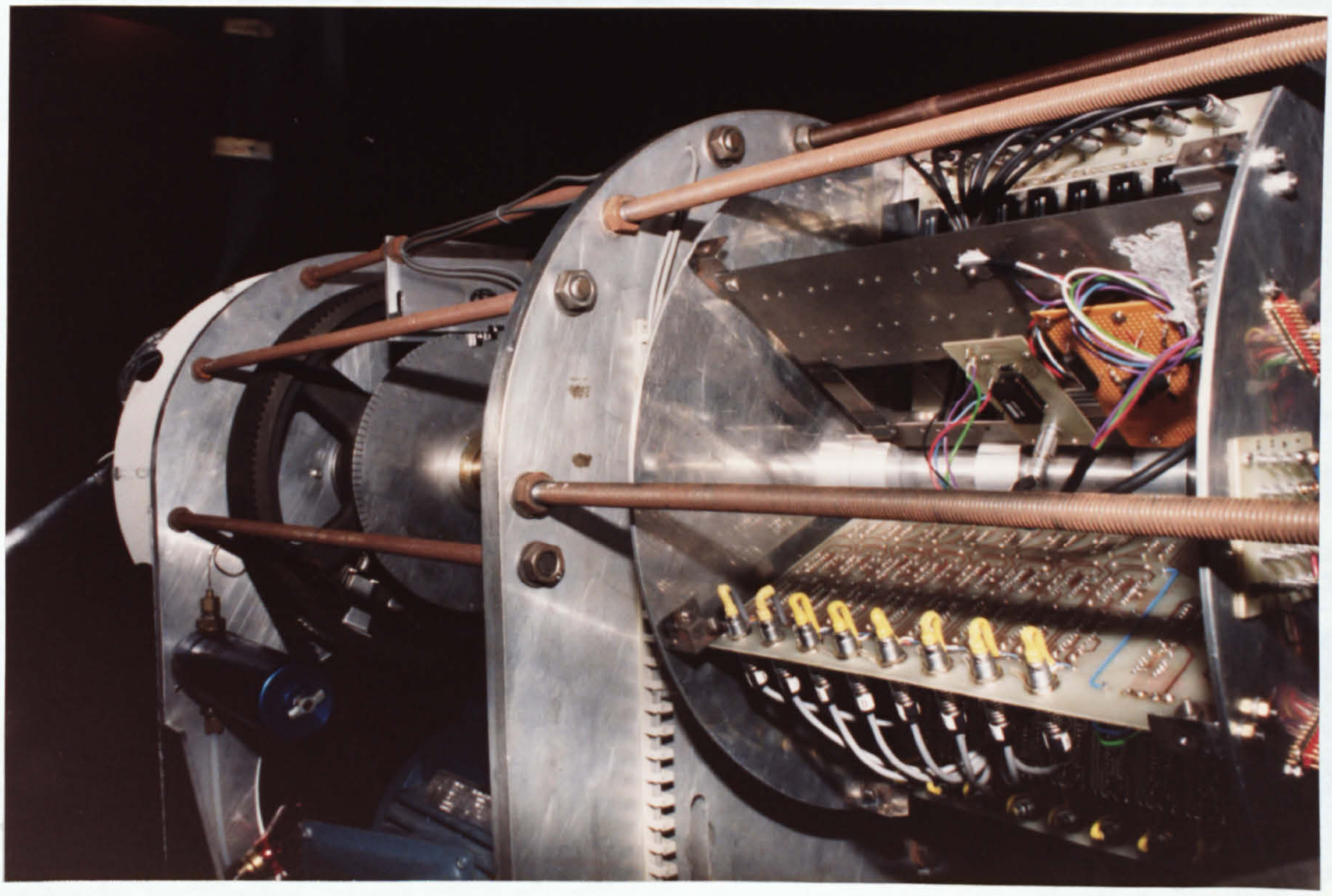

Plate 2 On-Rotor Signal Processing.

Plate 3 The Performance Test Facility.

Plate 4 The Mobile Test Facility.

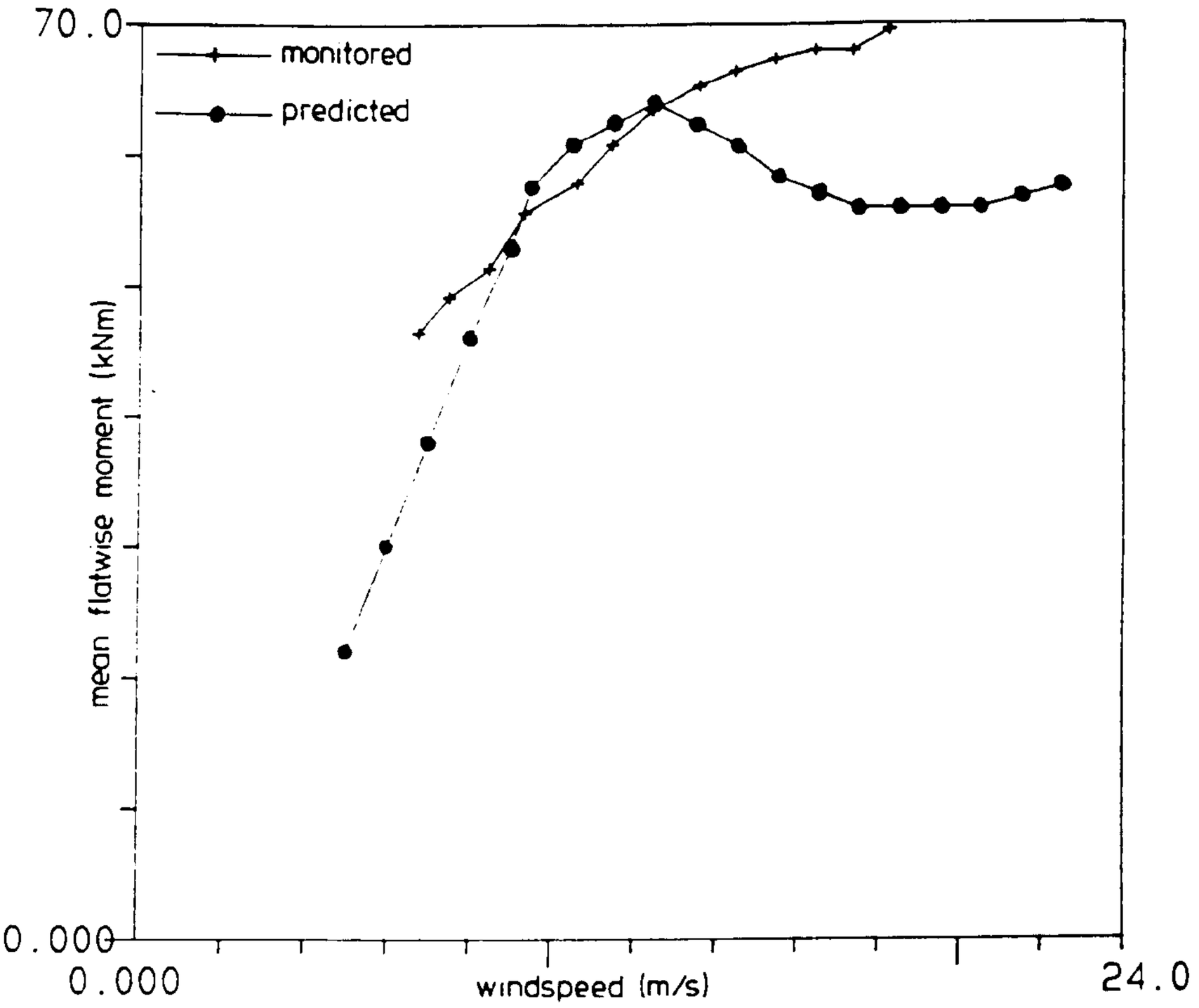

Figure 1.1 Measured and predicted blade flapwise bending moments vs. windspeed (from [1.12]).

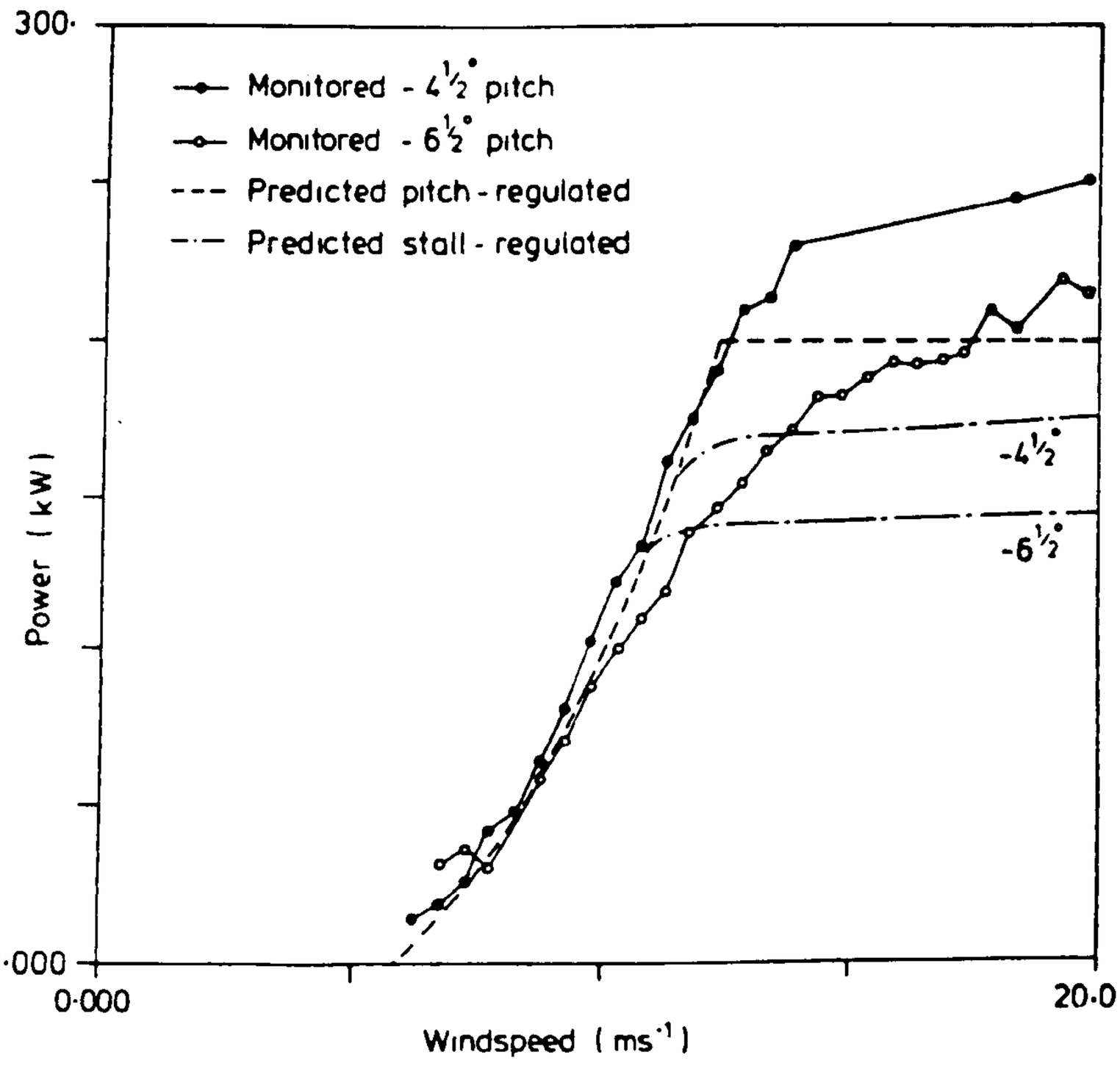

Figure 1.2 Measured and predicted power vs. windspeed (from [1.12]).

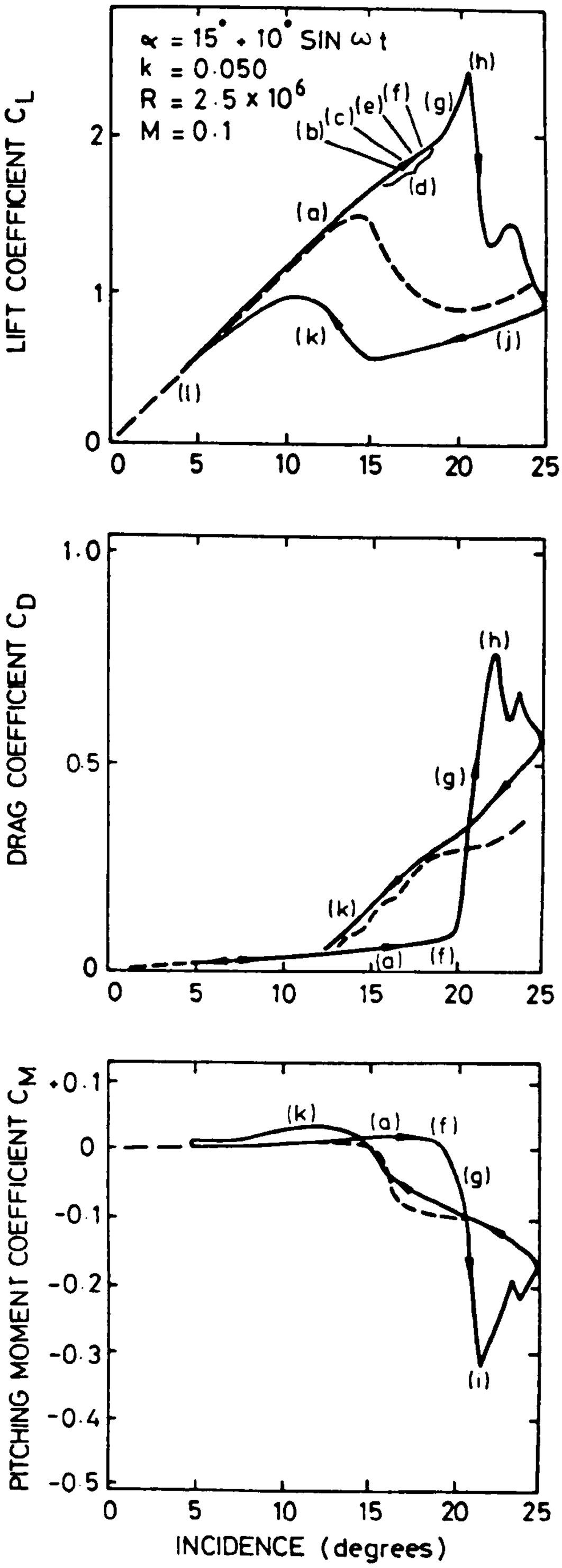

Figure 2.1 Dynamic stall events on a NACA 0012 aerofoil (from [2.26] and [2.27])

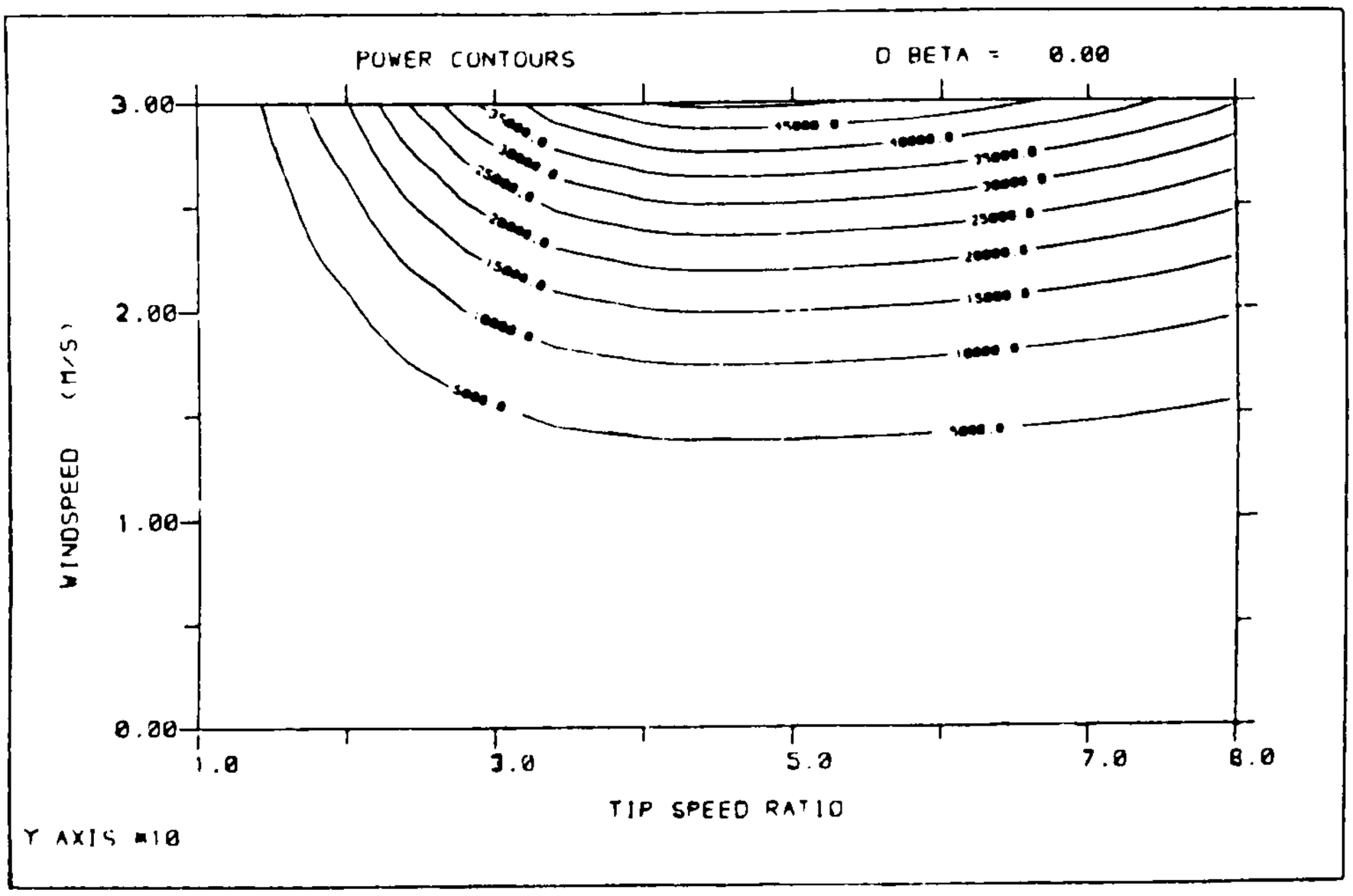

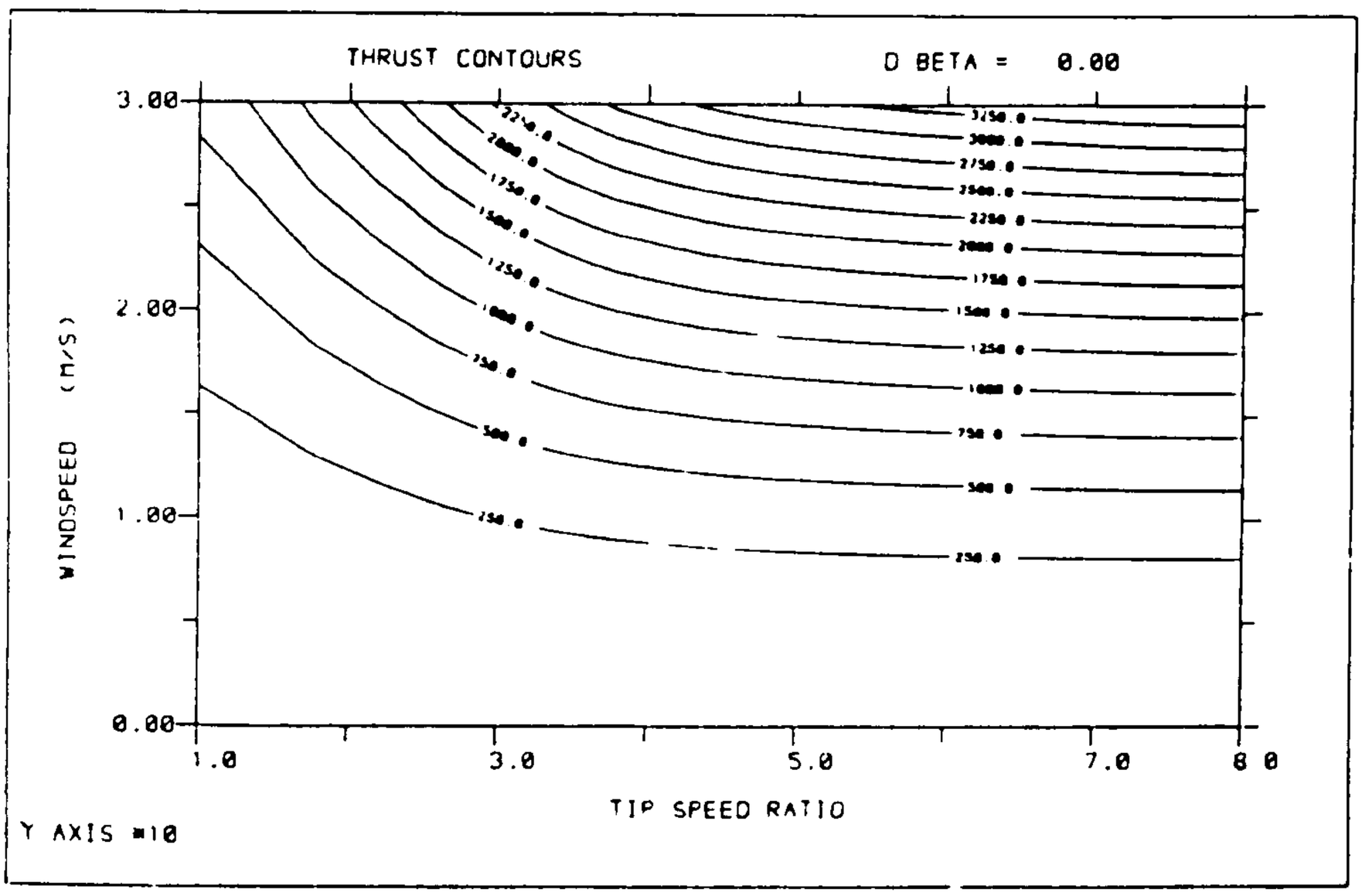

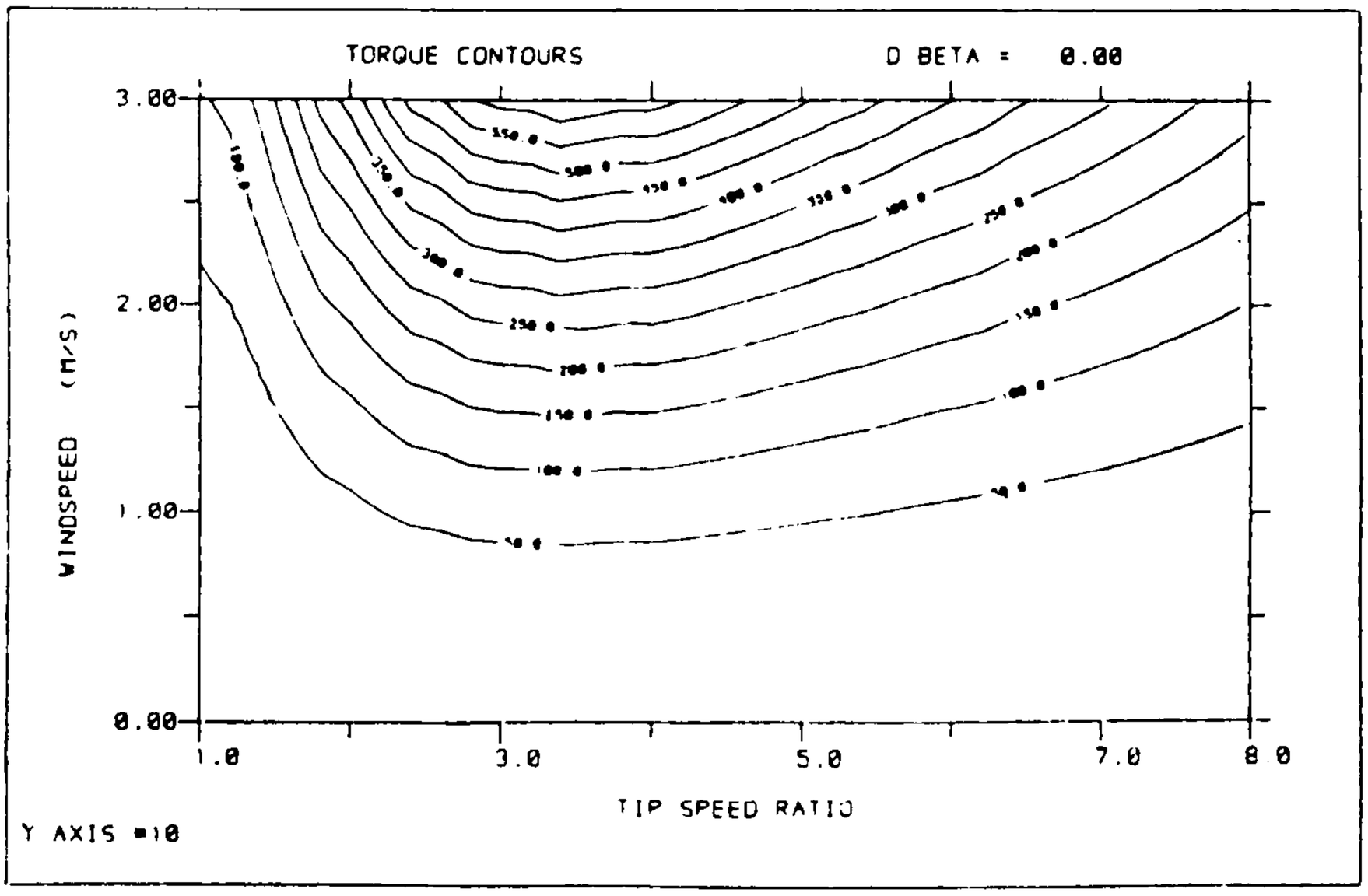

Figure 3.1 Preliminary design study: rotor power, thrust and torque contours.

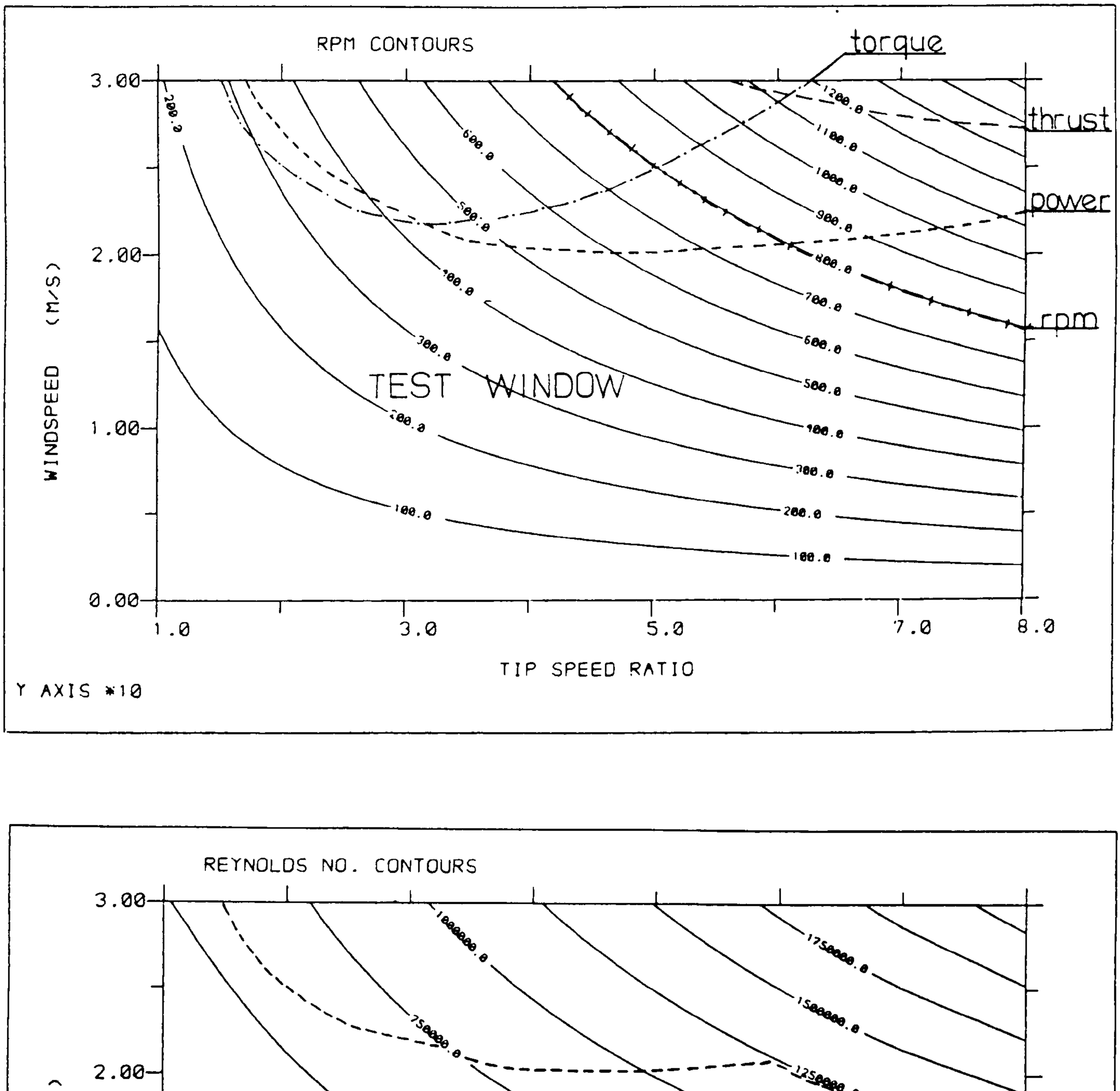

Figure 3.2 Preliminary design study: test window boundaries.

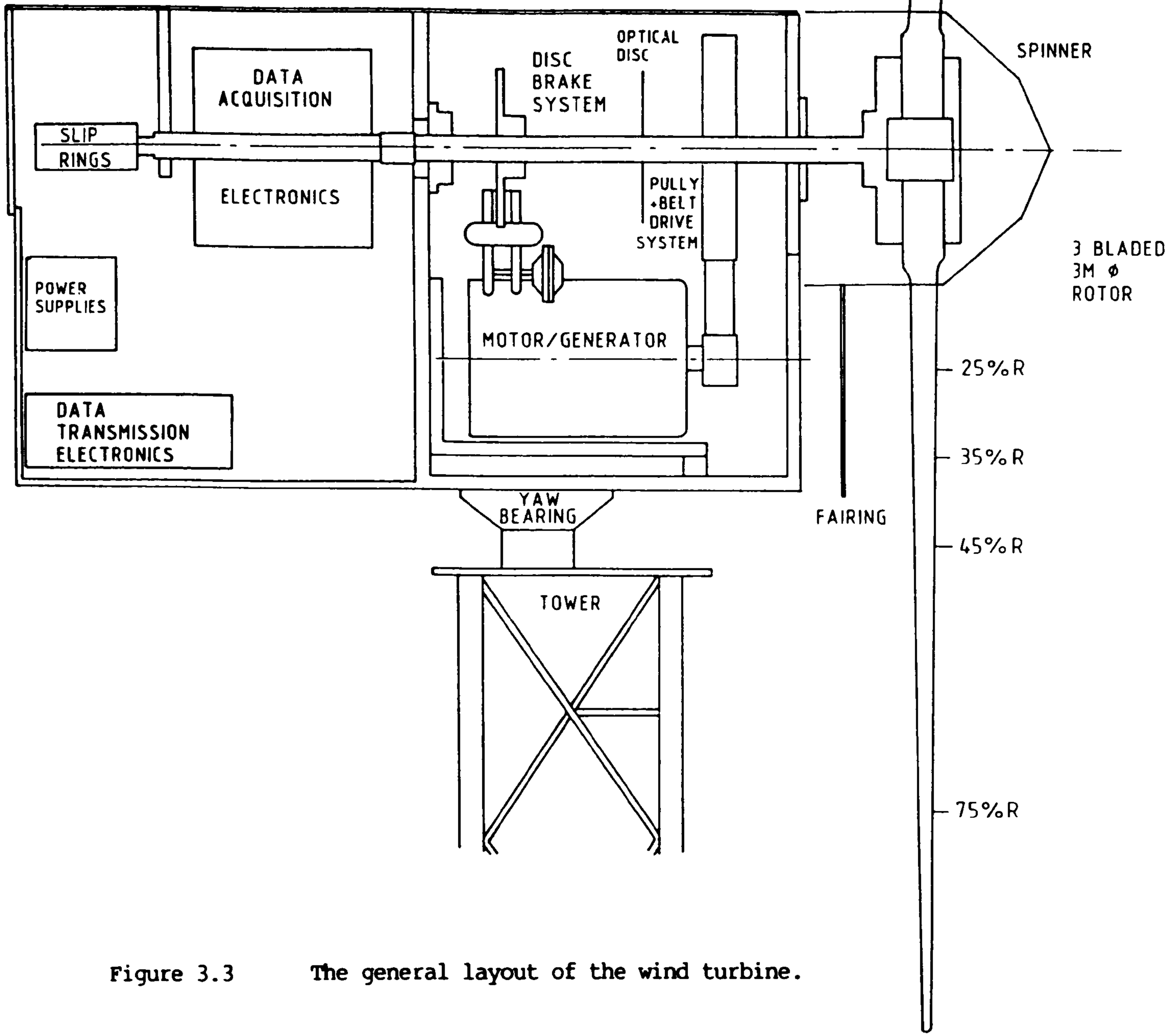

Figure 3.3 The general layout of the wind turbine.

a) "Wesco" tail-vane

b) "CIT" tail-vane

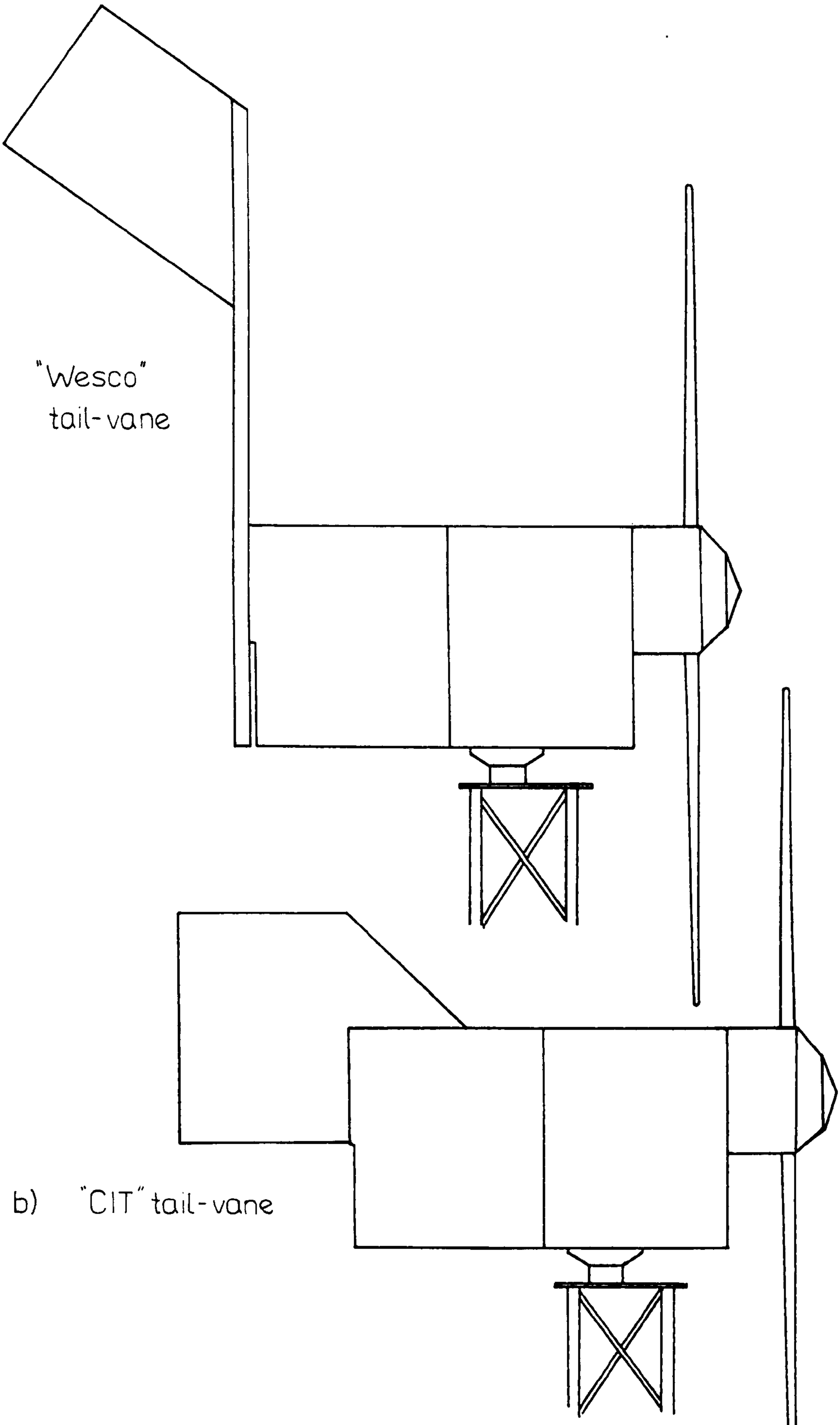

Figure 3.4 **Tail vane configurations.**

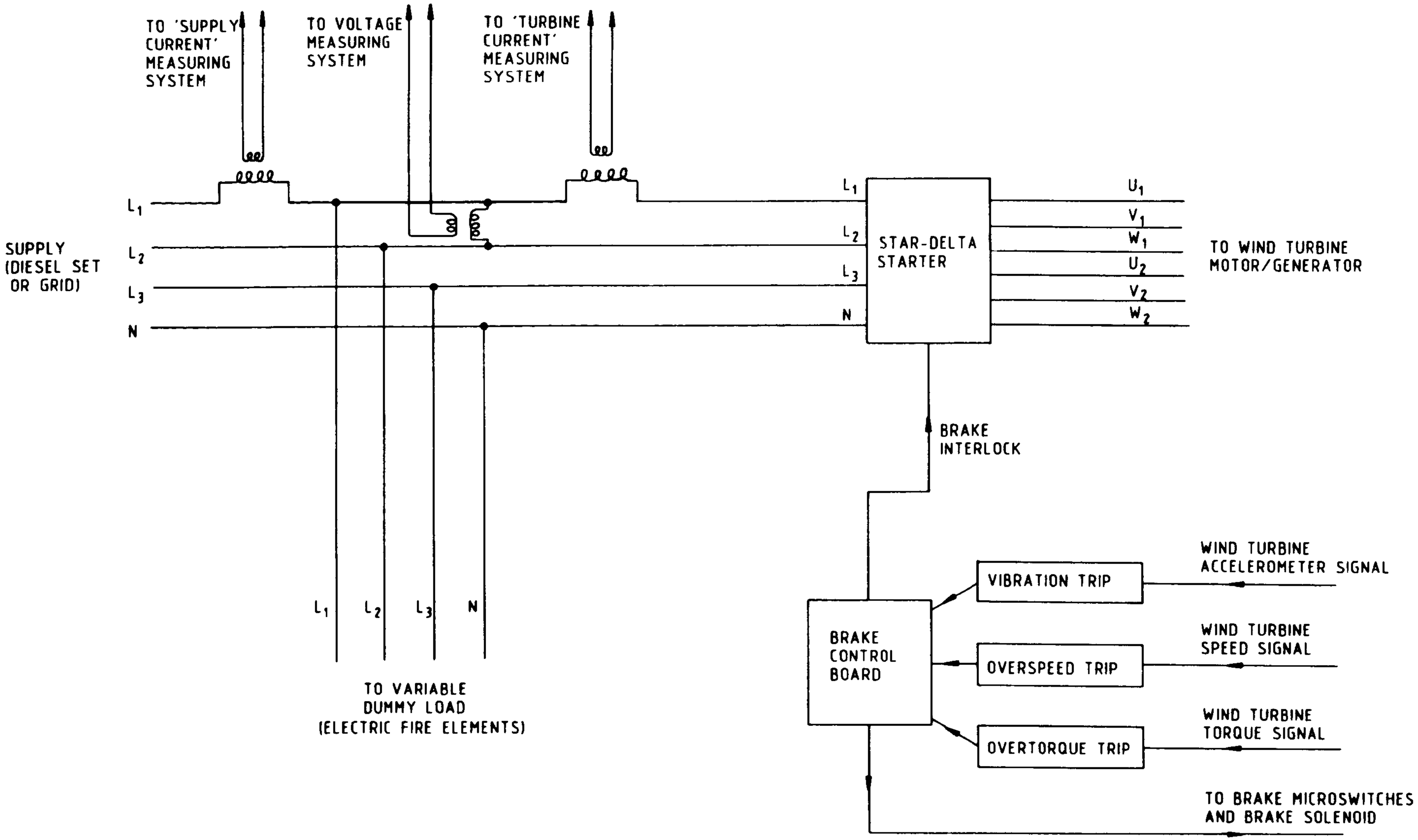

Figure 3.5 Wind turbine electrical system.

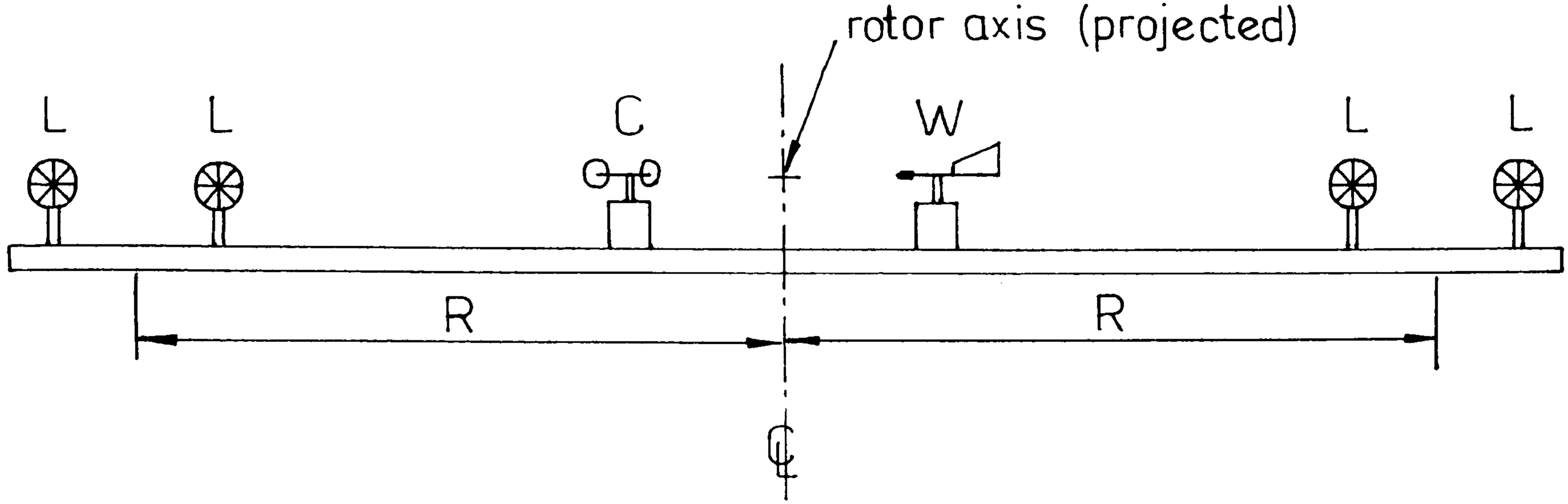

Figure 4.1 Layout of anemometer tower instruments.

Circuit Input

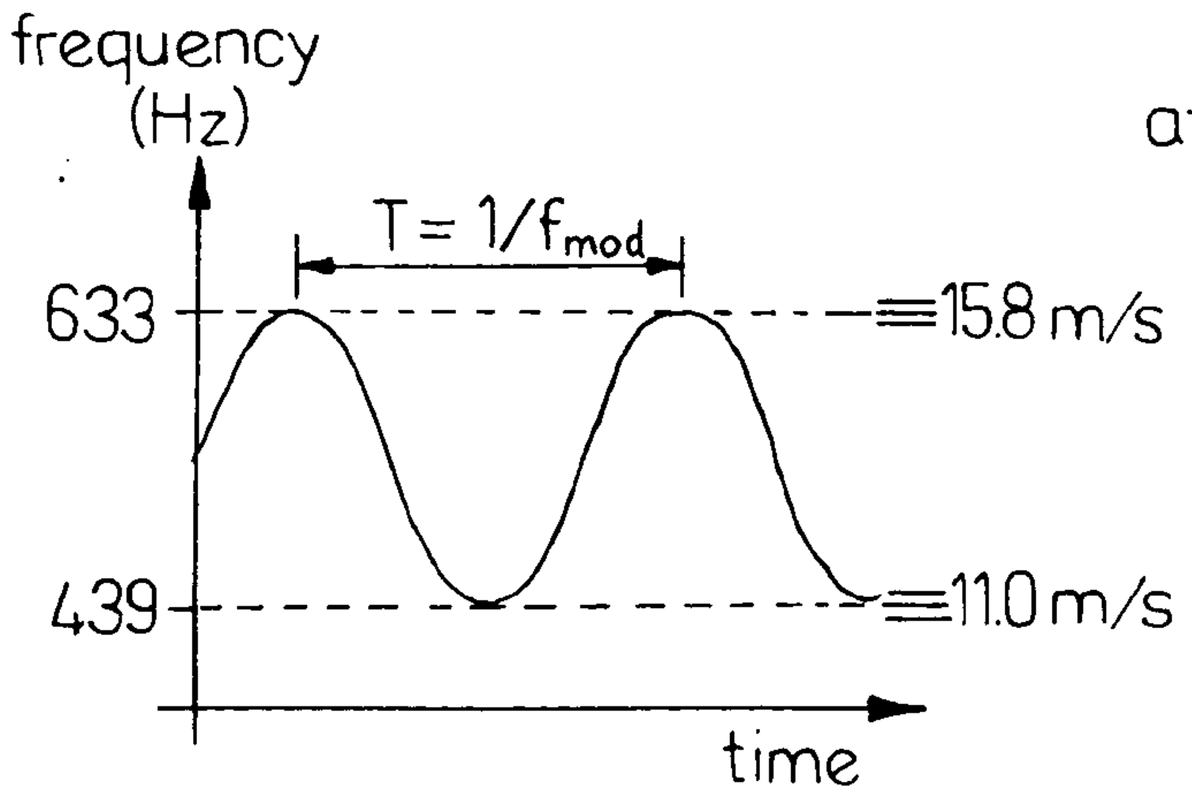

Circuit output is −3 dB down at 0.45 Hz modulation frequency. This is equivalent to 0.707 of the steady output for a windspeed rate of change of 7 m/s²

Circuit response

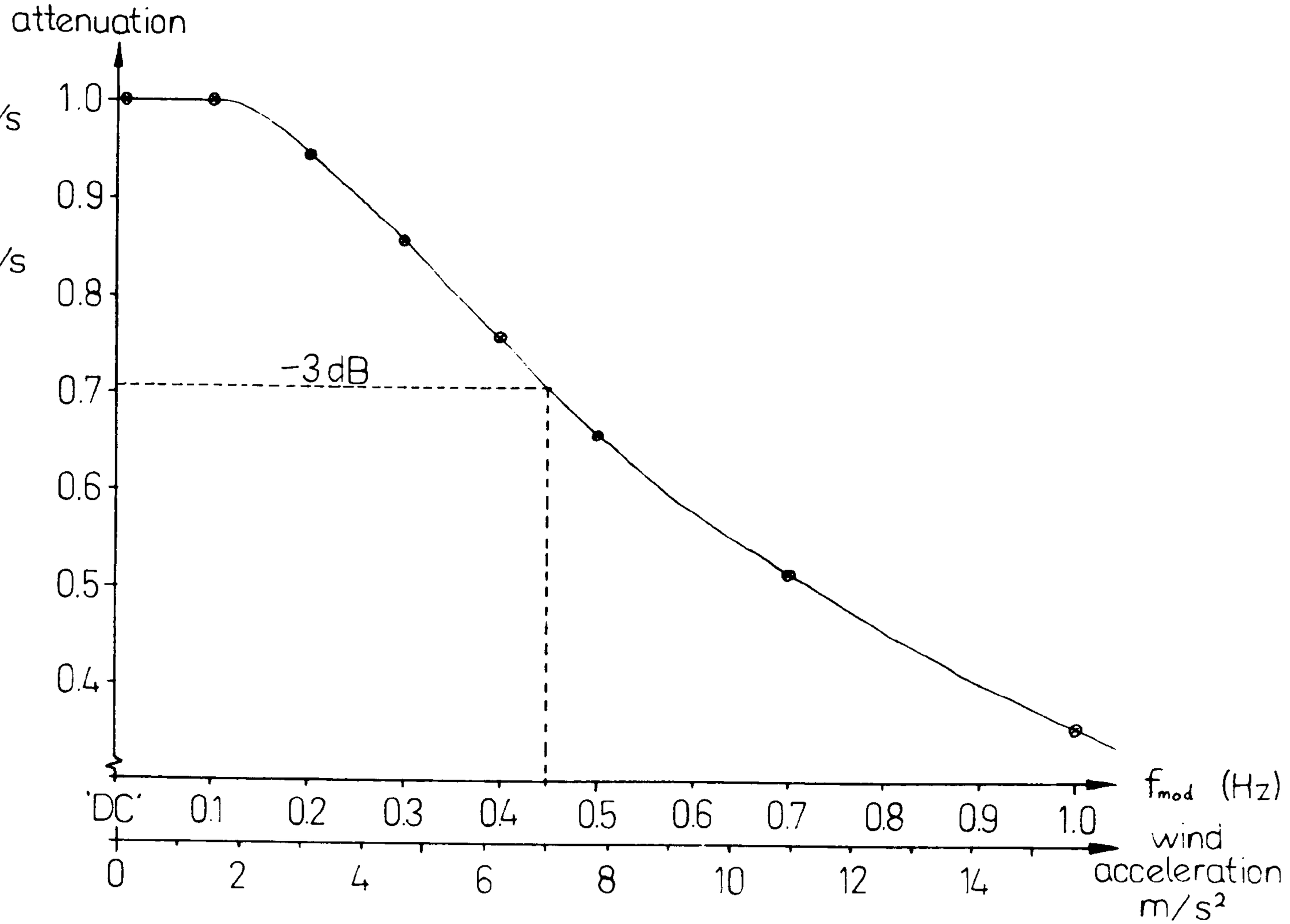

Figure 4.2 **Lowne anemometer channel frequency response.**

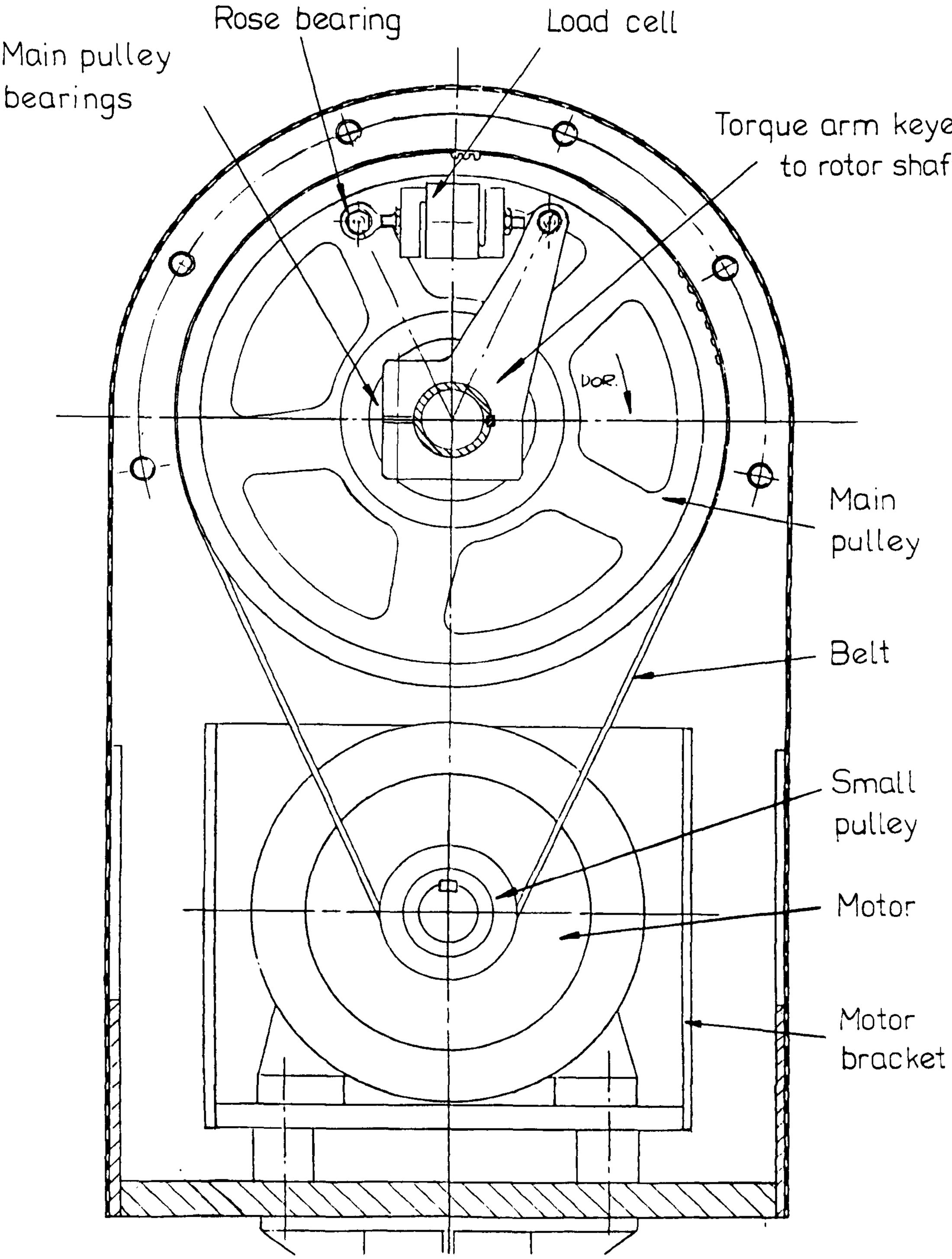

Figure 4.3 Rotor torque measurement system.

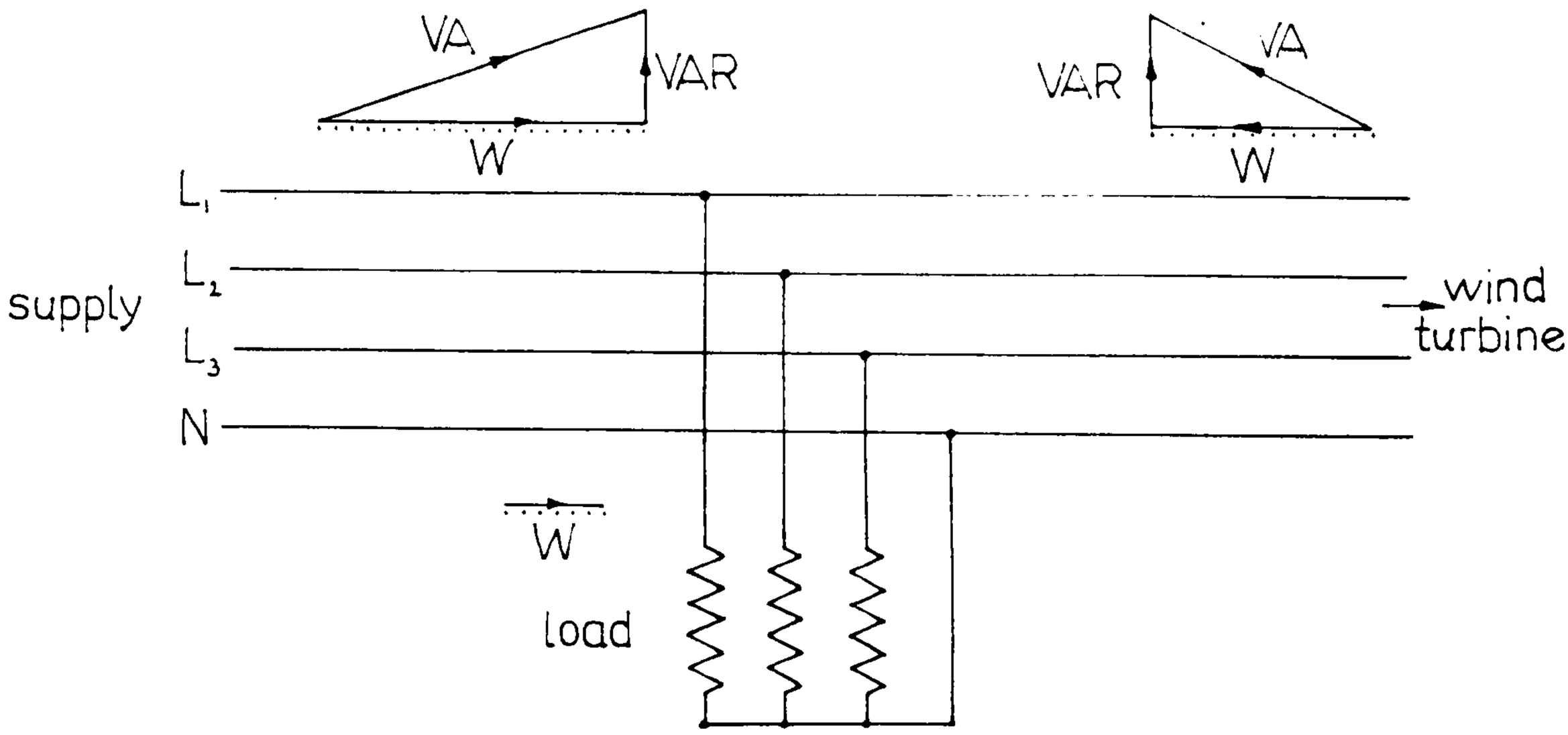

Figure 4.4 Typical phasor diagrams for the star electrical system.

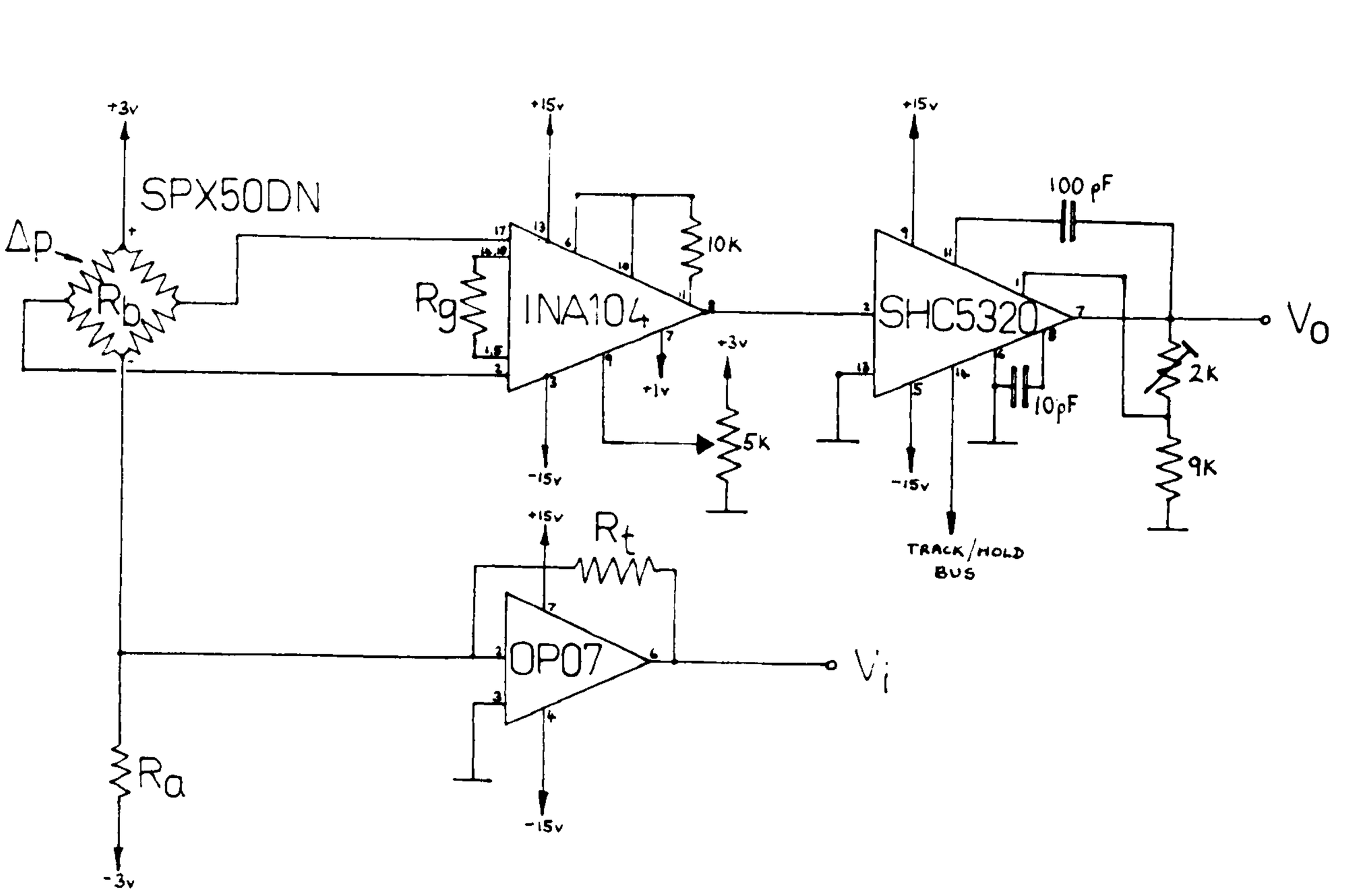

Figure 4.5 Pressure transducer signal processing circuit.

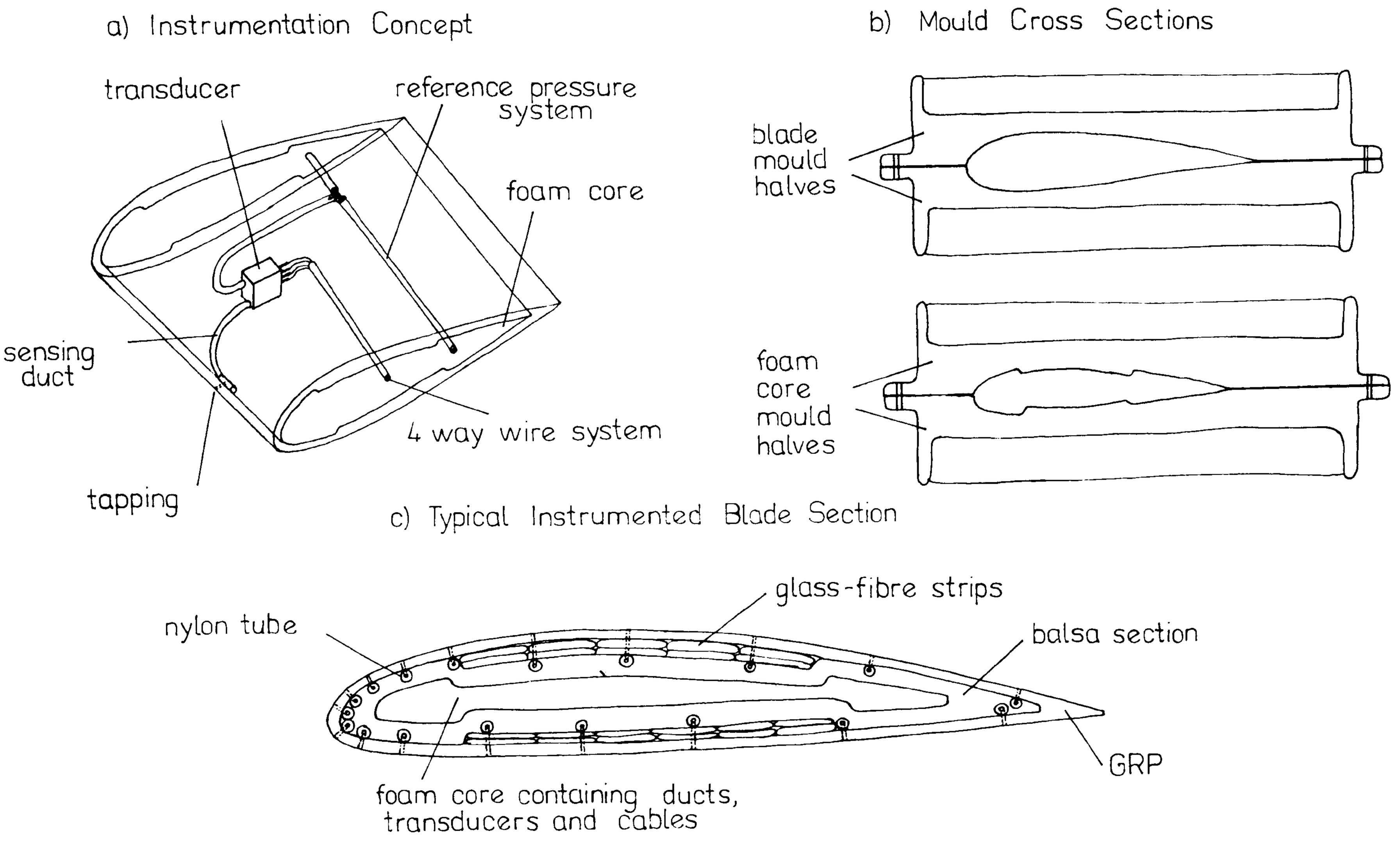

Figure 4.6 Blade manufacture and instrumentation.

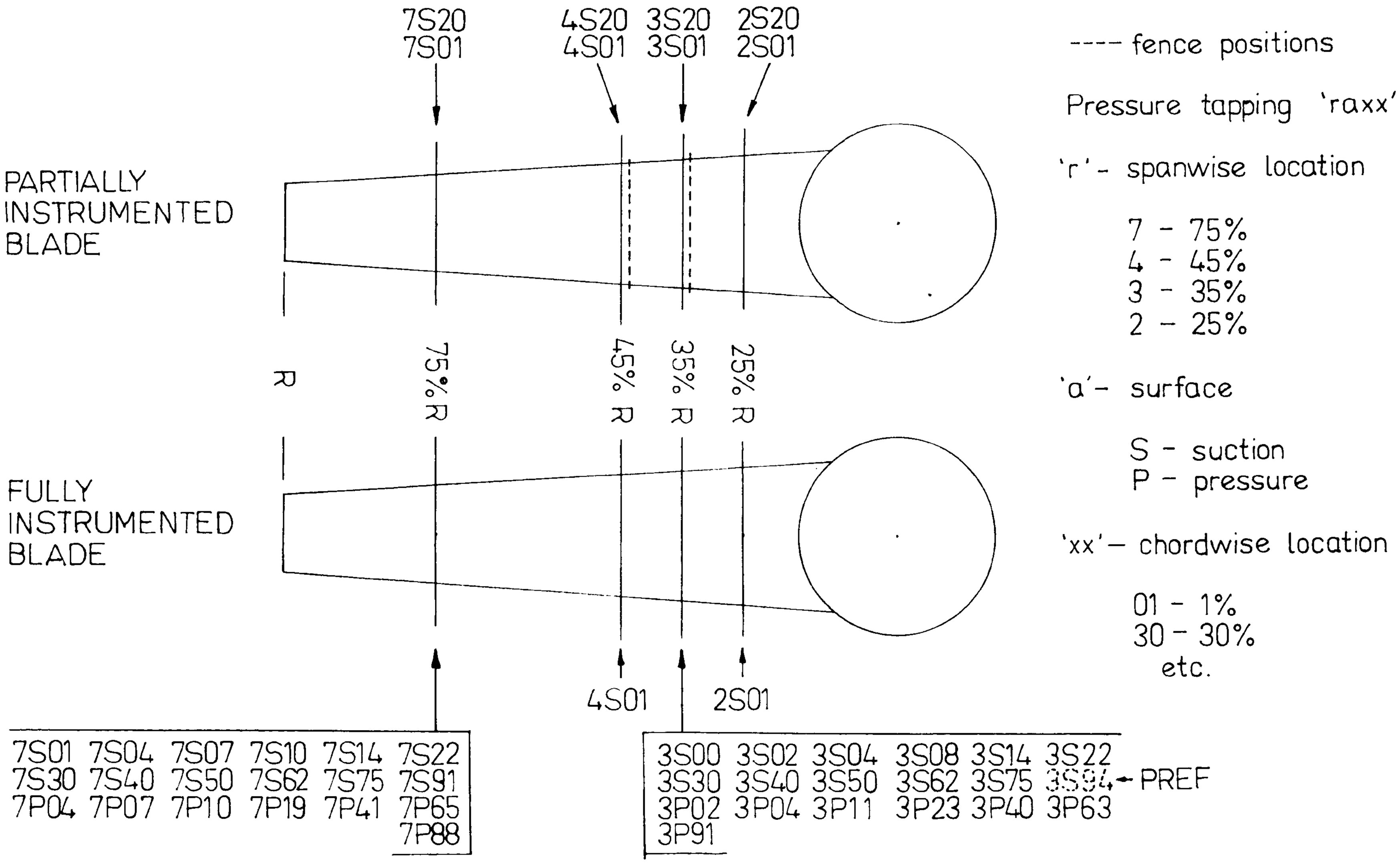

Figure 4.7 **Desired pressure tapping locations for partially and fully instrumented blades.**

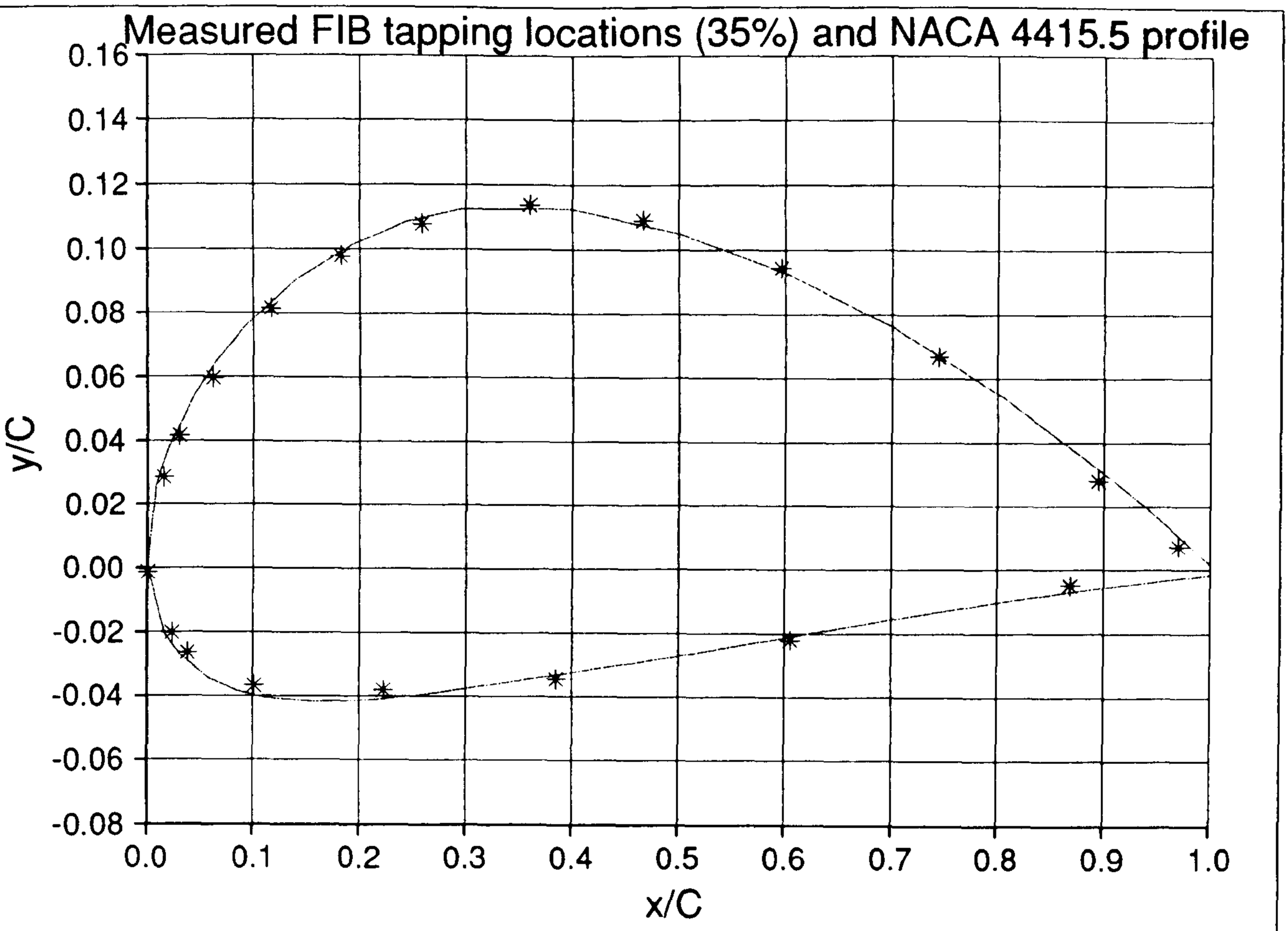

Figure 4.8 Achieved pressure tapping locations (symbols) and comparison with the NACA 44XX aerofoil.

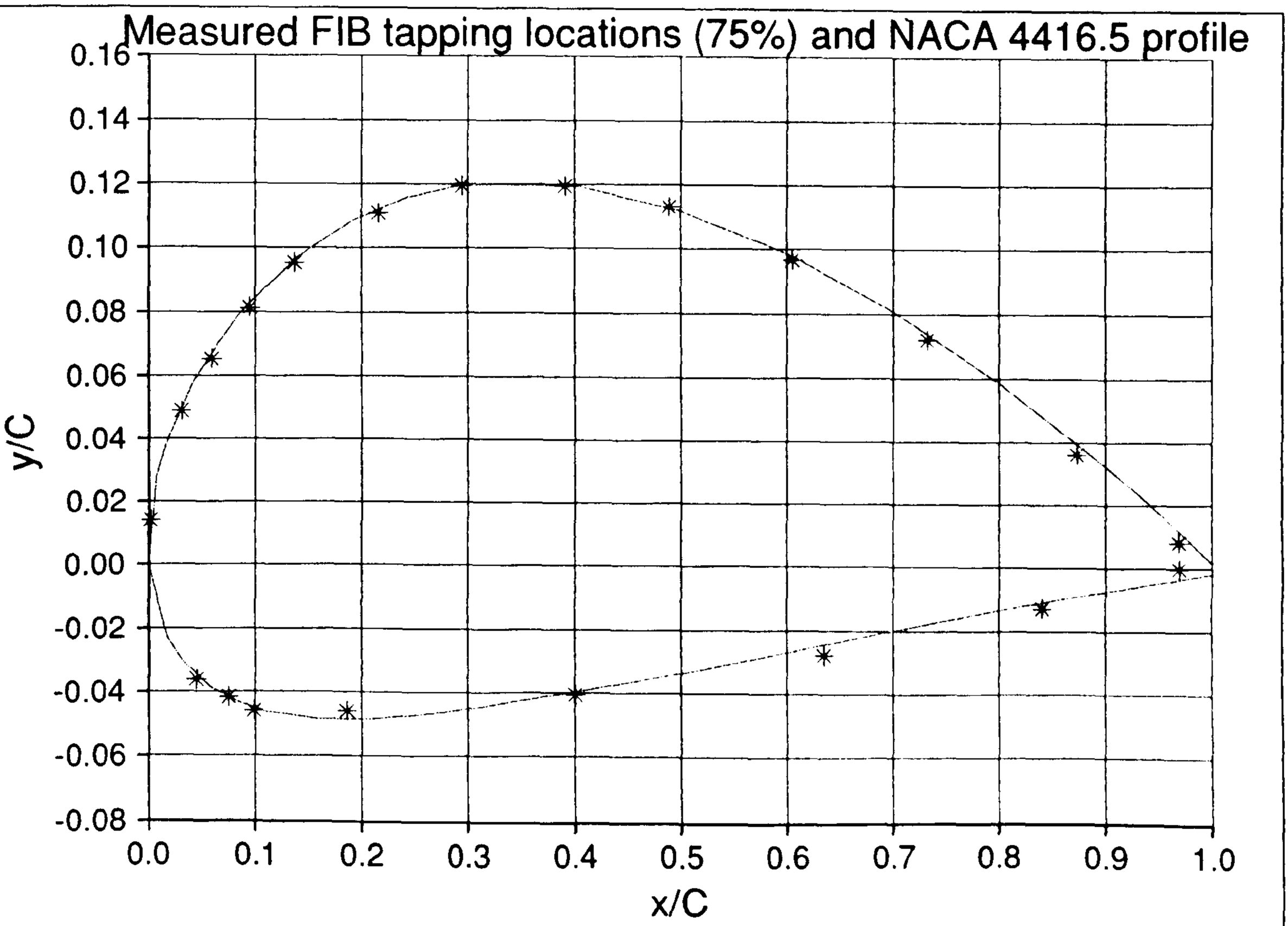

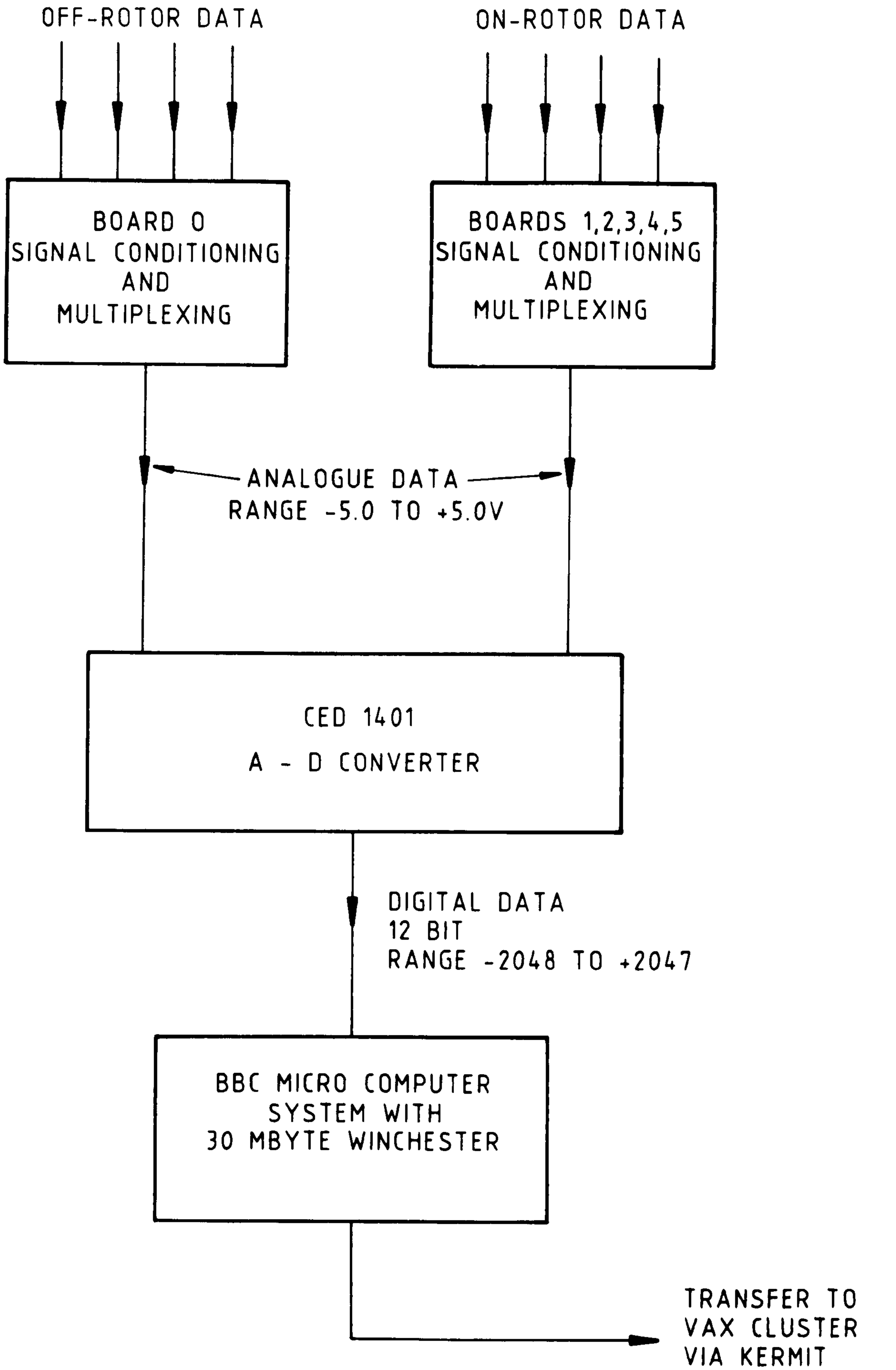

Figure 5.1 General layout of the data acquisition system.

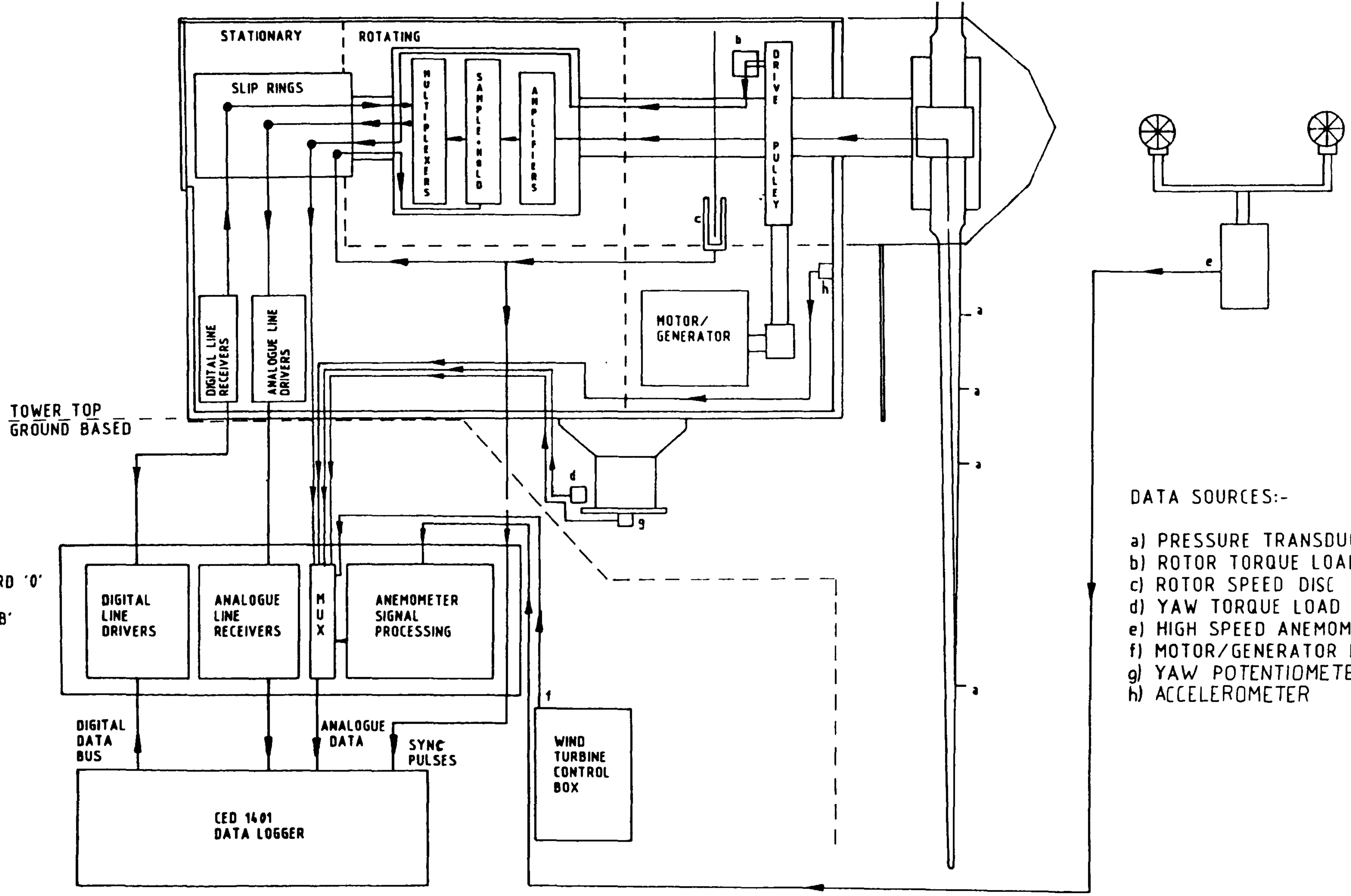

Figure 5.2 Arrangement of the wind turbine and data acquisition system.

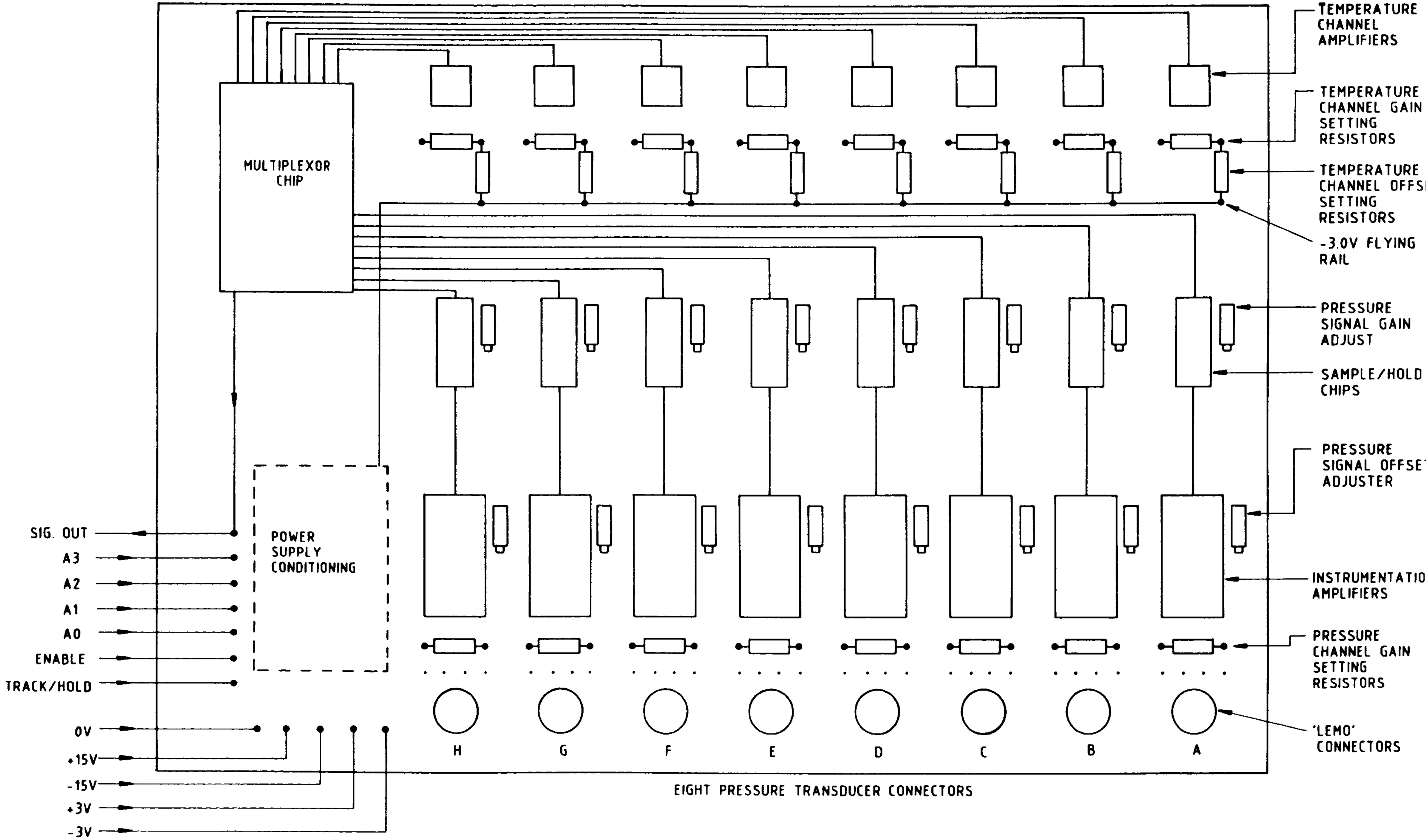

Figure 5.3 Circuit layout for Boards 1,2,3,4 and 5 - on rotor signal conditioning and multiplexing.

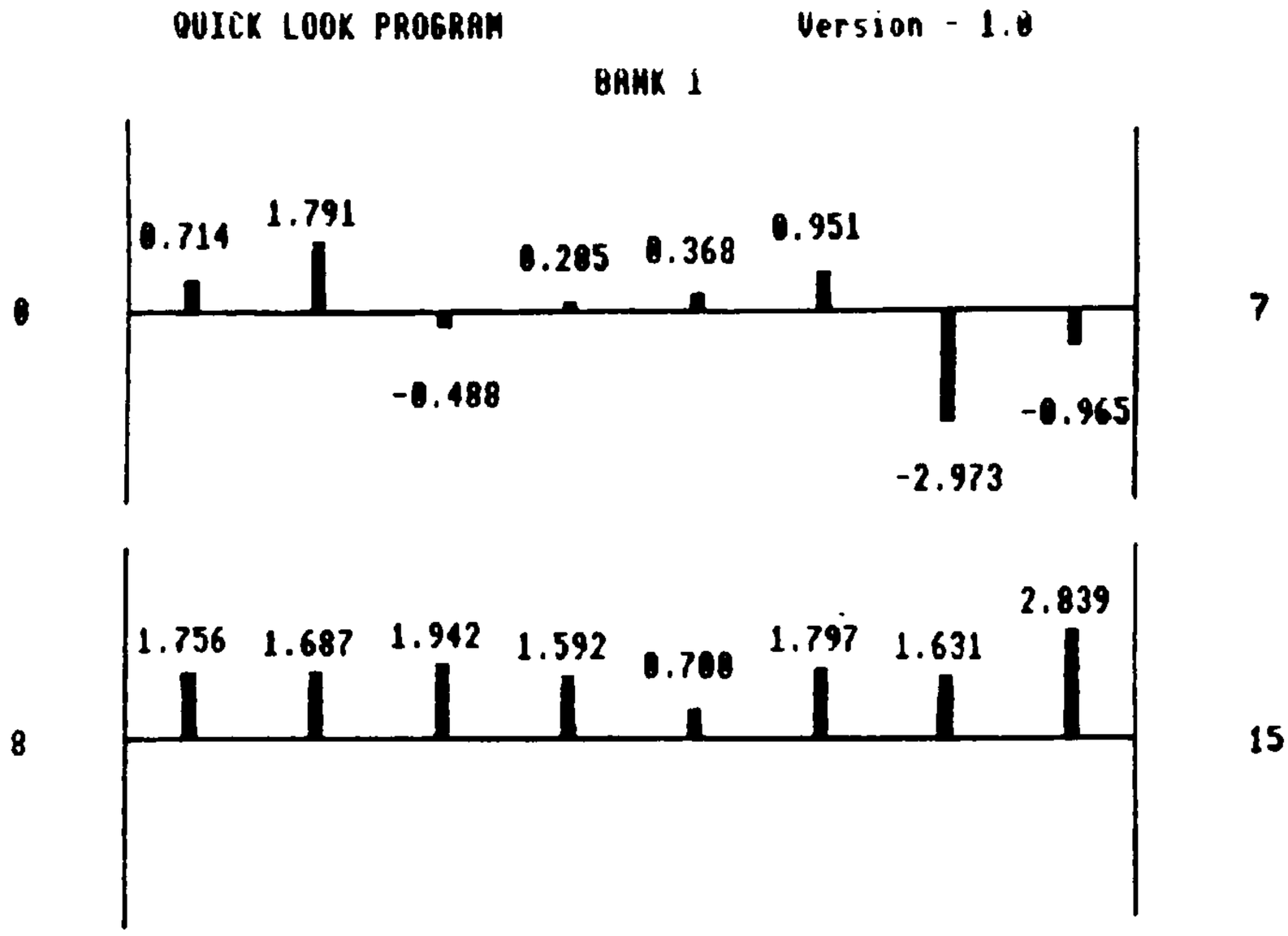

Bank 1 voltages at zero pressure

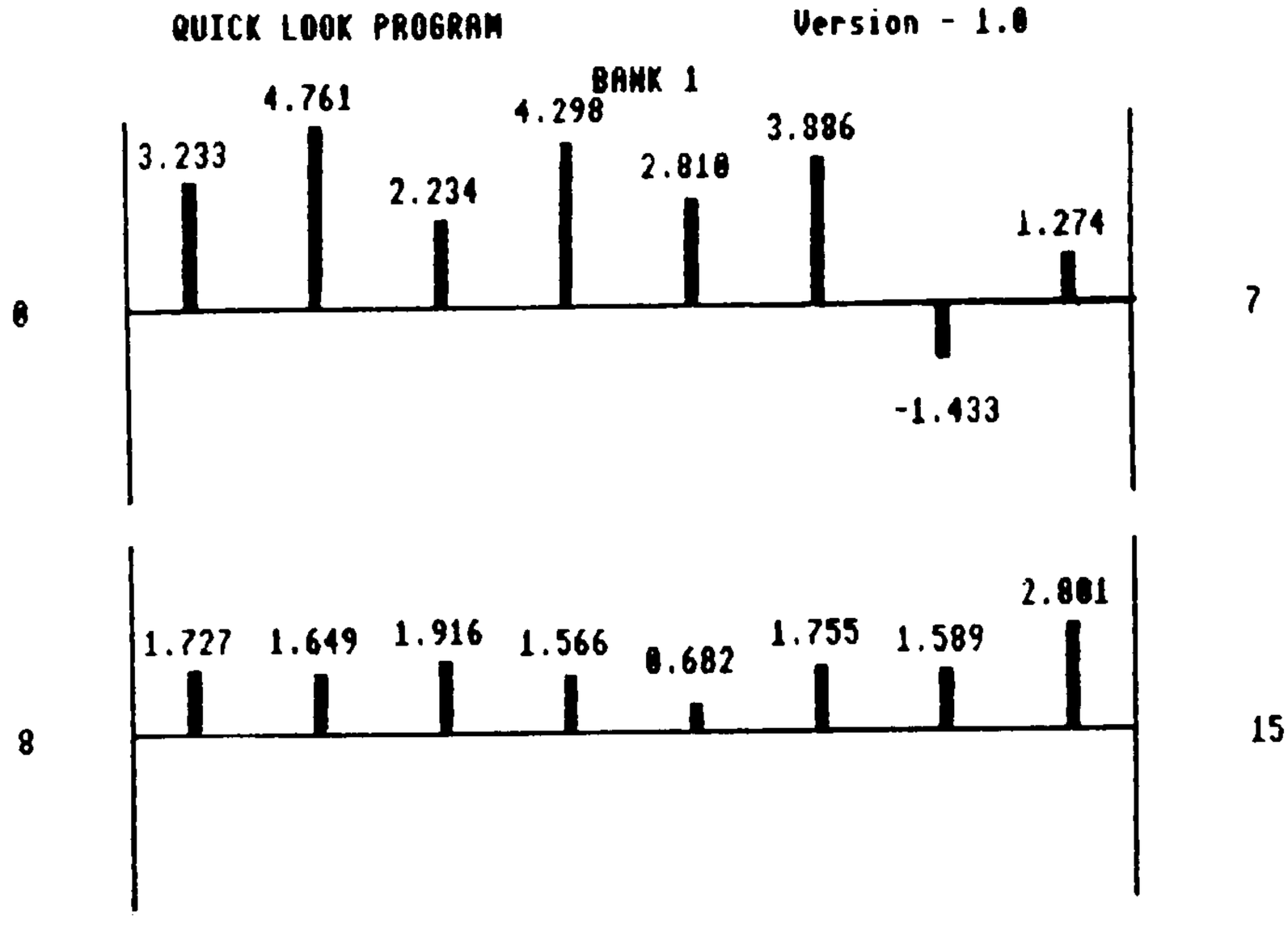

Bank 1 voltages at 300 mm water pressure

Figure 5.4 Typical monitor screen displays during execution of 'QLOOK'.

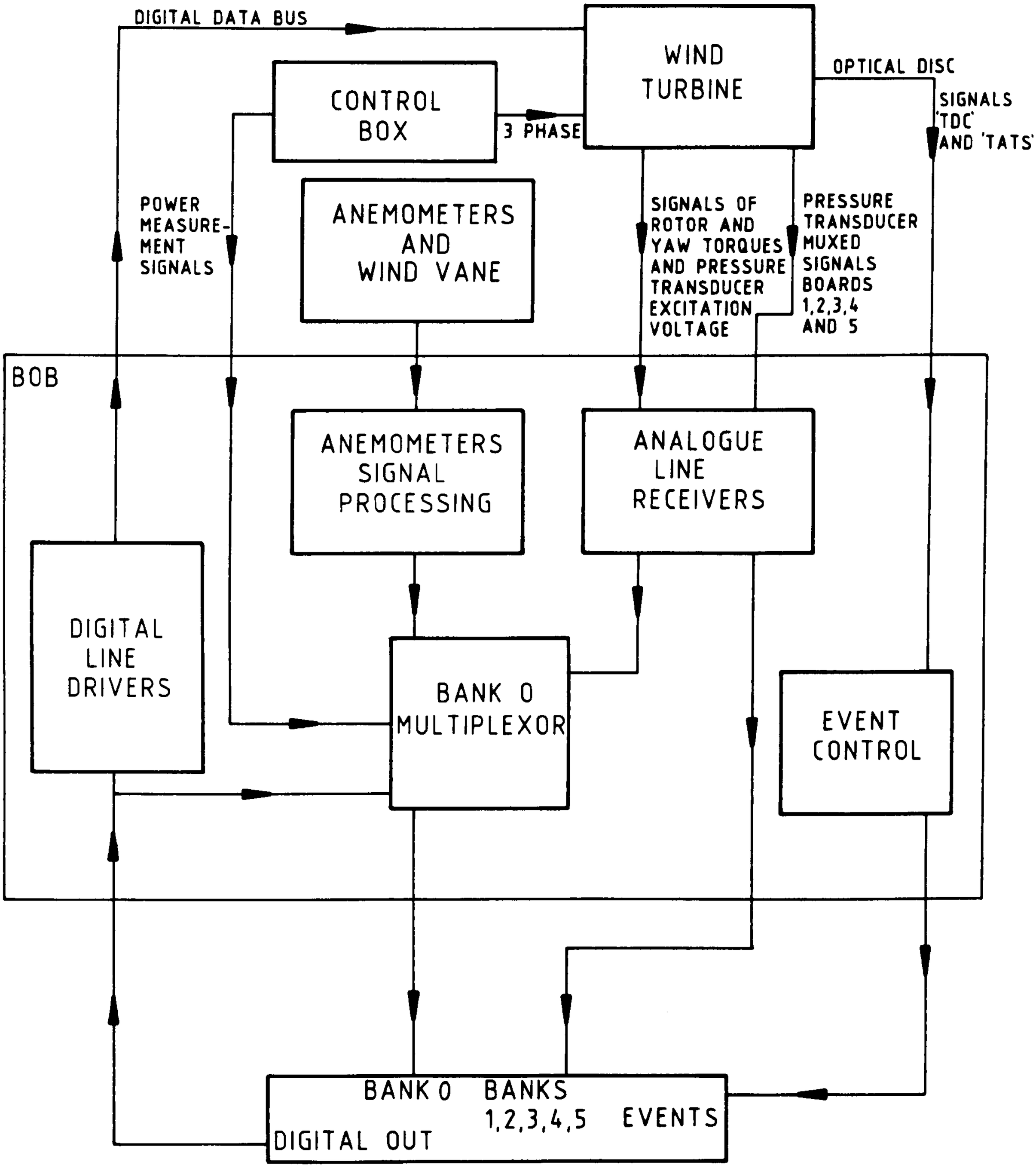

Figure 5.5 Schematic diagram of 'BOB' within the data acquisition system.

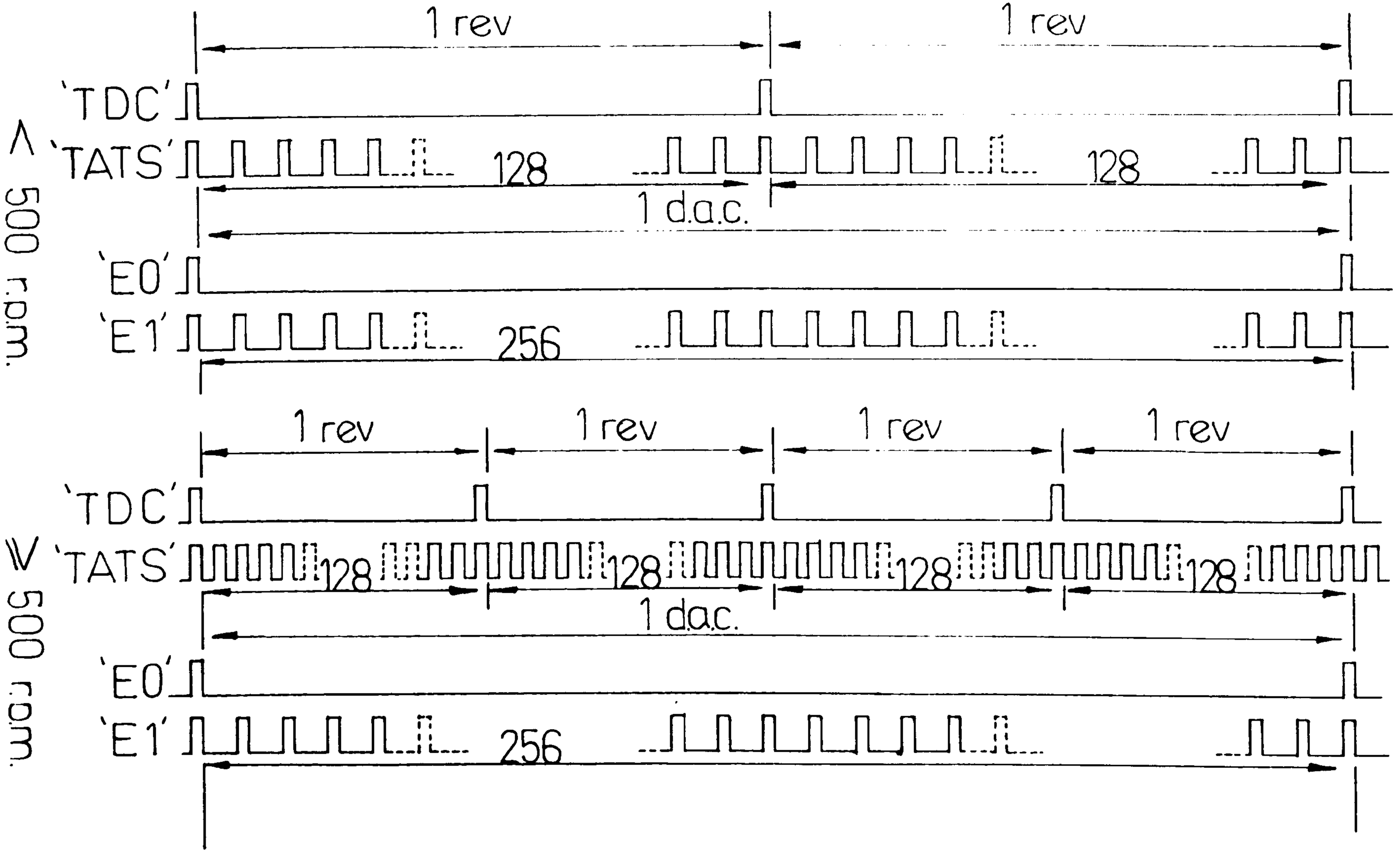

Figure 5.6 Relationship between the 'TDC', 'TATS', Event 0 and Event 1 pulse trains.

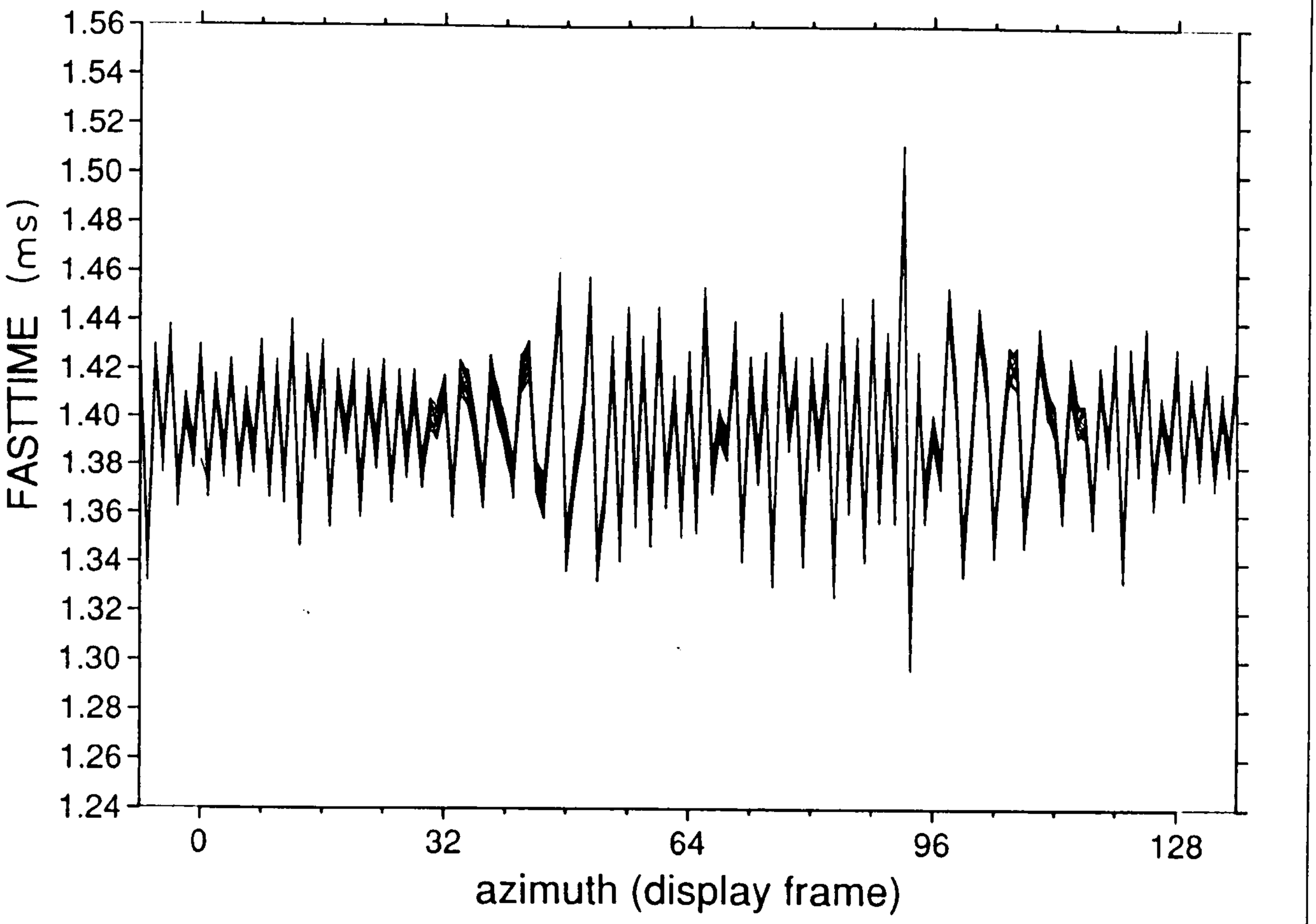

Figure 5.7 Time interval between successive azimuth slots before and after addition of PLL.

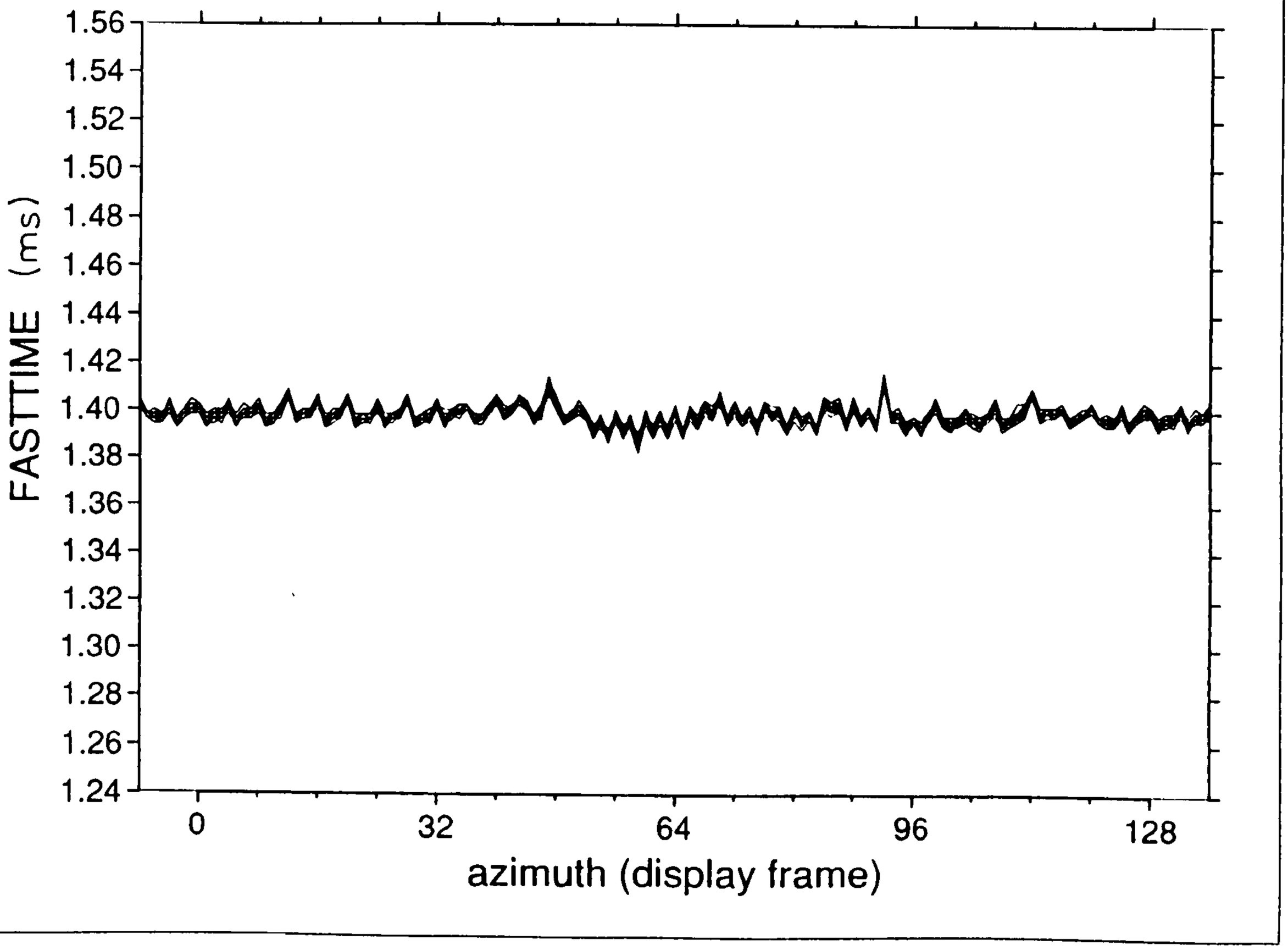

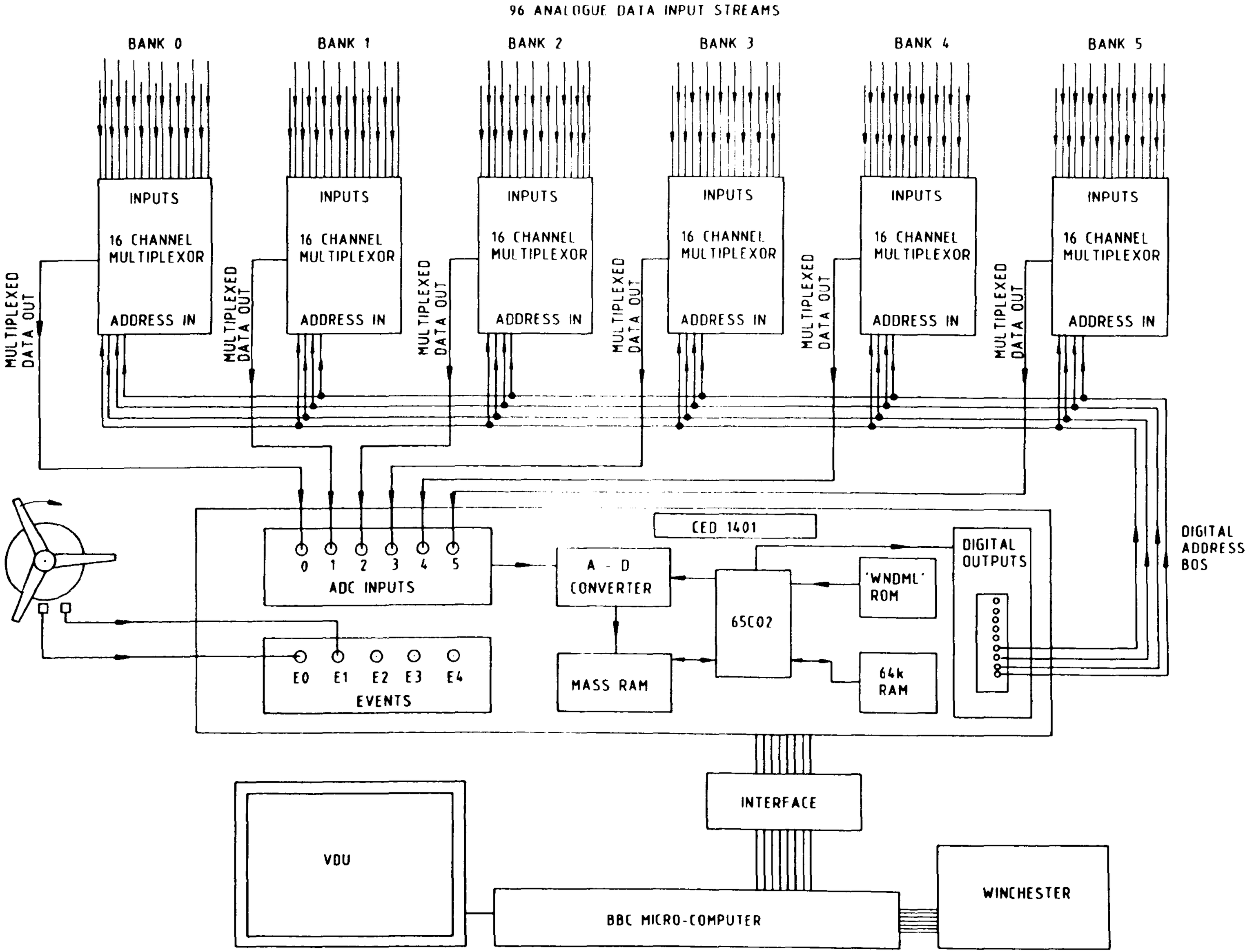

Figure 5.8 Detailed arrangement of the interfaces between the CED 1401 and the rest of the data acquisition system.

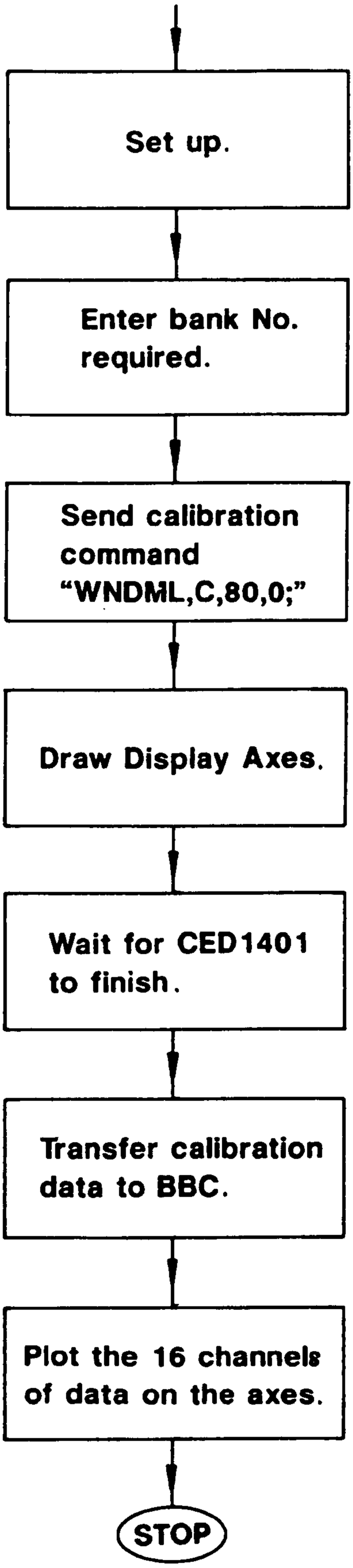

Figure 5.9 Block diagram of program 'QLOOK'.

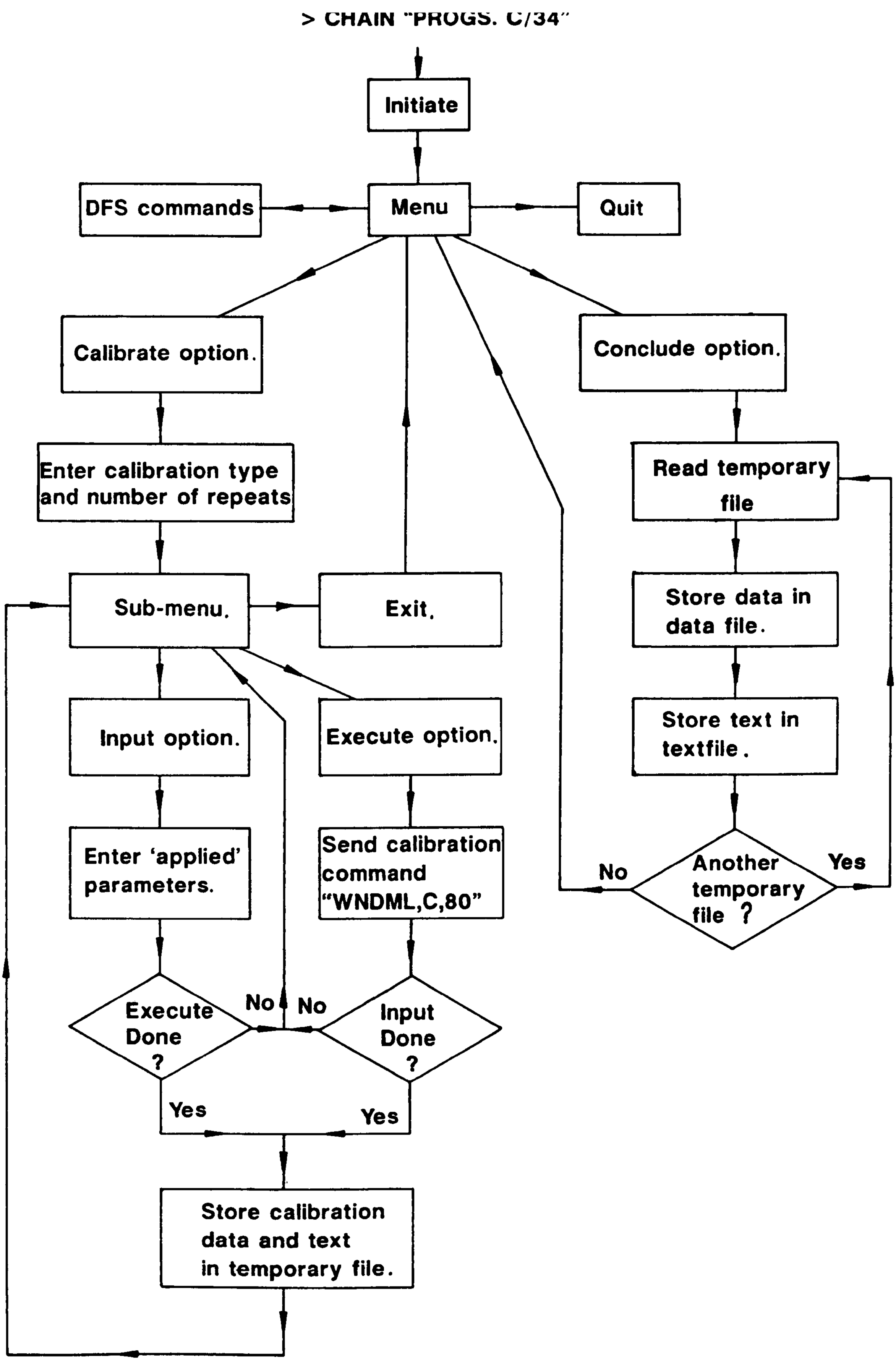

Figure 5.10 Block diagram of program 'C/34'.

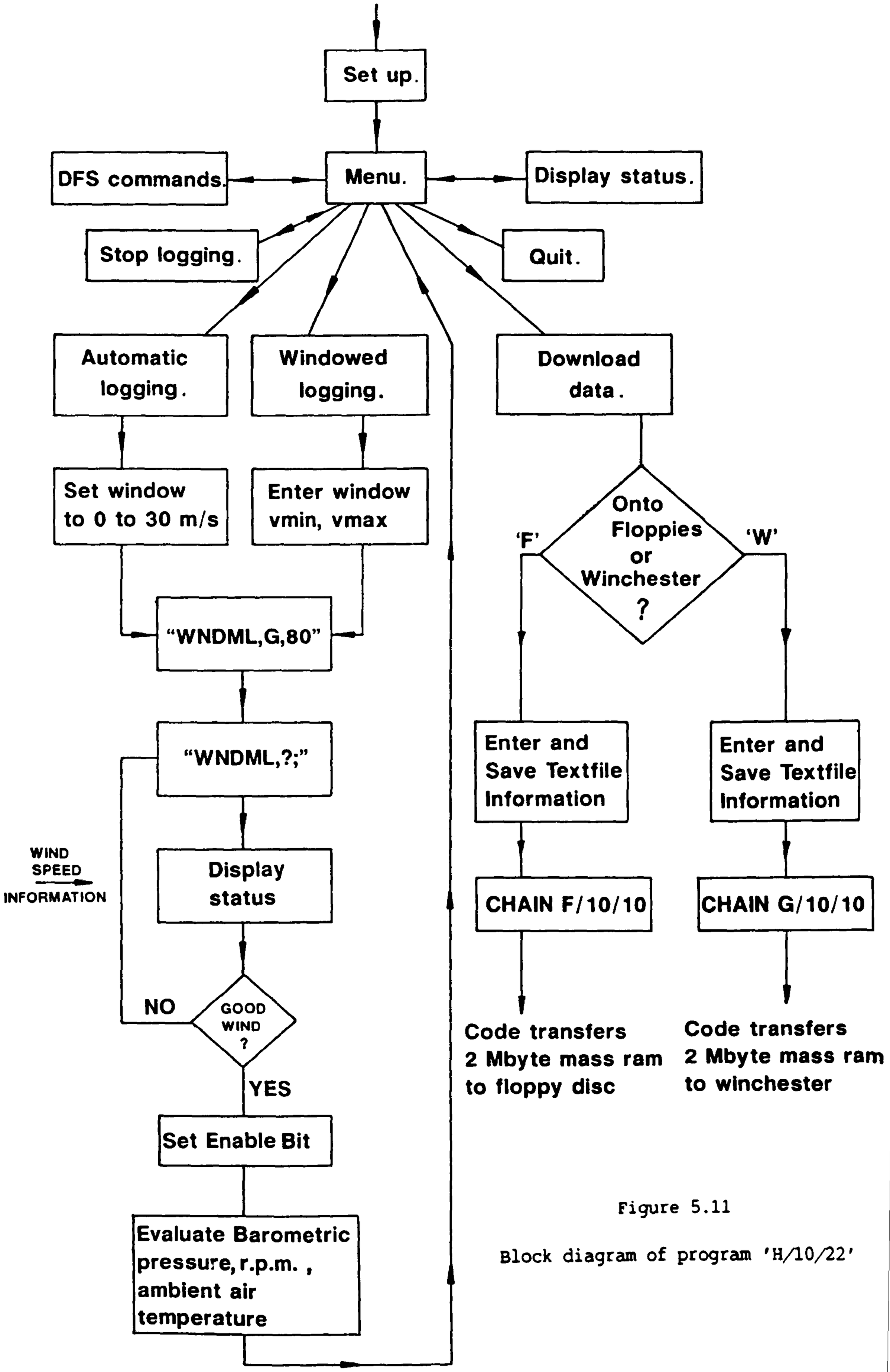

Figure 5.11

Block diagram of program 'H/10/22'

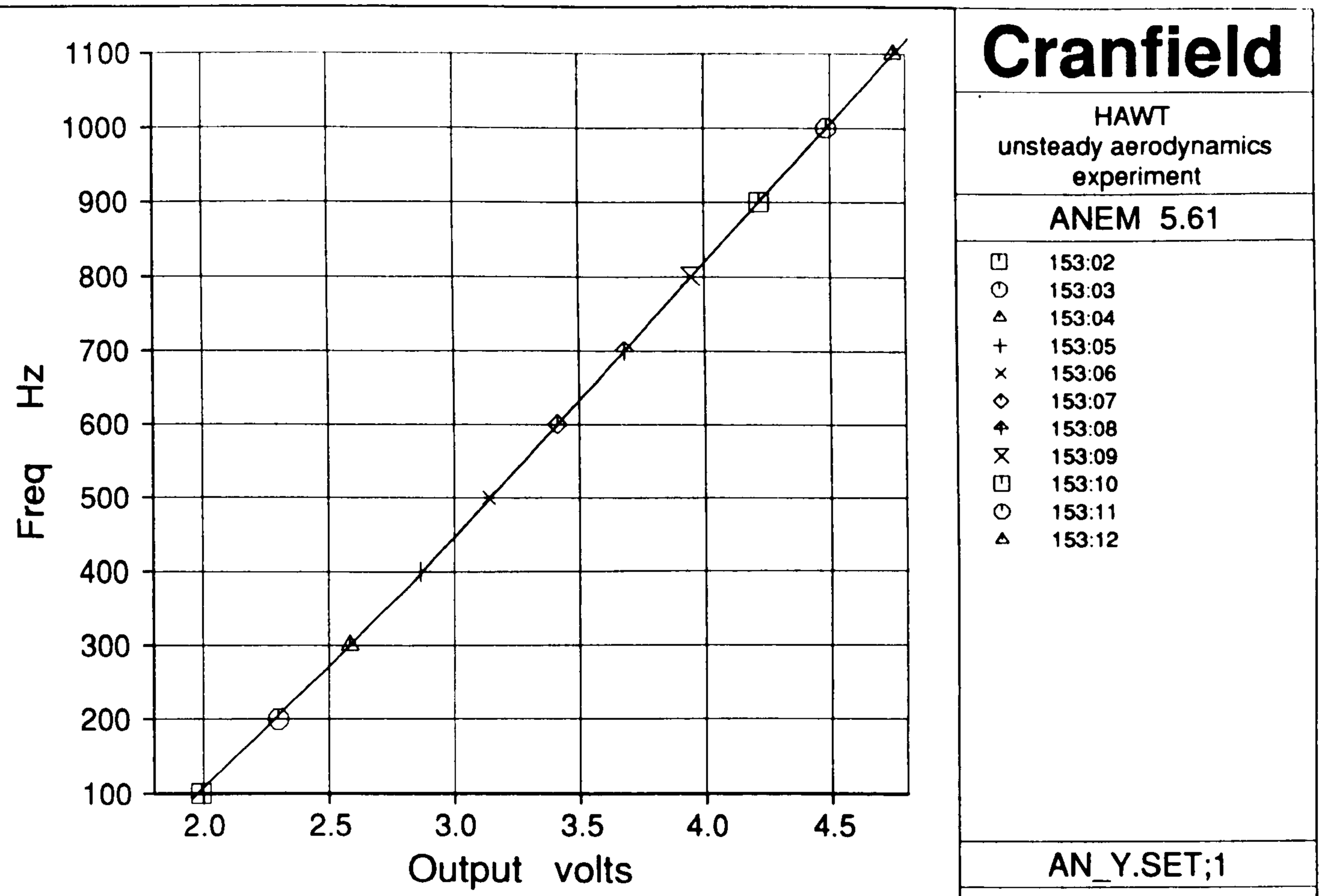

Figure 6.1 Typical calibration of Lowne anemometer (frequency to voltage).

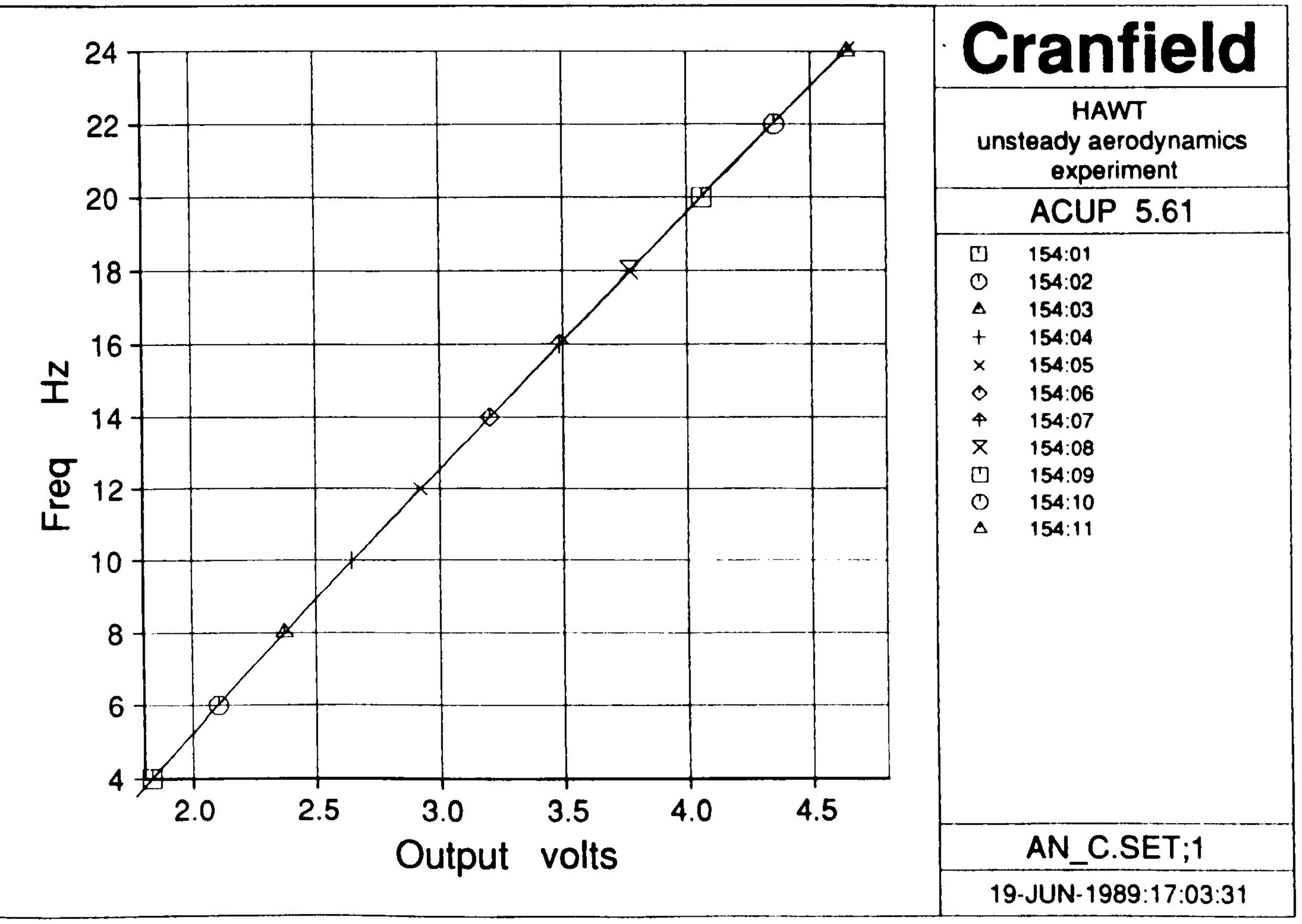

Figure 6.2 Typical calibration of cup anemometer (frequency to voltage).

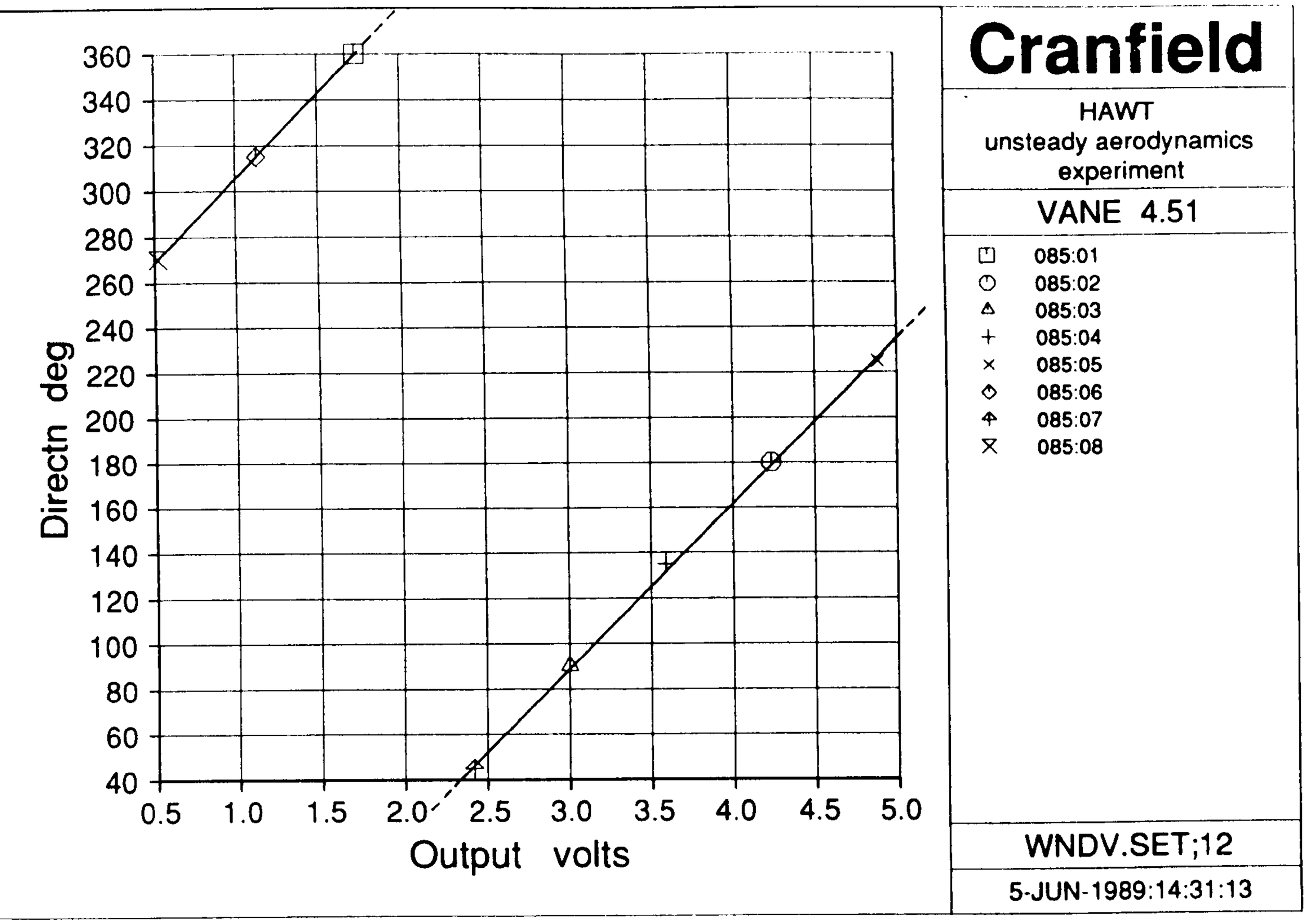

Figure 6.3 Typical calibration of wind vane (angle to voltage).

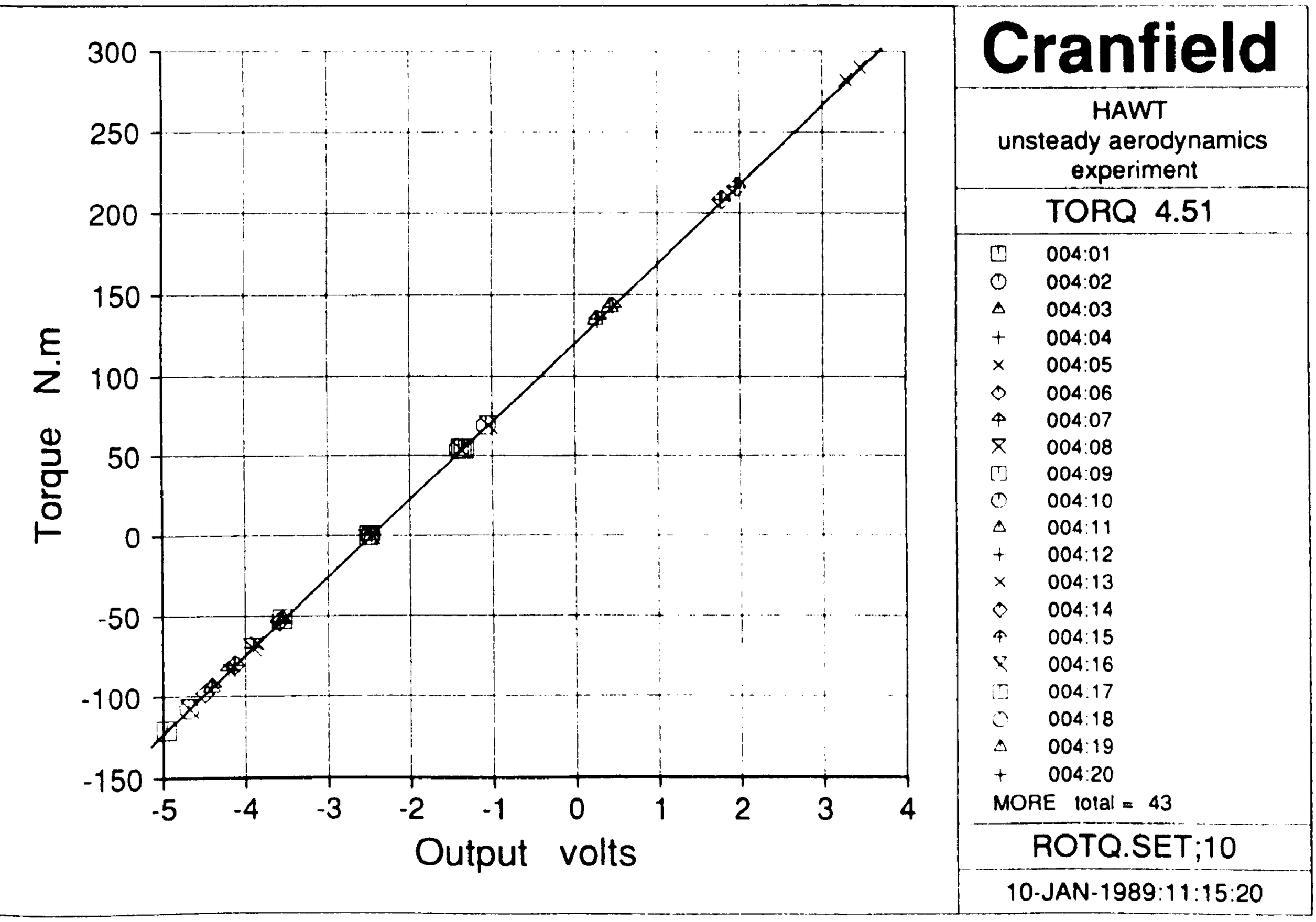

Figure 6.4 Typical calibration of rotor torque load cell (torque to voltage)

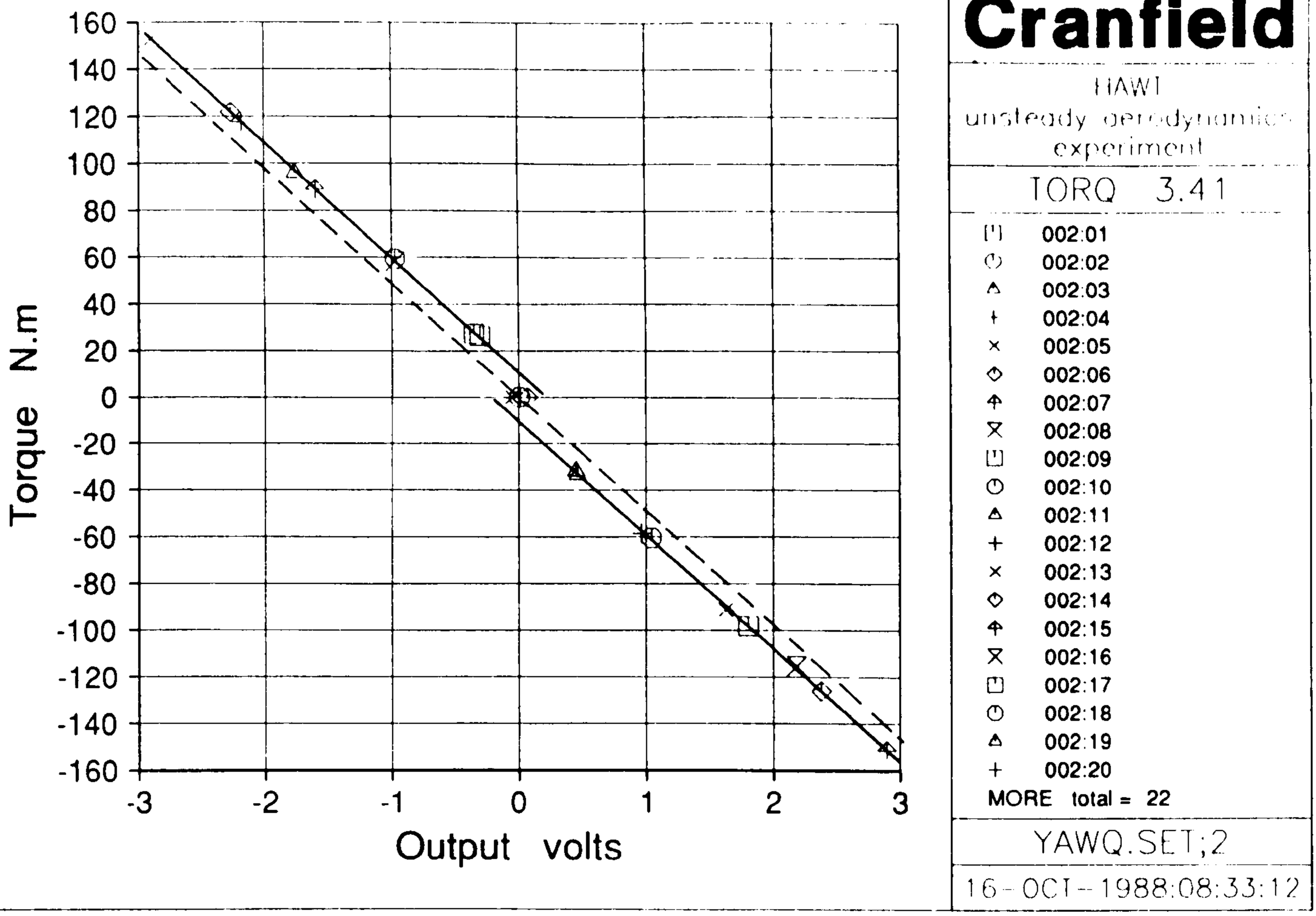

Figure 6.5 Typical calibration of yaw torque load cell (torque to voltage)

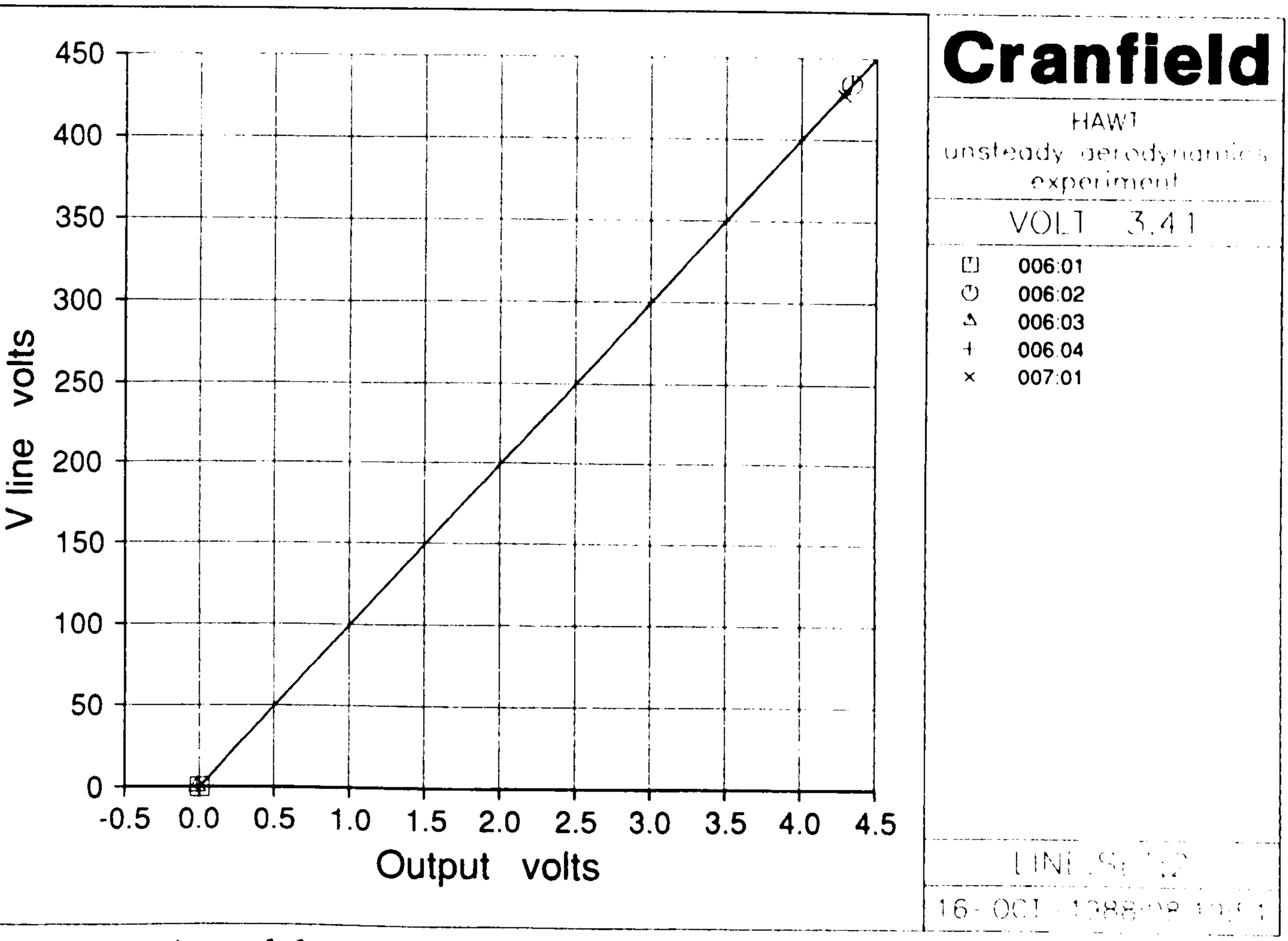

Figure 6.6 Typical calibration of the line voltage

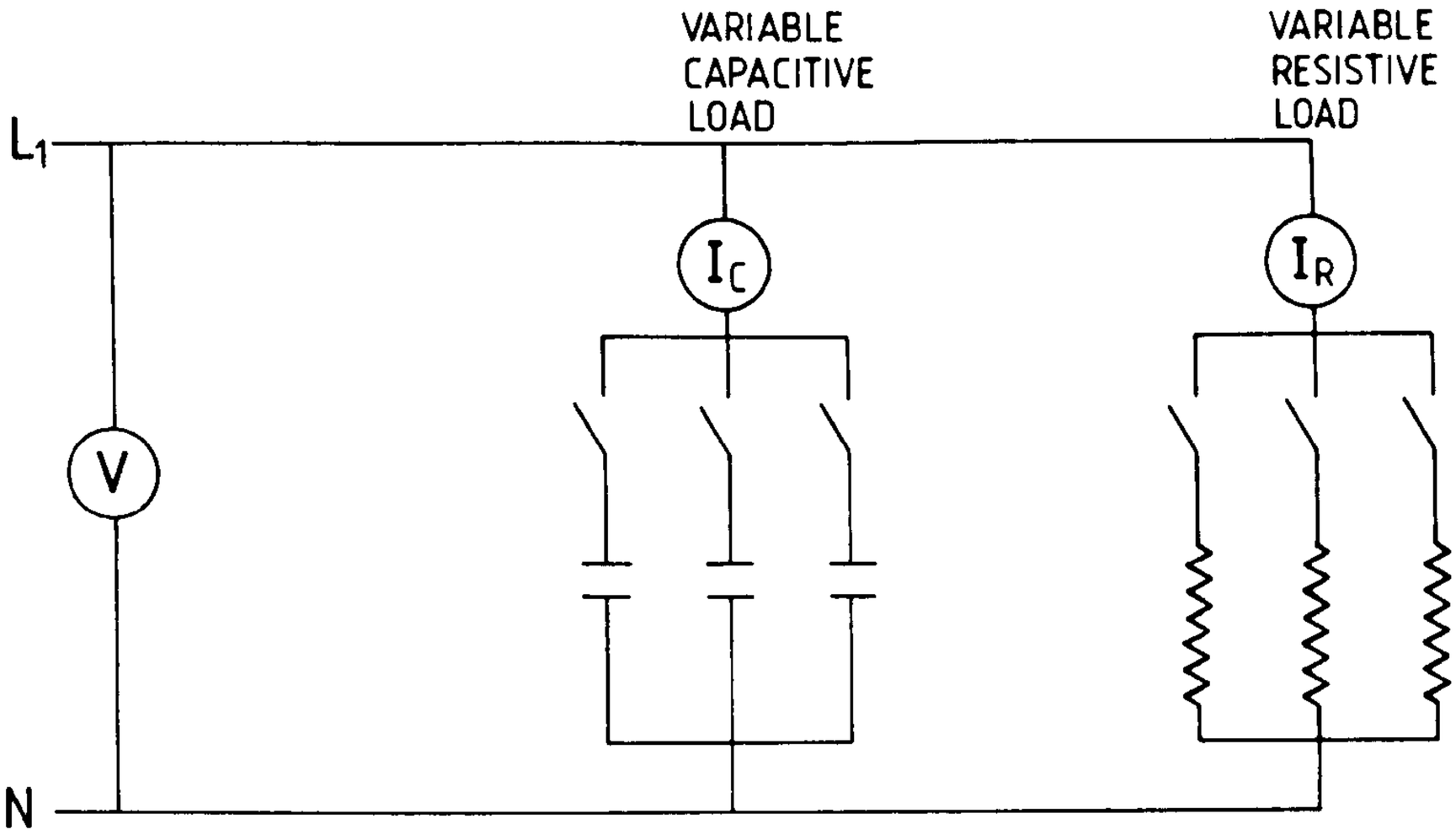

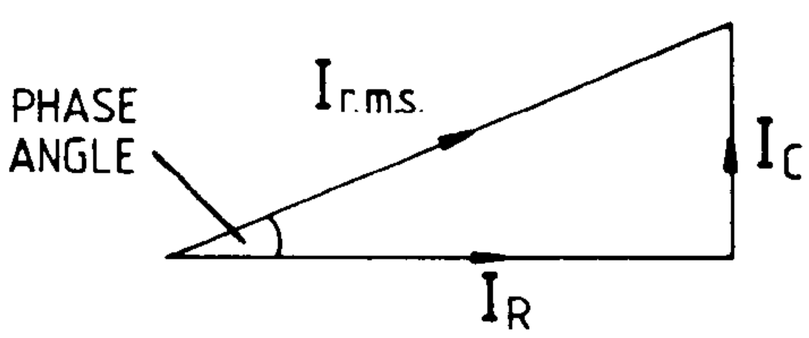

$$\text{REAL POWER} = I_R V \ (kW)$$

$$\text{R.M.S. CURRENT} = \sqrt{I_C^2 + I_R^2}$$

Figure 6.7 Circuit to allow variation of phase angle for current and power calibrations

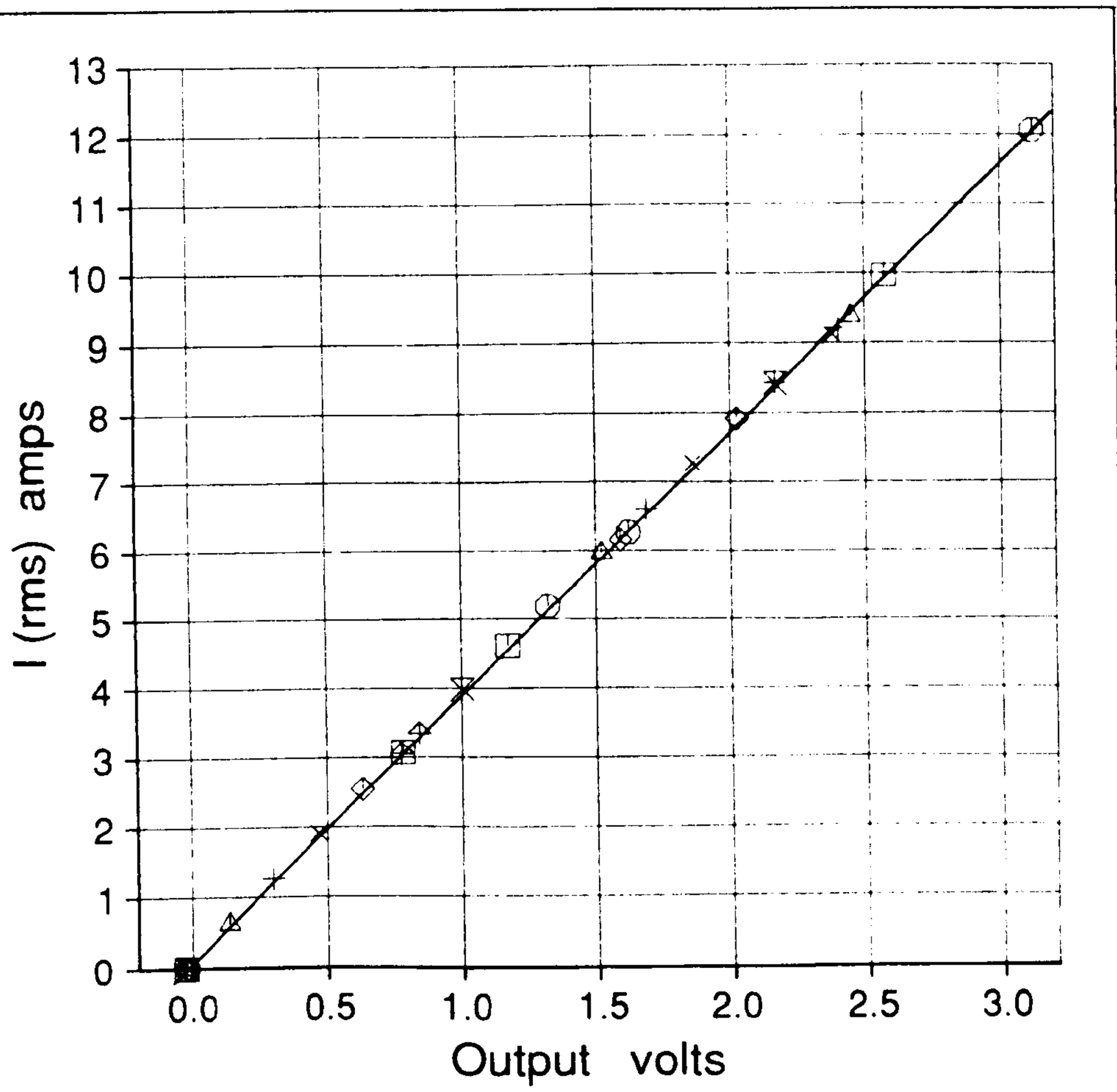

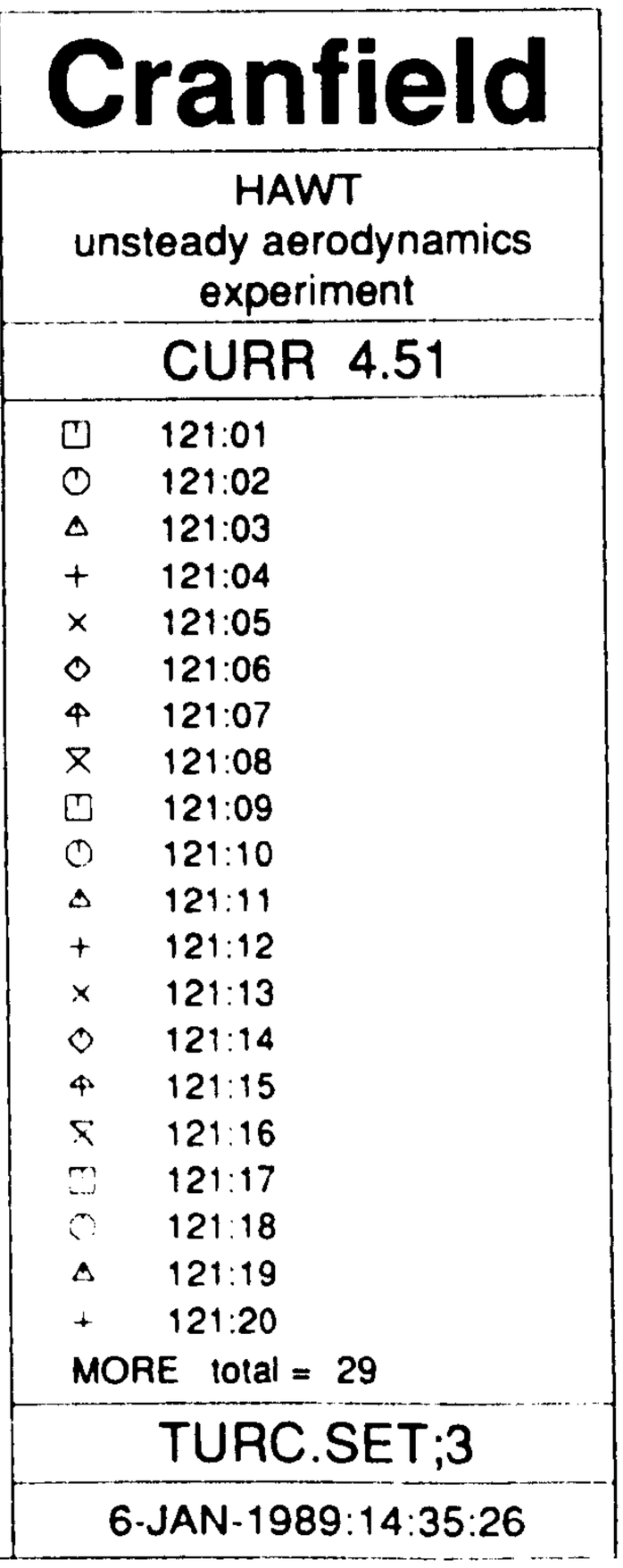

Figure 6.8 Typical calibration of the r.m.s. current circuit

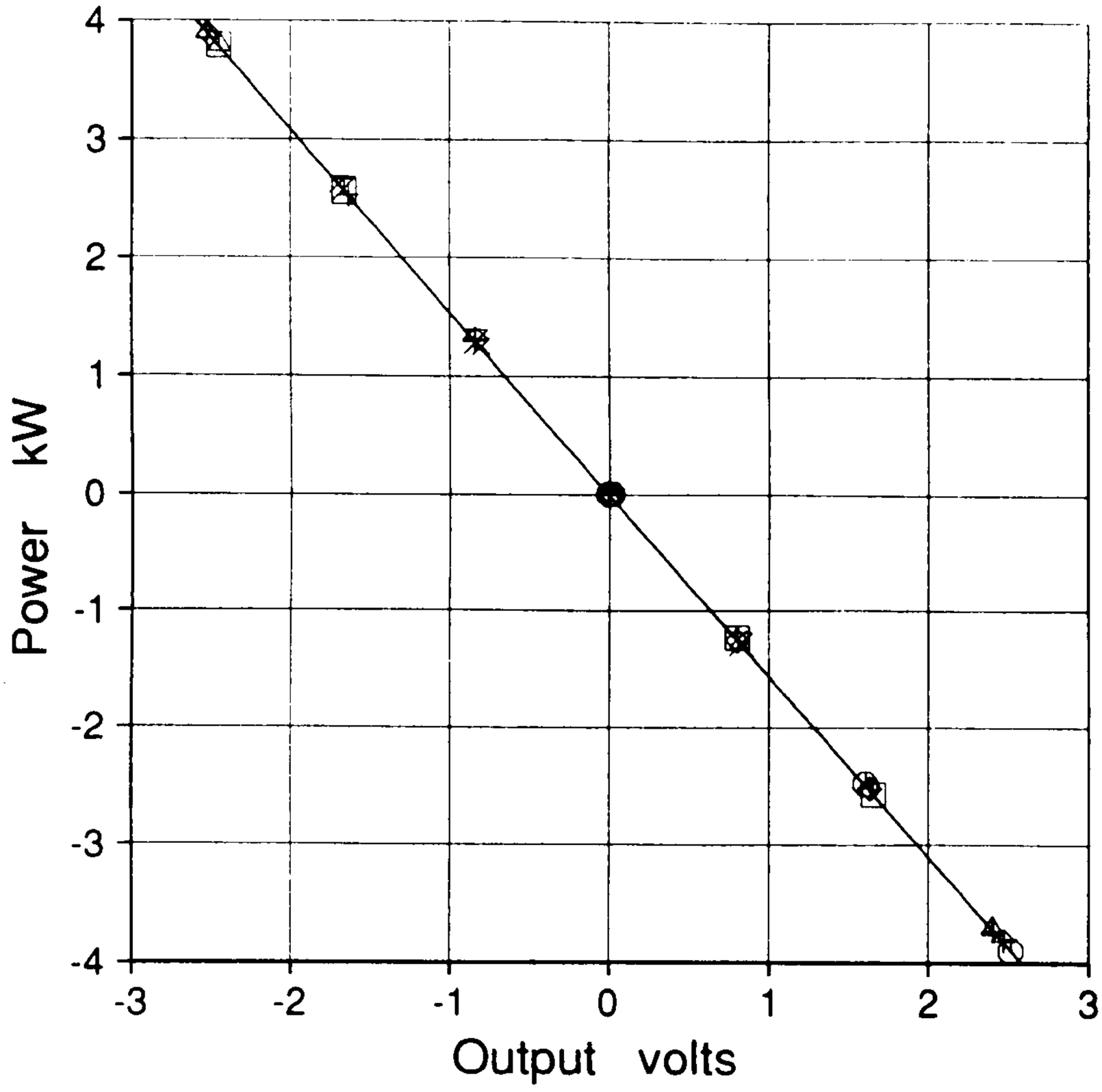

Figure 6.9 Typical calibration of the electrical power circuit

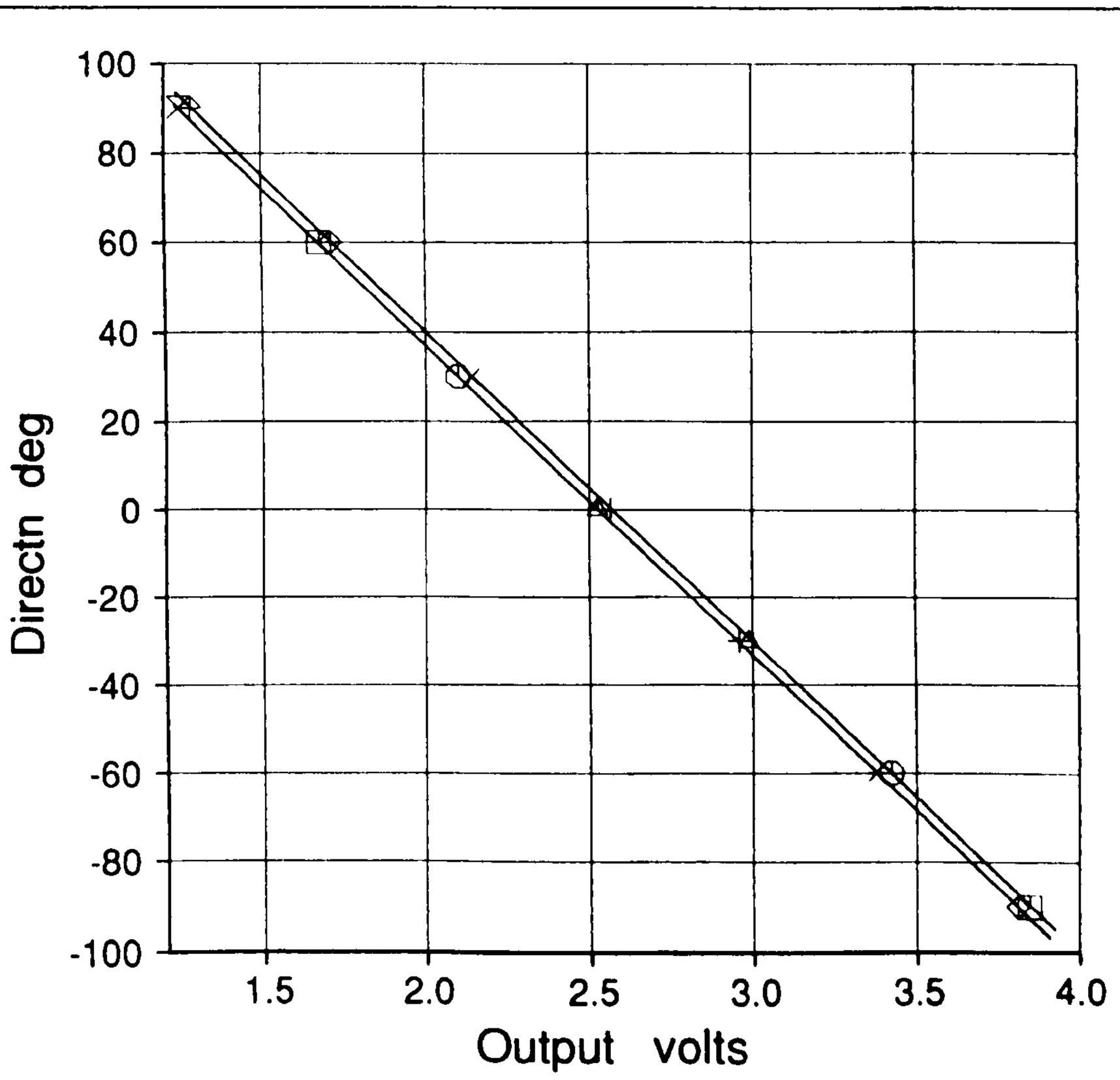

Figure 6.10 Typical calibration of the body (yaw) angle sensor

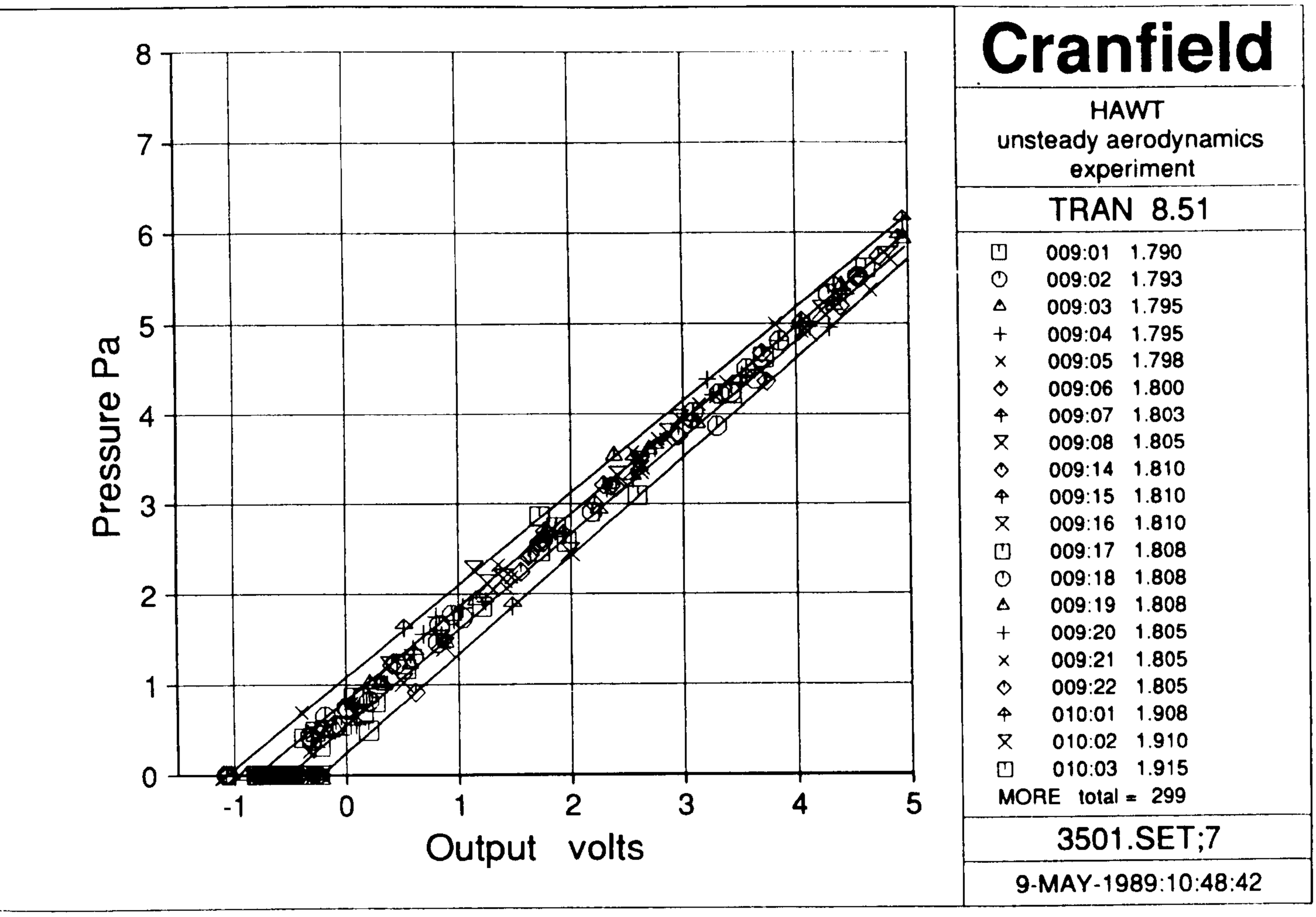

Figure 6.11 Typical calibration of a pressure transducer

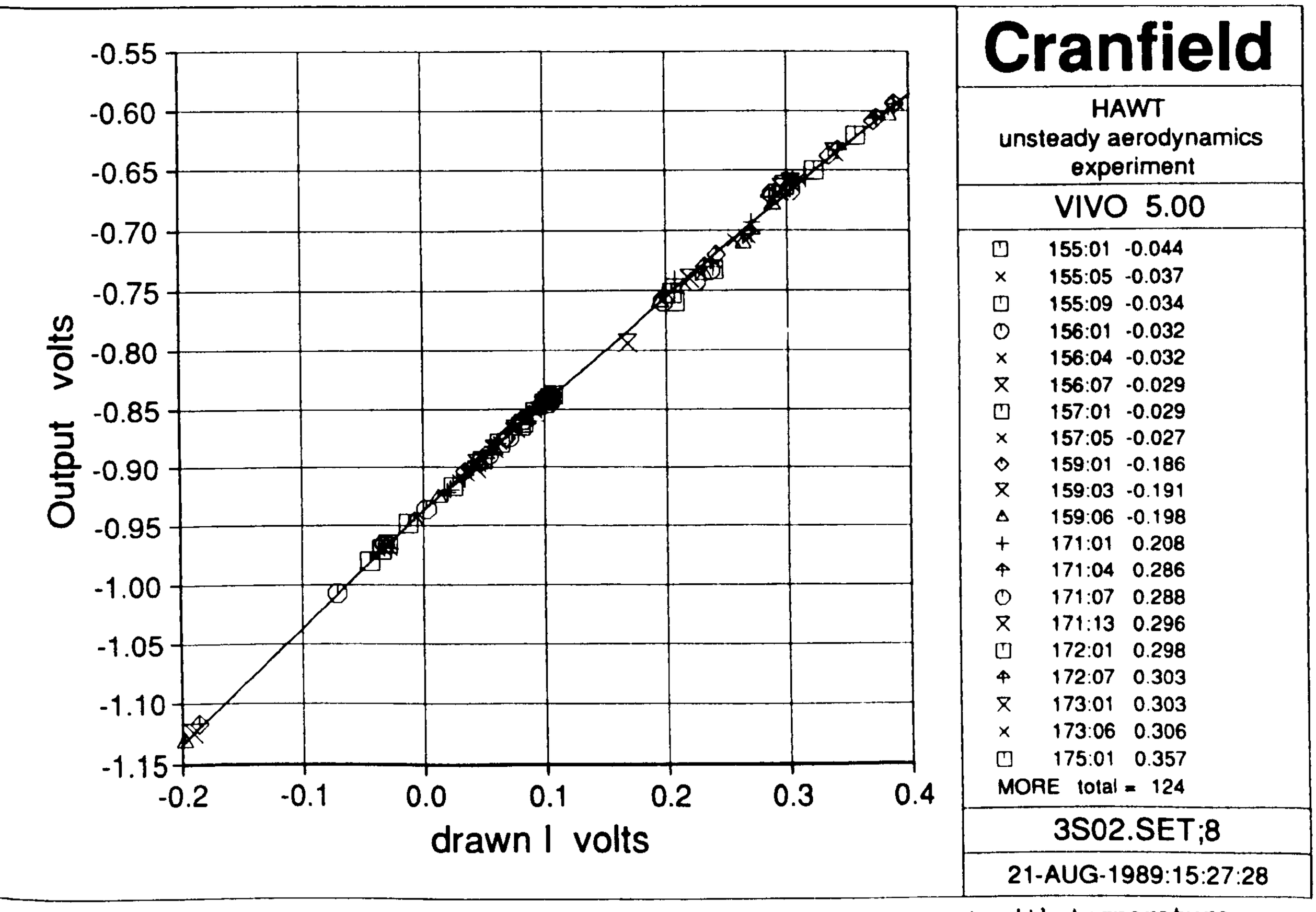

Figure 6.12 Typical correlation of pressure transducer output with temperature

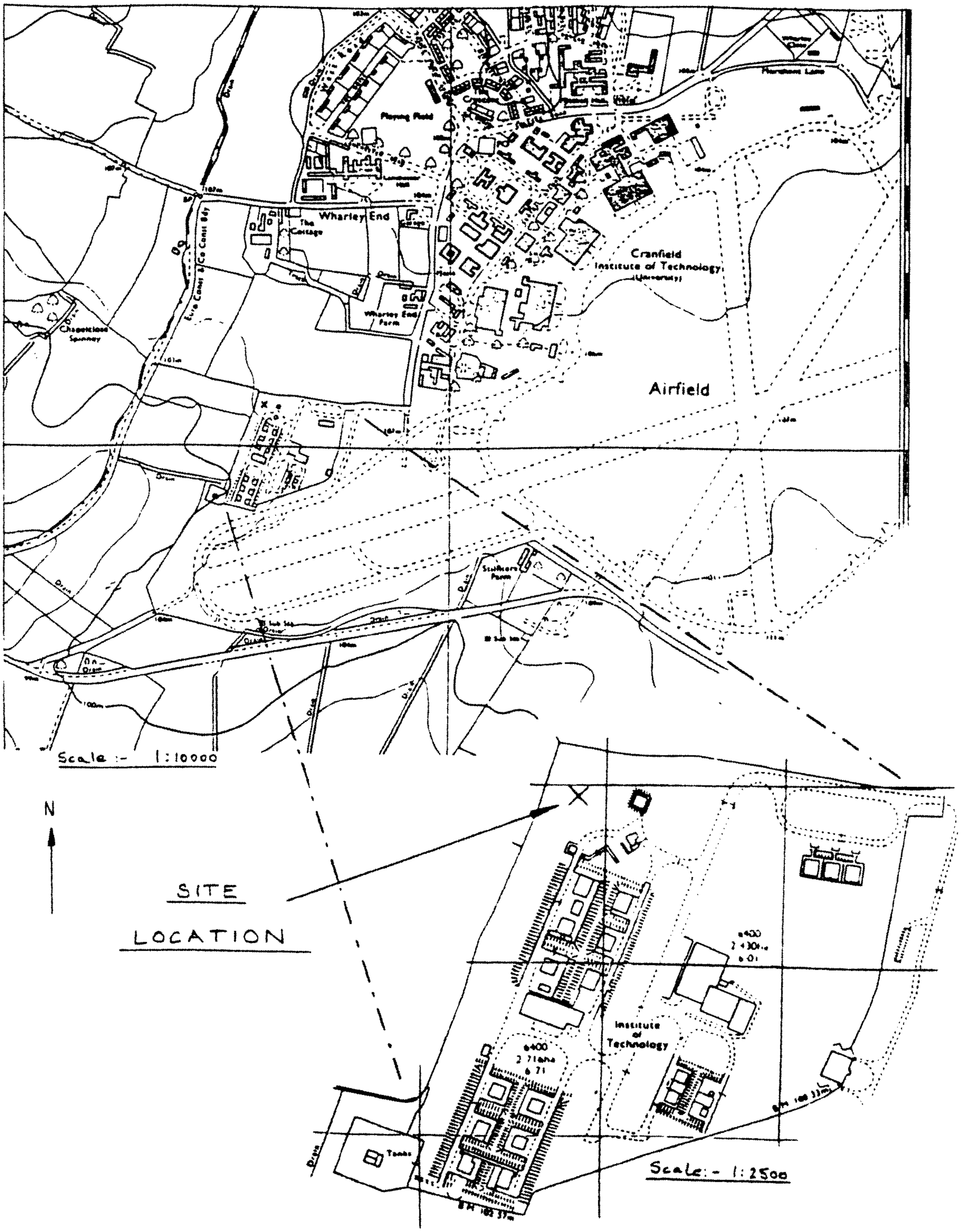

Figure 7.1 Map of the performance test facility

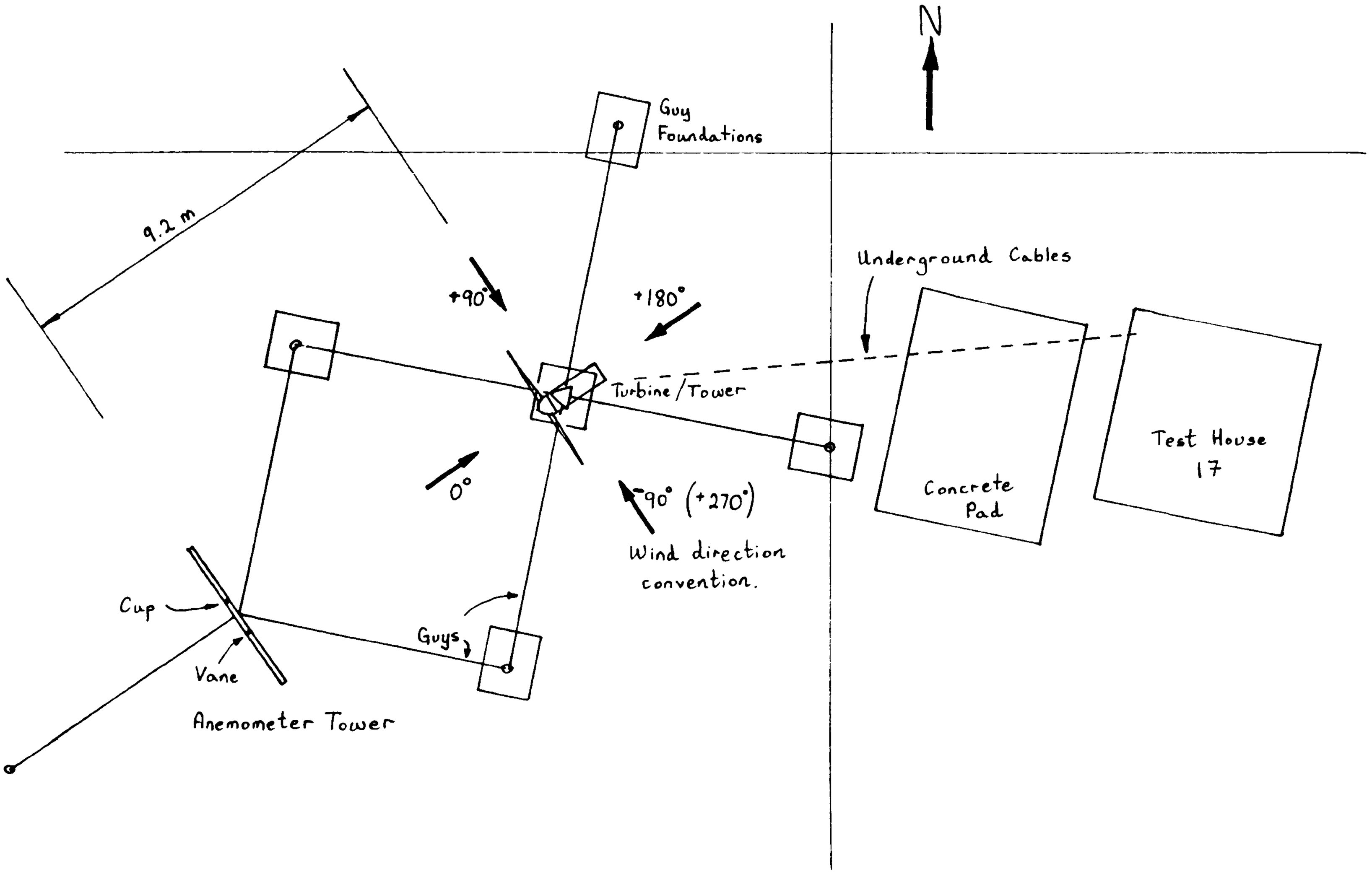

Figure 7.2 Plan and sign conventions for the performance test facility

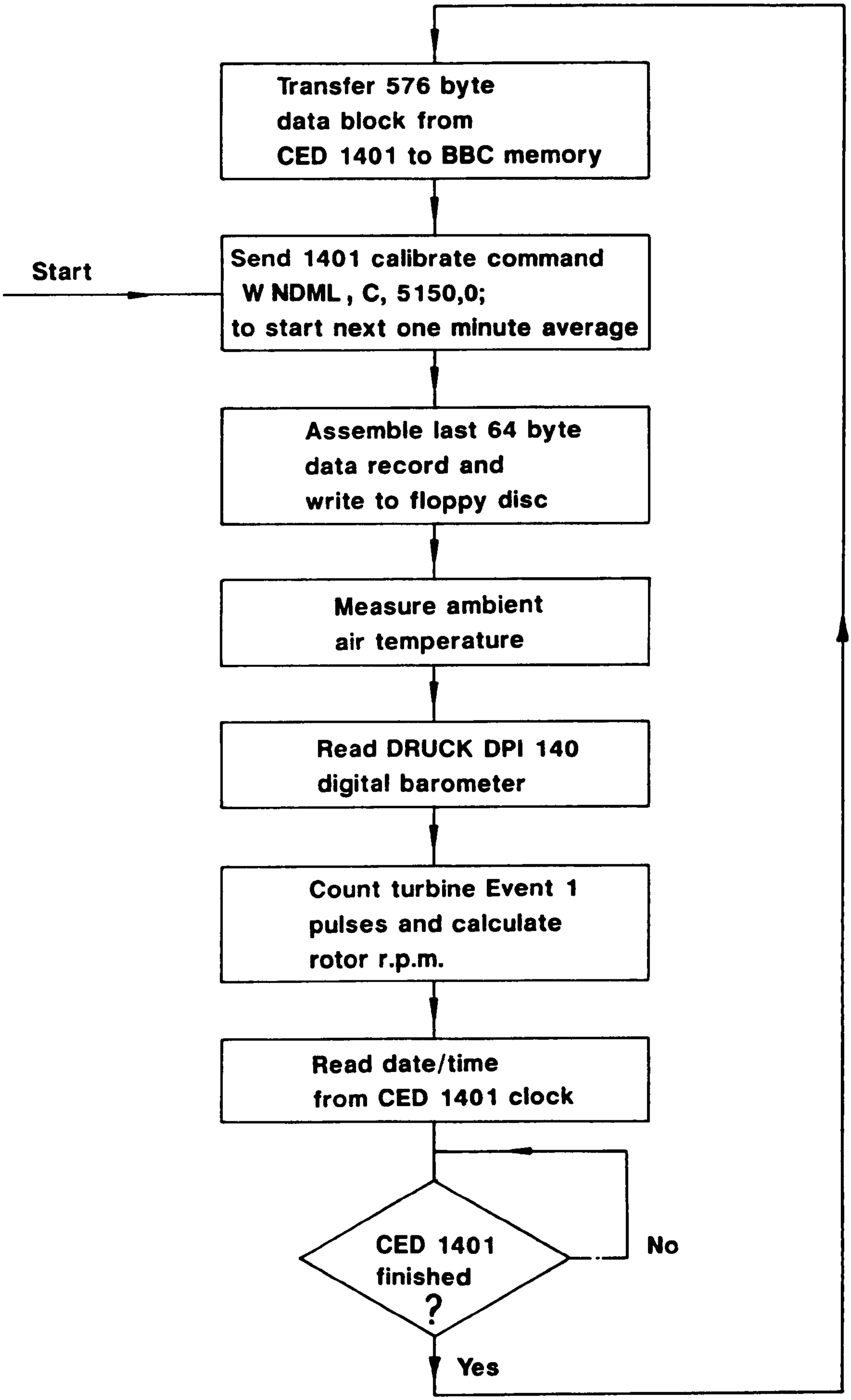

Figure 7.3 Block diagram of the BBC micro program "BANK0"

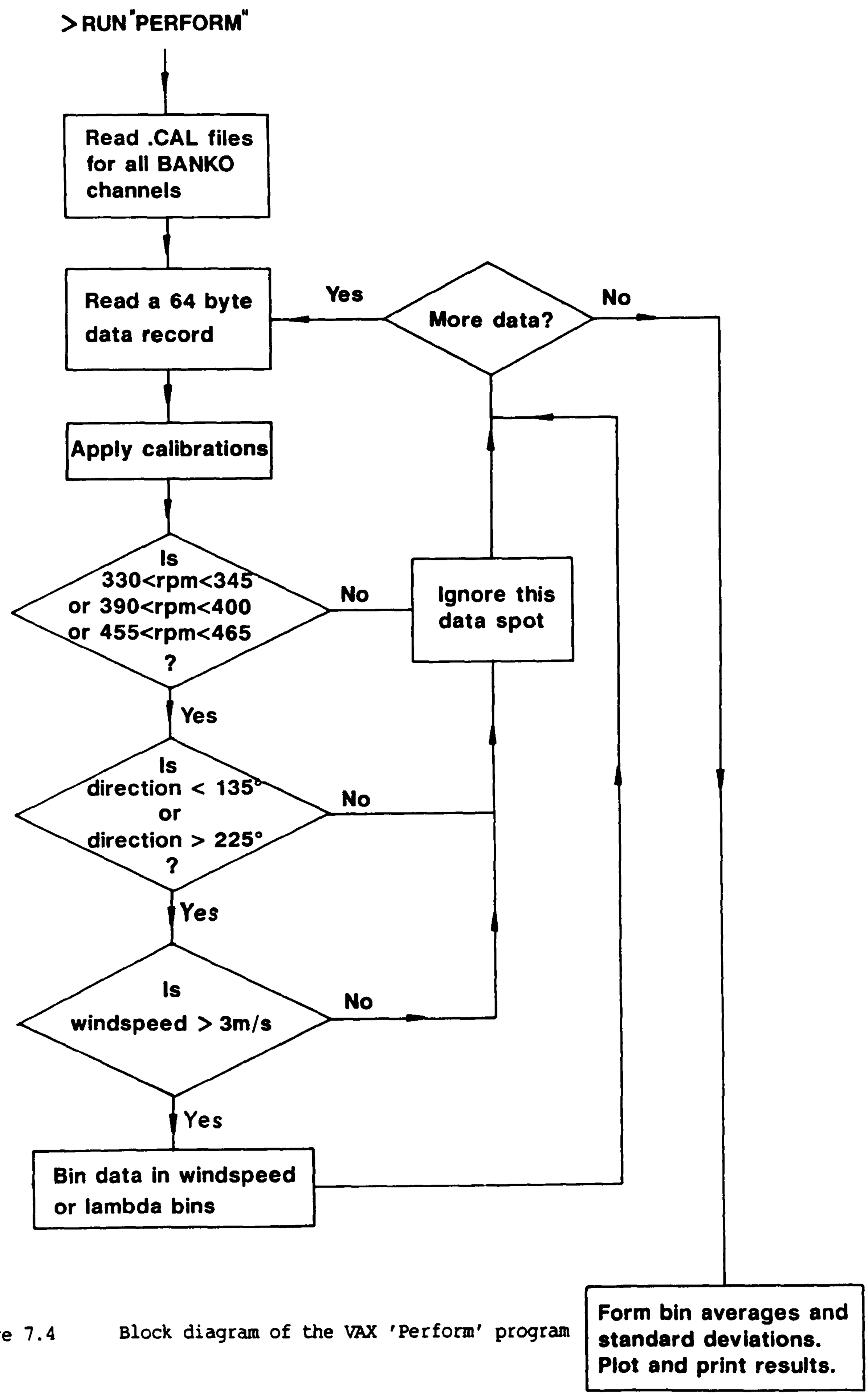

Figure 7.4 Block diagram of the VAX 'Perform' program

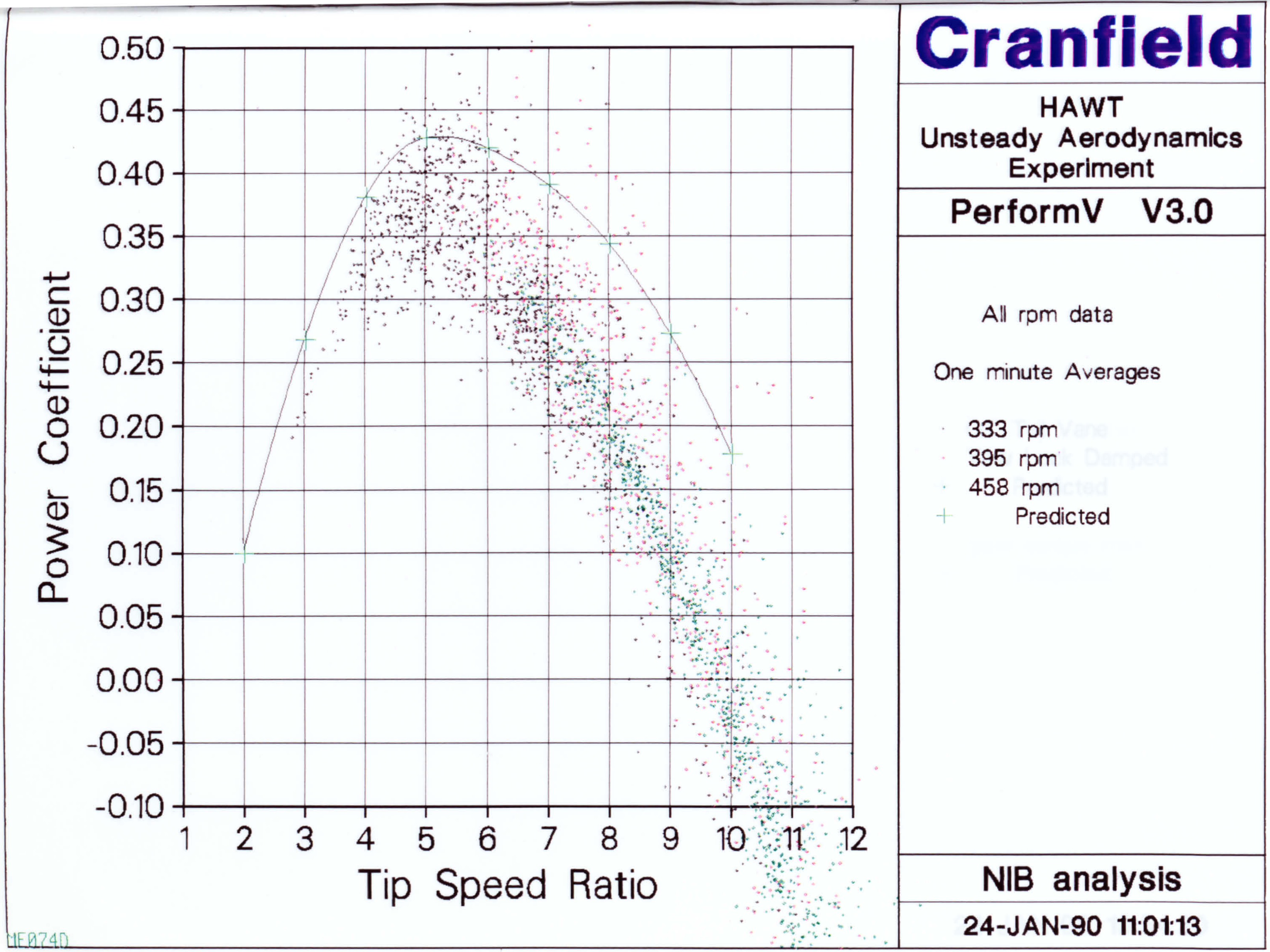

Figure 7.5 Scatter plot using r.p.m. criterion

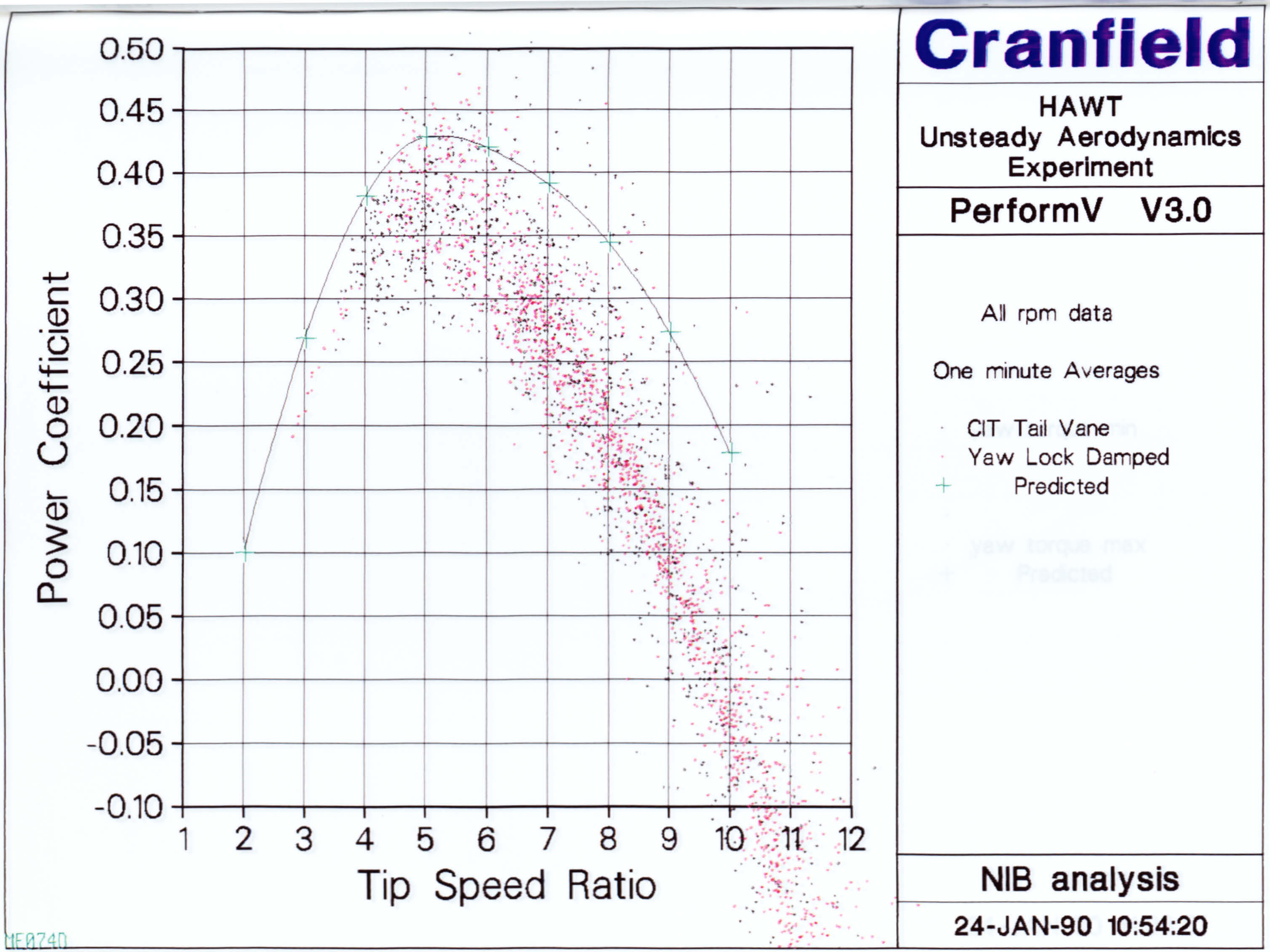

Figure 7.6 Scatter plot using yaw configuration criterion

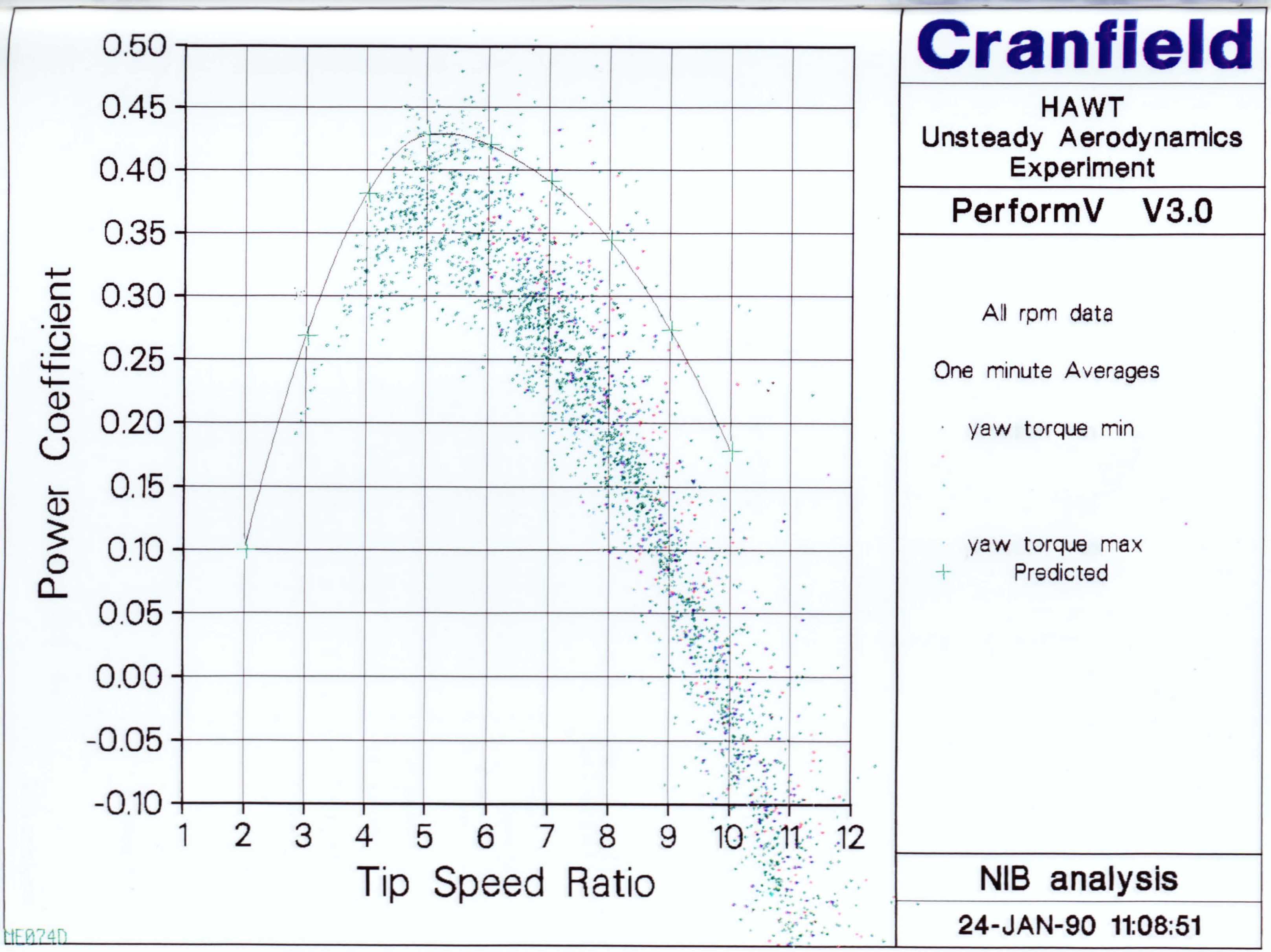

Figure 7.7 Scatter plot using yaw torque criterion

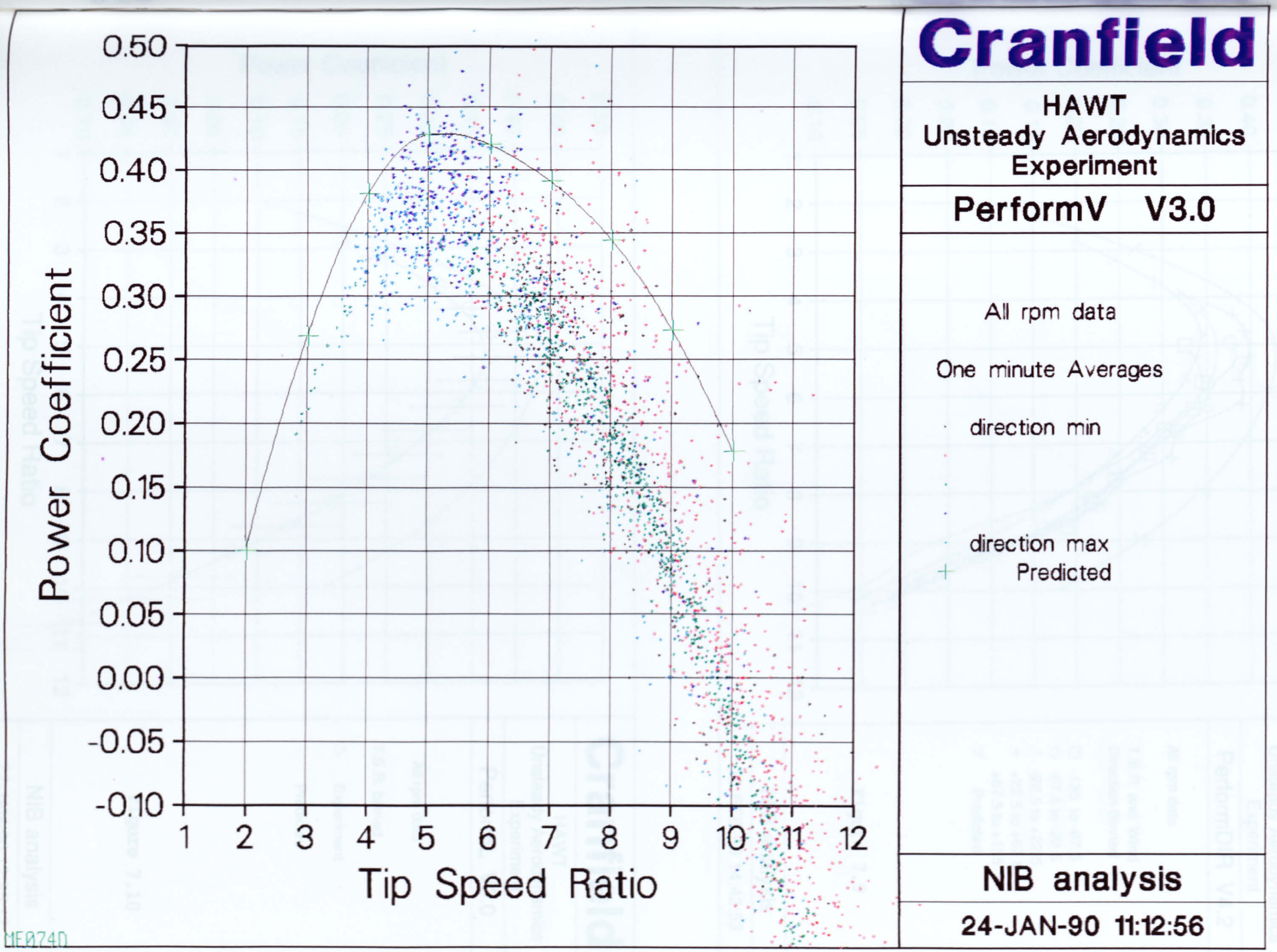

Figure 7.8 Scatter plot using wind direction criterion

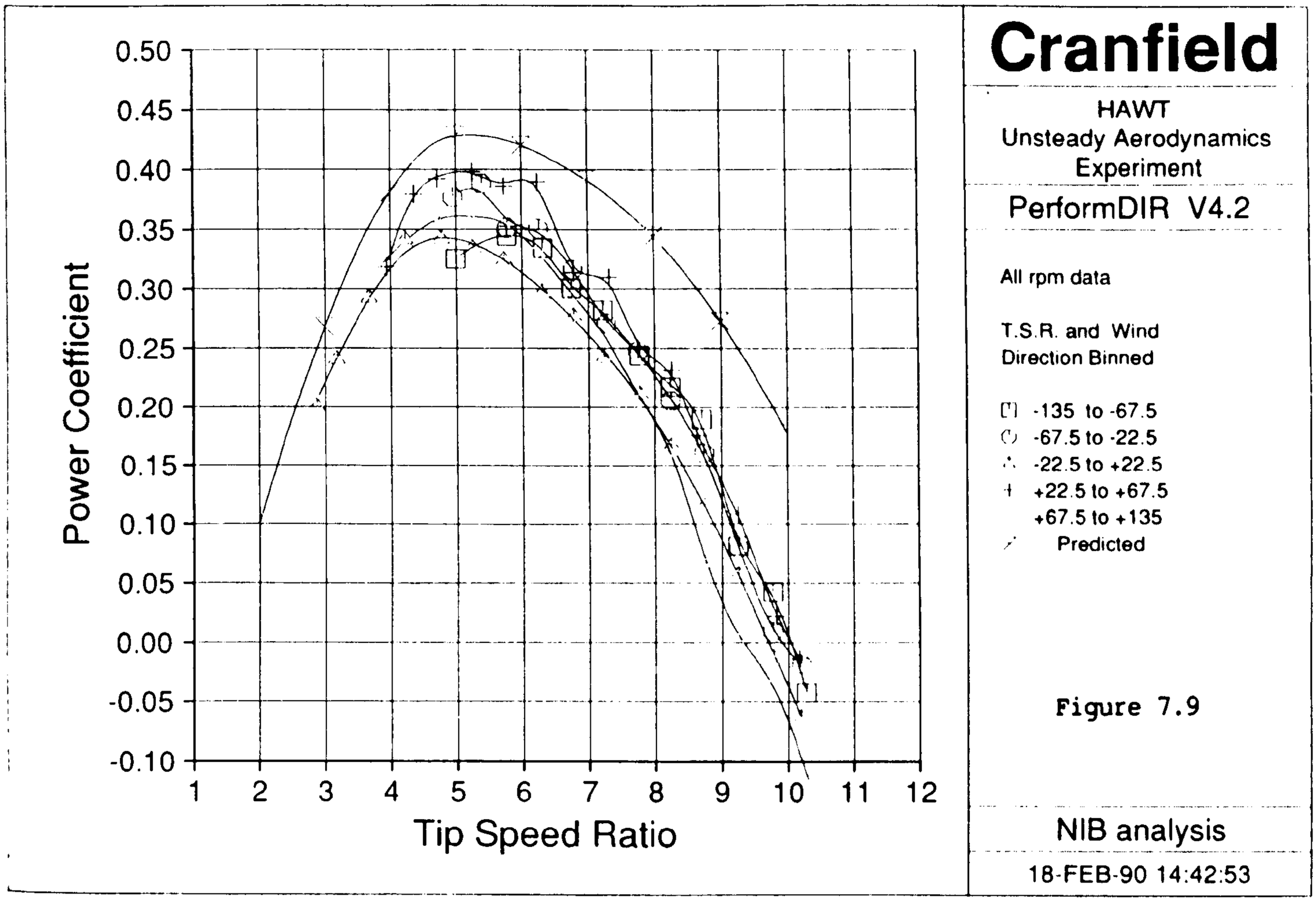
Power Coefficient
0.50
0.45
0.40
0.35
0.30
0.25
0.20
0.15
0.10
0.05
0.00
-0.05
-0.10
1
2
3
4
5
6
7
8
9
10
11
12
Tip Speed Ratio
Cranfield
HAWT
Unsteady Aerodynamics
Experiment
PerformDIR V4.2
All rpm data
T.S.R. and Wind
Direction Binned
-135 to -67.5
-67.5 to -22.5
-22.5 to +22.5
+22.5 to +67.5
+67.5 to +135
Predicted
Figure 7.9
NIB analysis
18-FEB-90 14:42:53

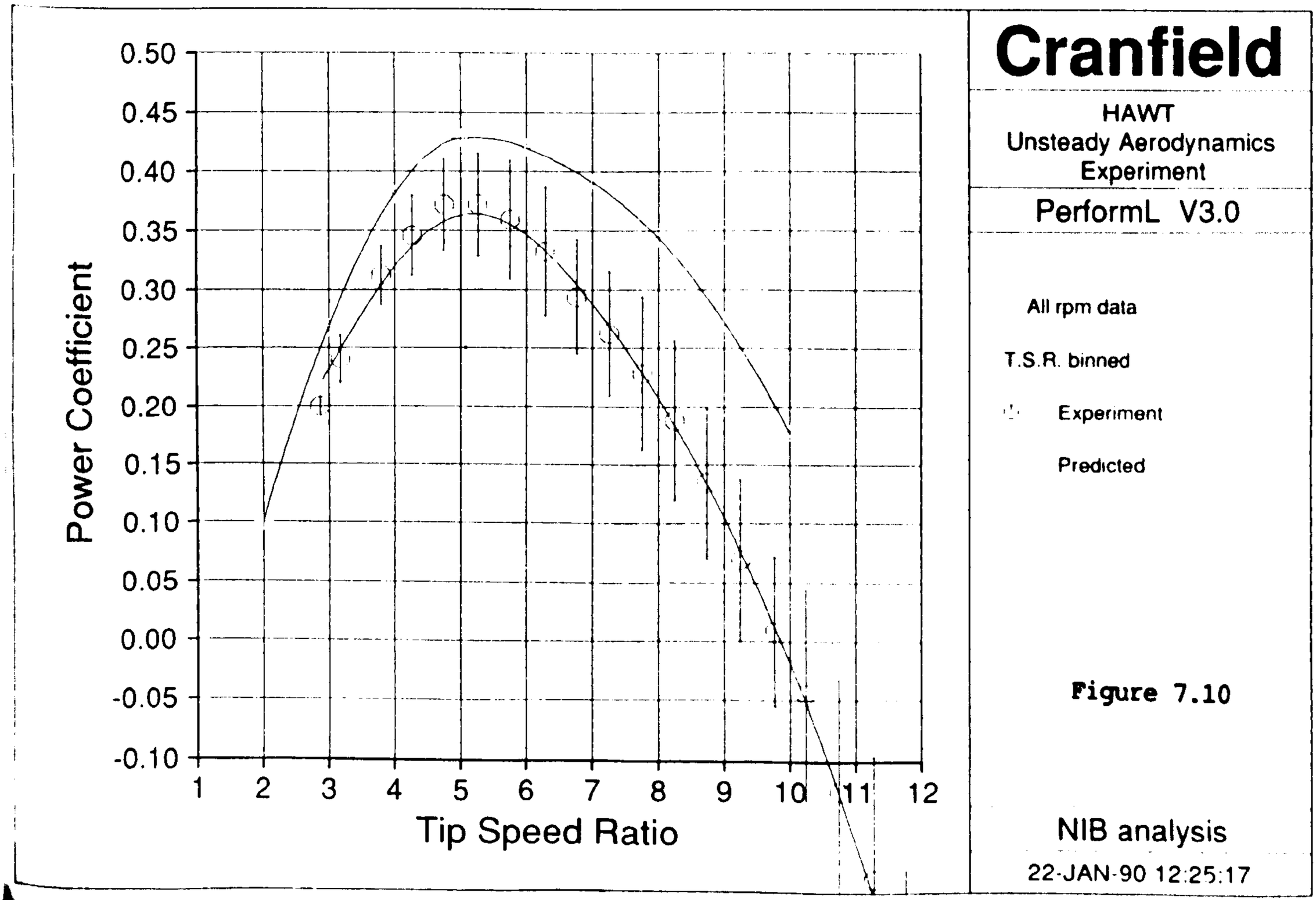
Power Coefficient
0.50
0.45
0.40
0.35
0.30
0.25
0.20
0.15
0.10
0.05
0.00
-0.05
-0.10
1
2
3
4
5
6
7
8
9
10
11
12
Tip Speed Ratio
Cranfield
HAWT
Unsteady Aerodynamics
Experiment
PerformL V3.0
All rpm data
T.S.R. binned
Experiment
Predicted
Figure 7.10
NIB analysis
22-JAN-90 12:25:17

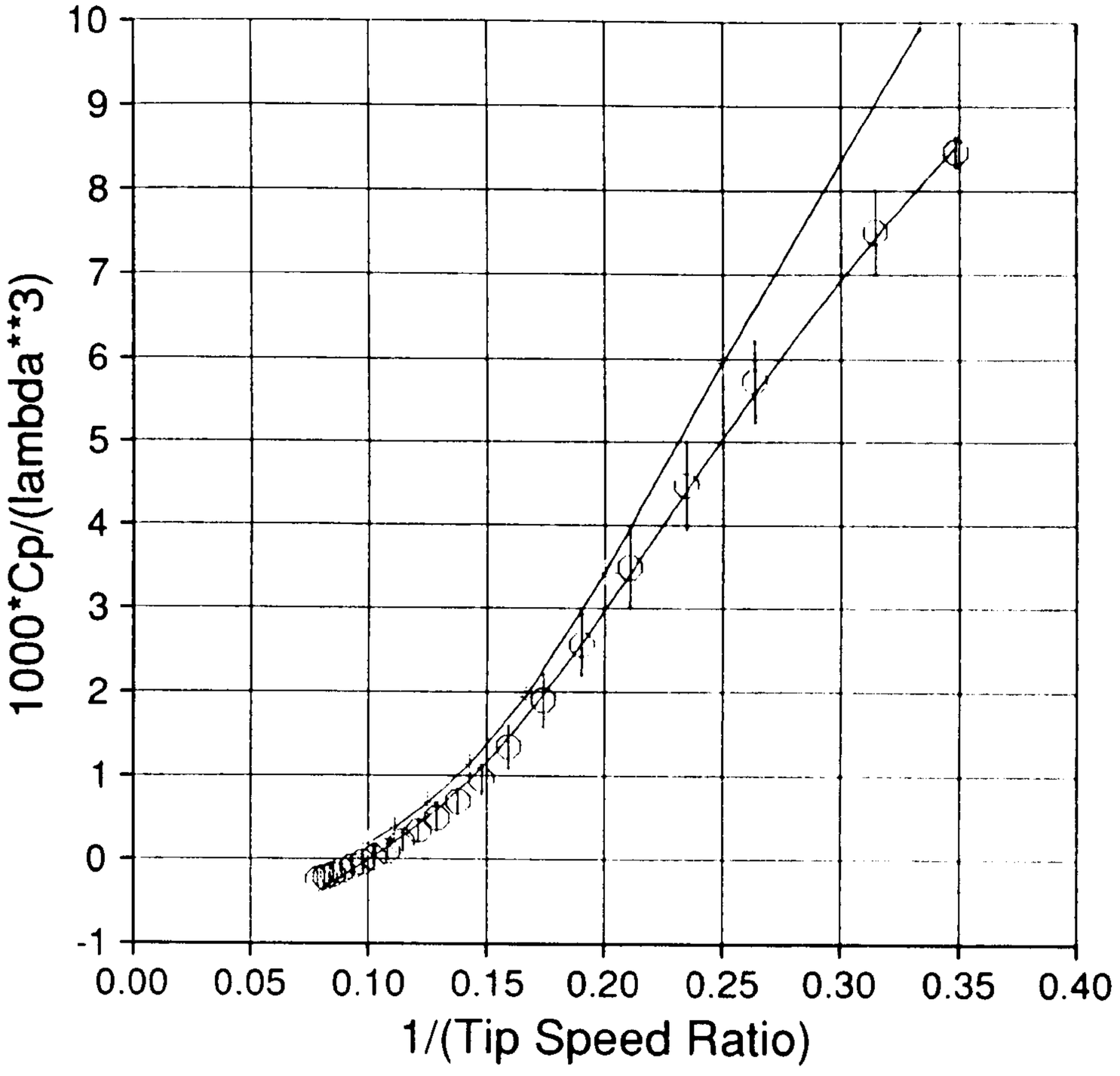

Cranfield

HAWT
Unsteady Aerodynamics
Experiment

PerformL V3.0

All rpm data

T.S.R. binned

Experiment

Predicted

Figure 7.11

NIB analysis

29-MAR-90 10:21:52

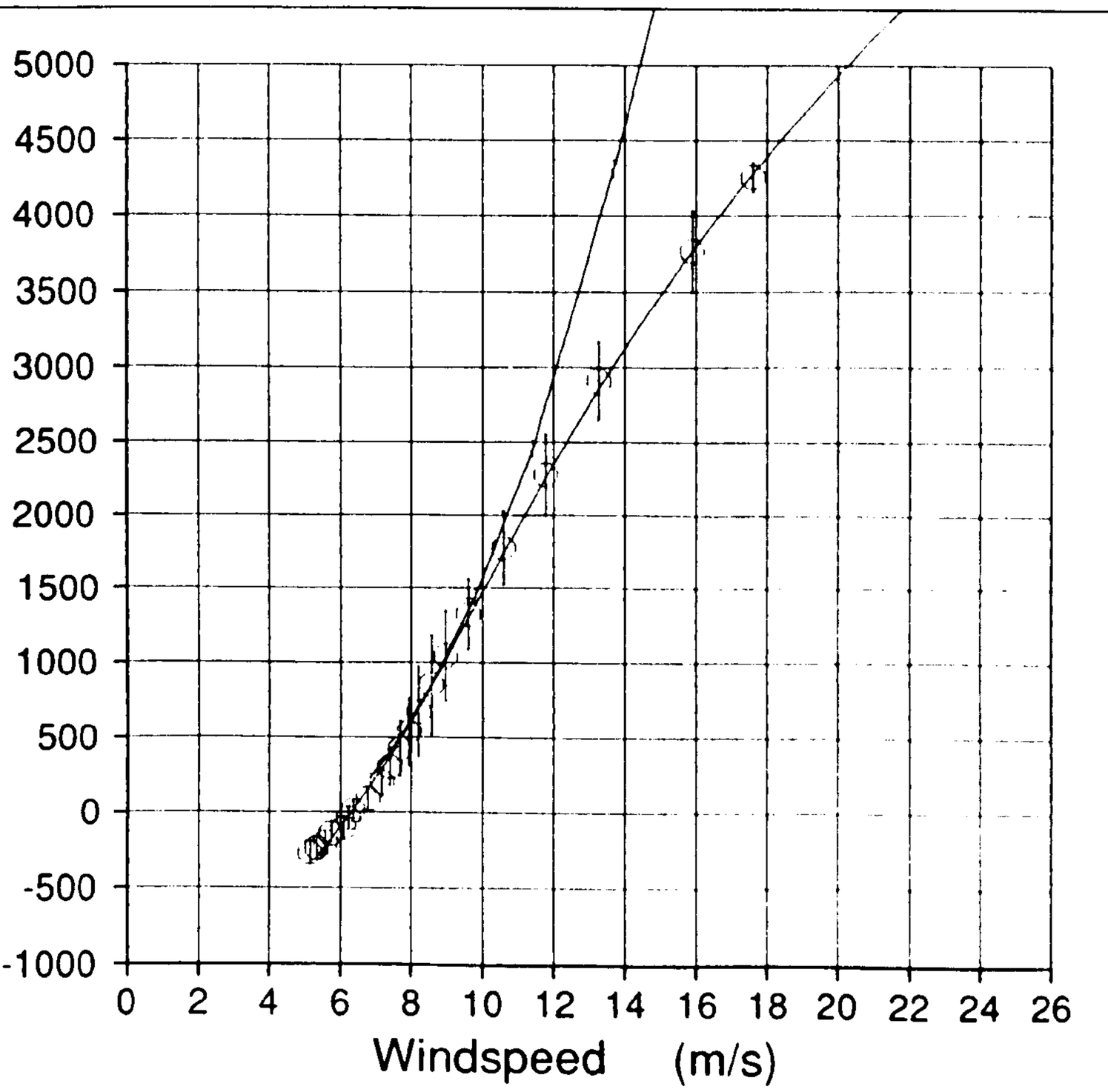

Cranfield

HAWT
Unsteady Aerodynamics
Experiment

PerformL V3.0

All rpm data

T.S.R. binned

Experiment

Predicted

Figure 7.12

NIB analysis

29-MAR-90 10:21:41

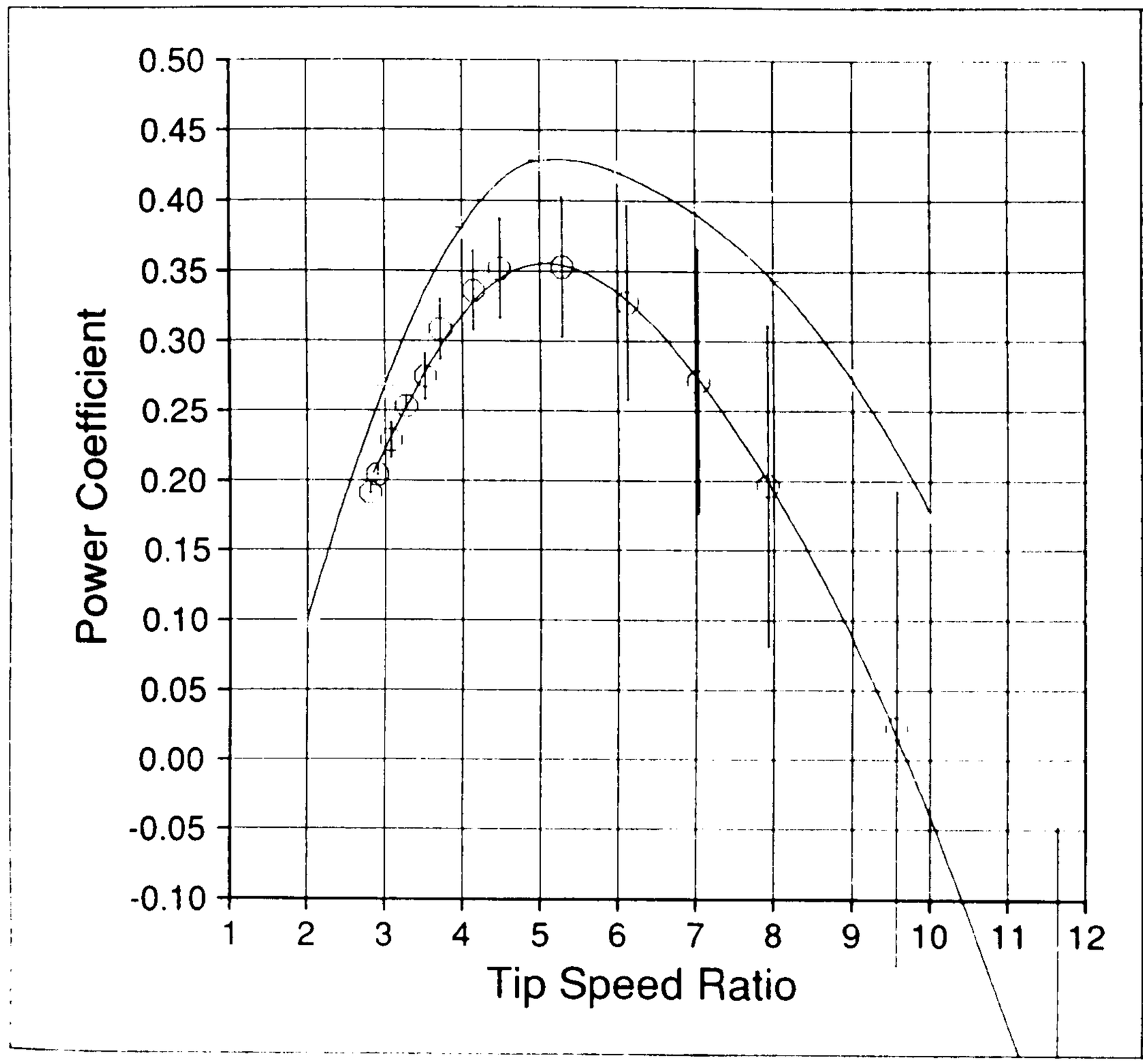

Cranfield

HAWT
Unsteady Aerodynamics
Experiment

PerformV V3.0

All rpm data

Velocity binned

Experiment

Predicted

Figure 7.13

NIB analysis

19-JAN-90 17:56:08

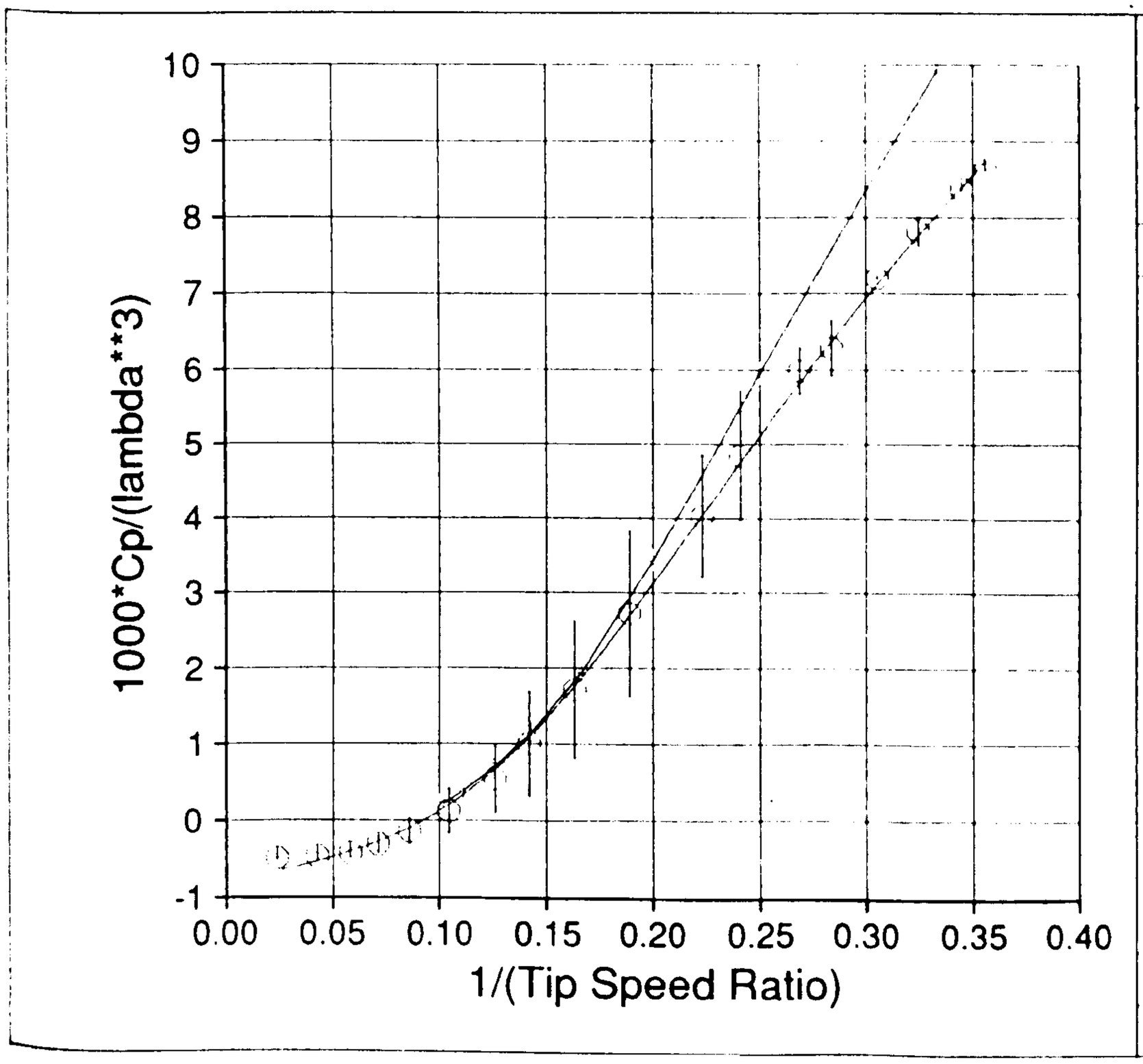

Cranfield

HAWT
Unsteady Aerodynamics
Experiment

PerformV V3.0

All rpm data

Velocity binned

Experiment

Predicted

Figure 7.14

NIB analysis

19-JAN-90 17:56:09

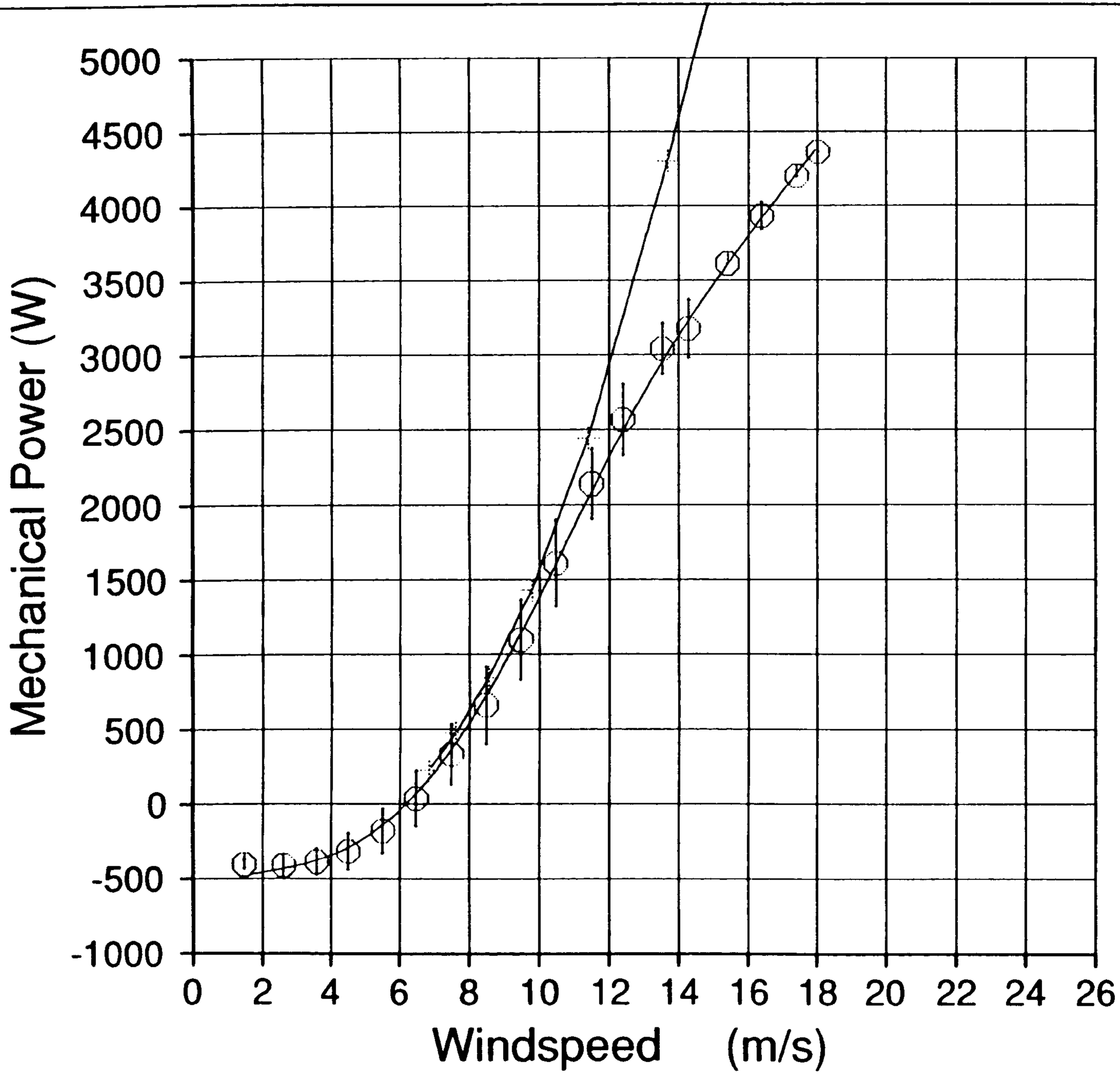

Cranfield

HAWT
Unsteady Aerodynamics
Experiment

PerformV V3.0

All rpm data

Velocity binned

Experiment

Predicted

Figure 7.15

NIB analysis

19-JAN-90 17:56:07

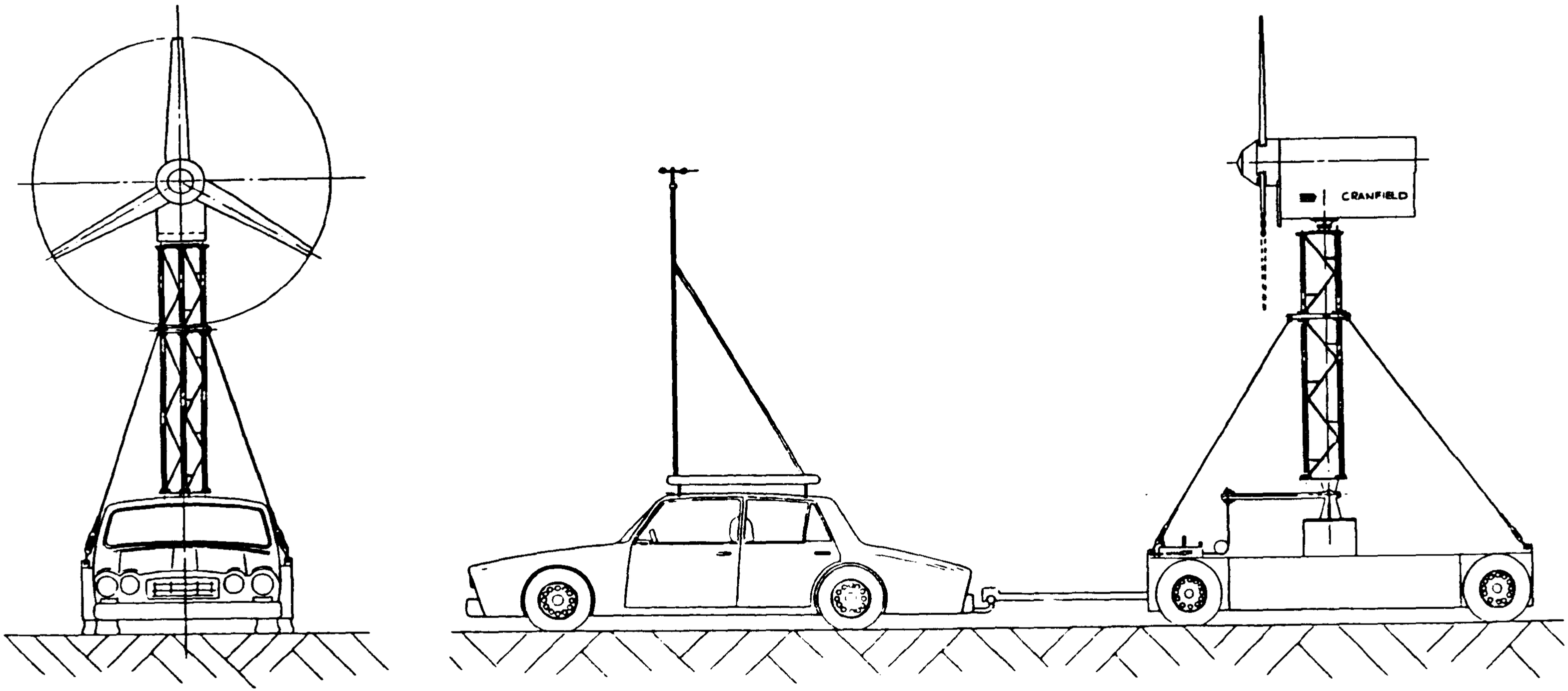

Figure 8.1 The mobile test facility

165.EXP;2 000-159 7-FEB-1990:10:46:41 WINDY 4.00

Anemometer tower direction = 0.00

Text file wind direction = 0.00

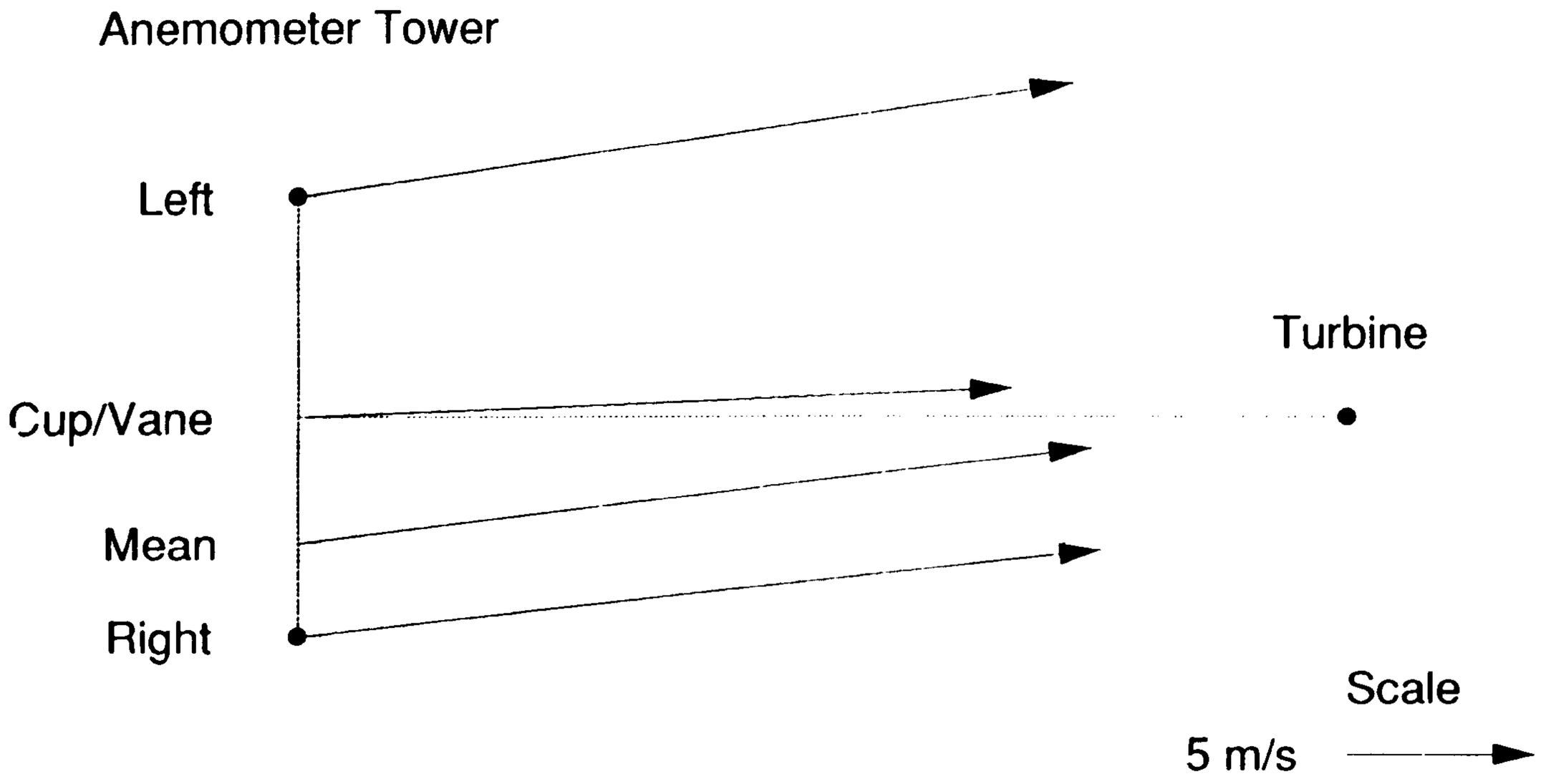

Figure 9.1 Program WINDY: scale plan of anemometer installation and wind vectors.

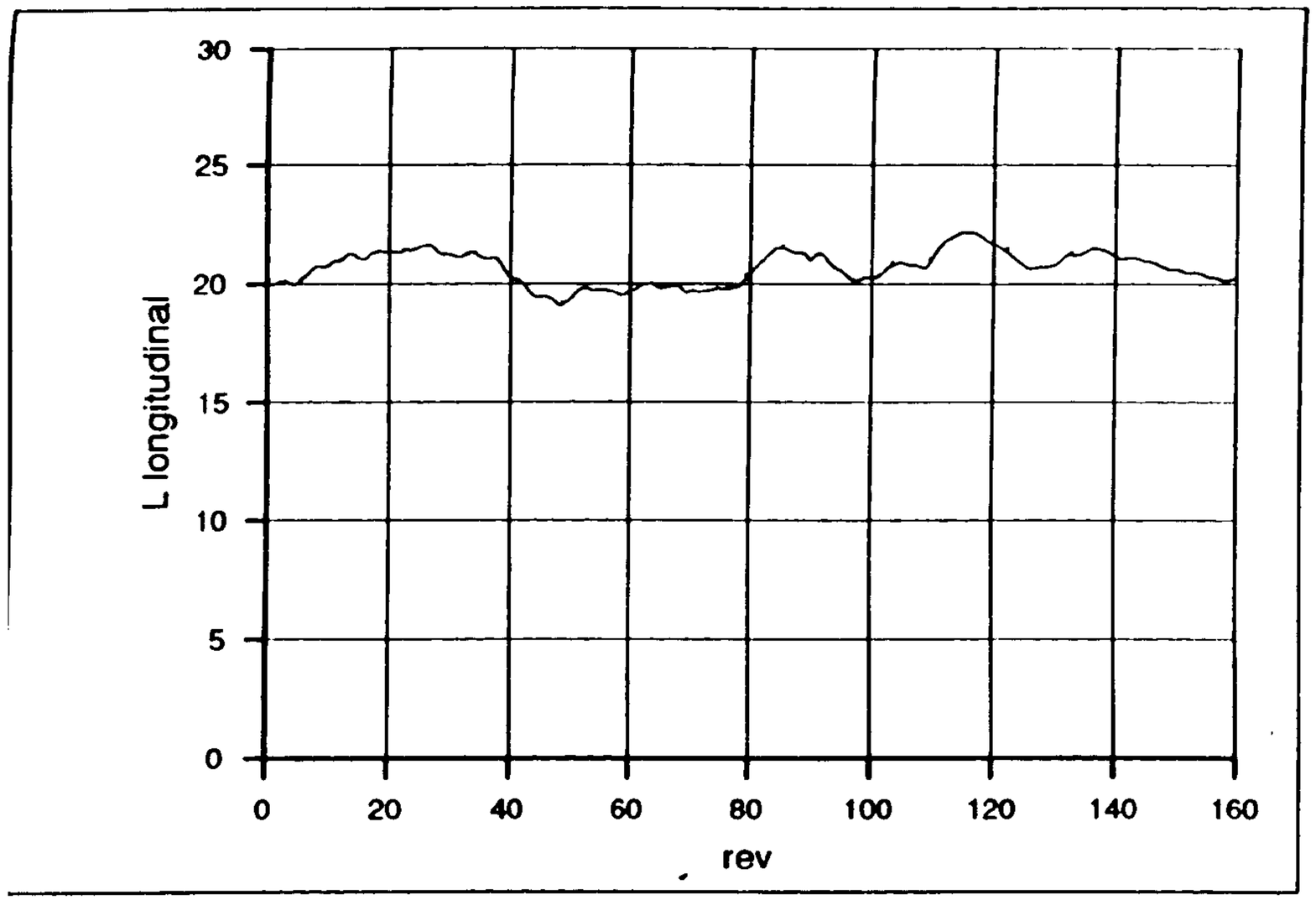

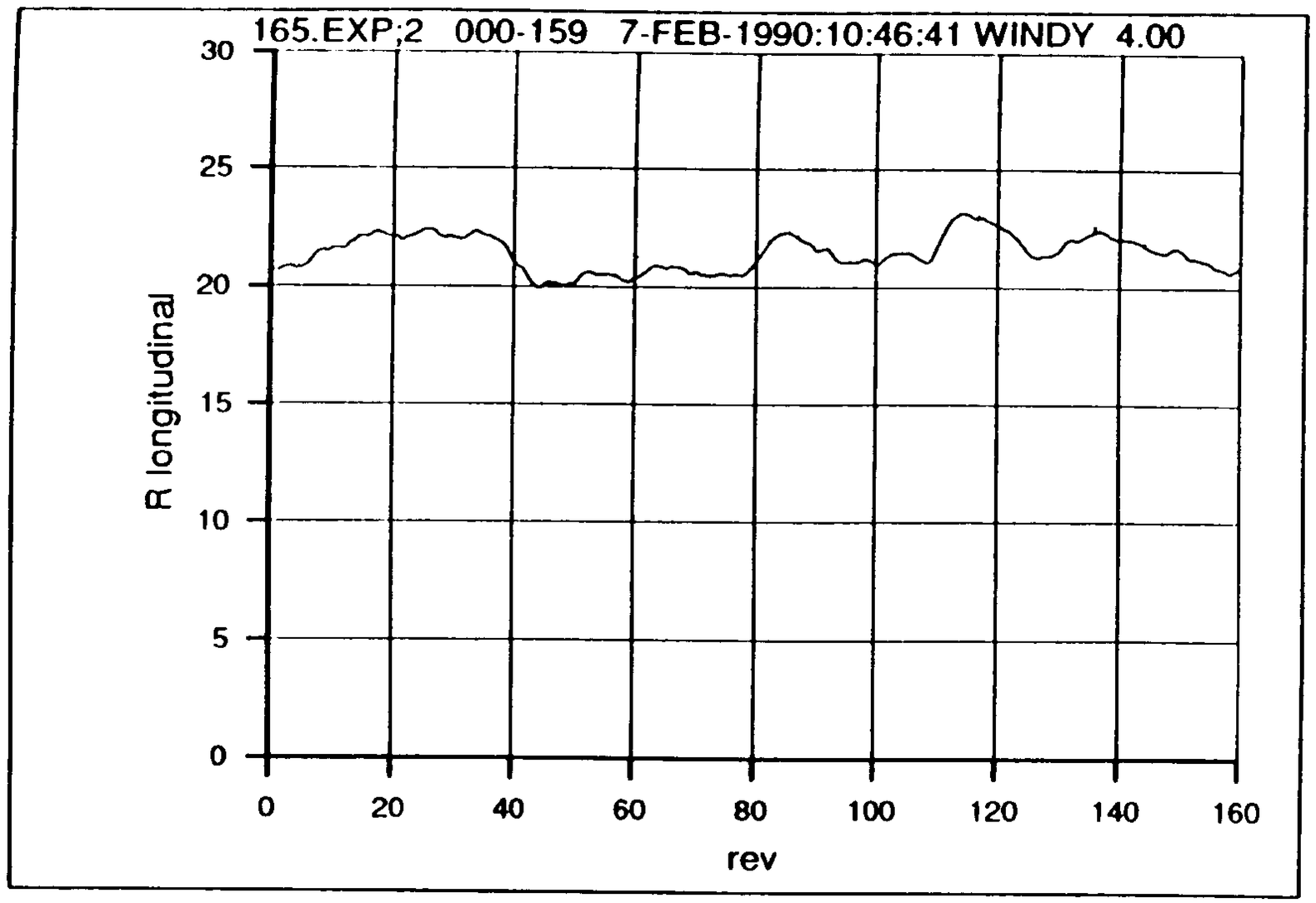

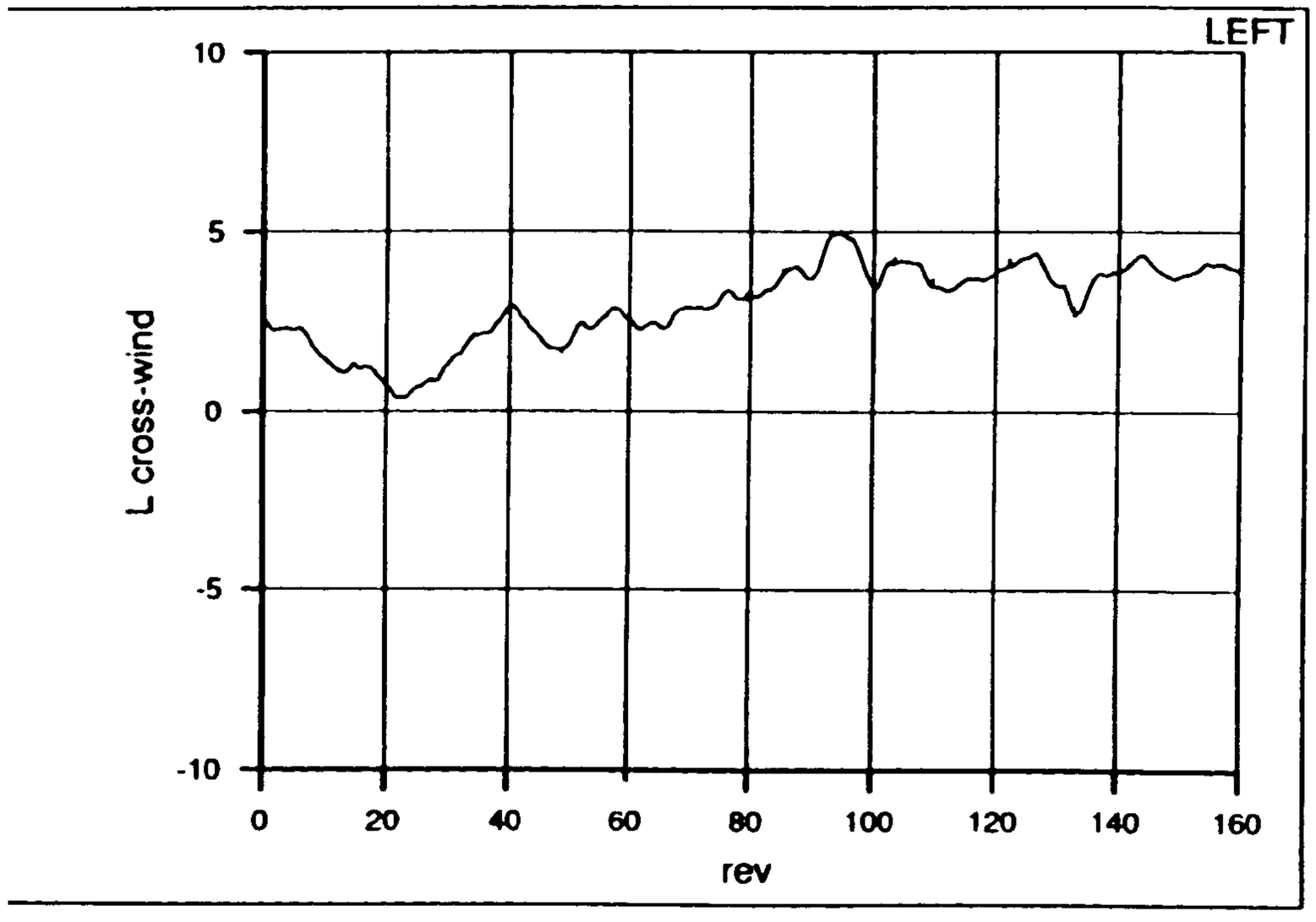

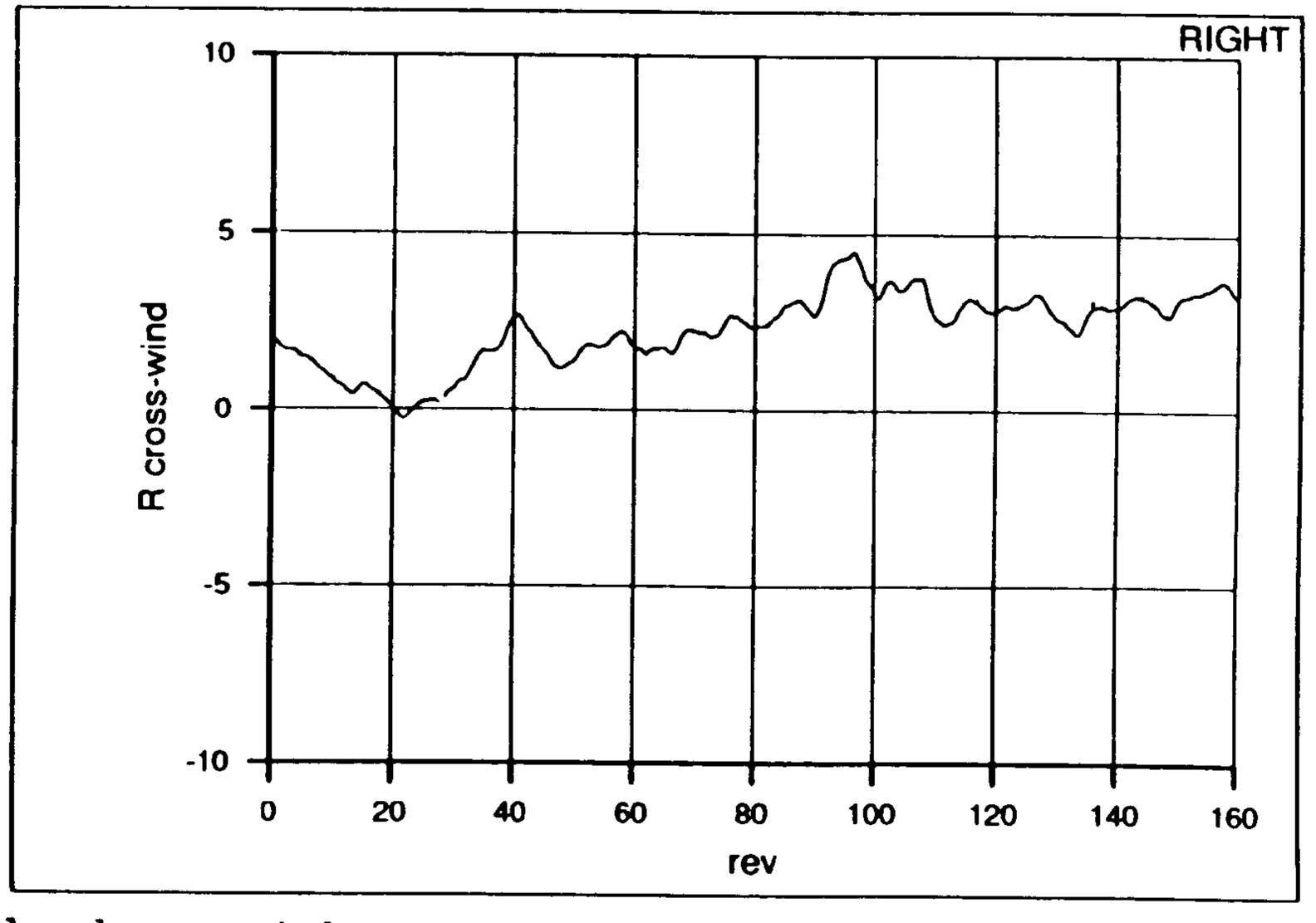

Figure 9.2 Program WINDY: time histories of longitudinal and cross-wind components derived from Lowne anemometers.

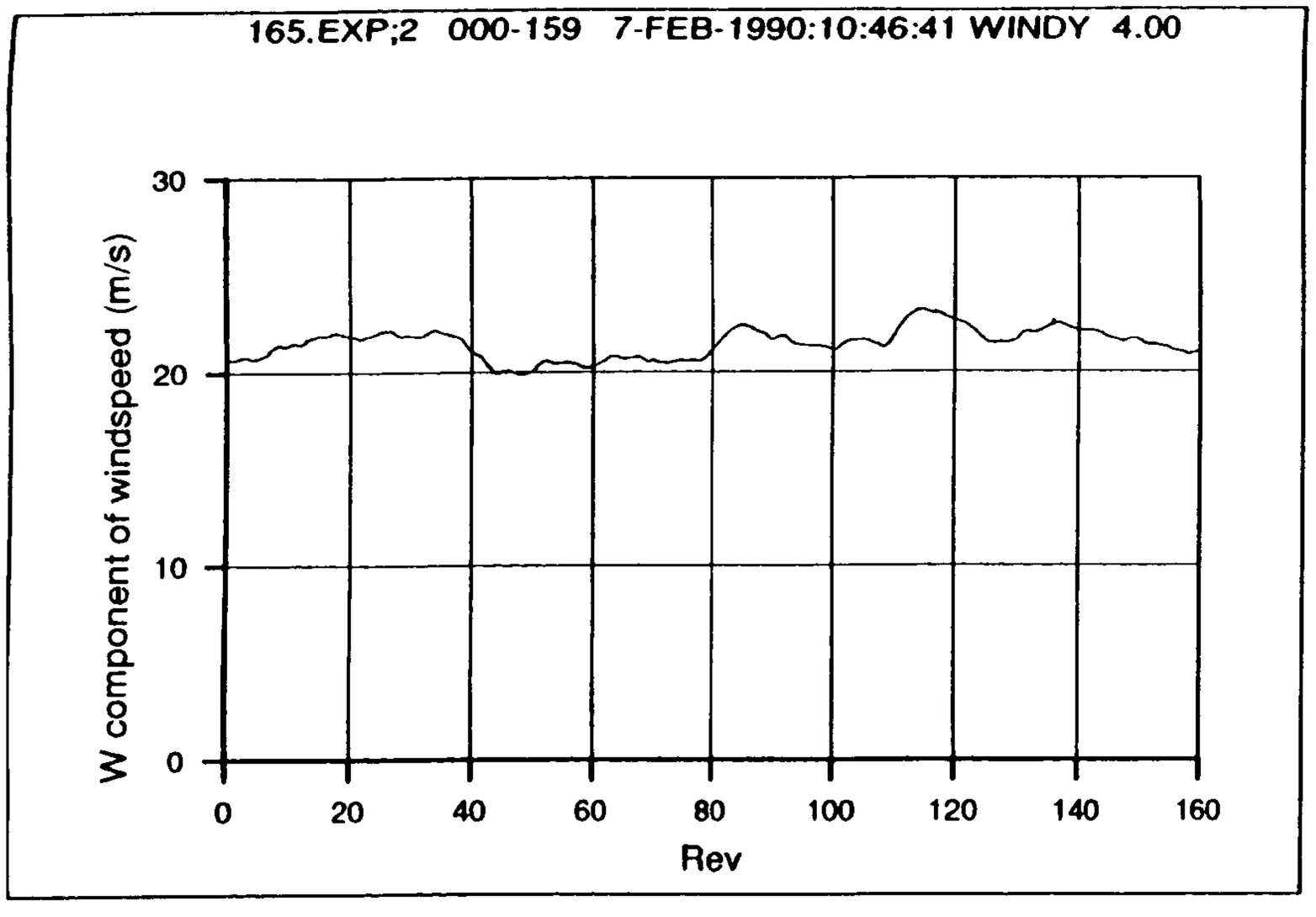

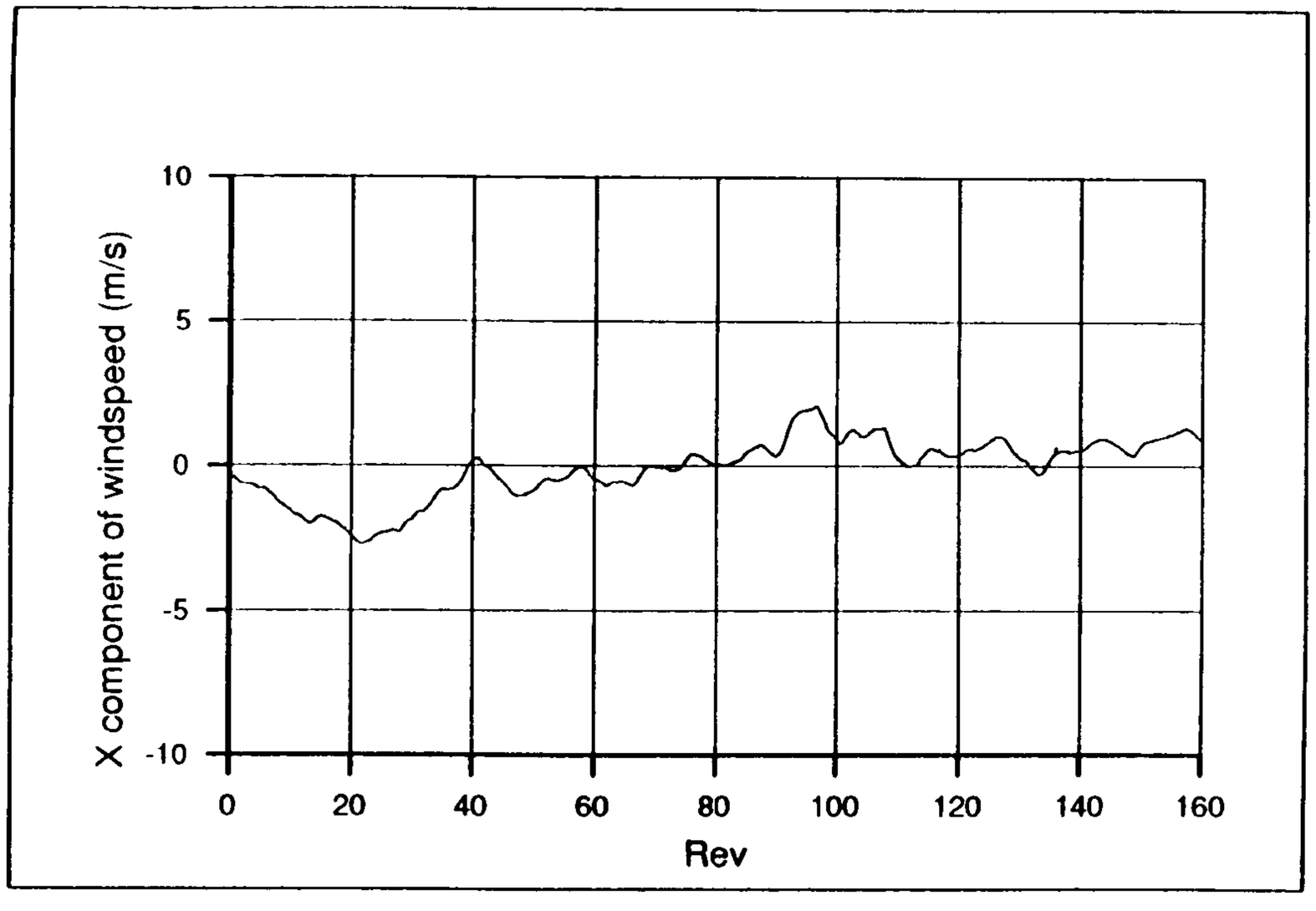

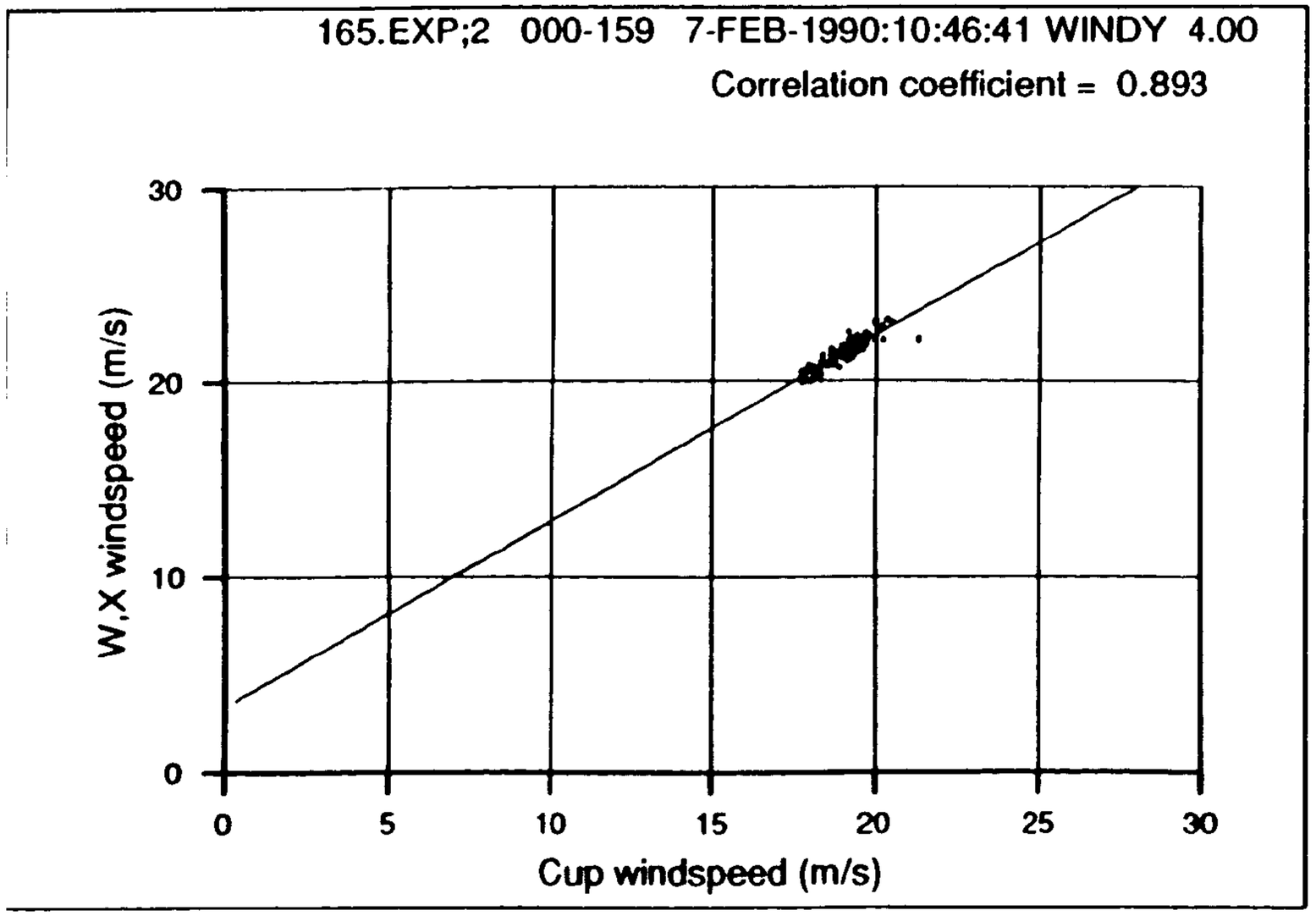

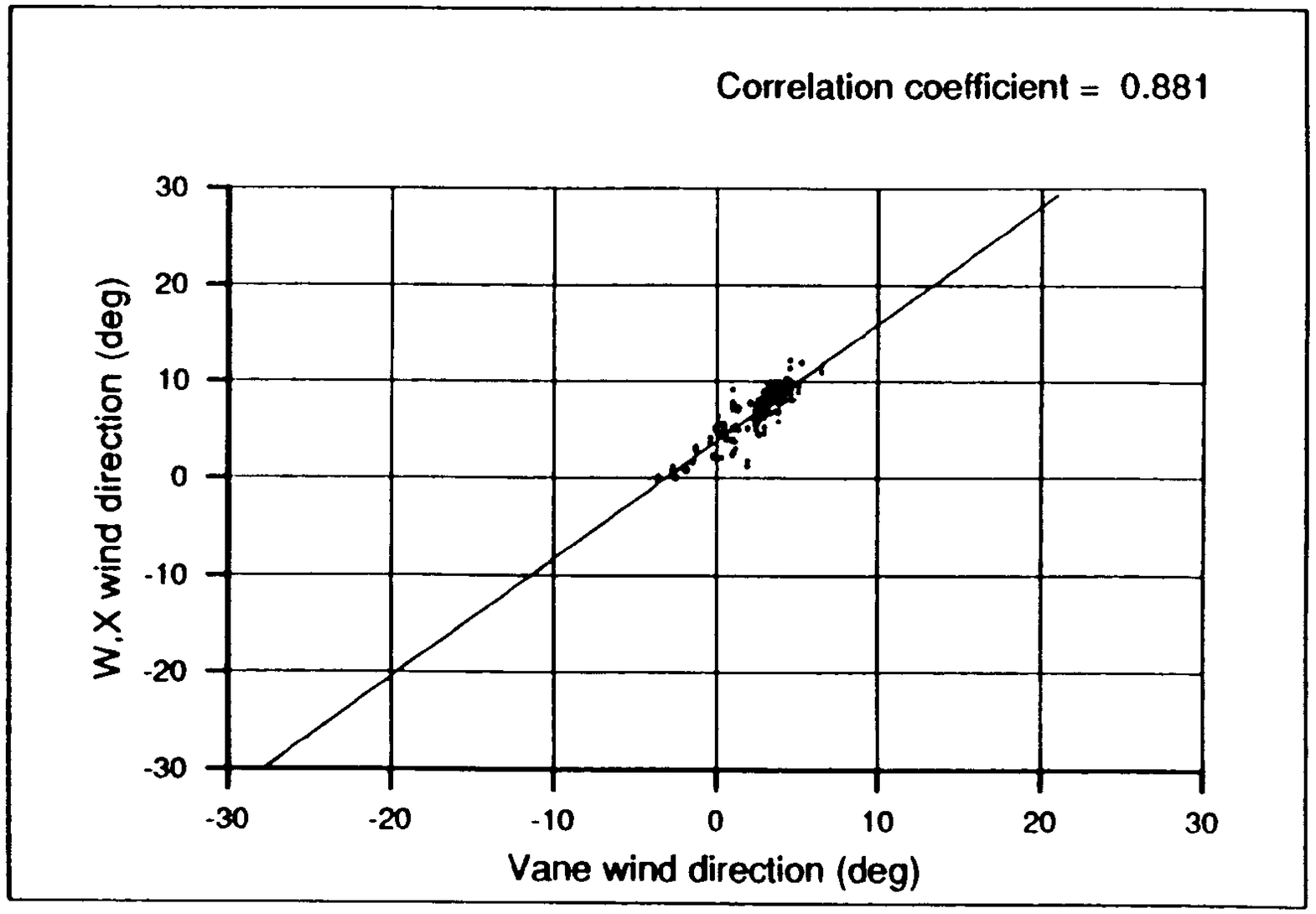

Figure 9.3 Program WINDY: time histories of mean-wind and mean-lateral components derived from Lowne anemometers.

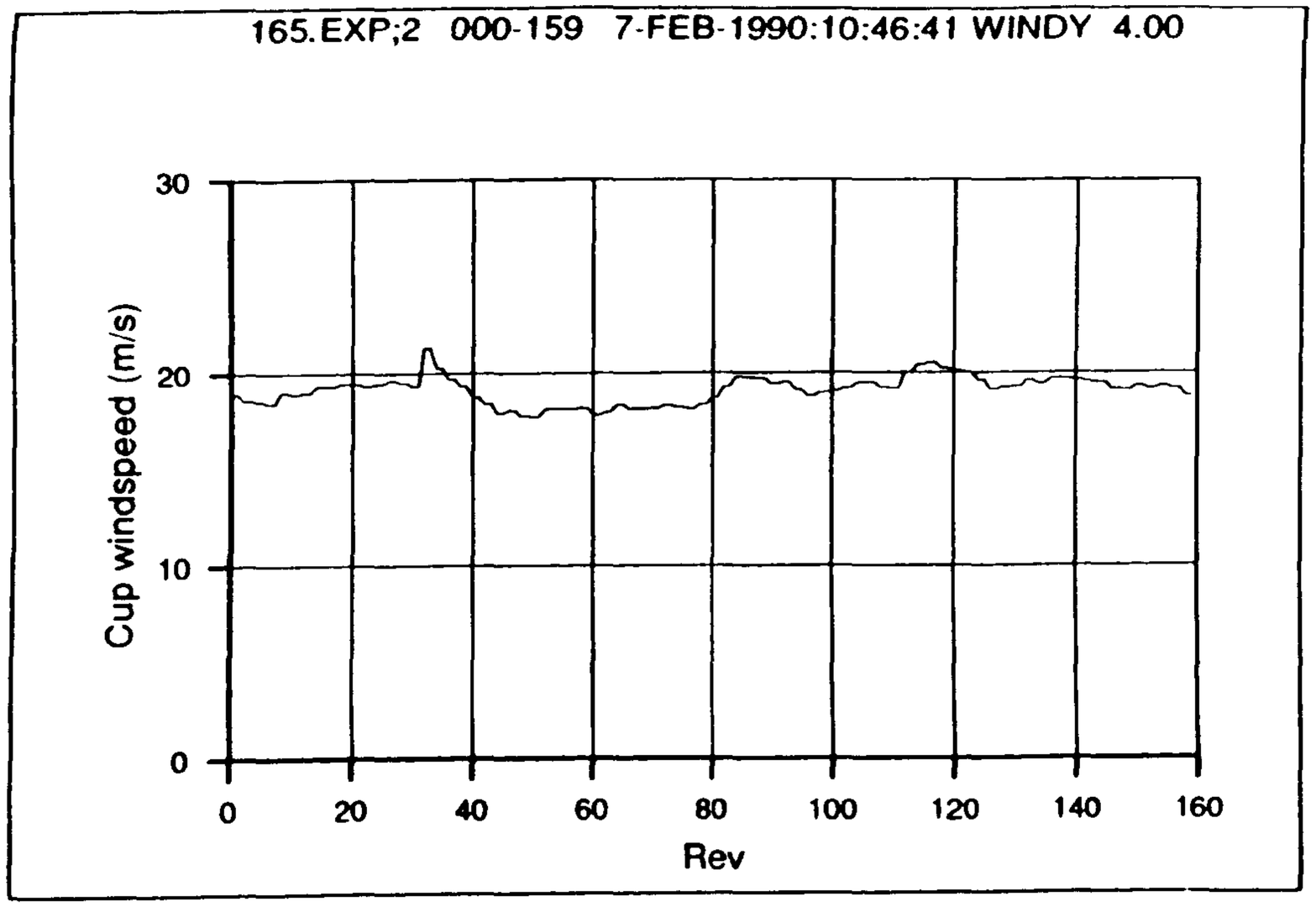

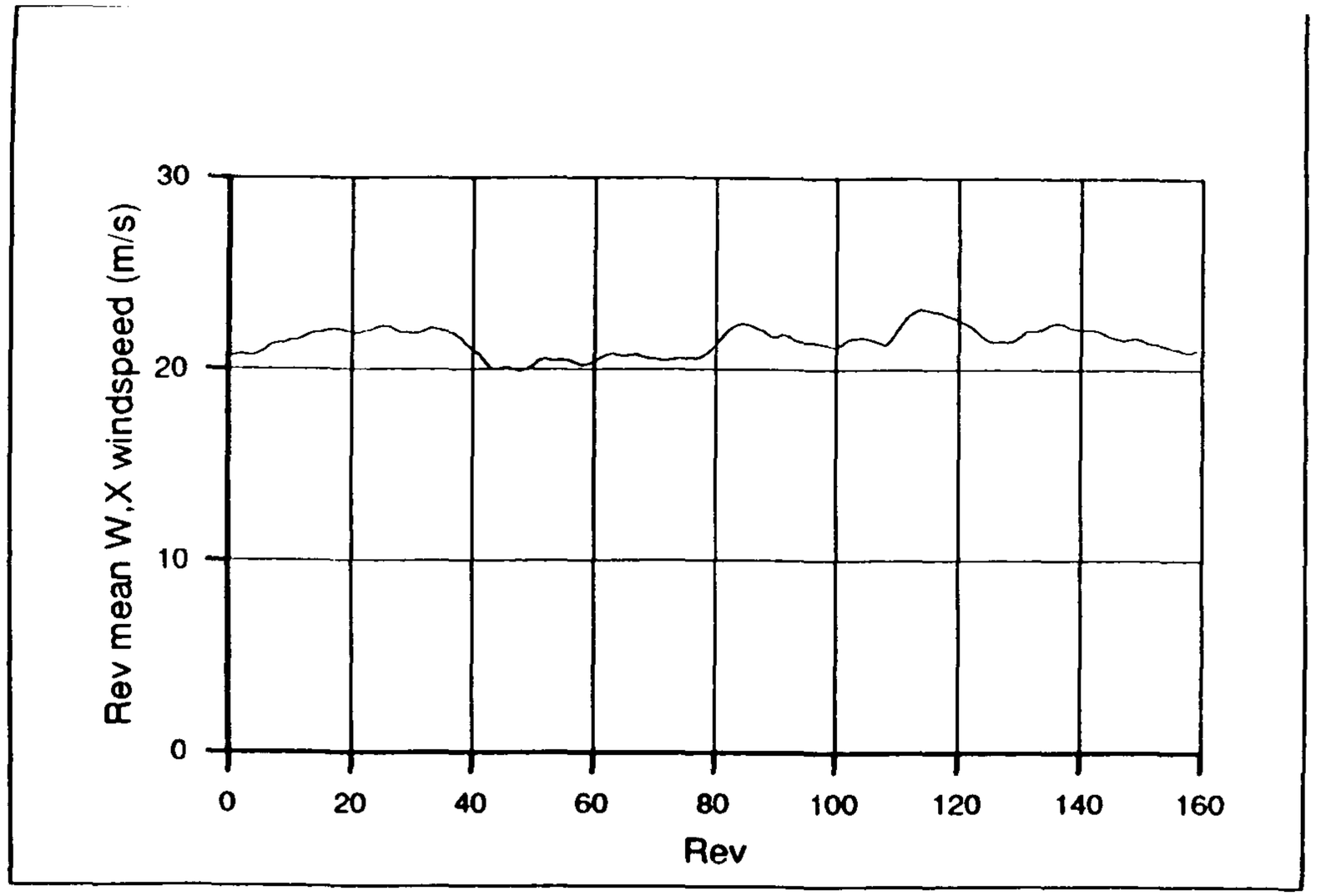

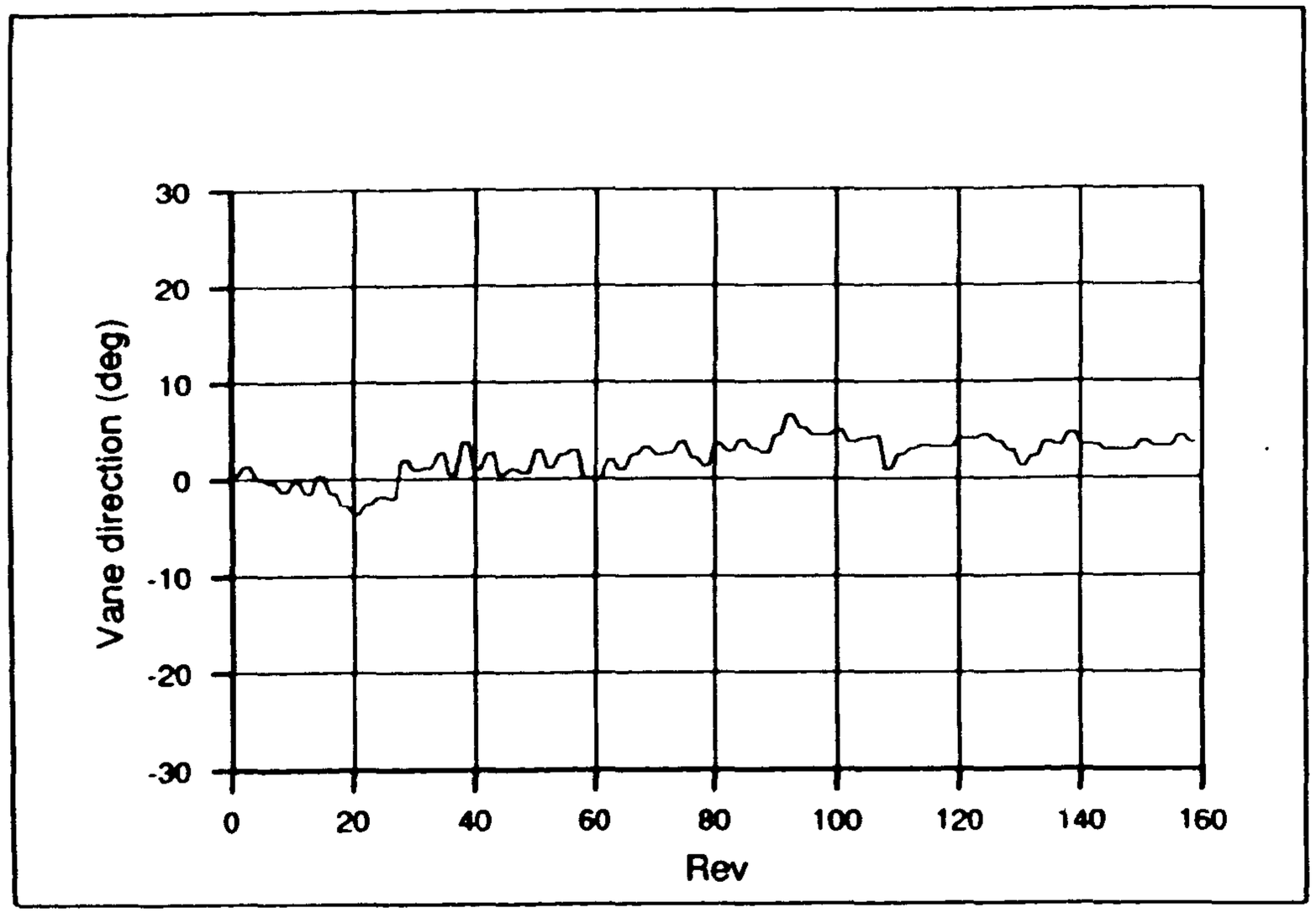

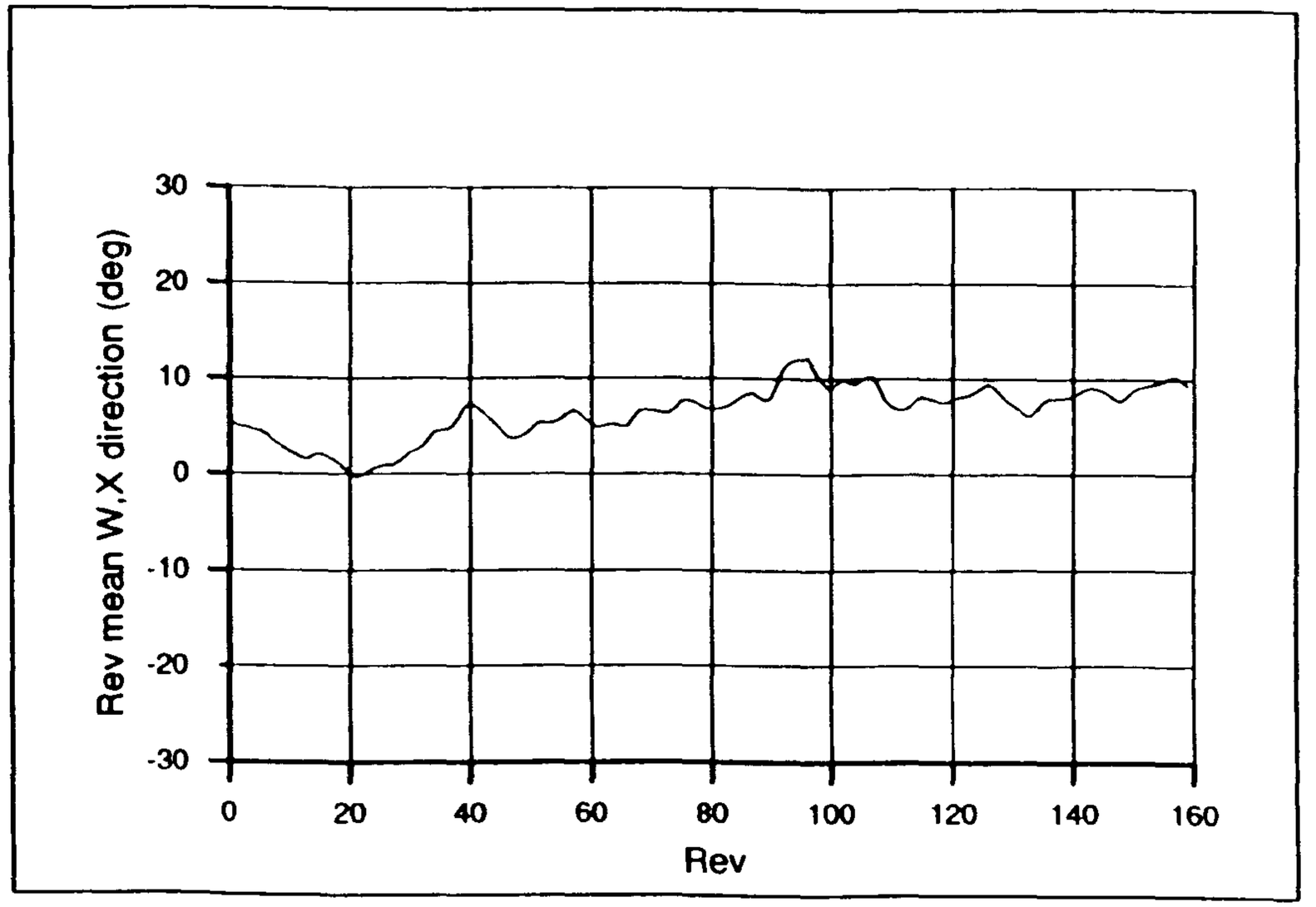

Figure 9.4 Program WINDY: rev-average time histories for wind speed and direction derived from Lownes and cup/vane instruments.

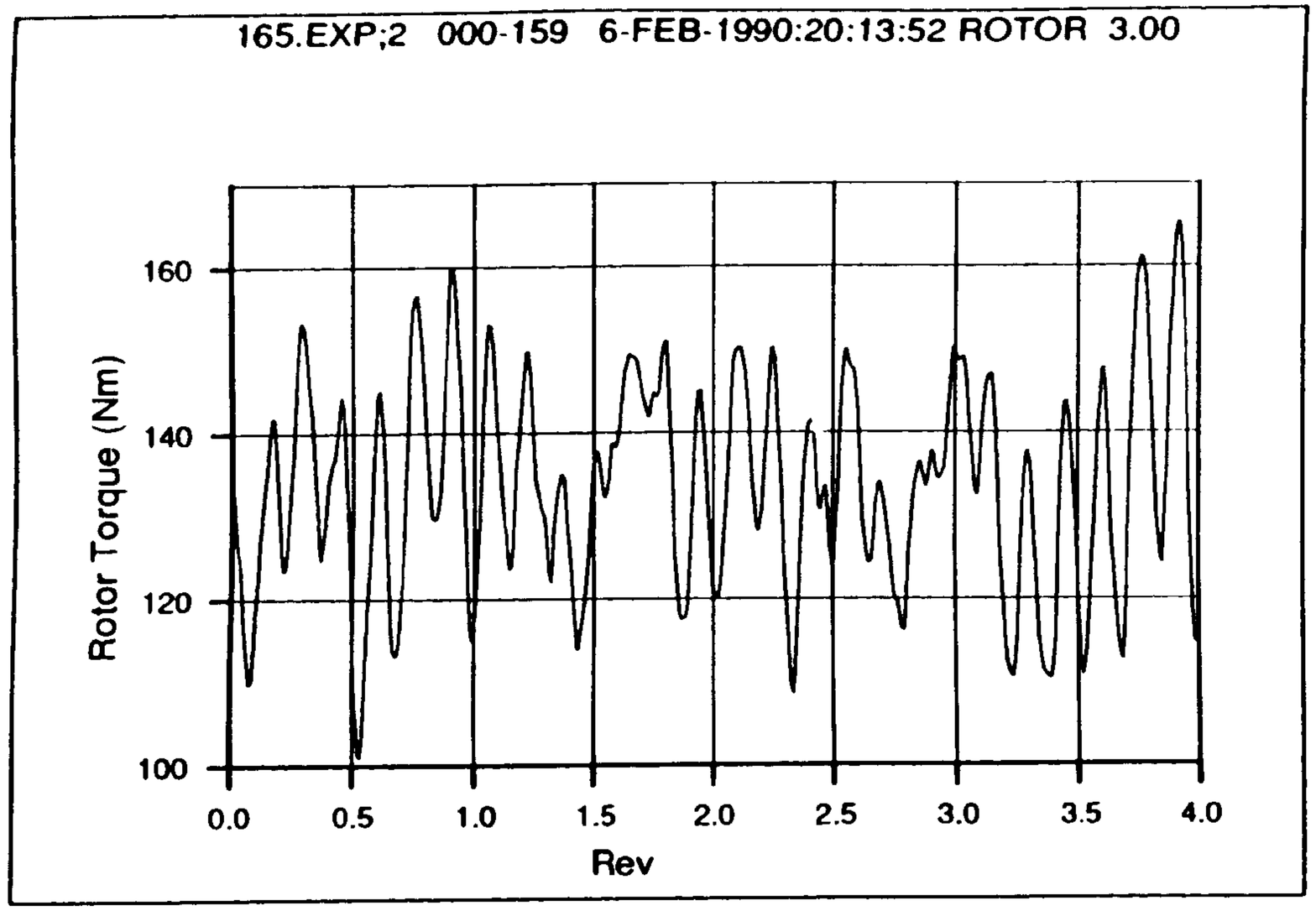

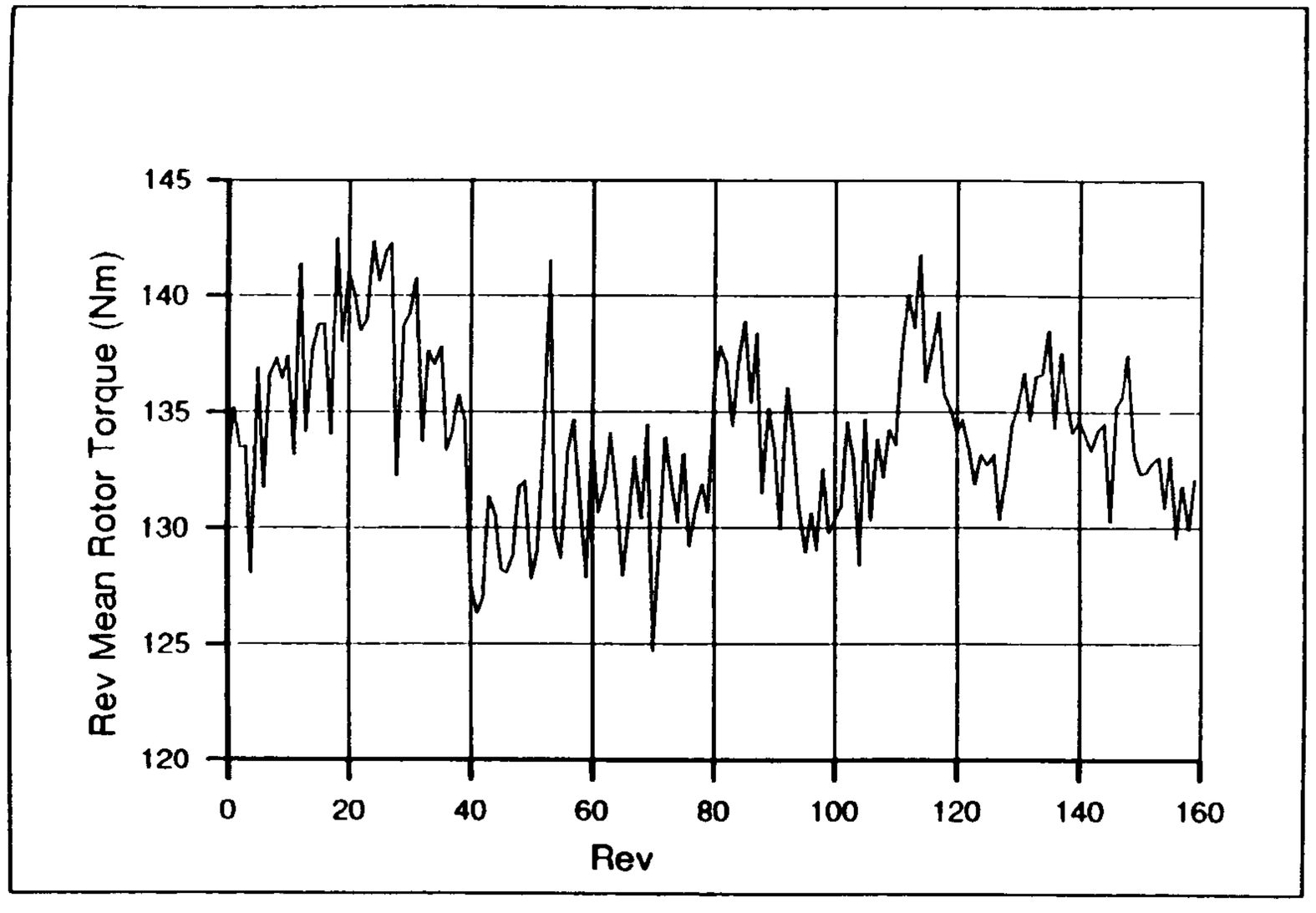

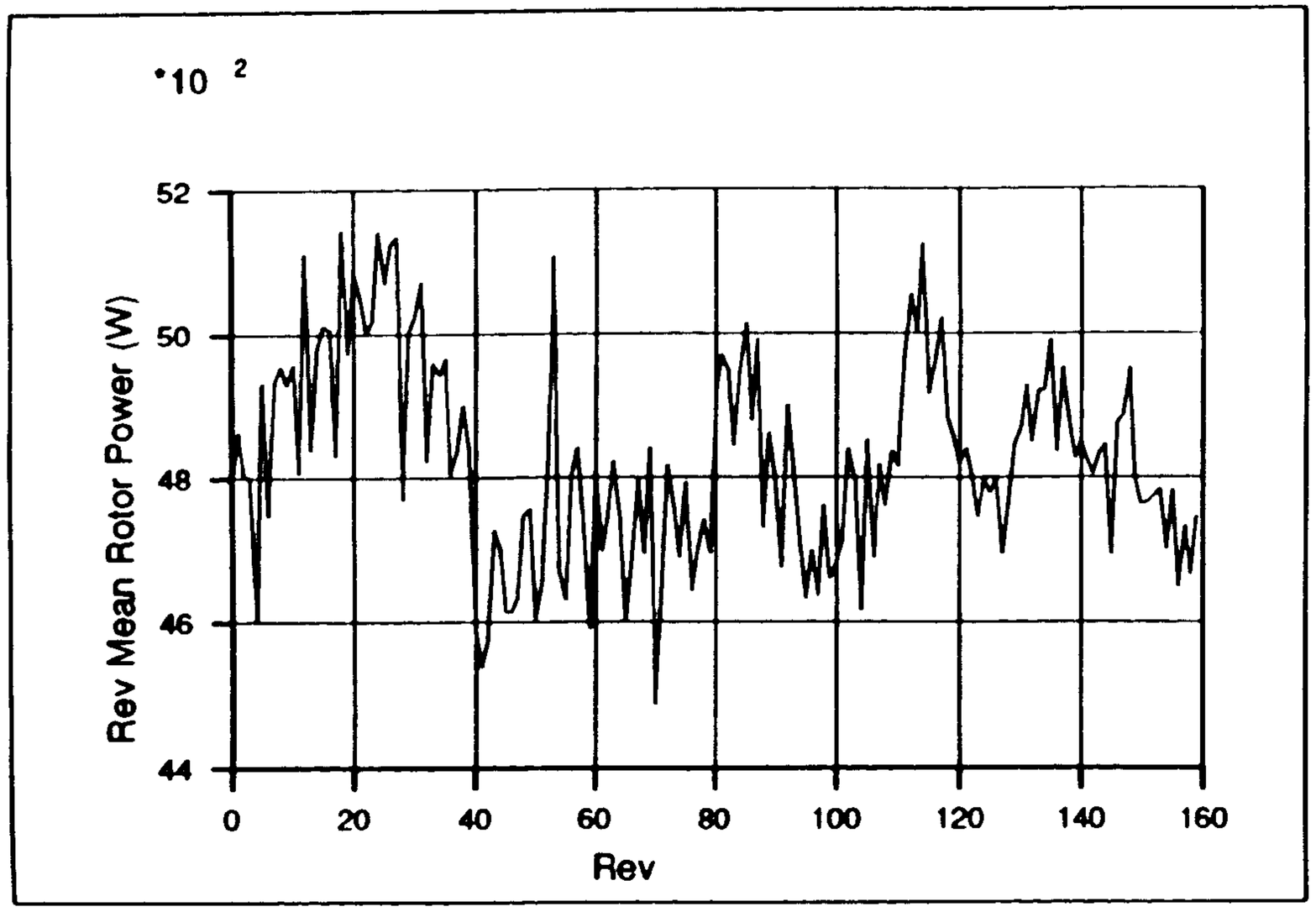

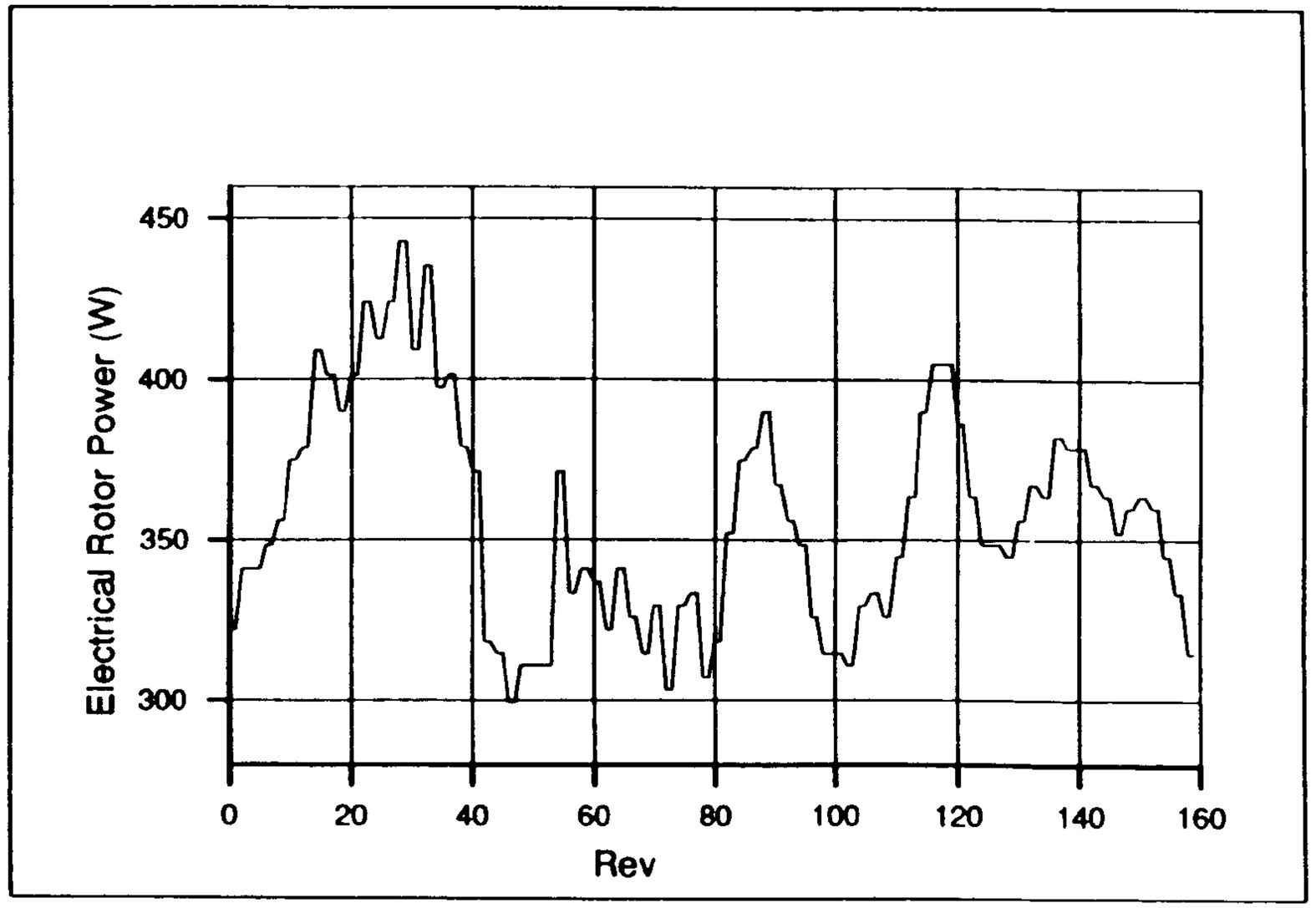

Figure 9.5 Program ROTOR: rev-average time histories of rotor torque, mechanical power and electrical power.

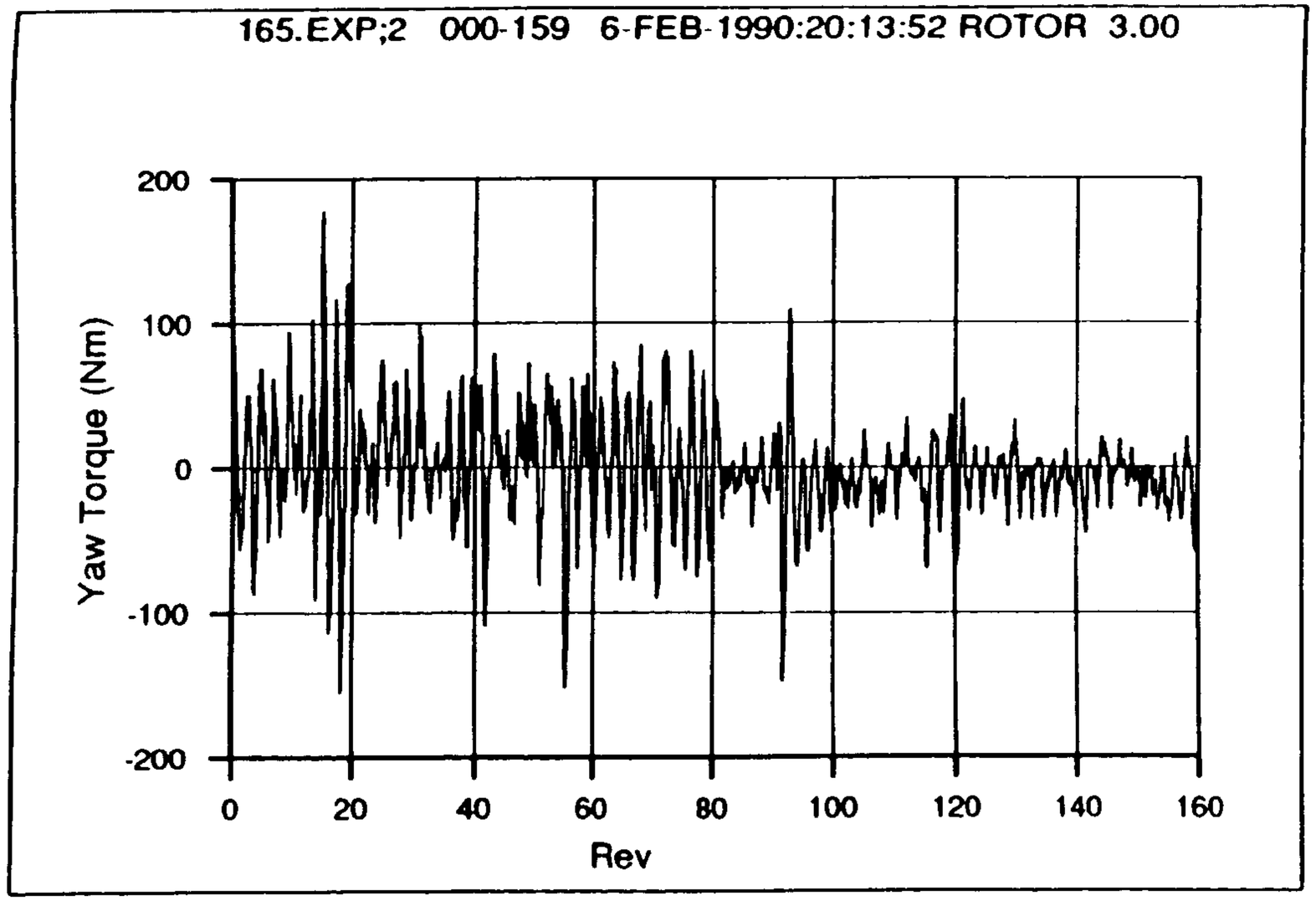

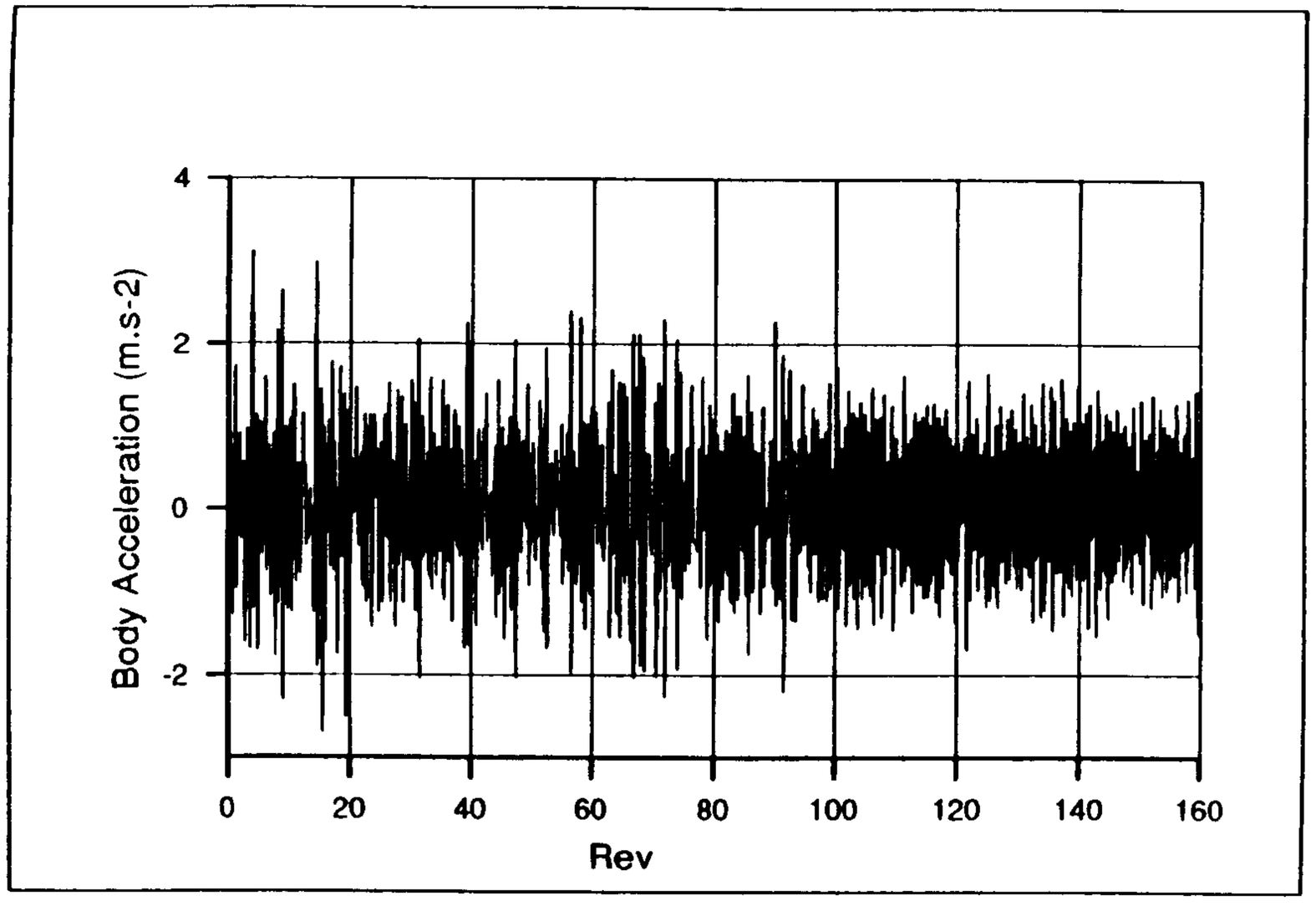

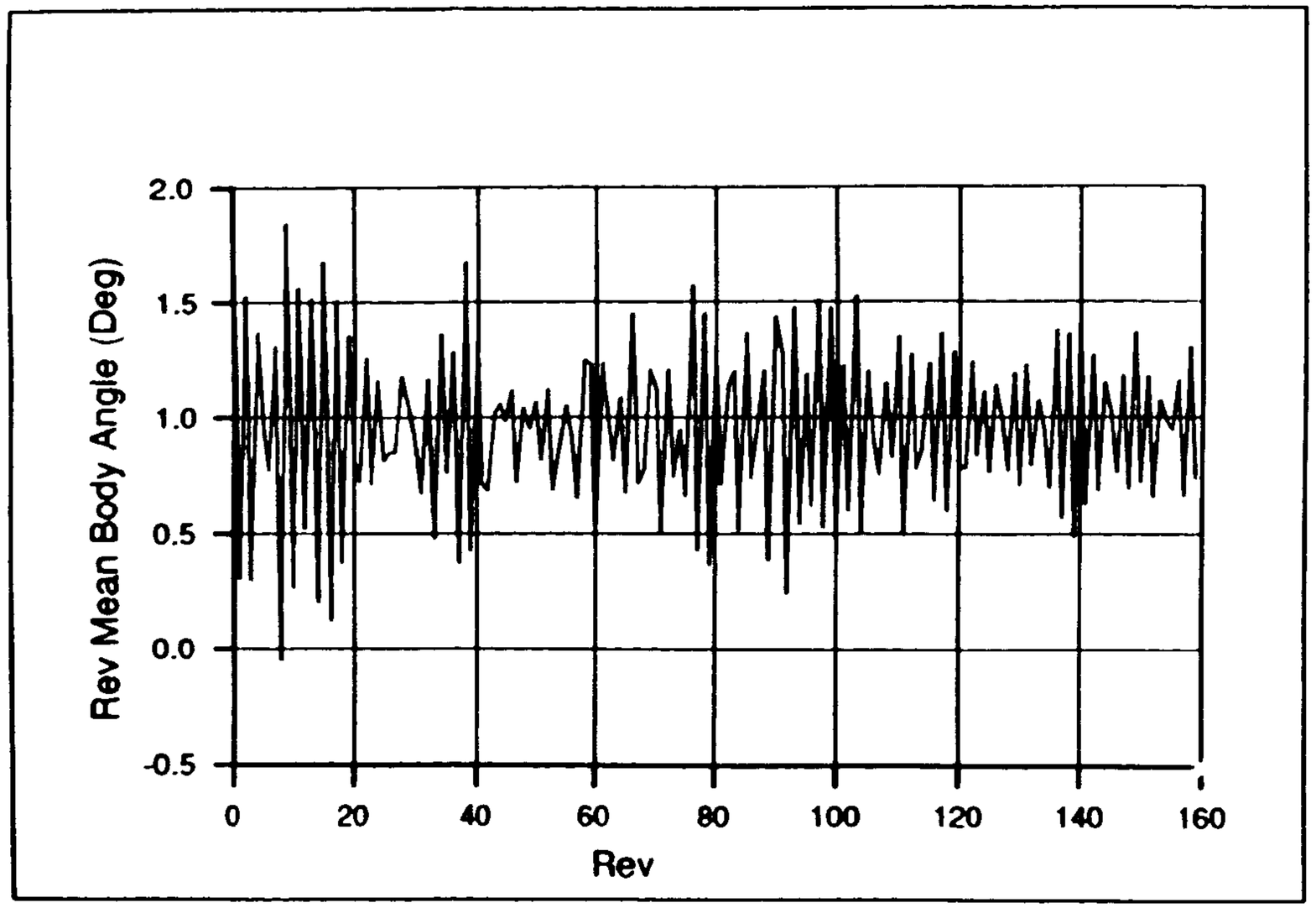

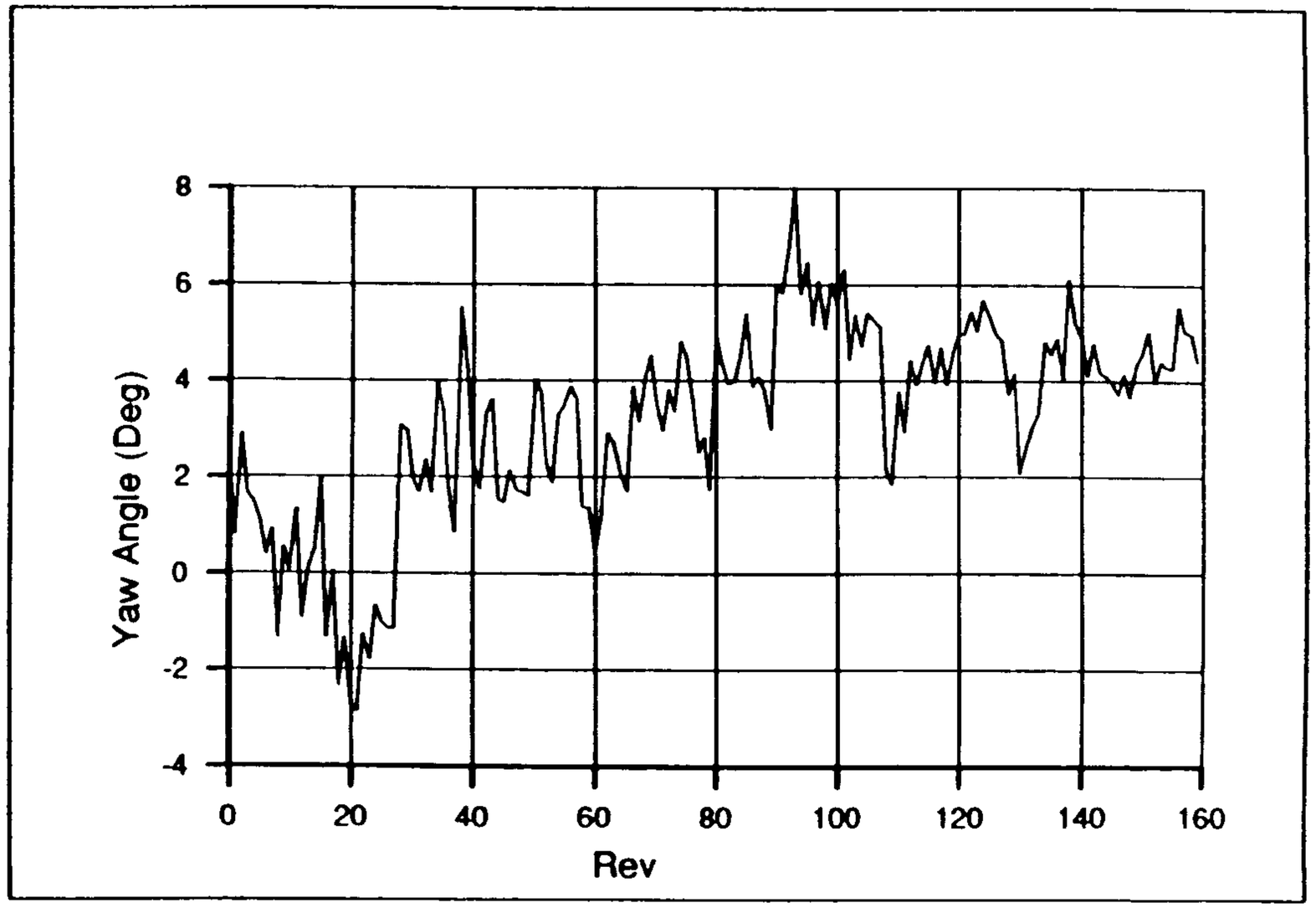

Figure 9.6 Program ROTOR: rev-average time histories of yaw torque, body acceleration, body angle, and derived yaw angle.

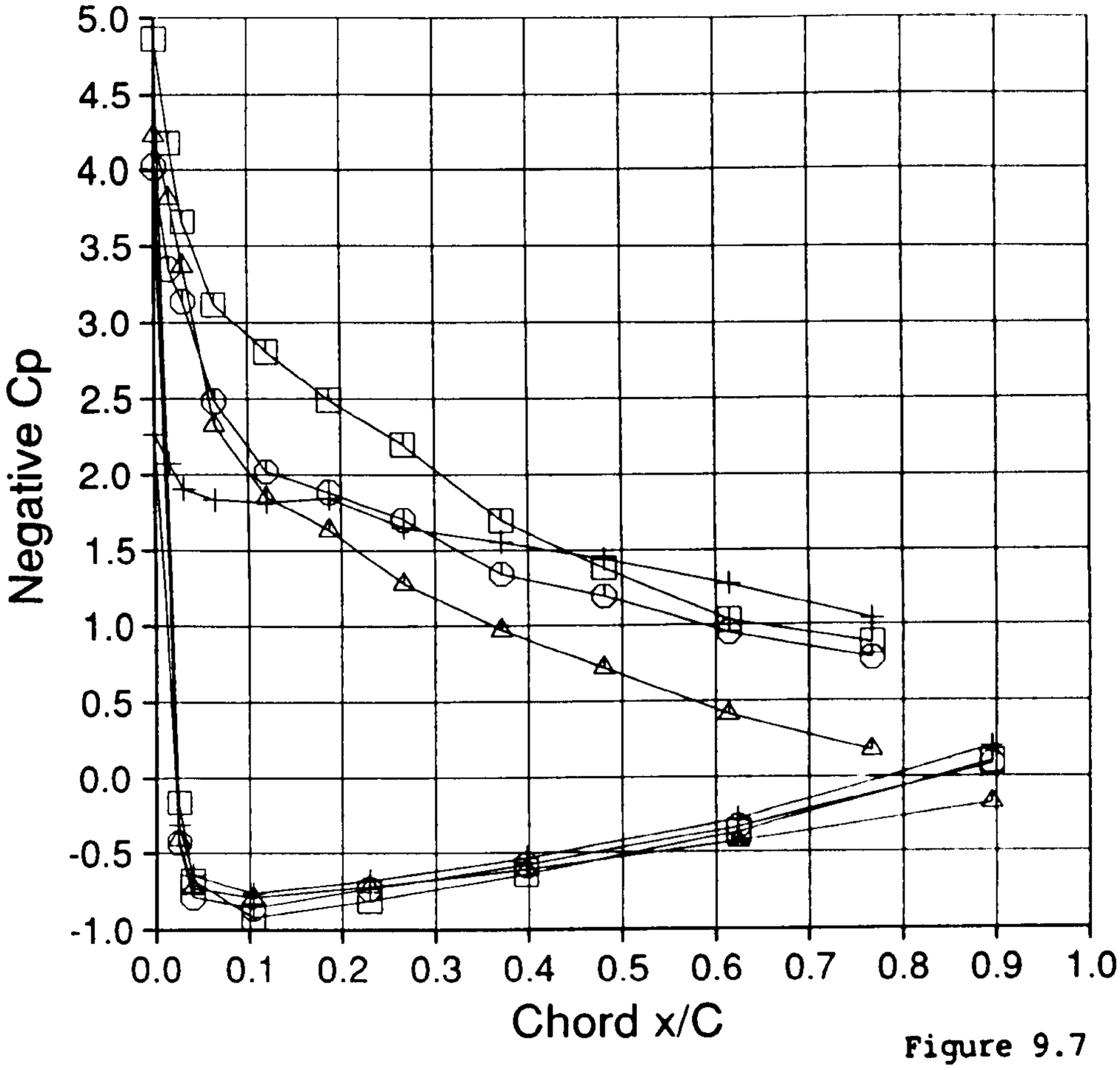

Figure 9.7

Cranfield

HAWT
Unsteady Aerodynamics
Experiment

Profiles V2.0

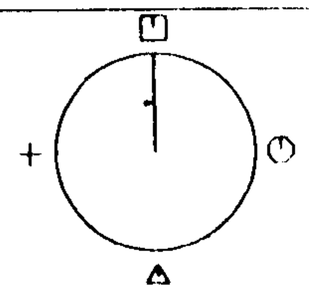

35% Span
Mean of Revs 040 TO 079
□ N = 164.0 N/m
○ N = 138.2 N/m
△ N = 111.8 N/m
\+ N = 138.2 N/m
Geometric alpha 39.6 deg
Rotor Speed 343.7 rpm
Body Angle 0.9 deg
Windspeed 18.1 m/s
Wind Angle -1.8 deg
Dynamic Head 400.1 Pa
Yaw Angle 2.8 deg
Tip Speed Ratio 2.8

165.EXP;2

7-FEB-1990:18:11:19

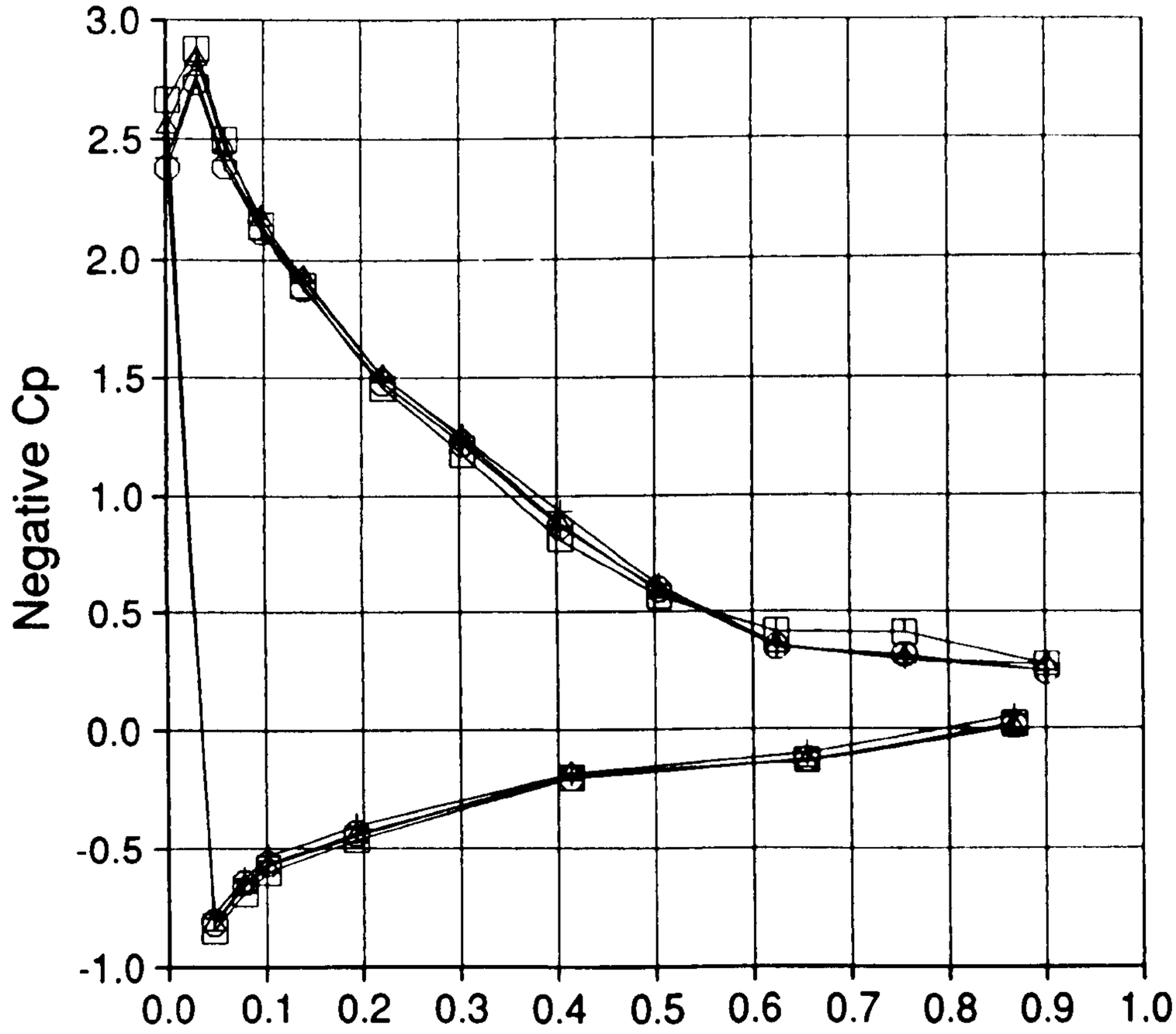

Figure 9.8

Cranfield

HAWT
Unsteady Aerodynamics
Experiment

Profiles V2.0

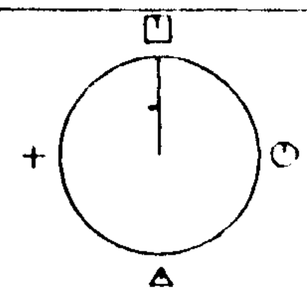

75% Span
Mean of Revs 040 TO 079
□ N = 175.4 N/m
○ N = 171.0 N/m
△ N = 173.9 N/m
\+ N = 169.5 N/m
Geometric alpha 19.5 deg
Rotor Speed 343.7 rpm
Body Angle 0.9 deg
Windspeed 18.1 m/s
Wind Angle -1.8 deg
Dynamic Head 1113.7 Pa
Yaw Angle 2.8 deg
Tip Speed Ratio 2.8

165.EXP;2

7-FEB-1990:18:11:19

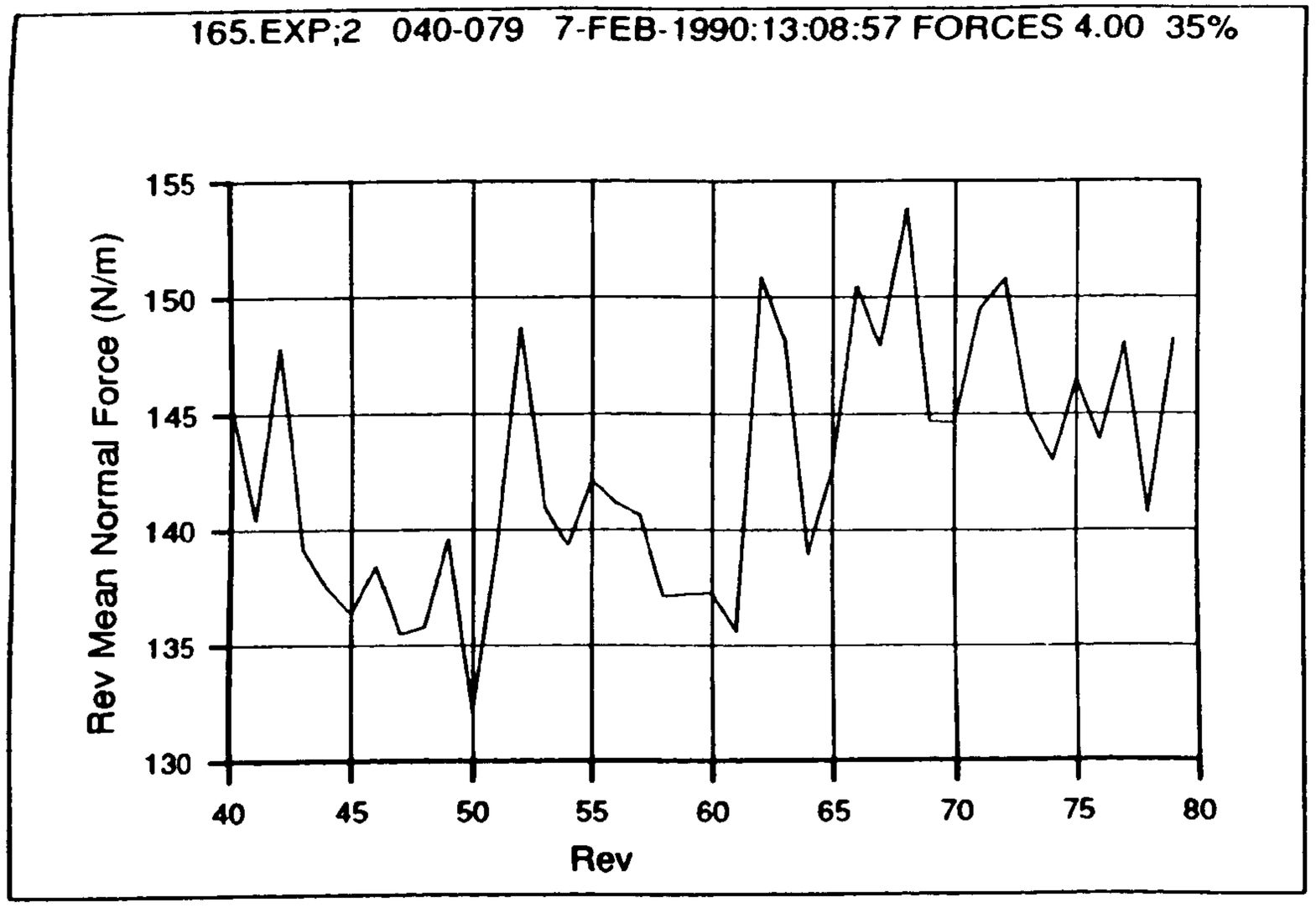

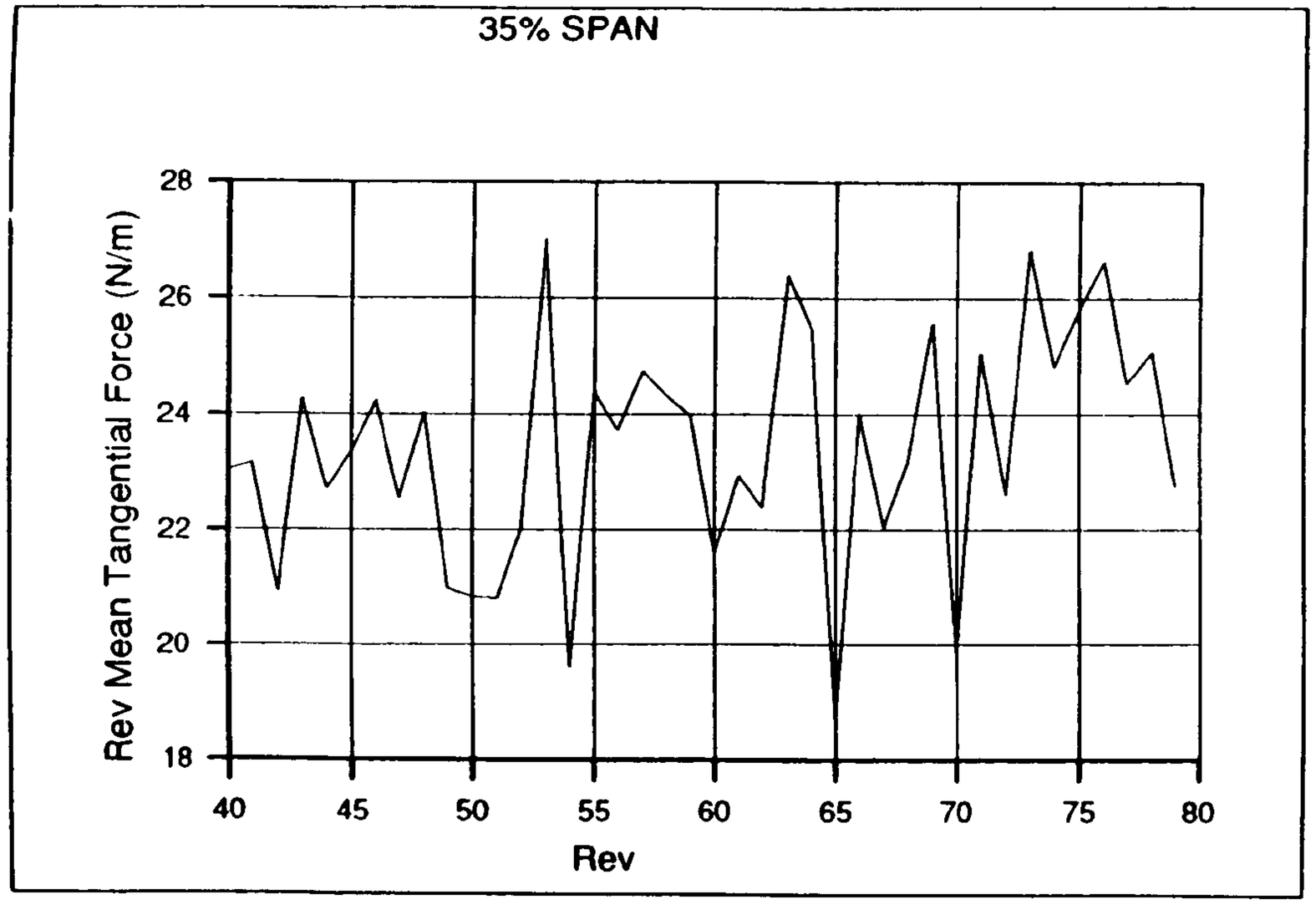

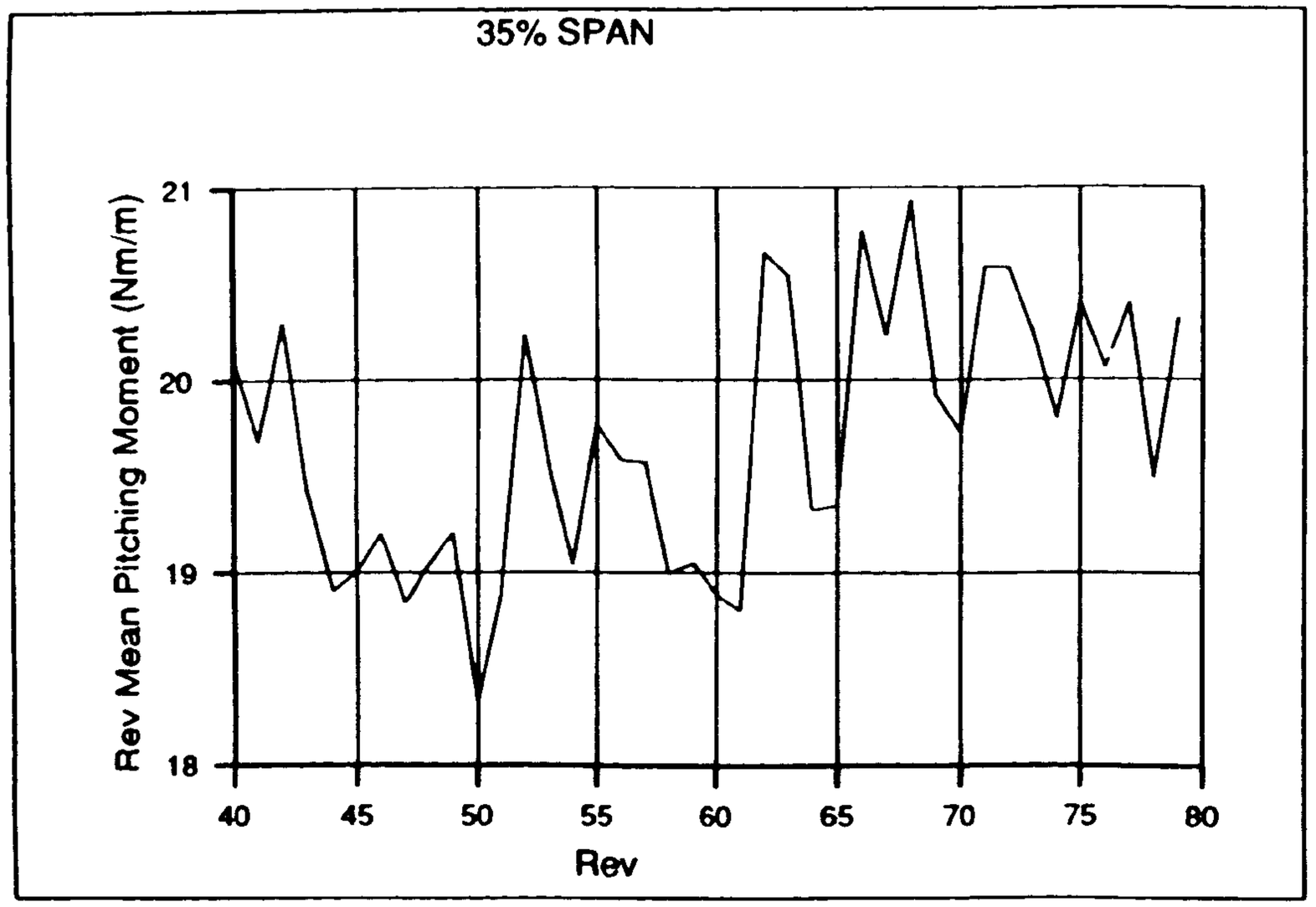

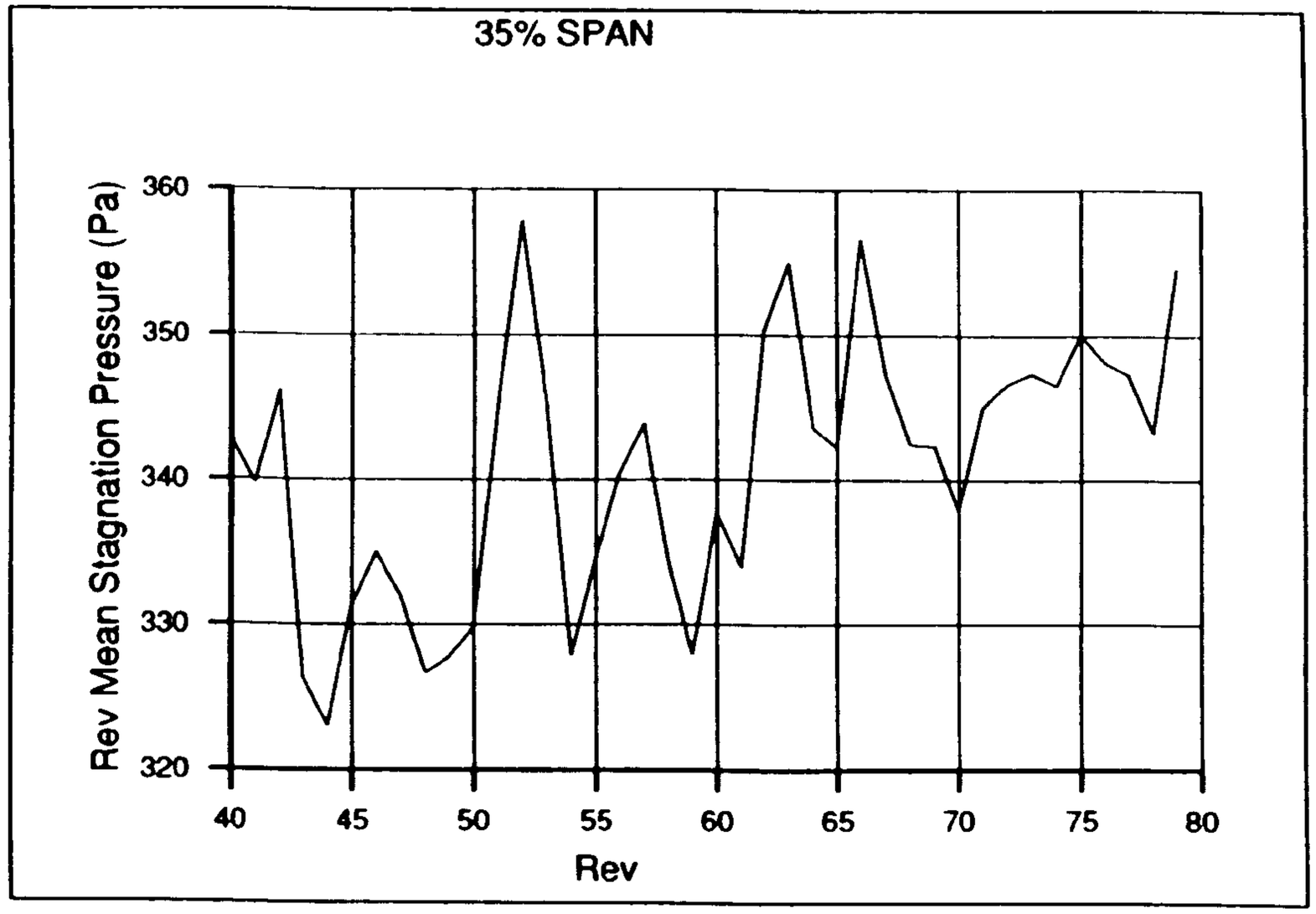

Figure 9.9 Program FORCES

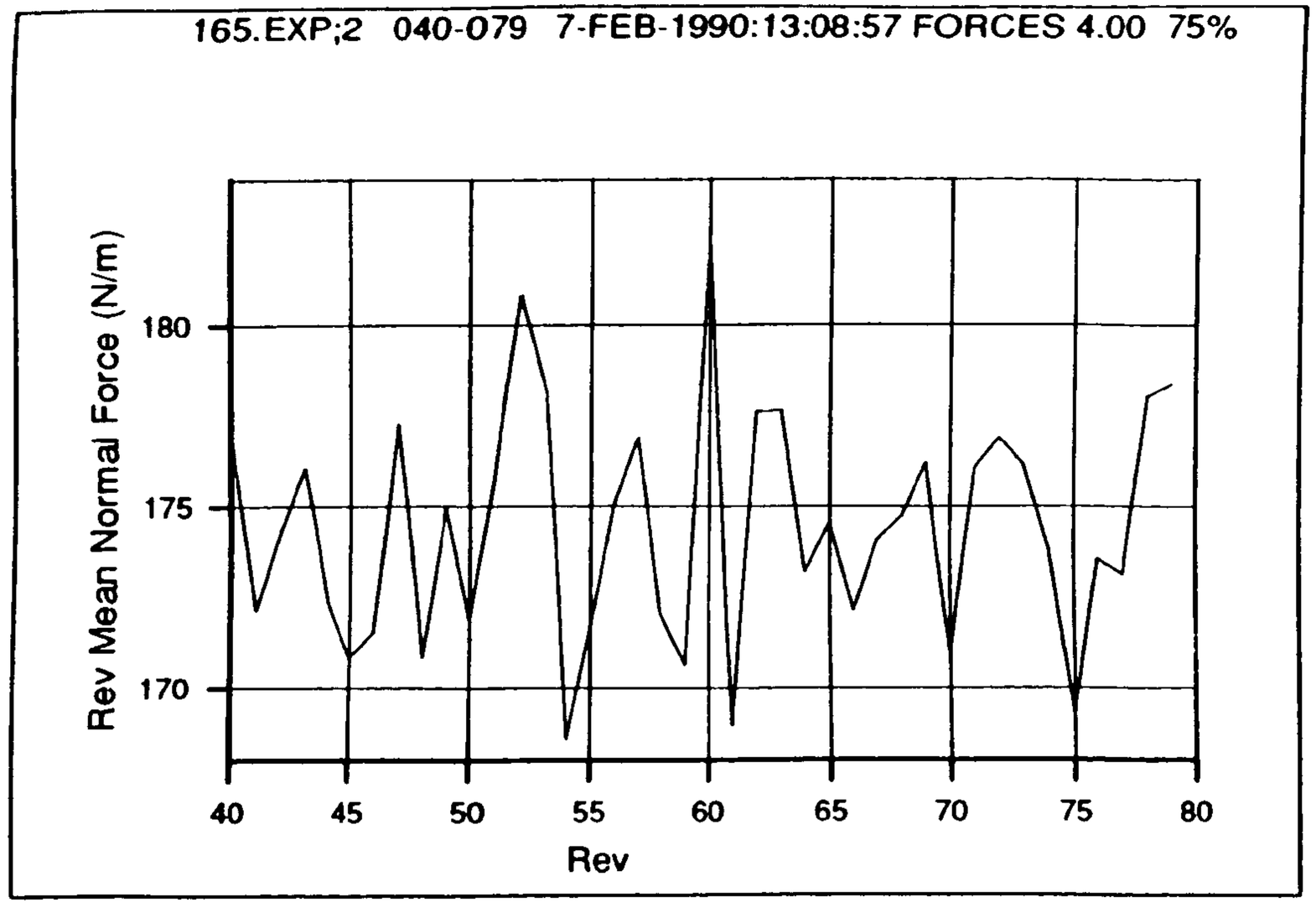

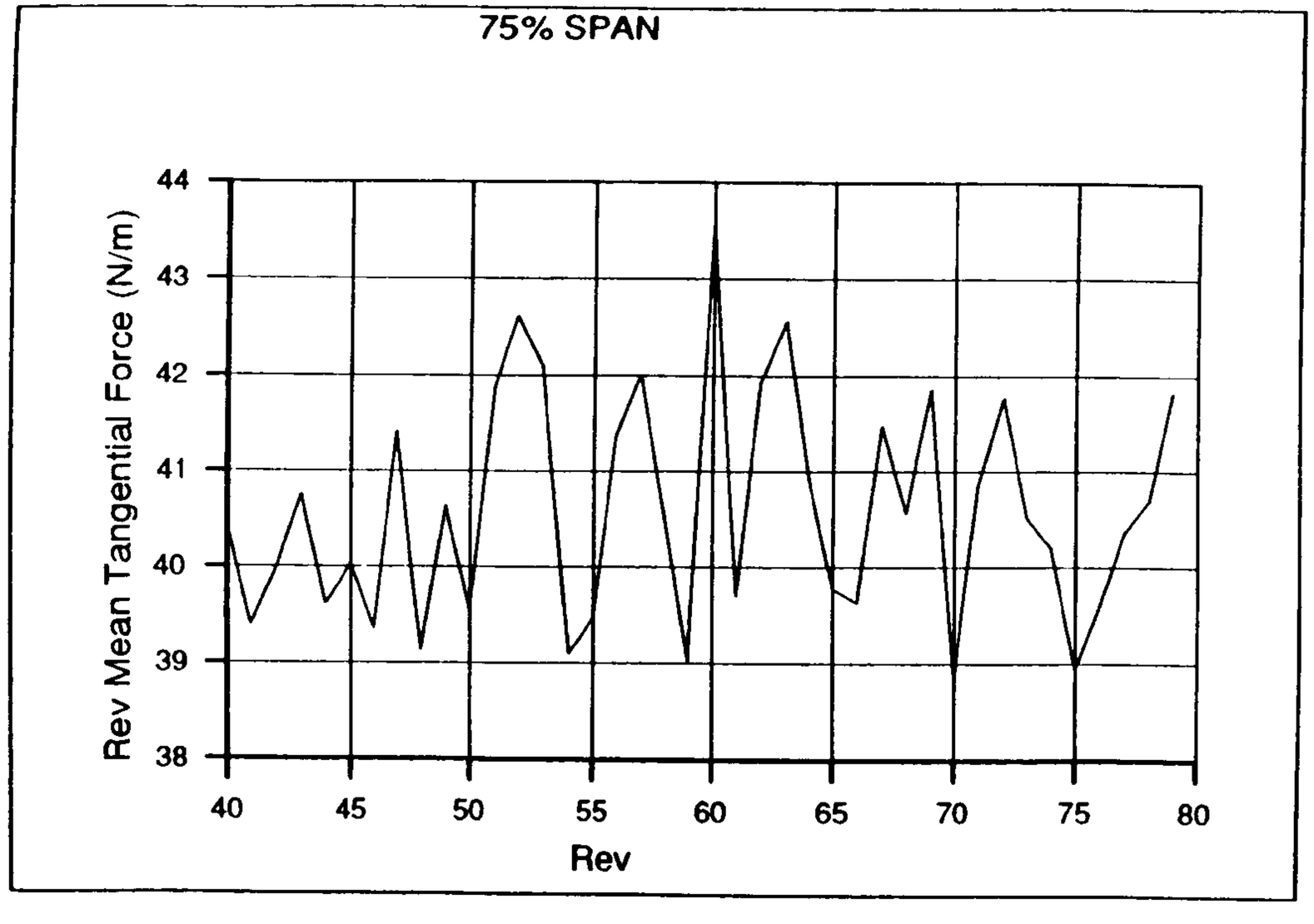

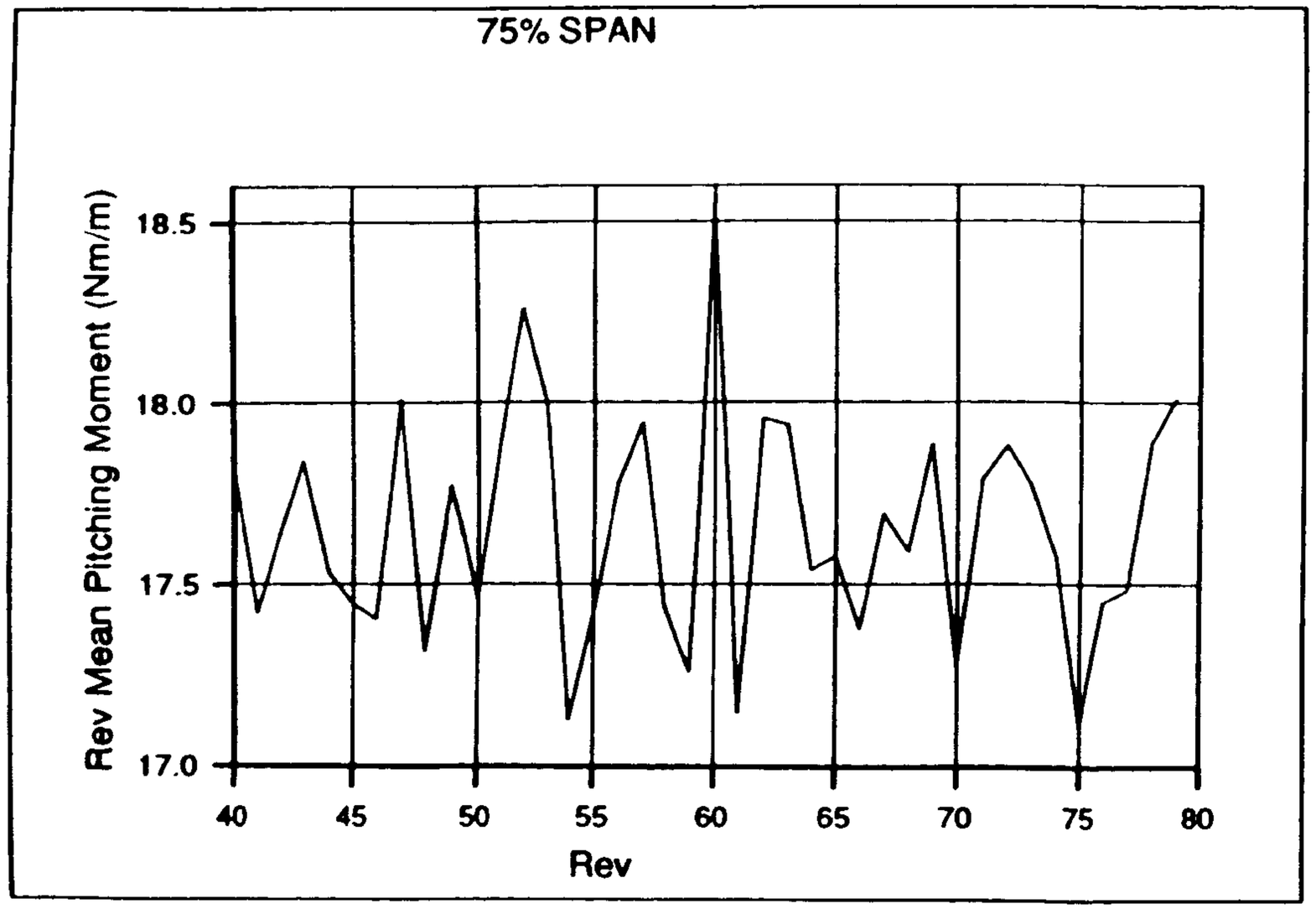

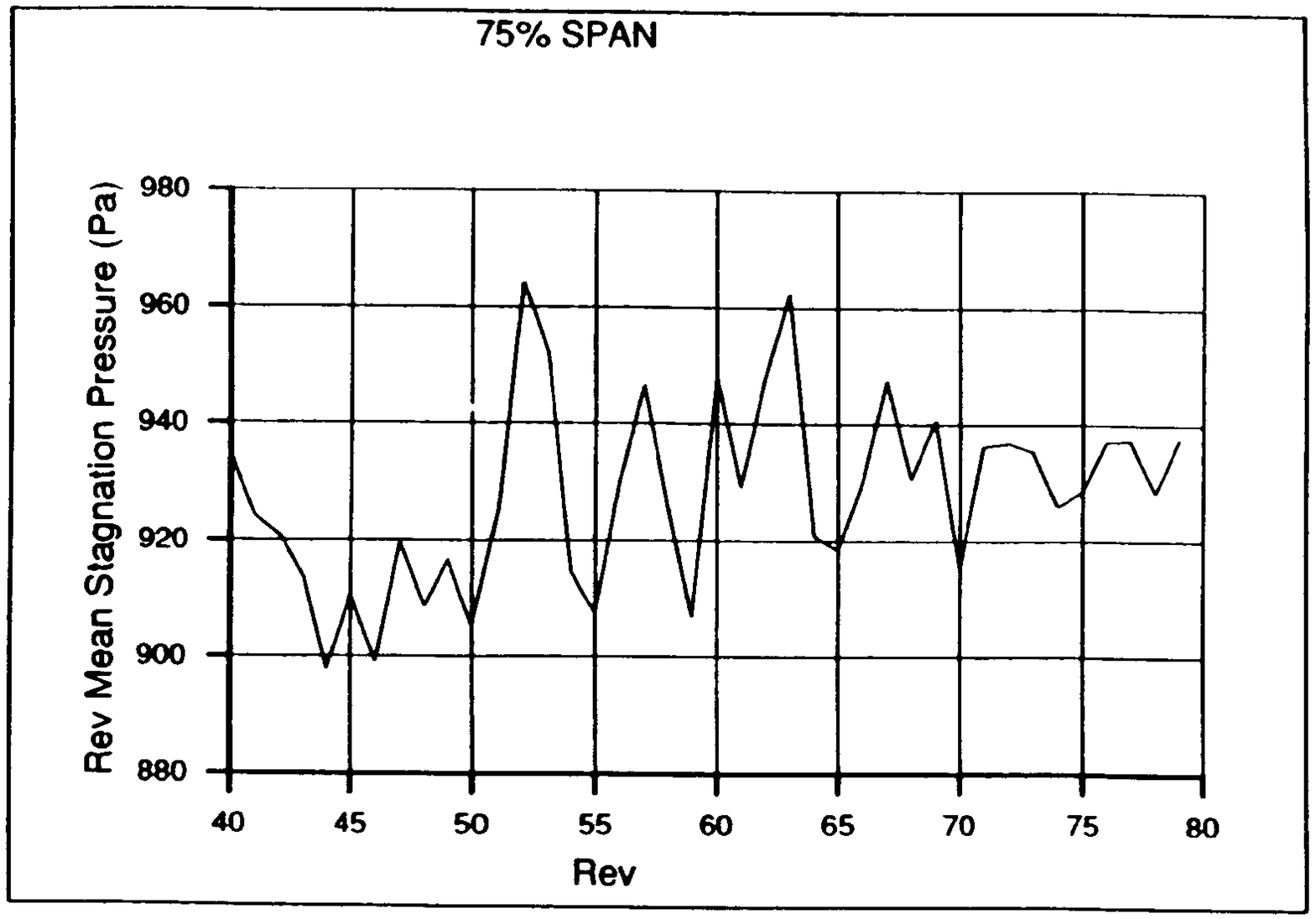

Figure 9.10 Program FORCES

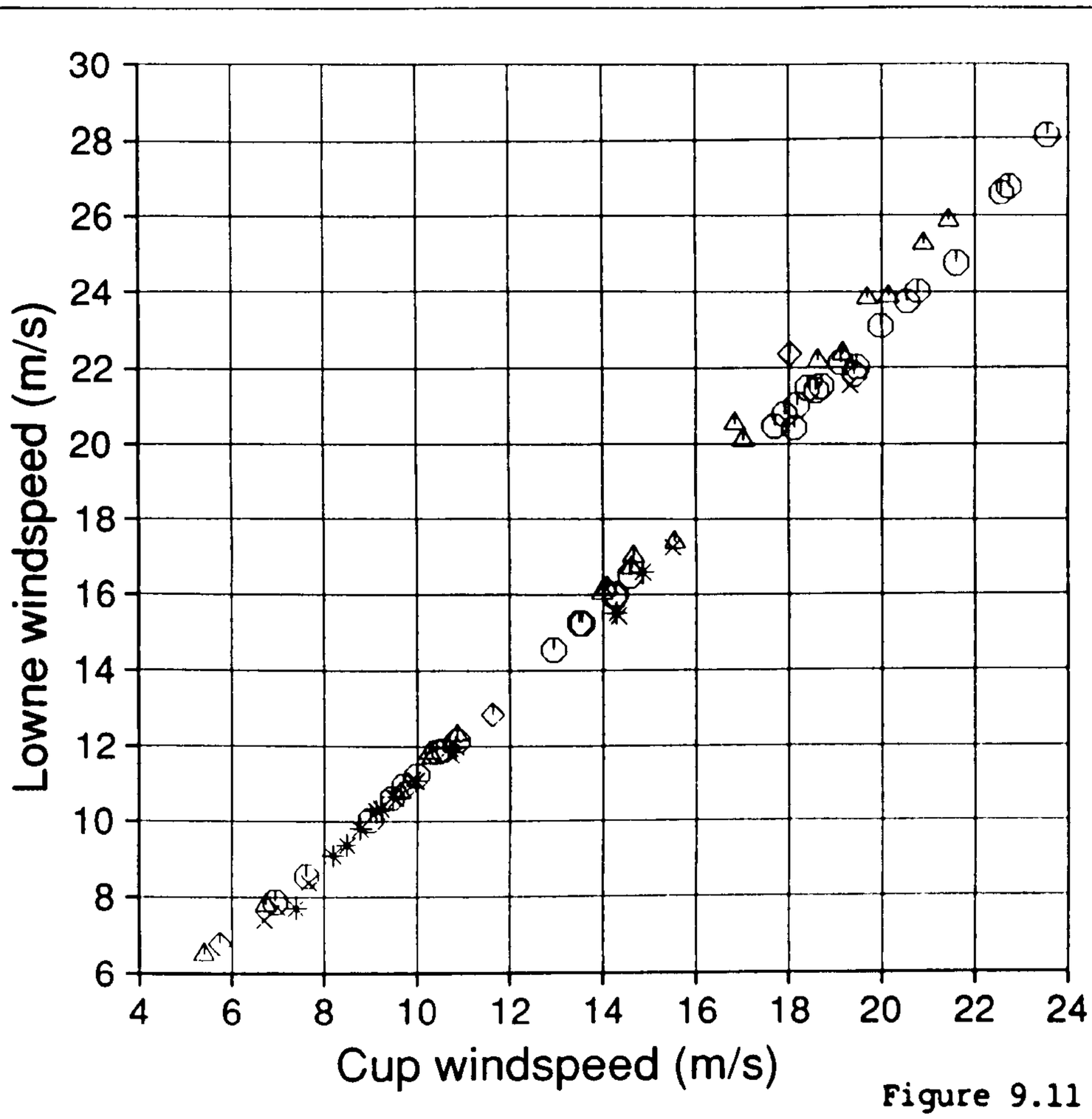

Figure 9.11

Cranfield

HAWT
Unsteady Aerodynamics
Experiment

Parametric Trends

Program V0.01

MARLEC Blades FI-1

76 sub-runs plotted
exactly 40 revs
in each sub run
derived parameters from
WINDY

z is vane angle
Y --- -20.0
✱ -20.0 --- -10.0
× -10.0 --- 0.0
◷ 0.0 --- 10.0
△ 10.0 --- 20.0
◇ 20.0 ---

TREND.DAT;38

28-FEB-1990: 9:59:59

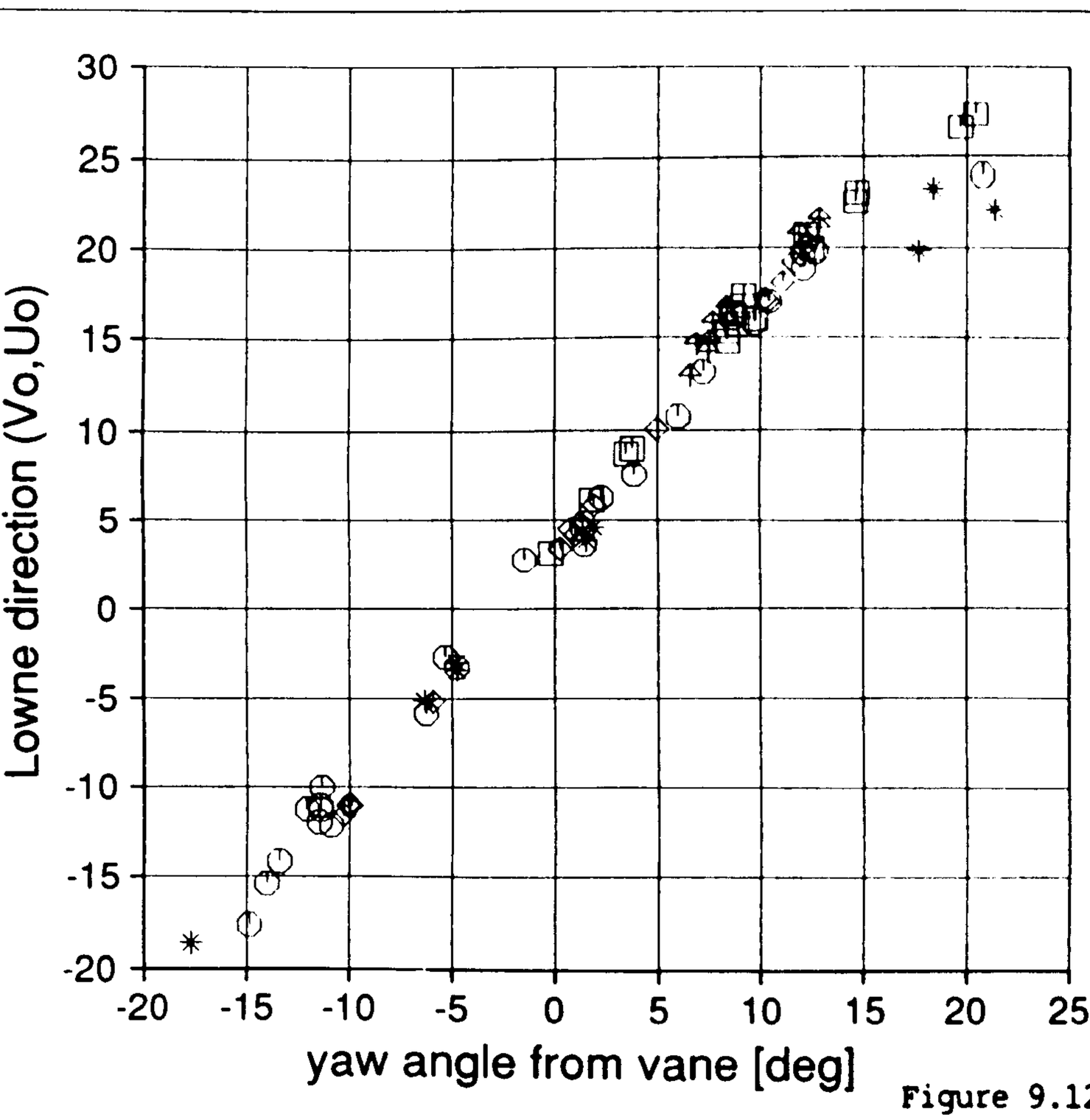

Figure 9.12

Cranfield

HAWT
Unsteady Aerodynamics
Experiment

Parametric Trends

Program V0.02

MARLEC Blades FI-1

76 sub-runs plotted
exactly 40 revs
in each sub run
derived parameters from
WINDY

z is wind speed
Y --- 4.0
✱ 4.0 --- 8.0
◷ 8.0 --- 12.0
◷ 12.0 --- 16.0
□ 16.0 --- 20.0
✱ 20.0 ---

TREND.DAT;51

28-FEB-1990:14:37:15

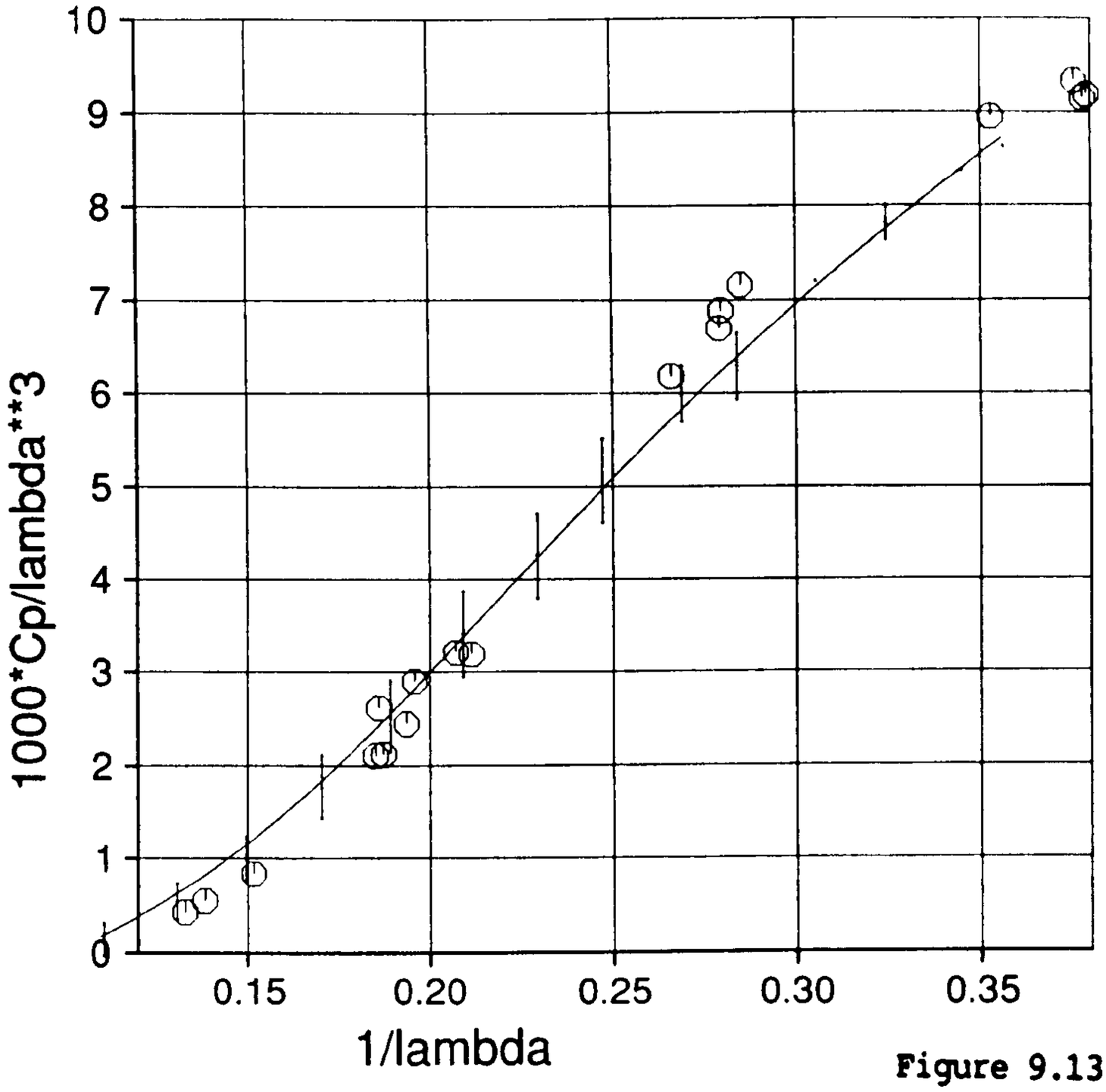

Figure 9.13

Cranfield

HAWT
Unsteady Aerodynamics
Experiment

Parametric Trends

Program V4.17

MARLEC Blades FI-1

18 sub-runs plotted
exactly 40 revs
in each sub run
derived parameters from
WINDY
ROTOR

z is yaw angle

Y	--- -37.5
✱	-37.5 --- -22.5
×	-22.5 --- -7.5
◷	-7.5 --- 7.5
△	7.5 --- 22.5
◇	22.5 --- 37.5
◫	37.5 --- 52.5
↟	52.5 ---

TREND.DAT;2

1-MAY-1990:11:41:59

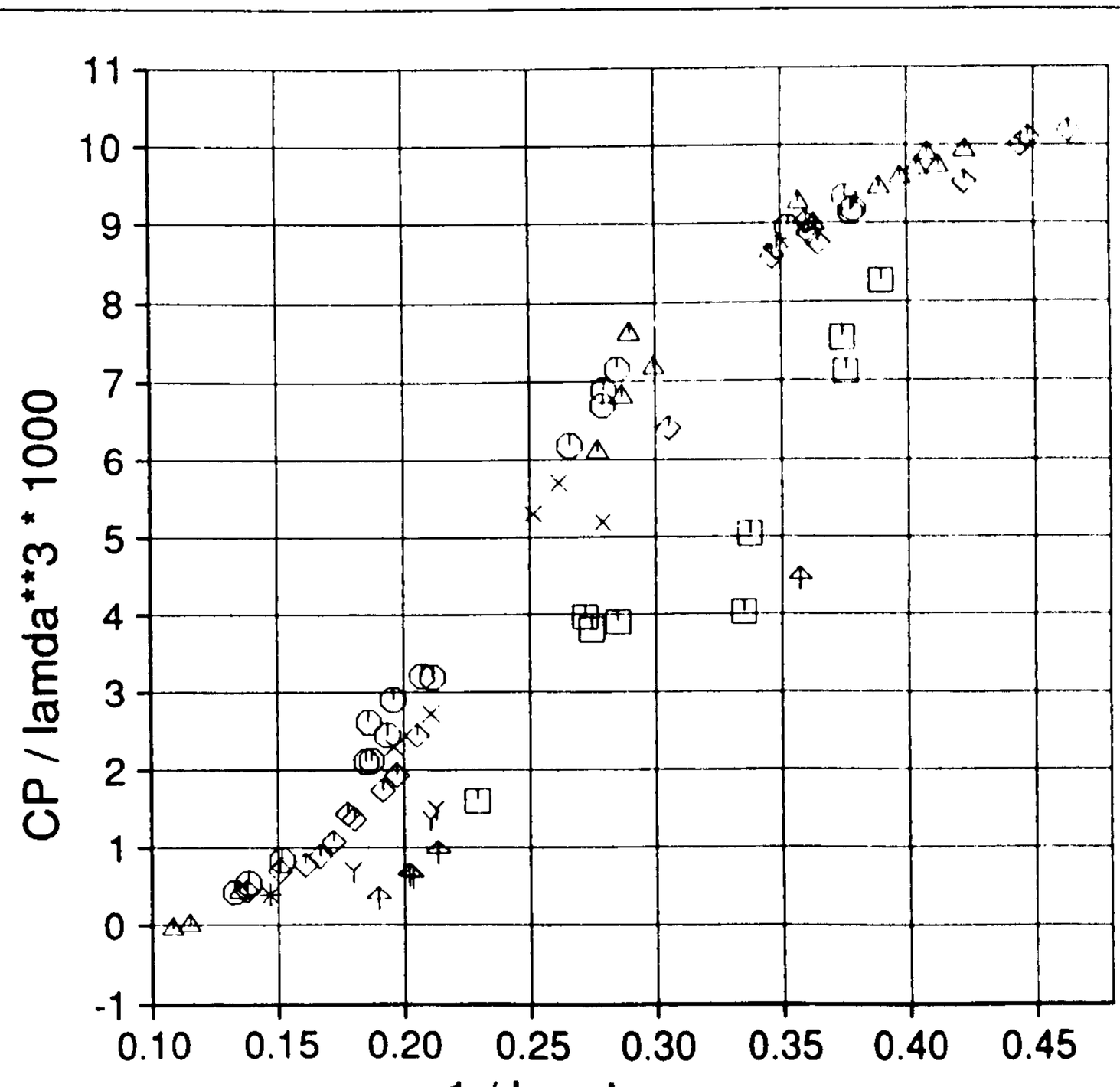

Figure 9.14

Cranfield

HAWT
Unsteady Aerodynamics
Experiment

Parametric Trends

Program V4.07

MARLEC Blades FI-1

76 sub-runs plotted
exactly 40 revs
in each sub run
derived parameters from
WINDY
ROTOR

z is yaw angle

Y	--- -37.5
✱	-37.5 --- -22.5
×	-22.5 --- -7.5
◷	-7.5 --- 7.5
△	7.5 --- 22.5
◇	22.5 --- 37.5
◫	37.5 --- 52.5
↟	52.5 ---

TREND.DAT;8

16-FEB-1990:13:54:30

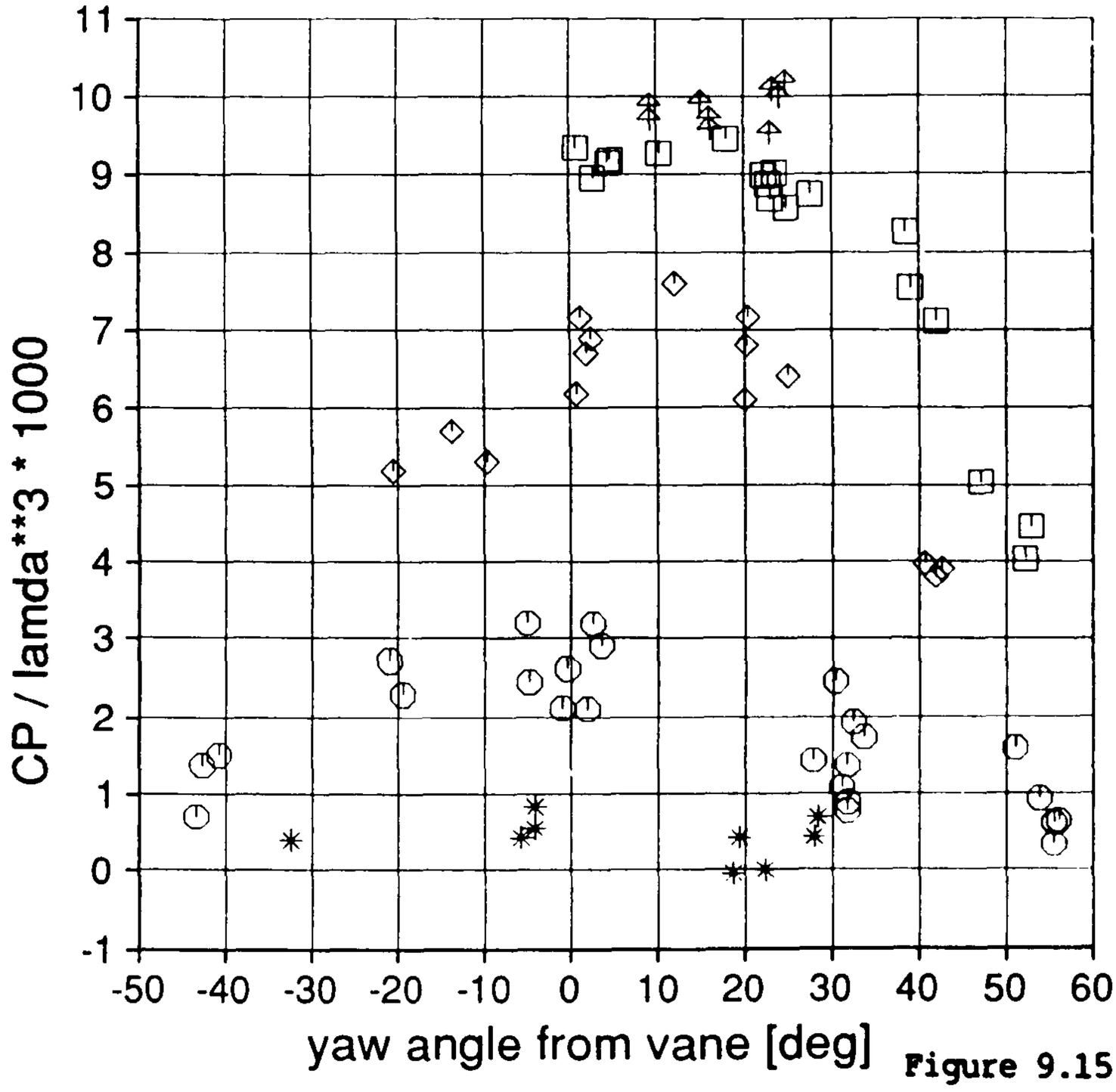

Cranfield

HAWT
Unsteady Aerodynamics
Experiment

Parametric Trends

Program V4.08

MARLEC Blades FI-1

76 sub-runs plotted
exactly 40 revs
in each sub run
derived parameters from
WINDY
ROTOR

z is wind speed

Y	--- 4.0
*	4.0 --- 8.0
O	8.0 --- 12.0
◇	12.0 --- 16.0
□	16.0 --- 20.0
↑	20.0 ---

TREND.DAT;10

16-FEB-1990:14:16:20

Figure 9.15

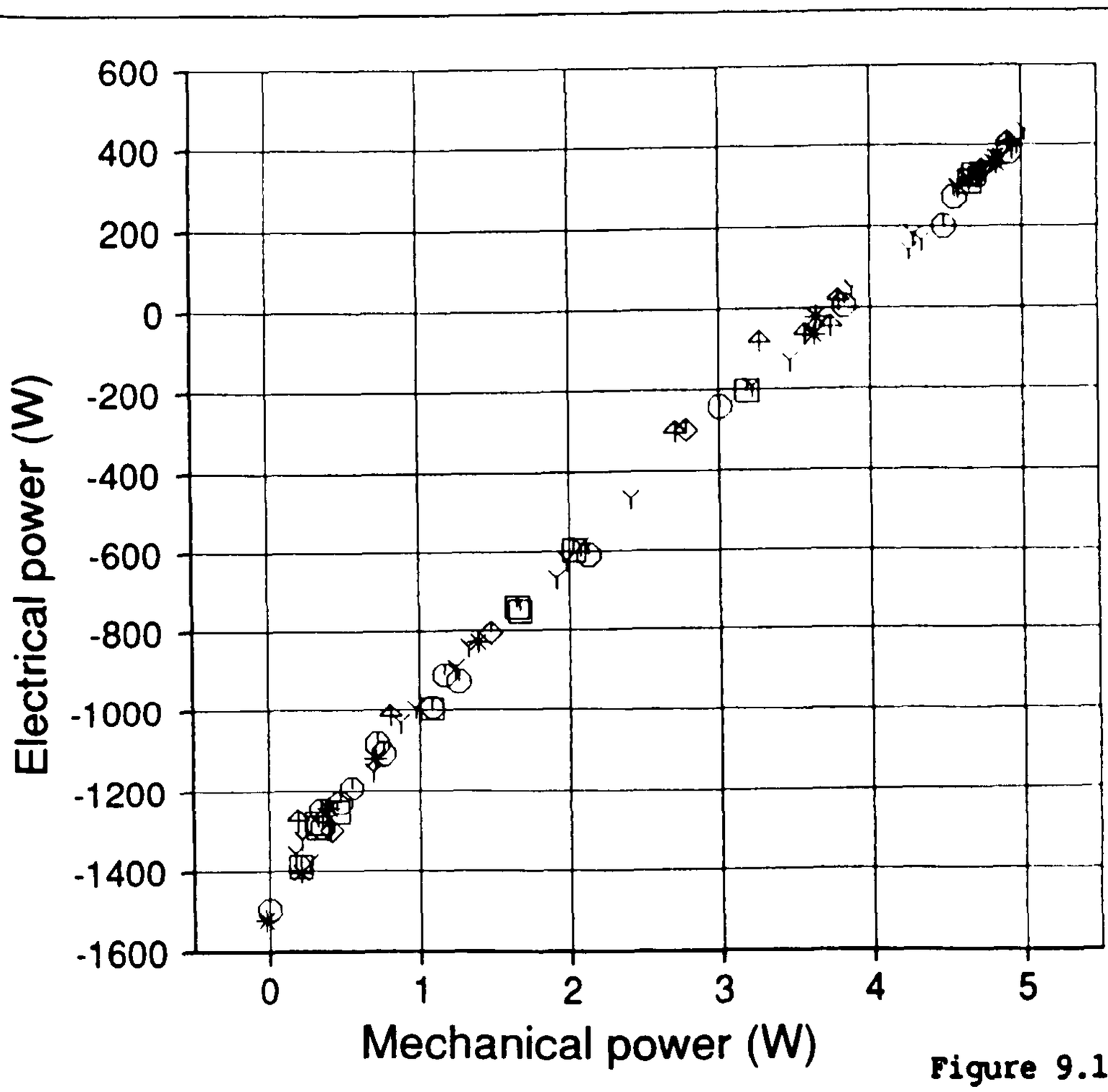

Cranfield

HAWT
Unsteady Aerodynamics
Experiment

Parametric Trends

Program V1.01

MARLEC Blades FI-1

76 sub-runs plotted
exactly 40 revs
in each sub run
derived parameters from
ROTOR

z is Correlation

Y	--- 0.5
*	0.5 --- 0.6
O	0.6 --- 0.7
◇	0.7 --- 0.8
□	0.8 --- 0.9
↑	0.9 ---

*10 3

TREND.DAT;49

28-FEB-1990:12:47:44

Figure 9.16

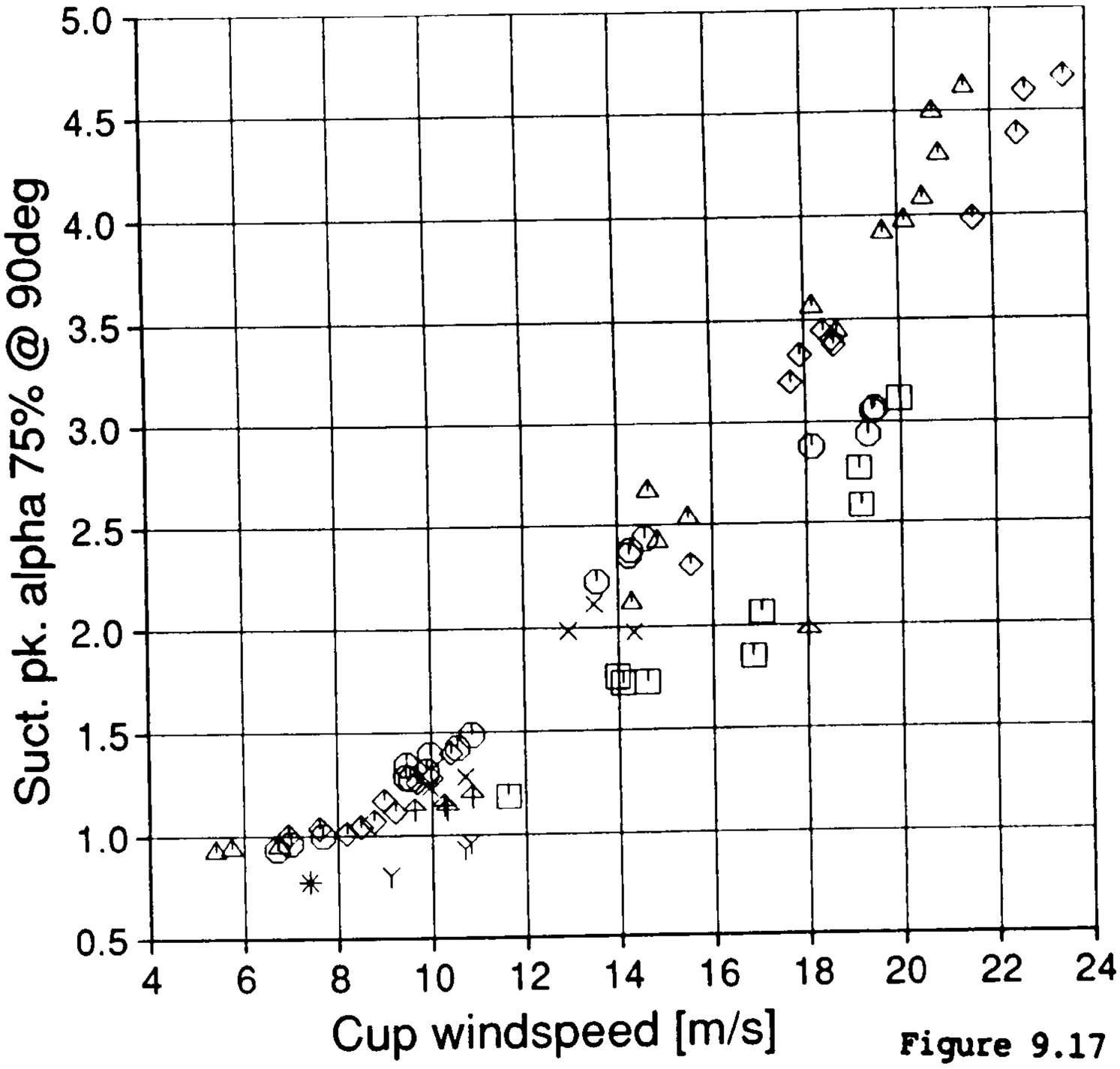

Figure 9.17

Cranfield

HAWT
Unsteady Aerodynamics
Experiment

Parametric Trends

Program V2.05

MARLEC Blades FI-1

76 sub-runs plotted
exactly 40 revs
in each sub run
derived parameters from
PROFILES

z is yaw angle

Y	--- -37.5
✱	-37.5 --- -22.5
×	-22.5 --- -7.5
○	-7.5 --- 7.5
△	7.5 --- 22.5
◇	22.5 --- 37.5
□	37.5 --- 52.5
✦	52.5 ---

TREND.DAT;57

28-FEB-1990:15:56:24

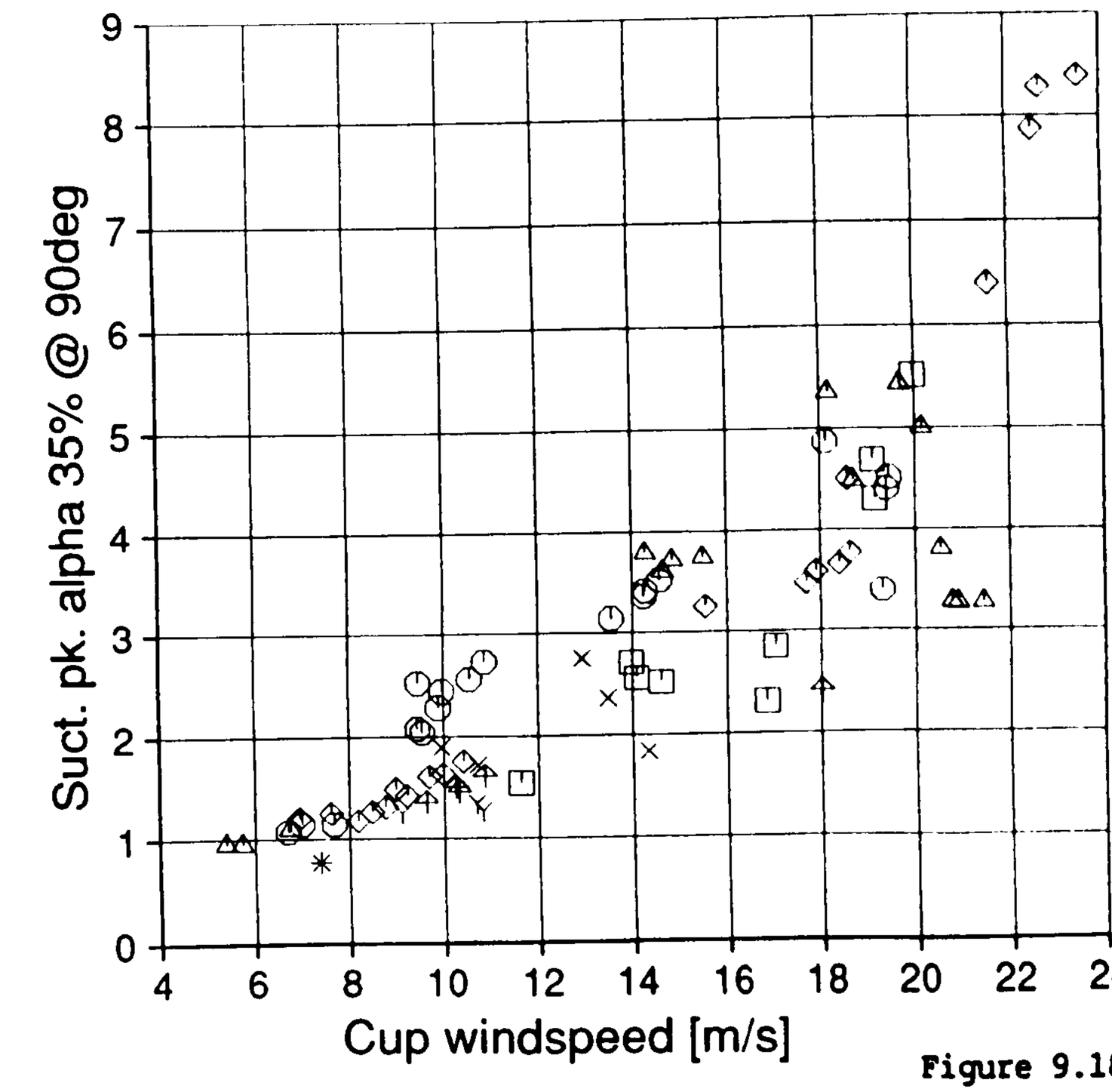

Figure 9.18

Cranfield

HAWT
Unsteady Aerodynamics
Experiment

Parametric Trends

Program V2.11

MARLEC Blades FI-1

76 sub-runs plotted
exactly 40 revs
in each sub run
derived parameters from
PROFILES

z is yaw angle

Y	--- -37.5
✱	-37.5 --- -22.5
×	-22.5 --- -7.5
○	-7.5 --- 7.5
△	7.5 --- 22.5
◇	22.5 --- 37.5
□	37.5 --- 52.5
✦	52.5 ---

TREND.DAT;63

28-FEB-1990:16:36:19

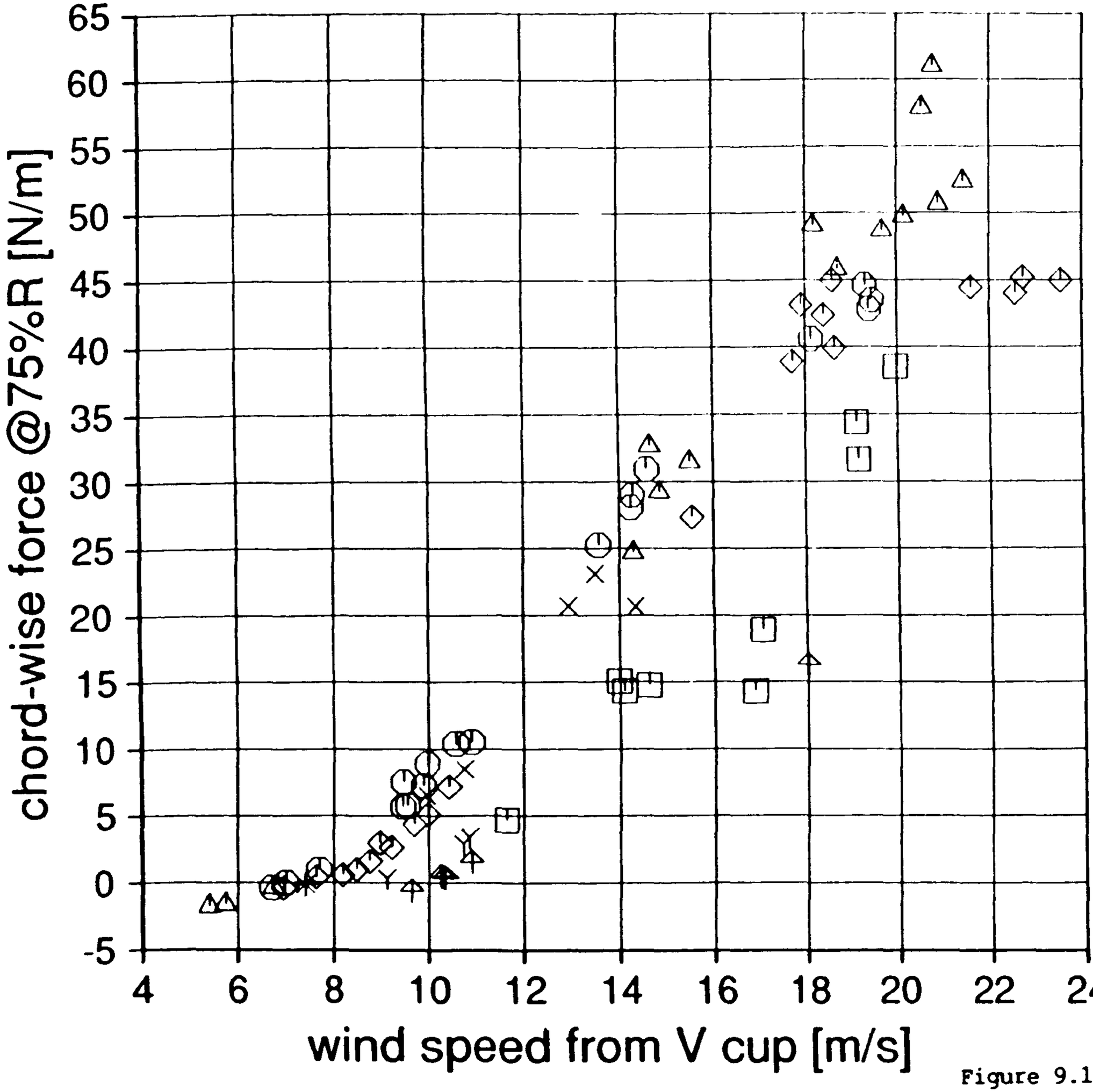

Figure 9.19

Cranfield

HAWT
Unsteady Aerodynamics
Experiment

Parametric Trends

Program V6.04

MARLEC Blades FI-1

76 sub-runs plotted
exactly 40 revs
in each sub run
derived parameters from
WINDY
FORCE

z is yaw angle

Y	--- -37.5
*	-37.5 --- -22.5
×	-22.5 --- -7.5
○	-7.5 --- 7.5
△	7.5 --- 22.5
◇	22.5 --- 37.5
□	37.5 --- 52.5
↑	52.5 ---

TREND.DAT;13

16-FEB-1990:15:07:43

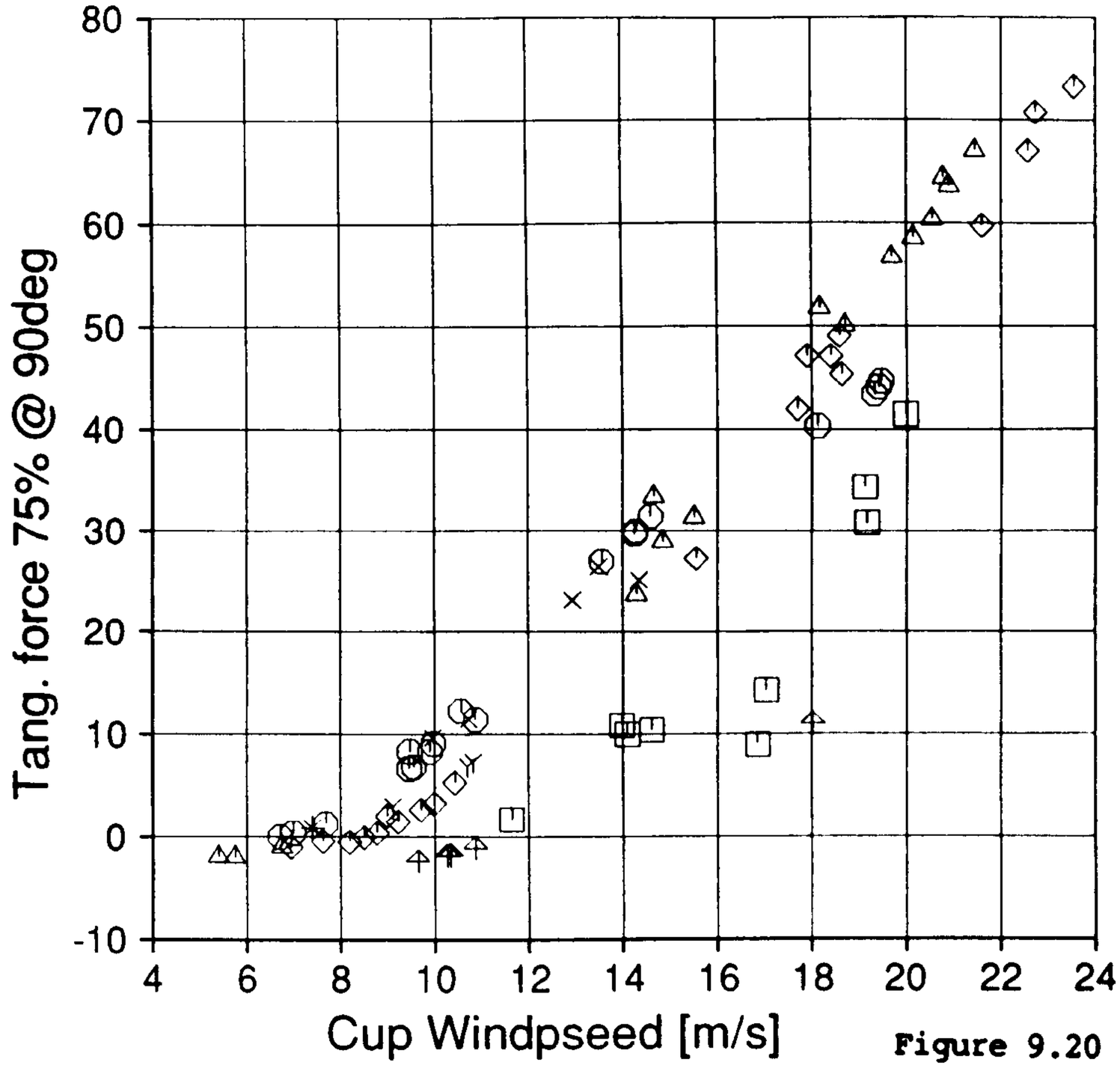

Figure 9.20

Cranfield

HAWT
Unsteady Aerodynamics
Experiment

Parametric Trends

Program V2.62

MARLEC Blades FI-1

76 sub-runs plotted
exactly 40 revs
in each sub run
derived parameters from
PROFILES

z is yaw angle

Y	--- -37.5
*	-37.5 --- -22.5
×	-22.5 --- -7.5
○	-7.5 --- 7.5
△	7.5 --- 22.5
◇	22.5 --- 37.5
□	37.5 --- 52.5
⏚	52.5 ---

TREND.DAT;142

19-MAR-1990:13:37:54

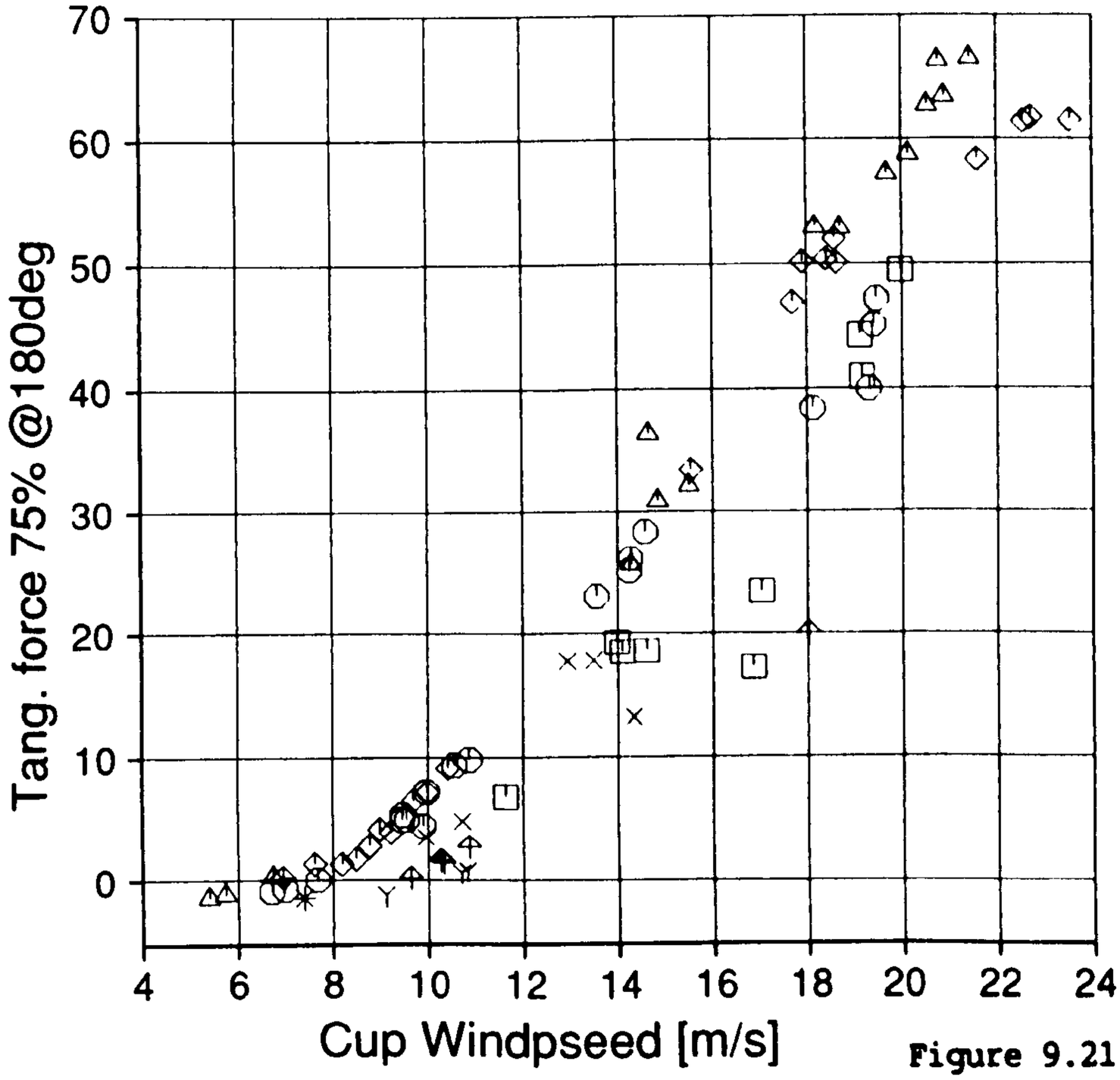

Figure 9.21

Cranfield

HAWT
Unsteady Aerodynamics
Experiment

Parametric Trends

Program V2.63

MARLEC Blades FI-1

76 sub-runs plotted
exactly 40 revs
in each sub run
derived parameters from
PROFILES

z is yaw angle

Y	--- -37.5
*	-37.5 --- -22.5
×	-22.5 --- -7.5
○	-7.5 --- 7.5
△	7.5 --- 22.5
◇	22.5 --- 37.5
□	37.5 --- 52.5
⏚	52.5 ---

TREND.DAT;143

19-MAR-1990:13:39:01

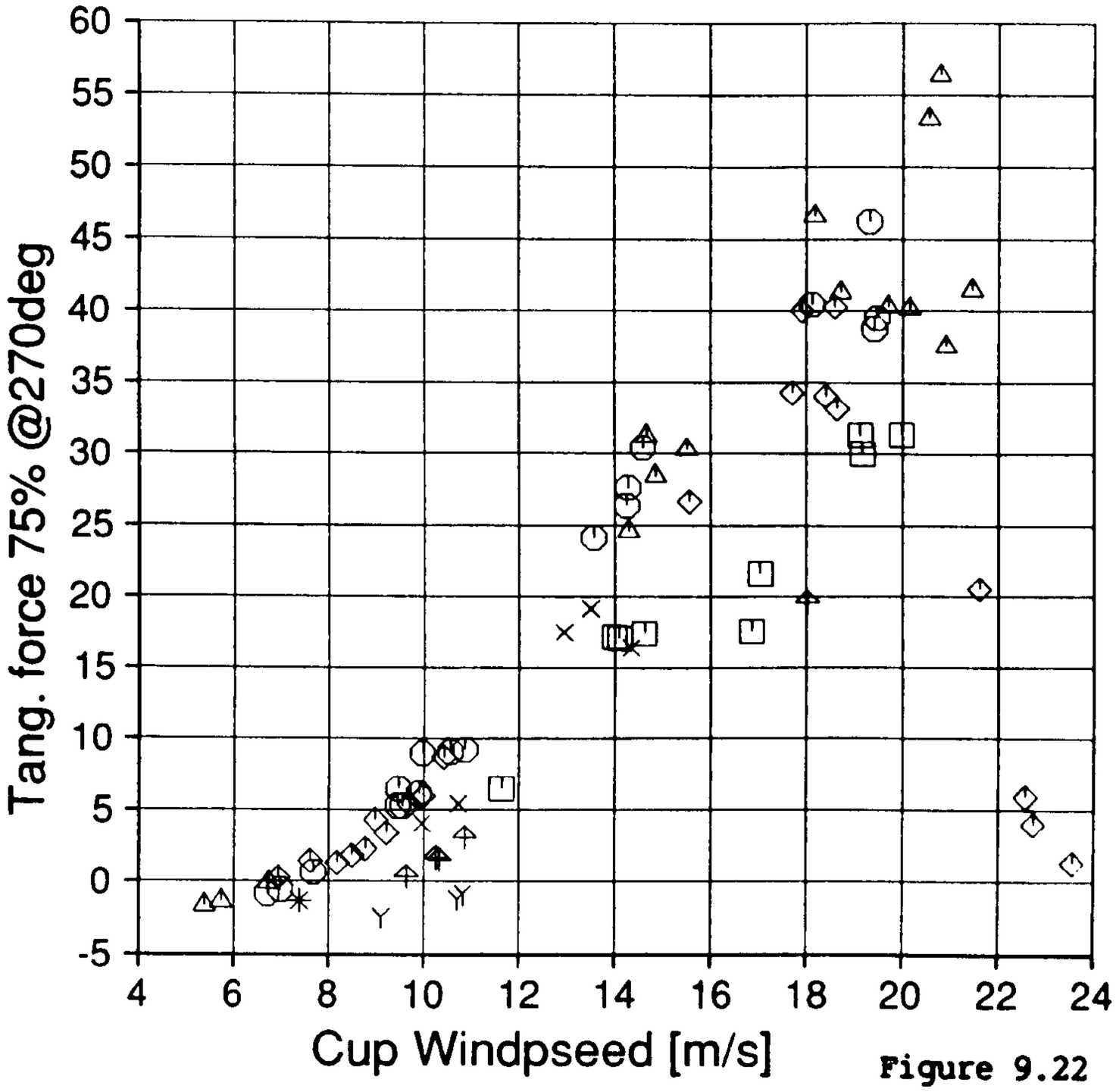

Figure 9.22

Cranfield

HAWT
Unsteady Aerodynamics
Experiment

Parametric Trends

Program V2.64

MARLEC Blades FI-1

76 sub-runs plotted
exactly 40 revs
in each sub run
derived parameters from
PROFILES

z is yaw angle

Y	--- -37.5
✱	-37.5 --- -22.5
×	-22.5 --- -7.5
○	-7.5 --- 7.5
△	7.5 --- 22.5
◇	22.5 --- 37.5
□	37.5 --- 52.5
⍏	52.5 ---

TREND.DAT;144

19-MAR-1990:13:39:14

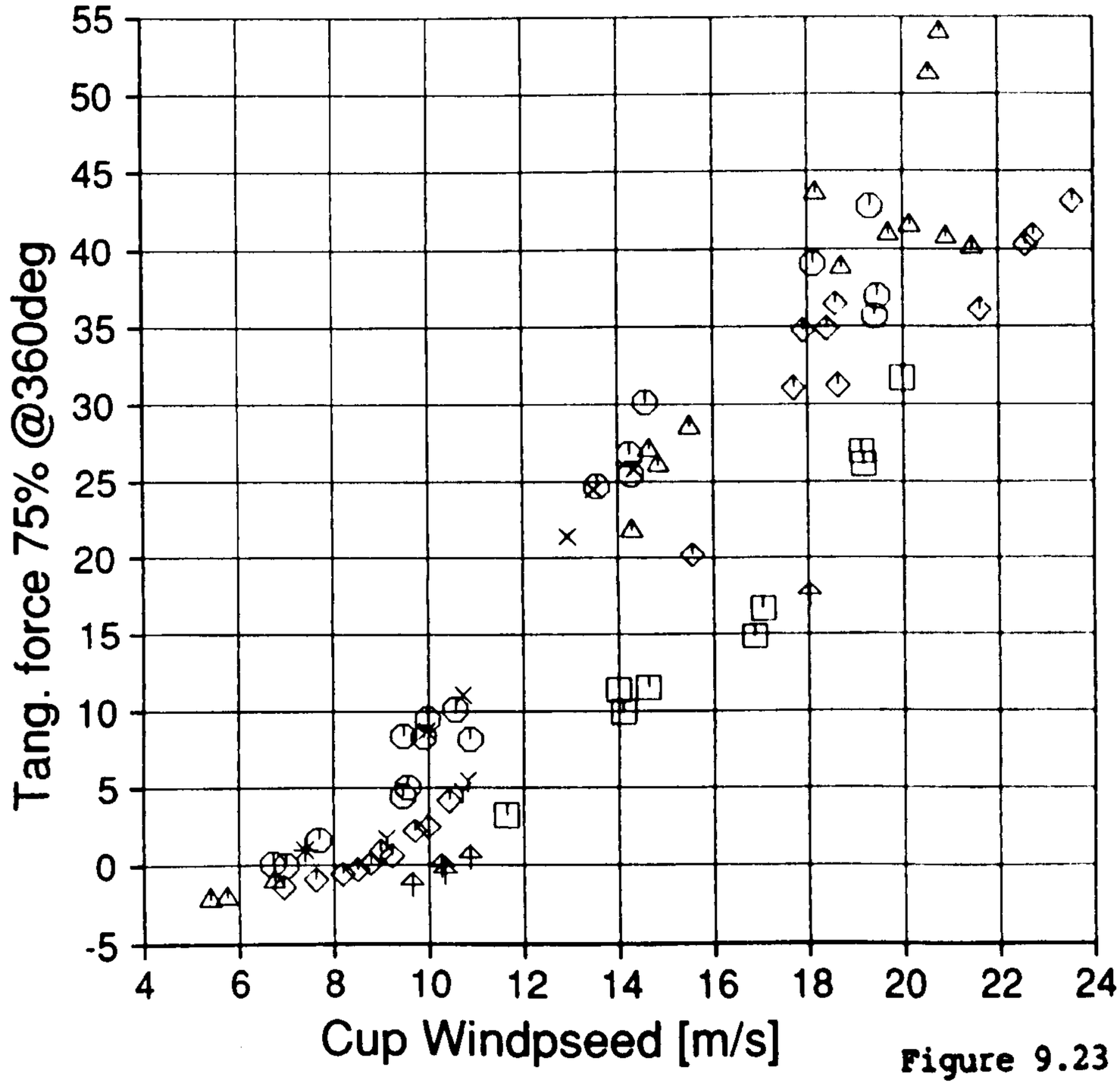

Figure 9.23

Cranfield

HAWT
Unsteady Aerodynamics
Experiment

Parametric Trends

Program V2.65

MARLEC Blades FI-1

76 sub-runs plotted
exactly 40 revs
in each sub run
derived parameters from
PROFILES

z is yaw angle

Y	--- -37.5
✱	-37.5 --- -22.5
×	-22.5 --- -7.5
○	-7.5 --- 7.5
△	7.5 --- 22.5
◇	22.5 --- 37.5
□	37.5 --- 52.5
⍏	52.5 ---

TREND.DAT;145

19-MAR-1990:13:39:34

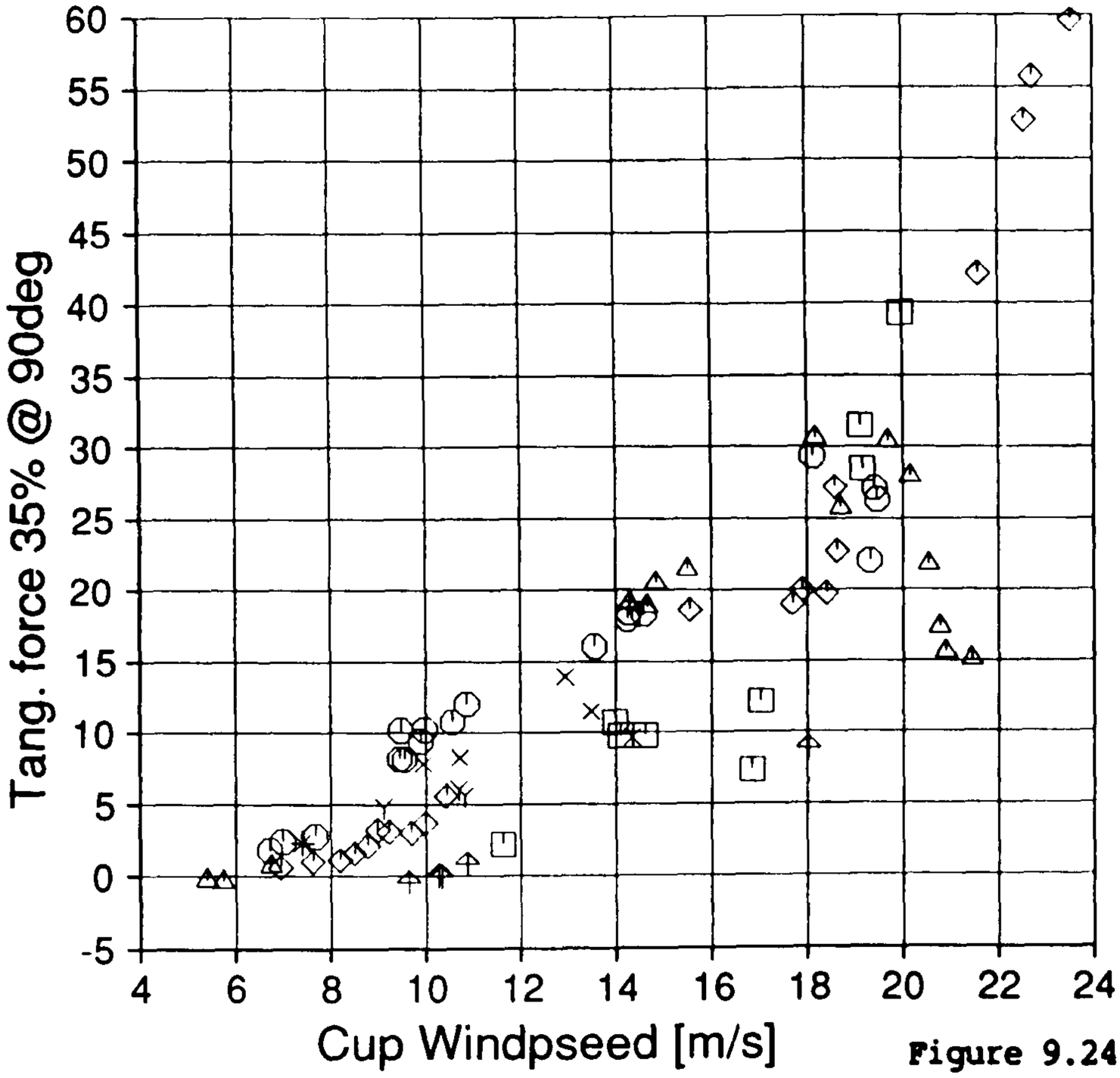

Figure 9.24

Cranfield

HAWT
Unsteady Aerodynamics
Experiment

Parametric Trends

Program V2.54

MARLEC Blades FI-1

76 sub-runs plotted
exactly 40 revs
in each sub run
derived parameters from
PROFILES

z is yaw angle

Y	--- -37.5
*	-37.5 --- -22.5
x	-22.5 --- -7.5
○	-7.5 --- 7.5
△	7.5 --- 22.5
◇	22.5 --- 37.5
□	37.5 --- 52.5
↑	52.5 ---

TREND.DAT;134

19-MAR-1990:13:35:31

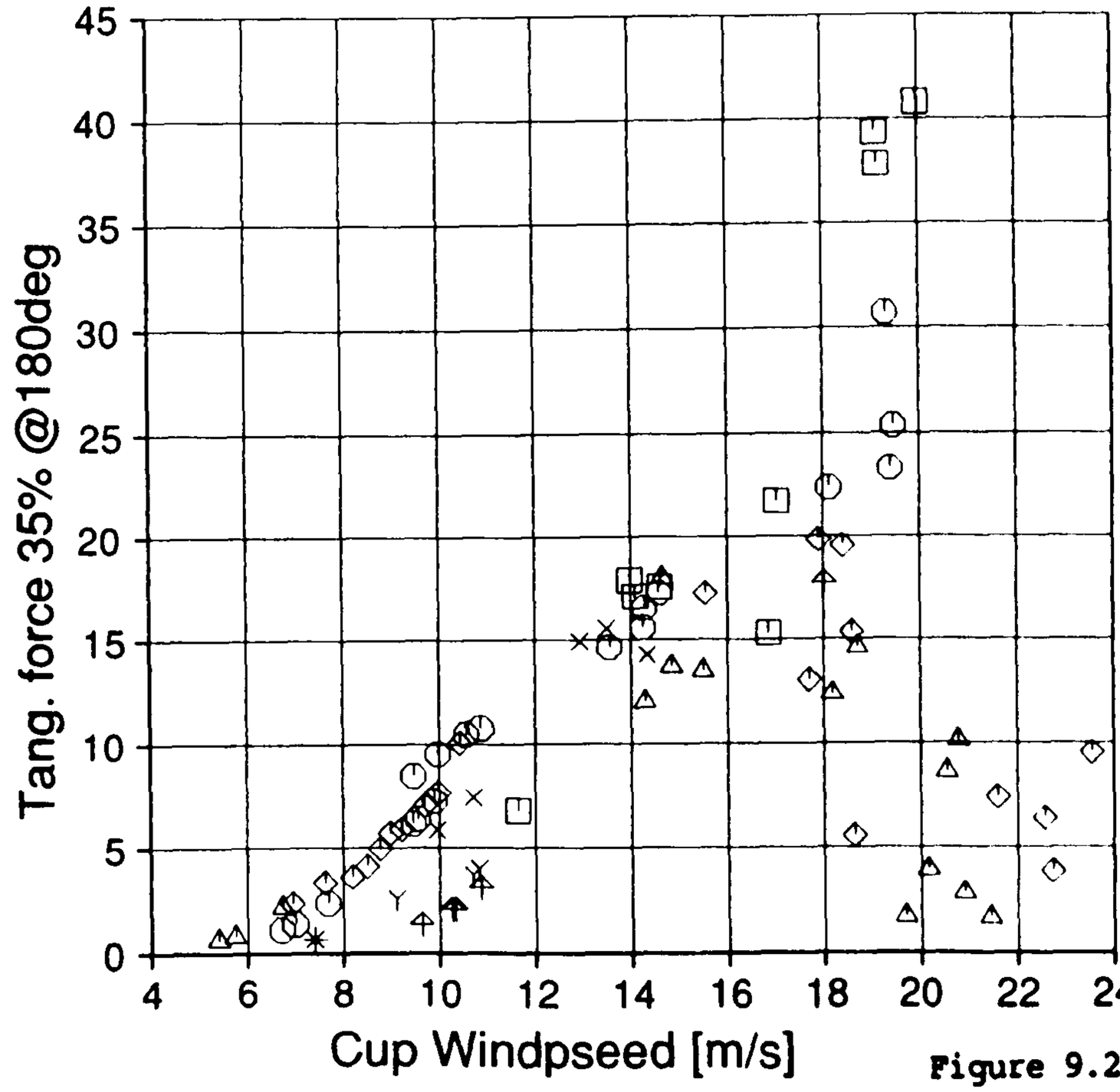

Figure 9.25

Cranfield

HAWT
Unsteady Aerodynamics
Experiment

Parametric Trends

Program V2.55

MARLEC Blades FI-1

76 sub-runs plotted
exactly 40 revs
in each sub run
derived parameters from
PROFILES

z is yaw angle

Y	--- -37.5
*	-37.5 --- -22.5
x	-22.5 --- -7.5
○	-7.5 --- 7.5
△	7.5 --- 22.5
◇	22.5 --- 37.5
□	37.5 --- 52.5
↑	52.5 ---

TREND.DAT;135

19-MAR-1990:13:35:50

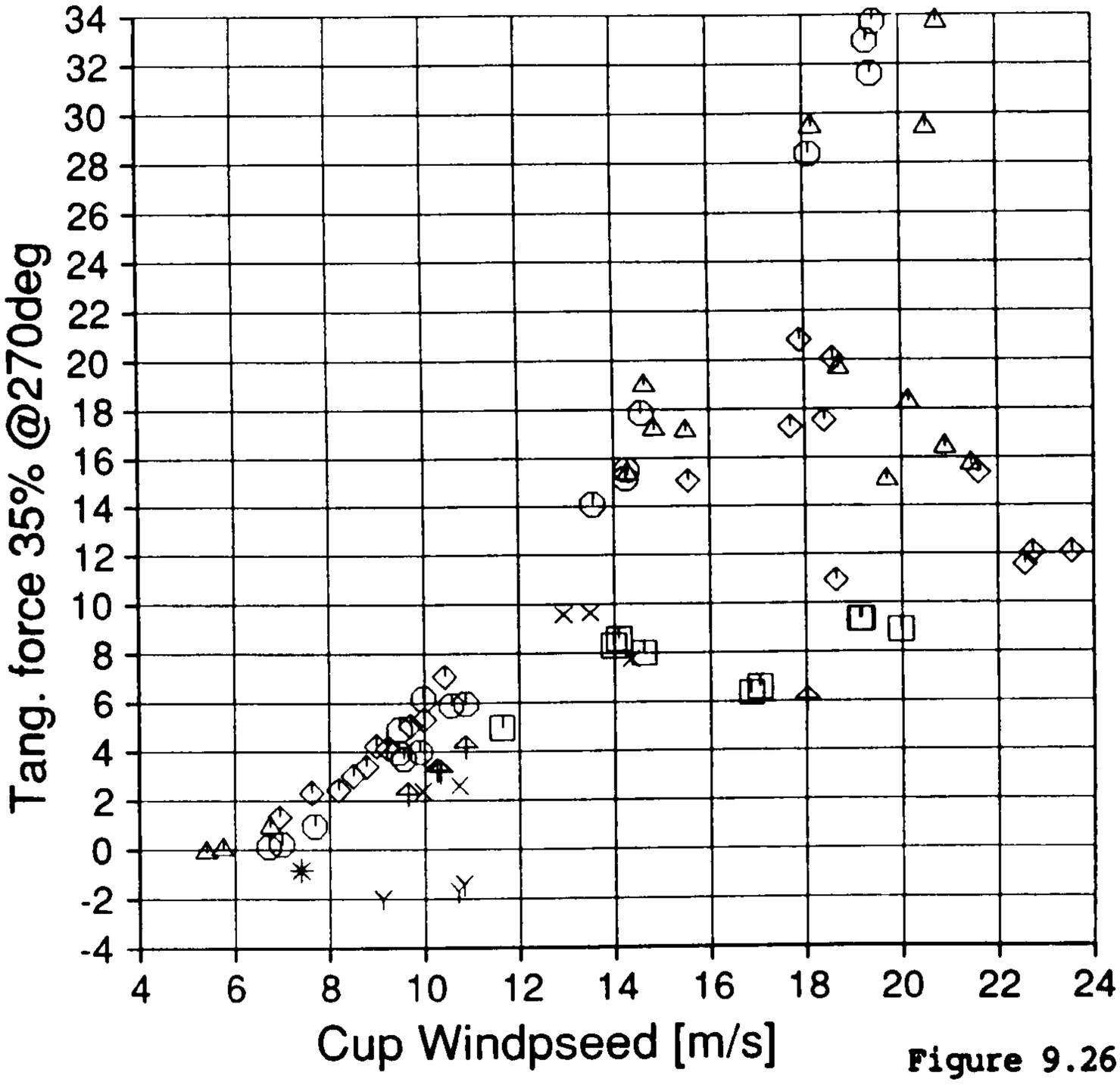

Figure 9.26

Cranfield

HAWT
Unsteady Aerodynamics
Experiment

Parametric Trends

Program V2.56

MARLEC Blades FI-1

76 sub-runs plotted
exactly 40 revs
in each sub run
derived parameters from
PROFILES

z is yaw angle

Y	--- -37.5
*	-37.5 --- -22.5
x	-22.5 --- -7.5
O	-7.5 --- 7.5
△	7.5 --- 22.5
◇	22.5 --- 37.5
□	37.5 --- 52.5
✦	52.5 ---

TREND.DAT;136

19-MAR-1990:13:36:08

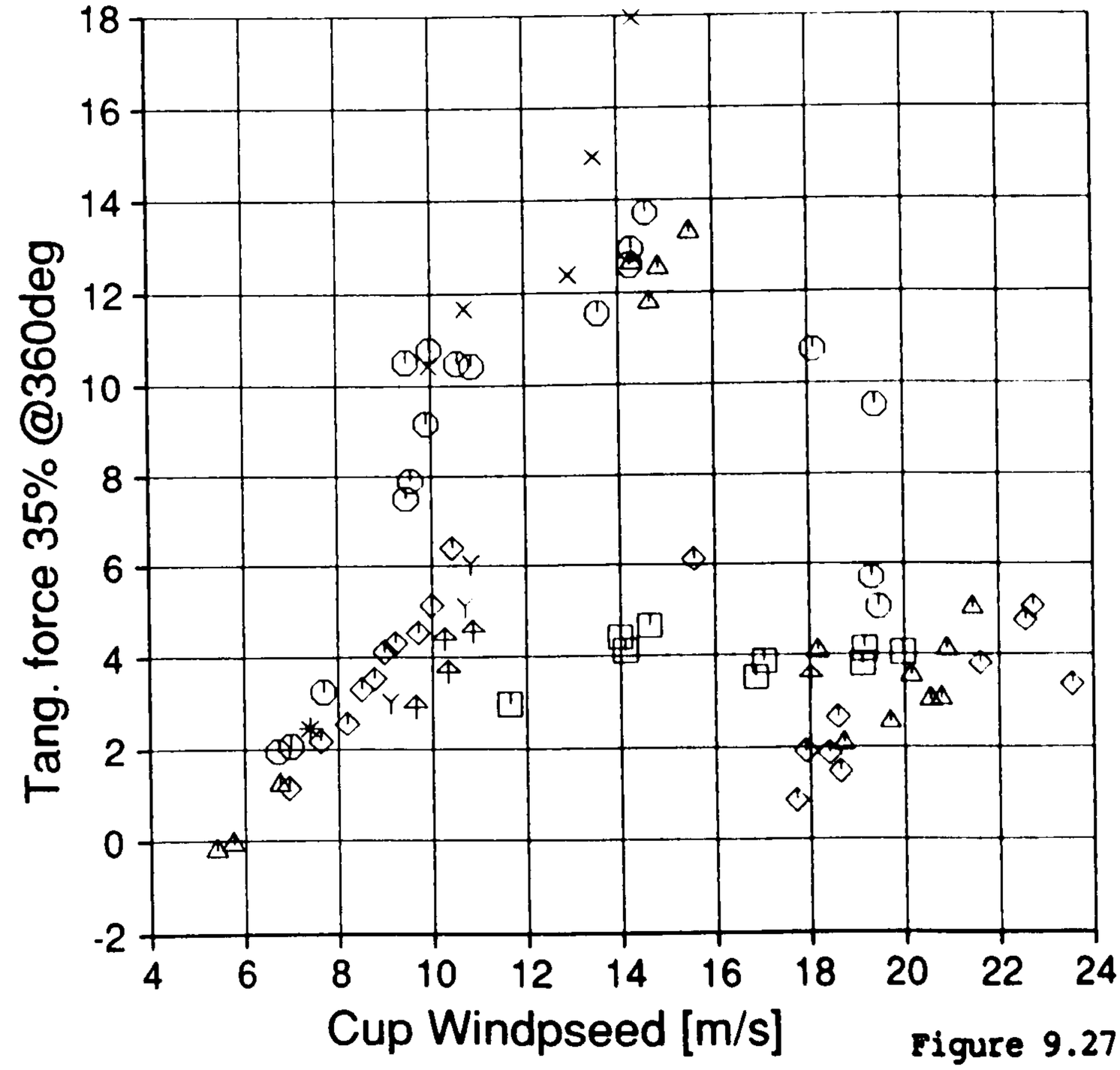

Figure 9.27

Cranfield

HAWT
Unsteady Aerodynamics
Experiment

Parametric Trends

Program V2.57

MARLEC Blades FI-1

76 sub-runs plotted
exactly 40 revs
in each sub run
derived parameters from
PROFILES

z is yaw angle

Y	--- -37.5
*	-37.5 --- -22.5
x	-22.5 --- -7.5
O	-7.5 --- 7.5
△	7.5 --- 22.5
◇	22.5 --- 37.5
□	37.5 --- 52.5
✦	52.5 ---

TREND.DAT;137

19-MAR-1990:13:36:23

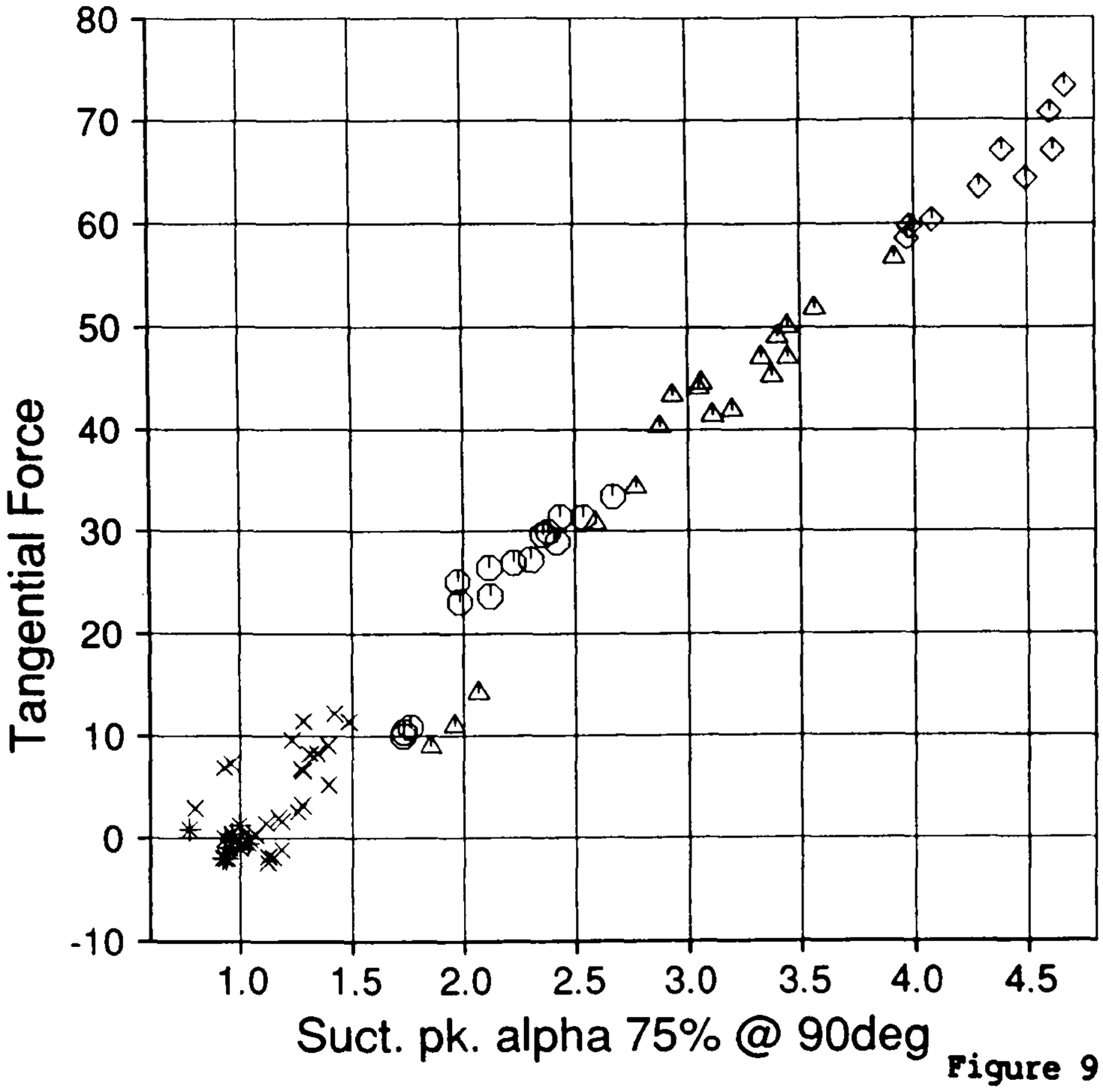

Figure 9.28

Cranfield

HAWT
Unsteady Aerodynamics
Experiment

Parametric Trends

Program V2.20

MARLEC Blades FI-1

76 sub-runs plotted
exactly 40 revs
in each sub run
derived parameters from
PROFILES

z is wind speed

Y	--- 4.0
✱	4.0 --- 8.0
×	8.0 --- 12.0
○	12.0 --- 16.0
△	16.0 --- 20.0
◇	20.0 ---

TREND.DAT;73

7-MAR-1990:12:20:08

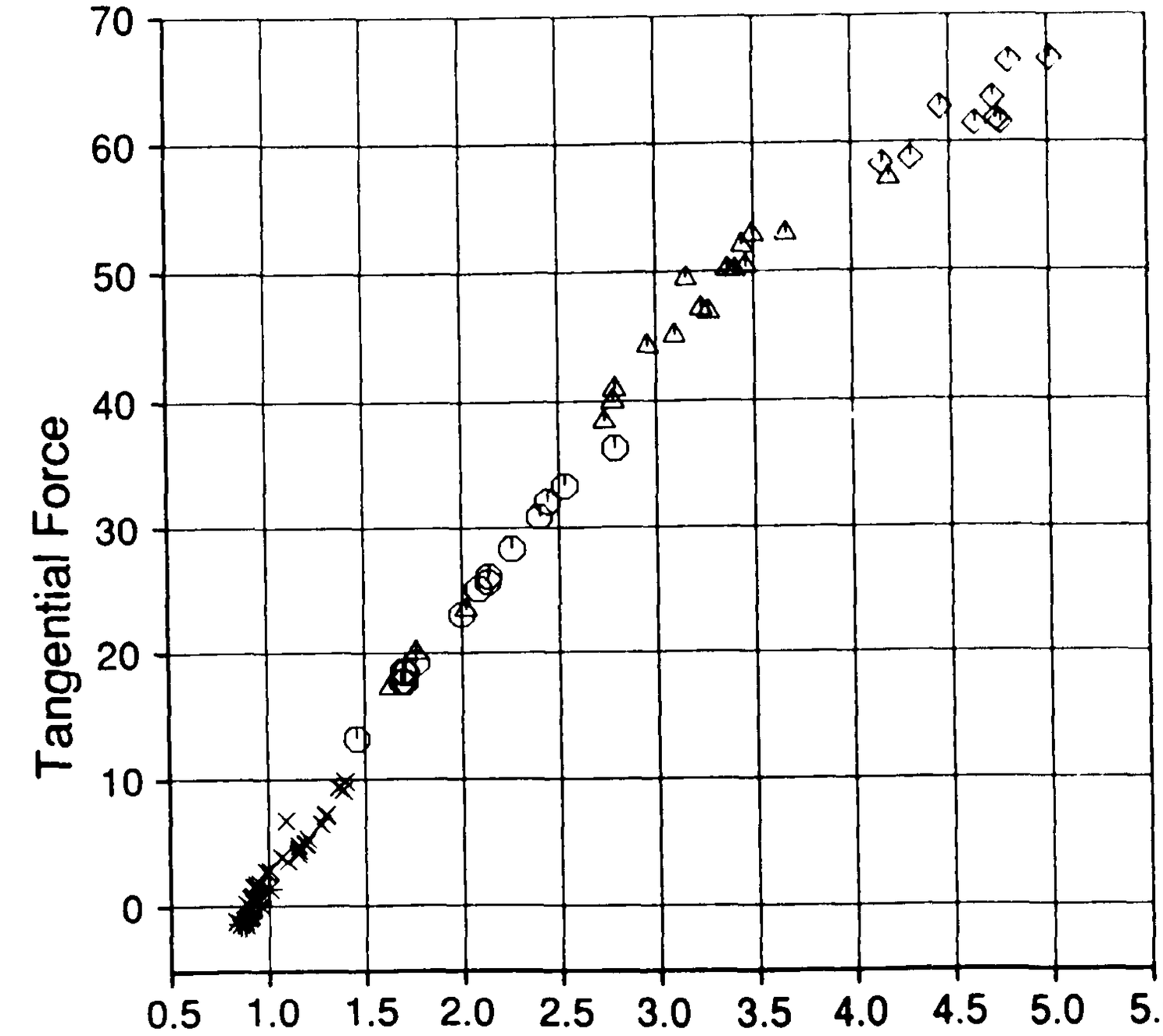

Figure 9.29

Cranfield

HAWT
Unsteady Aerodynamics
Experiment

Parametric Trends

Program V2.14

MARLEC Blades FI-1

76 sub-runs plotted
exactly 40 revs
in each sub run
derived parameters from
PROFILES

z is wind speed

Y	--- 4.0
✱	4.0 --- 8.0
×	8.0 --- 12.0
○	12.0 --- 16.0
△	16.0 --- 20.0
◇	20.0 ---

TREND.DAT;67

1-MAR-1990:11:08:44

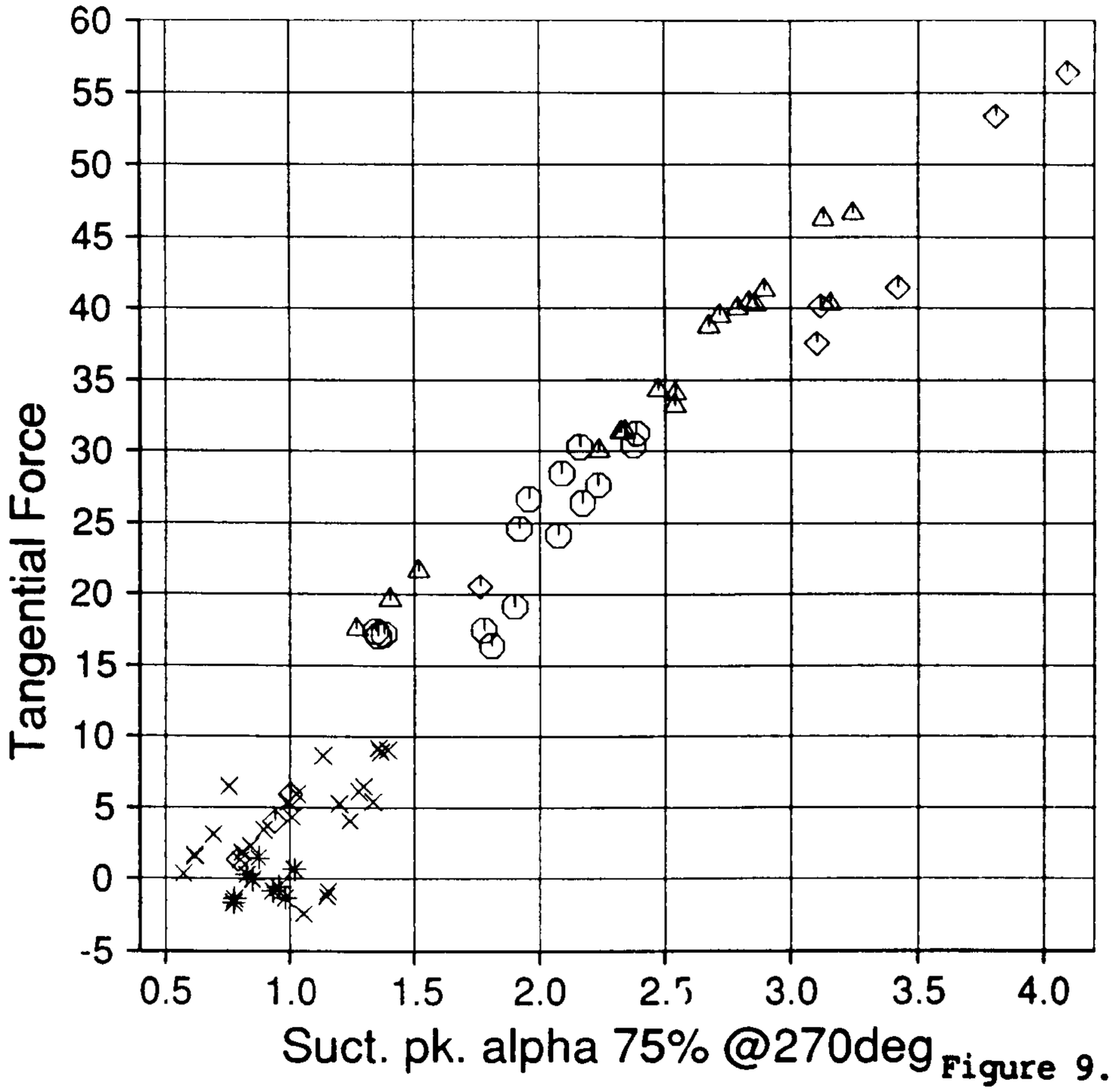

Figure 9.30

Cranfield

HAWT
Unsteady Aerodynamics
Experiment

Parametric Trends

Program V2.37

MARLEC Blades FI-1

76 sub-runs plotted
exactly 40 revs
in each sub run
derived parameters from
PROFILES

z is wind speed

Y	--- 4.0
*	4.0 --- 8.0
×	8.0 --- 12.0
◯	12.0 --- 16.0
△	16.0 --- 20.0
◇	20.0 ---

TREND.DAT;109

19-MAR-1990: 9:30:36

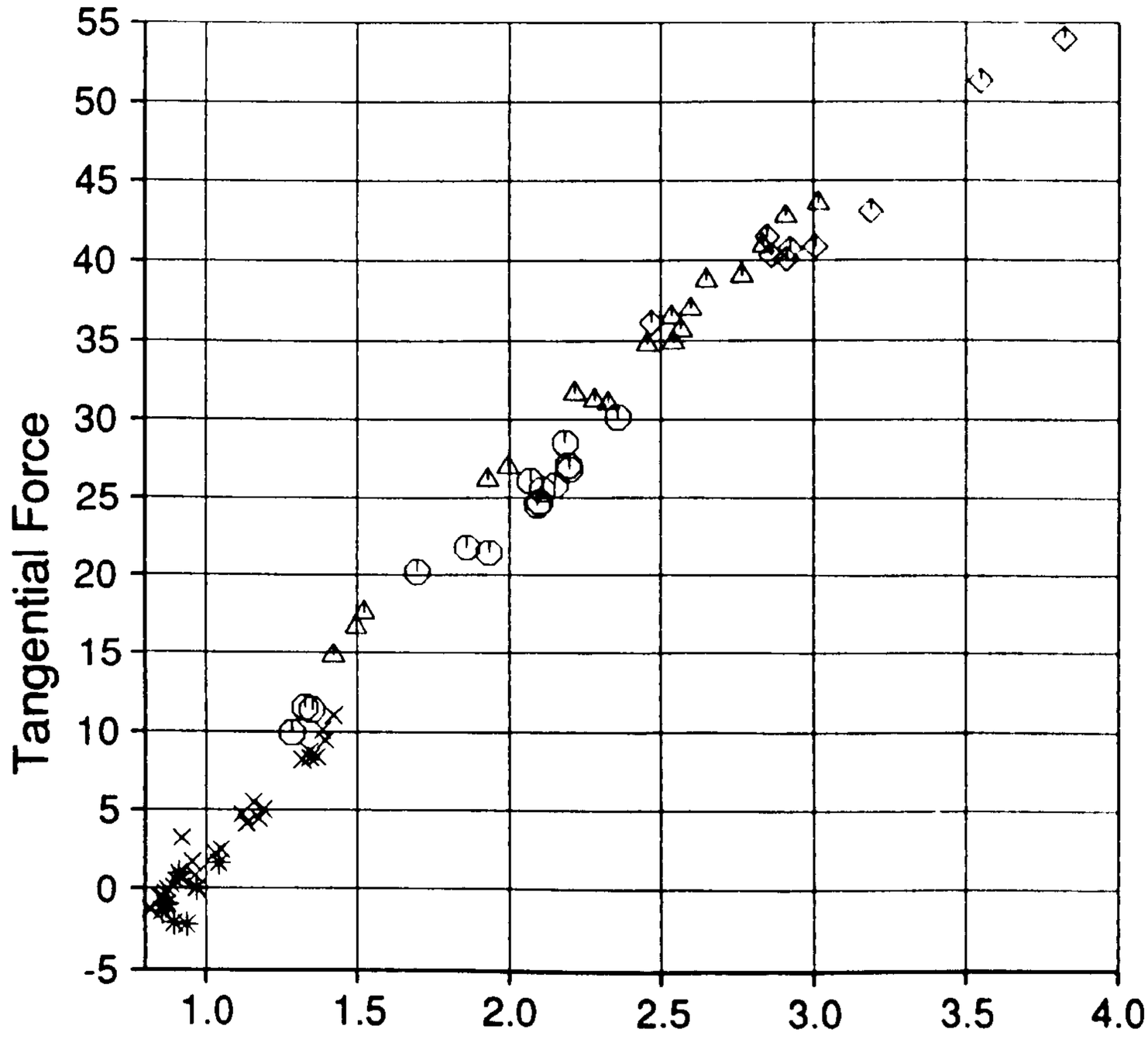

Figure 9.31

Cranfield

HAWT
Unsteady Aerodynamics
Experiment

Parametric Trends

Program V2.39

MARLEC Blades FI-1

76 sub-runs plotted
exactly 40 revs
in each sub run
derived parameters from
PROFILES

z is wind speed

Y	--- 4.0
*	4.0 --- 8.0
×	8.0 --- 12.0
◯	12.0 --- 16.0
△	16.0 --- 20.0
◇	20.0 ---

TREND.DAT;111

19-MAR-1990: 9:32:16

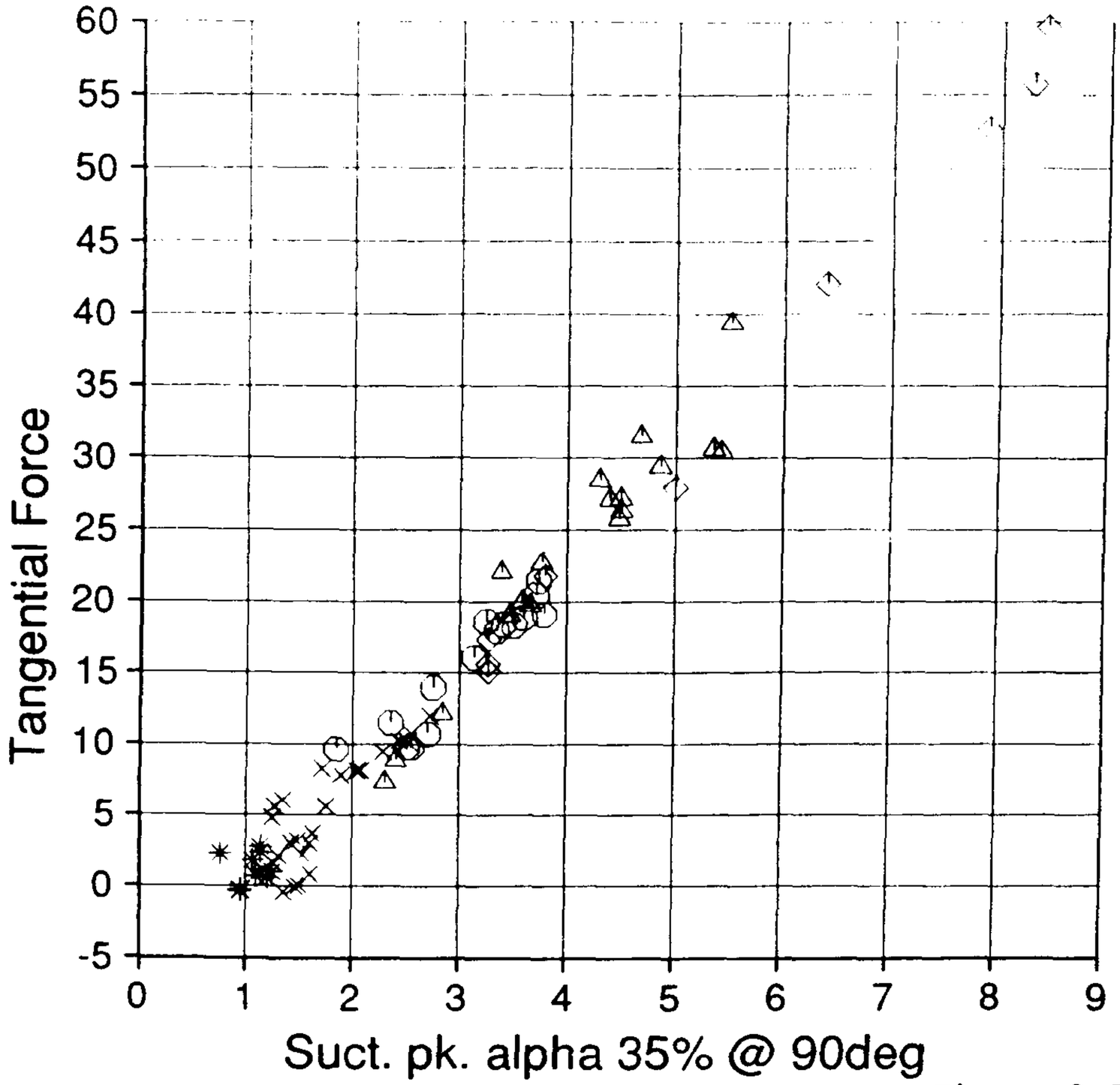

Figure 9.32

Cranfield

HAWT
Unsteady Aerodynamics
Experiment

Parametric Trends

Program V2.26

MARLEC Blades FI-1

76 sub-runs plotted
exactly 40 revs
in each sub run
derived parameters from
PROFILES

z is wind speed

Y	--- 4.0
✱	4.0 --- 8.0
×	8.0 --- 12.0
⏲	12.0 --- 16.0
△	16.0 --- 20.0
◇	20.0 ---

TREND.DAT;79

7-MAR-1990:12:24:47

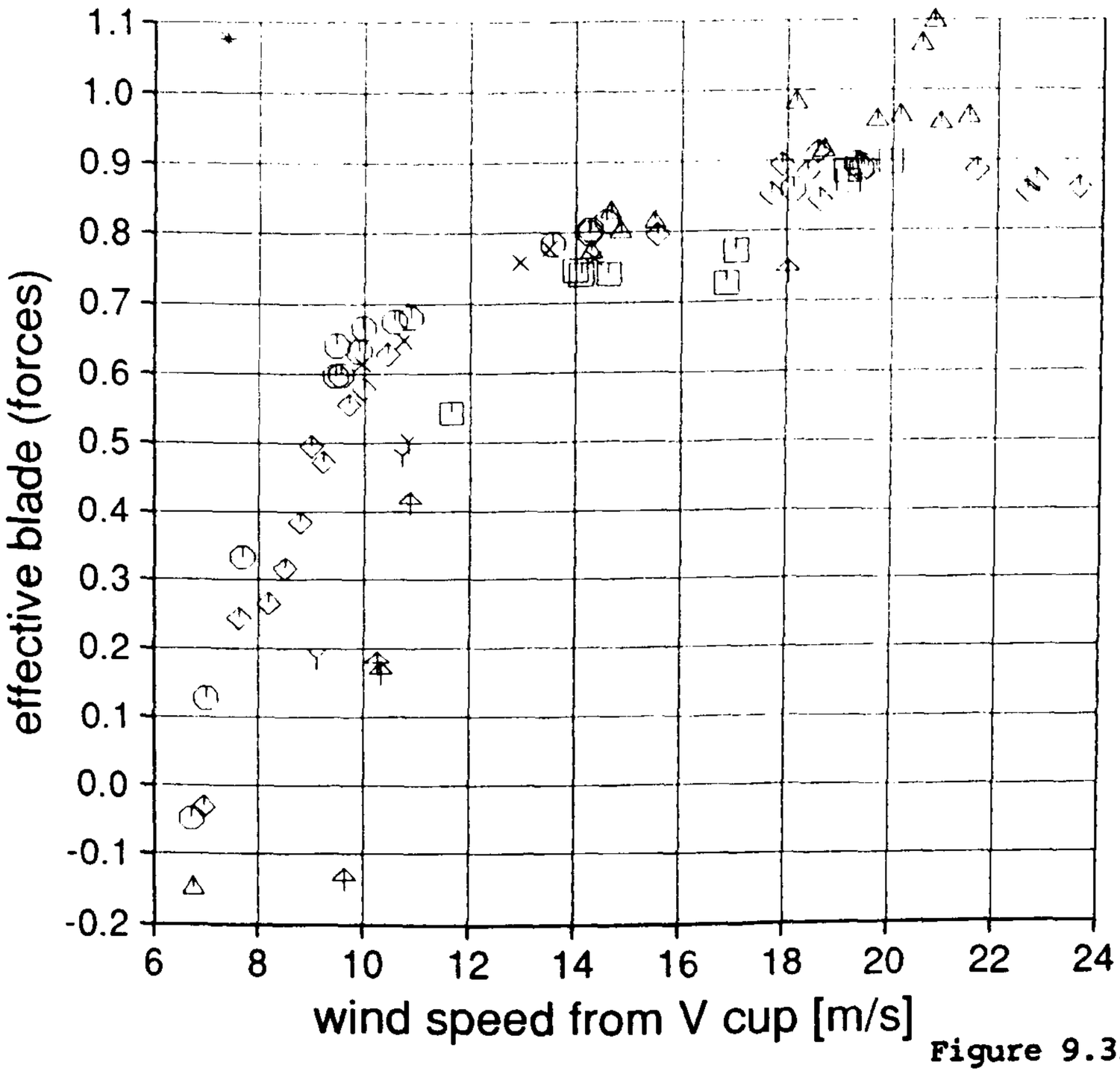

Figure 9.33

Cranfield

HAWT
Unsteady Aerodynamics
Experiment

Parametric Trends

Program V6.08

MARLEC Blades FI-1

74 sub-runs plotted
exactly 40 revs
in each sub run
derived parameters from
WINDY
FORCE

z is yaw angle

Y	--- -37.5
✱	-37.5 --- -22.5
×	-22.5 --- -7.5
⏲	-7.5 --- 7.5
△	7.5 --- 22.5
◇	22.5 --- 37.5
⏍	37.5 --- 52.5
⏃	52.5 ---

TREND.DAT;21

16-FEB-1990:20:20:30

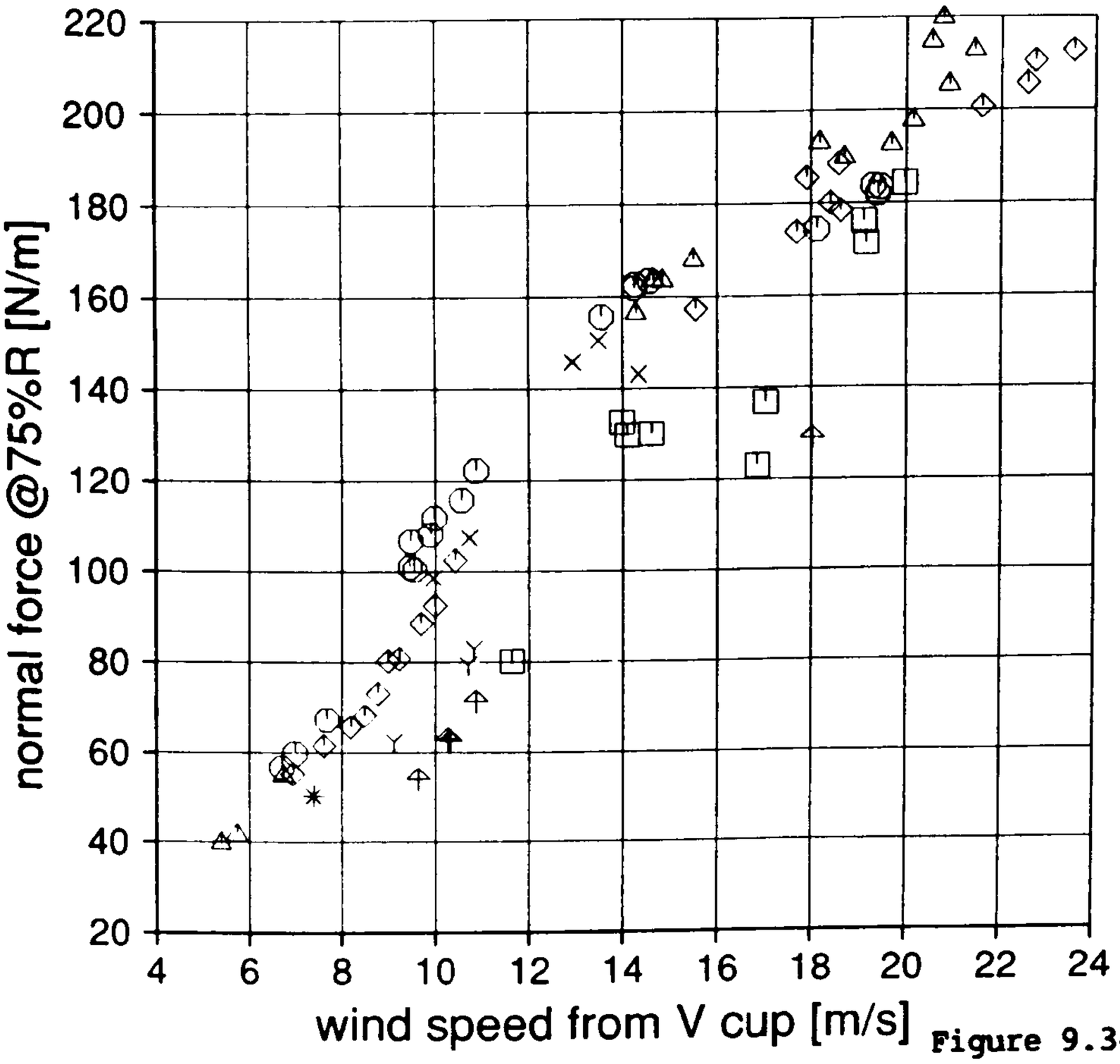

Cranfield

HAWT
Unsteady Aerodynamics
Experiment

Parametric Trends

Program V6.20

MARLEC Blades FI-1

76 sub-runs plotted
exactly 40 revs
in each sub run
derived parameters from
WINDY
FORCE

z is yaw angle

Y	--- -37.5
*	-37.5 --- -22.5
×	-22.5 --- -7.5
○	-7.5 --- 7.5
△	7.5 --- 22.5
◇	22.5 --- 37.5
□	37.5 --- 52.5
⏚	52.5 ---

TREND.DAT;125

19-MAR-1990:12:56:29

Figure 9.34

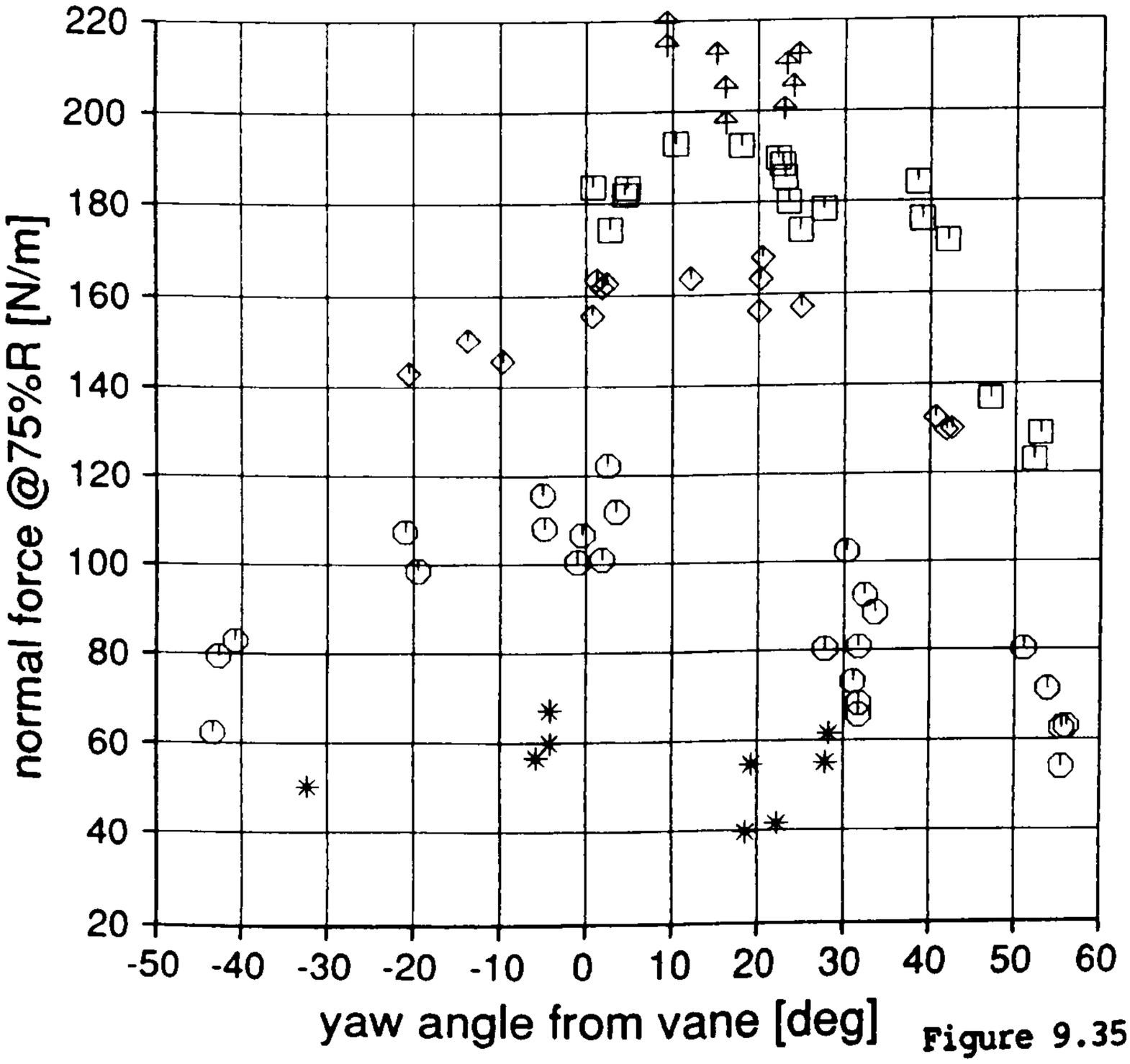

Cranfield

HAWT
Unsteady Aerodynamics
Experiment

Parametric Trends

Program V6.23

MARLEC Blades FI-1

76 sub-runs plotted
exactly 40 revs
in each sub run
derived parameters from
WINDY
FORCE

z is wind speed

Y	--- 4.0
*	4.0 --- 8.0
○	8.0 --- 12.0
◇	12.0 --- 16.0
□	16.0 --- 20.0
⏚	20.0 ---

TREND.DAT;128

19-MAR-1990:13:07:50

Figure 9.35

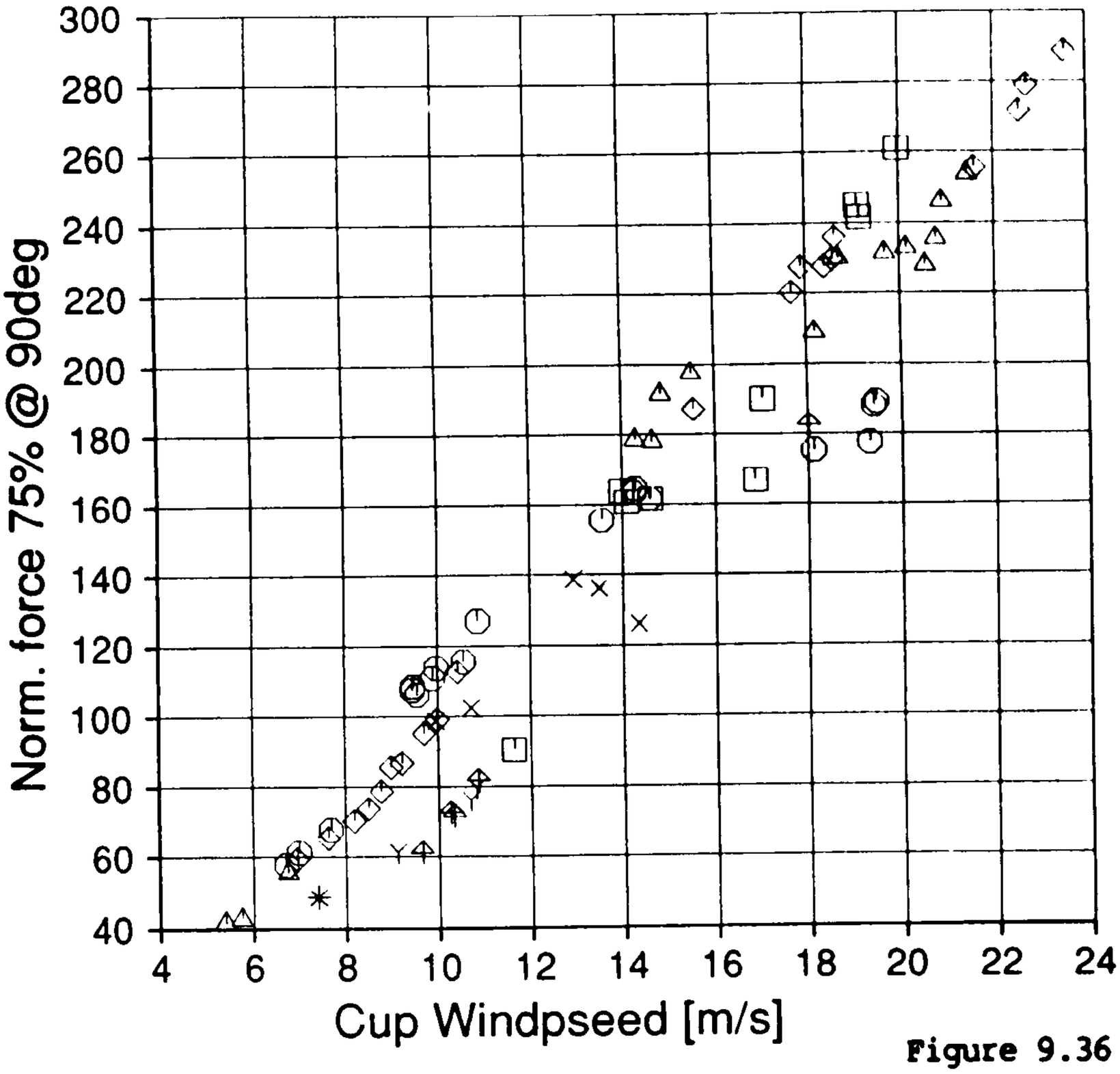

Cranfield

HAWT
Unsteady Aerodynamics
Experiment

Parametric Trends

Program V2.58

MARLEC Blades FI-1

76 sub-runs plotted
exactly 40 revs
in each sub run
derived parameters from
PROFILES

z is yaw angle

Y	--- -37.5
*	-37.5 --- -22.5
x	-22.5 --- -7.5
○	-7.5 --- 7.5
△	7.5 --- 22.5
◇	22.5 --- 37.5
□	37.5 --- 52.5
↑	52.5 ---

TREND.DAT;138

19-MAR-1990:13:36:41

Figure 9.36

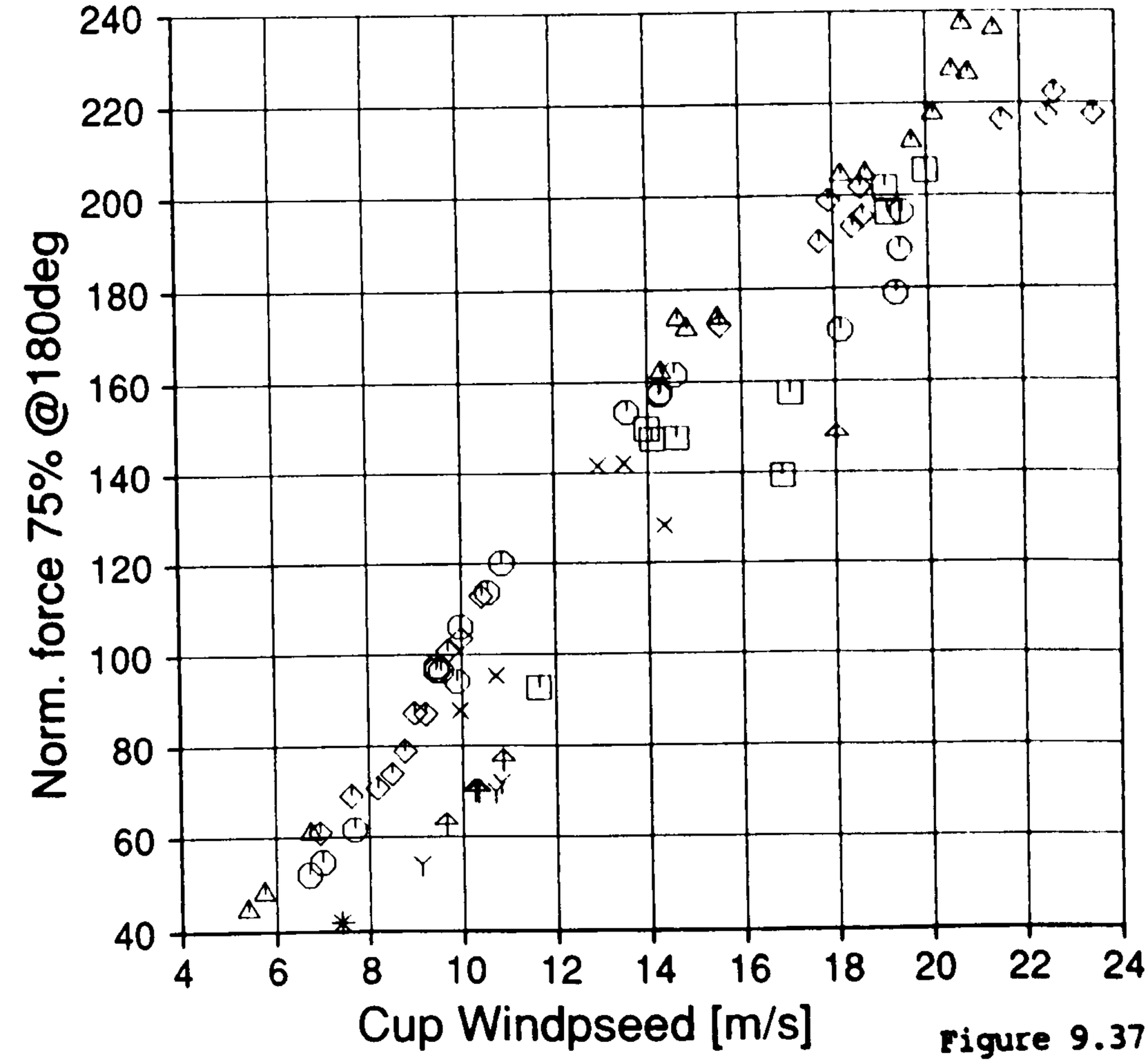

Cranfield

HAWT
Unsteady Aerodynamics
Experiment

Parametric Trends

Program V2.59

MARLEC Blades FI-1

76 sub-runs plotted
exactly 40 revs
in each sub run
derived parameters from
PROFILES

z is yaw angle

Y	--- -37.5
*	-37.5 --- -22.5
x	-22.5 --- -7.5
○	-7.5 --- 7.5
△	7.5 --- 22.5
◇	22.5 --- 37.5
□	37.5 --- 52.5
↑	52.5 ---

TREND.DAT;139

19-MAR-1990:13:36:59

Figure 9.37

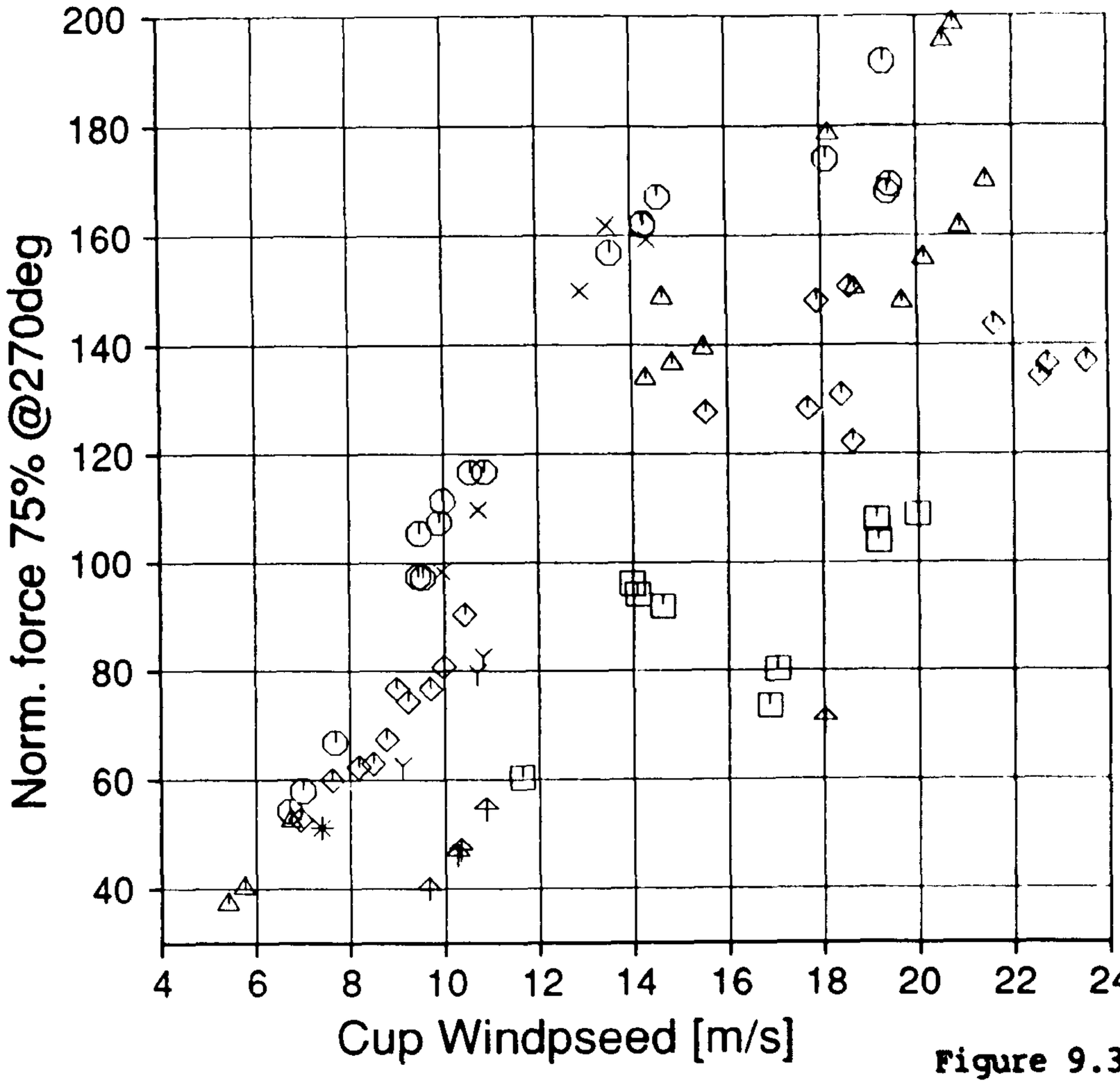

Cranfield

HAWT
Unsteady Aerodynamics
Experiment

Parametric Trends

Program V2.60

MARLEC Blades FI-1

76 sub-runs plotted
exactly 40 revs
in each sub run
derived parameters from
PROFILES

z is yaw angle

Y	--- -37.5
*	-37.5 --- -22.5
x	-22.5 --- -7.5
○	-7.5 --- 7.5
△	7.5 --- 22.5
◇	22.5 --- 37.5
□	37.5 --- 52.5
↑	52.5 ---

TREND.DAT;140

19-MAR-1990:13:37:15

Figure 9.38

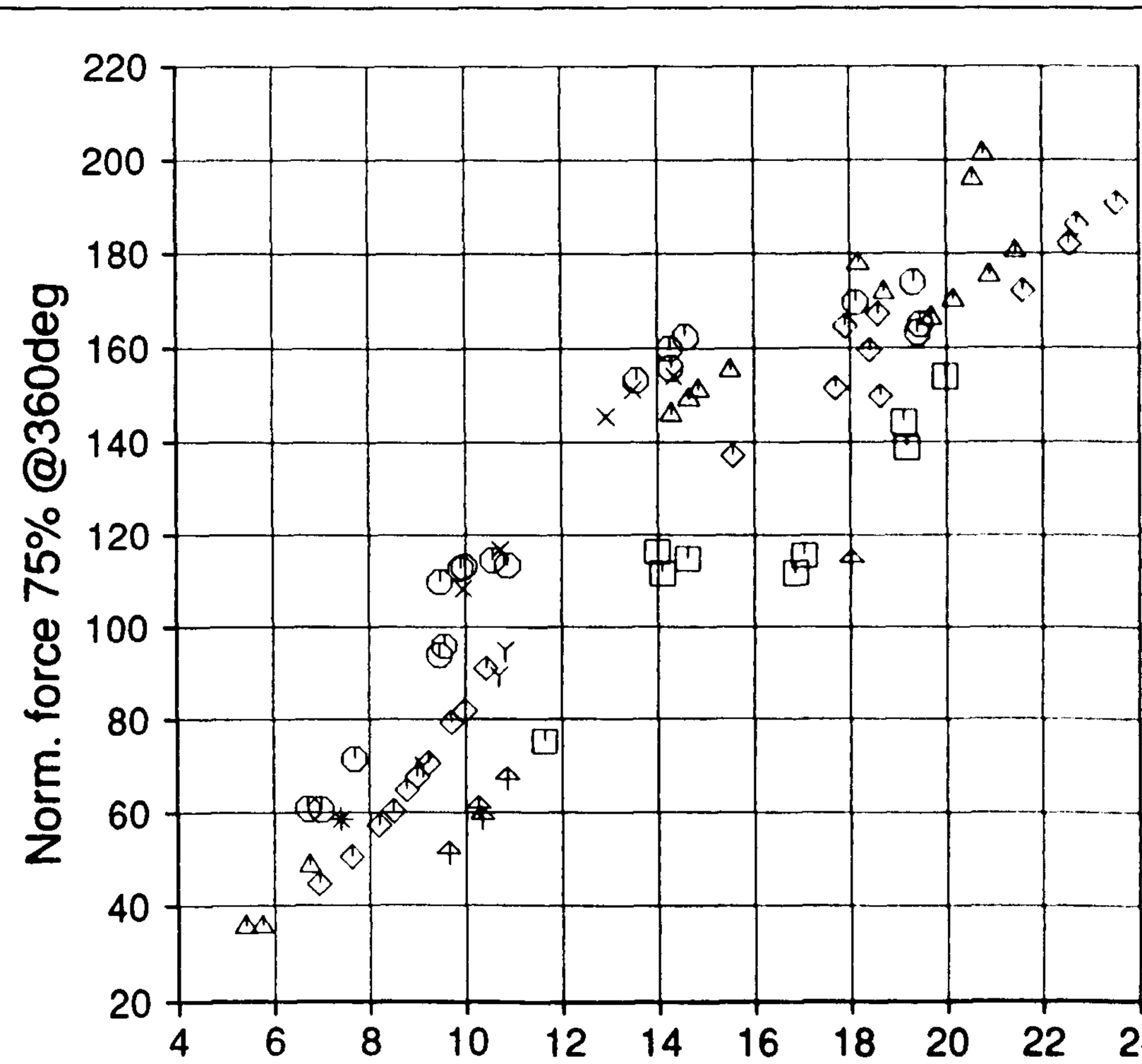

Cranfield

HAWT
Unsteady Aerodynamics
Experiment

Parametric Trends

Program V2.61

MARLEC Blades FI-1

76 sub-runs plotted
exactly 40 revs
in each sub run
derived parameters from
PROFILES

z is yaw angle

Y	--- -37.5
*	-37.5 --- -22.5
x	-22.5 --- -7.5
○	-7.5 --- 7.5
△	7.5 --- 22.5
◇	22.5 --- 37.5
□	37.5 --- 52.5
↑	52.5 ---

TREND.DAT;141

19-MAR-1990:13:37:28

Figure 9.39

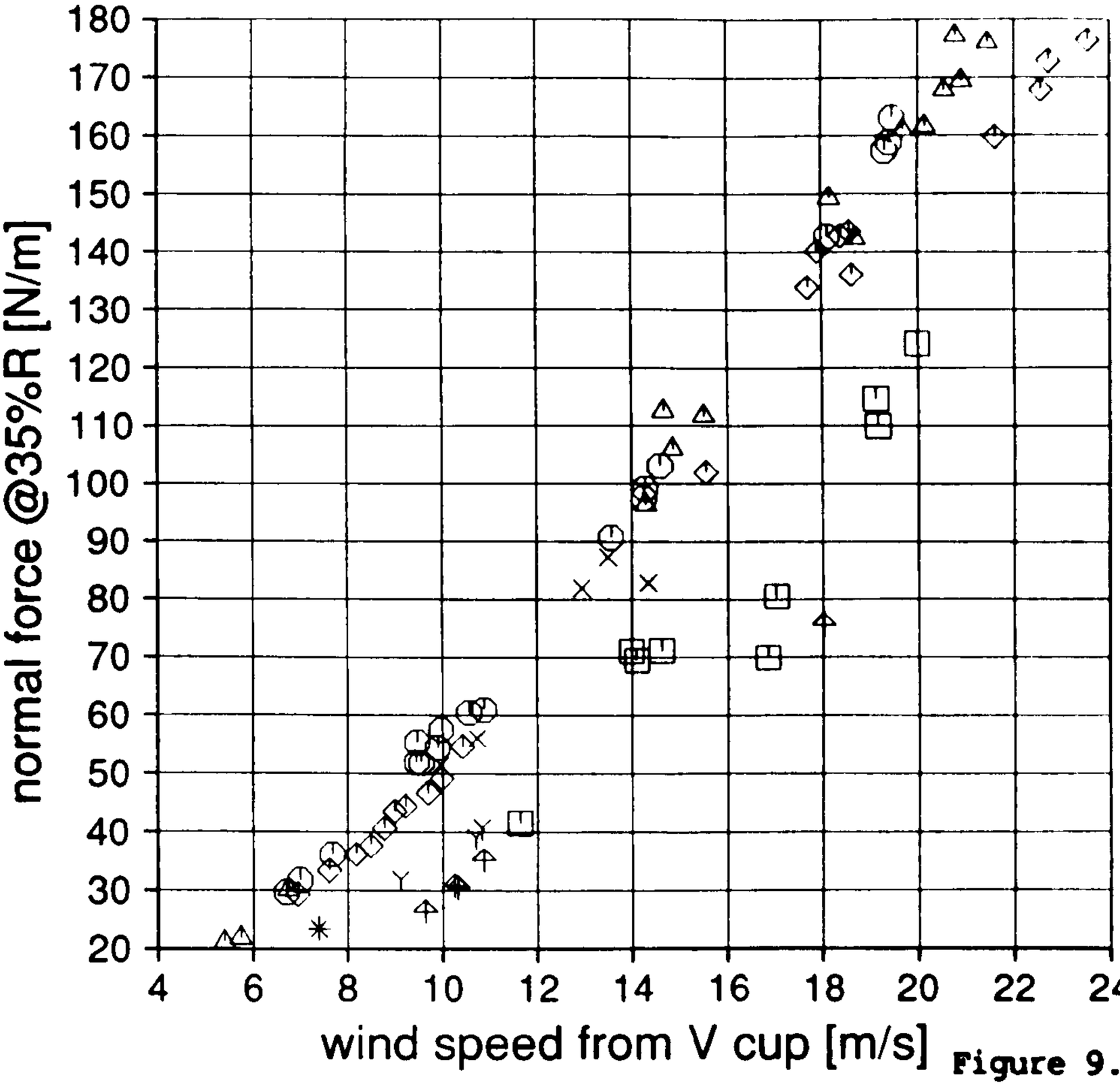

Figure 9.40

Cranfield

HAWT
Unsteady Aerodynamics
Experiment

Parametric Trends

Program V6.20

MARLEC Blades FI-1

76 sub-runs plotted
exactly 40 revs
in each sub run
derived parameters from
WINDY
FORCE

z is yaw angle

Y	--- -37.5
*	-37.5 --- -22.5
x	-22.5 --- -7.5
O	-7.5 --- 7.5
△	7.5 --- 22.5
◇	22.5 --- 37.5
□	37.5 --- 52.5
⚘	52.5 ---

TREND.DAT;126

19-MAR-1990:13:02:38

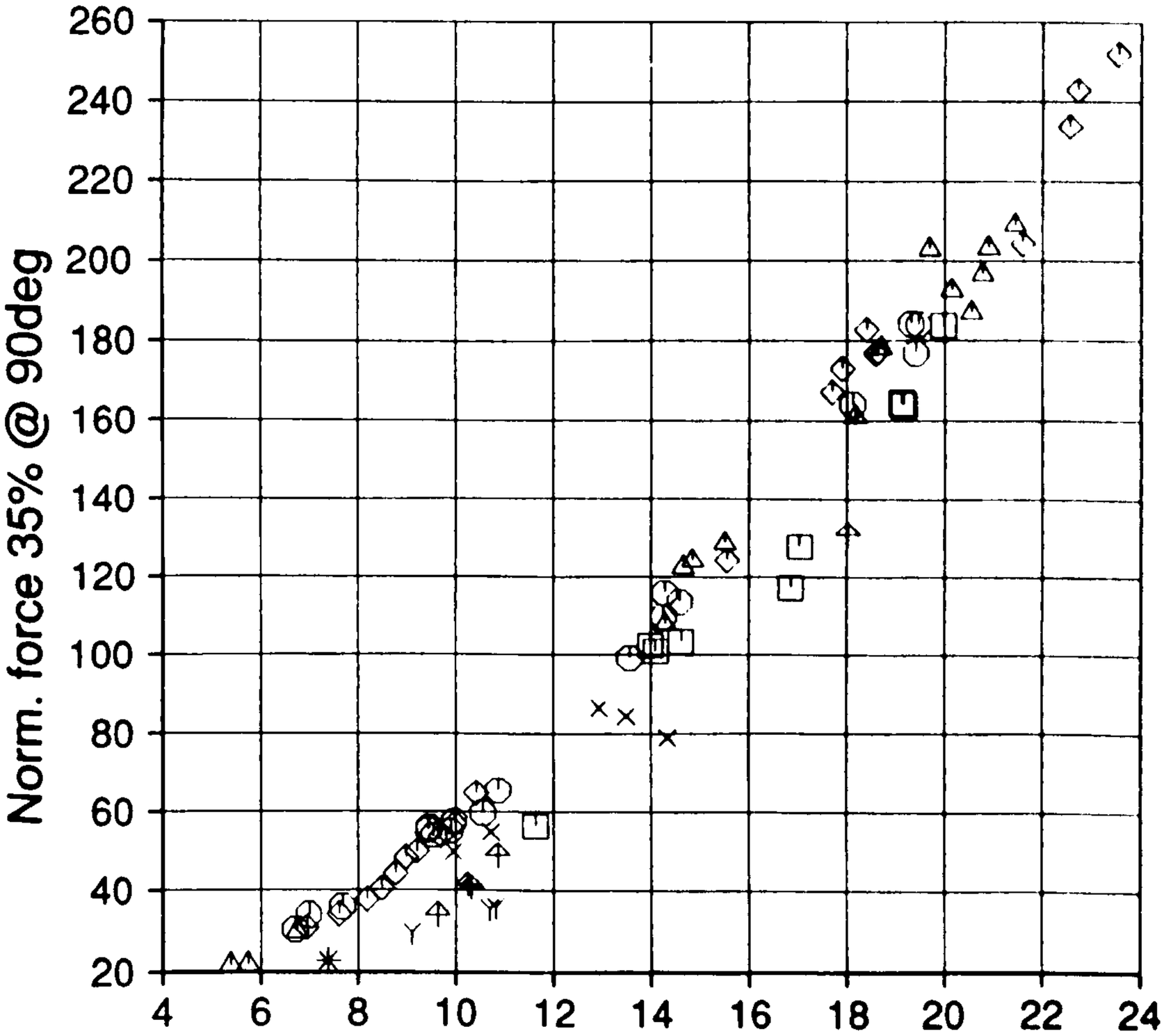

Figure 9.41

Cranfield

HAWT
Unsteady Aerodynamics
Experiment

Parametric Trends

Program V2.50

MARLEC Blades FI-1

76 sub-runs plotted
exactly 40 revs
in each sub run
derived parameters from
PROFILES

z is yaw angle

Y	--- -37.5
*	-37.5 --- -22.5
x	-22.5 --- -7.5
O	-7.5 --- 7.5
△	7.5 --- 22.5
◇	22.5 --- 37.5
□	37.5 --- 52.5
⚘	52.5 ---

TREND.DAT;130

19-MAR-1990:13:30:35

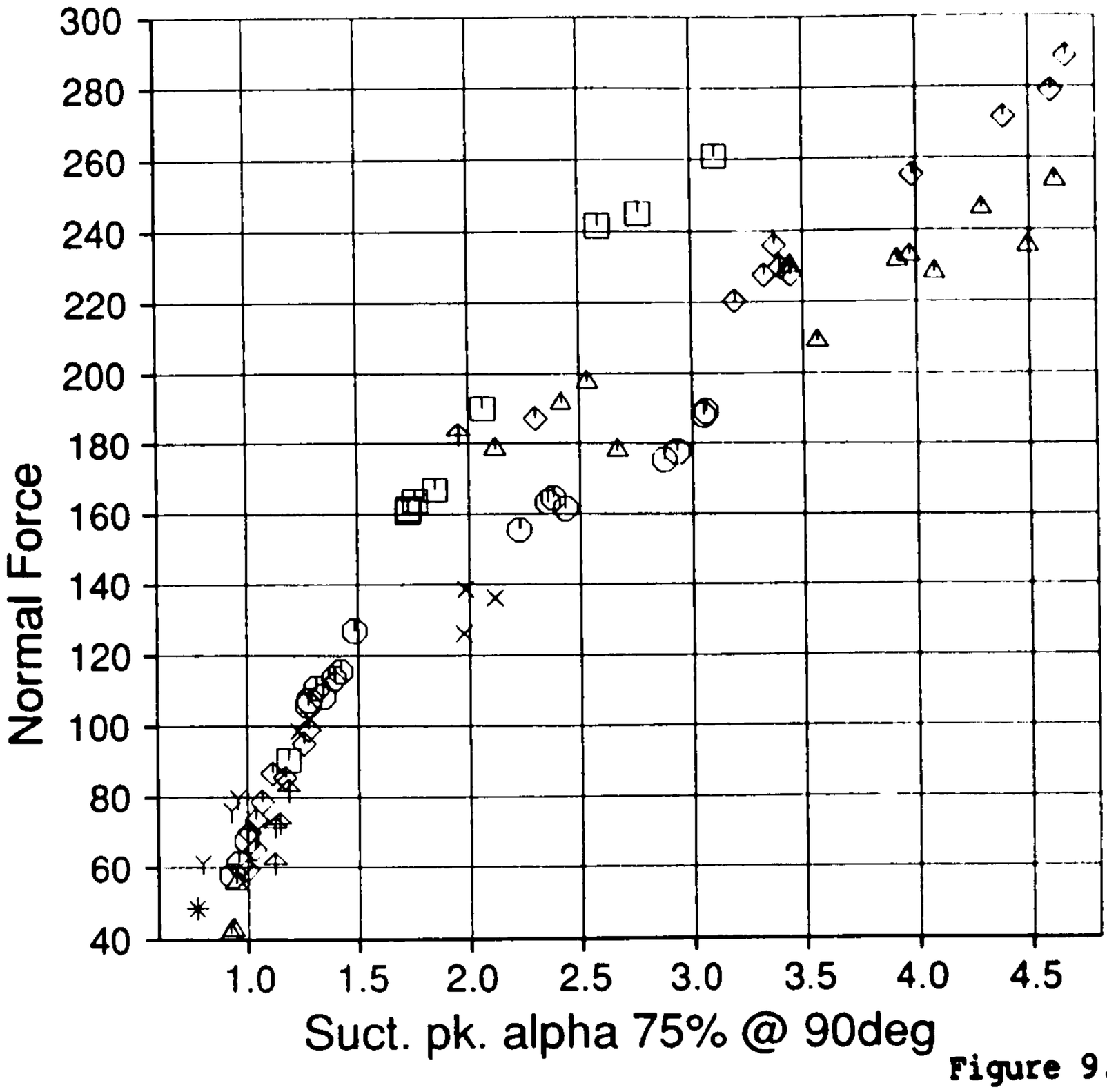

Figure 9.42

Cranfield

HAWT
Unsteady Aerodynamics
Experiment

Parametric Trends

Program V2.19

MARLEC Blades FI-1

76 sub-runs plotted
exactly 40 revs
in each sub run
derived parameters from
PROFILES

z is yaw angle

Y	--- -37.5
*	-37.5 --- -22.5
x	-22.5 --- -7.5
◯	-7.5 --- 7.5
△	7.5 --- 22.5
◇	22.5 --- 37.5
□	37.5 --- 52.5
✦	52.5 ---

TREND.DAT;72

7-MAR-1990:12:19:03

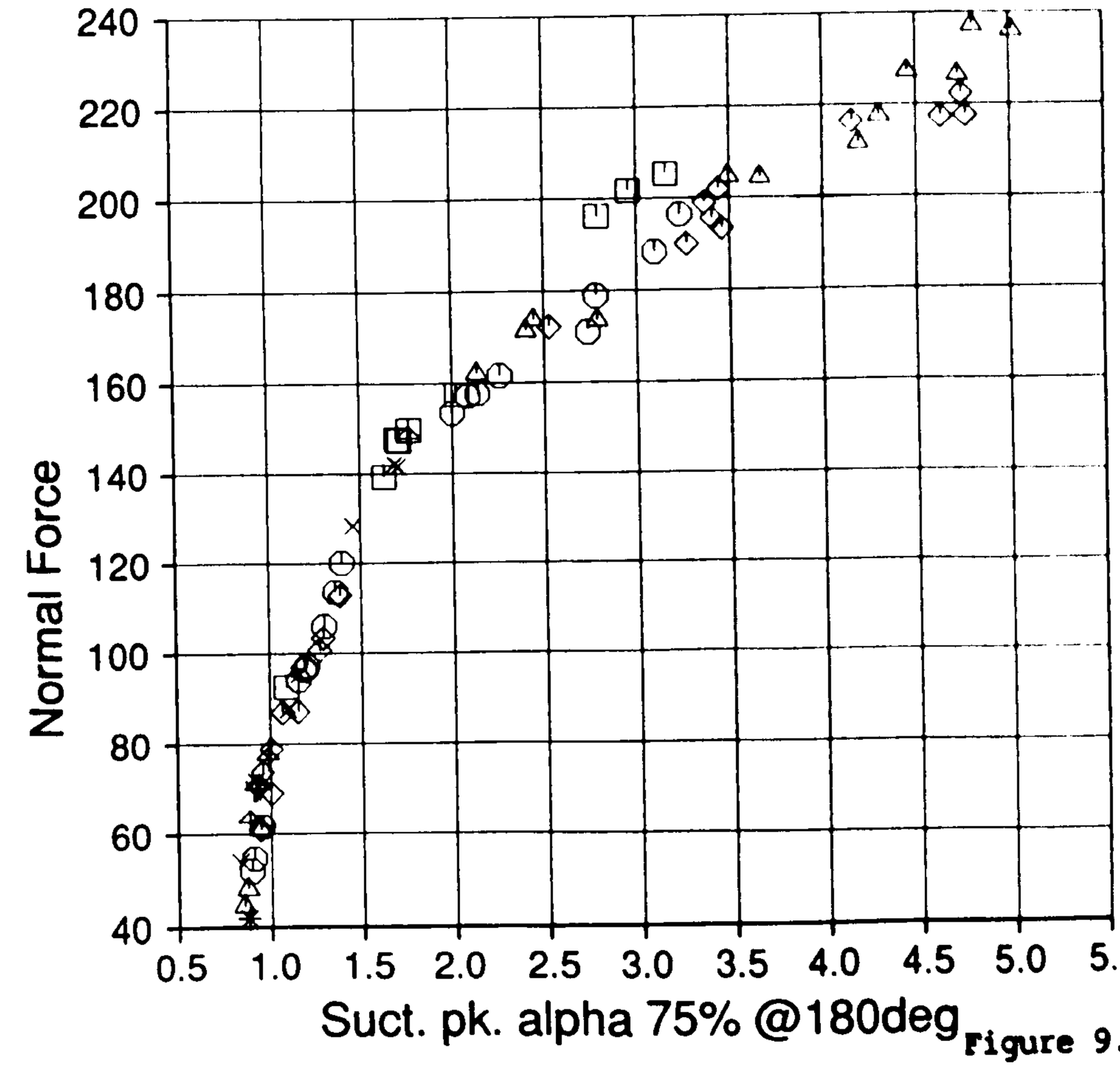

Figure 9.43

Cranfield

HAWT
Unsteady Aerodynamics
Experiment

Parametric Trends

Program V2.15

MARLEC Blades FI-1

76 sub-runs plotted
exactly 40 revs
in each sub run
derived parameters from
PROFILES

z is yaw angle

Y	--- -37.5
*	-37.5 --- -22.5
x	-22.5 --- -7.5
◯	-7.5 --- 7.5
△	7.5 --- 22.5
◇	22.5 --- 37.5
□	37.5 --- 52.5
✦	52.5 ---

TREND.DAT;68

1-MAR-1990:11:09:23

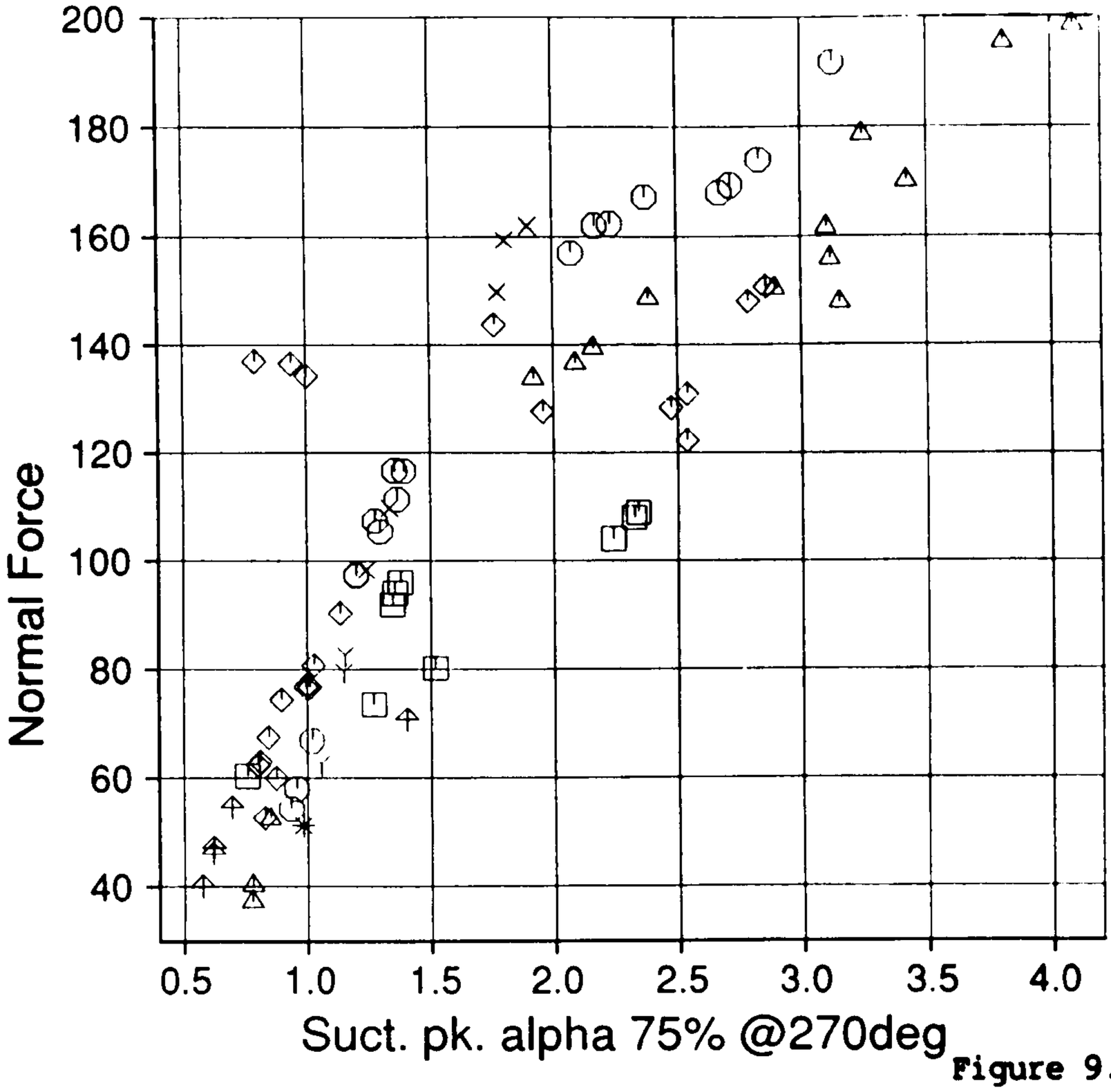

Figure 9.44

Cranfield

HAWT
Unsteady Aerodynamics
Experiment

Parametric Trends

Program V2.30

MARLEC Blades FI-1

76 sub-runs plotted
exactly 40 revs
in each sub run
derived parameters from
PROFILES

z is yaw angle

Y	--- -37.5
*	-37.5 --- -22.5
x	-22.5 --- -7.5
◯	-7.5 --- 7.5
△	7.5 --- 22.5
◇	22.5 --- 37.5
□	37.5 --- 52.5
+	52.5 ---

TREND.DAT;102

19-MAR-1990: 9:16:46

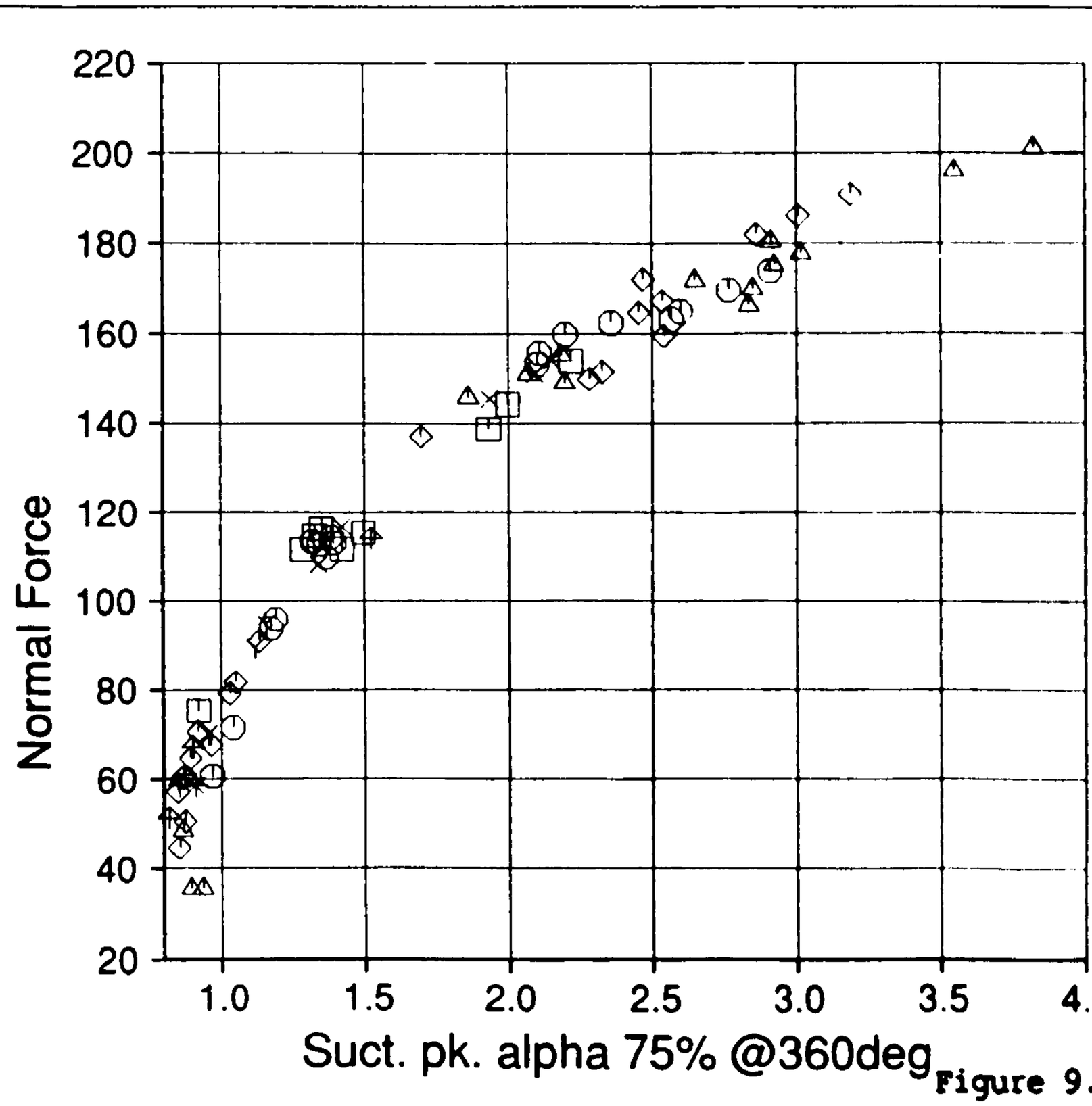

Figure 9.45

Cranfield

HAWT
Unsteady Aerodynamics
Experiment

Parametric Trends

Program V2.32

MARLEC Blades FI-1

76 sub-runs plotted
exactly 40 revs
in each sub run
derived parameters from
PROFILES

z is yaw angle

Y	--- -37.5
*	-37.5 --- -22.5
x	-22.5 --- -7.5
◯	-7.5 --- 7.5
△	7.5 --- 22.5
◇	22.5 --- 37.5
□	37.5 --- 52.5
+	52.5 ---

TREND.DAT;104

19-MAR-1990: 9:23:34

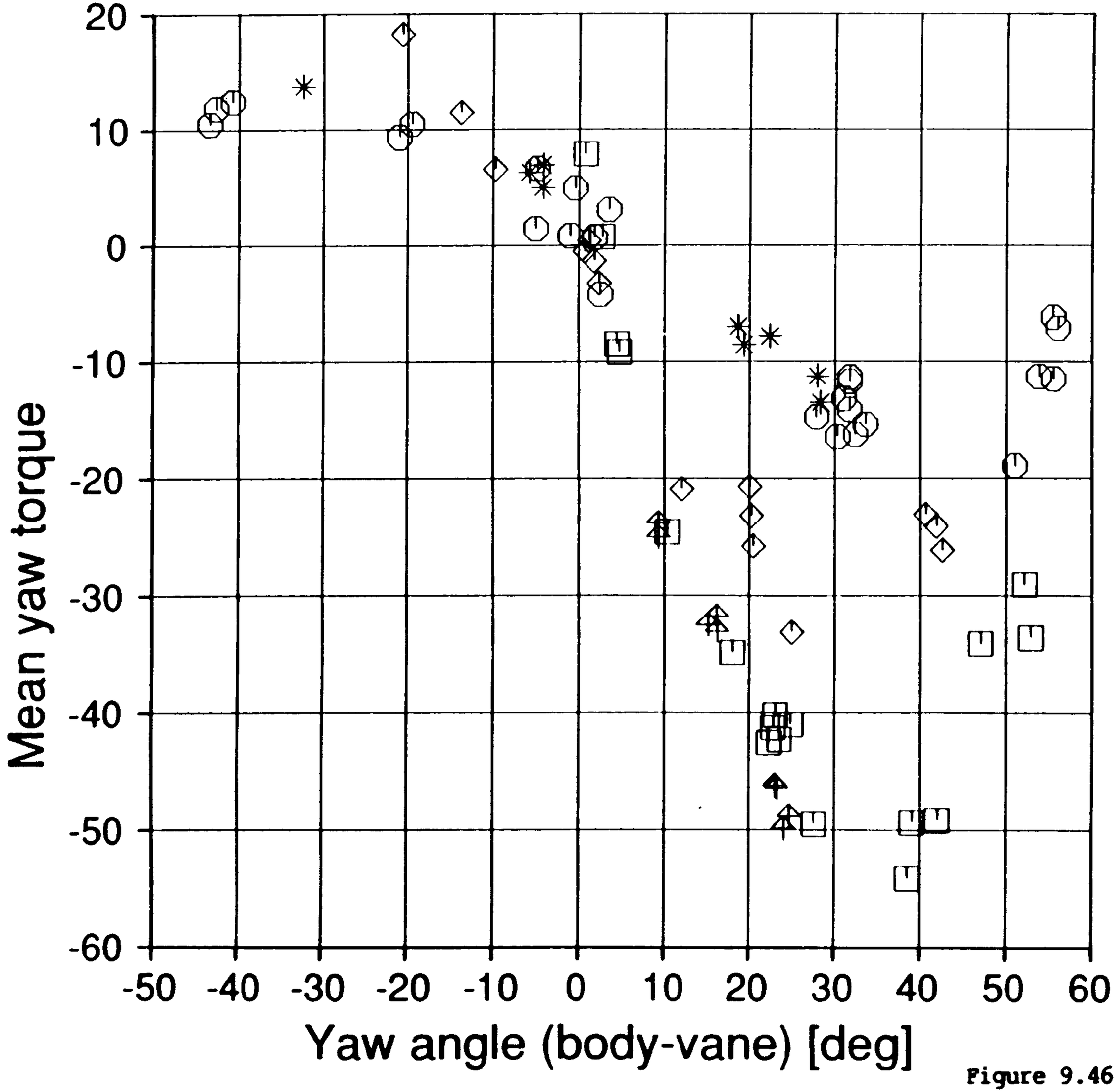

Figure 9.46

Cranfield

HAWT
Unsteady Aerodynamics
Experiment

Parametric Trends

Program V4.09

MARLEC Blades FI-1

76 sub-runs plotted
exactly 40 revs
in each sub run
derived parameters from
WINDY
ROTOR

z is wind speed

Y	--- 4.0
*	4.0 --- 8.0
○	8.0 --- 12.0
◇	12.0 --- 16.0
□	16.0 --- 20.0
↑	20.0 ---

TREND.DAT;119

19-MAR-1990:10:57:22

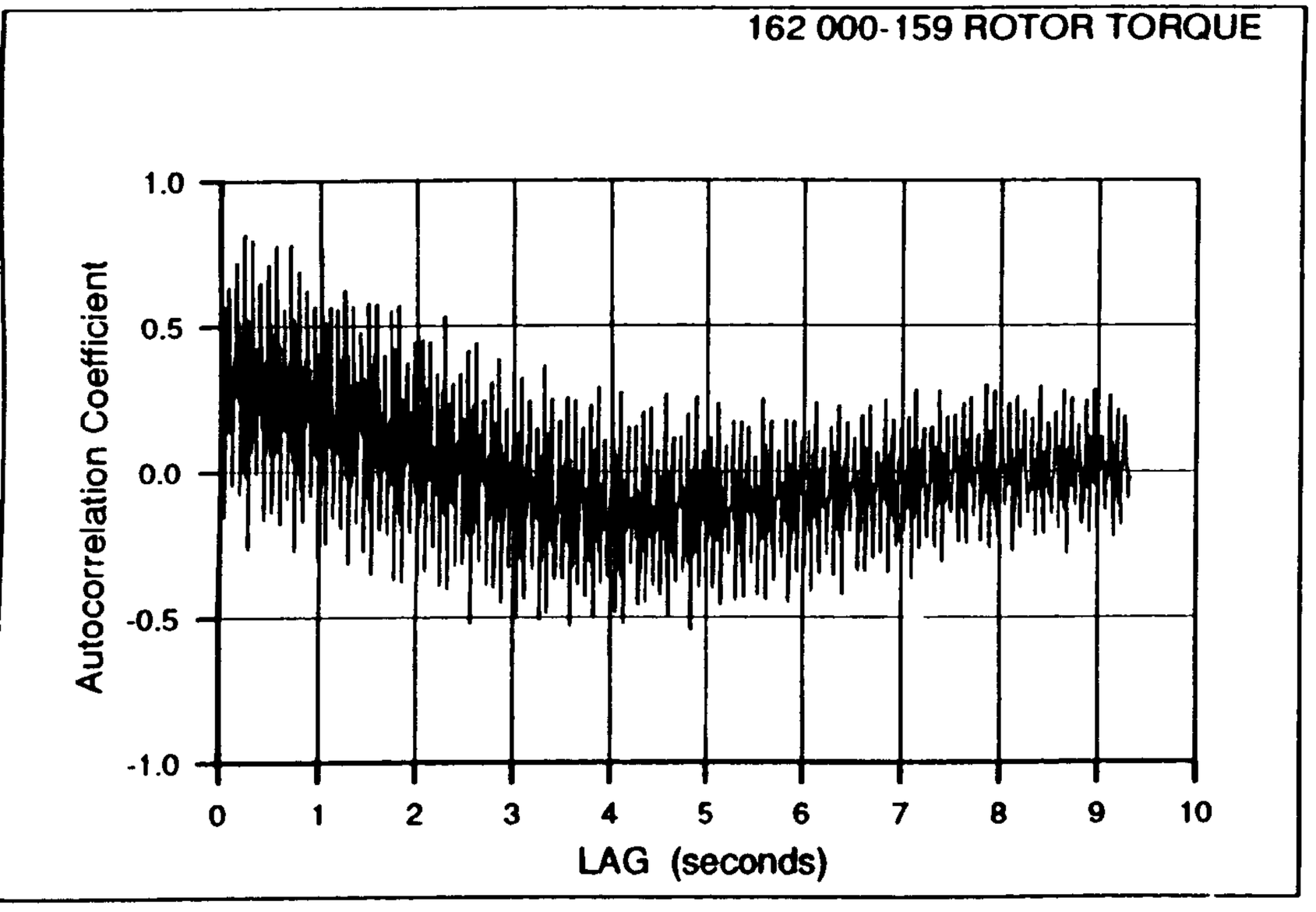
162 000-159 ROTOR TORQUE
Autocorrelation Coefficient
1.0
0.5
0.0
-0.5
-1.0
0
1
2
3
4
5
6
7
8
9
10
LAG (seconds)

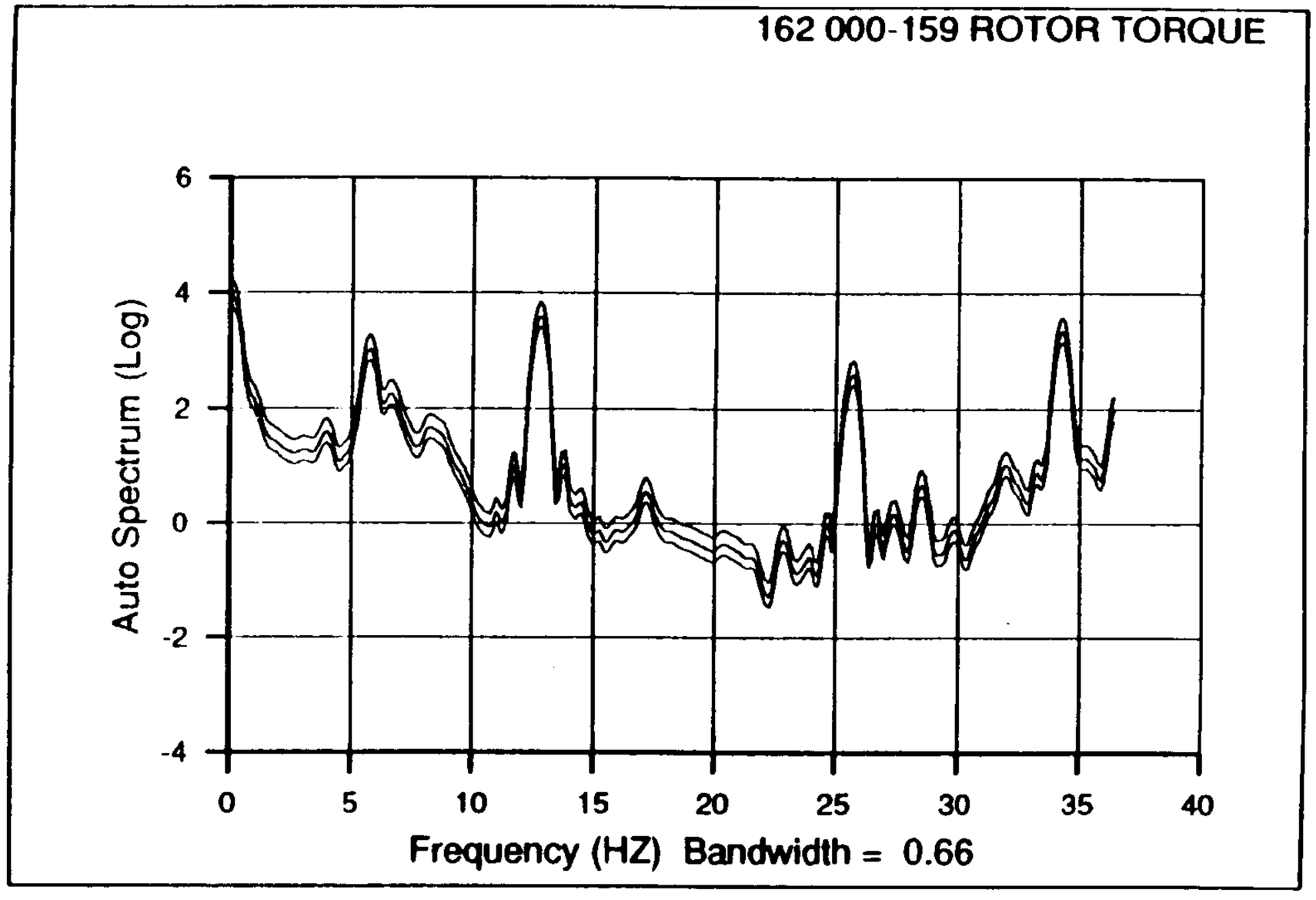
162 000-159 ROTOR TORQUE
Auto Spectrum (Log)
6
4
2
0
-2
-4
0
5
10
15
20
25
30
35
40
Frequency (HZ) Bandwidth = 0.66

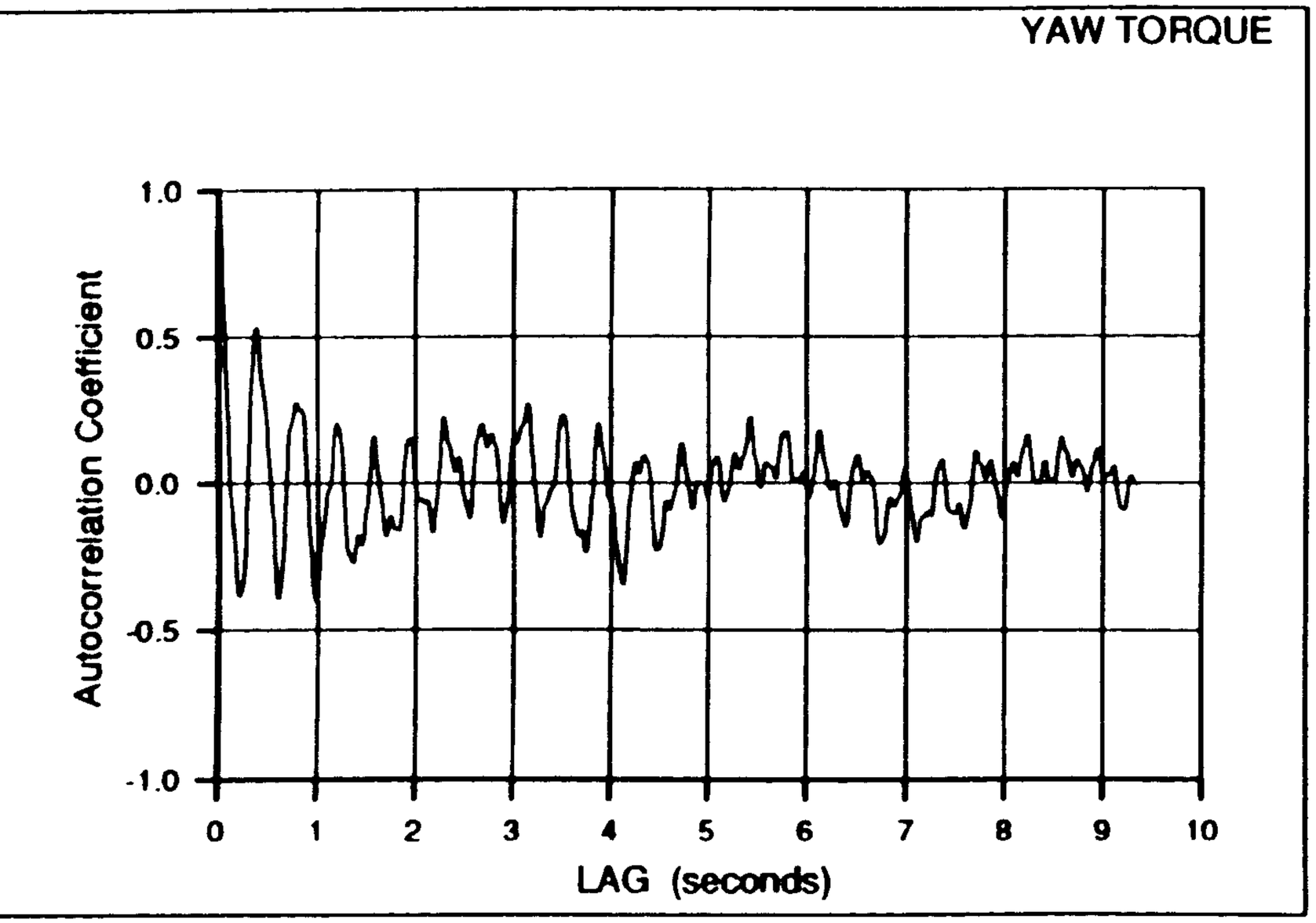
YAW TORQUE
Autocorrelation Coefficient
1.0
0.5
0.0
-0.5
-1.0
0
1
2
3
4
5
6
7
8
9
10
LAG (seconds)

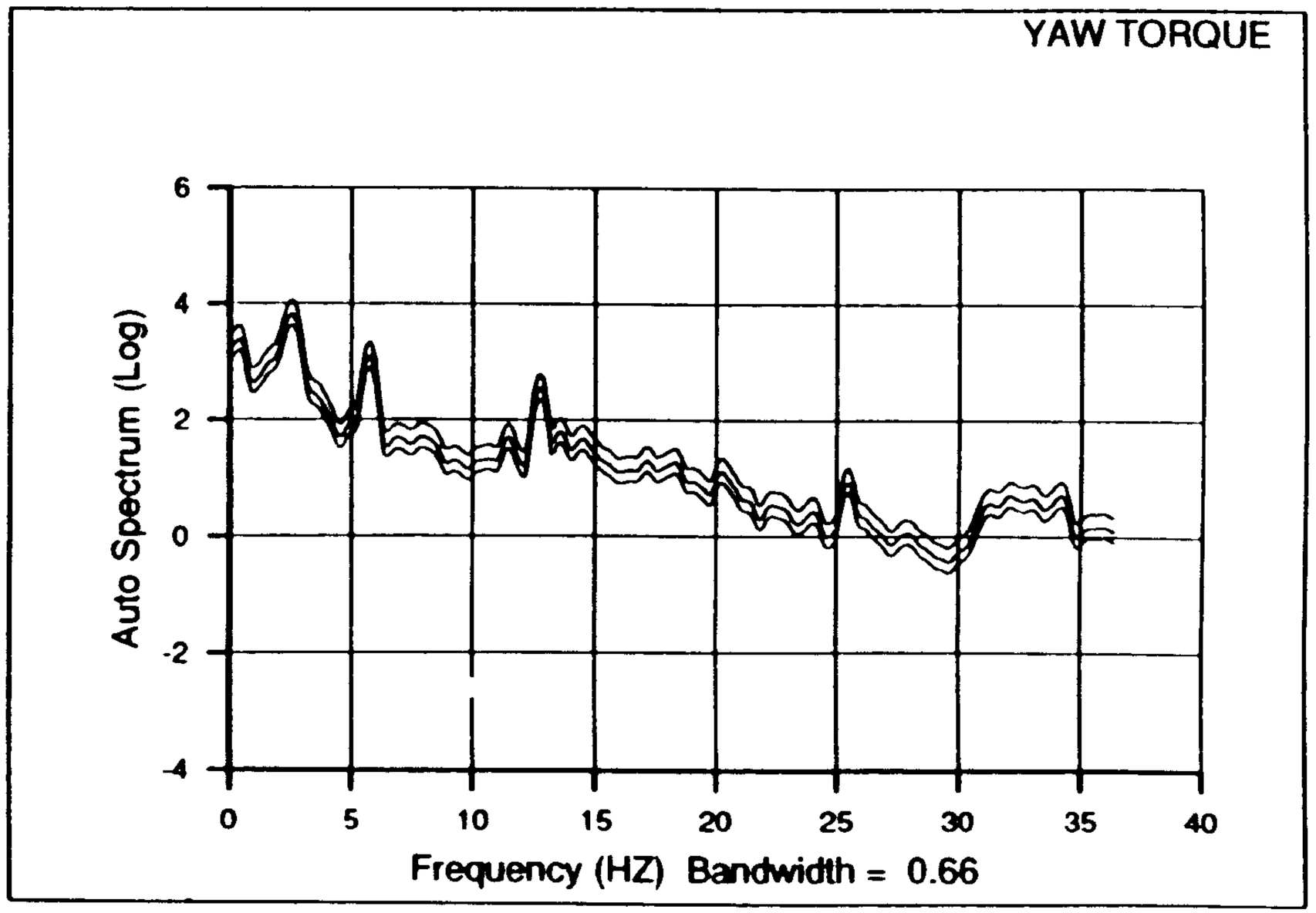
YAW TORQUE
Auto Spectrum (Log)
6
4
2
0
-2
-4
0
5
10
15
20
25
30
35
40
Frequency (HZ) Bandwidth = 0.66

Figure 9.47

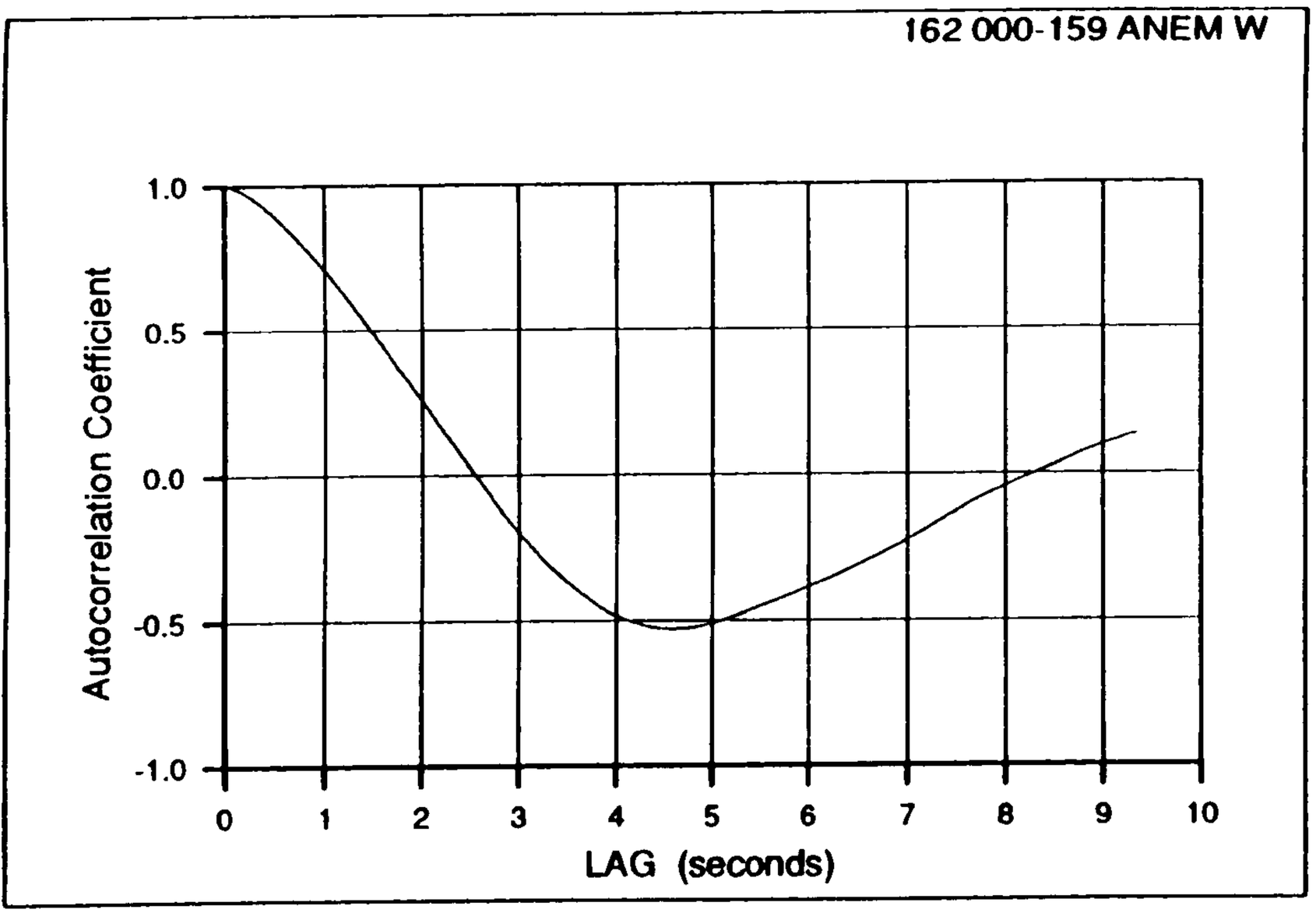
162 000-159 ANEM W
Autocorrelation Coefficient
1.0
0.5
0.0
-0.5
-1.0
0 1 2 3 4 5 6 7 8 9 10
LAG (seconds)

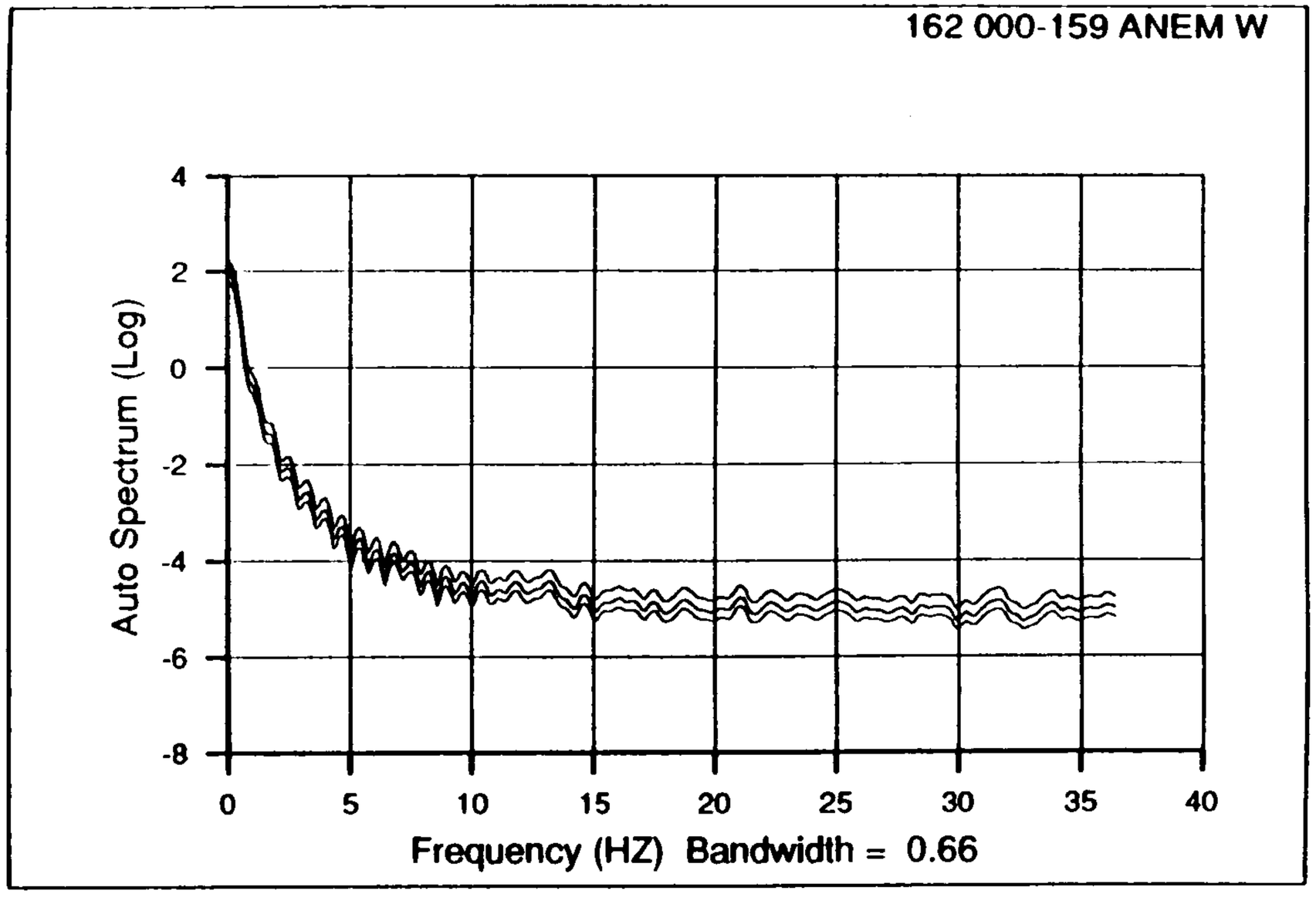
162 000-159 ANEM W
Auto Spectrum (Log)
4
2
0
-2
-4
-6
-8
0 5 10 15 20 25 30 35 40
Frequency (HZ) Bandwidth = 0.66

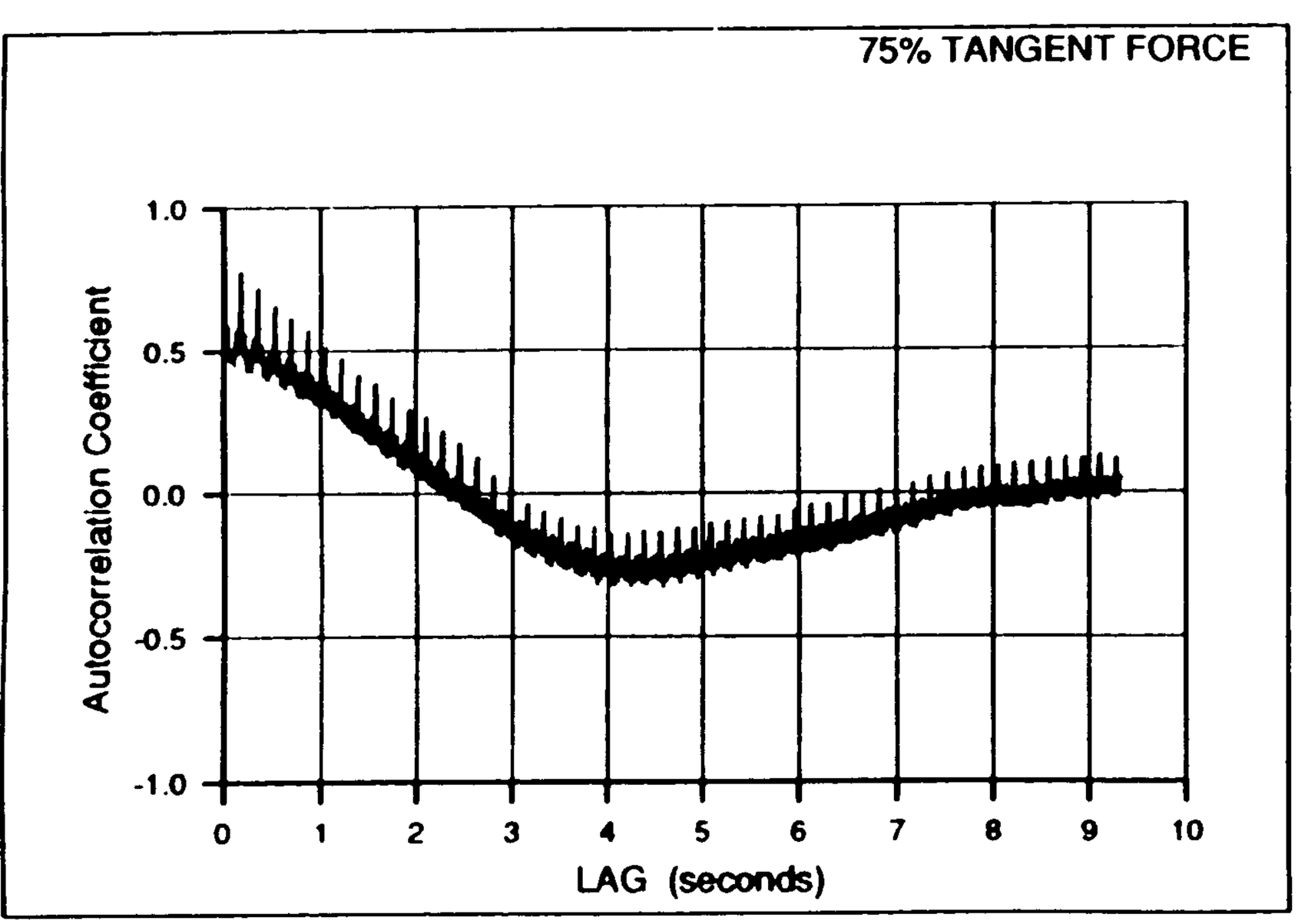
75% TANGENT FORCE
Autocorrelation Coefficient
1.0
0.5
0.0
-0.5
-1.0
0 1 2 3 4 5 6 7 8 9 10
LAG (seconds)

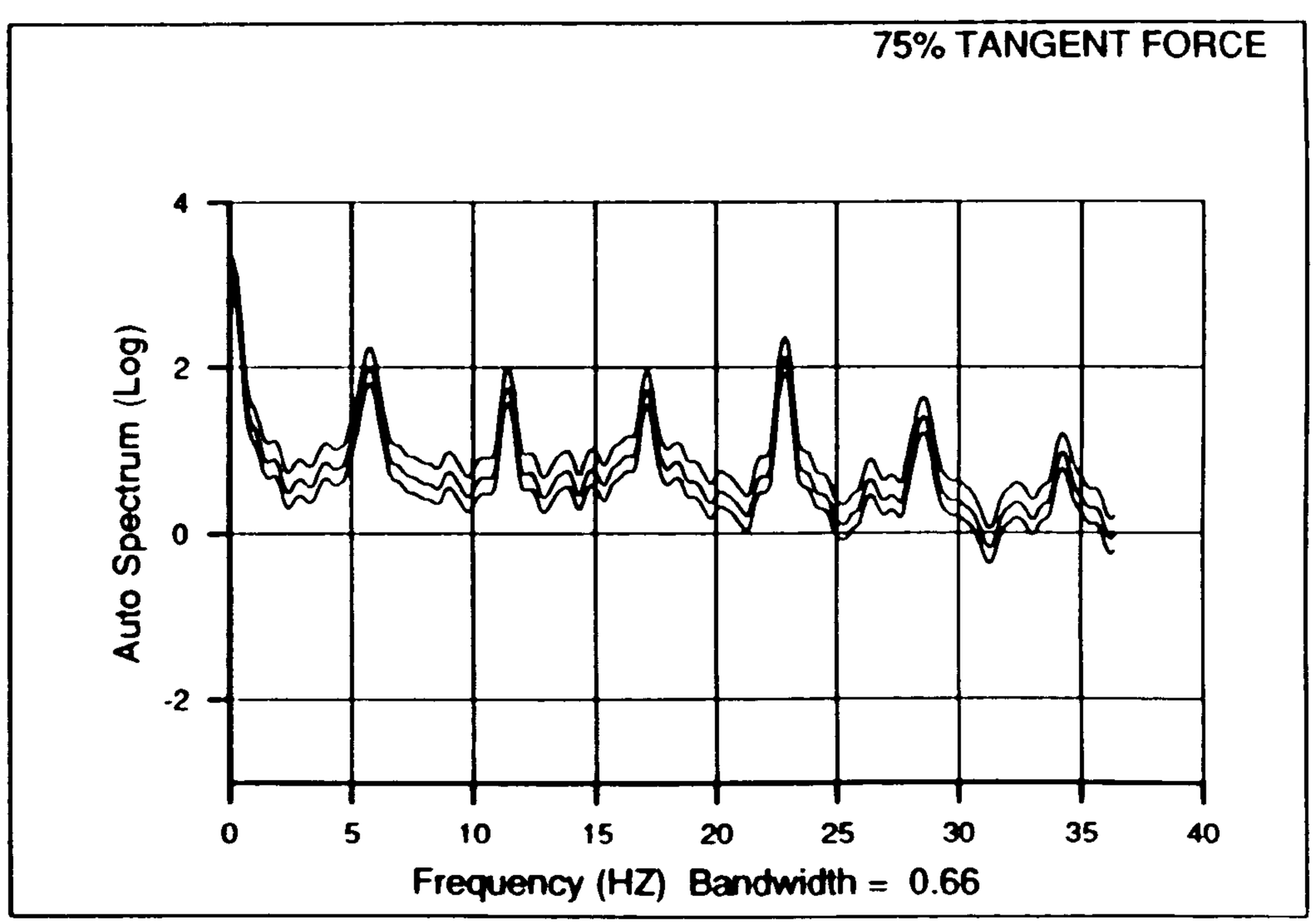
75% TANGENT FORCE
Auto Spectrum (Log)
4
2
0
-2
0 5 10 15 20 25 30 35 40
Frequency (HZ) Bandwidth = 0.66

Figure 9.48

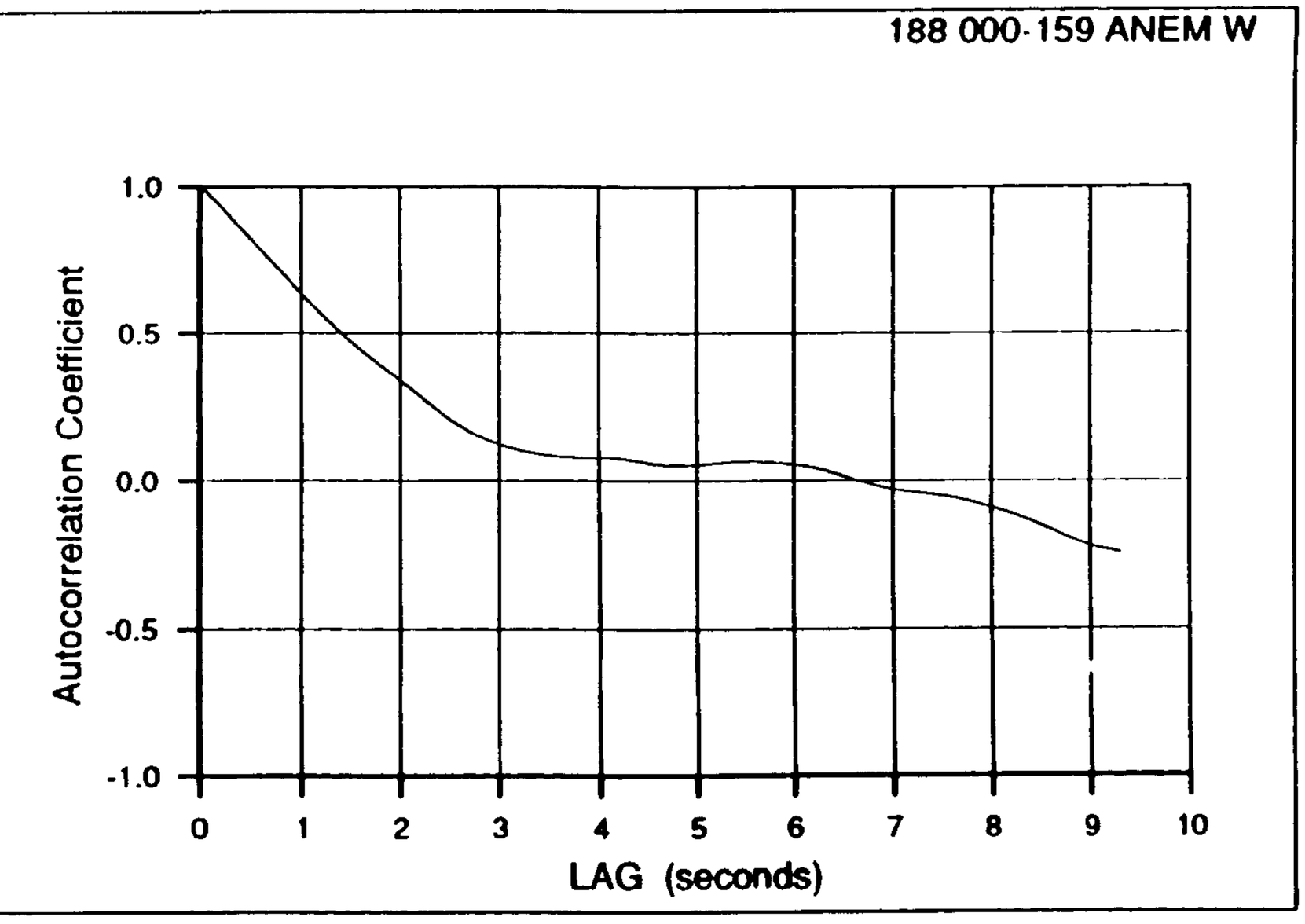
188 000-159 ANEM W
Autocorrelation Coefficient
1.0
0.5
0.0
-0.5
-1.0
0 1 2 3 4 5 6 7 8 9 10
LAG (seconds)

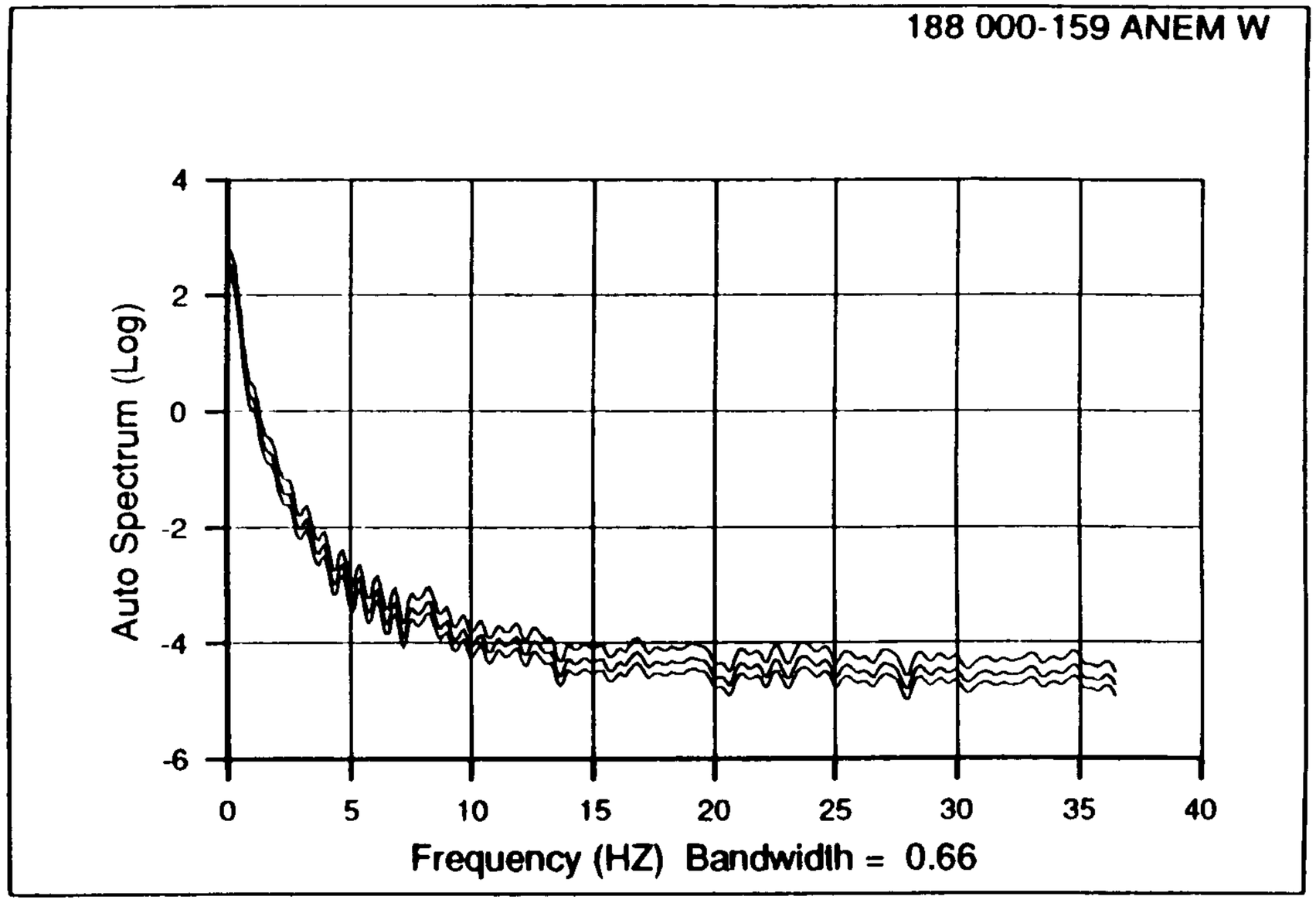
188 000-159 ANEM W
Auto Spectrum (Log)
4
2
0
-2
-4
-6
0 5 10 15 20 25 30 35 40
Frequency (HZ) Bandwidth = 0.66

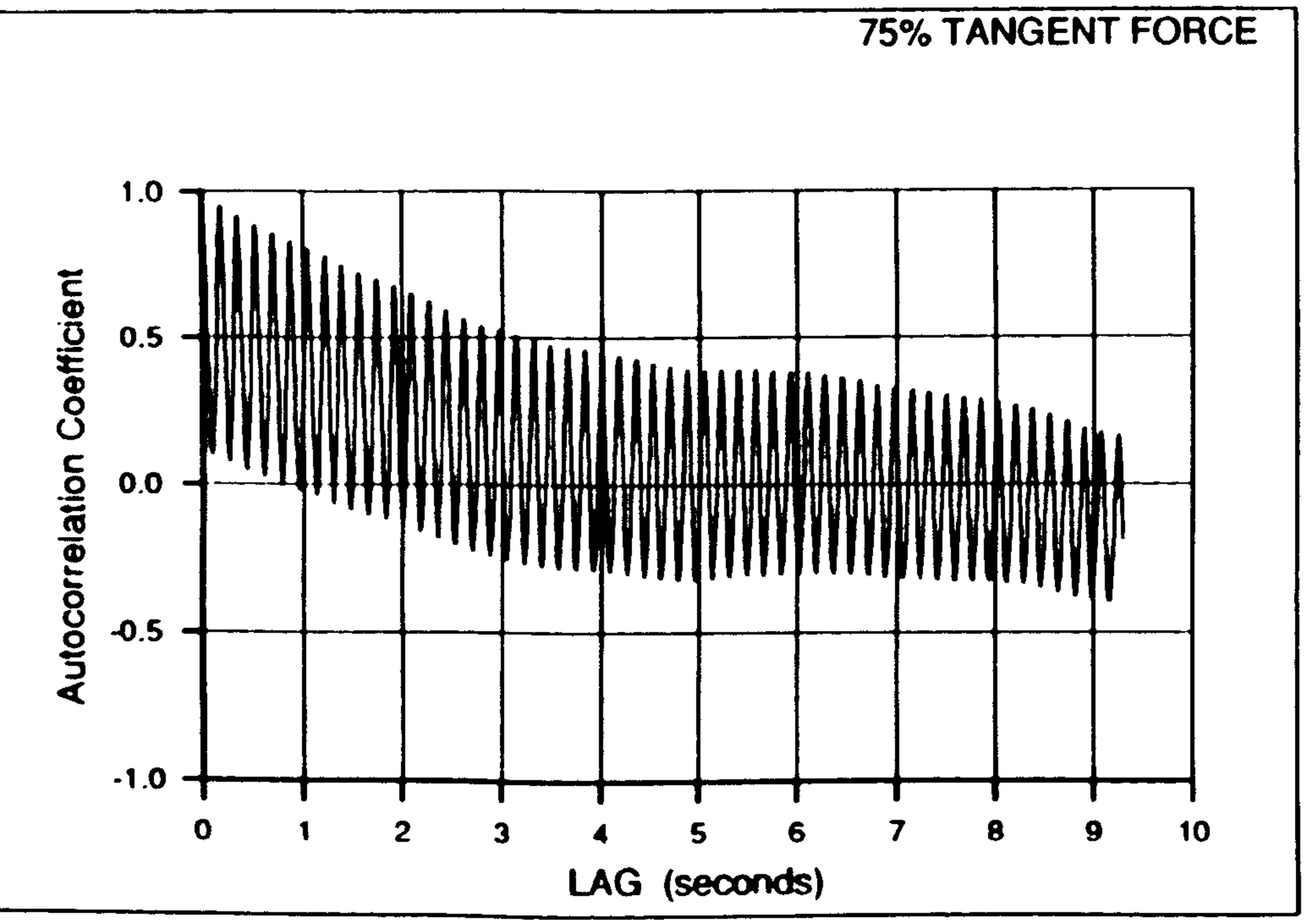
75% TANGENT FORCE
Autocorrelation Coefficient
1.0
0.5
0.0
-0.5
-1.0
0 1 2 3 4 5 6 7 8 9 10
LAG (seconds)

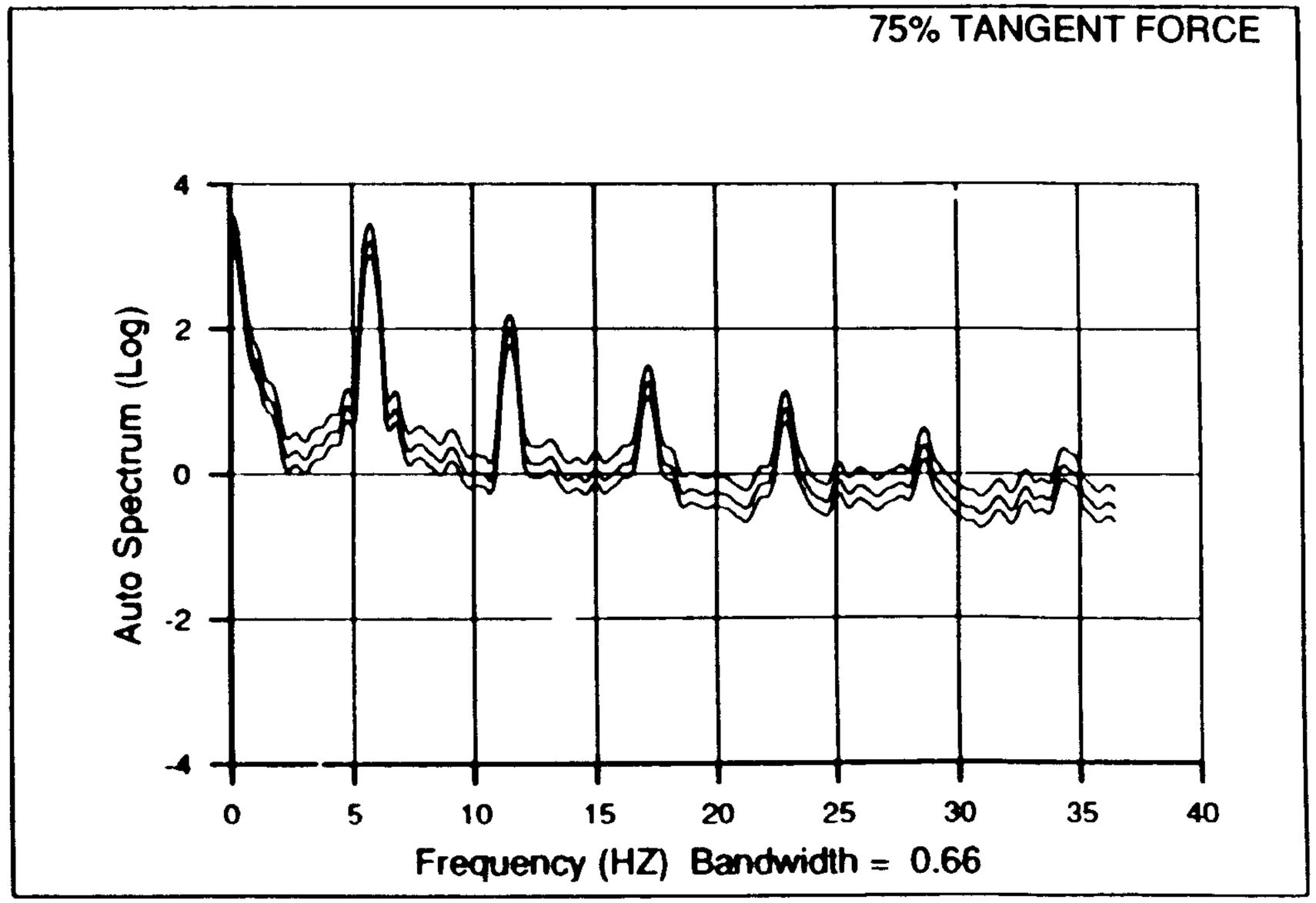
75% TANGENT FORCE
Auto Spectrum (Log)
4
2
0
-2
-4
0 5 10 15 20 25 30 35 40
Frequency (HZ) Bandwidth = 0.66

Figure 9.49

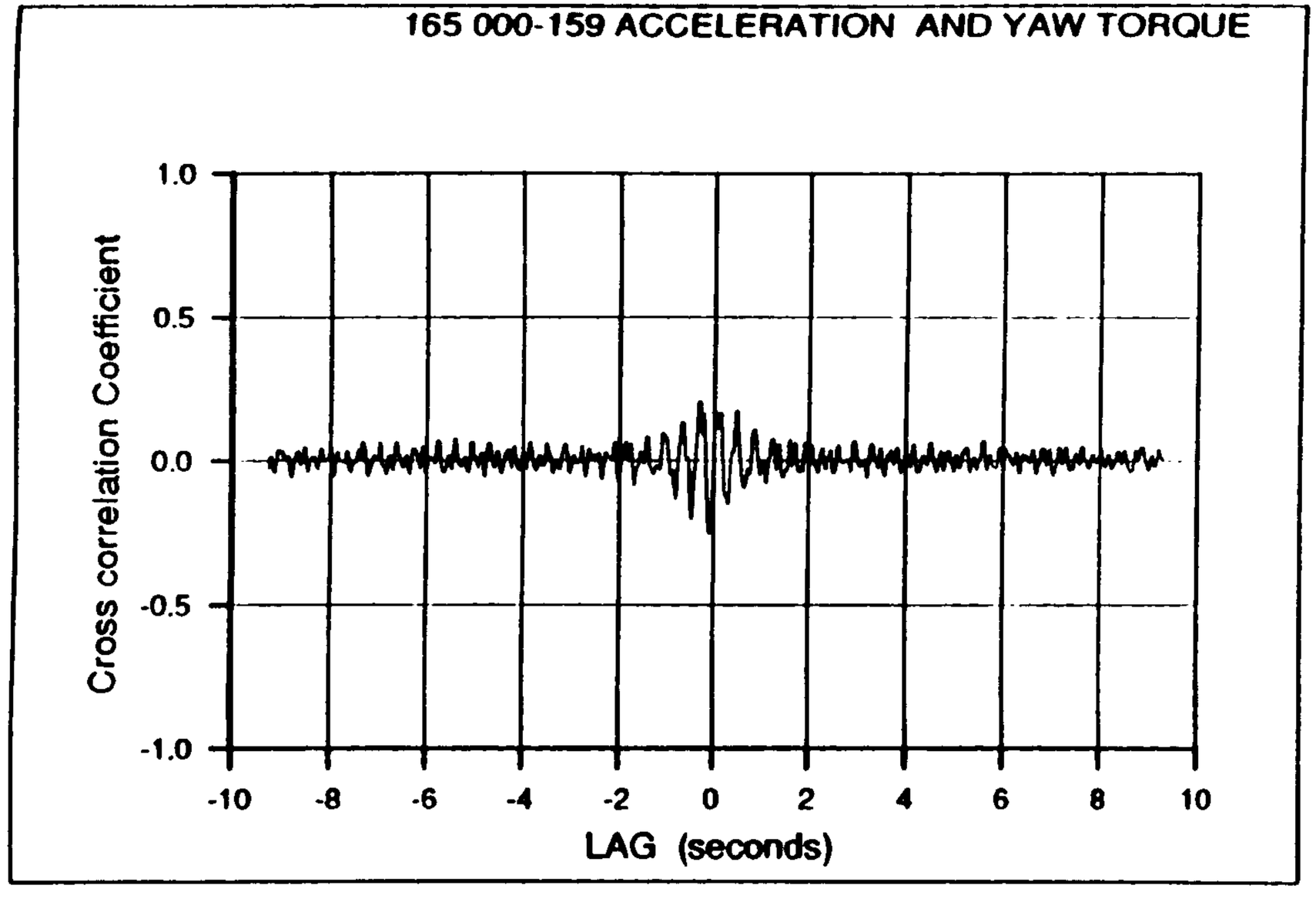
165 000-159 ACCELERATION AND YAW TORQUE
Cross correlation Coefficient
1.0
0.5
0.0
-0.5
-1.0
-10
-8
-6
-4
-2
0
2
4
6
8
10
LAG (seconds)

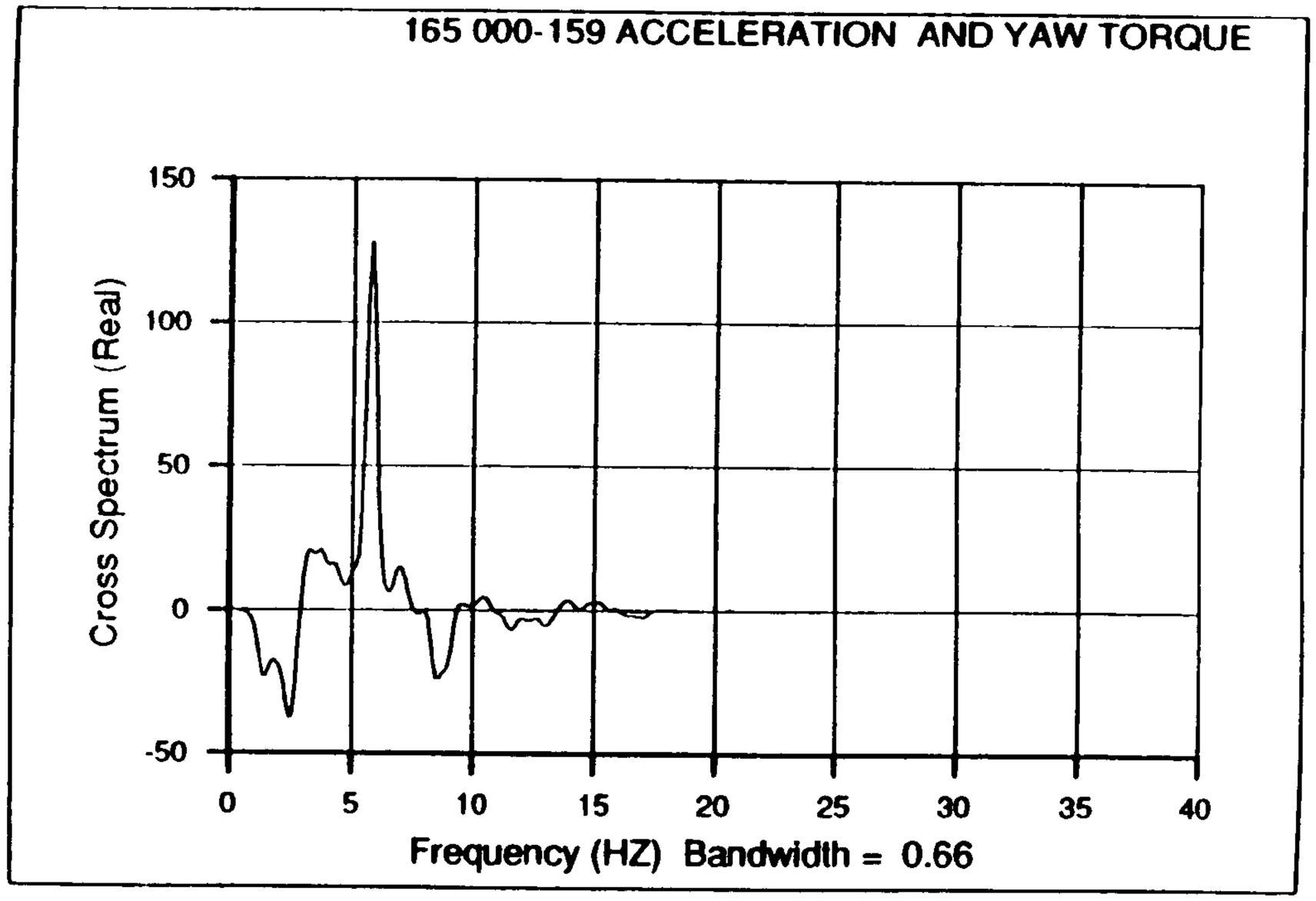
165 000-159 ACCELERATION AND YAW TORQUE
Cross Spectrum (Real)
150
100
50
0
-50
0
5
10
15
20
25
30
35
40
Frequency (HZ) Bandwidth = 0.66

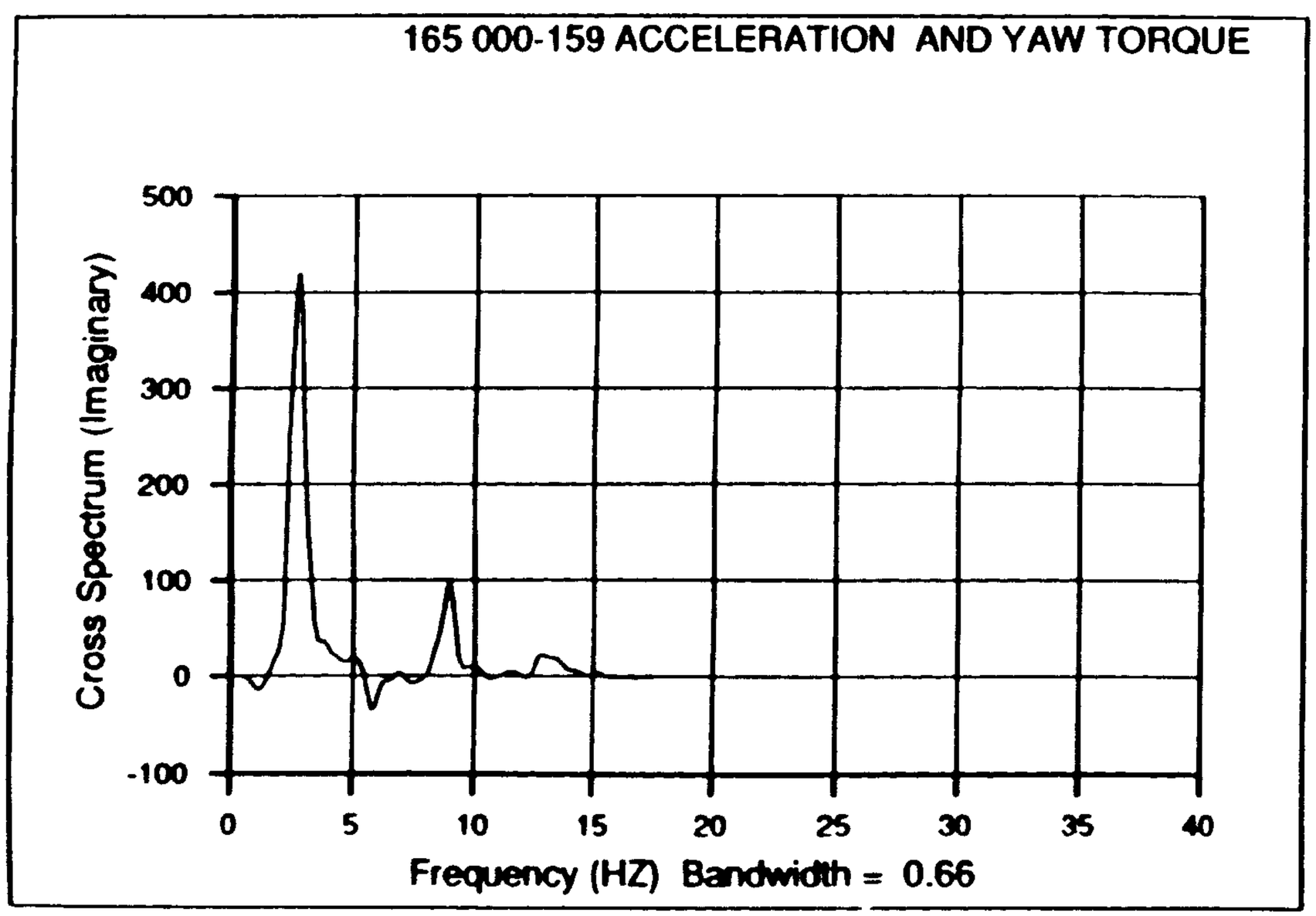
165 000-159 ACCELERATION AND YAW TORQUE
Cross Spectrum (Imaginary)
500
400
300
200
100
0
-100
0
5
10
15
20
25
30
35
40
Frequency (HZ) Bandwidth = 0.66

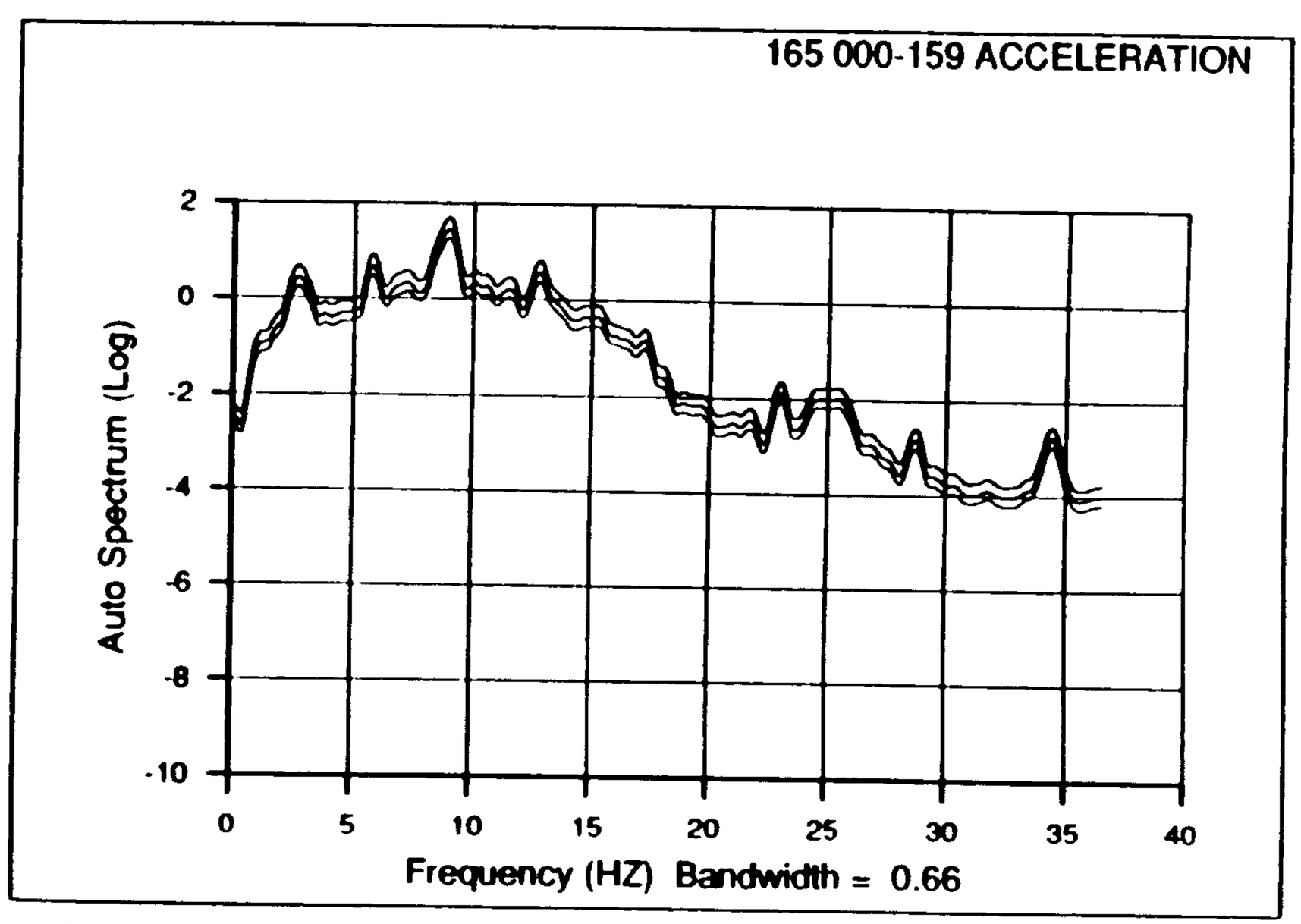
165 000-159 ACCELERATION
Auto Spectrum (Log)
2
0
-2
-4
-6
-8
-10
0
5
10
15
20
25
30
35
40
Frequency (HZ) Bandwidth = 0.66

Figure 9.50

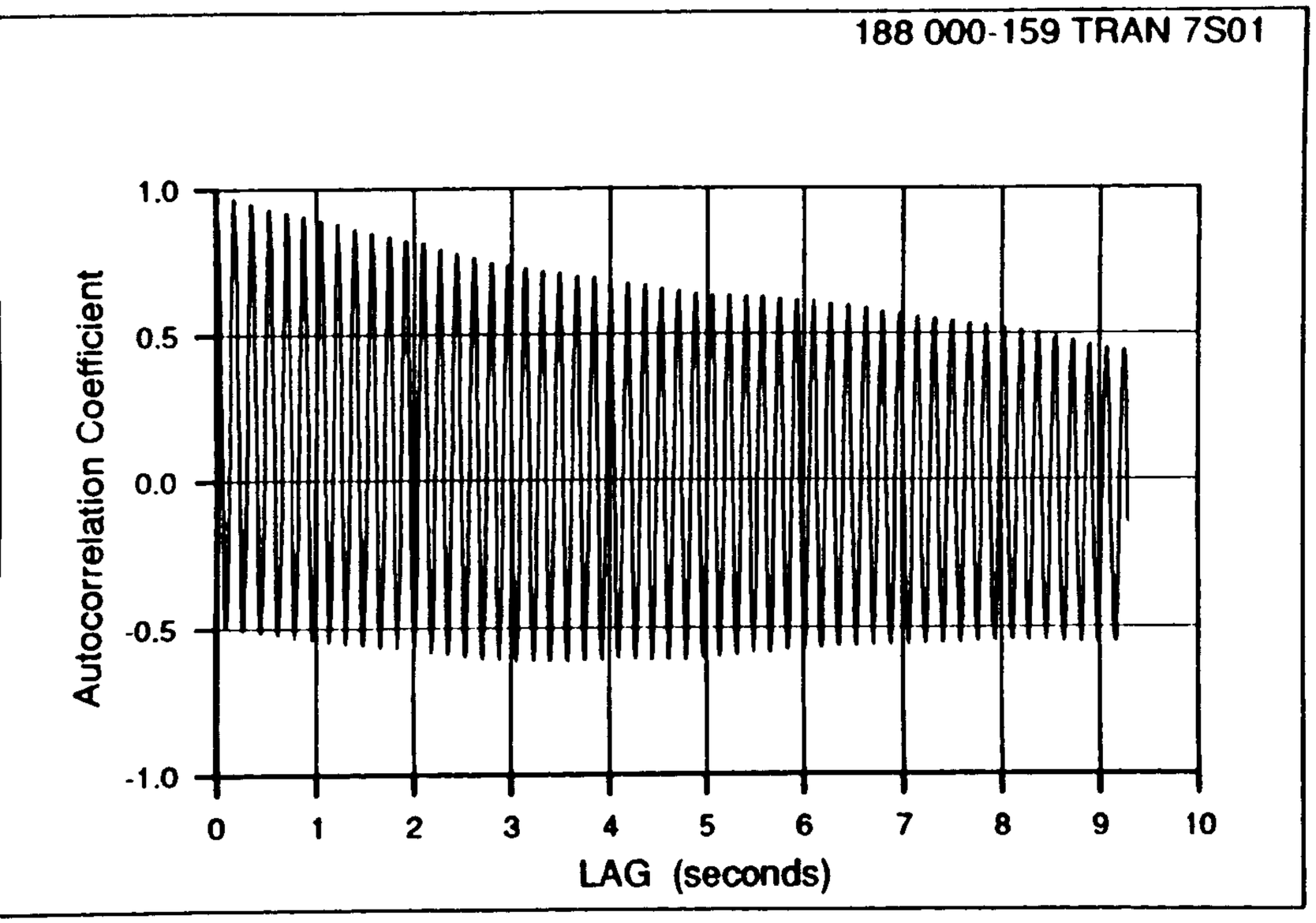
188 000-159 TRAN 7S01
Autocorrelation Coefficient
1.0
0.5
0.0
-0.5
-1.0
0 1 2 3 4 5 6 7 8 9 10
LAG (seconds)

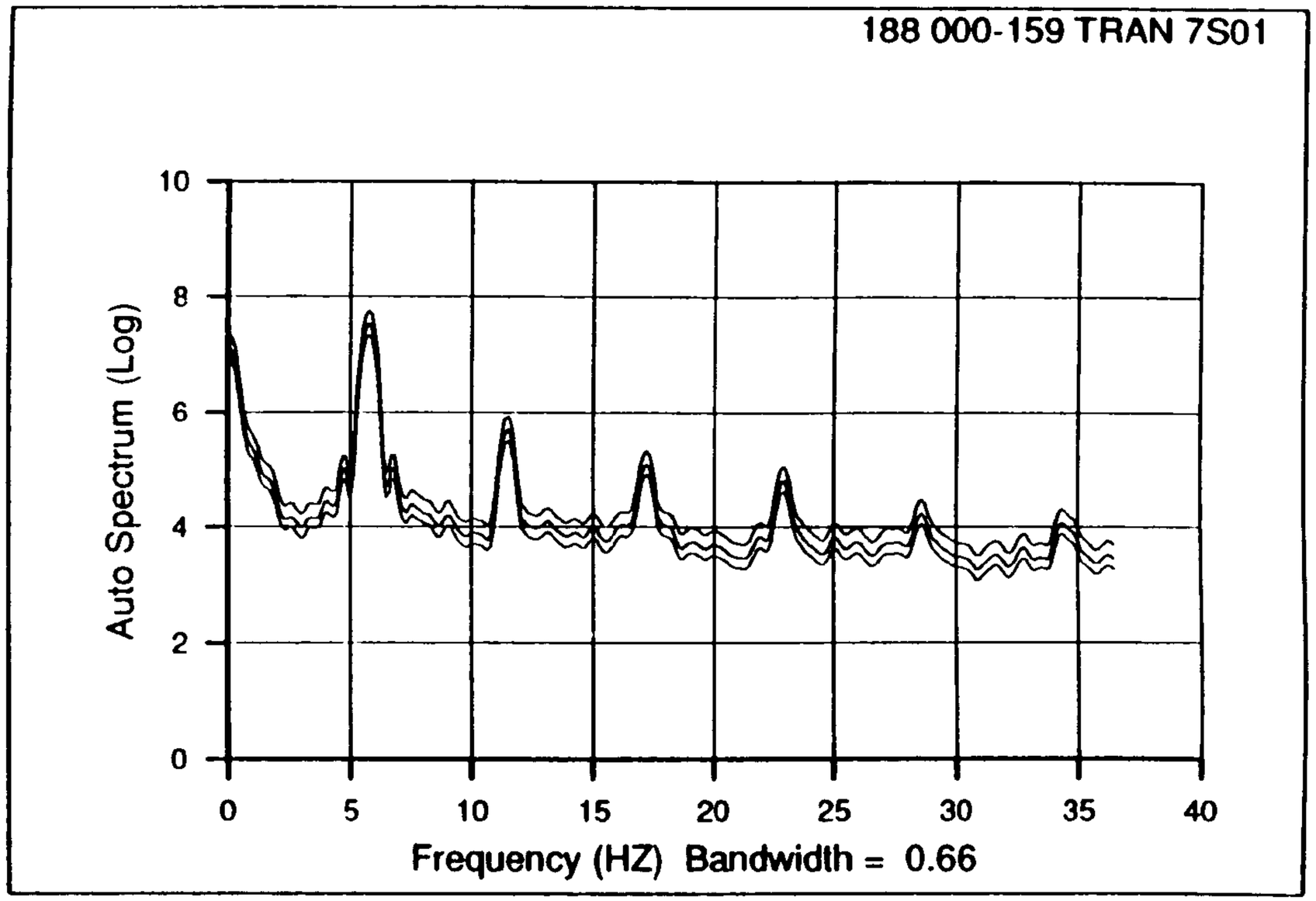
188 000-159 TRAN 7S01
Auto Spectrum (Log)
10
8
6
4
2
0
0 5 10 15 20 25 30 35 40
Frequency (HZ) Bandwidth = 0.66

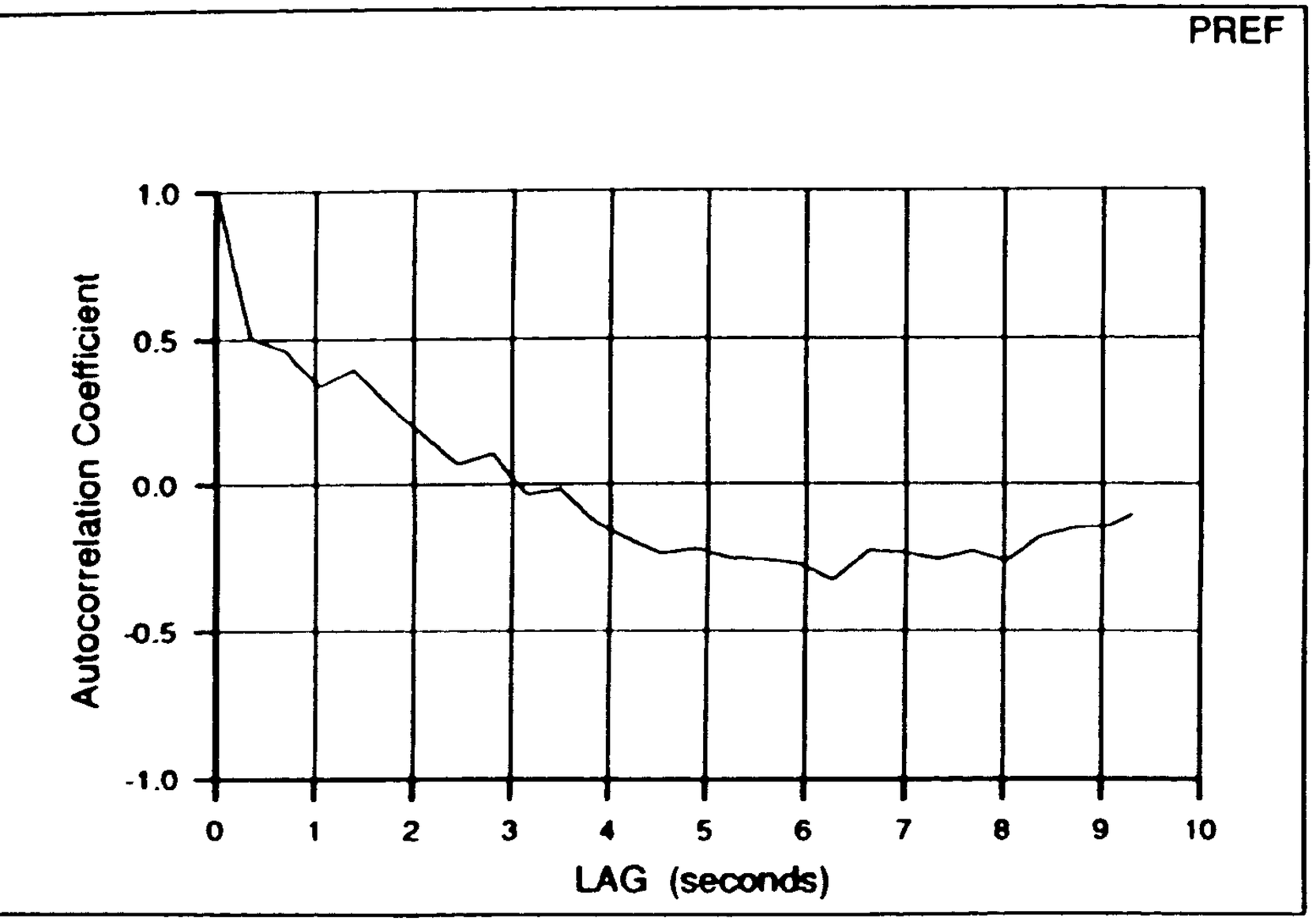
PREF
Autocorrelation Coefficient
1.0
0.5
0.0
-0.5
-1.0
0 1 2 3 4 5 6 7 8 9 10
LAG (seconds)

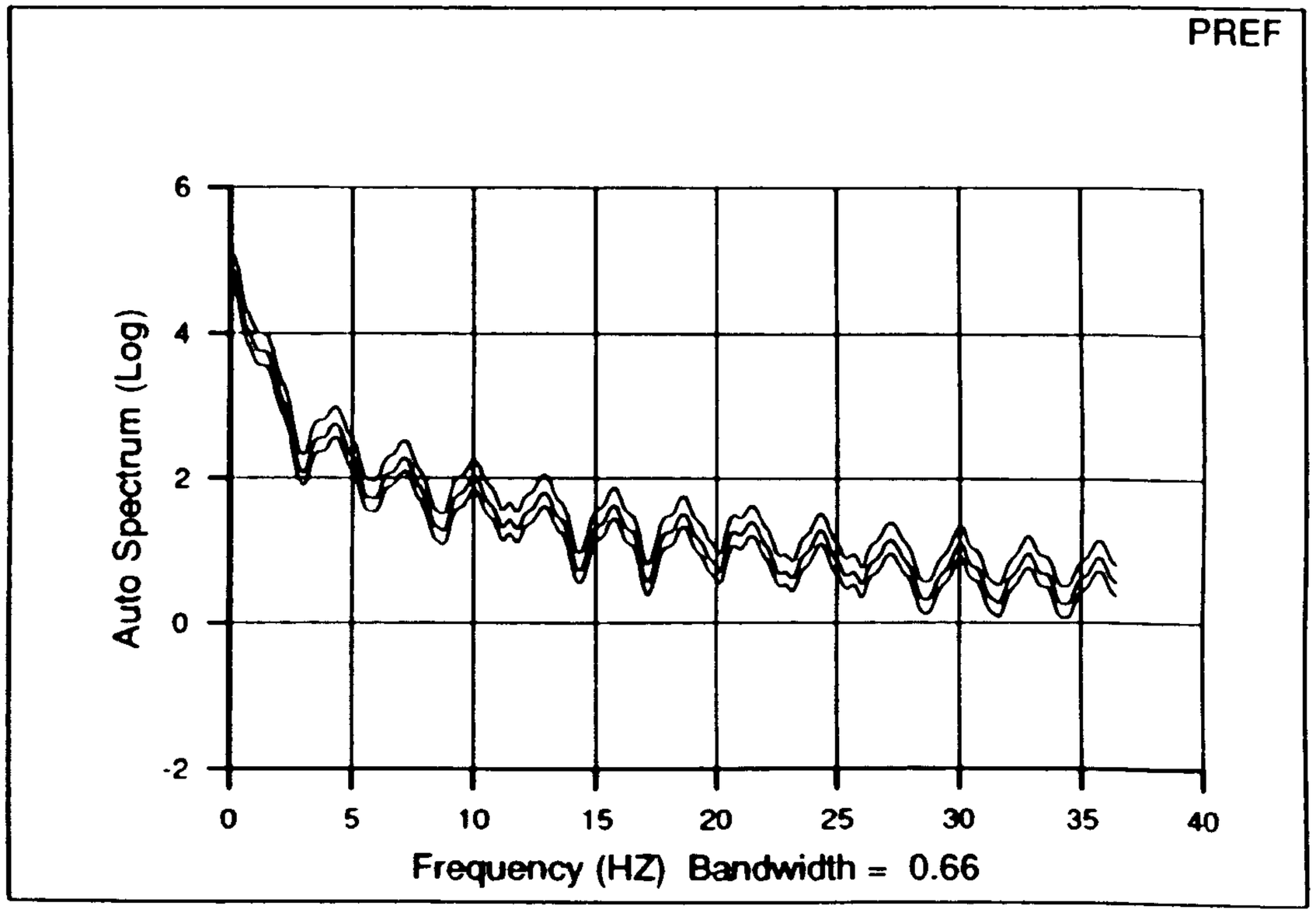
PREF
Auto Spectrum (Log)
6
4
2
0
-2
0 5 10 15 20 25 30 35 40
Frequency (HZ) Bandwidth = 0.66

Figure 9.51

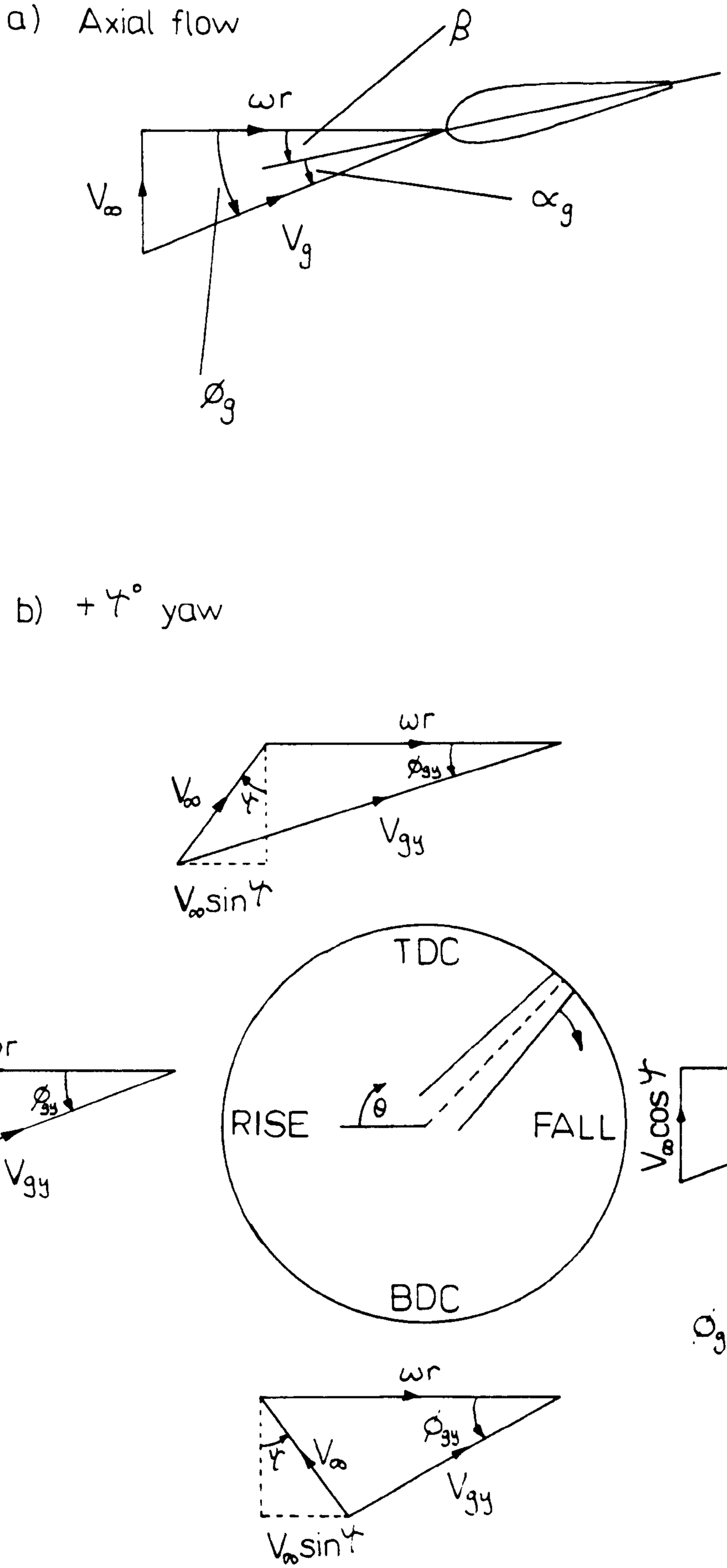

Figure 10.1 Blade section velocity and incidence (with and without yaw but with no induced effects).

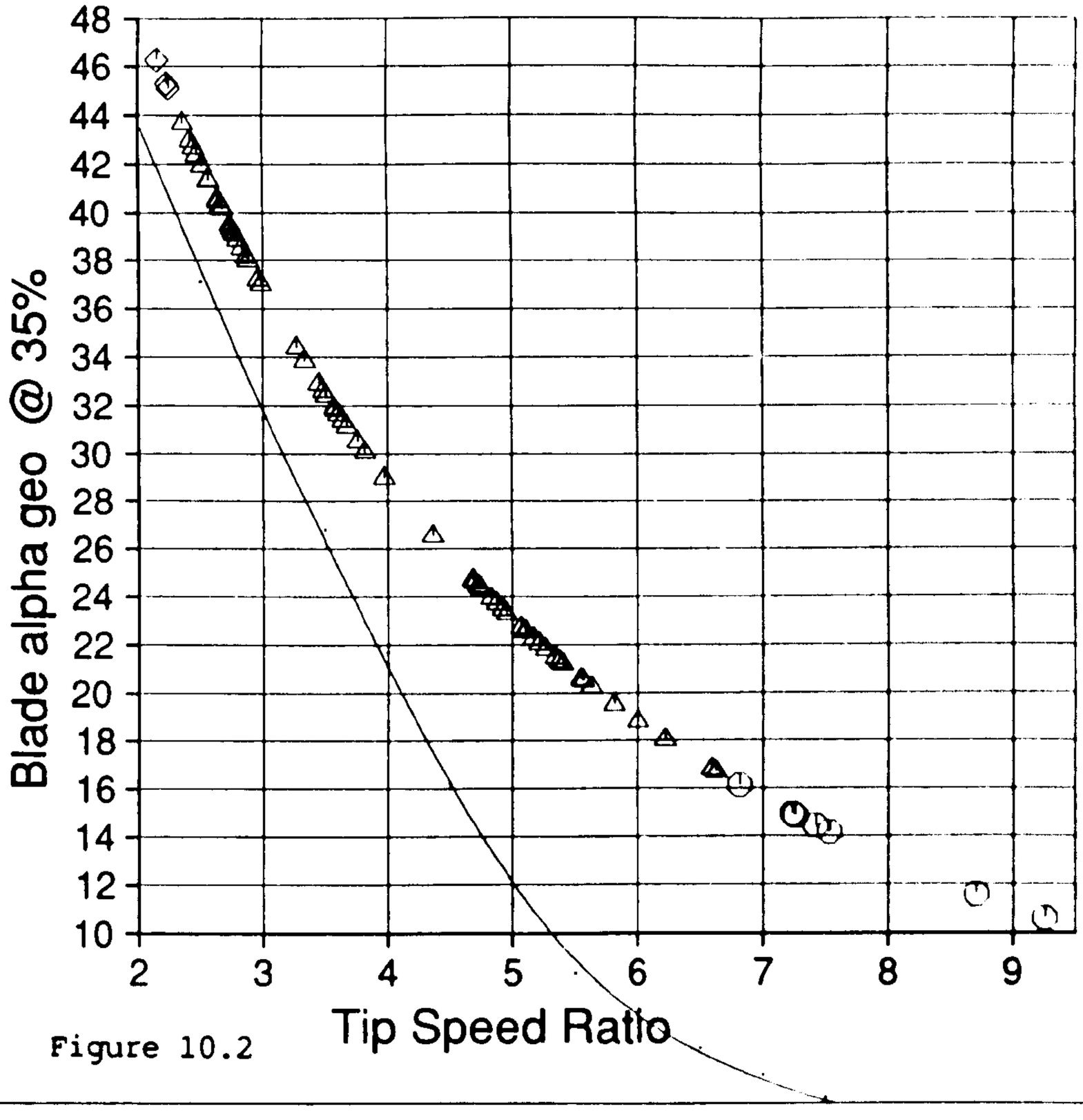

Figure 10.2

Cranfield

HAWT
Unsteady Aerodynamics
Experiment

Parametric Trends

Program V2.01

MARLEC Blades FI-1

76 sub-runs plotted
exactly 40 revs
in each sub run
derived parameters from
PROFILES

z is wind speed

	--- 4.0
*	4.0 --- 8.0
	8.0 --- 12.0
	12.0 --- 16.0
	16.0 --- 20.0
	20.0 ---

TREND.DAT;1

1-MAY-1990:10:20:20

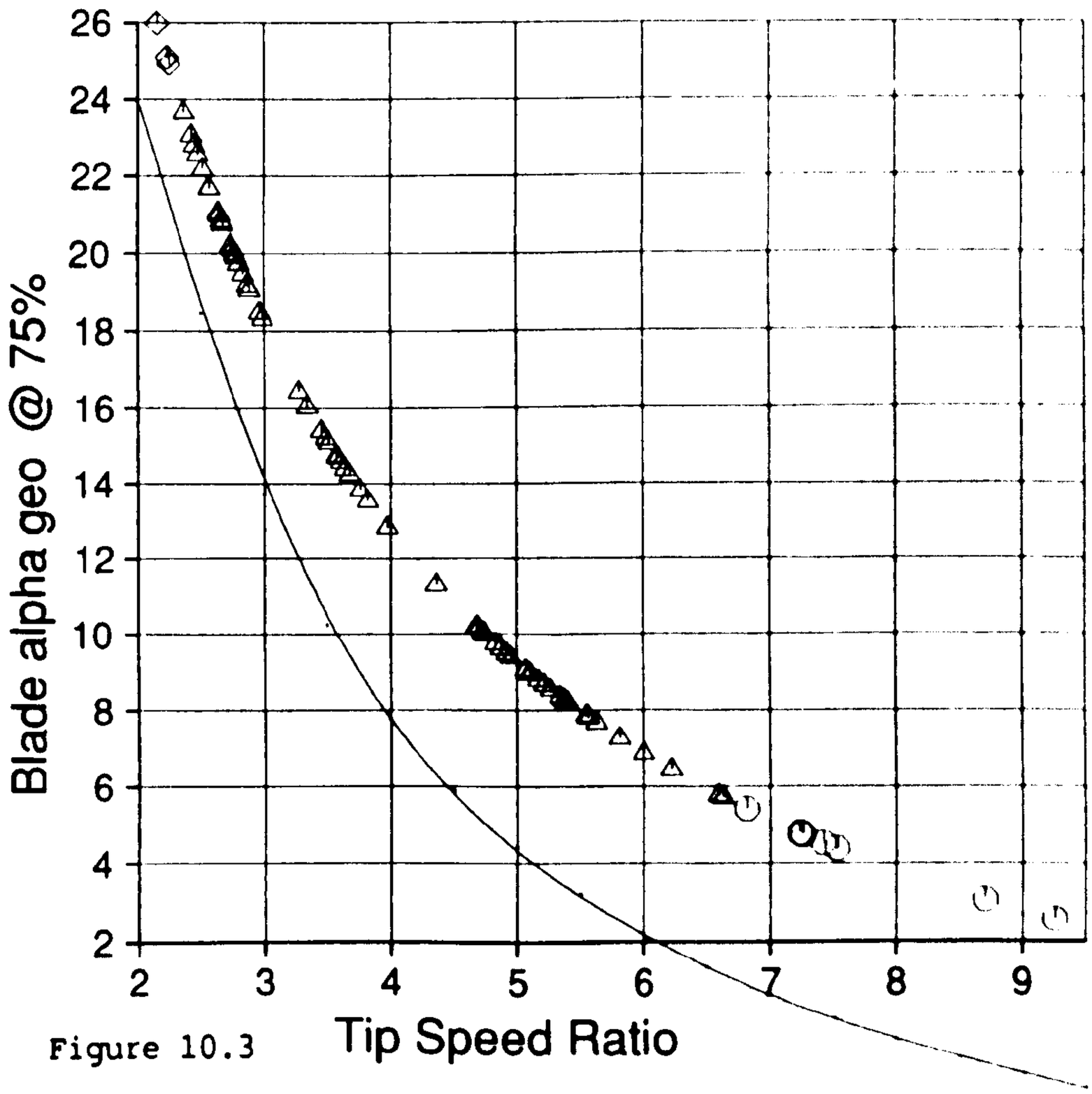

Figure 10.3

Cranfield

HAWT
Unsteady Aerodynamics
Experiment

Parametric Trends

Program V2.02

MARLEC Blades FI-1

76 sub-runs plotted
exactly 40 revs
in each sub run
derived parameters from
PROFILES

z is wind speed

	--- 4.0
*	4.0 --- 8.0
	8.0 --- 12.0
	12.0 --- 16.0
	16.0 --- 20.0
	20.0 ---

TREND.DAT;2

1-MAY-1990:10:20:55

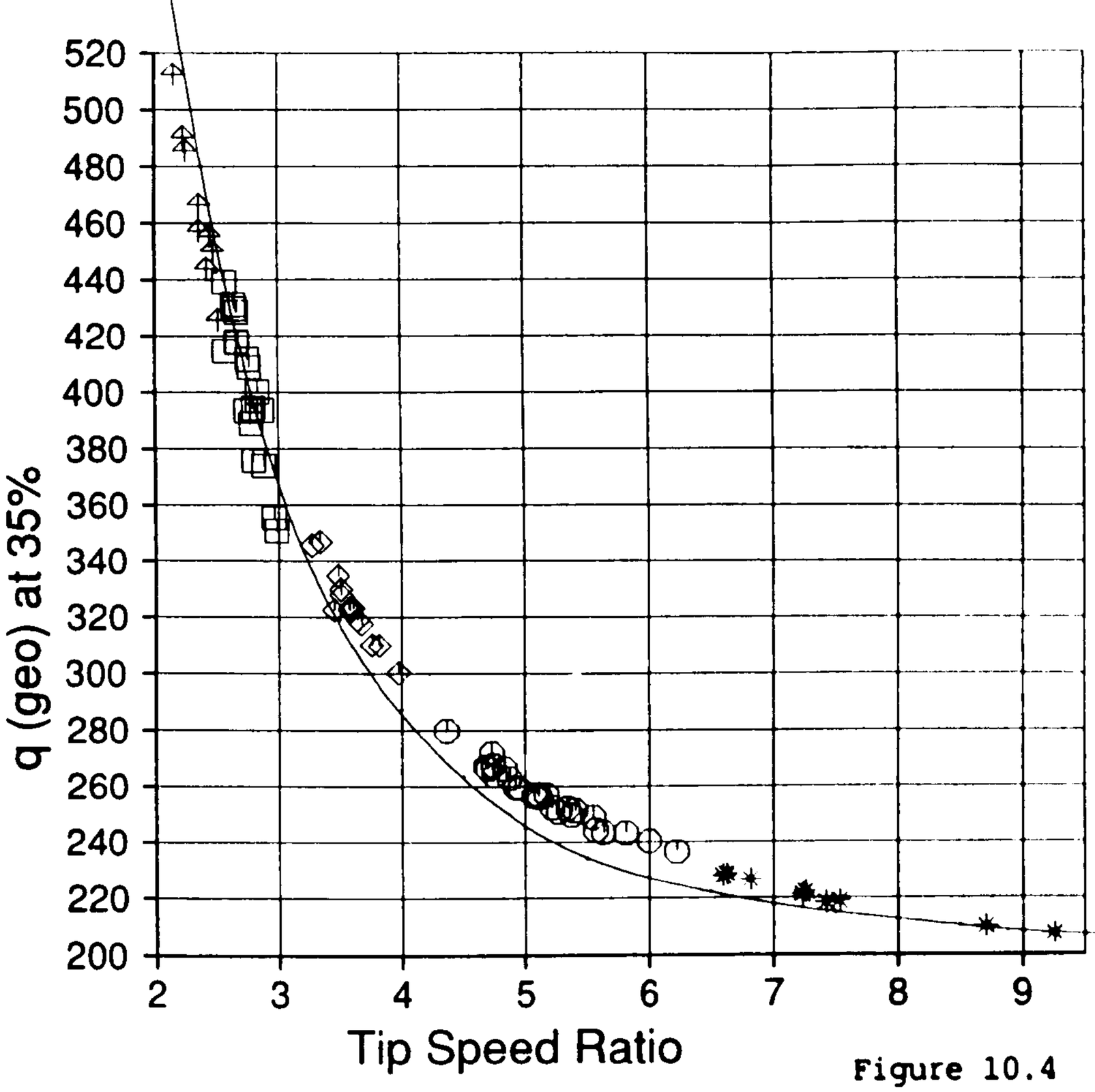

Figure 10.4

Cranfield

HAWT
Unsteady Aerodynamics
Experiment

Parametric Trends

Program V2.01

MARLEC Blades FI-1

76 sub-runs plotted
exactly 40 revs
in each sub run
derived parameters from
PROFILES

z is wind speed

Y	--- 4.0
*	4.0 --- 8.0
O	8.0 --- 12.0
◇	12.0 --- 16.0
□	16.0 --- 20.0
↑	20.0 ---

TREND.DAT;23

23-MAY-1990:15:11:24

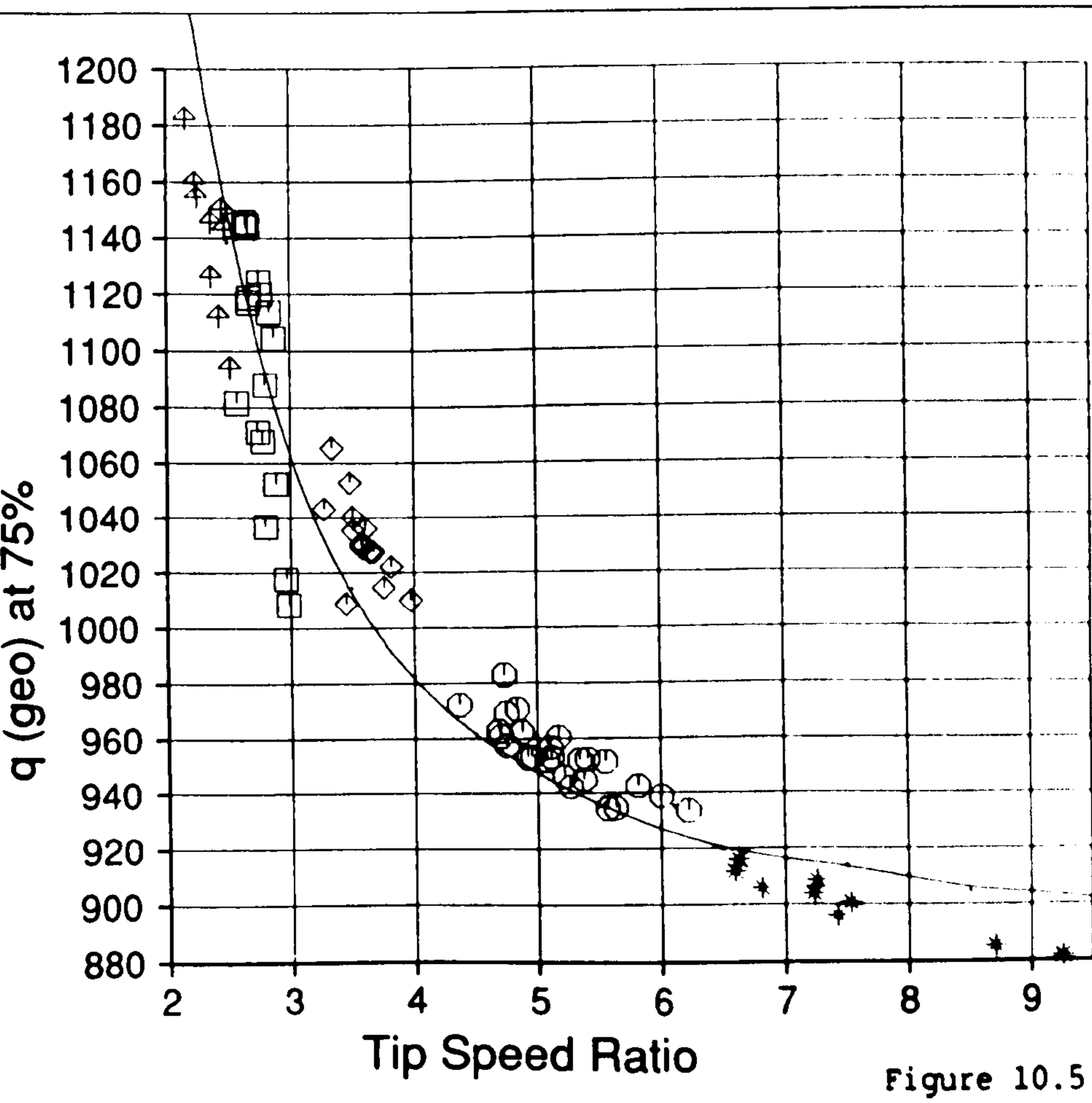

Figure 10.5

Cranfield

HAWT
Unsteady Aerodynamics
Experiment

Parametric Trends

Program V2.02

MARLEC Blades FI-1

76 sub-runs plotted
exactly 40 revs
in each sub run
derived parameters from
PROFILES

z is wind speed

Y	--- 4.0
*	4.0 --- 8.0
O	8.0 --- 12.0
◇	12.0 --- 16.0
□	16.0 --- 20.0
↑	20.0 ---

TREND.DAT;24

23-MAY-1990:15:13:47

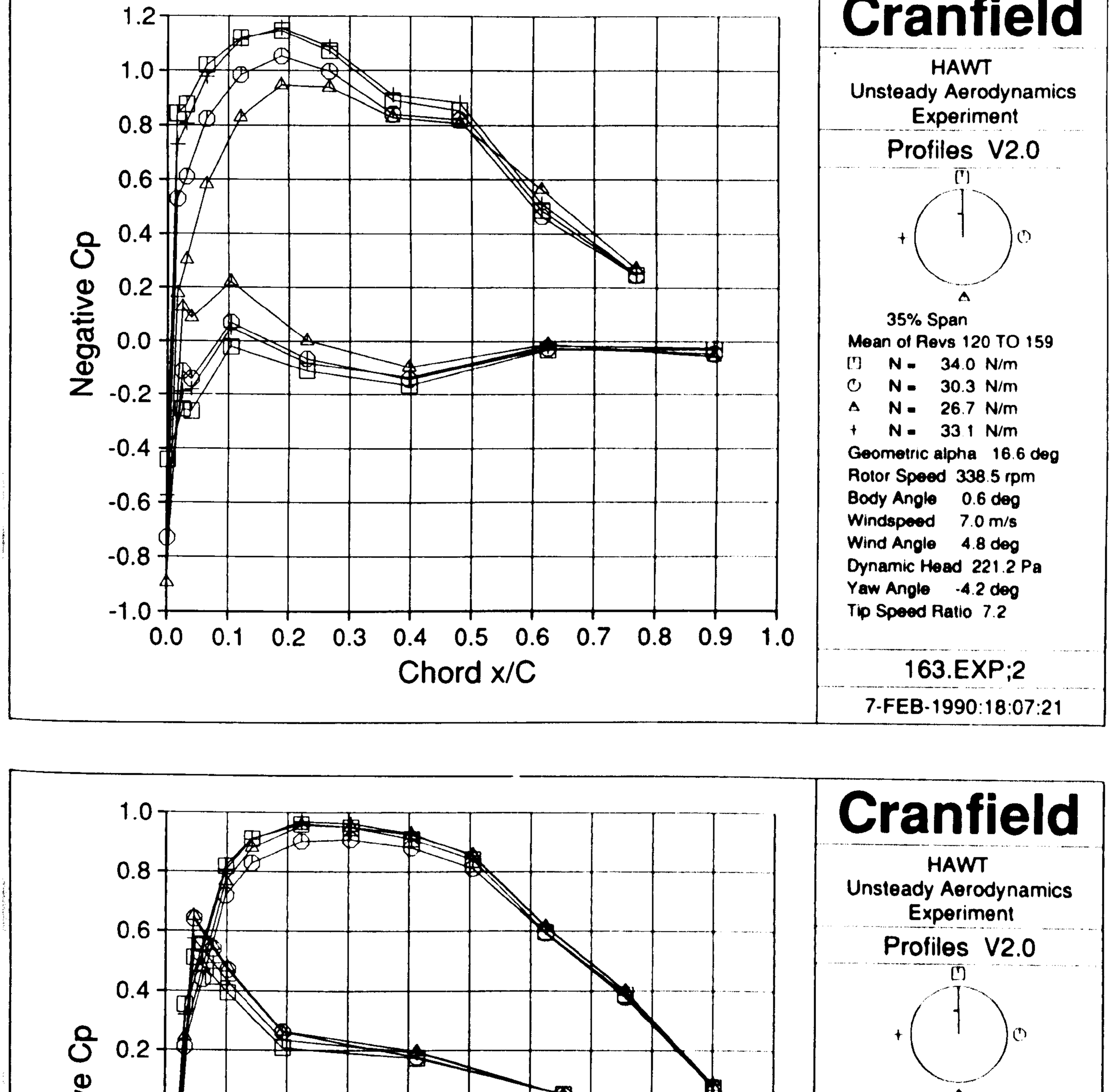
Cranfield
HAWT
Unsteady Aerodynamics
Experiment
Profiles V2.0
35% Span
Mean of Revs 120 TO 159
N = 34.0 N/m
N = 30.3 N/m
N = 26.7 N/m
N = 33.1 N/m
Geometric alpha 16.6 deg
Rotor Speed 338.5 rpm
Body Angle 0.6 deg
Windspeed 7.0 m/s
Wind Angle 4.8 deg
Dynamic Head 221.2 Pa
Yaw Angle -4.2 deg
Tip Speed Ratio 7.2
163.EXP;2
7-FEB-1990:18:07:21
Negative Cp
1.2
1.0
0.8
0.6
0.4
0.2
0.0
-0.2
-0.4
-0.6
-0.8
-1.0
0.0 0.1 0.2 0.3 0.4 0.5 0.6 0.7 0.8 0.9 1.0
Chord x/C
Cranfield
HAWT
Unsteady Aerodynamics
Experiment
Profiles V2.0
75% Span
Mean of Revs 120 TO 159
N = 61.3 N/m
N = 54.6 N/m
N = 58.0 N/m
N = 60.6 N/m
Geometric alpha 4.8 deg
Rotor Speed 338.5 rpm
Body Angle 0.6 deg
Windspeed 7.0 m/s
Wind Angle 4.8 deg
Dynamic Head 903.8 Pa
Yaw Angle -4.2 deg
Tip Speed Ratio 7.2
163.EXP;2
7-FEB-1990:18:07:21
Negative Cp
1.0
0.8
0.6
0.4
0.2
0.0
-0.2
-0.4
-0.6
-0.8
-1.0
0.0 0.1 0.2 0.3 0.4 0.5 0.6 0.7 0.8 0.9 1.0
Chord x/C

Figure 10.6

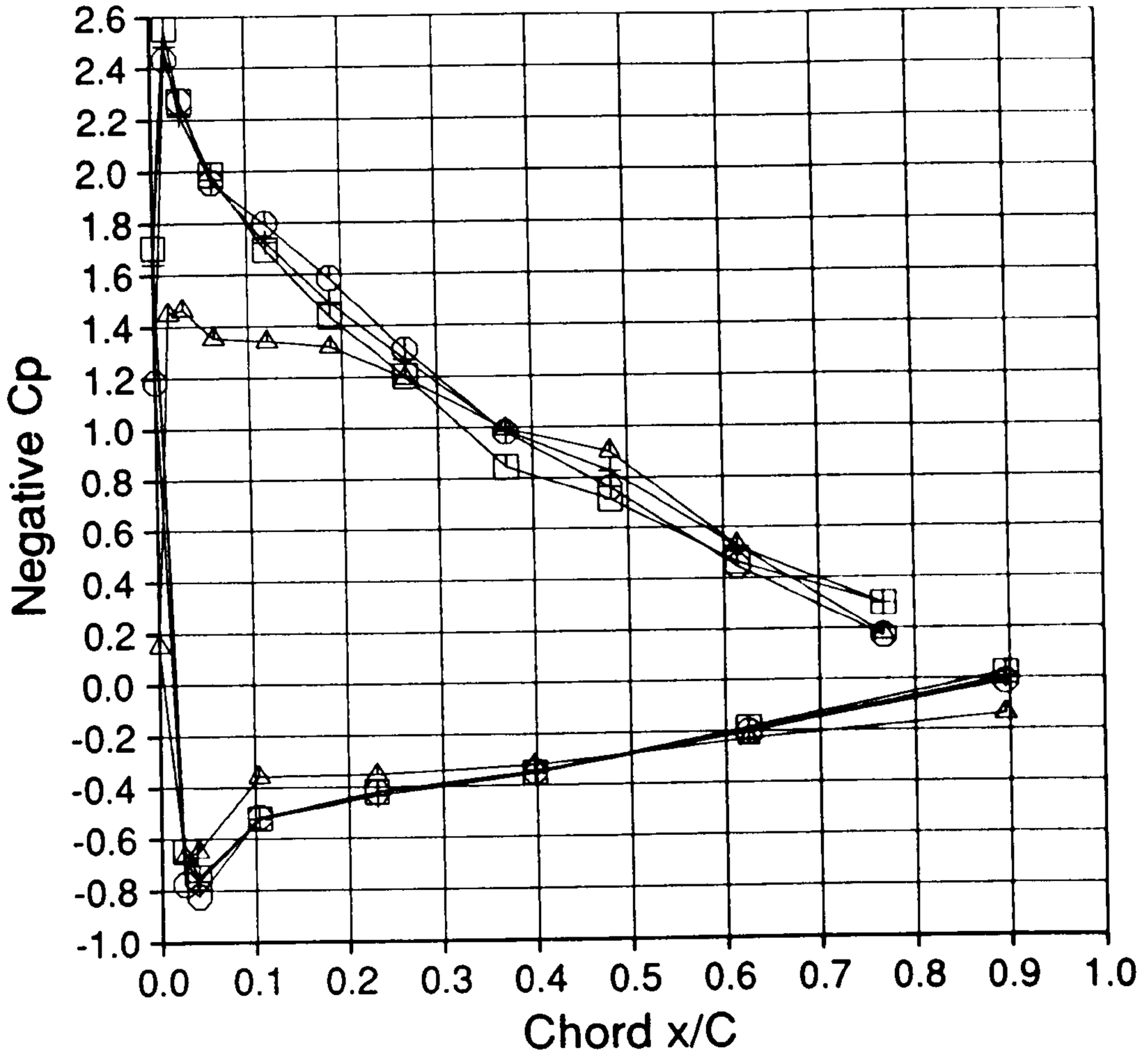

Cranfield

HAWT
Unsteady Aerodynamics
Experiment

Profiles V2.0

35% Span
Mean of Revs 120 TO 159
N = 59.6 N/m
N = 61.2 N/m
N = 55.8 N/m
N = 62.7 N/m
Geometric alpha 25.5 deg
Rotor Speed 341.3 rpm
Body Angle -14.7 deg
Windspeed 10.6 m/s
Wind Angle -9.7 deg
Dynamic Head 266.2 Pa
Yaw Angle -5.0 deg
Tip Speed Ratio 4.8

167.EXP;2

7-FEB-1990:18:16:47

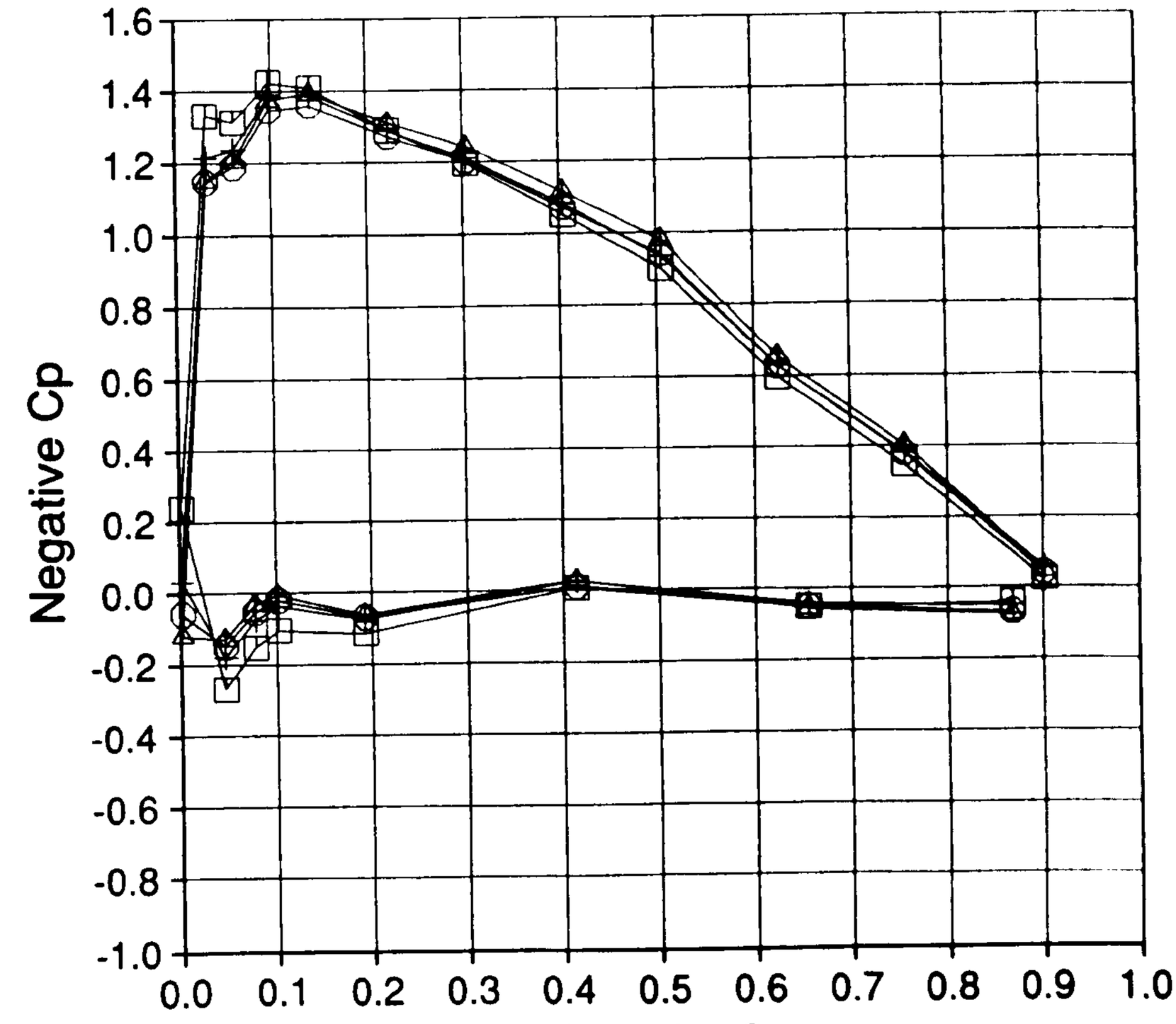

Cranfield

HAWT
Unsteady Aerodynamics
Experiment

Profiles V2.0

75% Span
Mean of Revs 120 TO 159
N = 115.4 N/m
N = 113.7 N/m
N = 116.7 N/m
N = 114.4 N/m
Geometric alpha 9.7 deg
Rotor Speed 341.3 rpm
Body Angle -14.7 deg
Windspeed 10.6 m/s
Wind Angle -9.7 deg
Dynamic Head 970.5 Pa
Yaw Angle -5.0 deg
Tip Speed Ratio 4.8

167.EXP;2

7-FEB-1990:18:16:47

Figure 10.7

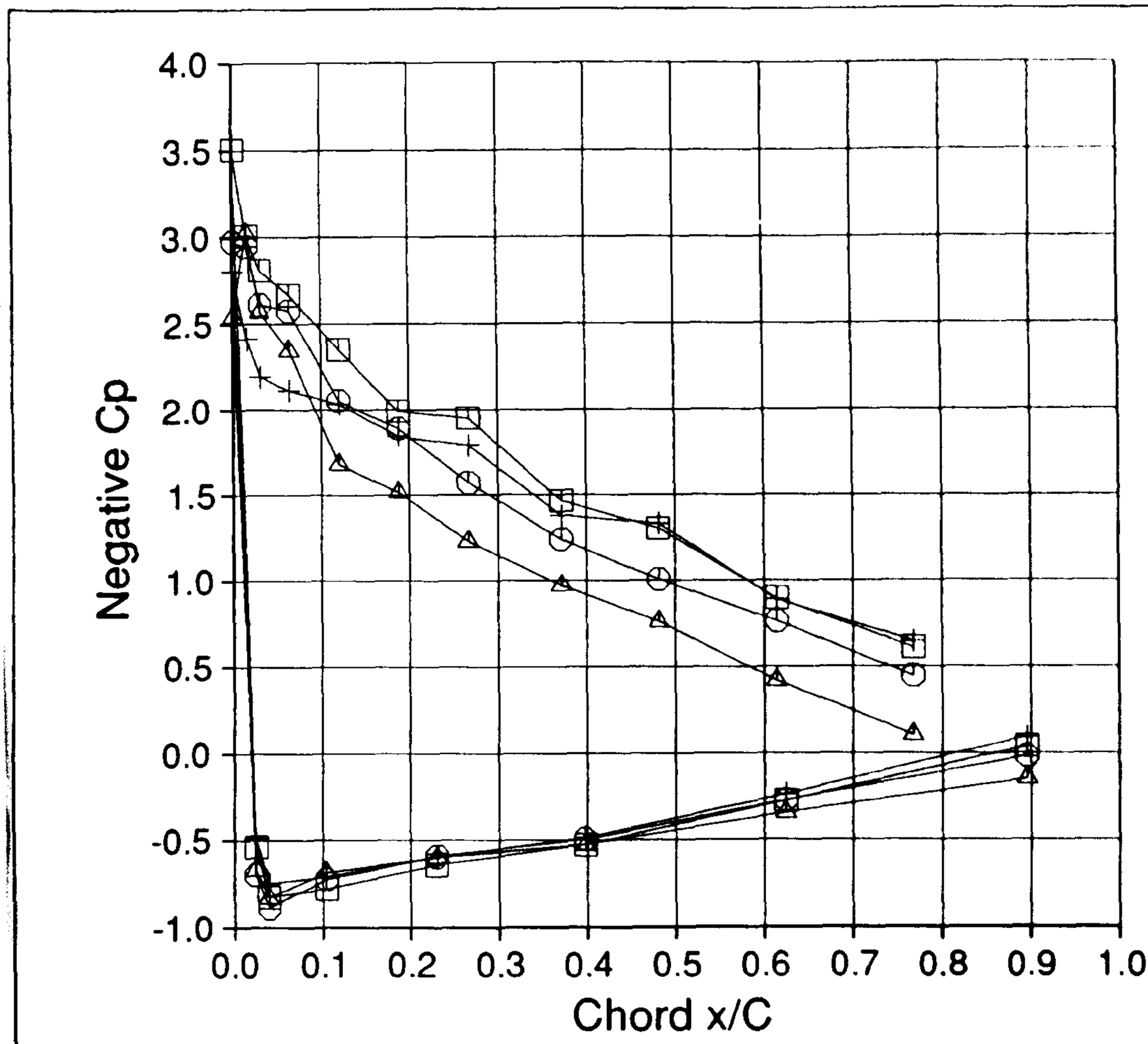

Cranfield

HAWT
Unsteady Aerodynamics
Experiment

Profiles V2.0

35% Span
Mean of Revs 000 TO 039
N = 113.5 N/m
N = 100.4 N/m
N = 84.1 N/m
N = 104.3 N/m
Geometric alpha 33.7 deg
Rotor Speed 342.6 rpm
Body Angle 0.4 deg
Windspeed 14.6 m/s
Wind Angle -0.7 deg
Dynamic Head 329.8 Pa
Yaw Angle 1.2 deg
Tip Speed Ratio 3.5

162.EXP;2

7-FEB-1990:18:02:36

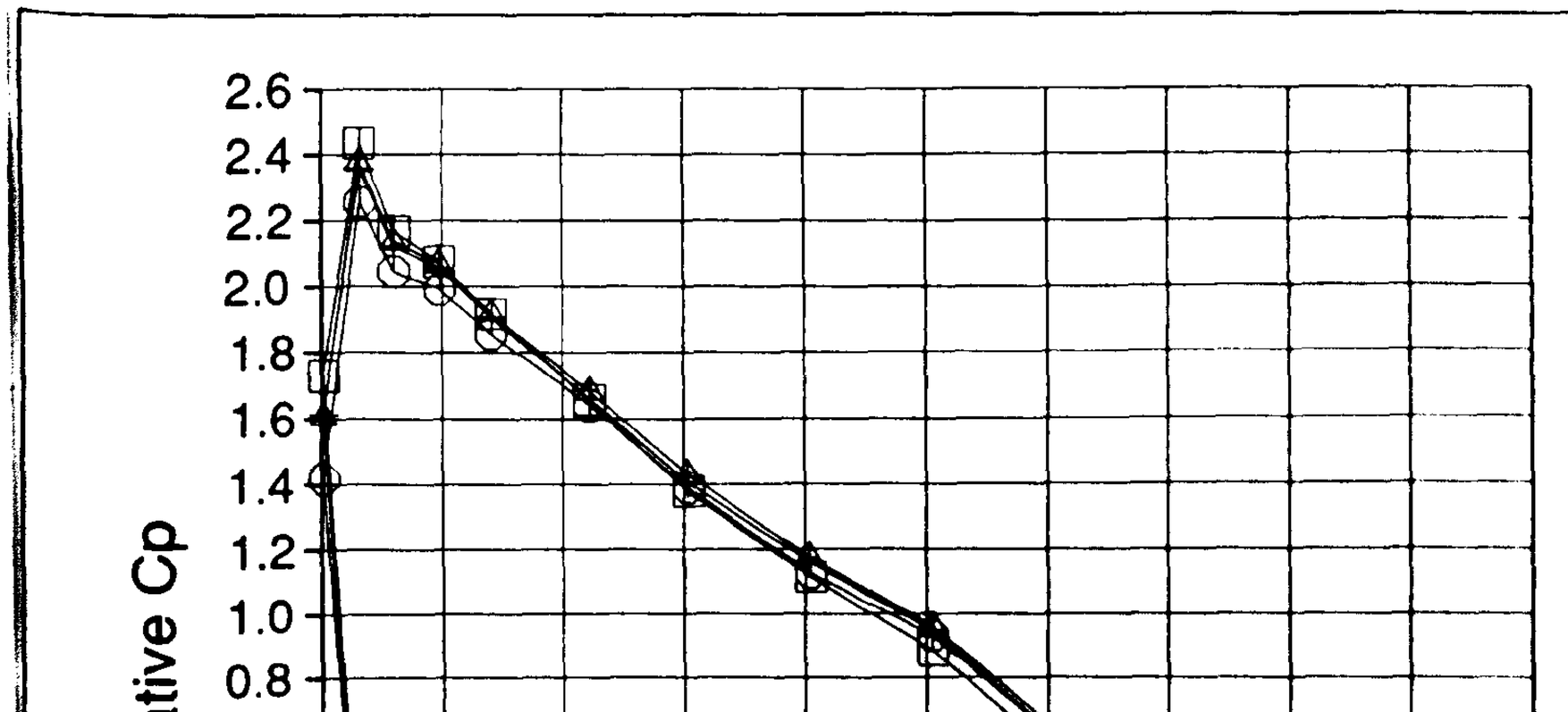

Cranfield

HAWT
Unsteady Aerodynamics
Experiment

Profiles V2.0

75% Span
Mean of Revs 000 TO 039
N = 161.6 N/m
N = 161.6 N/m
N = 167.2 N/m
N = 162.4 N/m
Geometric alpha 15.1 deg
Rotor Speed 342 6 rpm
Body Angle 0 4 deg
Windspeed 14.6 m/s
Wind Angle -0.7 deg
Dynamic Head 1040.1 Pa
Yaw Angle 1.2 deg
Tip Speed Ratio 3.5

162.EXP;2

7-FEB-1990:18:02:36

Figure 10.8

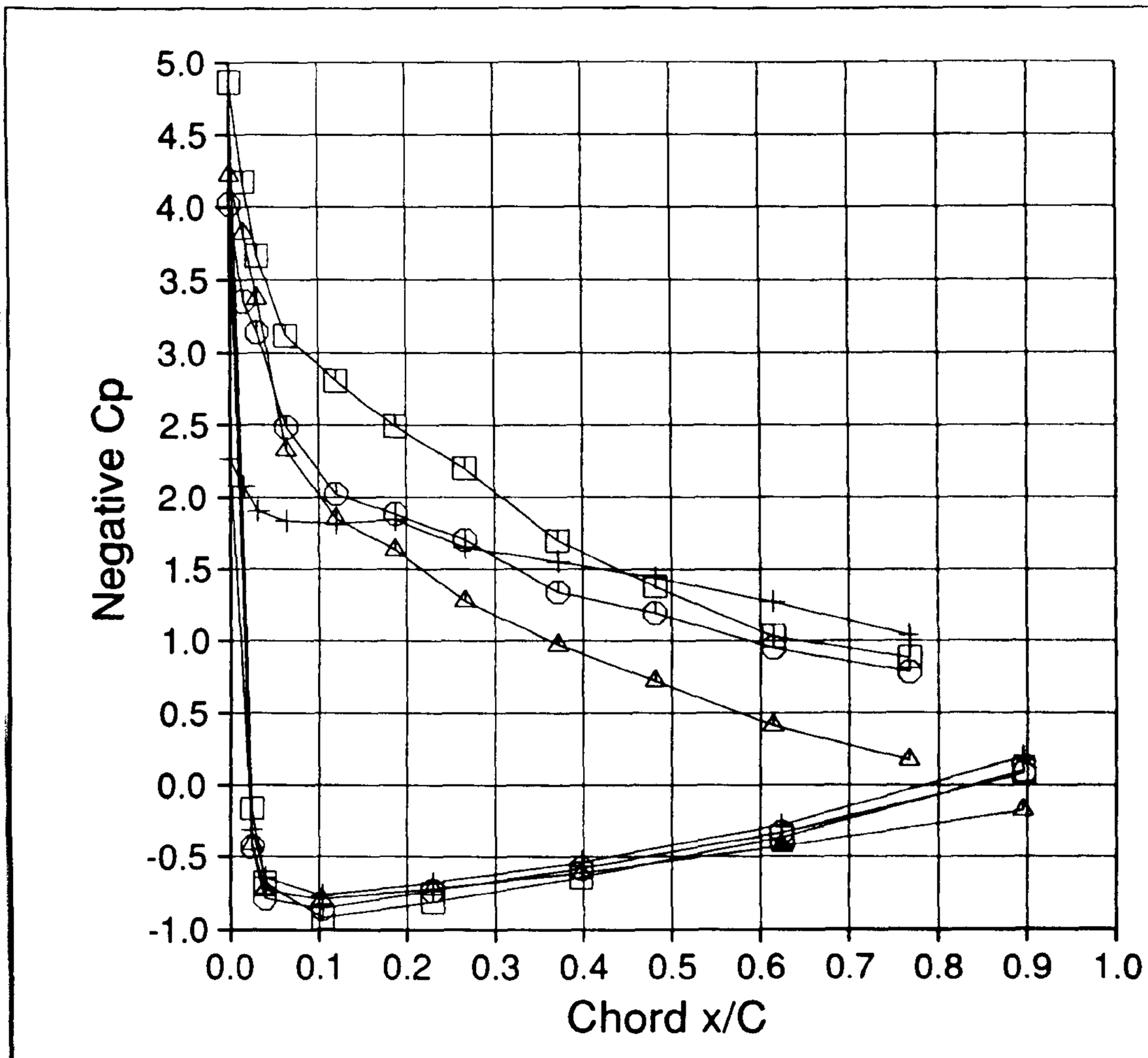

Cranfield

HAWT
Unsteady Aerodynamics
Experiment

Profiles V2.0

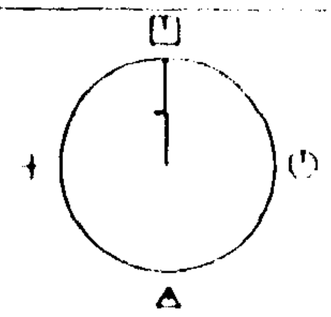

35% Span
Mean of Revs 040 TO 079
□ N = 164.0 N/m
○ N = 138.2 N/m
△ N = 111.8 N/m
\+ N = 138.2 N/m
Geometric alpha 39.6 deg
Rotor Speed 343.7 rpm
Body Angle 0.9 deg
Windspeed 18.1 m/s
Wind Angle -1.8 deg
Dynamic Head 400.1 Pa
Yaw Angle 2.8 deg
Tip Speed Ratio 2.8

165.EXP;2

7-FEB-1990:18:11:19

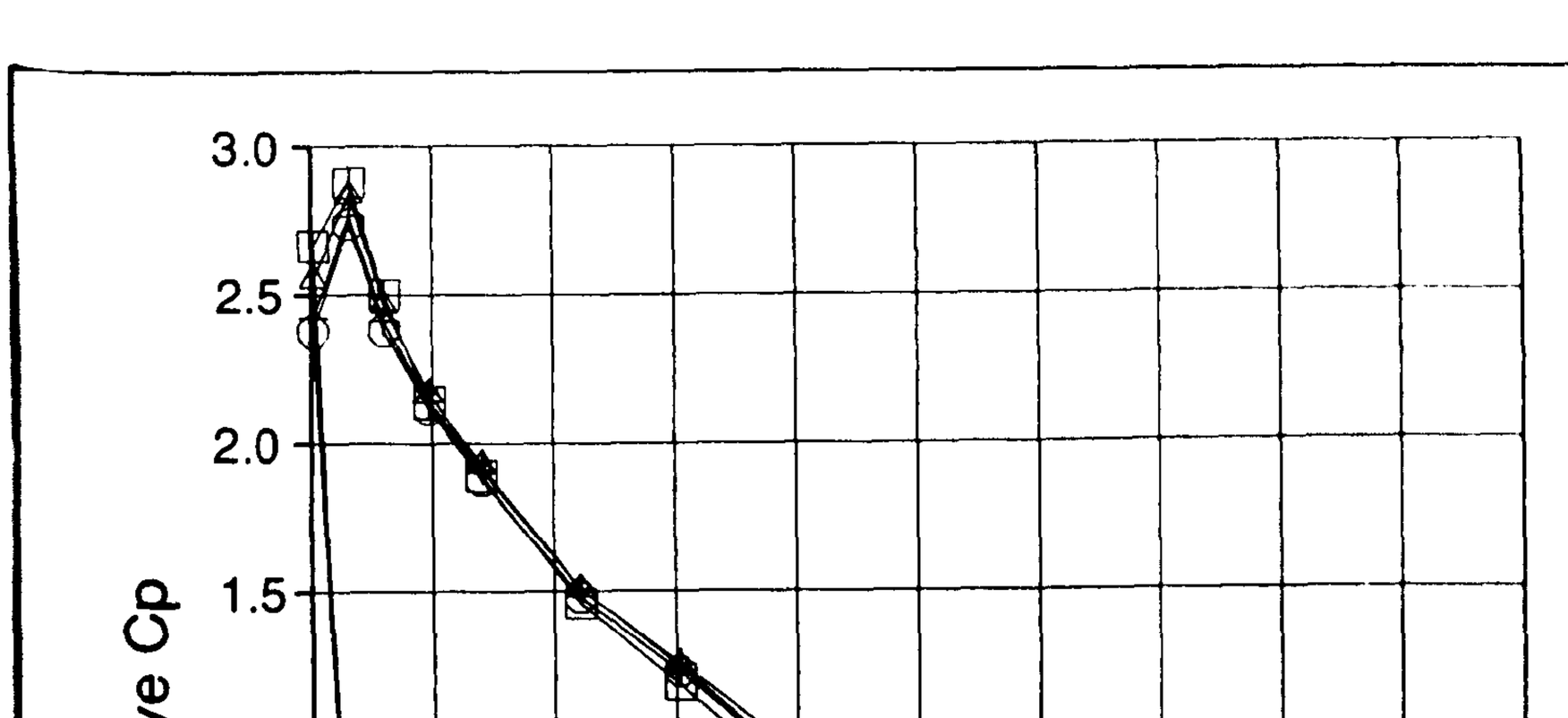

Cranfield

HAWT
Unsteady Aerodynamics
Experiment

Profiles V2.0

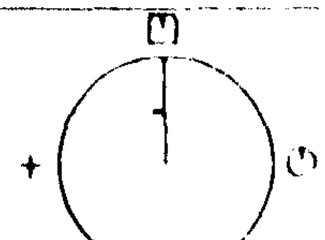

75% Span
Mean of Revs 040 TO 079
□ N = 175.4 N/m
○ N = 171.0 N/m
△ N = 173.9 N/m
\+ N = 169.5 N/m
Geometric alpha 19.5 deg
Rotor Speed 343.7 rpm
Body Angle 0.9 deg
Windspeed 18.1 m/s
Wind Angle -1.8 deg
Dynamic Head 1113.7 Pa
Yaw Angle 2.8 deg
Tip Speed Ratio 2.8

165.EXP;2

7-FEB-1990:18:11:19

Figure 10.9

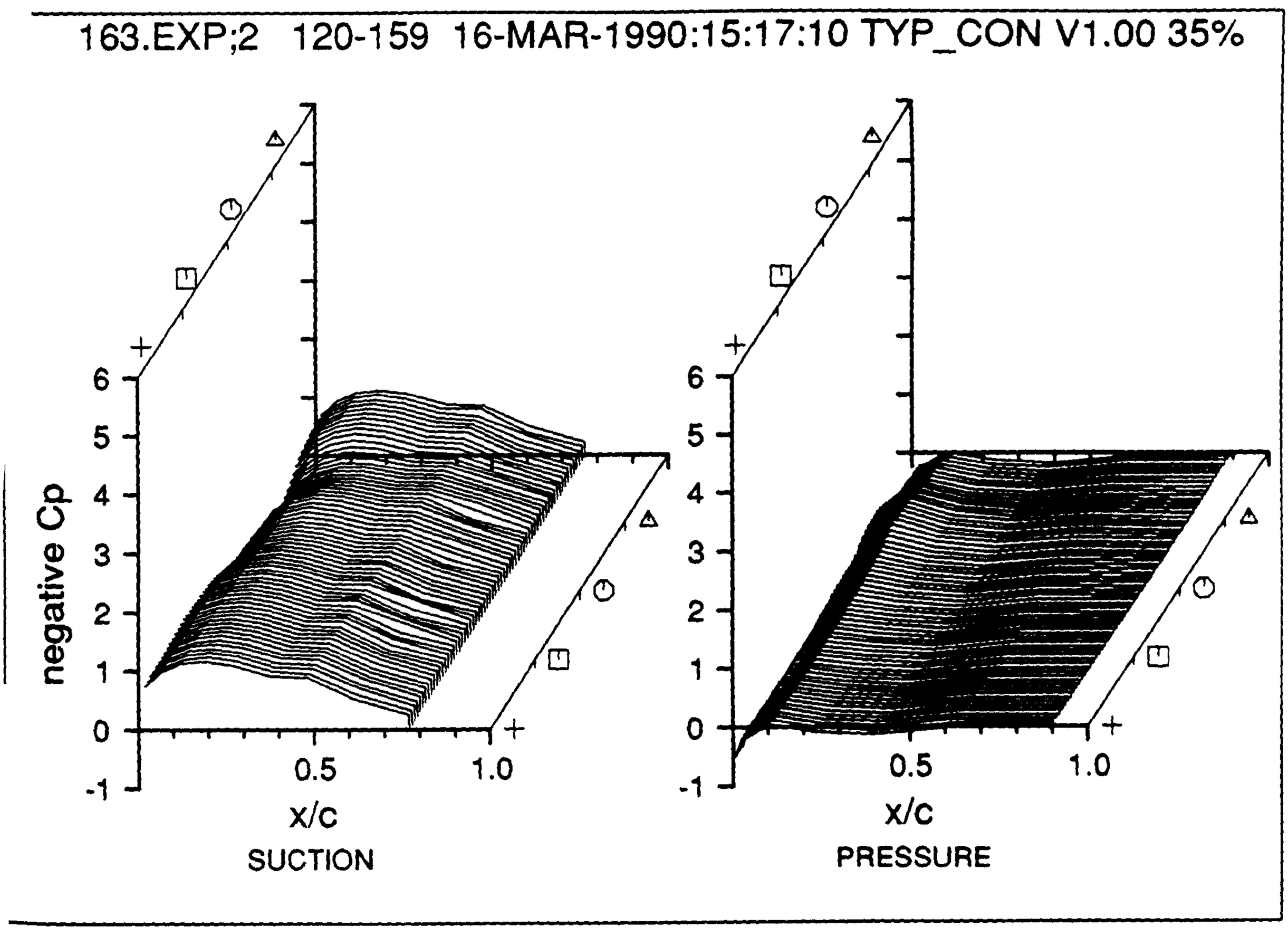
163.EXP;2 120-159 16-MAR-1990:15:17:10 TYP_CON V1.00 35%
negative Cp
6
5
4
3
2
1
0
-1
0.5
1.0
X/C
SUCTION
PRESSURE
163.EXP;2 120-159 16-MAR-1990:15:17:10 TYP_CON V1.00 75%
negative Cp
SUCTION
PRESSURE

Figure 10.10

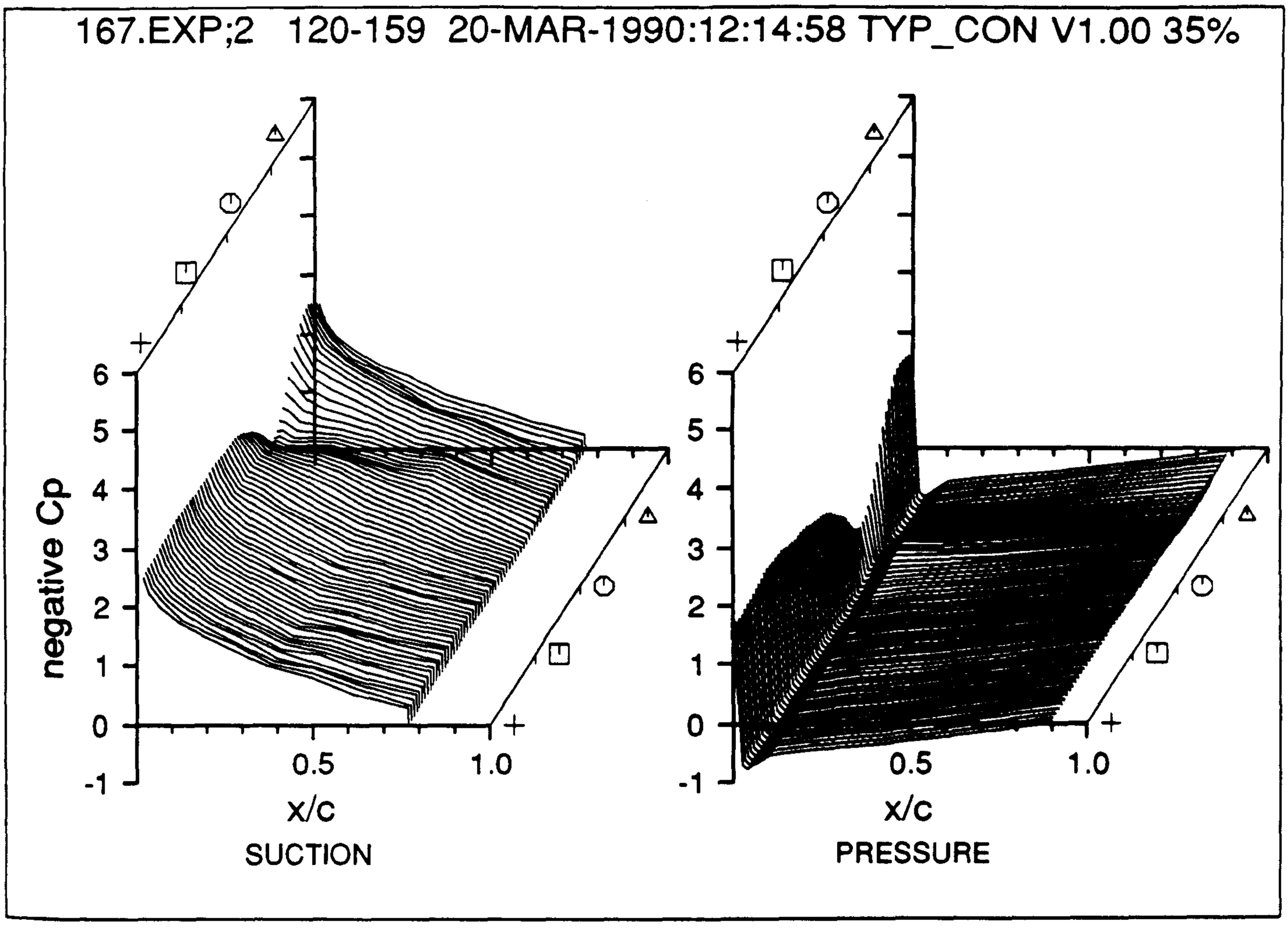
167.EXP;2 120-159 20-MAR-1990:12:14:58 TYP_CON V1.00 35%
negative Cp
6
5
4
3
2
1
0
-1
0.5
1.0
x/c
SUCTION
PRESSURE
167.EXP;2 120-159 20-MAR-1990:12:14:58 TYP_CON V1.00 75%

Figure 10.11

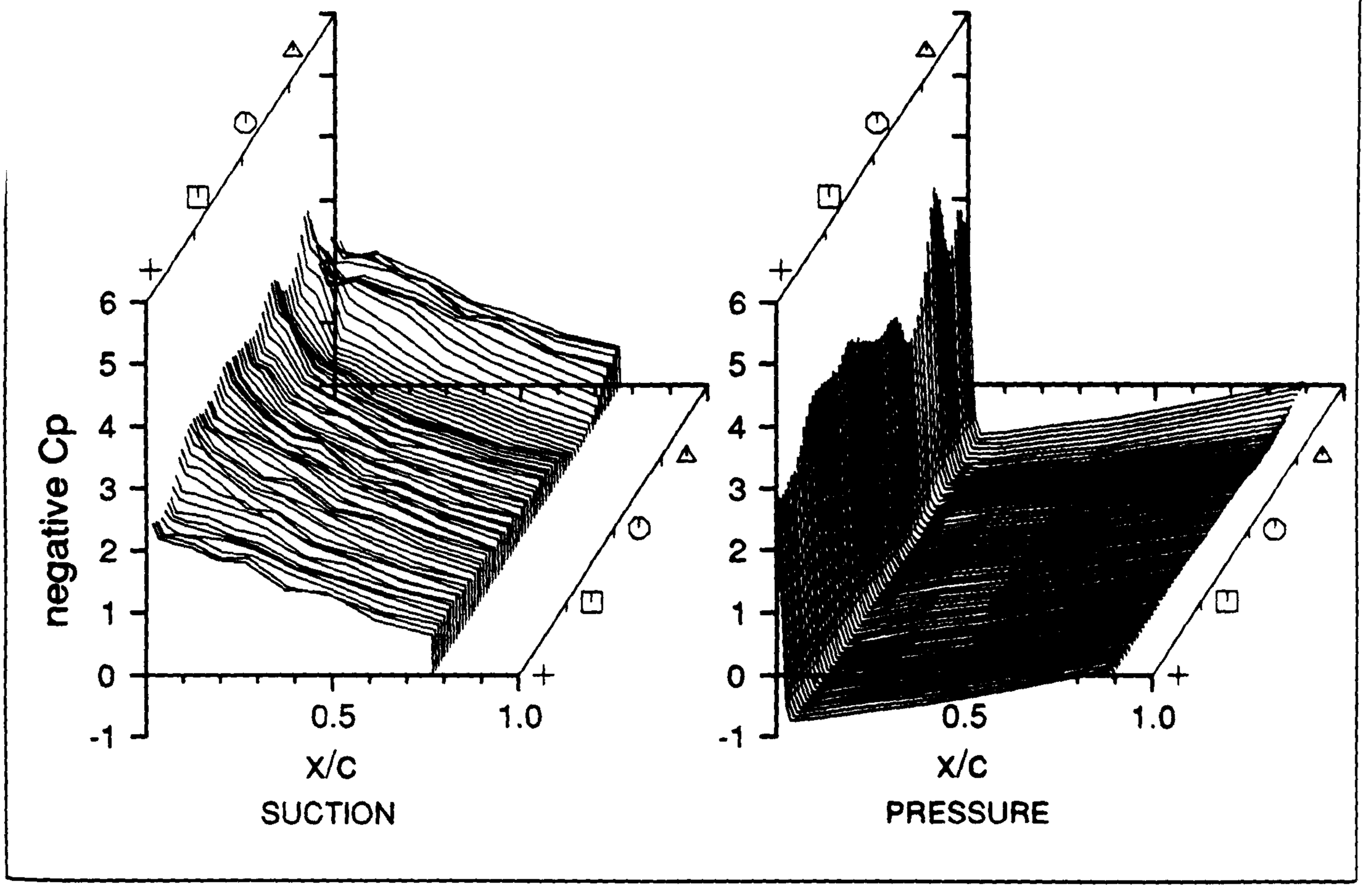
162.EXP;2 000-039 16-MAR-1990:15:09:07 TYP_CON V1.00 35%
negative Cp
6
5
4
3
2
1
0
-1
0.5
1.0
X/C
SUCTION
PRESSURE

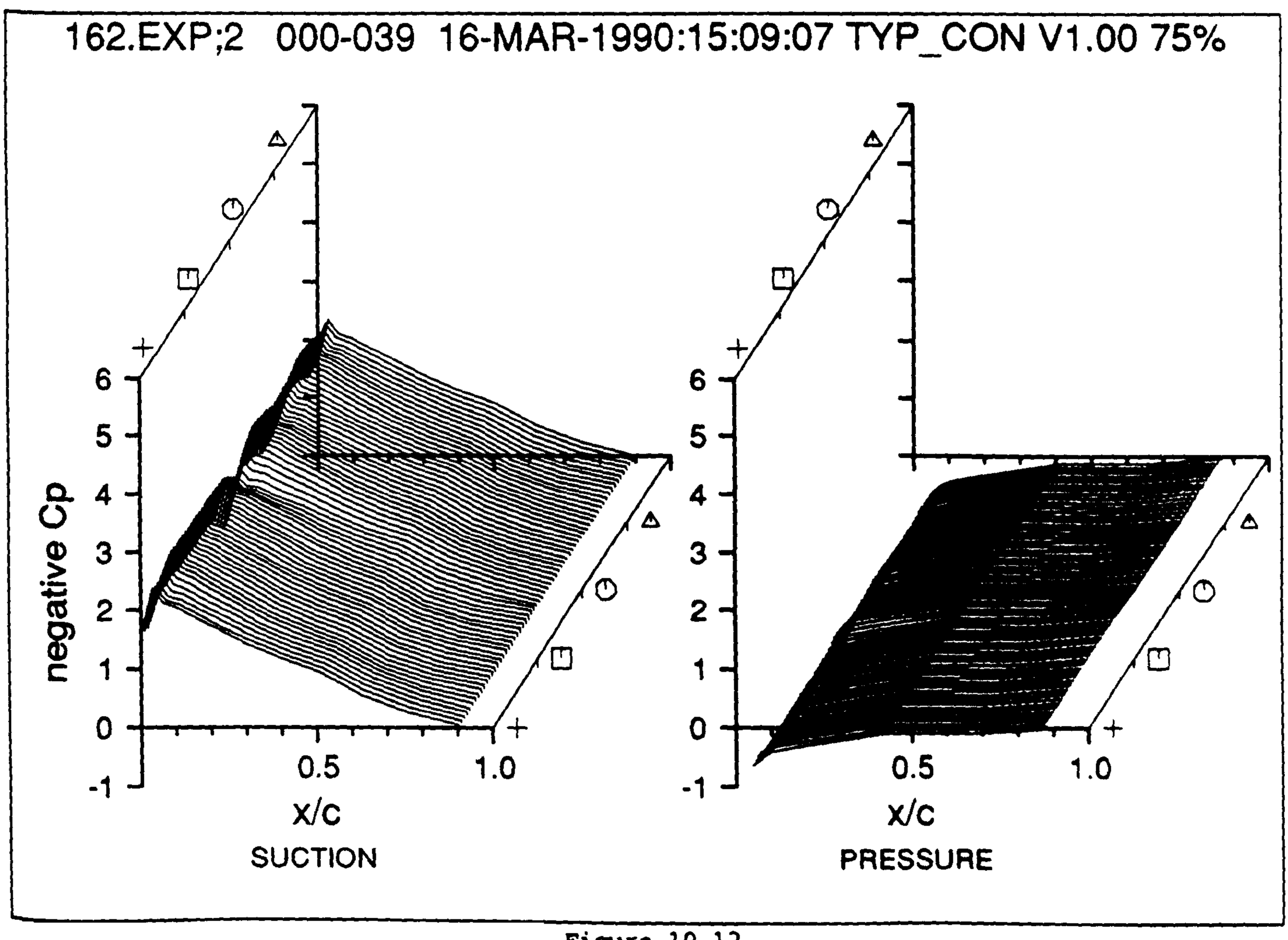
162.EXP;2 000-039 16-MAR-1990:15:09:07 TYP_CON V1.00 75%
negative Cp
6
5
4
3
2
1
0
-1
0.5
1.0
X/C
SUCTION
PRESSURE

Figure 10.12

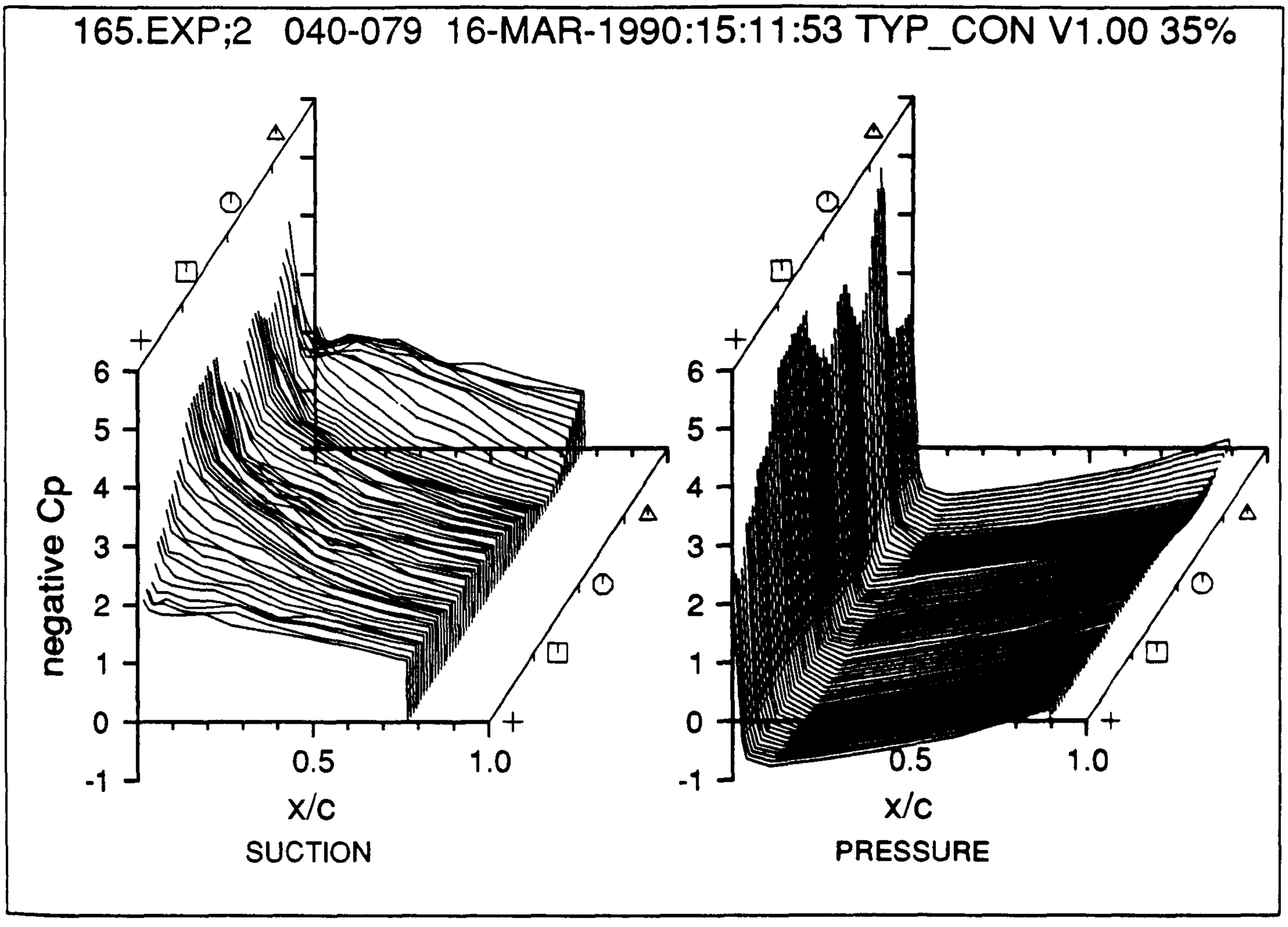
165.EXP;2 040-079 16-MAR-1990:15:11:53 TYP_CON V1.00 35%
negative Cp
6
5
4
3
2
1
0
-1
0.5
1.0
X/C
SUCTION
PRESSURE
165.EXP;2 040-079 16-MAR-1990:15:11:53 TYP_CON V1.00 75%

Figure 10.13

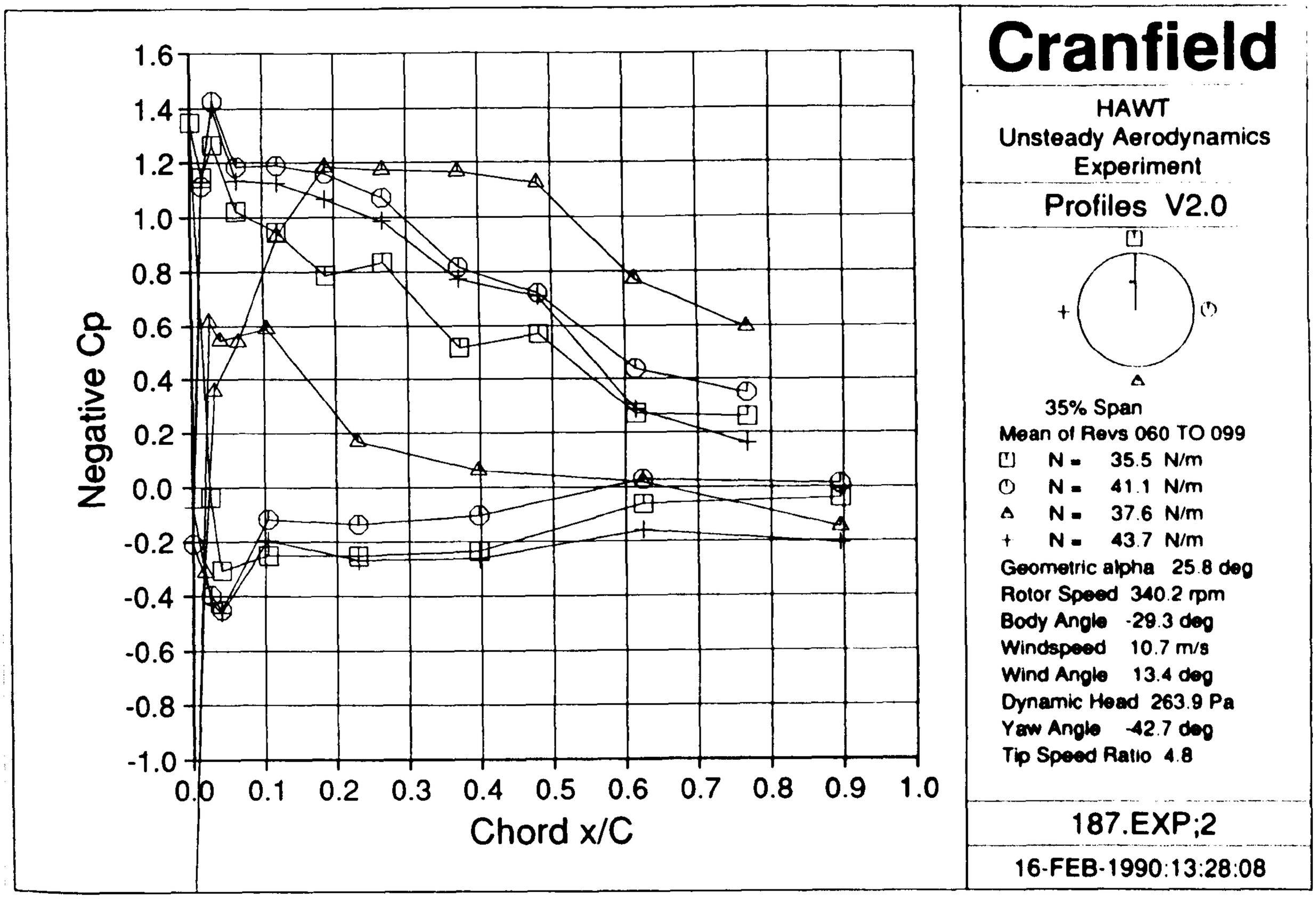
Cranfield
HAWT
Unsteady Aerodynamics
Experiment
Profiles V2.0
35% Span
Mean of Revs 060 TO 099
N = 35.5 N/m
N = 41.1 N/m
N = 37.6 N/m
N = 43.7 N/m
Geometric alpha 25.8 deg
Rotor Speed 340.2 rpm
Body Angle -29.3 deg
Windspeed 10.7 m/s
Wind Angle 13.4 deg
Dynamic Head 263.9 Pa
Yaw Angle -42.7 deg
Tip Speed Ratio 4.8
187.EXP;2
16-FEB-1990:13:28:08
Negative Cp
1.6
1.4
1.2
1.0
0.8
0.6
0.4
0.2
0.0
-0.2
-0.4
-0.6
-0.8
-1.0
0.0 0.1 0.2 0.3 0.4 0.5 0.6 0.7 0.8 0.9 1.0
Chord x/C

Cranfield
HAWT
Unsteady Aerodynamics
Experiment
Profiles V2.0
75% Span
Mean of Revs 060 TO 099
N = 76.1 N/m
N = 69.9 N/m
N = 79.6 N/m
N = 89.5 N/m
Geometric alpha 10.0 deg
Rotor Speed 340.2 rpm
Body Angle -29.3 deg
Windspeed 10.7 m/s
Wind Angle 13.4 deg
Dynamic Head 957.2 Pa
Yaw Angle -42.7 deg
Tip Speed Ratio 4.8
187.EXP;2
16-FEB-1990:13:28:08
Negative Cp
1.2
1.0
0.8
0.6
0.4
0.2
0.0
-0.2
-0.4
-0.6
-0.8
-1.0
0.0 0.1 0.2 0.3 0.4 0.5 0.6 0.7 0.8 0.9 1.0
Chord x/C

Figure 10.14

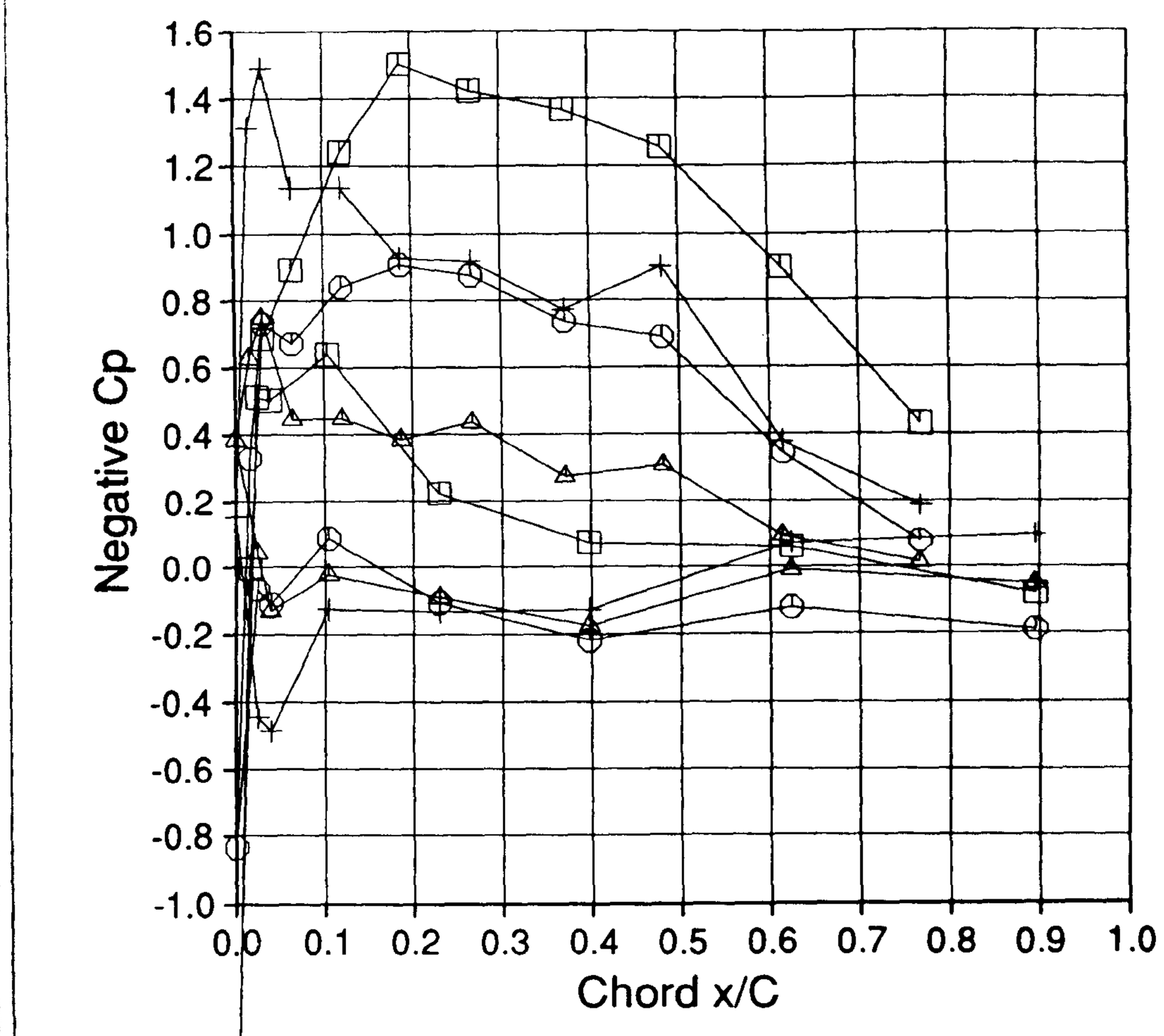

Cranfield

HAWT
Unsteady Aerodynamics
Experiment

Profiles V2.0

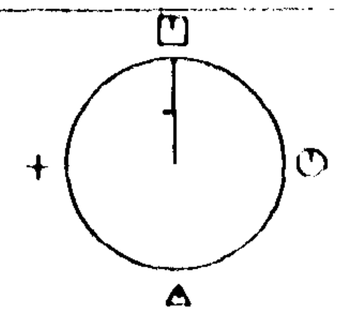

35% Span
Mean of Revs 000 TO 039

□	N =	41.4 N/m
○	N =	32.5 N/m
△	N =	15.7 N/m
+	N =	36.2 N/m

Geometric alpha 24.8 deg
Rotor Speed 340.2 rpm
Body Angle 43.3 deg
Windspeed 10.3 m/s
Wind Angle -12.7 deg
Dynamic Head 259.2 Pa
Yaw Angle 56.0 deg
Tip Speed Ratio 5.0

186.EXP;2

16-FEB-1990:13:34:17

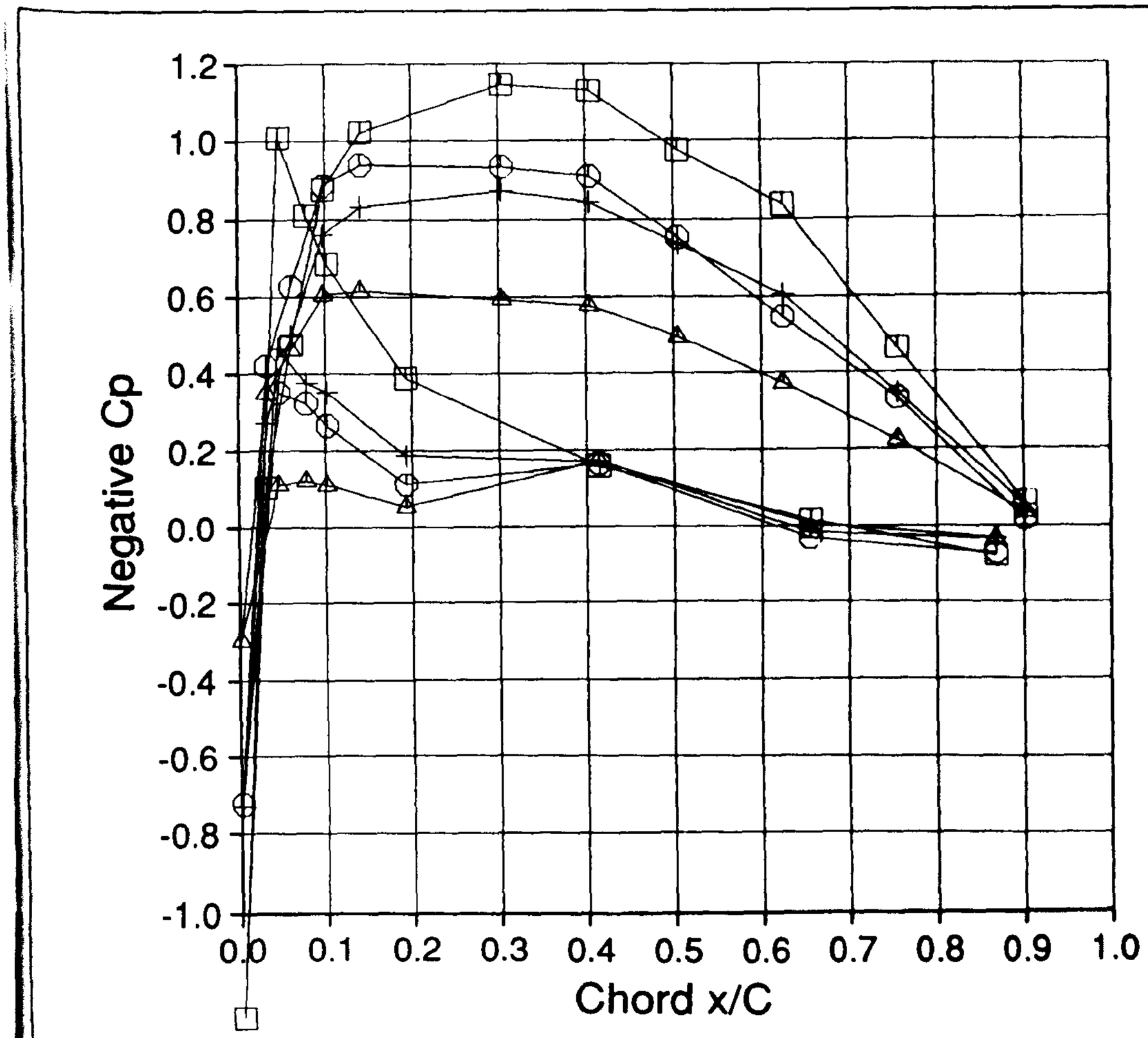

Cranfield

HAWT
Unsteady Aerodynamics
Experiment

Profiles V2.0

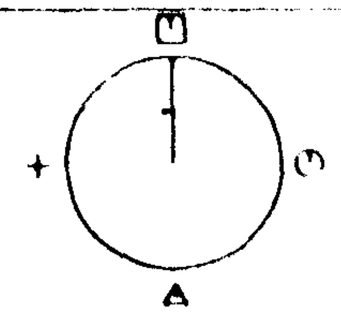

75% Span
Mean of Revs 000 TO 039

□	N =	72.5 N/m
○	N =	70.1 N/m
△	N =	46.0 N/m
+	N =	60.9 N/m

Geometric alpha 9.4 deg
Rotor Speed 340.2 rpm
Body Angle 43.3 deg
Windspeed 10.3 m/s
Wind Angle -12.7 deg
Dynamic Head 953.2 Pa
Yaw Angle 56.0 deg
Tip Speed Ratio 5.0

186.EXP;2

16-FEB-1990:13:34:17

Figure 10.15

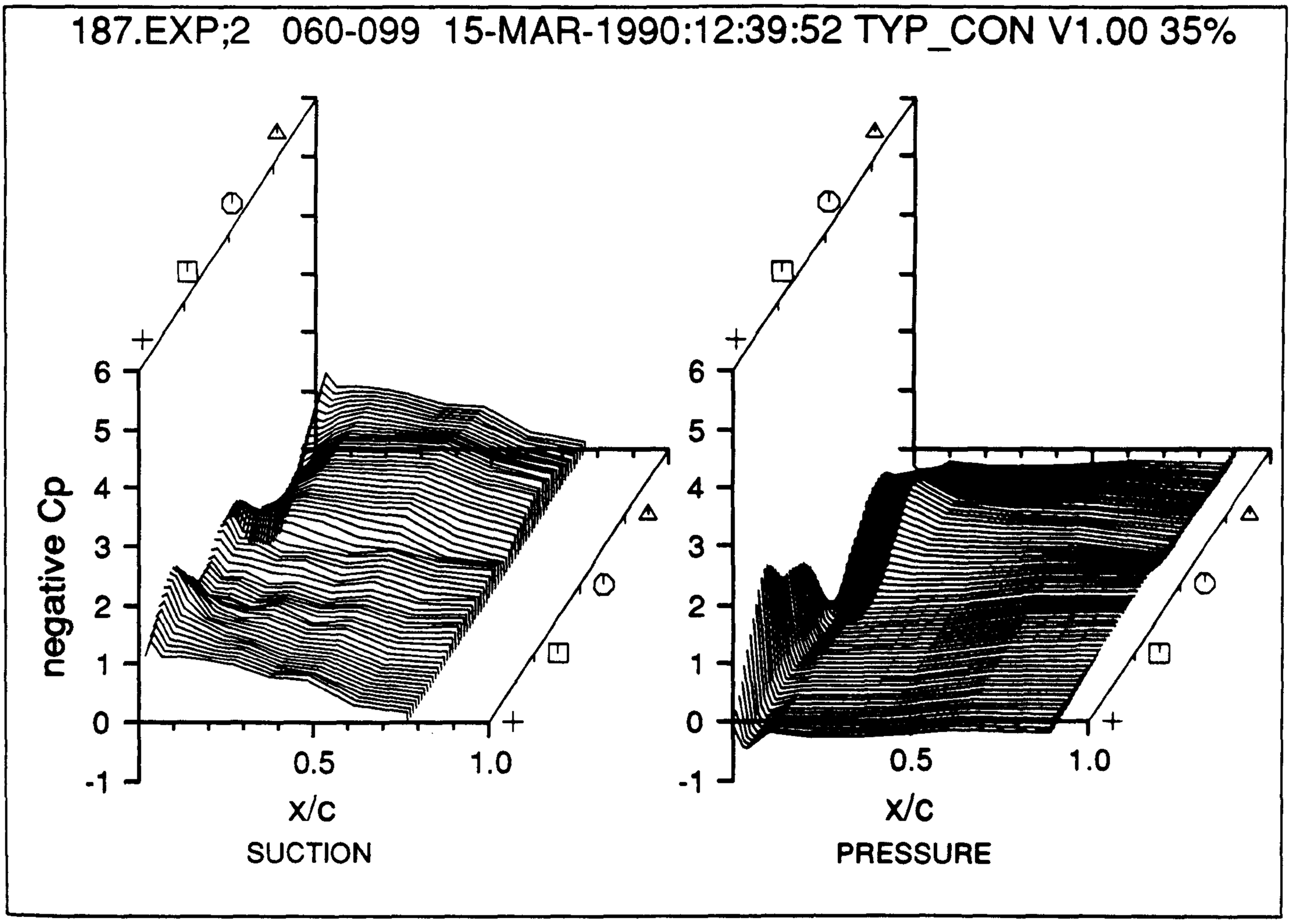
187.EXP;2 060-099 15-MAR-1990:12:39:52 TYP_CON V1.00 35%
negative Cp
6
5
4
3
2
1
0
-1
0.5
1.0
X/C
SUCTION
PRESSURE

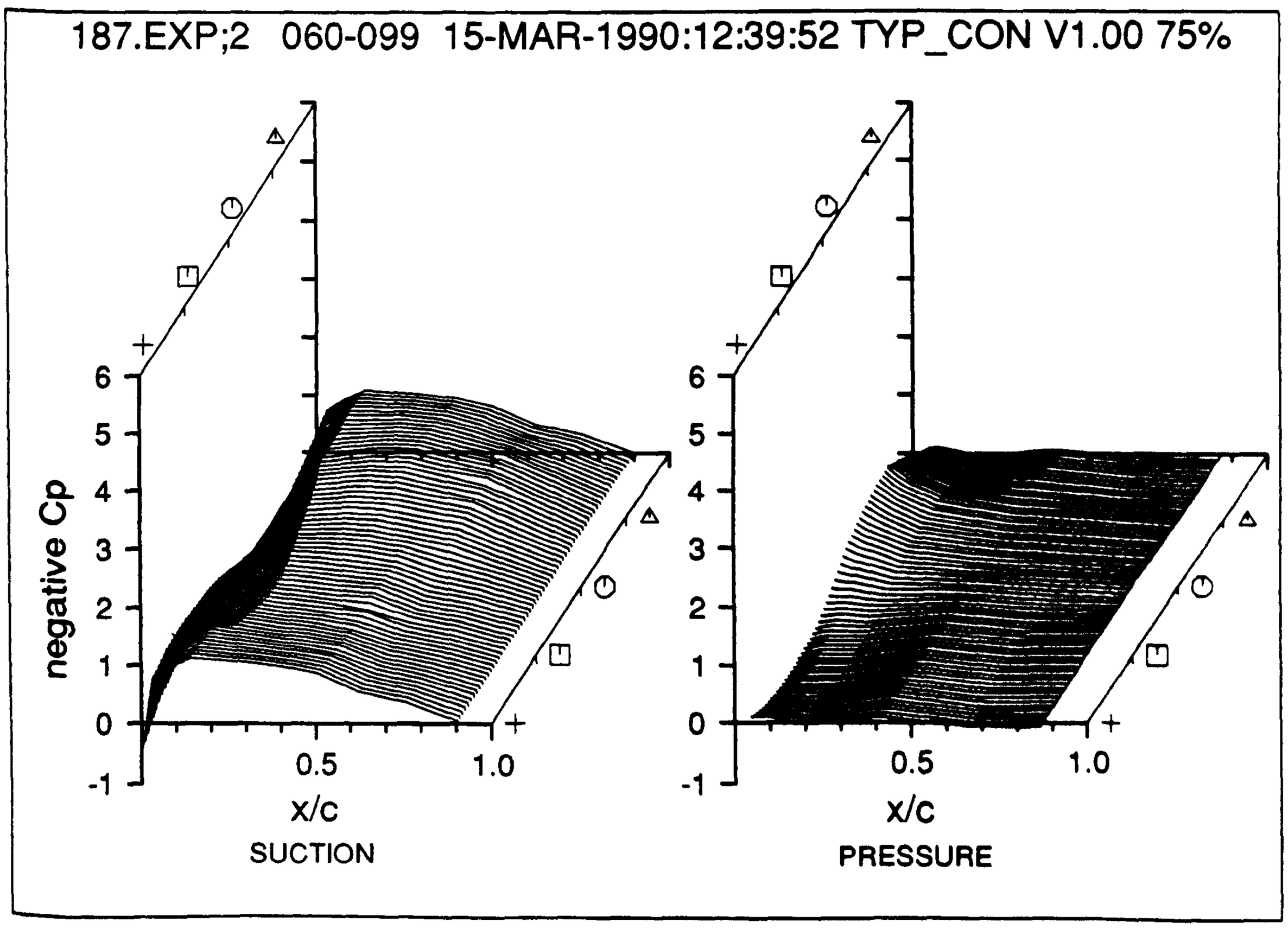
187.EXP;2 060-099 15-MAR-1990:12:39:52 TYP_CON V1.00 75%
negative Cp
6
5
4
3
2
1
0
-1
0.5
1.0
X/C
SUCTION
PRESSURE

Figure 10.16

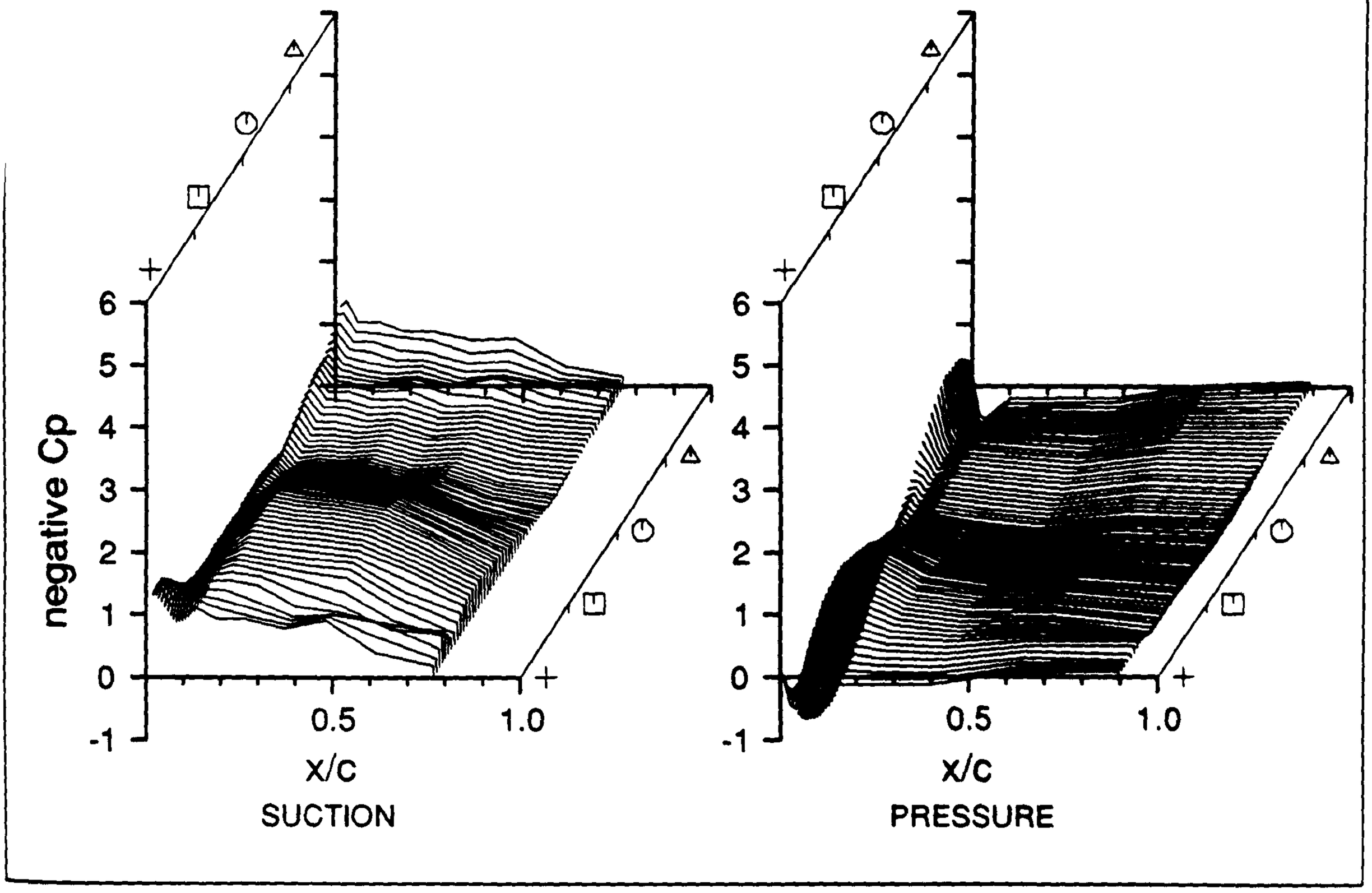
186.EXP;2 000-039 15-MAR-1990:12:37:10 TYP_CON V1.00 35%
negative Cp
6
5
4
3
2
1
0
-1
0.5
1.0
X/C
SUCTION
PRESSURE

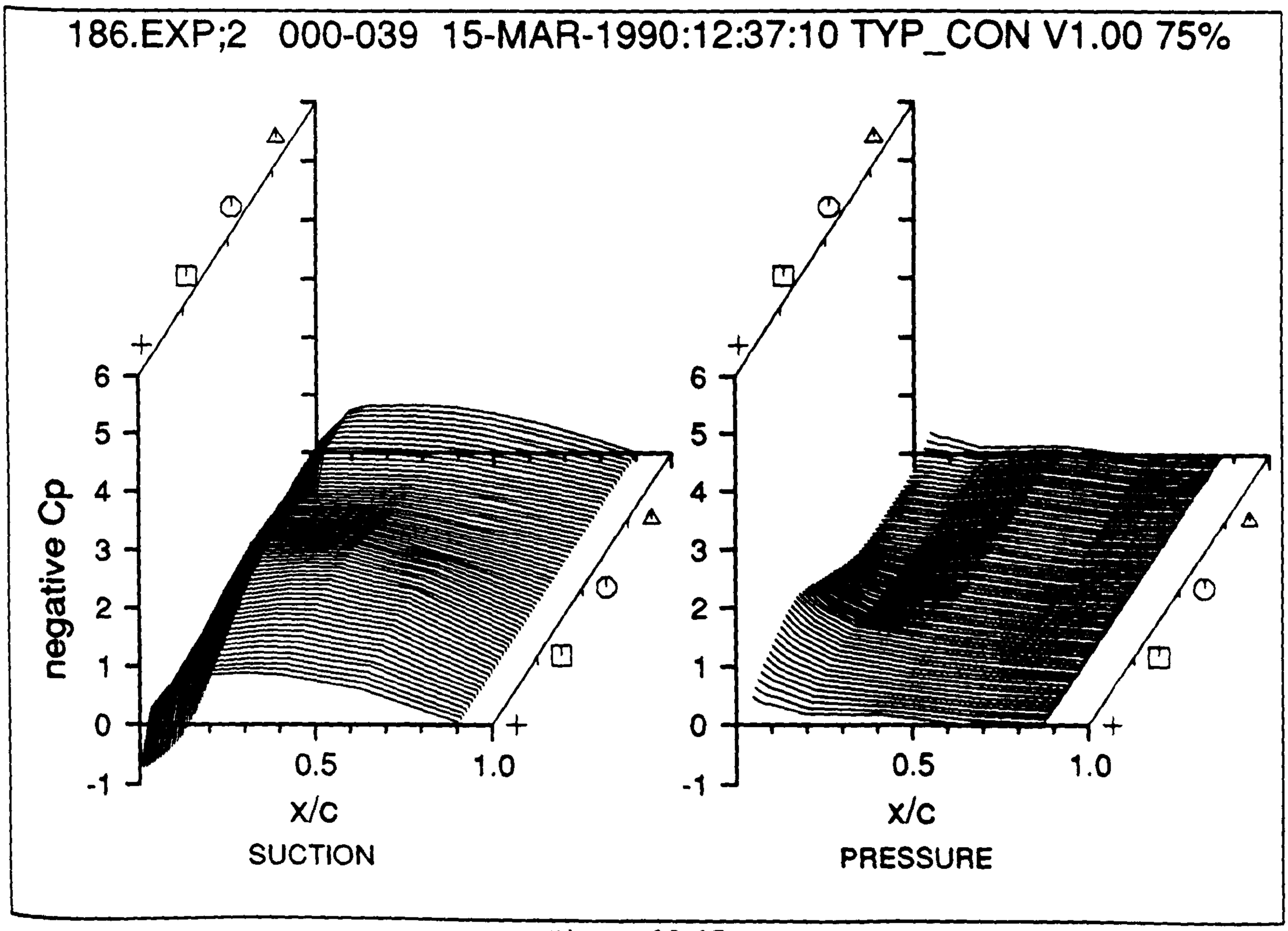
186.EXP;2 000-039 15-MAR-1990:12:37:10 TYP_CON V1.00 75%
negative Cp
6
5
4
3
2
1
0
-1
0.5
1.0
X/C
SUCTION
PRESSURE

Figure 10.17

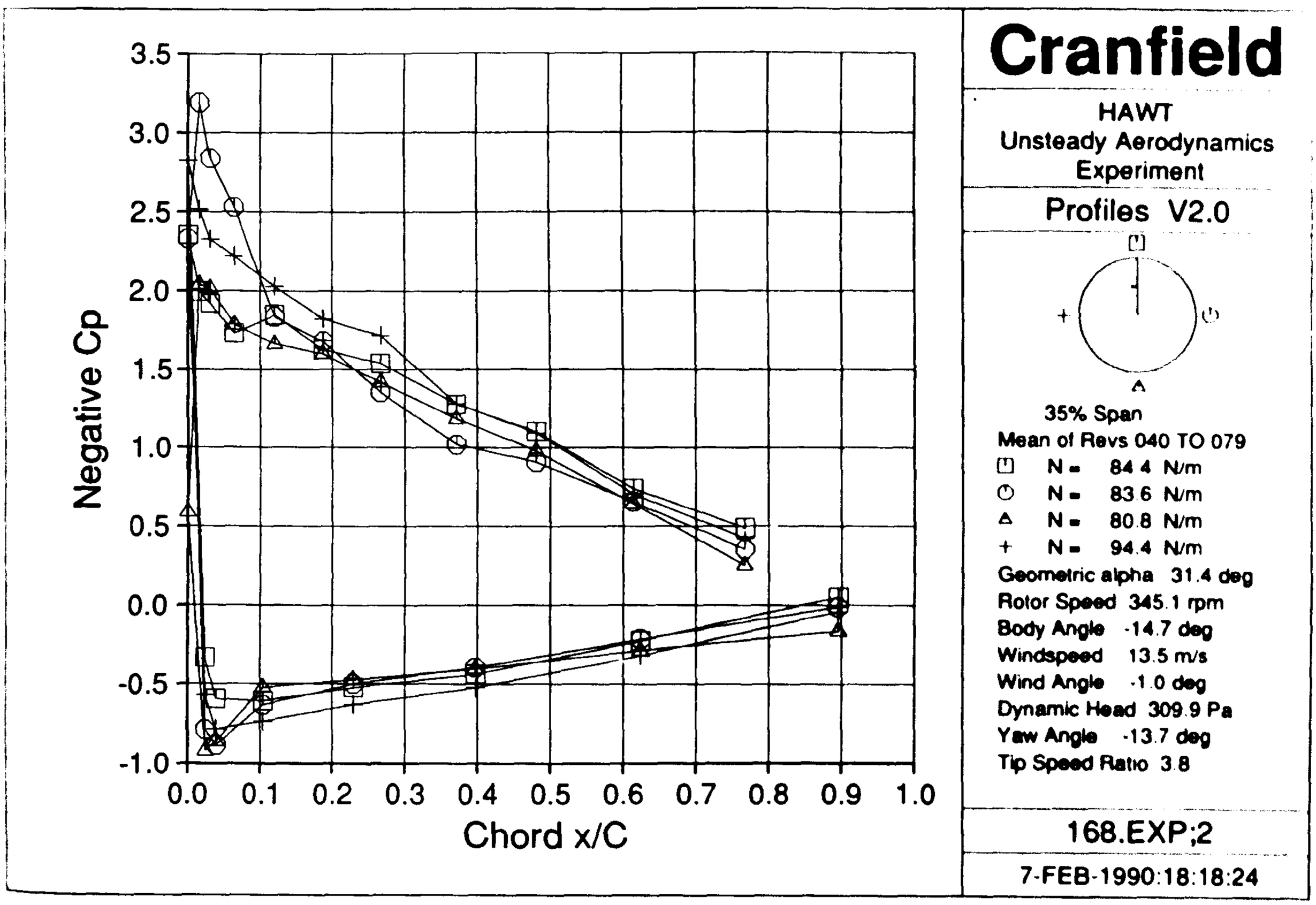
Cranfield
HAWT
Unsteady Aerodynamics
Experiment
Profiles V2.0
35% Span
Mean of Revs 040 TO 079
N = 84.4 N/m
N = 83.6 N/m
N = 80.8 N/m
N = 94.4 N/m
Geometric alpha 31.4 deg
Rotor Speed 345.1 rpm
Body Angle -14.7 deg
Windspeed 13.5 m/s
Wind Angle -1.0 deg
Dynamic Head 309.9 Pa
Yaw Angle -13.7 deg
Tip Speed Ratio 3.8
168.EXP;2
7-FEB-1990:18:18:24
Negative Cp
3.5
3.0
2.5
2.0
1.5
1.0
0.5
0.0
-0.5
-1.0
0.0 0.1 0.2 0.3 0.4 0.5 0.6 0.7 0.8 0.9 1.0
Chord x/C

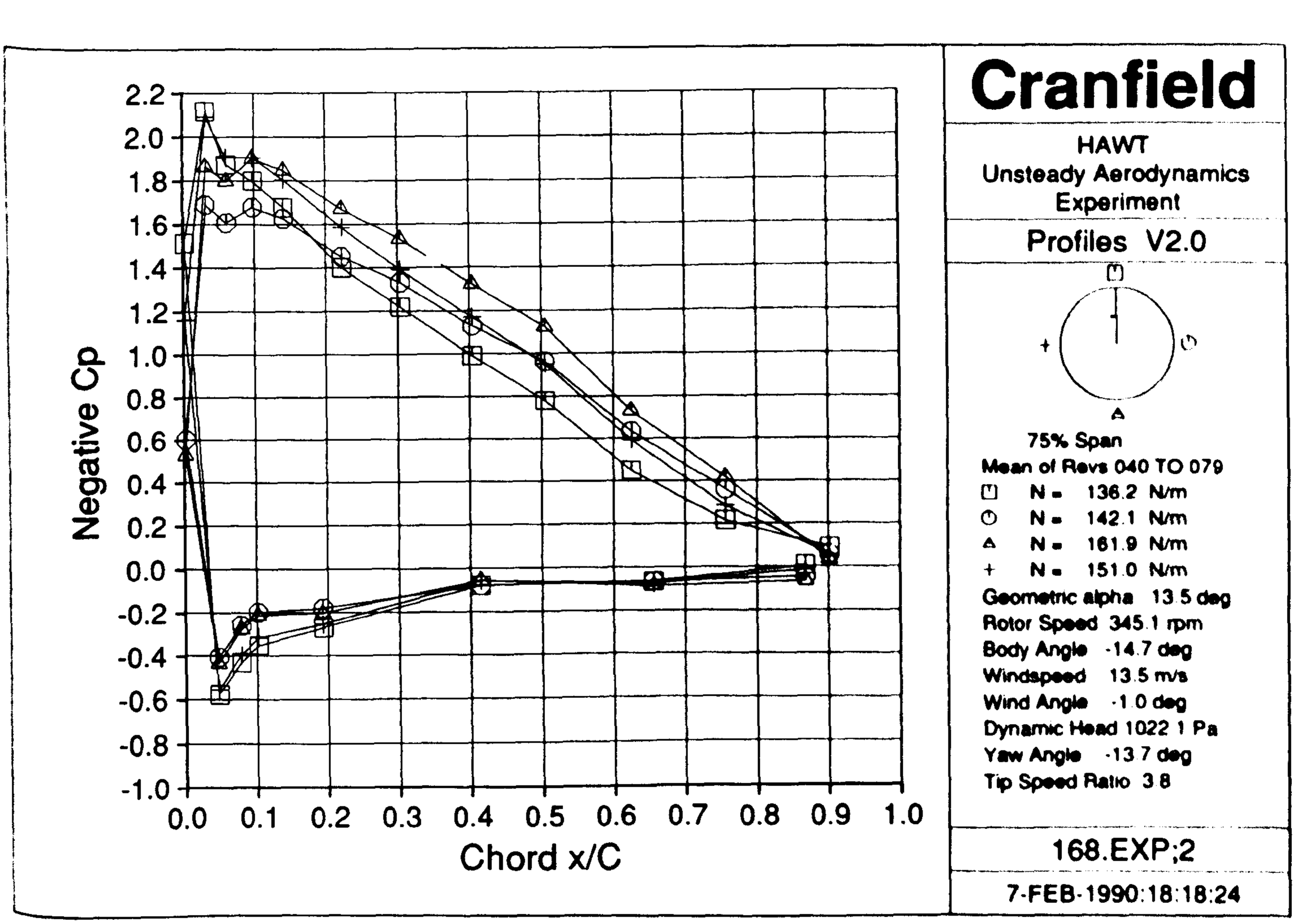
Cranfield
HAWT
Unsteady Aerodynamics
Experiment
Profiles V2.0
75% Span
Mean of Revs 040 TO 079
N = 136.2 N/m
N = 142.1 N/m
N = 161.9 N/m
N = 151.0 N/m
Geometric alpha 13.5 deg
Rotor Speed 345.1 rpm
Body Angle -14.7 deg
Windspeed 13.5 m/s
Wind Angle -1.0 deg
Dynamic Head 1022.1 Pa
Yaw Angle -13.7 deg
Tip Speed Ratio 3.8
168.EXP;2
7-FEB-1990:18:18:24
Negative Cp
2.2
2.0
1.8
1.6
1.4
1.2
1.0
0.8
0.6
0.4
0.2
0.0
-0.2
-0.4
-0.6
-0.8
-1.0
0.0 0.1 0.2 0.3 0.4 0.5 0.6 0.7 0.8 0.9 1.0
Chord x/C

Figure 10.18

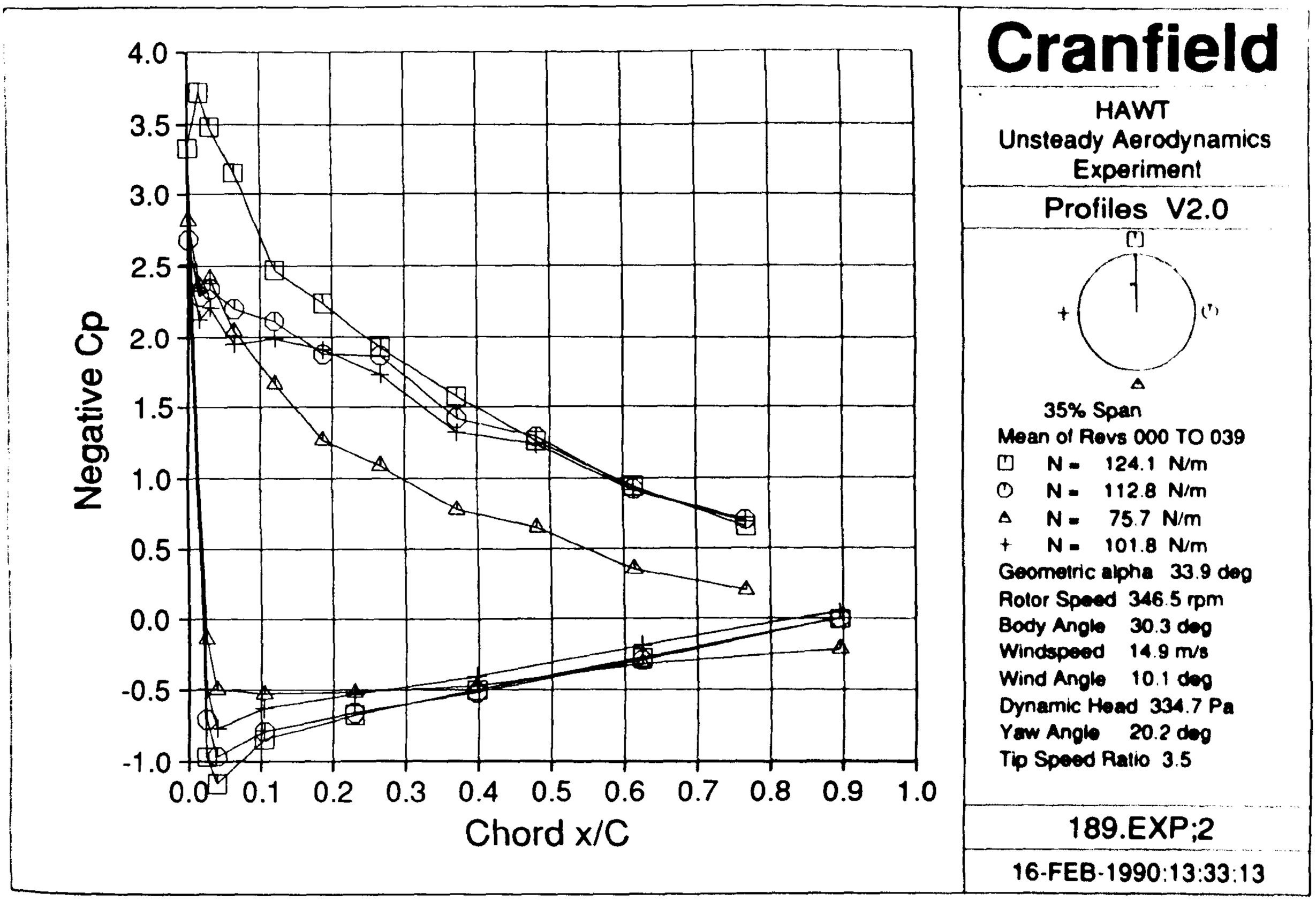
Negative Cp
4.0
3.5
3.0
2.5
2.0
1.5
1.0
0.5
0.0
-0.5
-1.0
0.0 0.1 0.2 0.3 0.4 0.5 0.6 0.7 0.8 0.9 1.0
Chord x/C
Cranfield
HAWT
Unsteady Aerodynamics
Experiment
Profiles V2.0
35% Span
Mean of Revs 000 TO 039
N = 124.1 N/m
N = 112.8 N/m
N = 75.7 N/m
N = 101.8 N/m
Geometric alpha 33.9 deg
Rotor Speed 346.5 rpm
Body Angle 30.3 deg
Windspeed 14.9 m/s
Wind Angle 10.1 deg
Dynamic Head 334.7 Pa
Yaw Angle 20.2 deg
Tip Speed Ratio 3.5
189.EXP;2
16-FEB-1990:13:33:13

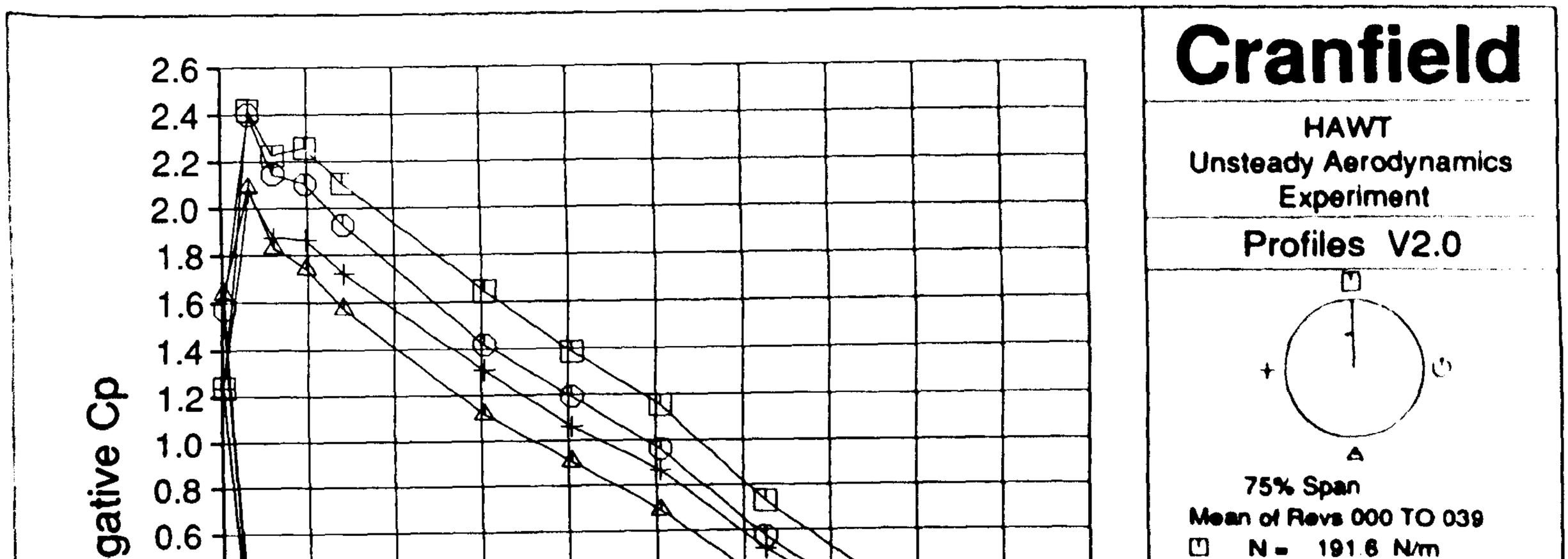
Negative Cp
2.6
2.4
2.2
2.0
1.8
1.6
1.4
1.2
1.0
0.8
0.6
0.4
0.2
0.0
-0.2
-0.4
-0.6
-0.8
-1.0
0.0 0.1 0.2 0.3 0.4 0.5 0.6 0.7 0.8 0.9 1.0
Chord x/C
Cranfield
HAWT
Unsteady Aerodynamics
Experiment
Profiles V2.0
75% Span
Mean of Revs 000 TO 039
N = 191.6 N/m
N = 171.4 N/m
N = 136.7 N/m
N = 150.9 N/m
Geometric alpha 15.2 deg
Rotor Speed 346.5 rpm
Body Angle 30.3 deg
Windspeed 14.9 m/s
Wind Angle 10.1 deg
Dynamic Head 1052.6 Pa
Yaw Angle 20.2 deg
Tip Speed Ratio 3.5
189.EXP;2
16-FEB-1990:13:33:13

Figure 10.19

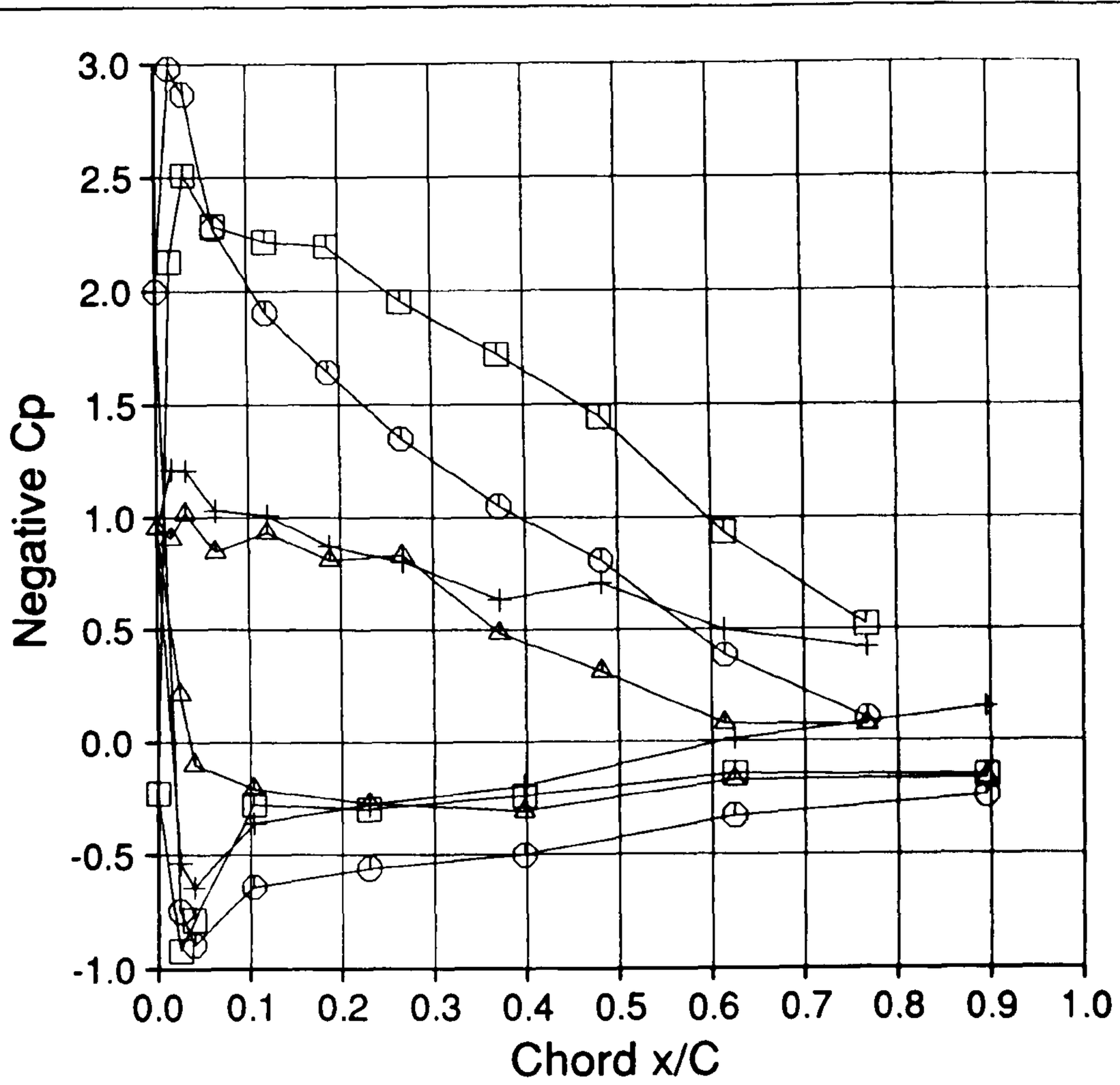

Cranfield

HAWT
Unsteady Aerodynamics
Experiment

Profiles V2.0

35% Span
Mean of Revs 080 TO 119
N = 103.4 N/m
N = 87.0 N/m
N = 39.2 N/m
N = 50.1 N/m
Geometric alpha 33.7 deg
Rotor Speed 343.4 rpm
Body Angle 30.3 deg
Windspeed 14.6 m/s
Wind Angle -12.3 deg
Dynamic Head 328.0 Pa
Yaw Angle 42.6 deg
Tip Speed Ratio 3.5

188.EXP;2

15-FEB-1990:16:05:29

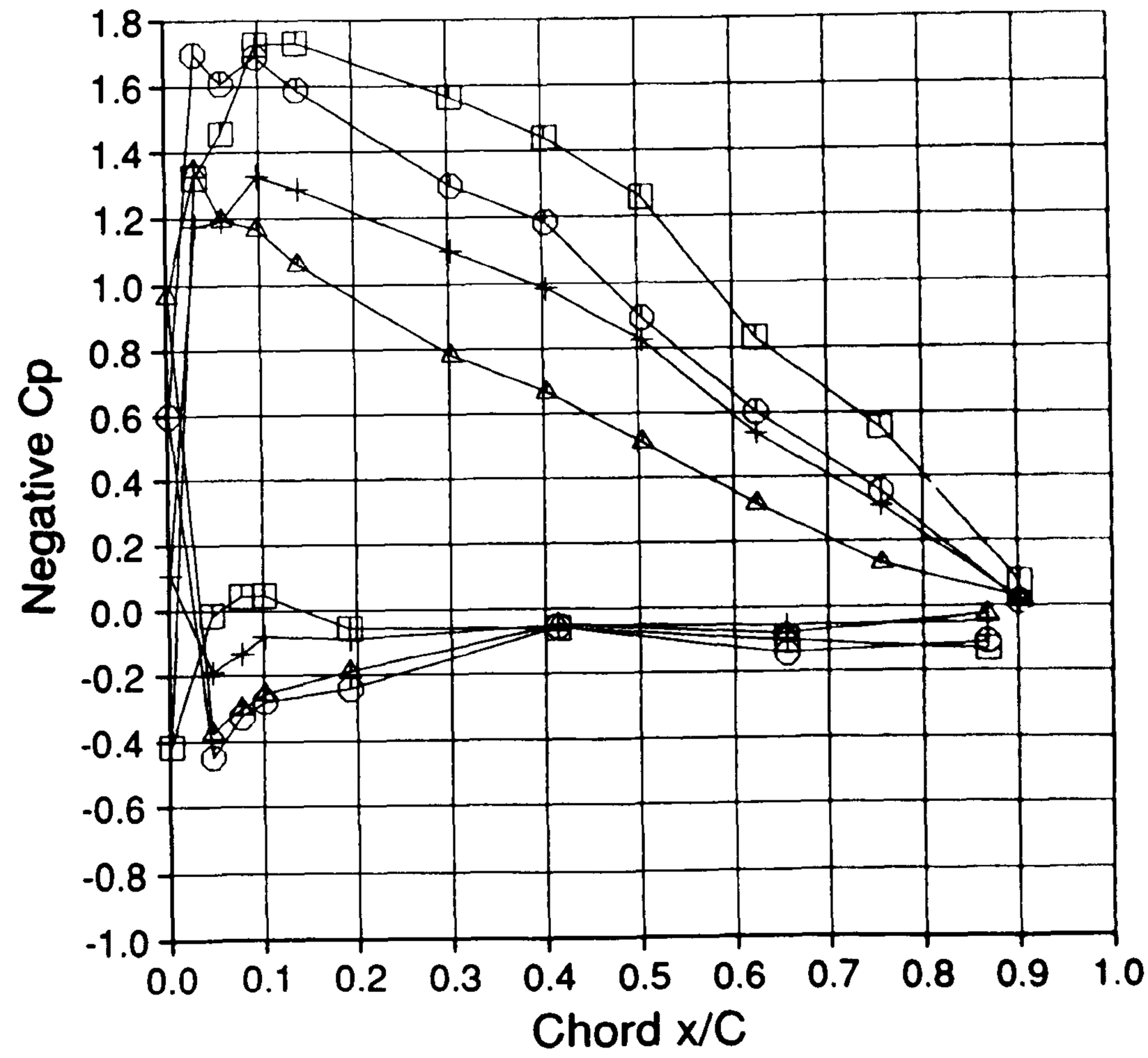

Cranfield

HAWT
Unsteady Aerodynamics
Experiment

Profiles V2.0

75% Span
Mean of Revs 080 TO 119
N = 161.4 N/m
N = 147.5 N/m
N = 91.9 N/m
N = 114.7 N/m
Geometric alpha 15.1 deg
Rotor Speed 343.4 rpm
Body Angle 30.3 deg
Windspeed 14.6 m/s
Wind Angle -12.3 deg
Dynamic Head 1035.3 Pa
Yaw Angle 42.6 deg
Tip Speed Ratio 3.5

188.EXP;2

15-FEB-1990:16:05:29

Figure 10.20

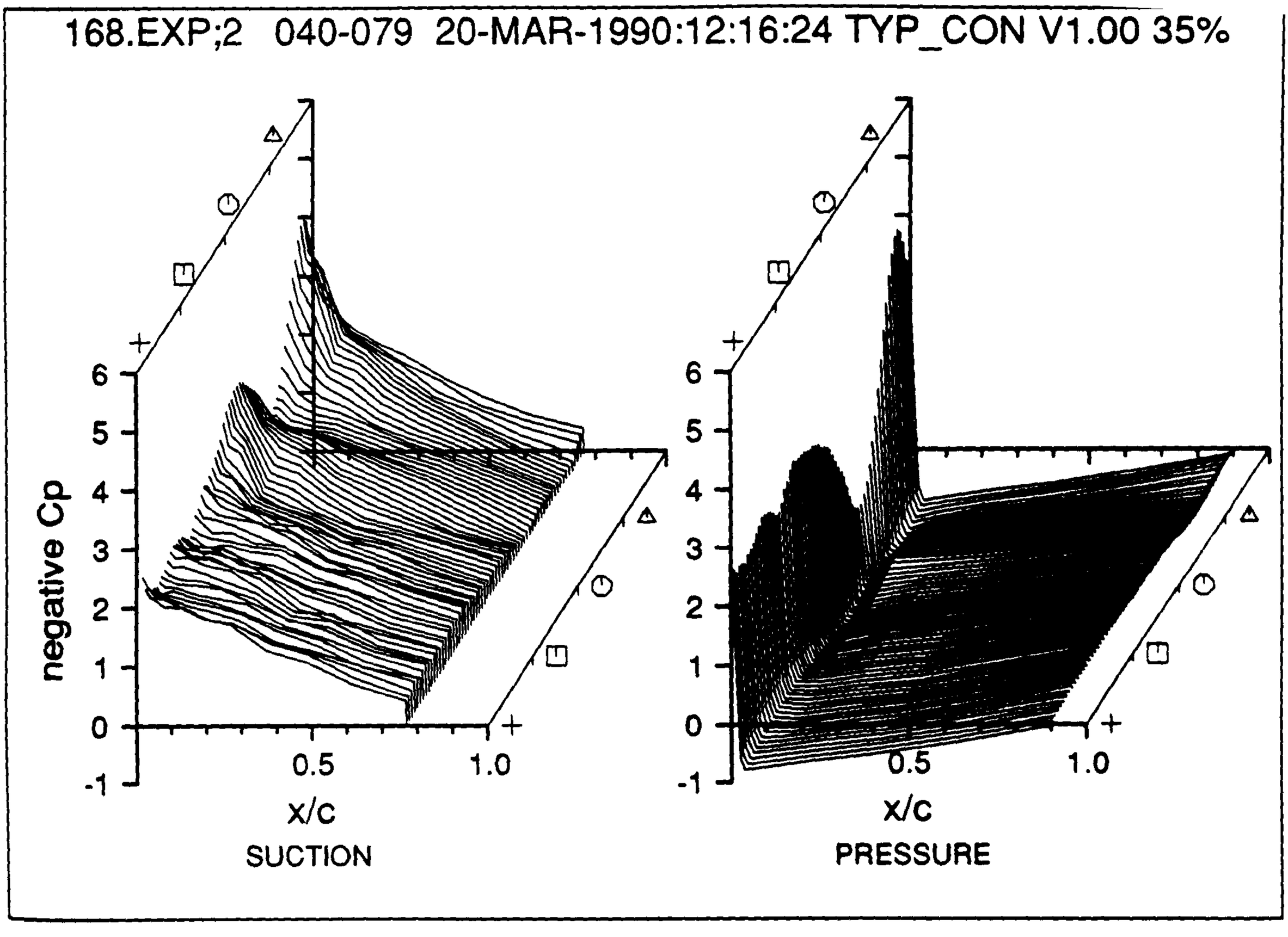
168.EXP;2 040-079 20-MAR-1990:12:16:24 TYP_CON V1.00 35%
negative Cp
6
5
4
3
2
1
0
-1
0.5
1.0
X/C
SUCTION
PRESSURE
168.EXP;2 040-079 20-MAR-1990:12:16:24 TYP_CON V1.00 75%
negative Cp
X/C
SUCTION
PRESSURE

Figure 10.21

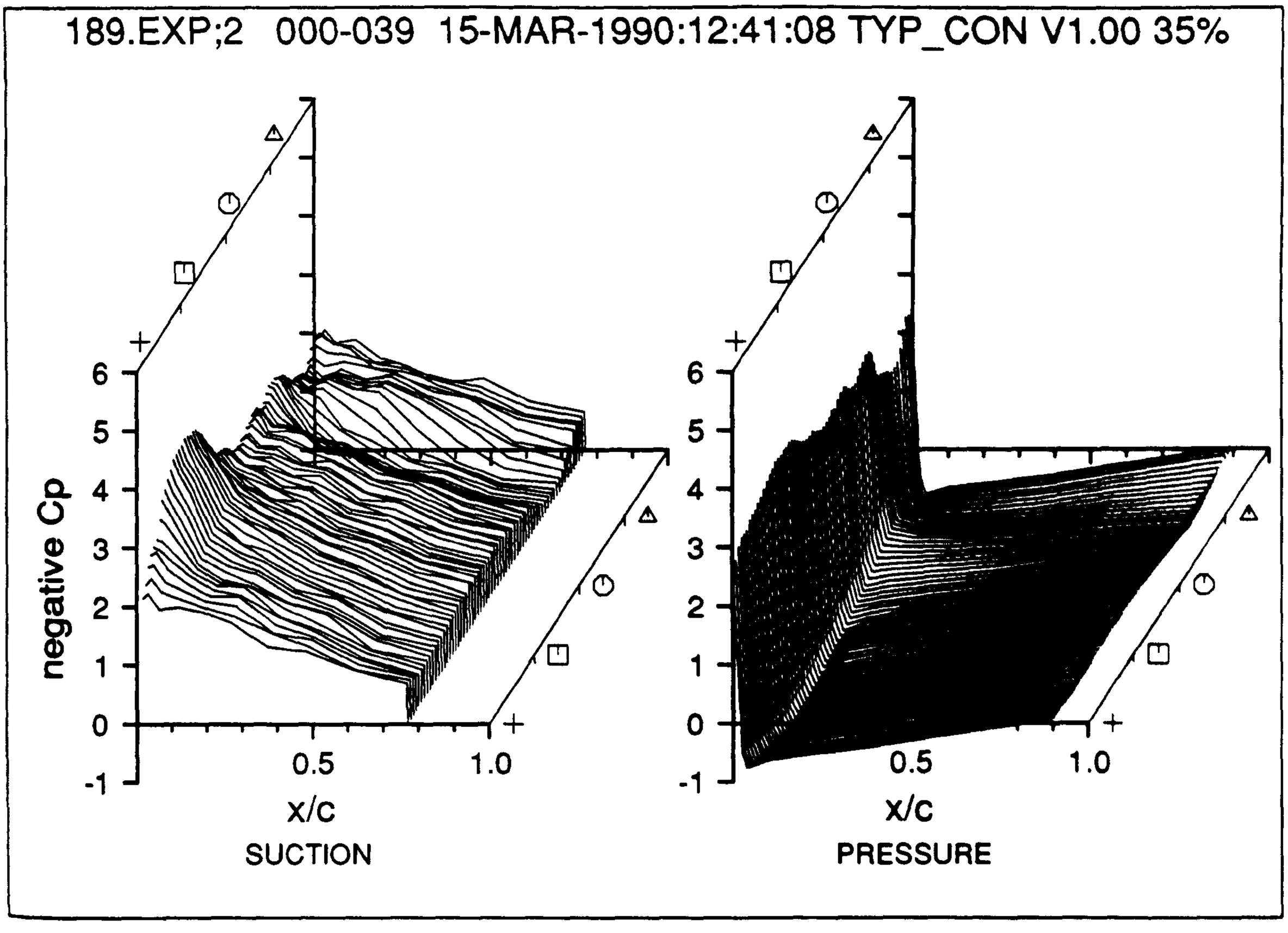
189.EXP;2 000-039 15-MAR-1990:12:41:08 TYP_CON V1.00 35%
negative Cp
6
5
4
3
2
1
0
-1
0.5
1.0
X/C
SUCTION
PRESSURE
189.EXP;2 000-039 15-MAR-1990:12:41:08 TYP_CON V1.00 75%
negative Cp
SUCTION
PRESSURE

Figure 10.22

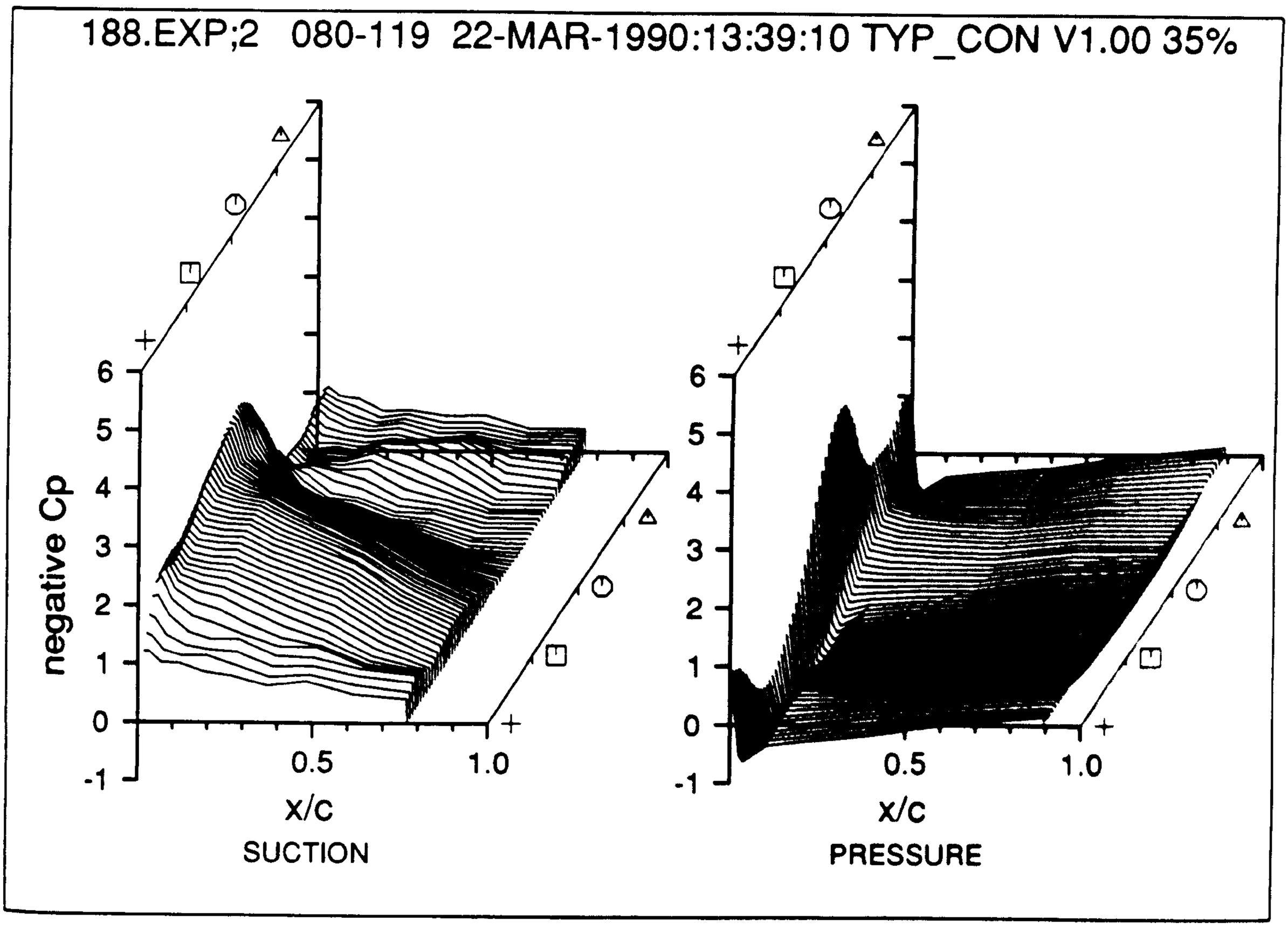
188.EXP;2 080-119 22-MAR-1990:13:39:10 TYP_CON V1.00 35%
negative Cp
6
5
4
3
2
1
0
-1
0.5
1.0
X/C
SUCTION
PRESSURE
188.EXP;2 080-119 22-MAR-1990:13:39:10 TYP_CON V1.00 75%
negative Cp
SUCTION
PRESSURE

Figure 10.23

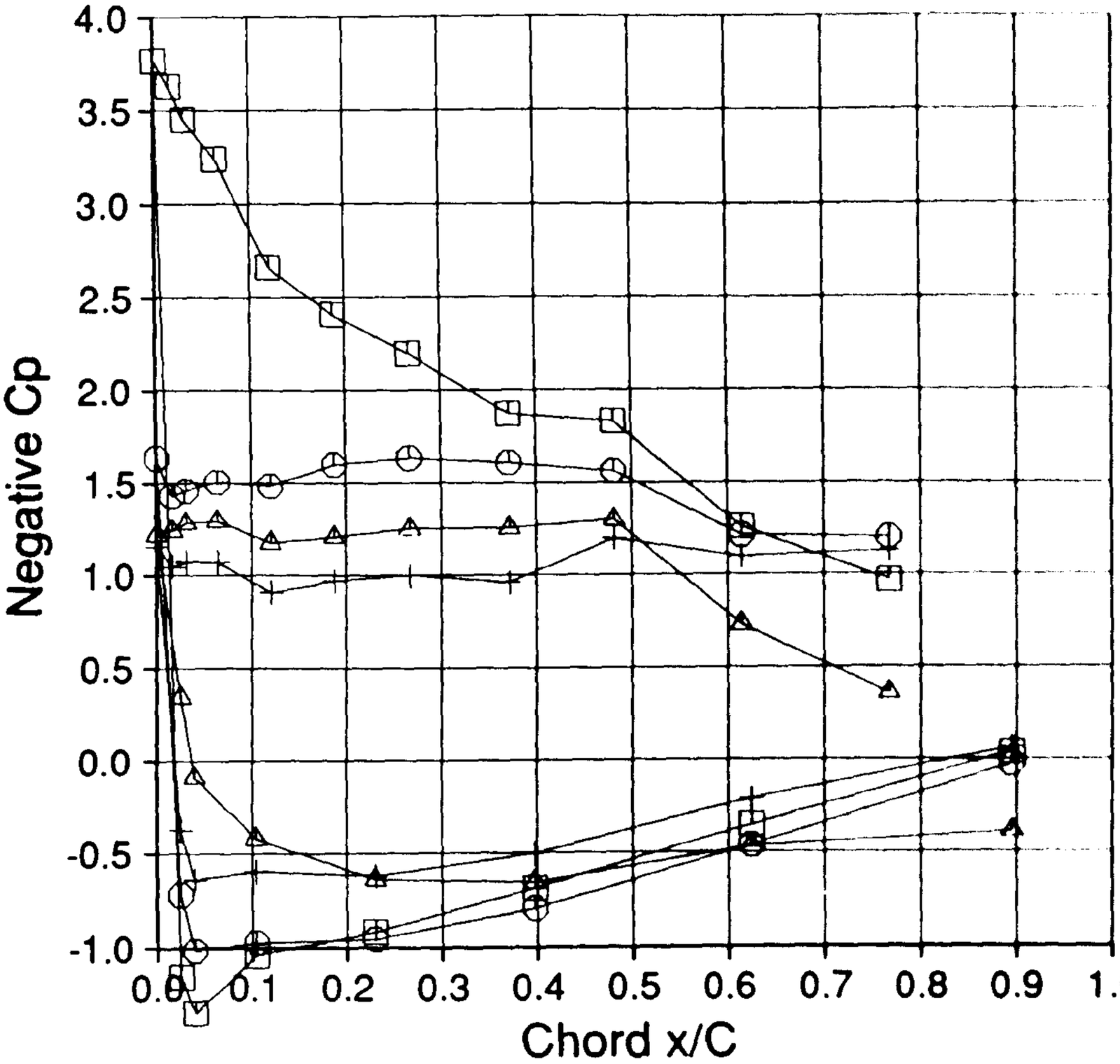

Cranfield

HAWT
Unsteady Aerodynamics
Experiment

Profiles V2.0

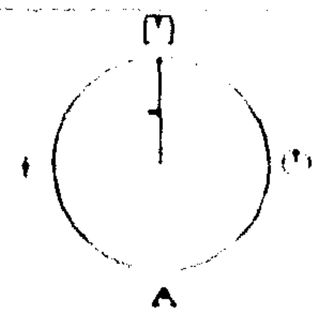

35% Span
Mean of Revs 100 TO 139
N = 177.2 N/m
N = 151.5 N/m
N = 106.1 N/m
N = 105.5 N/m
Geometric alpha 40.6 deg
Rotor Speed 341.7 rpm
Body Angle 15.1 deg
Windspeed 18.6 m/s
Wind Angle -12.5 deg
Dynamic Head 393.4 Pa
Yaw Angle 27.6 deg
Tip Speed Ratio 2.7

199.EXP;2

15-FEB-1990 16:02:50

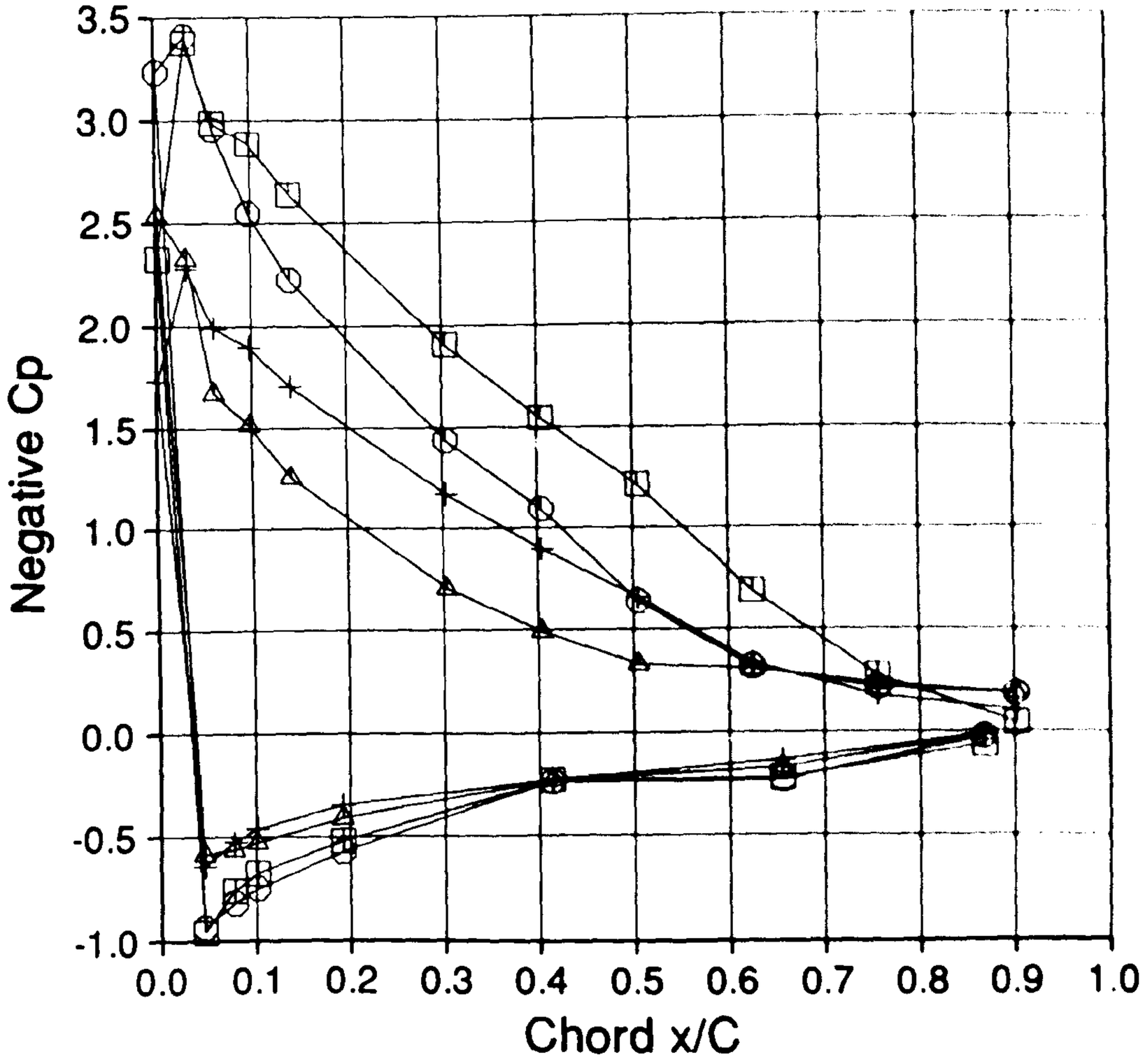

Cranfield

HAWT
Unsteady Aerodynamics
Experiment

Profiles V2.0

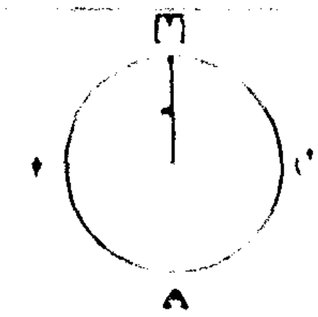

75% Span
Mean of Revs 100 TO 139
N = 235.9 N/m
N = 195.5 N/m
N = 122.3 N/m
N = 149.8 N/m
Geometric alpha 20.2 deg
Rotor Speed 341.7 rpm
Body Angle 15.1 deg
Windspeed 18.6 m/s
Wind Angle -12.5 deg
Dynamic Head 1071.2 Pa
Yaw Angle 27.6 deg
Tip Speed Ratio 2.7

199.EXP;2

15-FEB-1990 16:02:50

Figure 10.24

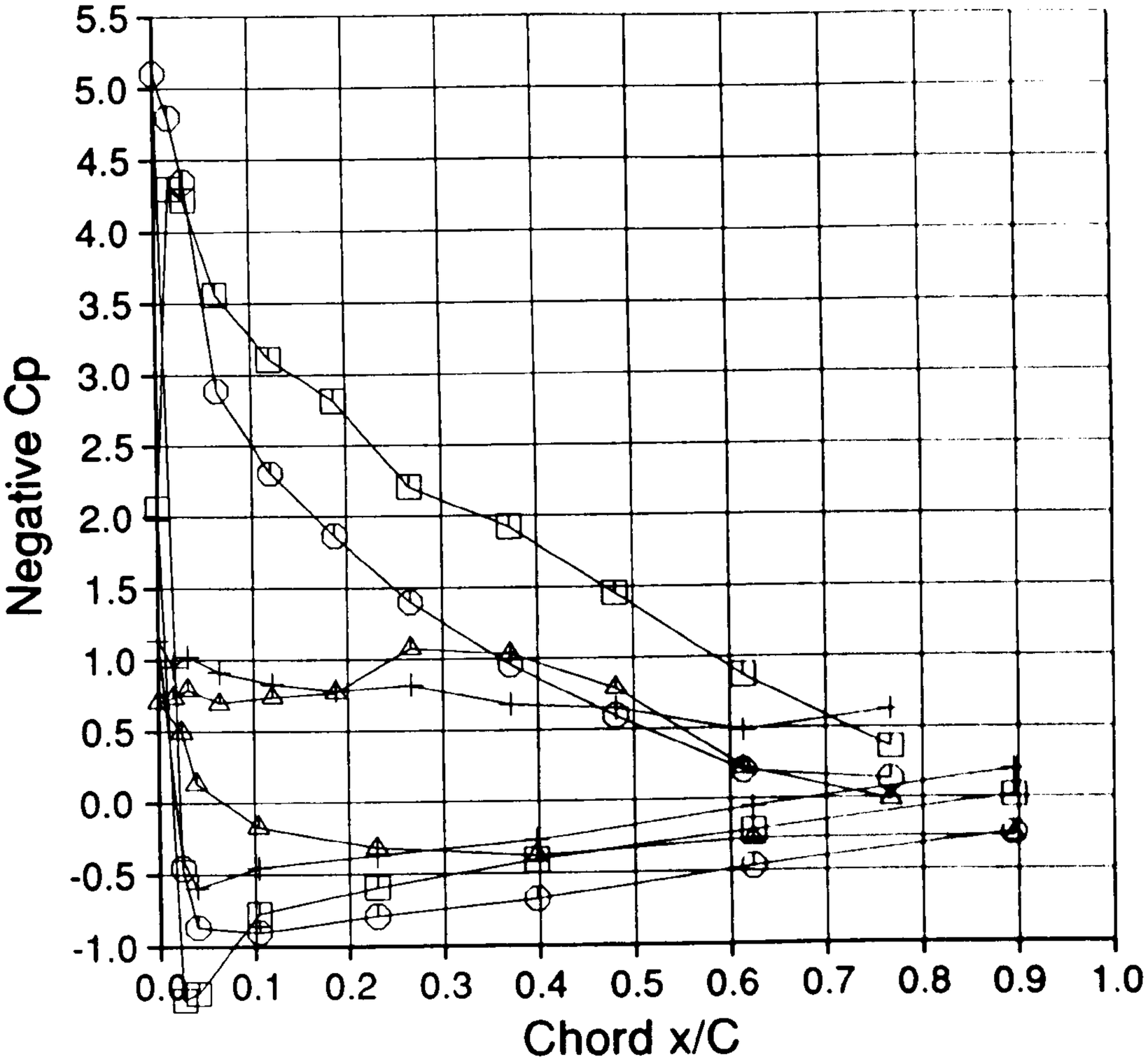

Cranfield

HAWT
Unsteady Aerodynamics
Experiment

Profiles V2.0

35% Span
Mean of Revs 100 TO 139
N = 163.9 N/m
N = 127.4 N/m
N = 63.7 N/m
N = 68.5 N/m
Geometric alpha 41.3 deg
Rotor Speed 341.7 rpm
Body Angle 29.8 deg
Windspeed 19.2 m/s
Wind Angle -12.2 deg
Dynamic Head 417.8 Pa
Yaw Angle 42.0 deg
Tip Speed Ratio 2.7

191.EXP;2

16-FEB-1990:13:36:19

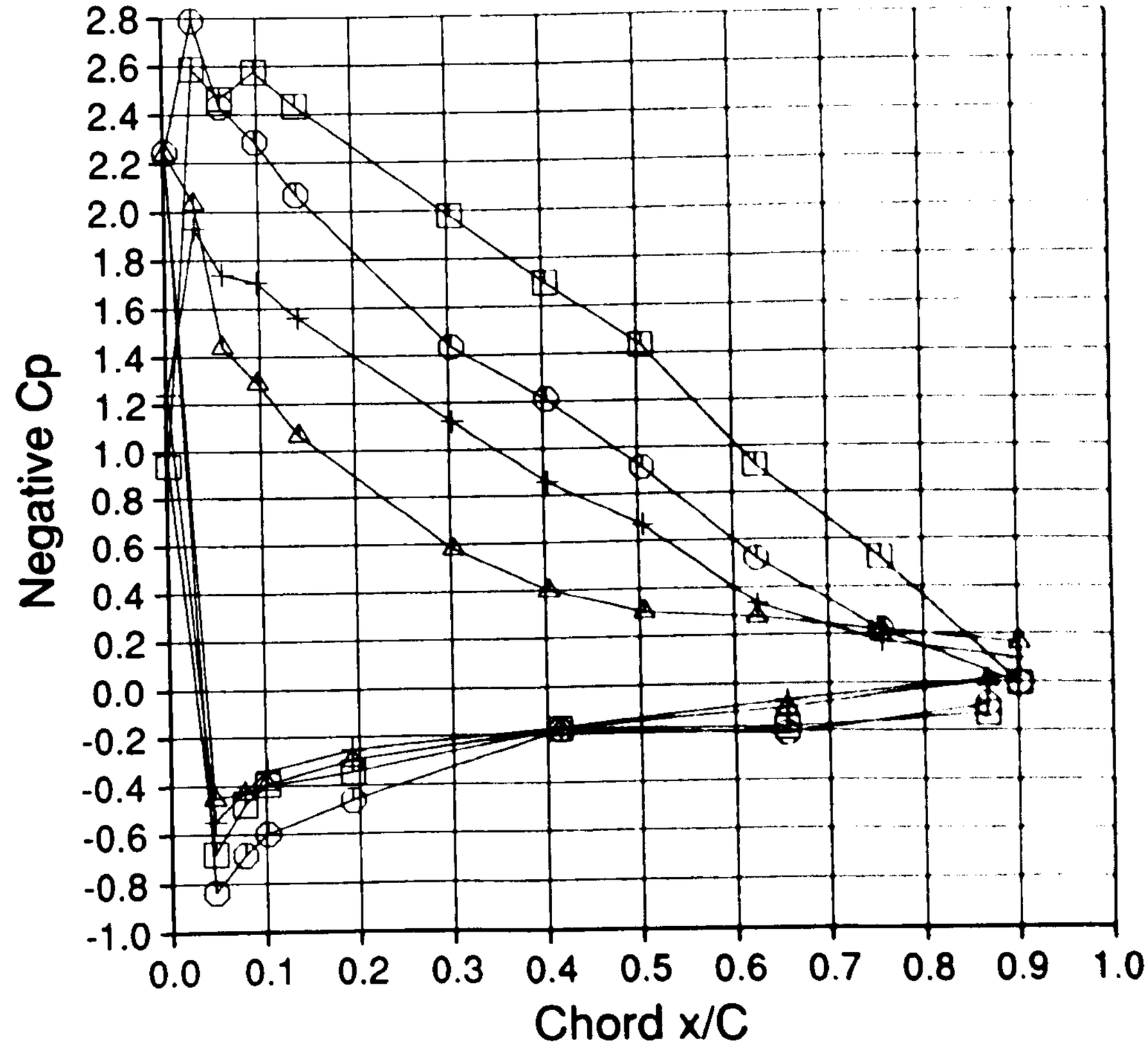

Cranfield

HAWT
Unsteady Aerodynamics
Experiment

Profiles V2.0

75% Span
Mean of Revs 100 TO 139
N = 241.5 N/m
N = 196.2 N/m
N = 104.0 N/m
N = 138.7 N/m
Geometric alpha 20.8 deg
Rotor Speed 341.7 rpm
Body Angle 29.8 deg
Windspeed 19.2 m/s
Wind Angle -12.2 deg
Dynamic Head 1117.1 Pa
Yaw Angle 42.0 deg
Tip Speed Ratio 2.7

191.EXP;2

16-FEB-1990:13:36:19

Figure 10.25

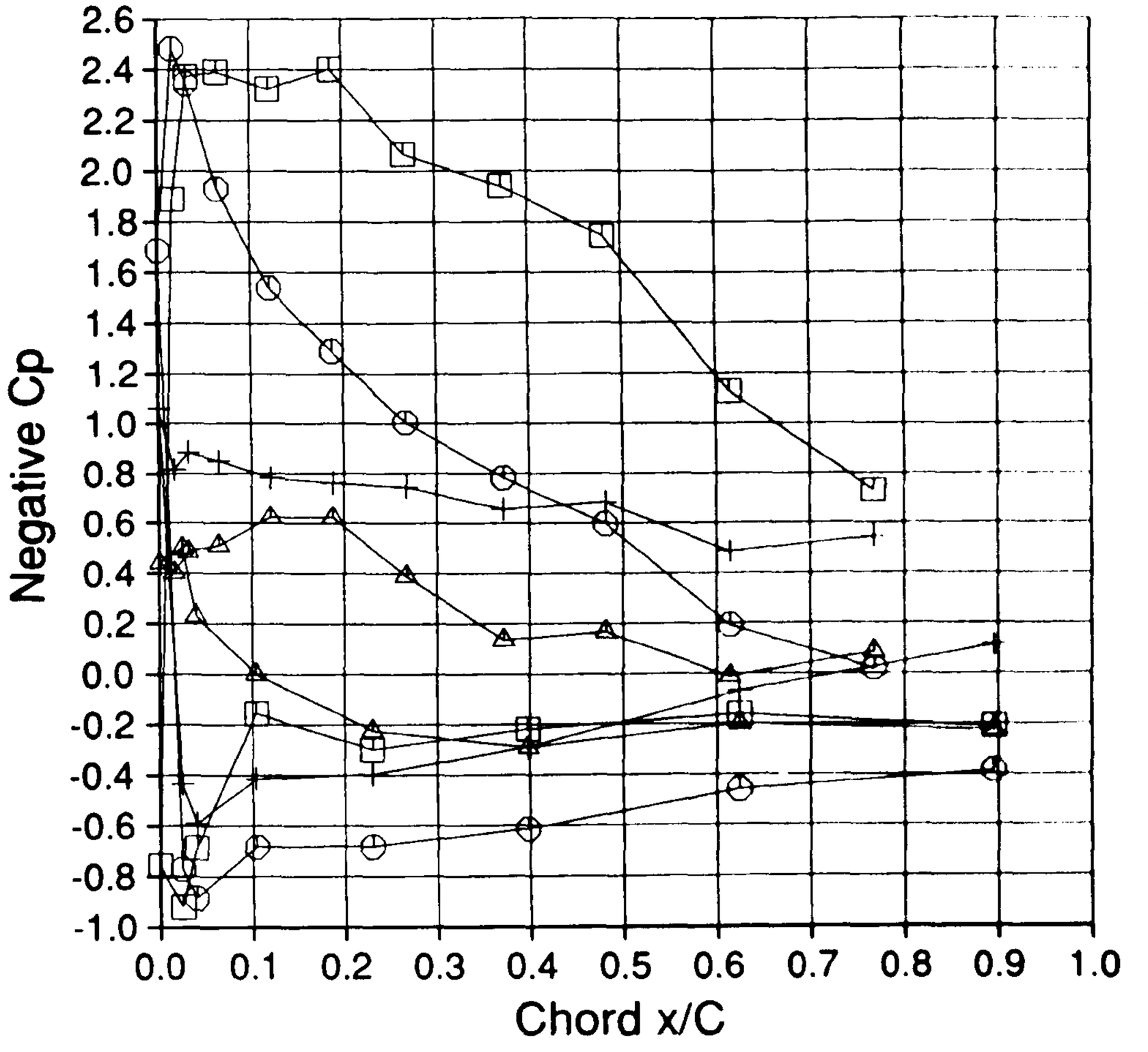

Cranfield

HAWT
Unsteady Aerodynamics
Experiment

Profiles V2.0

35% Span
Mean of Revs 010 TO 049
□ N = 131.0 N/m
○ N = 90.6 N/m
△ N = 28.8 N/m
+ N = 60.5 N/m
Geometric alpha 40.0 deg
Rotor Speed 337.7 rpm
Body Angle 32.4 deg
Windspeed 18.0 m/s
Wind Angle -20.4 deg
Dynamic Head 375.5 Pa
Yaw Angle 52.9 deg
Tip Speed Ratio 2.8

200.EXP;2

15-FEB-1990 16:06:36

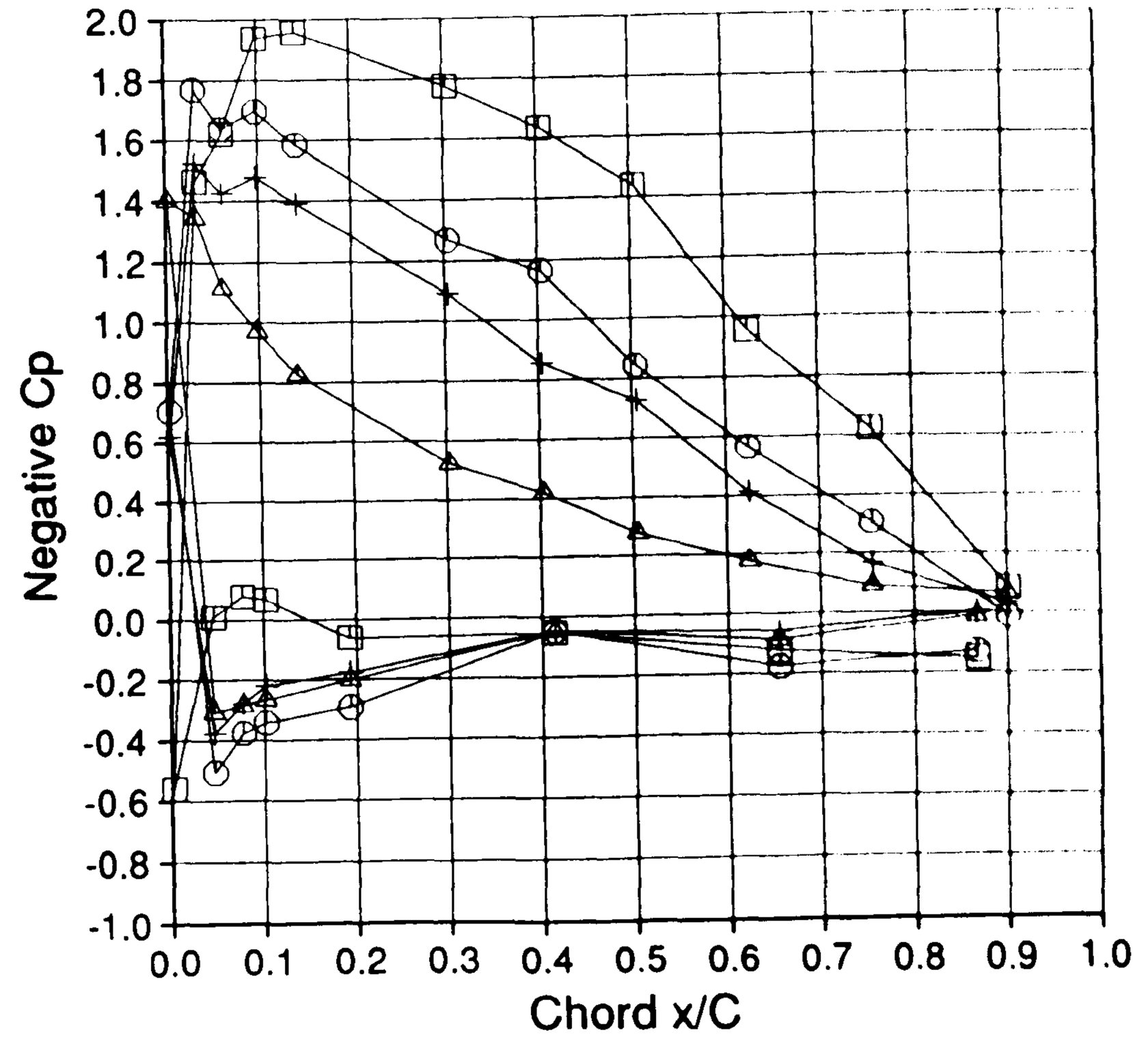

Cranfield

HAWT
Unsteady Aerodynamics
Experiment

Profiles V2.0

75% Span
Mean of Revs 010 TO 049
□ N = 182.5 N/m
○ N = 147.9 N/m
△ N = 70.6 N/m
+ N = 114.0 N/m
Geometric alpha 19.7 deg
Rotor Speed 337.7 rpm
Body Angle 32.4 deg
Windspeed 18.0 m/s
Wind Angle -20.4 deg
Dynamic Head 1036.7 Pa
Yaw Angle 52.9 deg
Tip Speed Ratio 2.8

200.EXP;2

15-FEB-1990 16:06:36

Figure 10.26

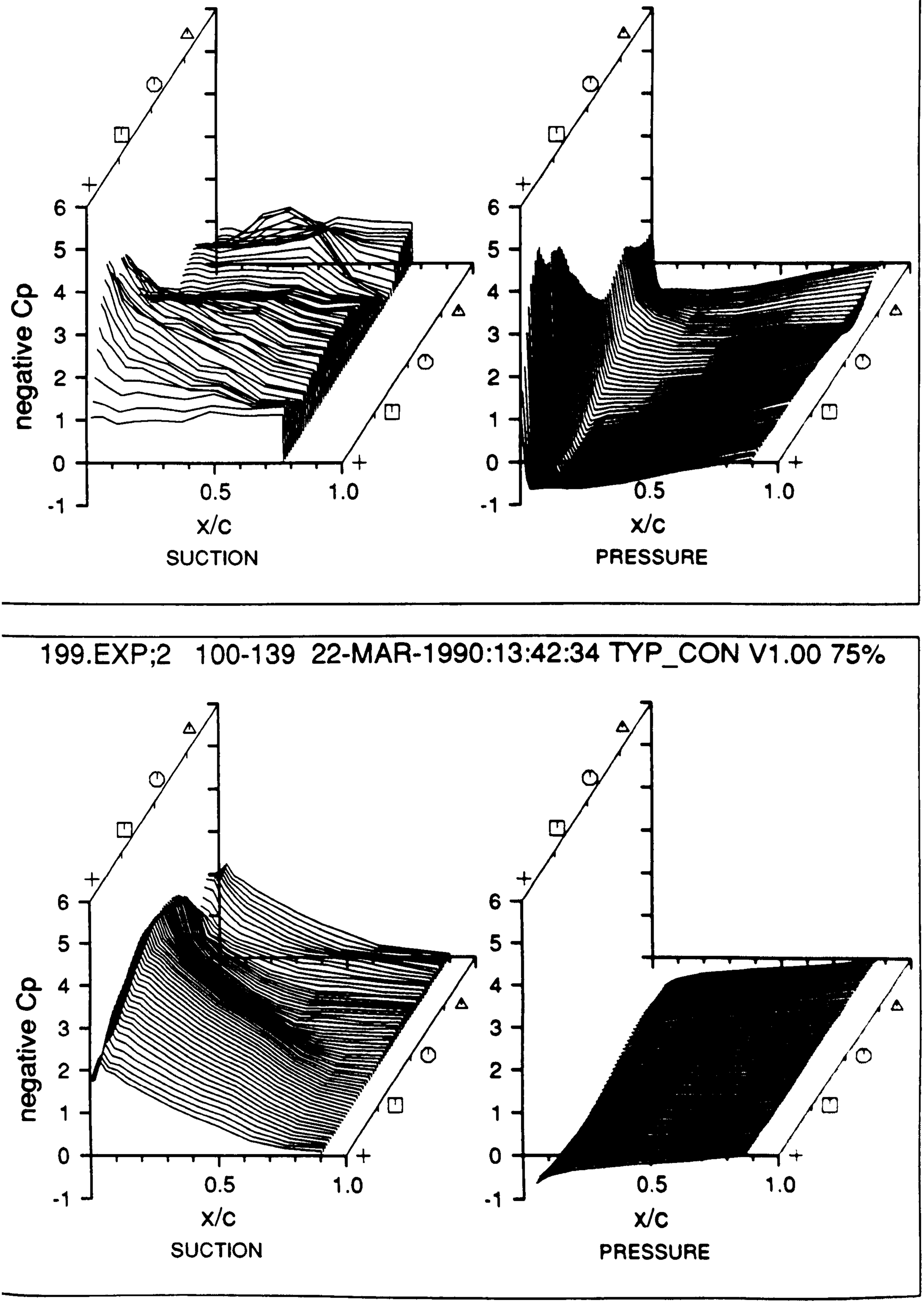
199.EXP;2 100-139 22-MAR-1990:13:42:34 TYP_CON V1.00 35%
negative Cp
6
5
4
3
2
1
0
-1
0.5
1.0
X/C
SUCTION
PRESSURE
199.EXP;2 100-139 22-MAR-1990:13:42:34 TYP_CON V1.00 75%

Figure 10.27

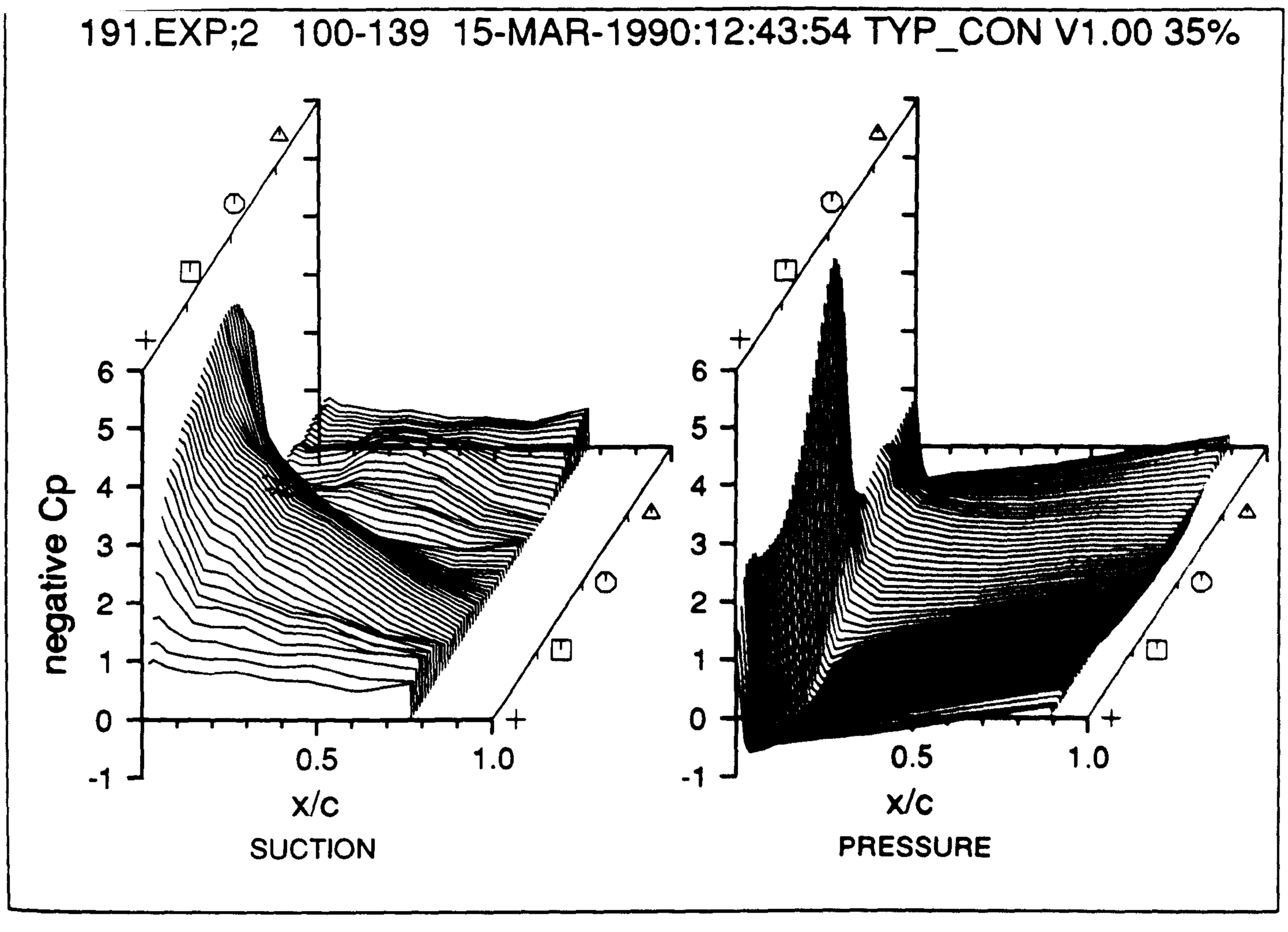
191.EXP;2 100-139 15-MAR-1990:12:43:54 TYP_CON V1.00 35%
negative Cp
6
5
4
3
2
1
0
-1
0.5
1.0
x/c
SUCTION
PRESSURE

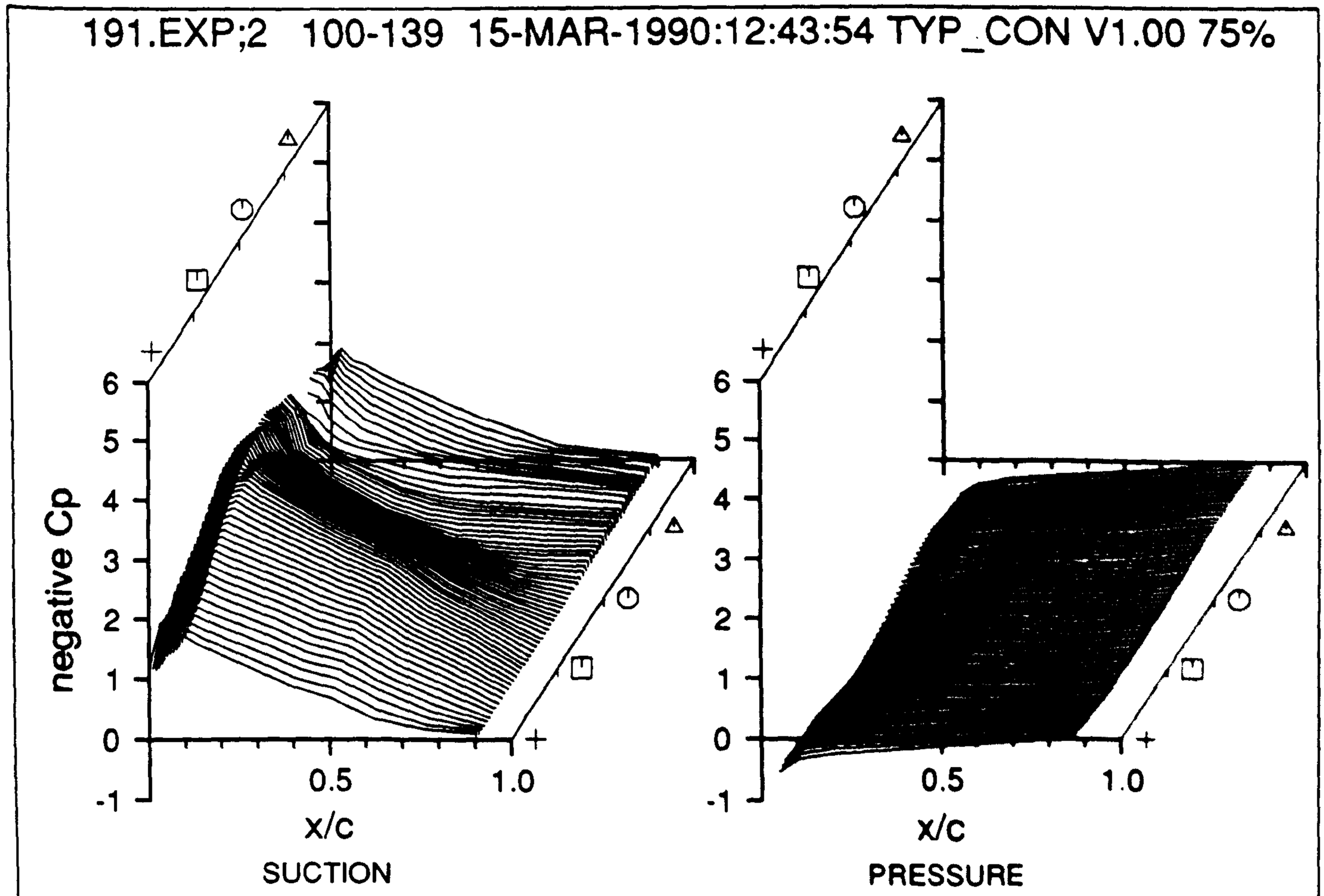
191.EXP;2 100-139 15-MAR-1990:12:43:54 TYP_CON V1.00 75%
negative Cp
6
5
4
3
2
1
0
-1
0.5
1.0
x/c
SUCTION
PRESSURE

Figure 10.28

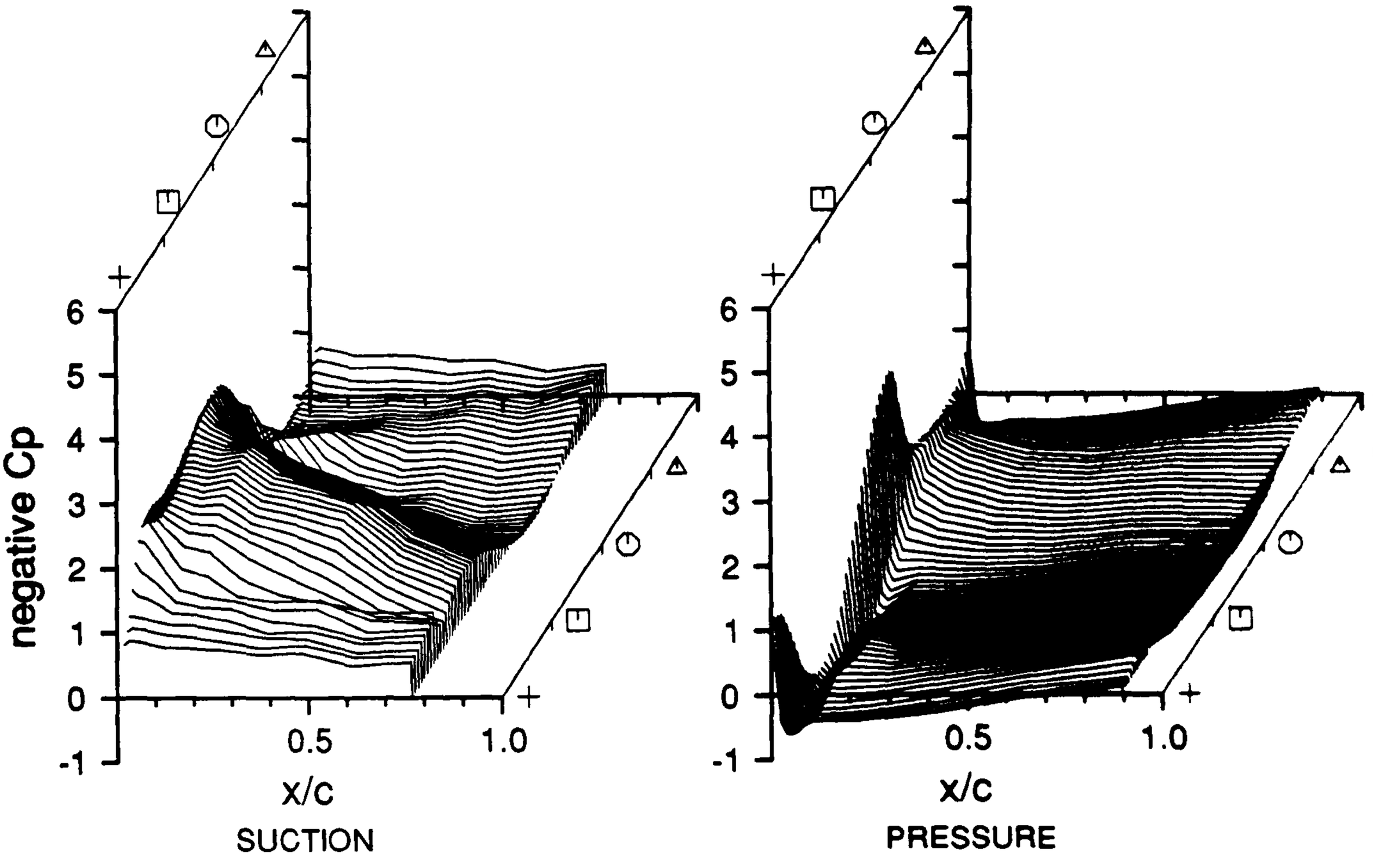
200.EXP;2 010-049 22-MAR-1990:13:42:55 TYP_CON V1.00 35%
negative Cp
6
5
4
3
2
1
0
-1
0.5
1.0
X/C
SUCTION
PRESSURE

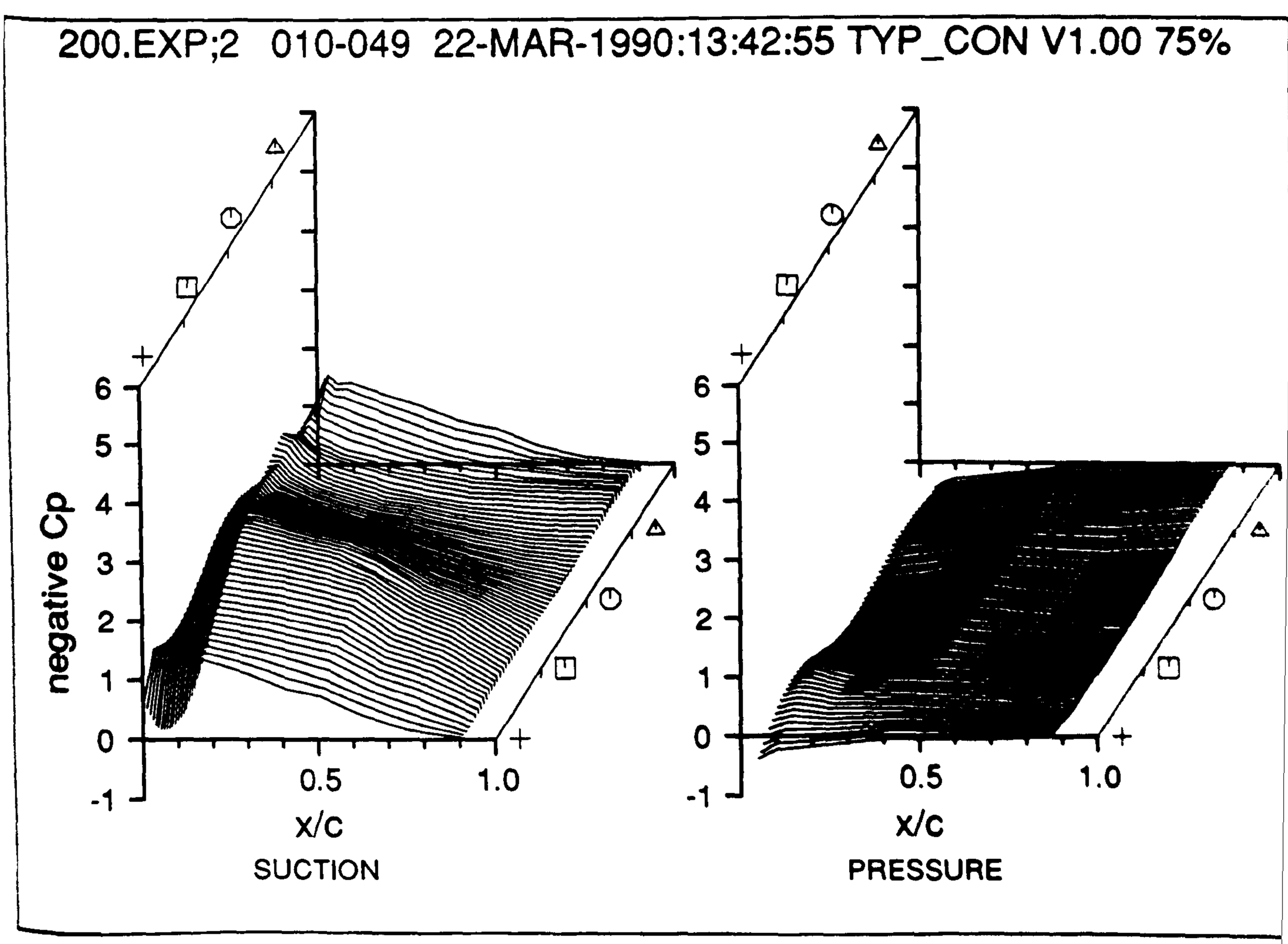
200.EXP;2 010-049 22-MAR-1990:13:42:55 TYP_CON V1.00 75%
negative Cp
6
5
4
3
2
1
0
-1
0.5
1.0
X/C
SUCTION
PRESSURE

Figure 10.29

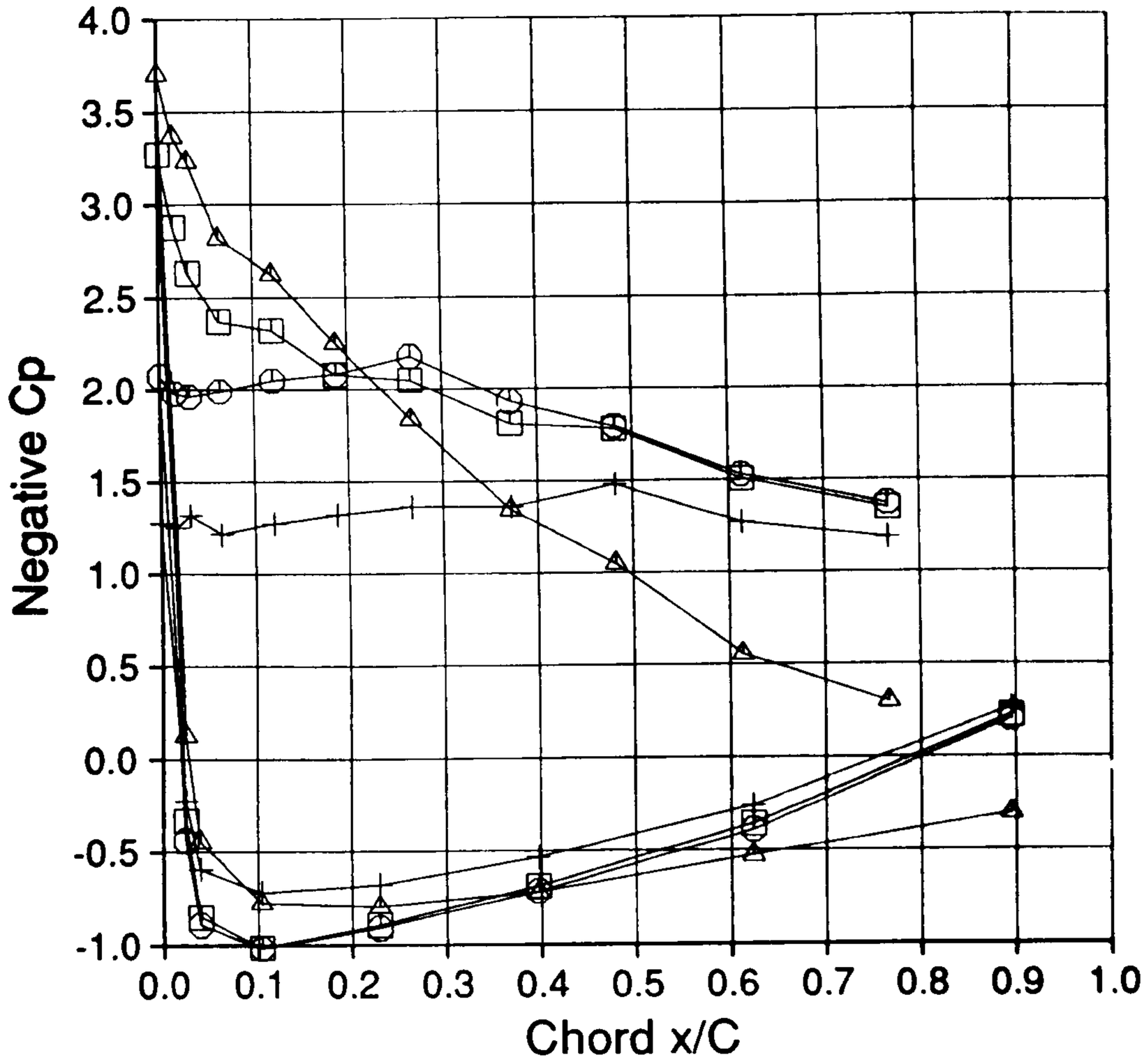

Cranfield

HAWT
Unsteady Aerodynamics
Experiment

Profiles V2.0

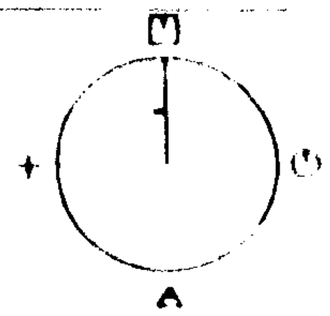

35% Span
Mean of Revs 080 TO 119
□ N = 196.6 N/m
○ N = 196.7 N/m
△ N = 159.6 N/m
+ N = 142.3 N/m
Geometric alpha 43.7 deg
Rotor Speed 340.8 rpm
Body Angle 1.8 deg
Windspeed 20.8 m/s
Wind Angle -7.5 deg
Dynamic Head 455.4 Pa
Yaw Angle 9.3 deg
Tip Speed Ratio 2.5

192.EXP;2

16-FEB-1990 13:37:26

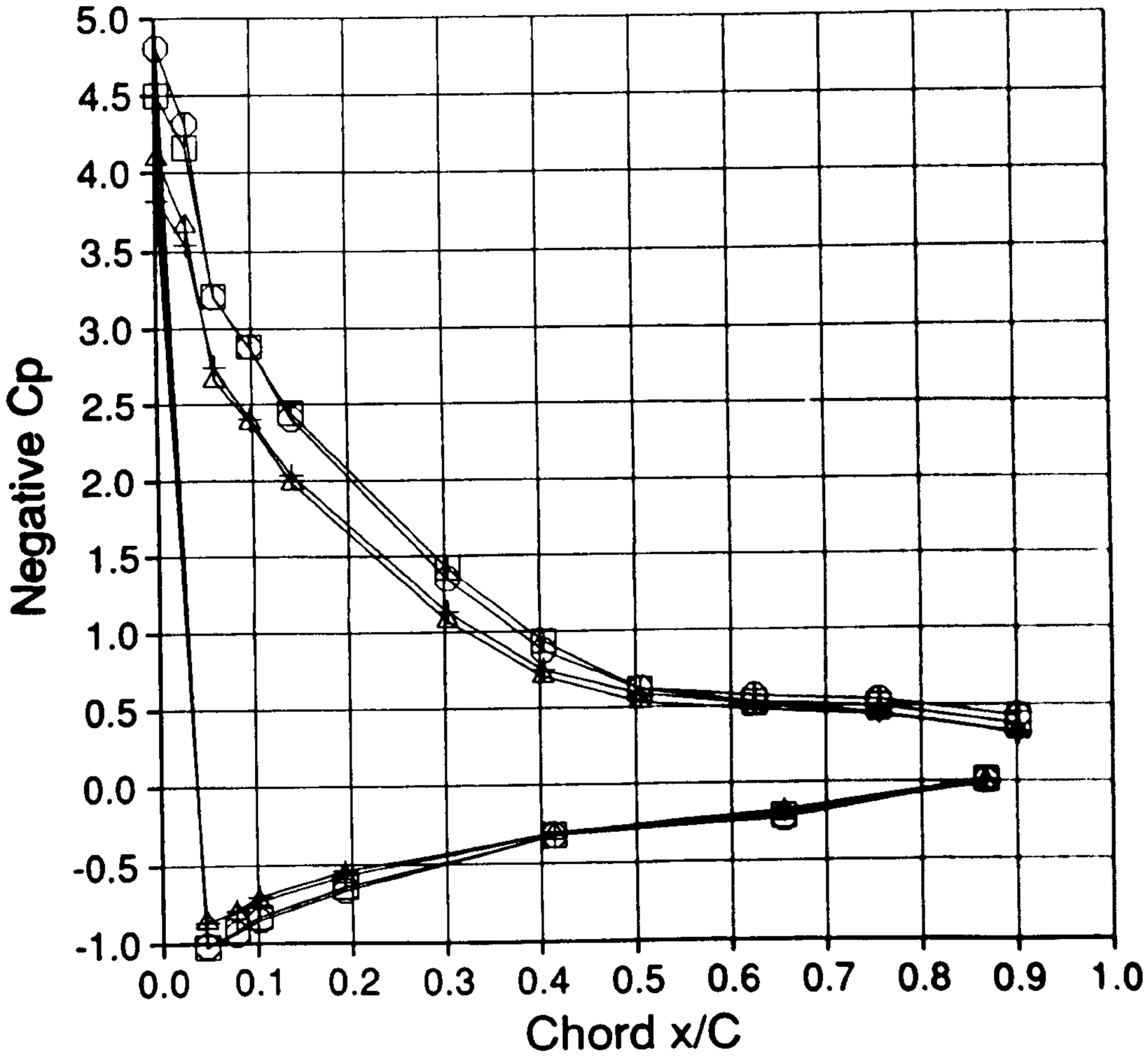

Cranfield

HAWT
Unsteady Aerodynamics
Experiment

Profiles V2.0

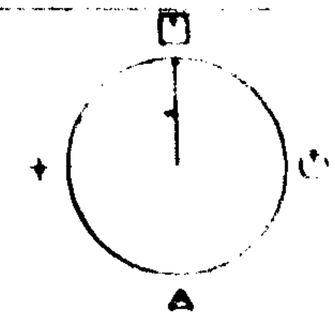

75% Span
Mean of Revs 080 TO 119
□ N = 235.4 N/m
○ N = 237.1 N/m
△ N = 198.4 N/m
+ N = 201.1 N/m
Geometric alpha 22.8 deg
Rotor Speed 340.8 rpm
Body Angle 1.8 deg
Windspeed 20.8 m/s
Wind Angle -7.5 deg
Dynamic Head 1150.2 Pa
Yaw Angle 9.3 deg
Tip Speed Ratio 2.5

192.EXP;2

16-FEB-1990 13:37:26

Figure 10.30

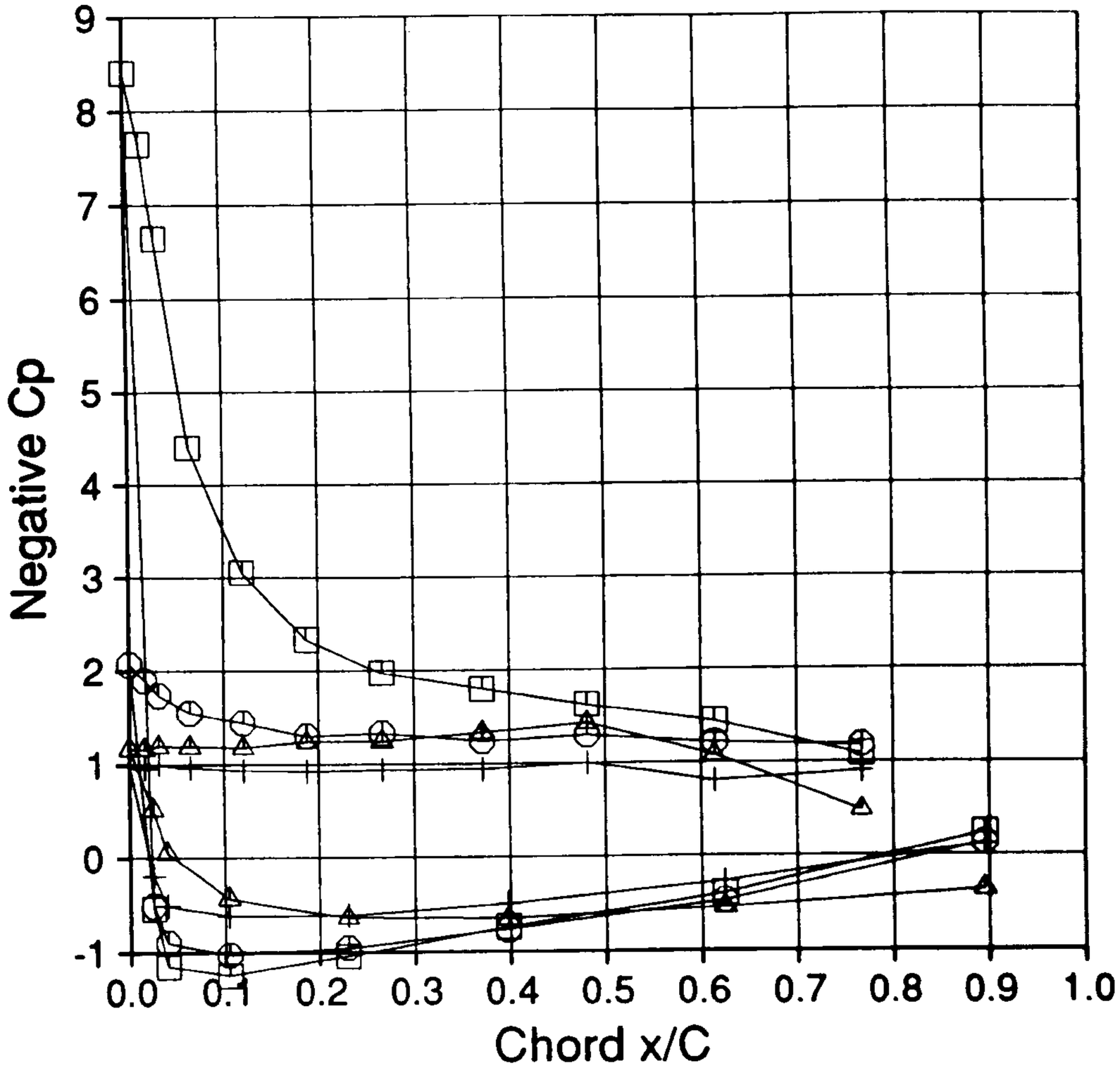

Cranfield

HAWT
Unsteady Aerodynamics
Experiment

Profiles V2.0

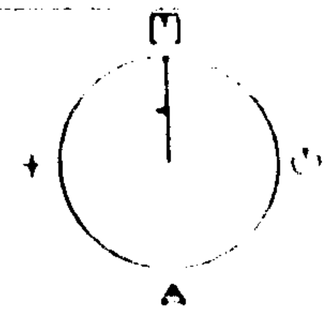

35% Span
Mean of Revs 040 TO 079
□ N = 252.0 N/m
○ N = 181.9 N/m
△ N = 149.1 N/m
\+ N = 122.4 N/m
Geometric alpha 47.2 deg
Rotor Speed 339.6 rpm
Body Angle 16.4 deg
Windspeed 23.5 m/s
Wind Angle -8.4 deg
Dynamic Head 512.3 Pa
Yaw Angle 24.7 deg
Tip Speed Ratio 2.2

202.EXP;2

15-FEB-1990 16:23:06

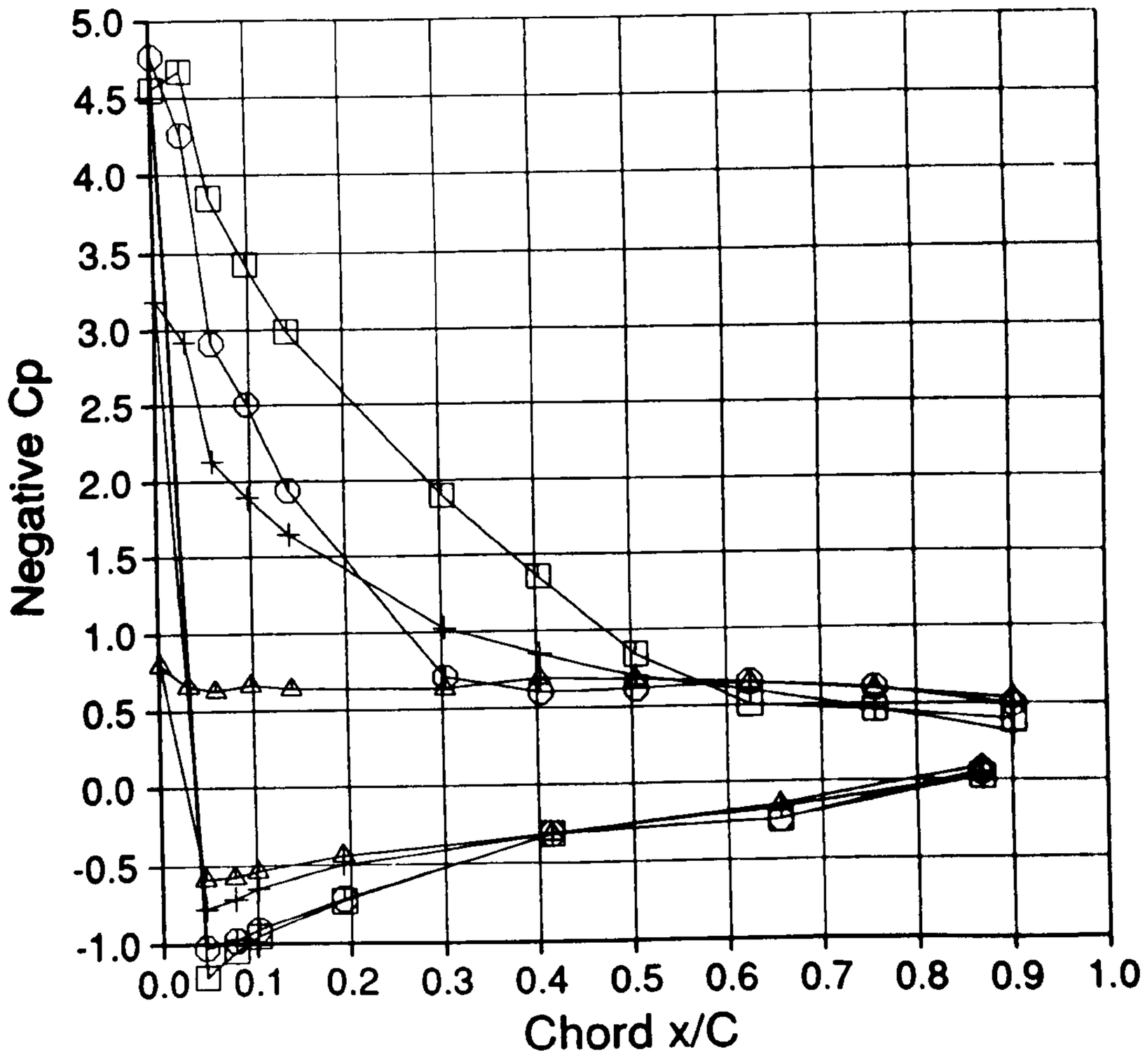

Cranfield

HAWT
Unsteady Aerodynamics
Experiment

Profiles V2.0

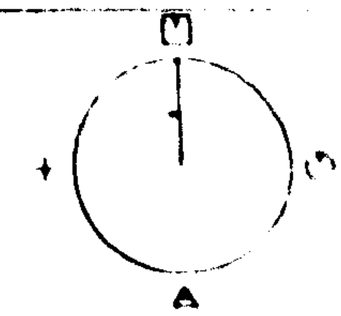

75% Span
Mean of Revs 040 TO 079
□ N = 288.5 N/m
○ N = 217.5 N/m
△ N = 137.0 N/m
\+ N = 190.8 N/m
Geometric alpha 26.0 deg
Rotor Speed 339.6 rpm
Body Angle 16.4 deg
Windspeed 23.5 m/s
Wind Angle -8.4 deg
Dynamic Head 1182.3 Pa
Yaw Angle 24.7 deg
Tip Speed Ratio 2.2

202.EXP;2

15-FEB-1990 16:23:06

Figure 10.31

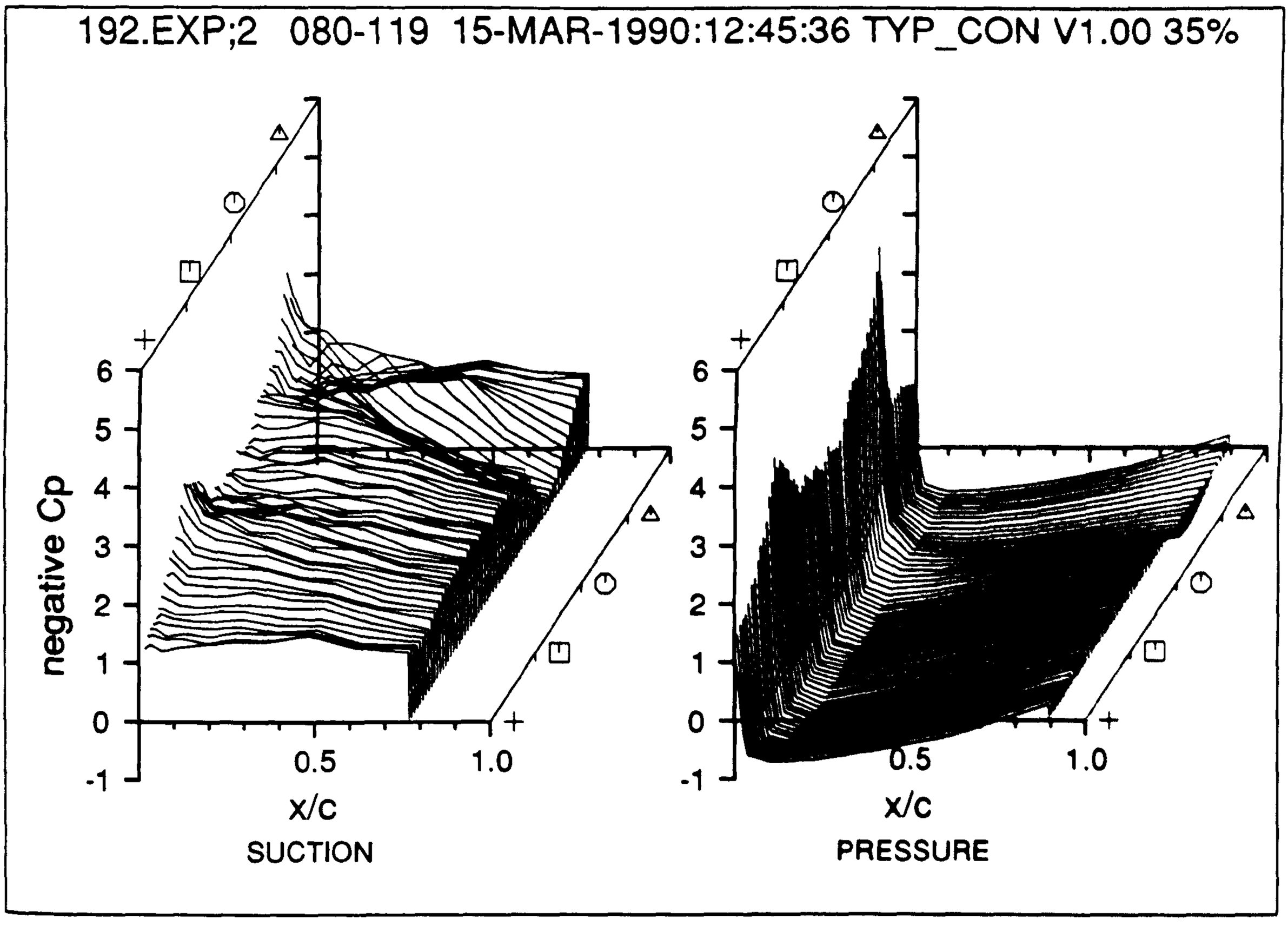
192.EXP;2 080-119 15-MAR-1990:12:45:36 TYP_CON V1.00 35%
negative Cp
6
5
4
3
2
1
0
-1
0.5
1.0
X/C
SUCTION
PRESSURE
192.EXP;2 080-119 15-MAR-1990:12:45:36 TYP_CON V1.00 75%
negative Cp
X/C
SUCTION
PRESSURE

Figure 10.32

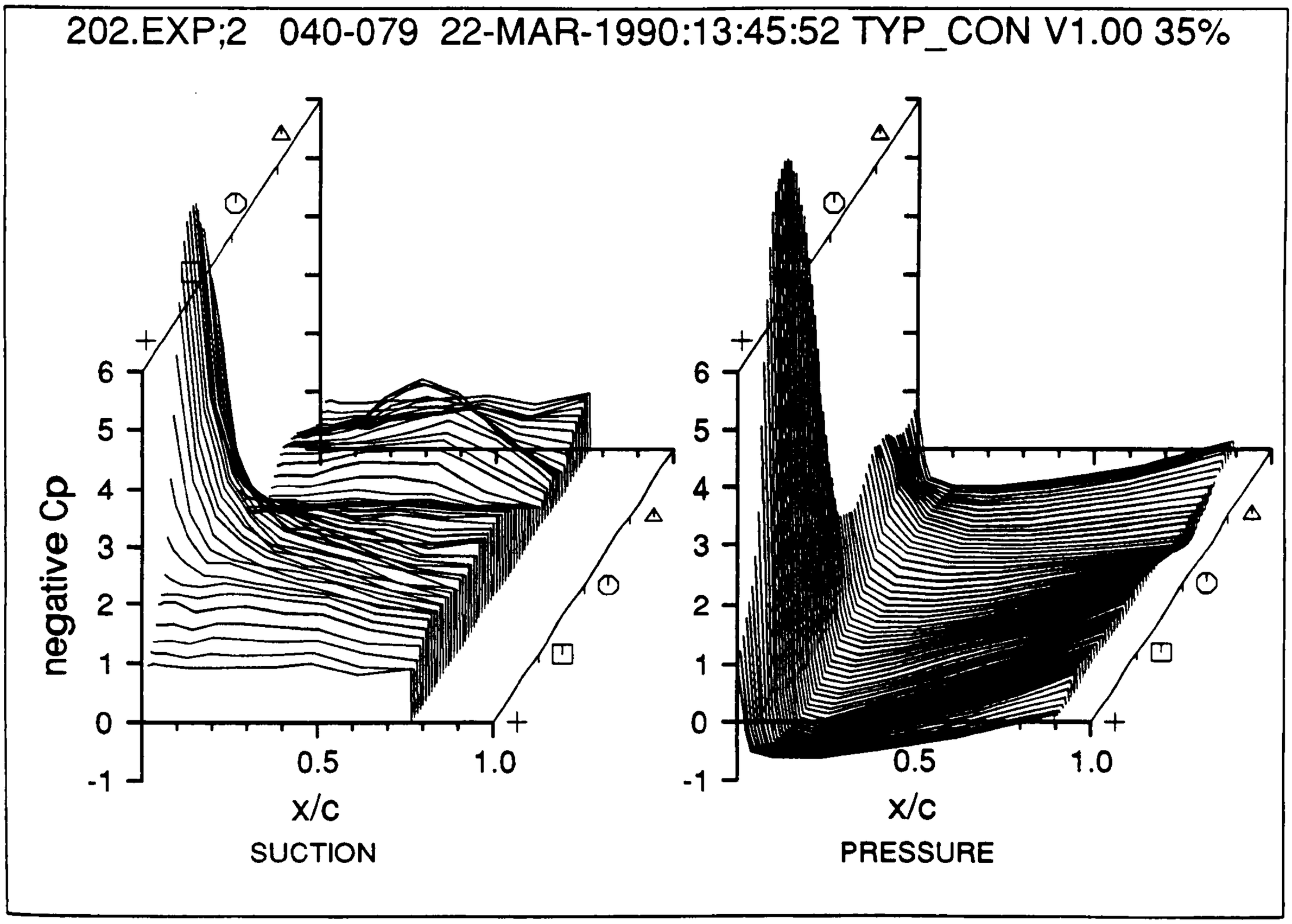
202.EXP;2 040-079 22-MAR-1990:13:45:52 TYP_CON V1.00 35%
negative Cp
6
5
4
3
2
1
0
-1
0.5
1.0
X/C
SUCTION
PRESSURE

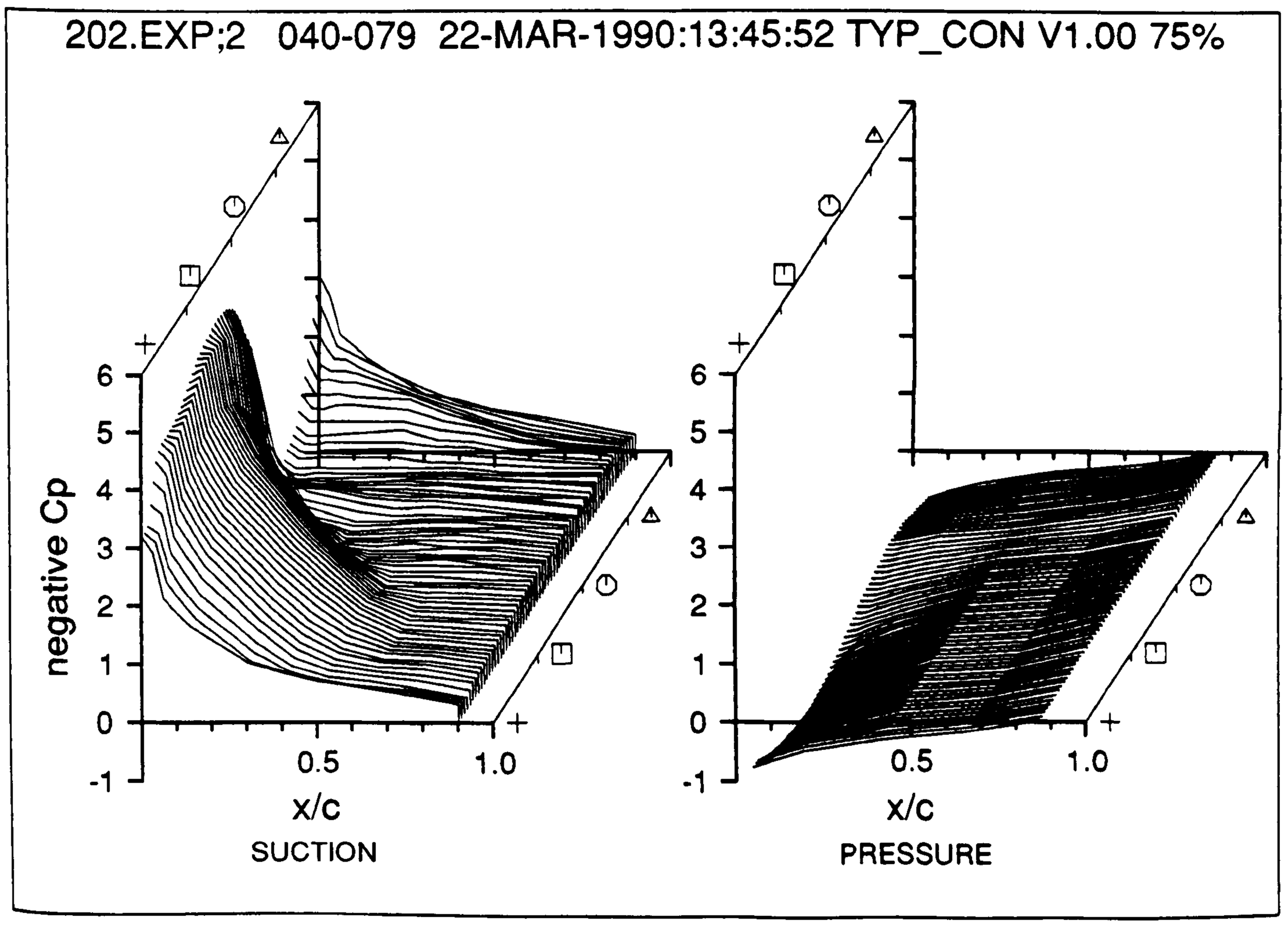
202.EXP;2 040-079 22-MAR-1990:13:45:52 TYP_CON V1.00 75%
negative Cp
6
5
4
3
2
1
0
-1
0.5
1.0
X/C
SUCTION
PRESSURE

Figure 10.33

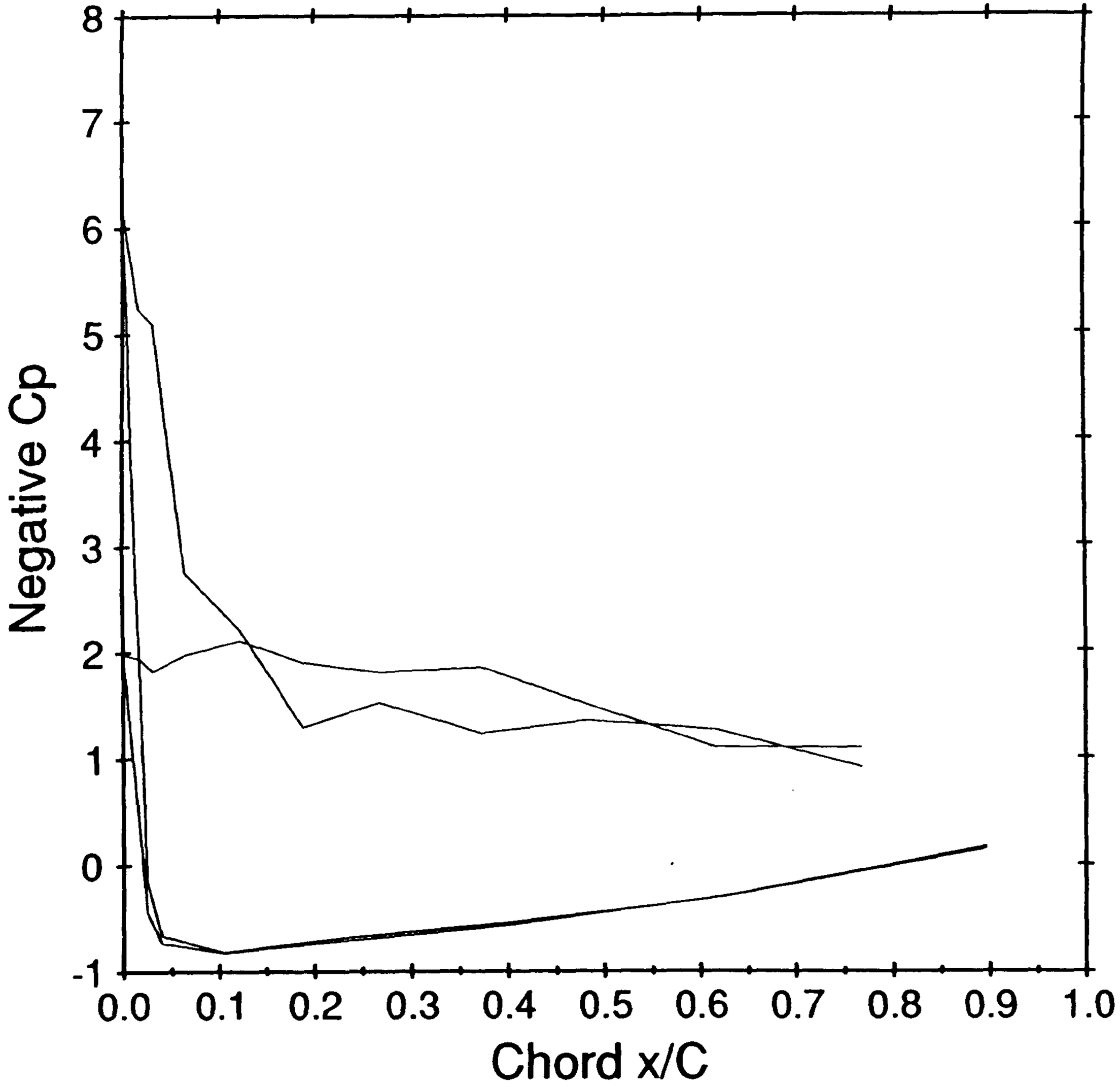

Cranfield

HAWT
Unsteady Aerodynamics
Experiment

Pres Profil V1.0

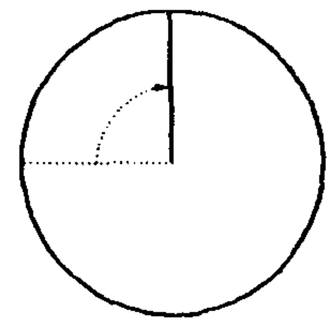

35% Span
Rev-Range [040,079]
Geometric alpha 38.5 deg
Rotor Speed 343.7 rpm
Body Angle 0.9 deg
Windspeed 18.1 m/s
Wind Angle -1.8 deg
Dynamic Head 400.1 Pa
Yaw Angle 2.8 deg
Tip Speed Ratio 2.8

165.EXP;2

4-MAY-1990:17:53:06

Figure 10.34

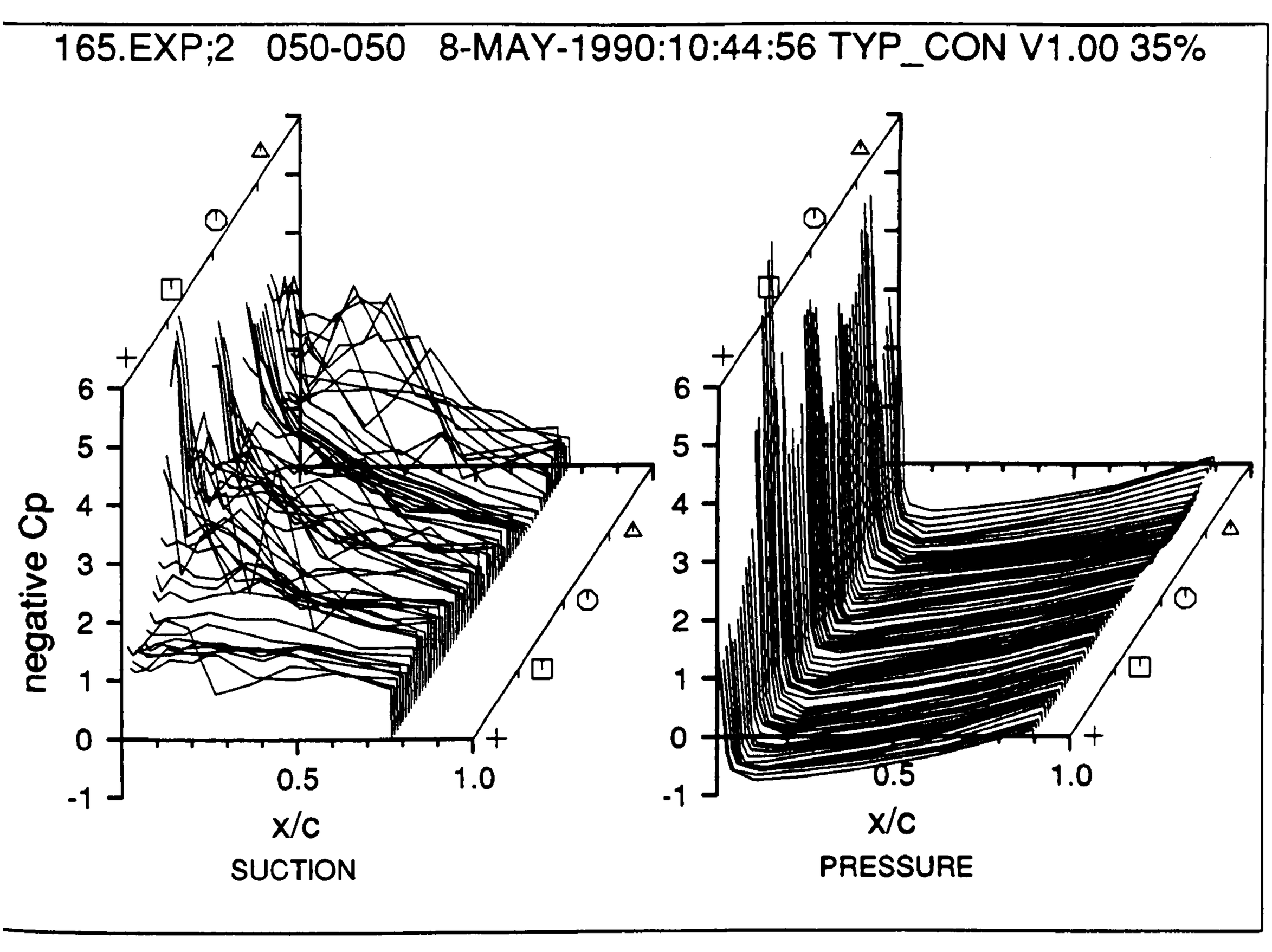
165.EXP;2 050-050 8-MAY-1990:10:44:56 TYP_CON V1.00 35%
negative Cp
6
5
4
3
2
1
0
-1
0.5
1.0
X/C
SUCTION
PRESSURE
165.EXP;2 050-050 8-MAY-1990:10:44:56 TYP_CON V1.00 75%

Figure 10.35

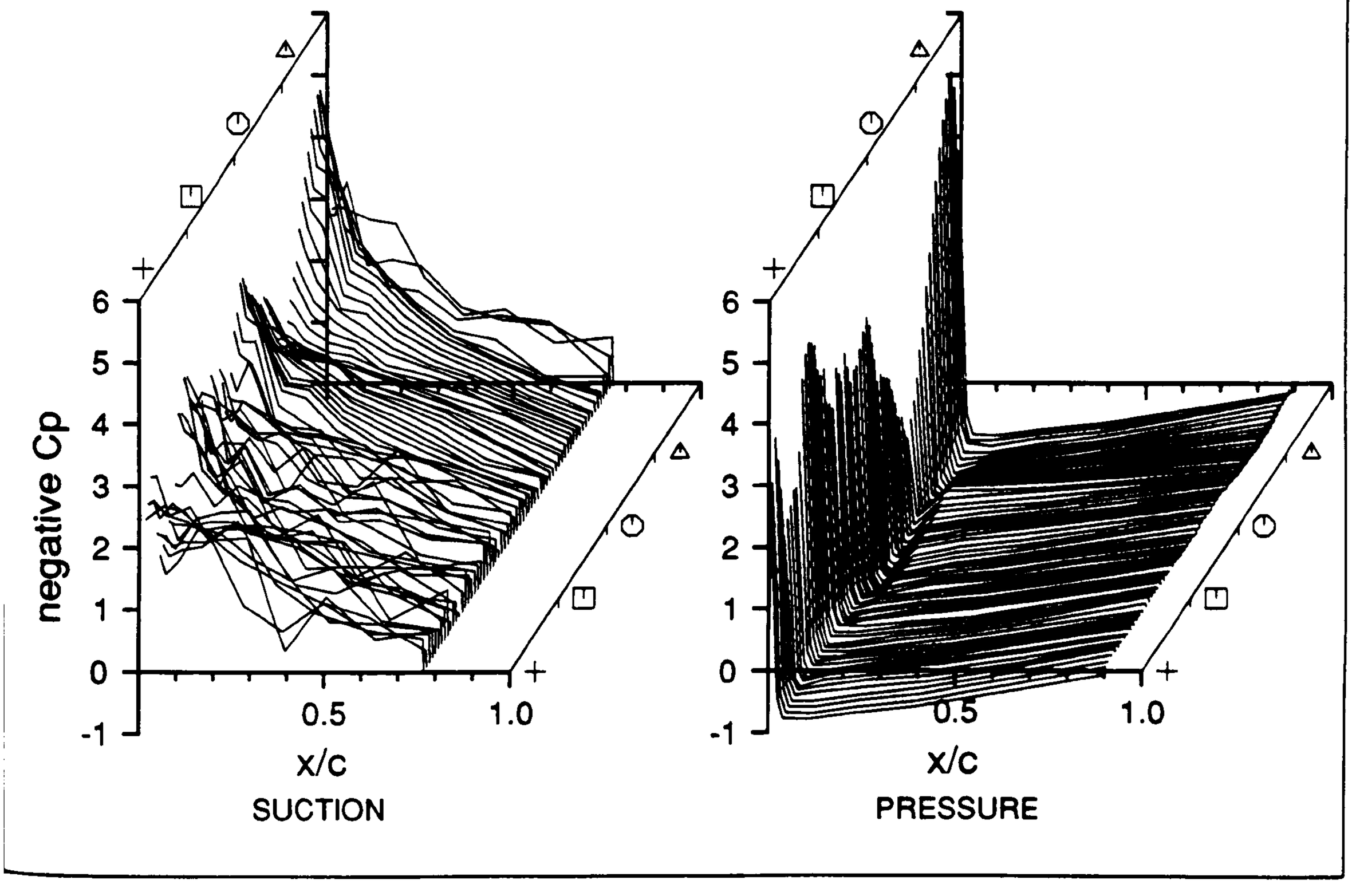
168.EXP;2 053-053 8-MAY-1990:10:46:27 TYP_CON V1.00 35%
negative Cp
6
5
4
3
2
1
0
-1
0.5
1.0
X/C
SUCTION
PRESSURE
168.EXP;2 053-053 8-MAY-1990:10:46:27 TYP_CON V1.00 75%
negative Cp
SUCTION
PRESSURE

Figure 10.36

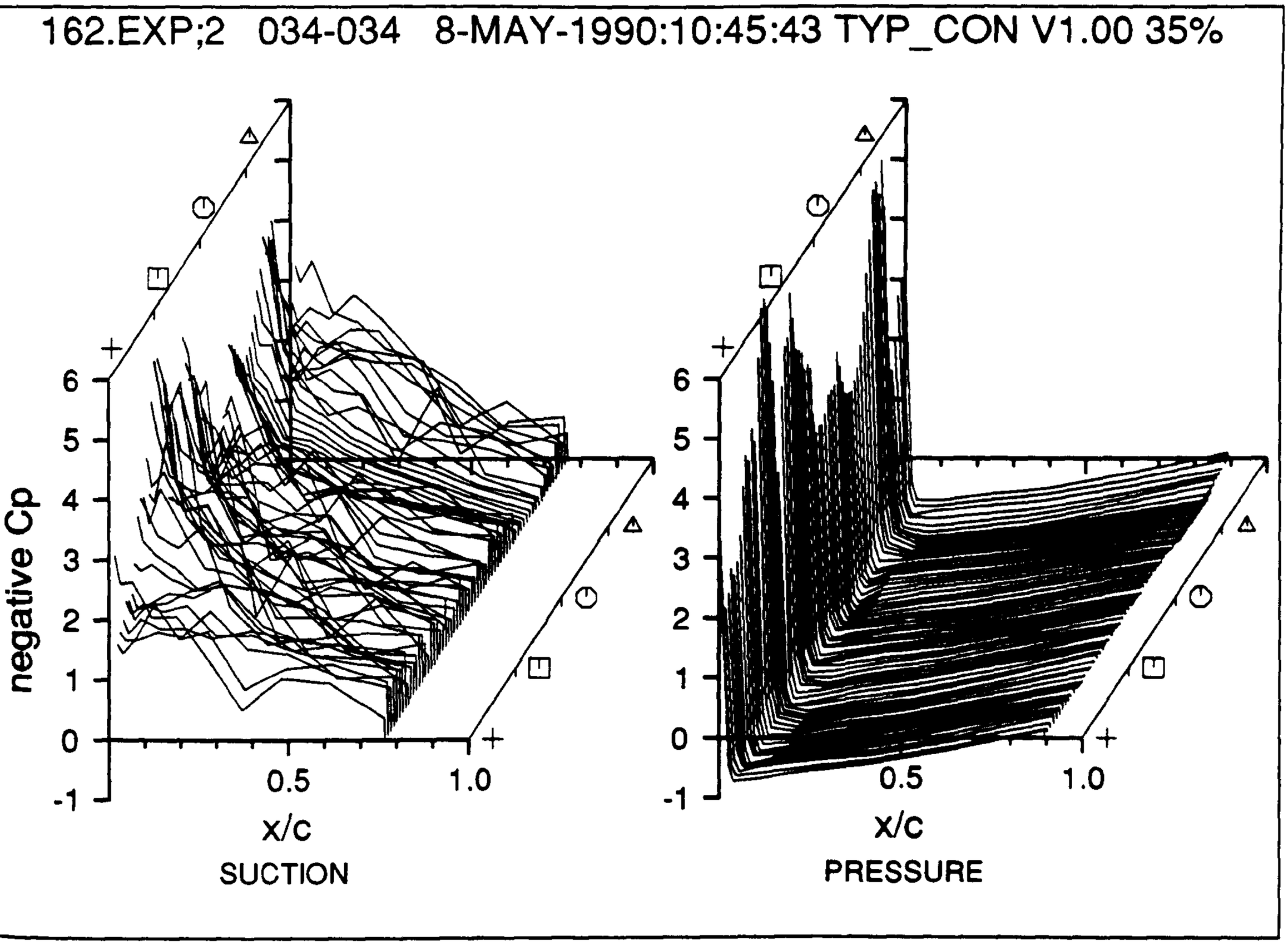
162.EXP;2 034-034 8-MAY-1990:10:45:43 TYP_CON V1.00 35%
negative Cp
6
5
4
3
2
1
0
-1
0.5
1.0
X/C
SUCTION
PRESSURE

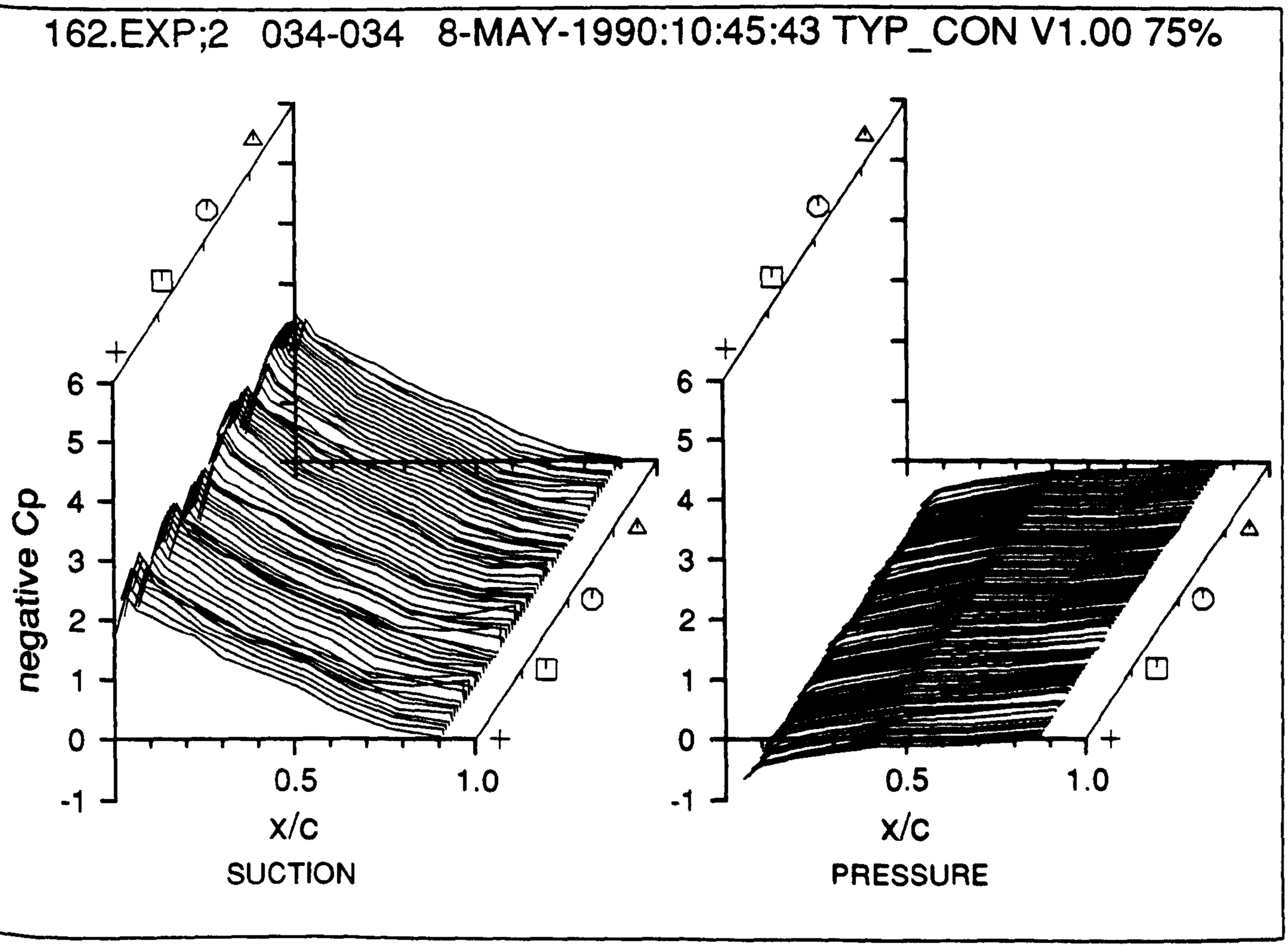
162.EXP;2 034-034 8-MAY-1990:10:45:43 TYP_CON V1.00 75%
negative Cp
6
5
4
3
2
1
0
-1
0.5
1.0
X/C
SUCTION
PRESSURE

Figure 10.37

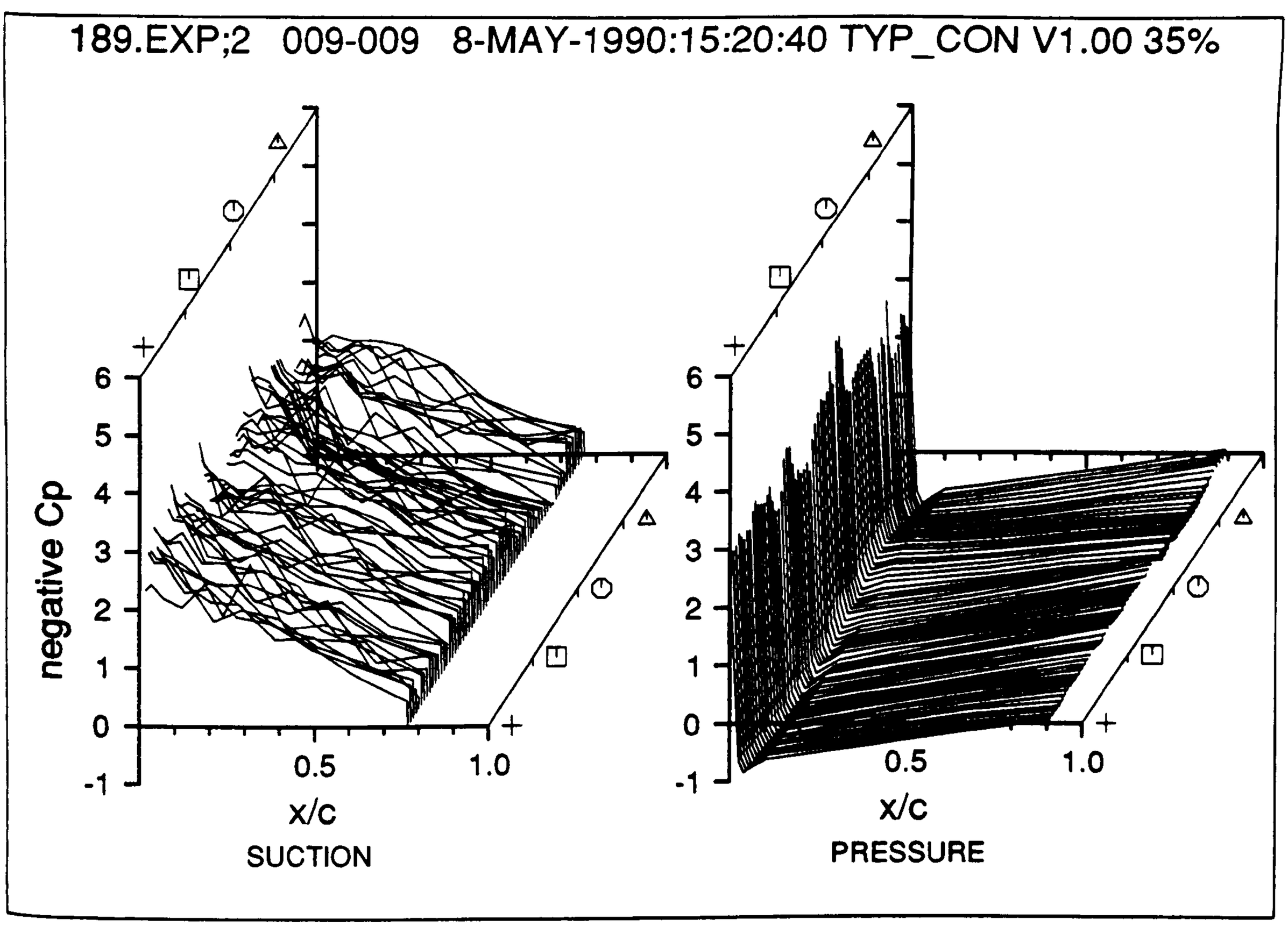
189.EXP;2 009-009 8-MAY-1990:15:20:40 TYP_CON V1.00 35%
negative Cp
6
5
4
3
2
1
0
-1
0.5
1.0
X/C
SUCTION
PRESSURE

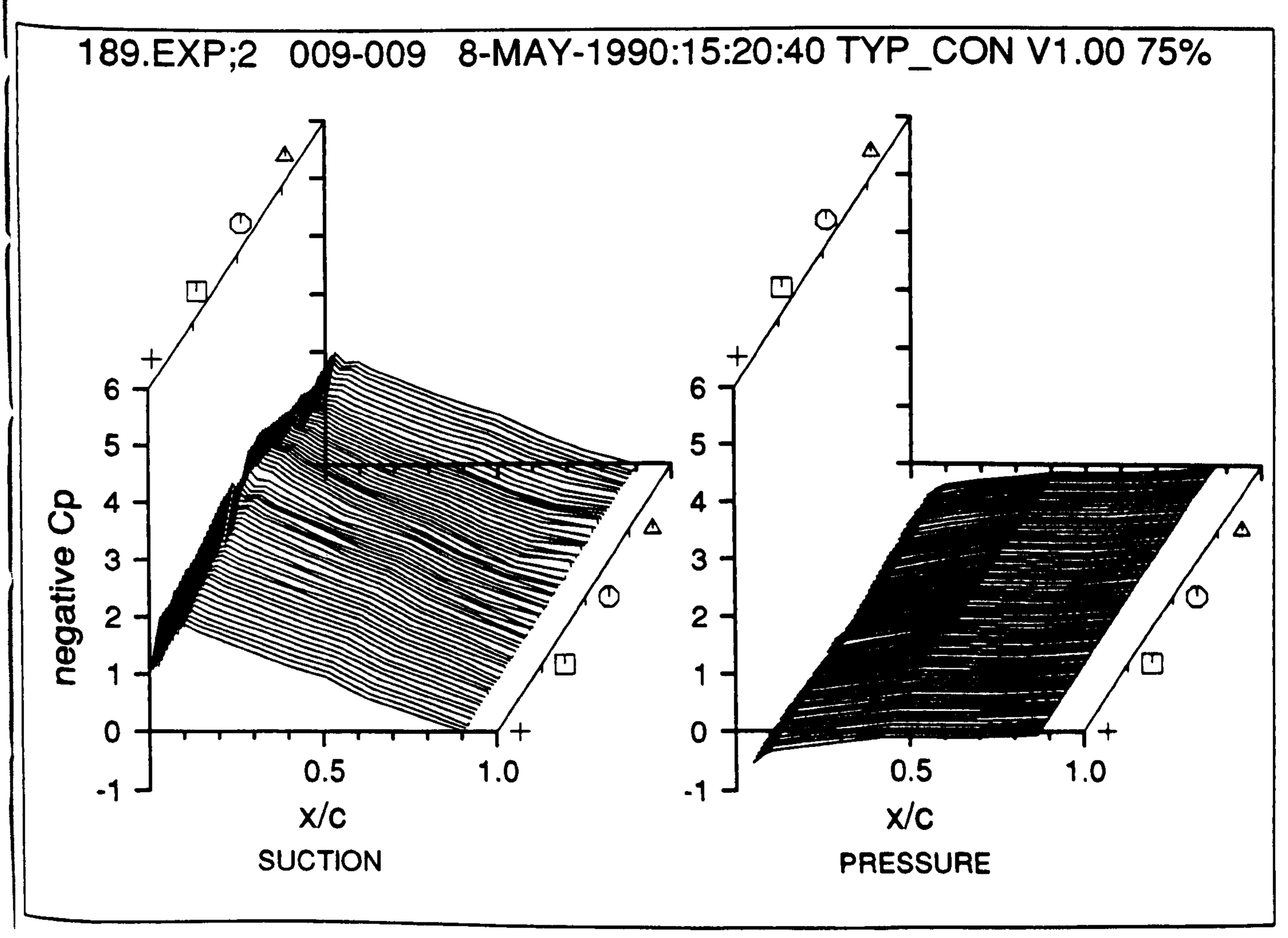
189.EXP;2 009-009 8-MAY-1990:15:20:40 TYP_CON V1.00 75%
negative Cp
6
5
4
3
2
1
0
-1
0.5
1.0
X/C
SUCTION
PRESSURE

Figure 10.38

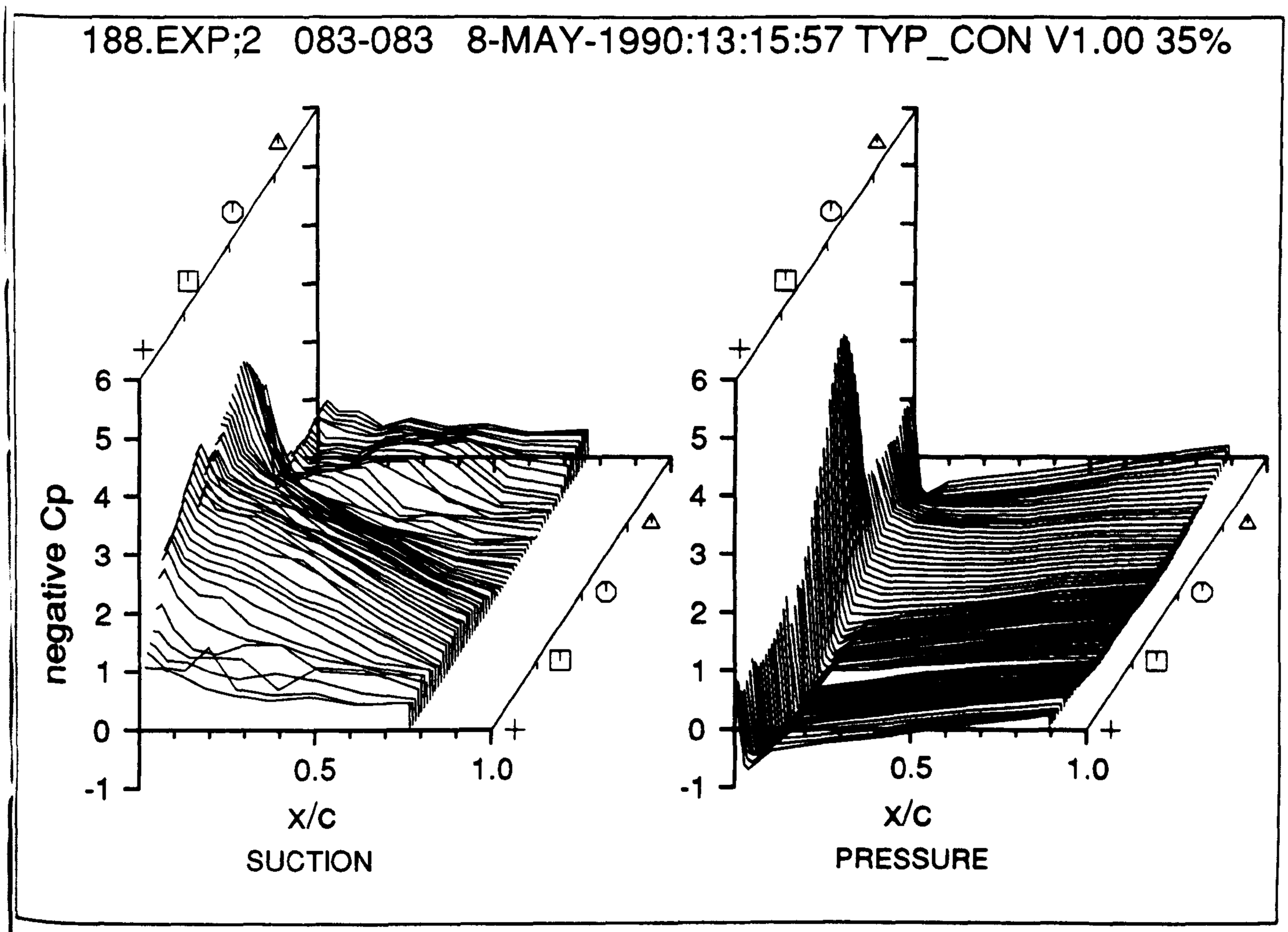
188.EXP;2 083-083 8-MAY-1990:13:15:57 TYP_CON V1.00 35%
negative Cp
6
5
4
3
2
1
0
-1
0.5
1.0
x/c
SUCTION
PRESSURE

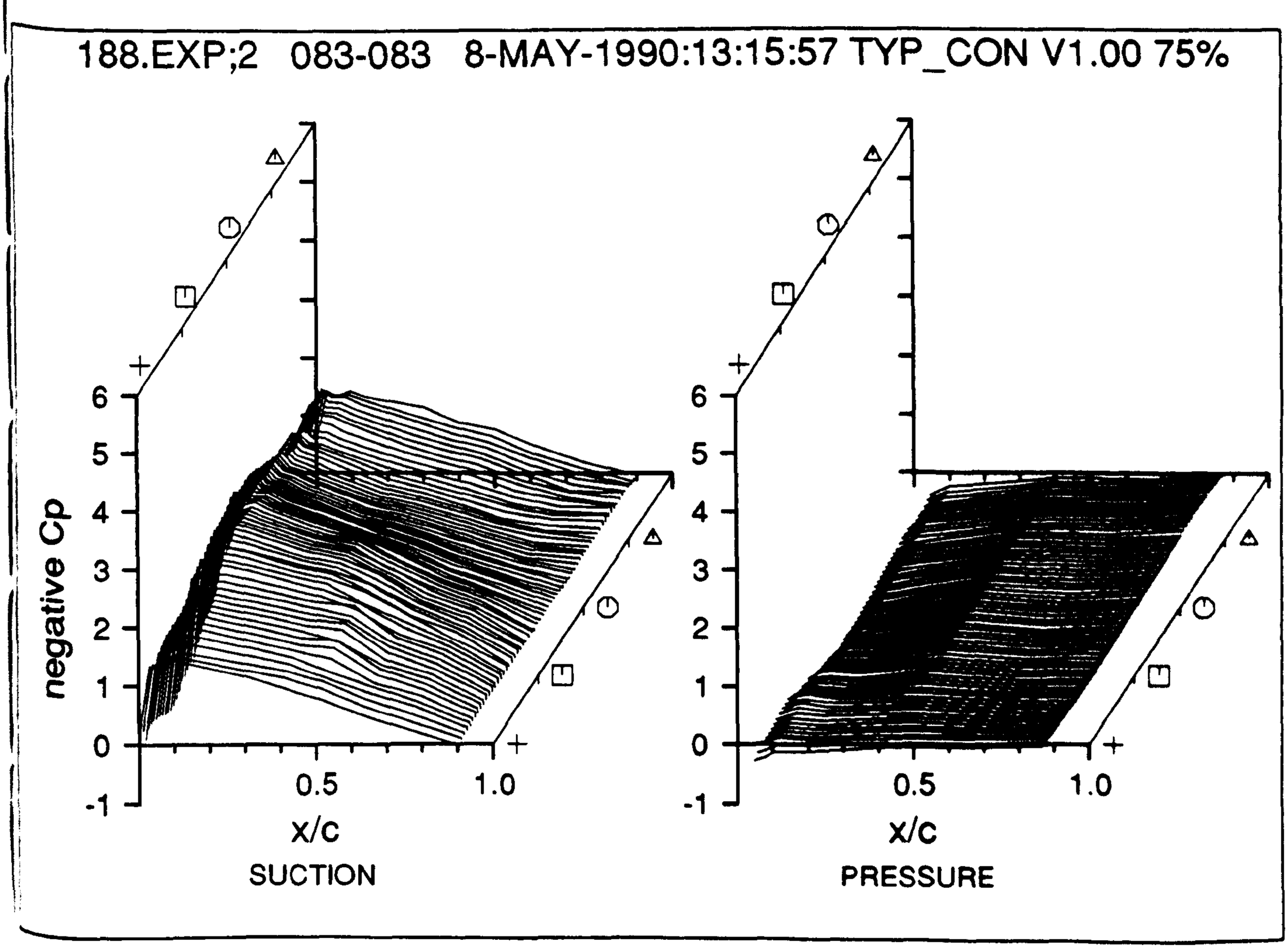
188.EXP;2 083-083 8-MAY-1990:13:15:57 TYP_CON V1.00 75%
negative Cp
6
5
4
3
2
1
0
-1
0.5
1.0
x/c
SUCTION
PRESSURE

Figure 10.39

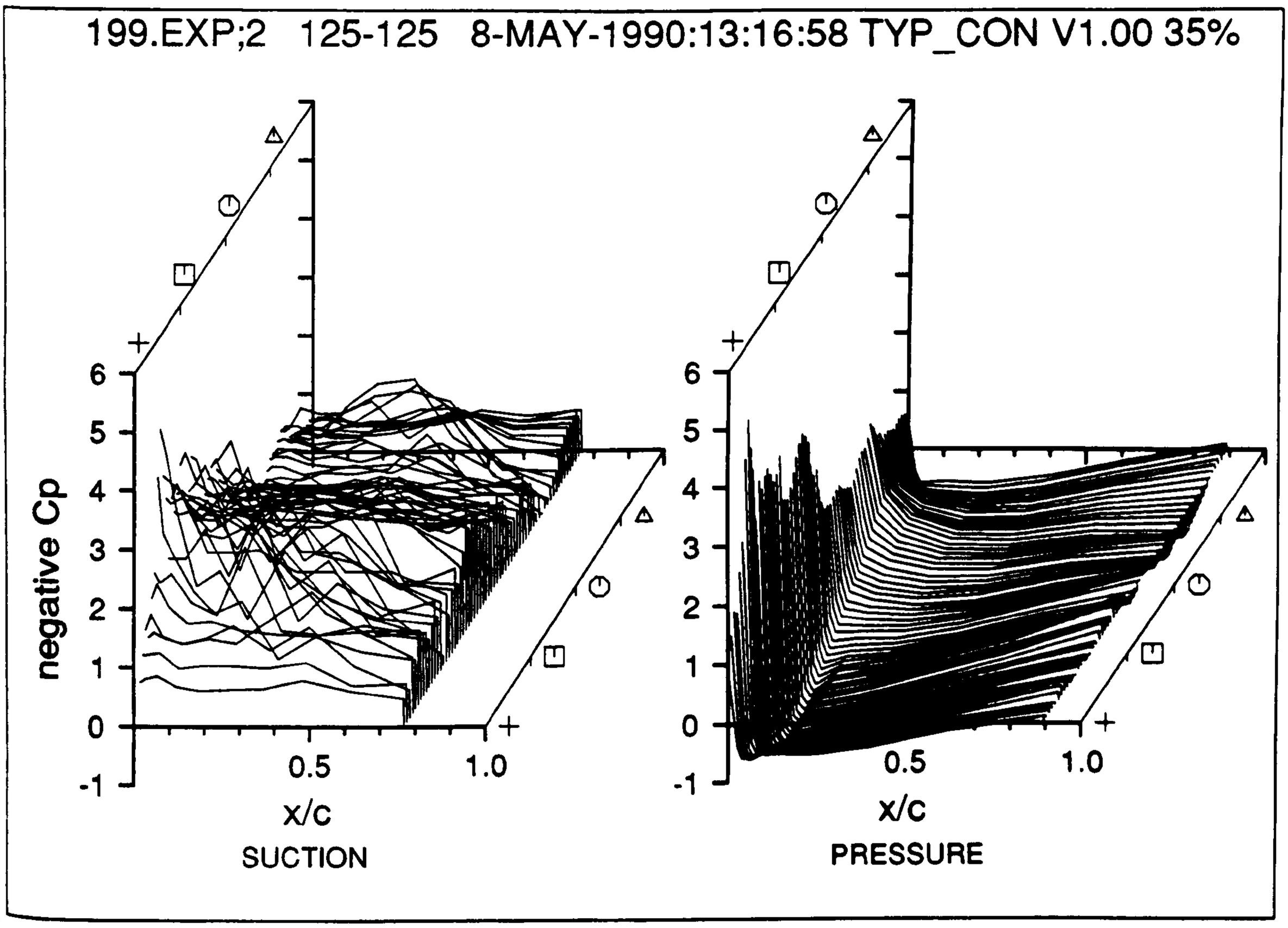
199.EXP;2 125-125 8-MAY-1990:13:16:58 TYP_CON V1.00 35%
negative Cp
6
5
4
3
2
1
0
-1
0.5
1.0
X/C
SUCTION
PRESSURE

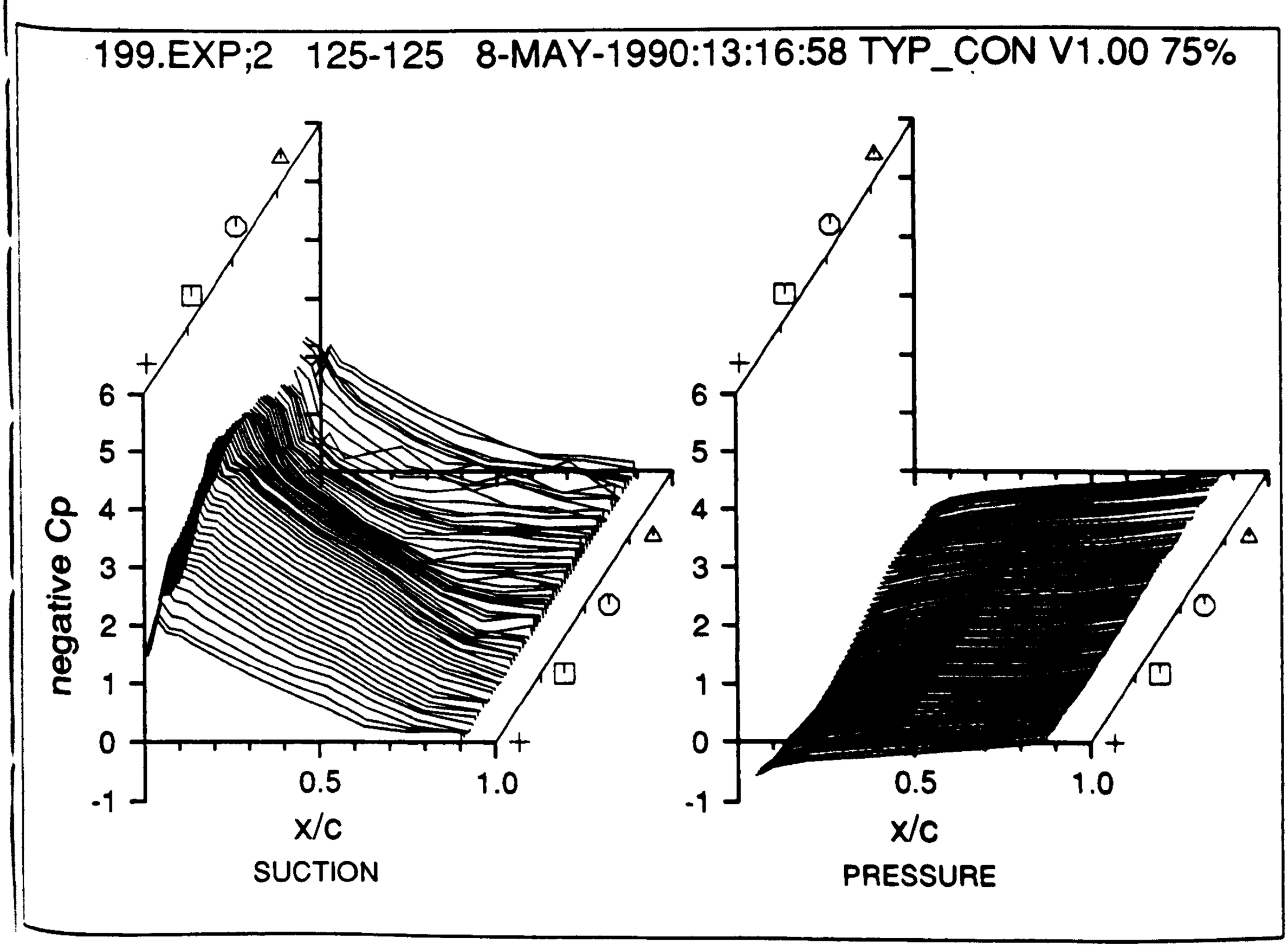
199.EXP;2 125-125 8-MAY-1990:13:16:58 TYP_CON V1.00 75%
negative Cp
6
5
4
3
2
1
0
-1
0.5
1.0
X/C
SUCTION
PRESSURE

Figure 10.40

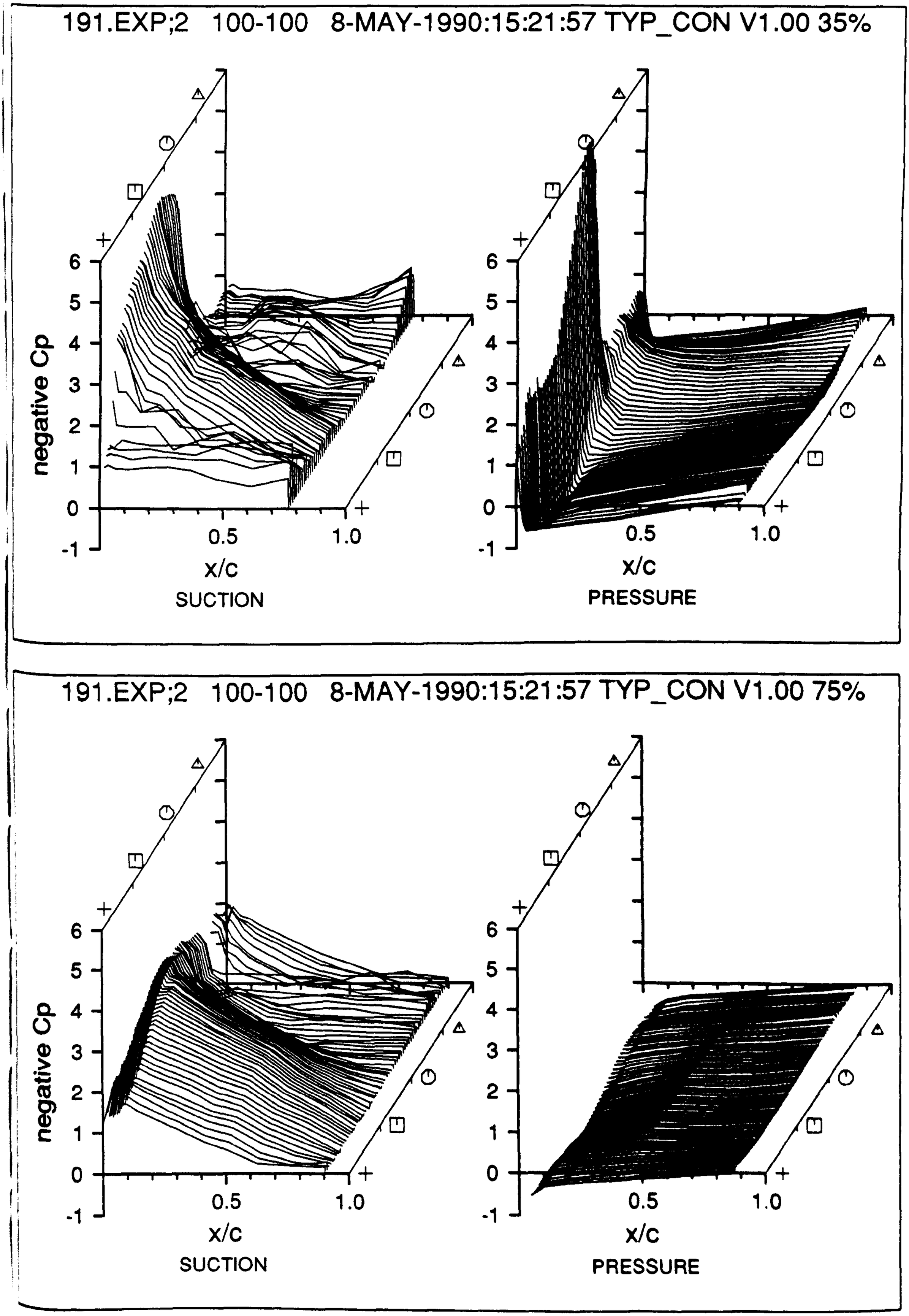
191.EXP;2 100-100 8-MAY-1990:15:21:57 TYP_CON V1.00 35%
negative Cp
6
5
4
3
2
1
0
-1
0.5
1.0
X/C
SUCTION
PRESSURE
191.EXP;2 100-100 8-MAY-1990:15:21:57 TYP_CON V1.00 75%

Figure 10.41

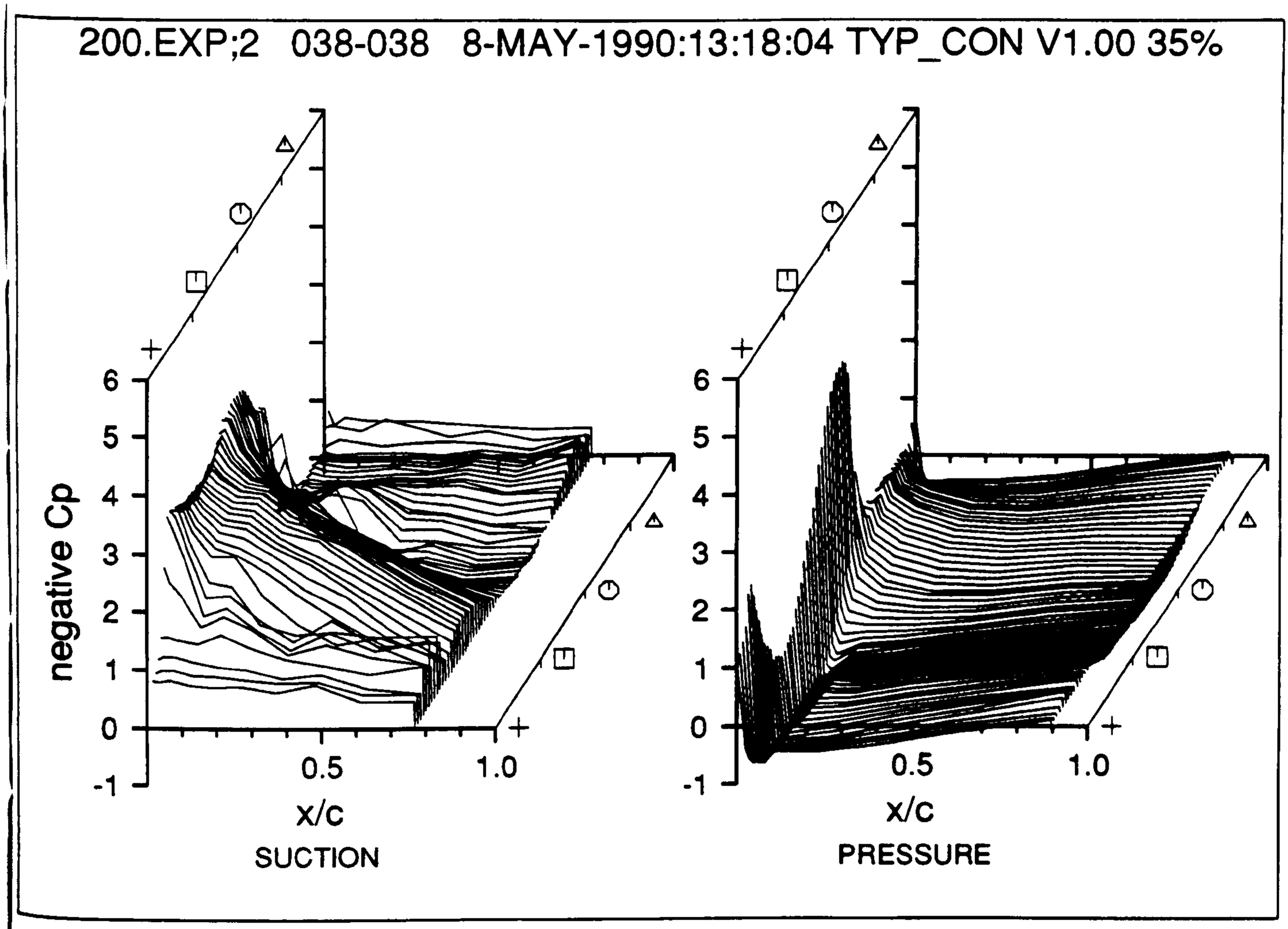
200.EXP;2 038-038 8-MAY-1990:13:18:04 TYP_CON V1.00 35%
negative Cp
6
5
4
3
2
1
0
-1
0.5
1.0
X/C
SUCTION
PRESSURE
200.EXP;2 038-038 8-MAY-1990:13:18:04 TYP_CON V1.00 75%

Figure 10.42

192.EXP;2 082-082 8-MAY-1990:15:23:32 TYP_CON V1.00 35%

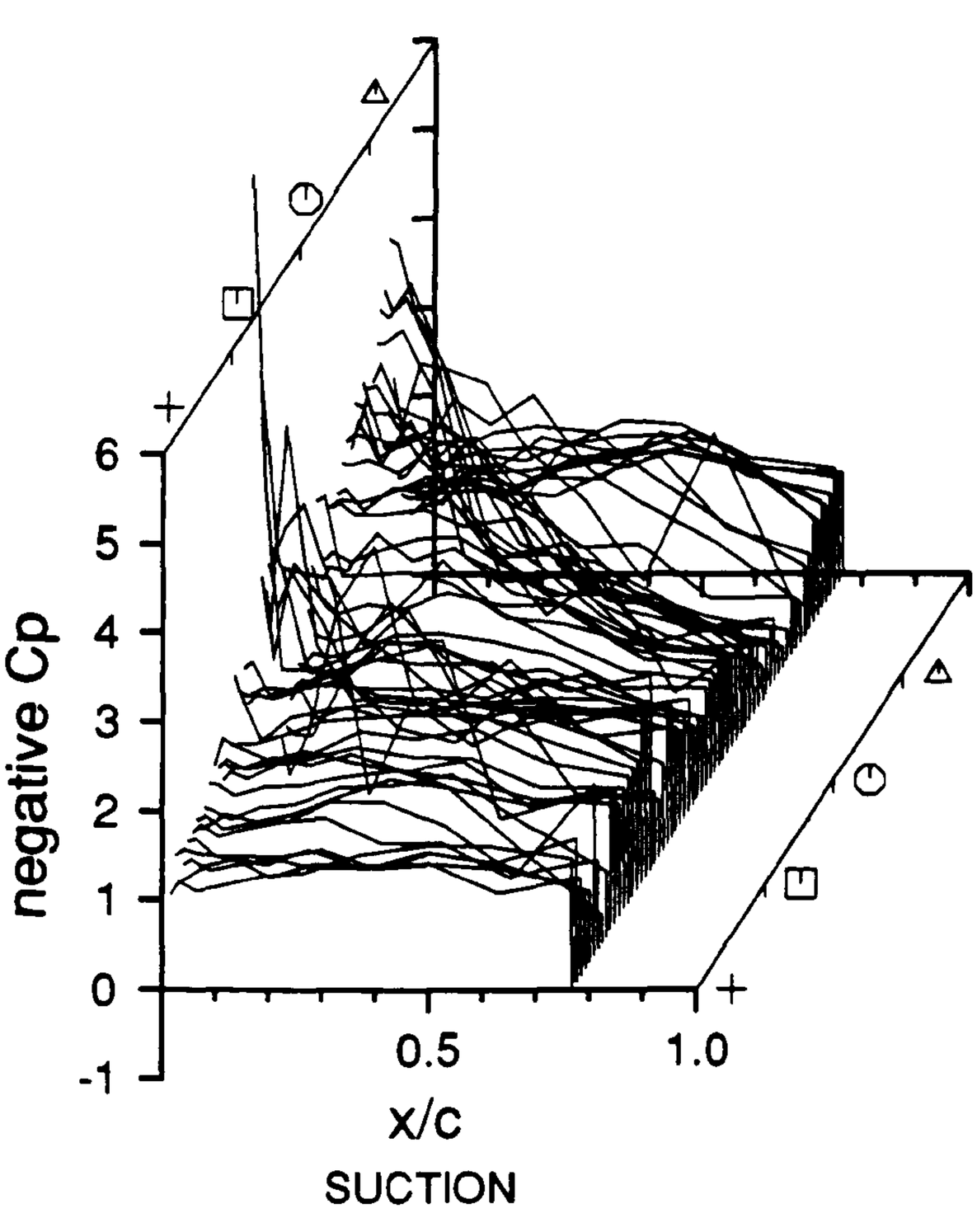

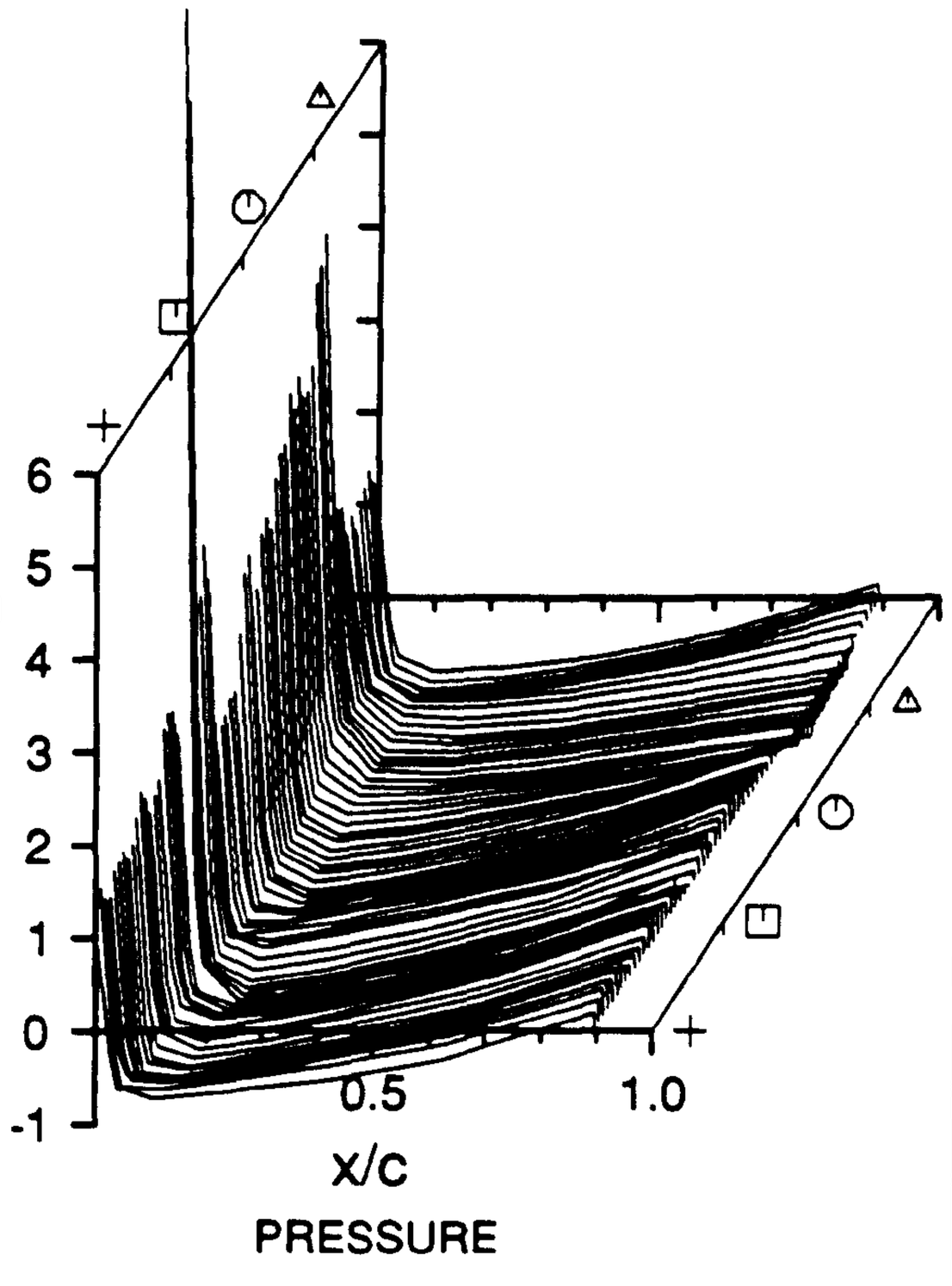

192.EXP;2 082-082 8-MAY-1990:15:23:32 TYP_CON V1.00 75%

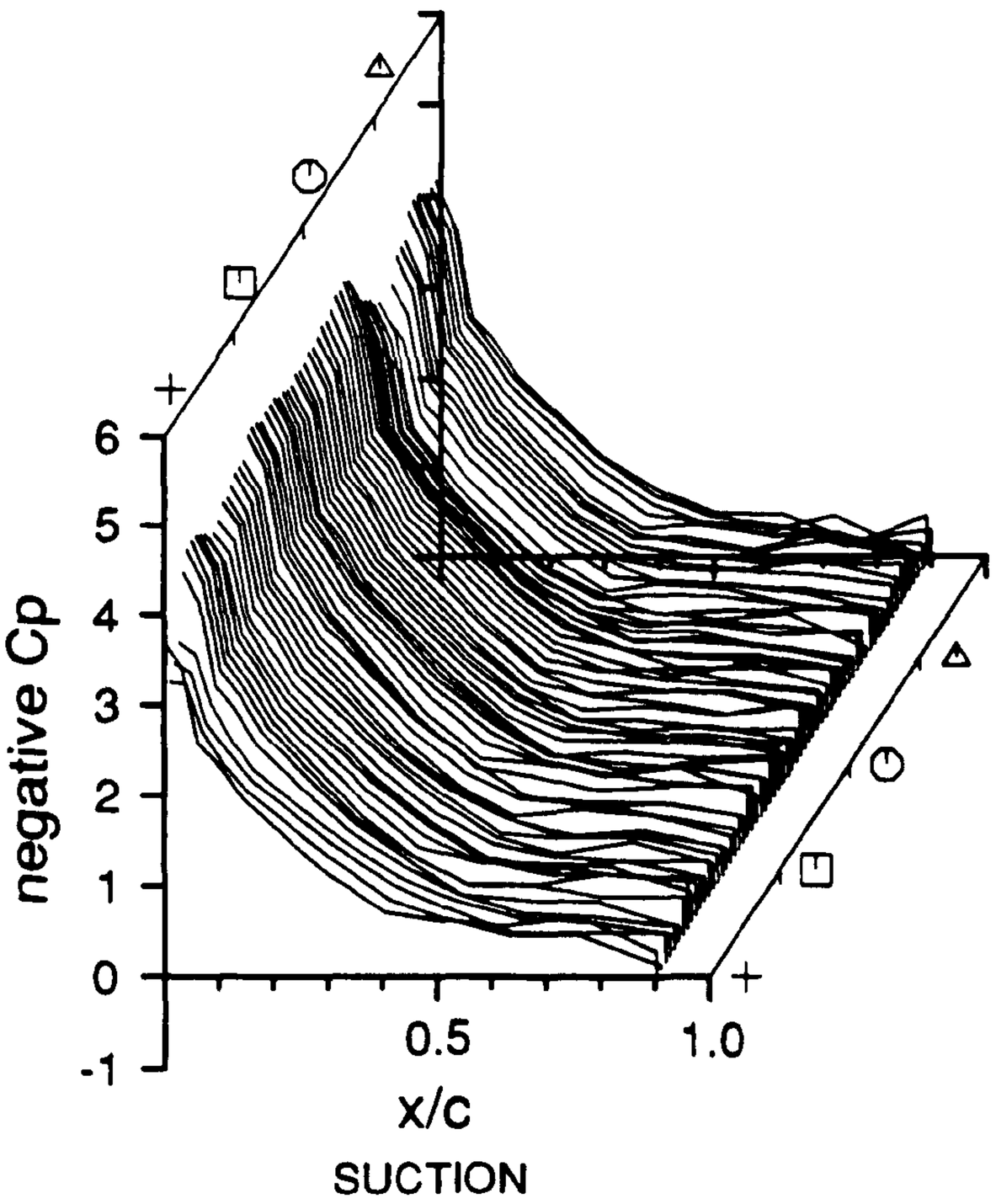

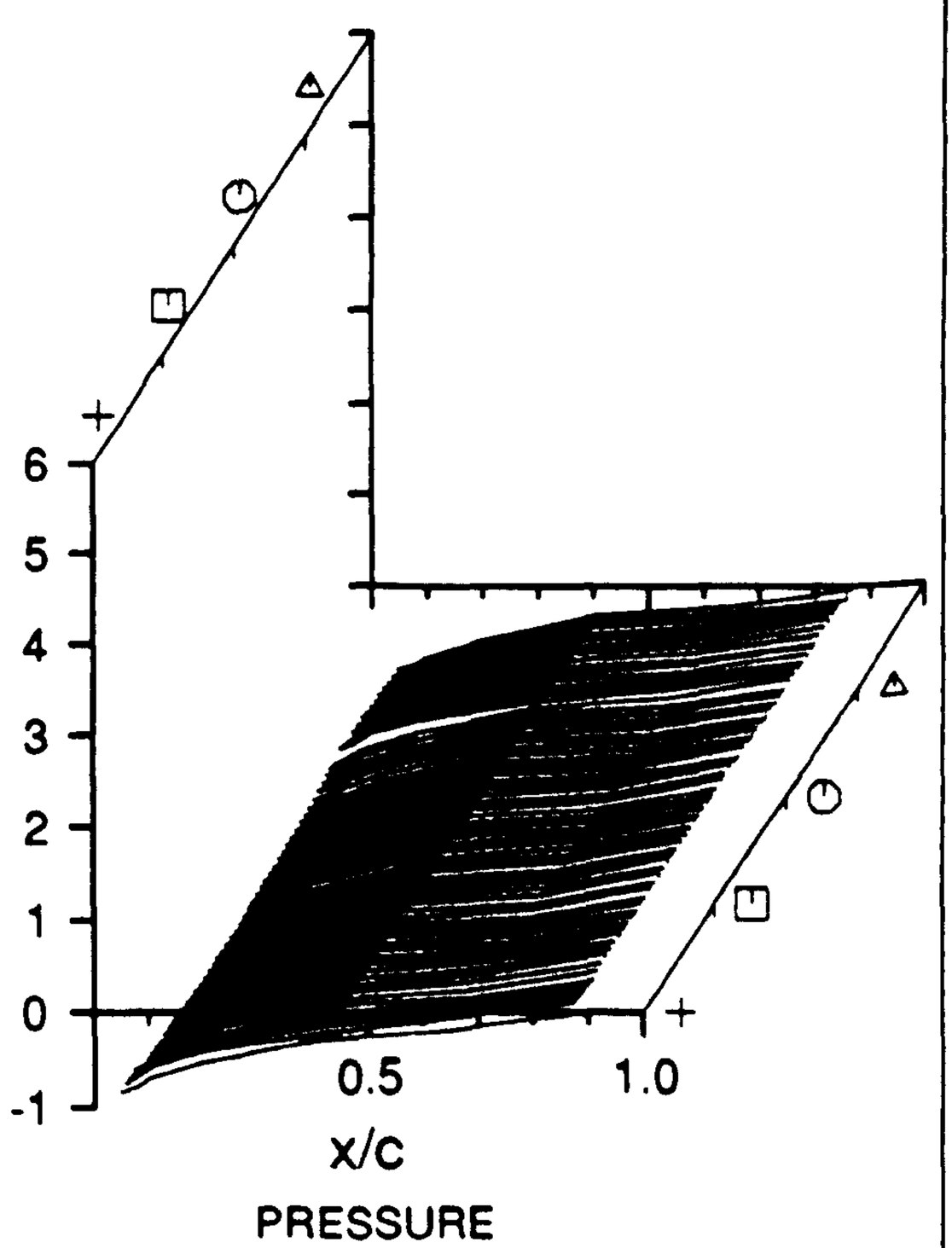

202.EXP;2 071-071 8-MAY-1990:13:18:57 TYP_CON V1.00 35%

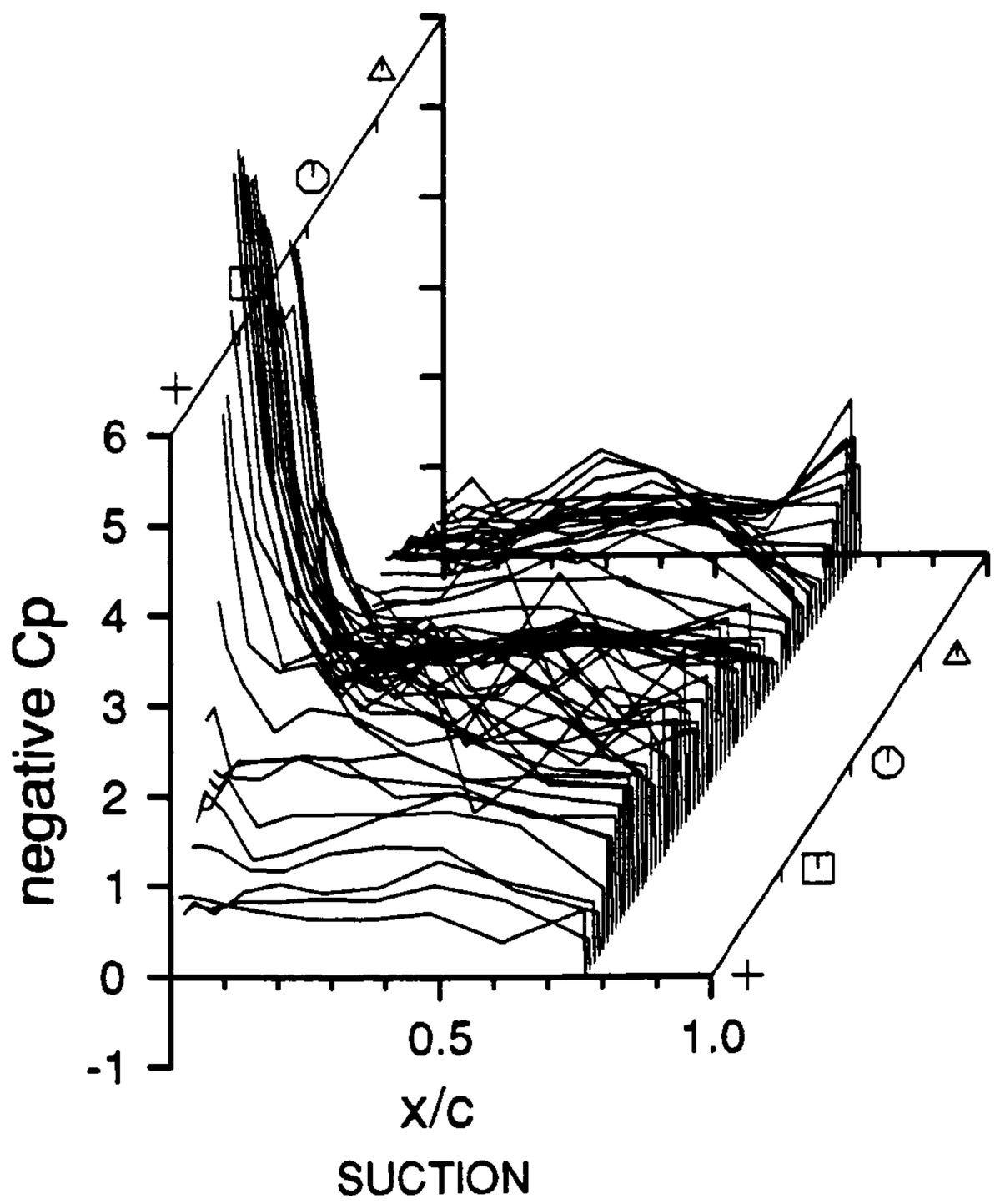

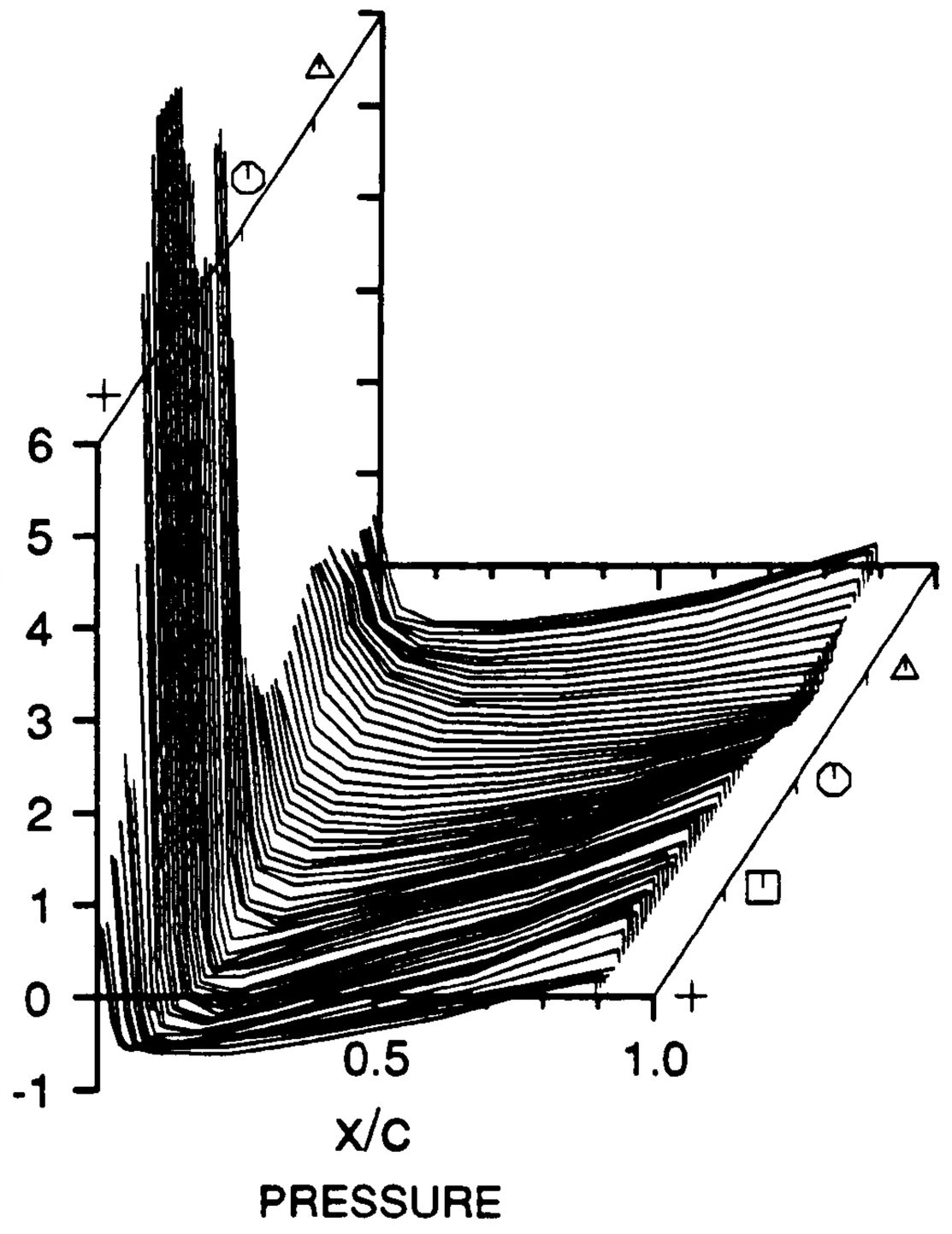

202.EXP;2 071-071 8-MAY-1990:13:18:57 TYP_CON V1.00 75%

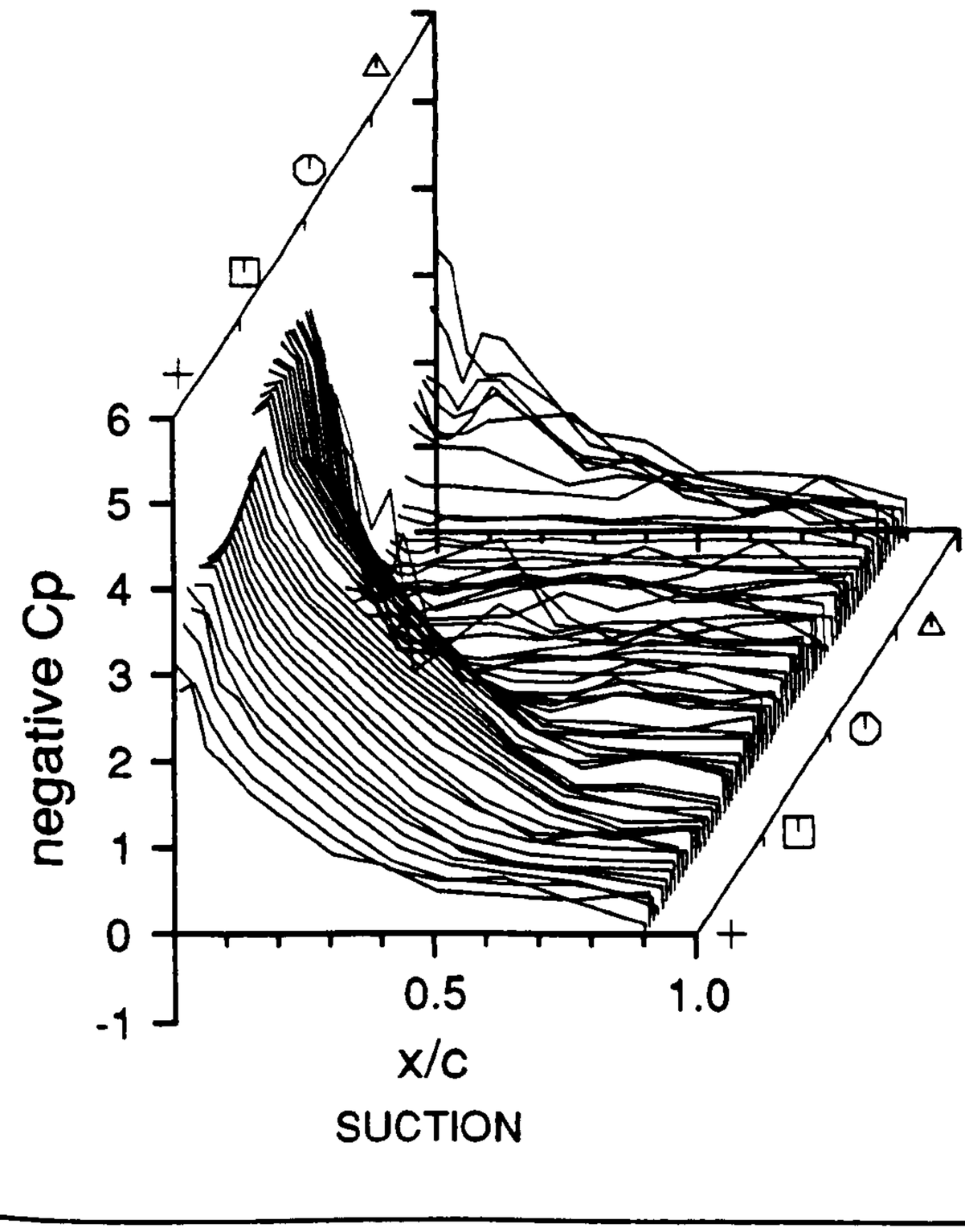

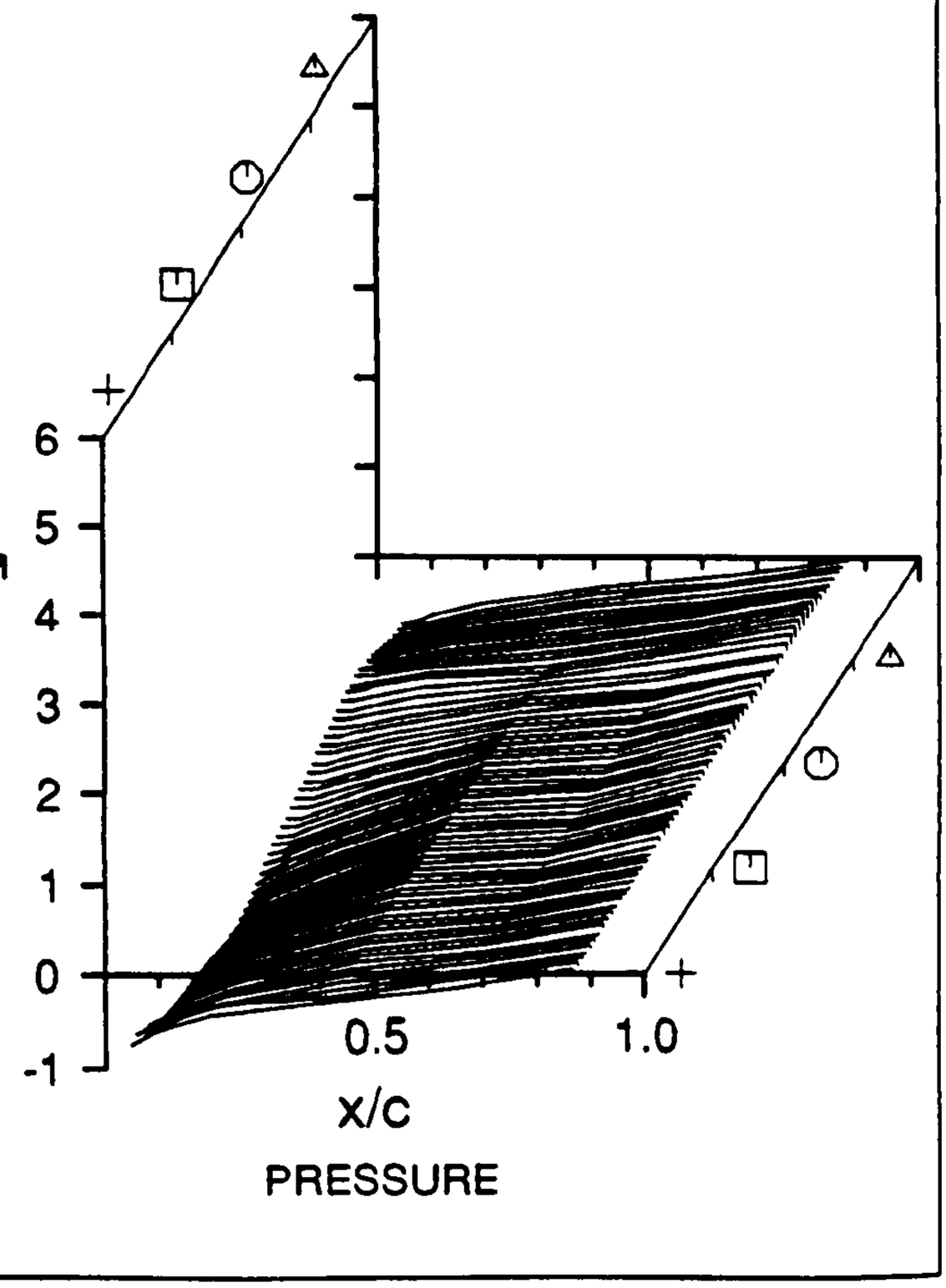

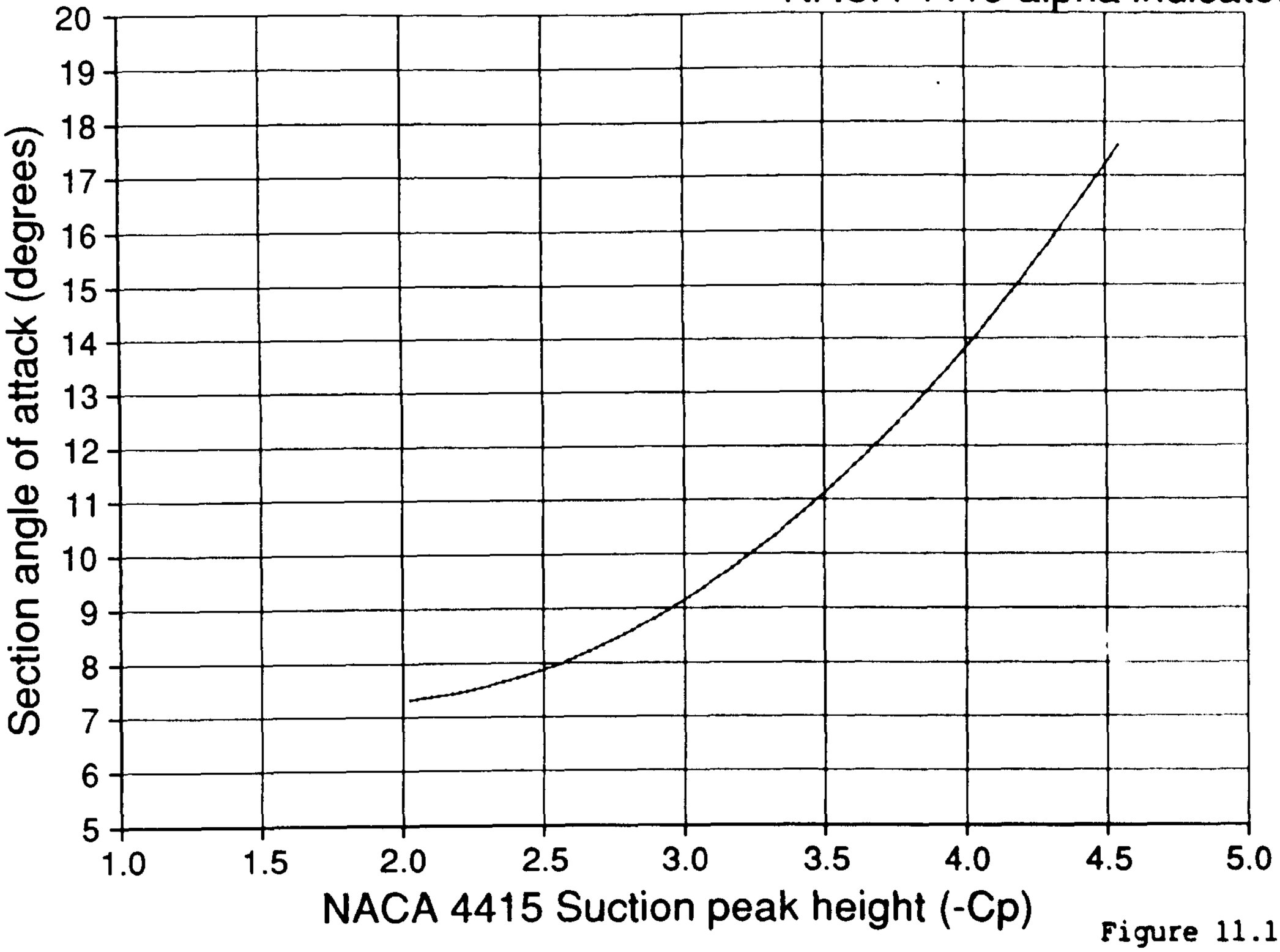

Figure 11.1

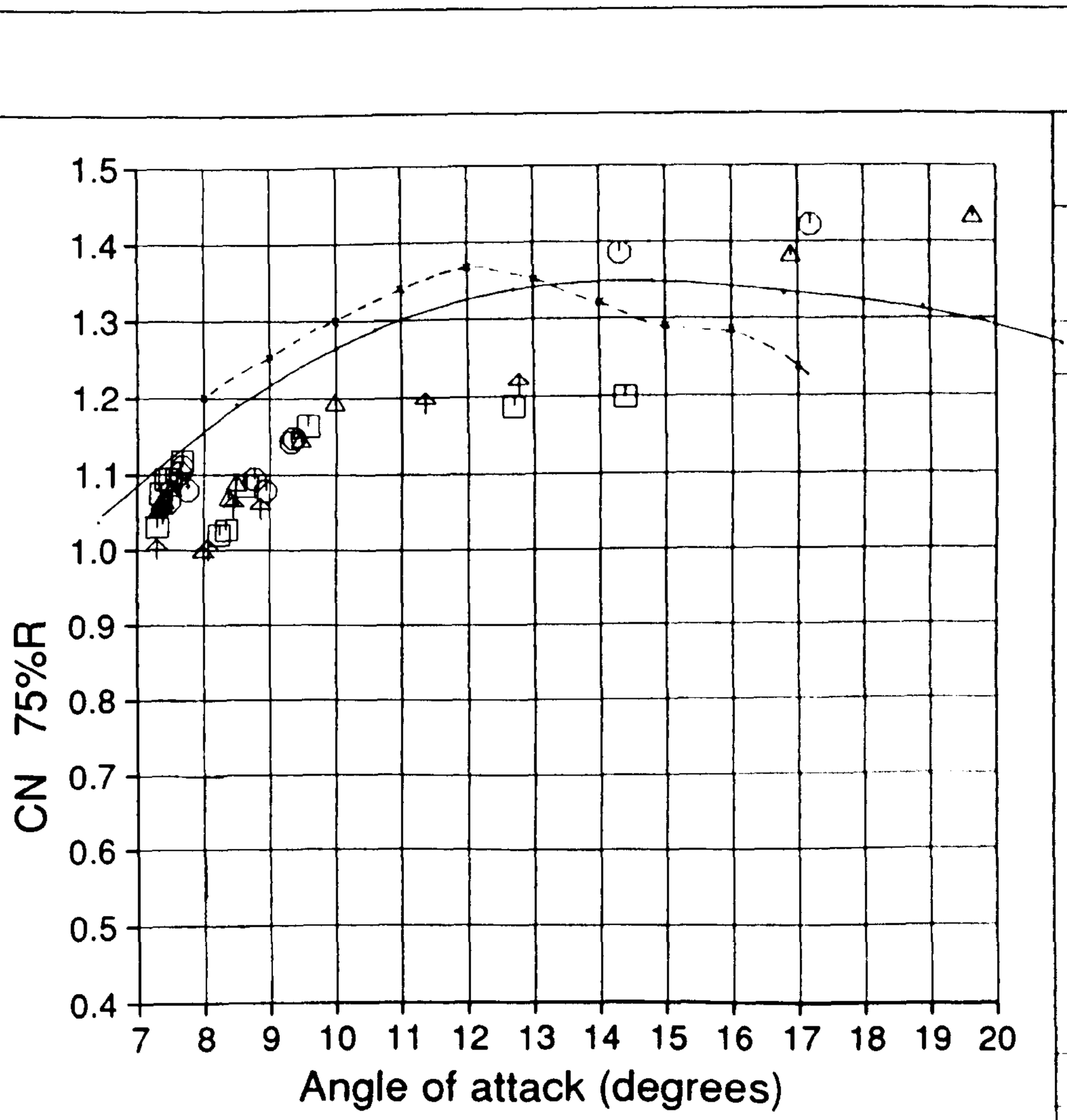

Cranfield

HAWT
Unsteady Aerodynamics
Experiment

Parametric Trends

Program V2.03

MARLEC Blades FI-1

84 sub-runs plotted
exactly 40 revs
in each sub run
derived parameters from
PROFILES

z is Blade azimut
× --- 90.0
○ 90.0 --- 180.0
△ 180.0 --- 270.0
□ 270.0 --- 360.0
✦ 360.0 ---

Figure 11.2

TREND.DAT;3

6-JUN-1990:15:33:55

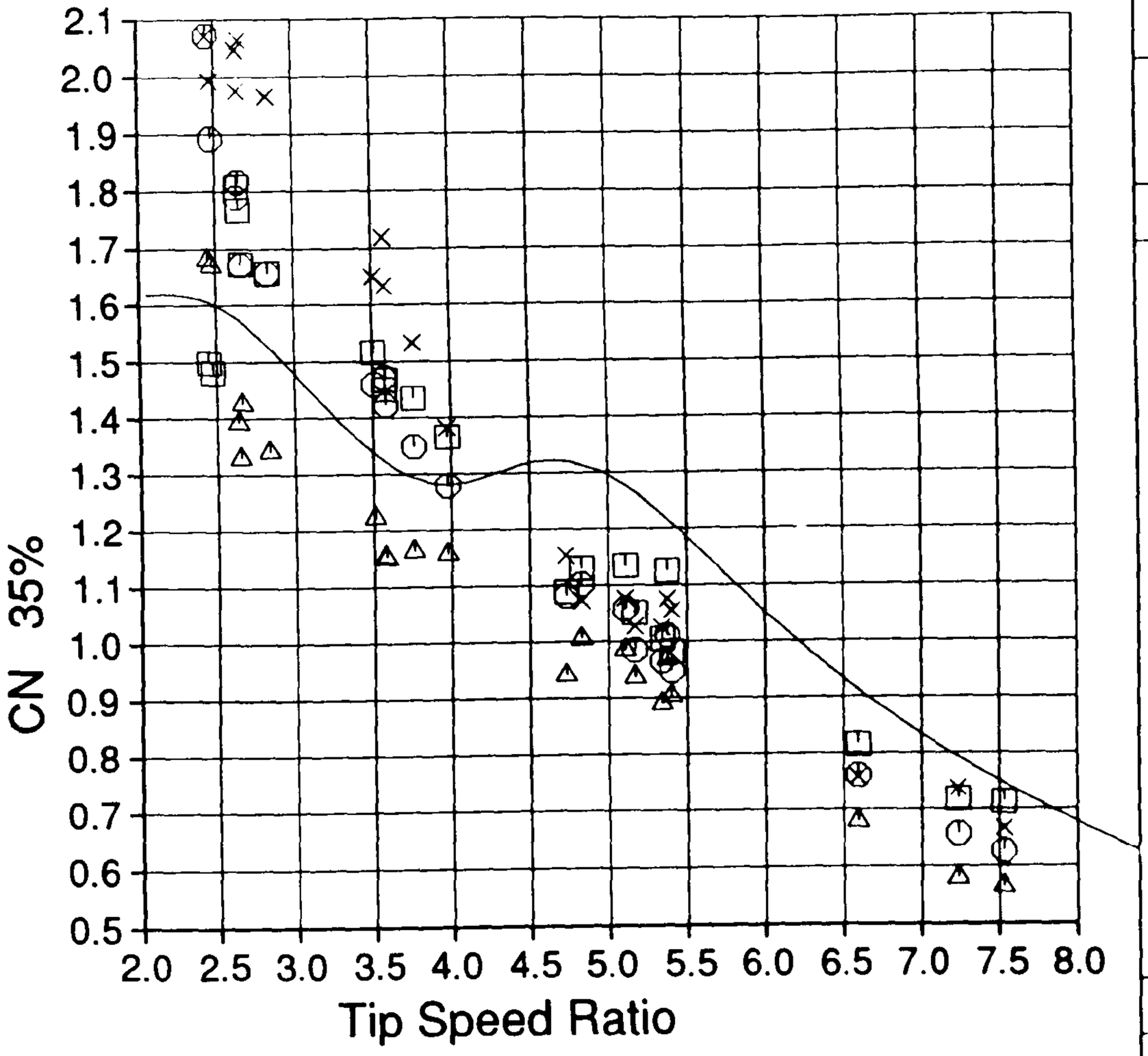

Cranfield

HAWT
Unsteady Aerodynamics
Experiment

Parametric Trends

Program V2.01

MARLEC Blades FI-1

84 sub-runs plotted
exactly 40 revs
in each sub run
Derived parameters from
PROFILES

z is Blade azimut
× --- 90.0
⏲ --- 180.0
△ --- 270.0
⊔ --- 360.0

Figure 11.3

TREND.DAT;1

27-APR-1990:15:12:11

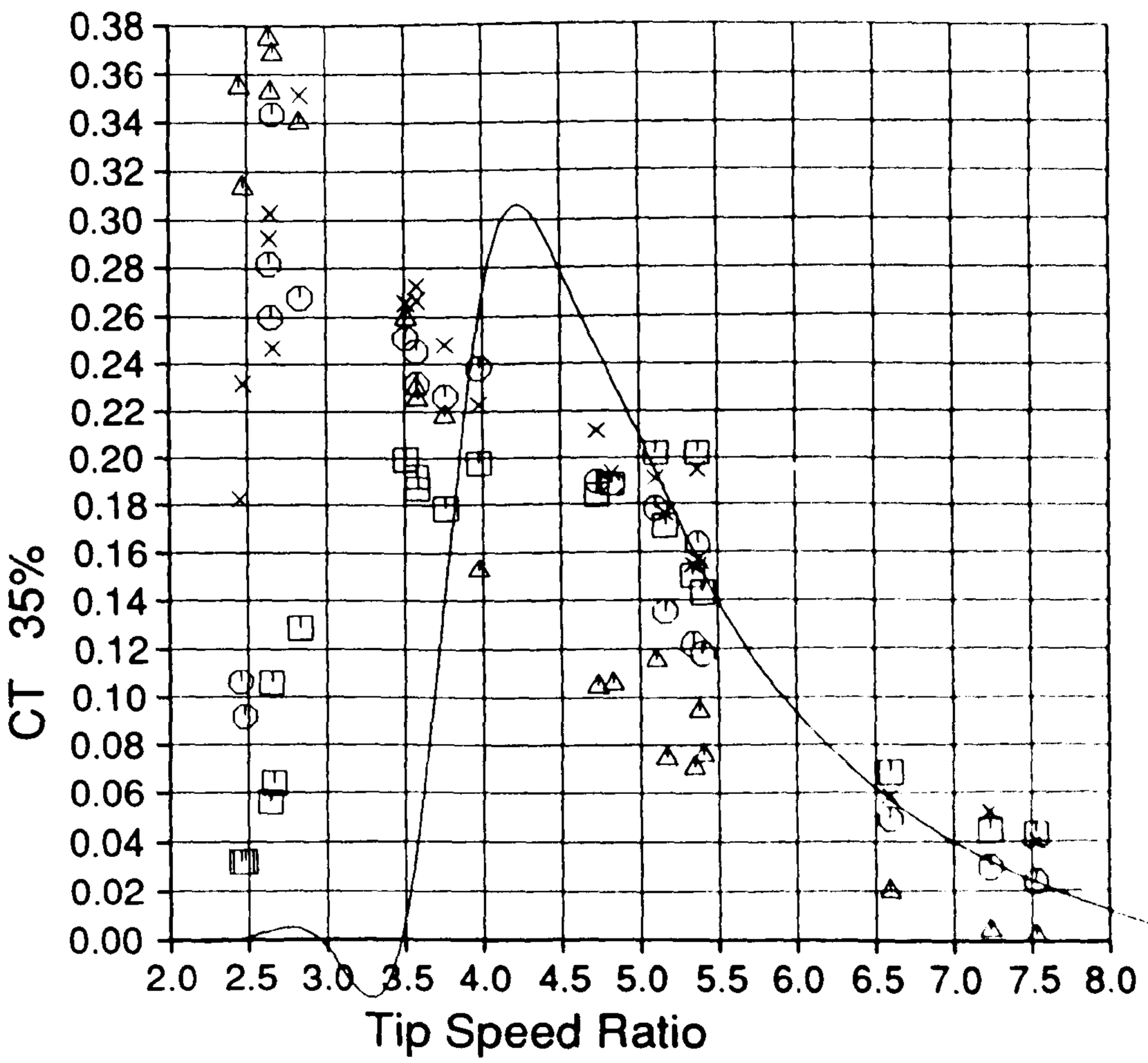

Cranfield

HAWT
Unsteady Aerodynamics
Experiment

Parametric Trends

Program V2.02

MARLEC Blades FI-1

84 sub-runs plotted
exactly 40 revs
in each sub run
Derived parameters from
PROFILES

z is Blade azimut
× --- 90.0
⏲ --- 180.0
△ --- 270.0
⊔ --- 360.0

Figure 11.4

TREND.DAT;2

27-APR-1990:15:12:50

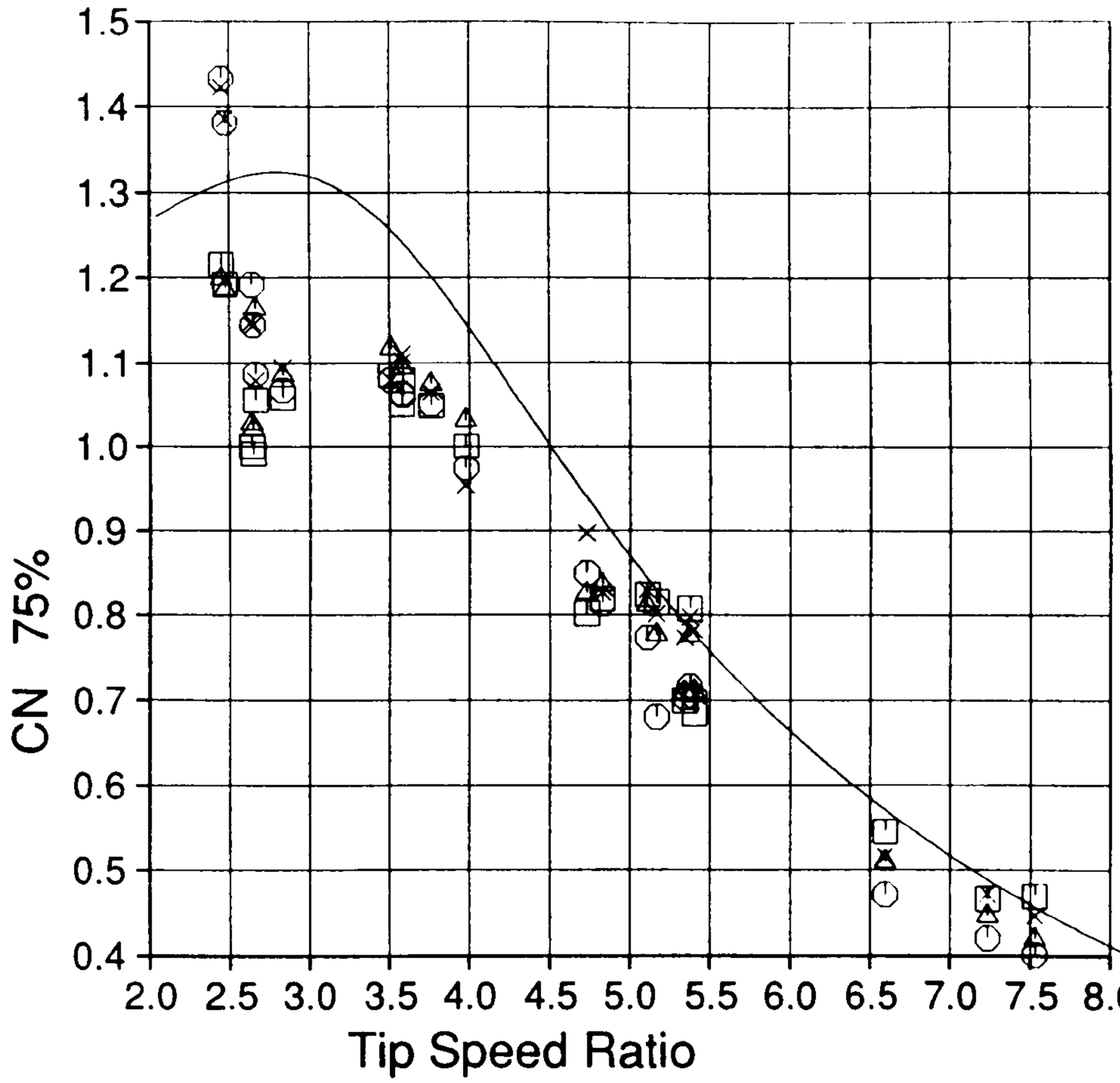

Cranfield

HAWT
Unsteady Aerodynamics
Experiment

Parametric Trends

Program V2.03

MARLEC Blades FI-1

84 sub-runs plotted
exactly 40 revs
in each sub run
Derived parameters from
PROFILES

z is Blade azimut
× --- 90.0
⏲ --- 180.0
△ --- 270.0
▯ --- 360.0

Figure 11.5

TREND.DAT;3

27-APR-1990:15:13:14

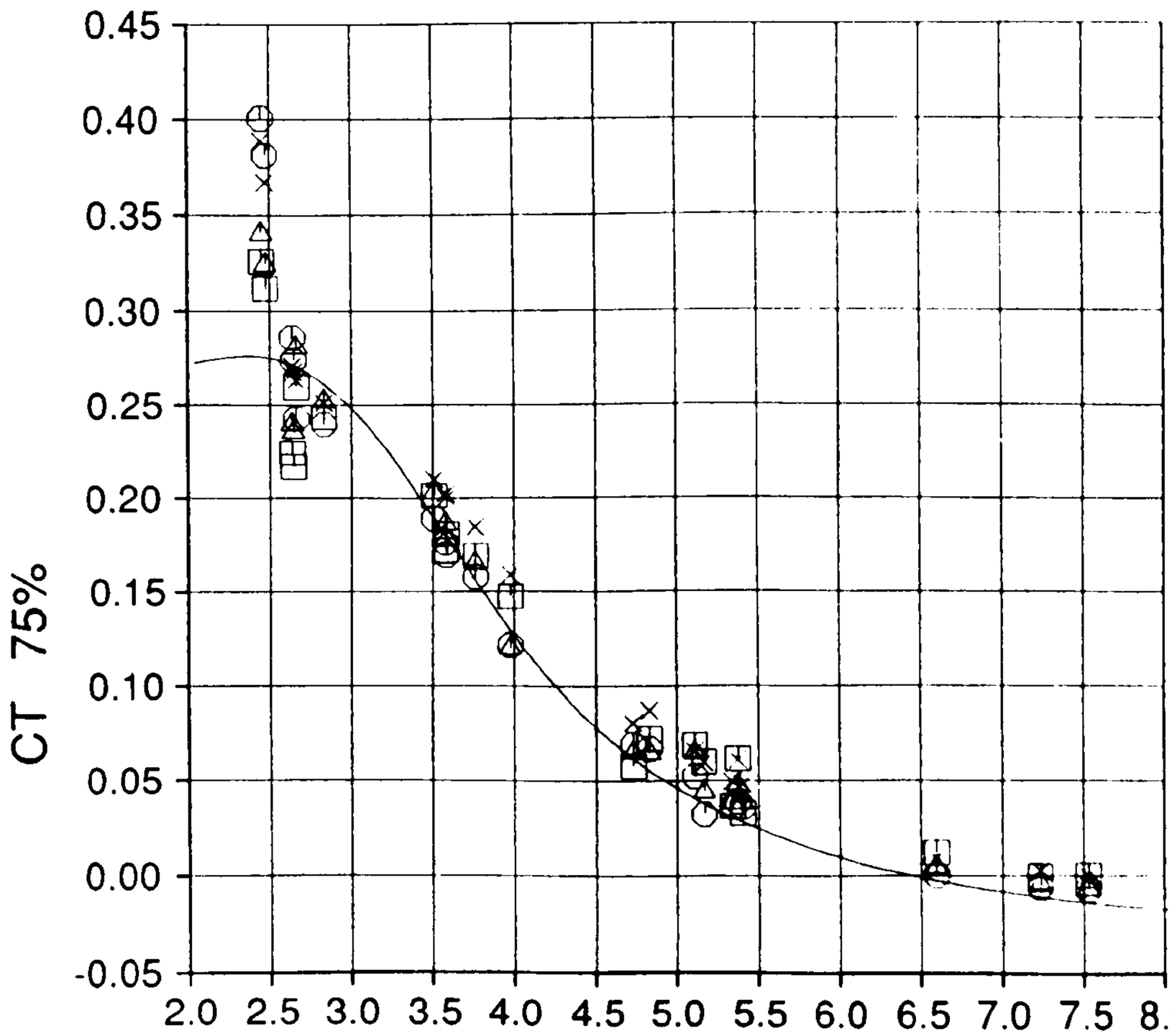

Cranfield

HAWT
Unsteady Aerodynamics
Experiment

Parametric Trends

Program V2.04

MARLEC Blades FI-1

84 sub-runs plotted
exactly 40 revs
in each sub run
Derived parameters from
PROFILES

z is Blade azimut
× --- 90.0
⏲ --- 180.0
△ --- 270.0
▯ --- 360.0

Figure 11.6

TREND.DAT;4

27-APR-1990:15:13:33

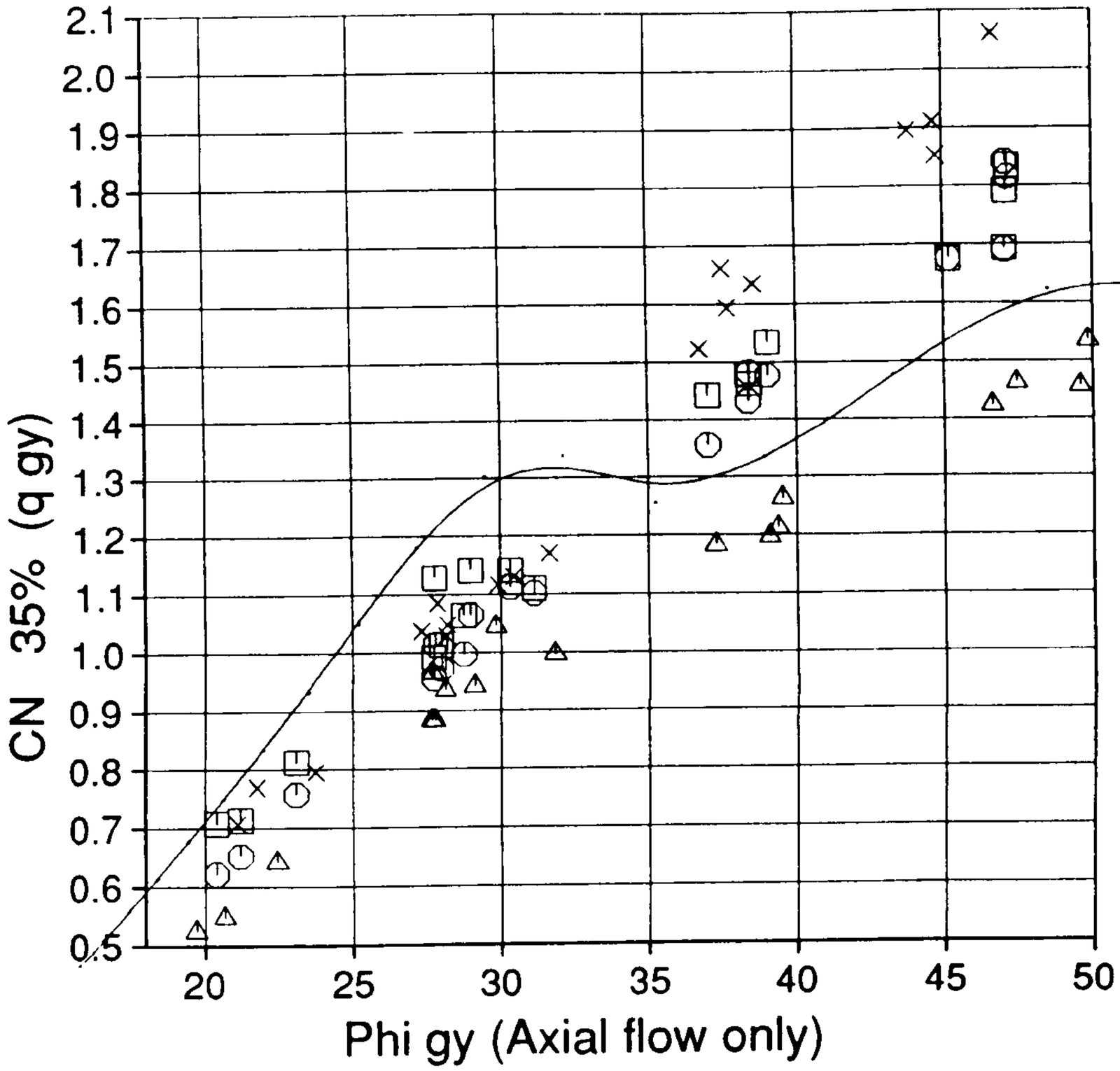

Cranfield

HAWT
Unsteady Aerodynamics
Experiment

Parametric Trends

Program V2.01

MARLEC Blades FI-1

72 sub-runs plotted
exactly 40 revs
in each sub run
Derived parameters from
PROFILES

z is Blade azimut
× --- 90.0
◷ --- 180.0
△ --- 270.0
⊓ --- 360.0

Figure 11.7

TREND.DAT;1

7-JUN-1990:10:39:11

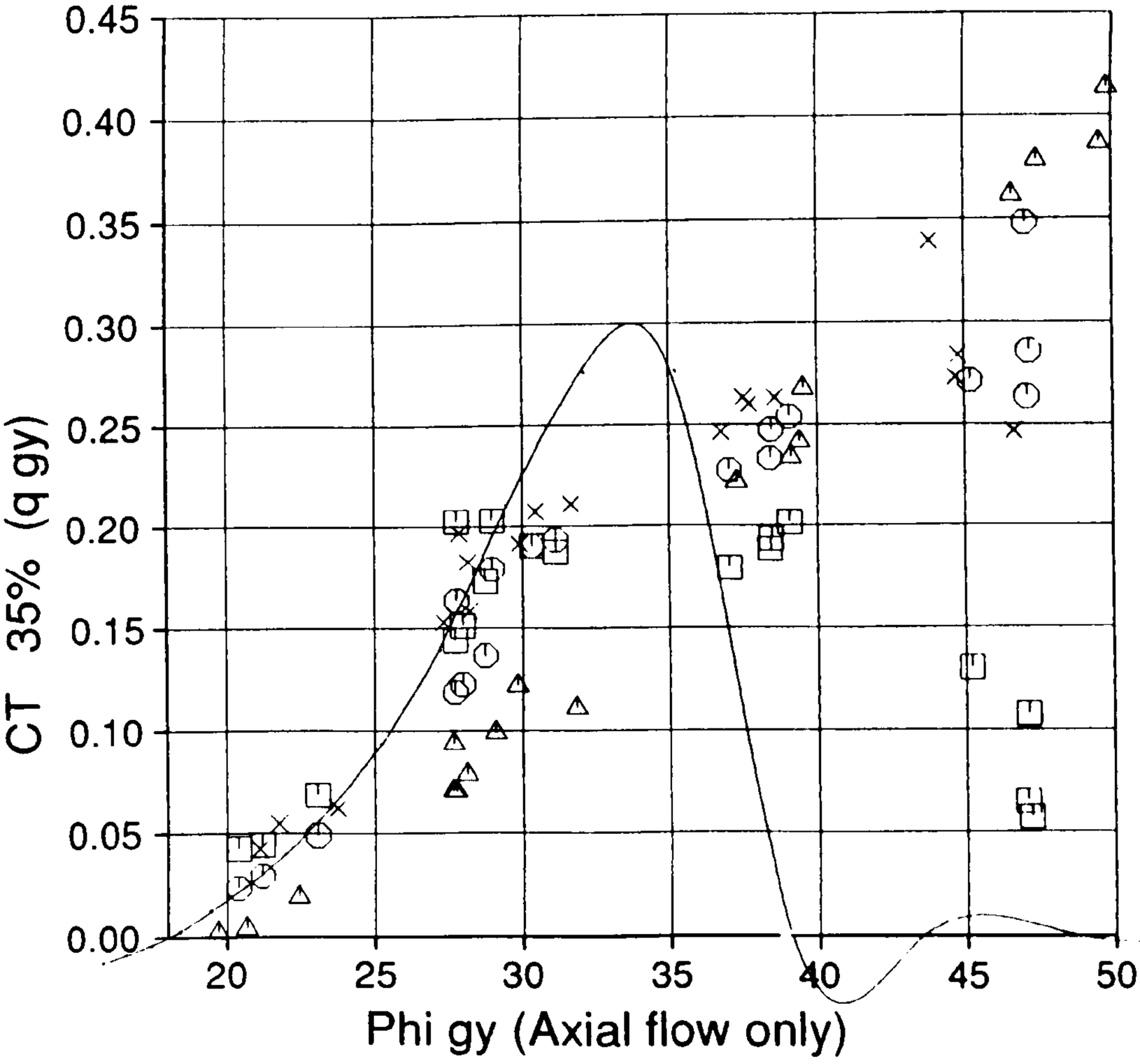

Cranfield

HAWT
Unsteady Aerodynamics
Experiment

Parametric Trends

Program V2.02

MARLEC Blades FI-1

72 sub-runs plotted
exactly 40 revs
in each sub run
Derived parameters from
PROFILES

z is Blade azimut
× --- 90.0
◷ --- 180.0
△ --- 270.0
⊓ --- 360.0

Figure 11.8

TREND.DAT;2

7-JUN-1990:10:39:45

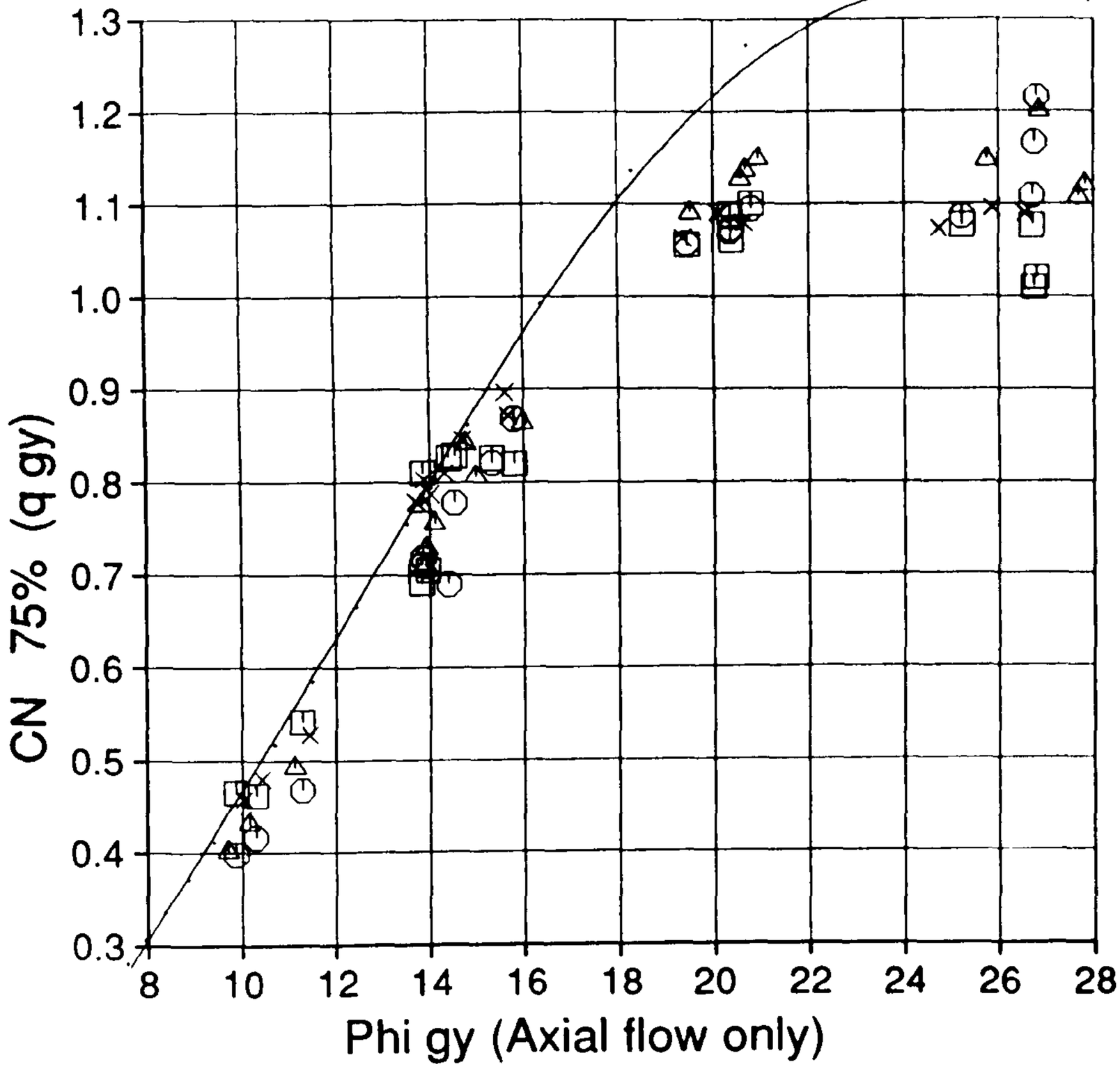

Cranfield

HAWT
Unsteady Aerodynamics
Experiment

Parametric Trends

Program V2.03

MARLEC Blades FI-1

72 sub-runs plotted
exactly 40 revs
in each sub run
Derived parameters from
PROFILES

z is Blade azimut
× --- 90.0
○ --- 180.0
△ --- 270.0
□ --- 360.0

Figure 11.9

TREND.DAT;3

7-JUN-1990:10:40:09

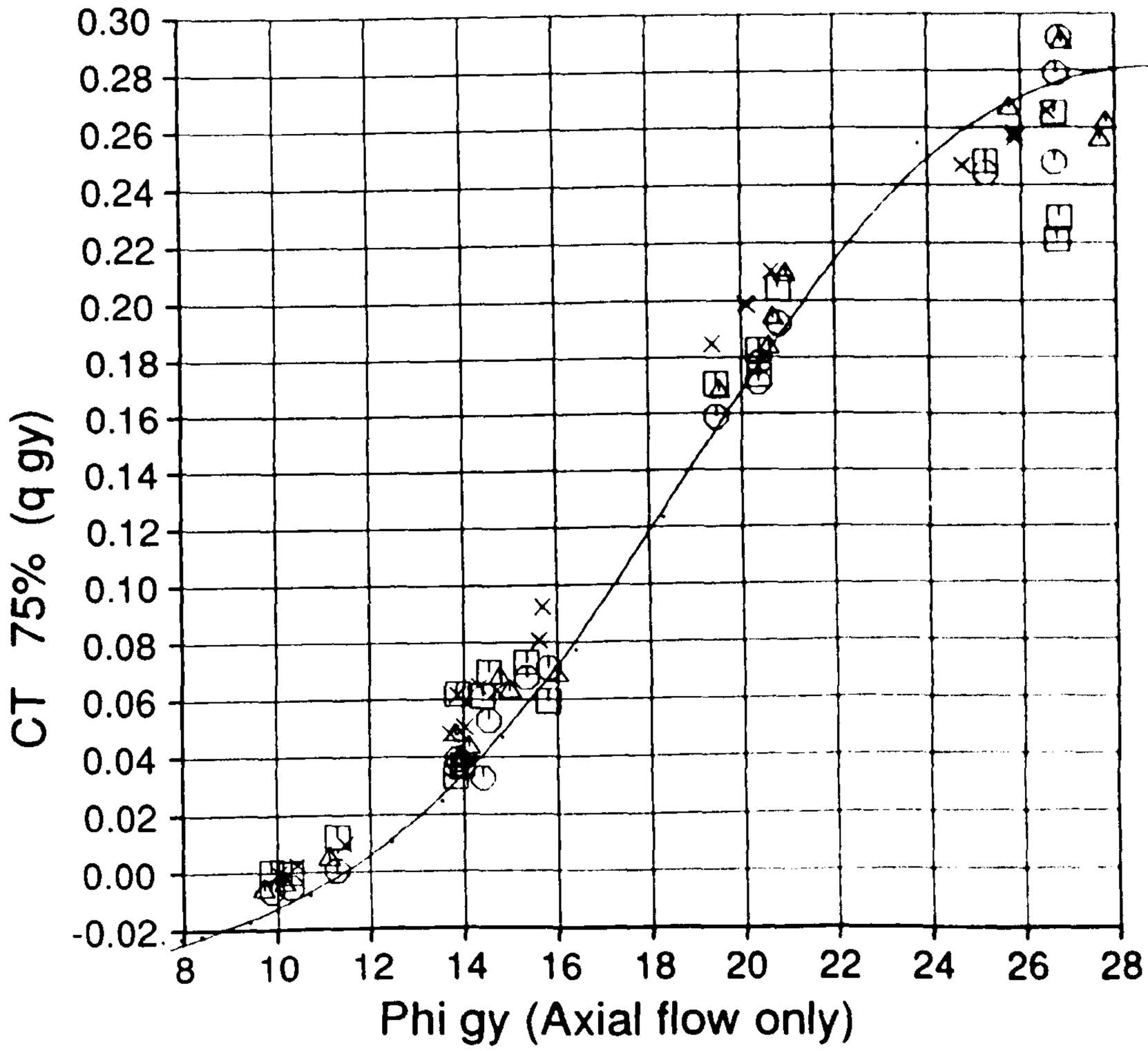

Cranfield

HAWT
Unsteady Aerodynamics
Experiment

Parametric Trends

Program V2.04

MARLEC Blades FI-1

72 sub-runs plotted
exactly 40 revs
in each sub run
Derived parameters from
PROFILES

z is Blade azimut
× --- 90.0
○ --- 180.0
△ --- 270.0
□ --- 360.0

Figure 11.10

TREND.DAT;4

7-JUN-1990:10:40:31

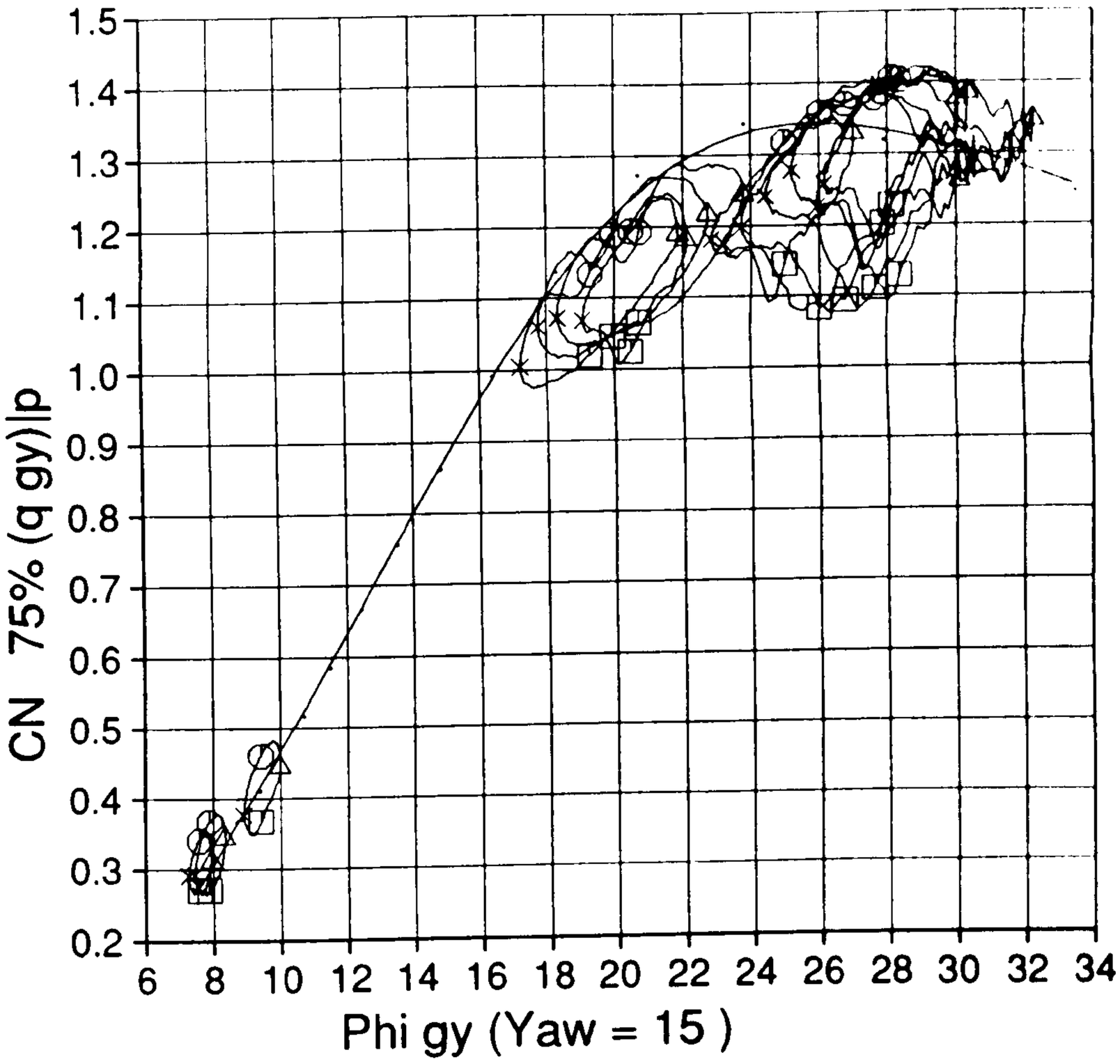

Cranfield

HAWT
Unsteady Aerodynamics
Experiment

Parametric Trends

Program V2.13

MARLEC Blades FI-1

14 sub-runs plotted
exactly 40 revs
in each sub run
Derived parameters from
PROFILES
TYPREV
z is Blade azimuth
× --- 90.0
○ --- 180.0
△ --- 270.0
□ --- 360.0

Figure 11.11

TREND.DAT;13

14-JUN-1990:10:08:16

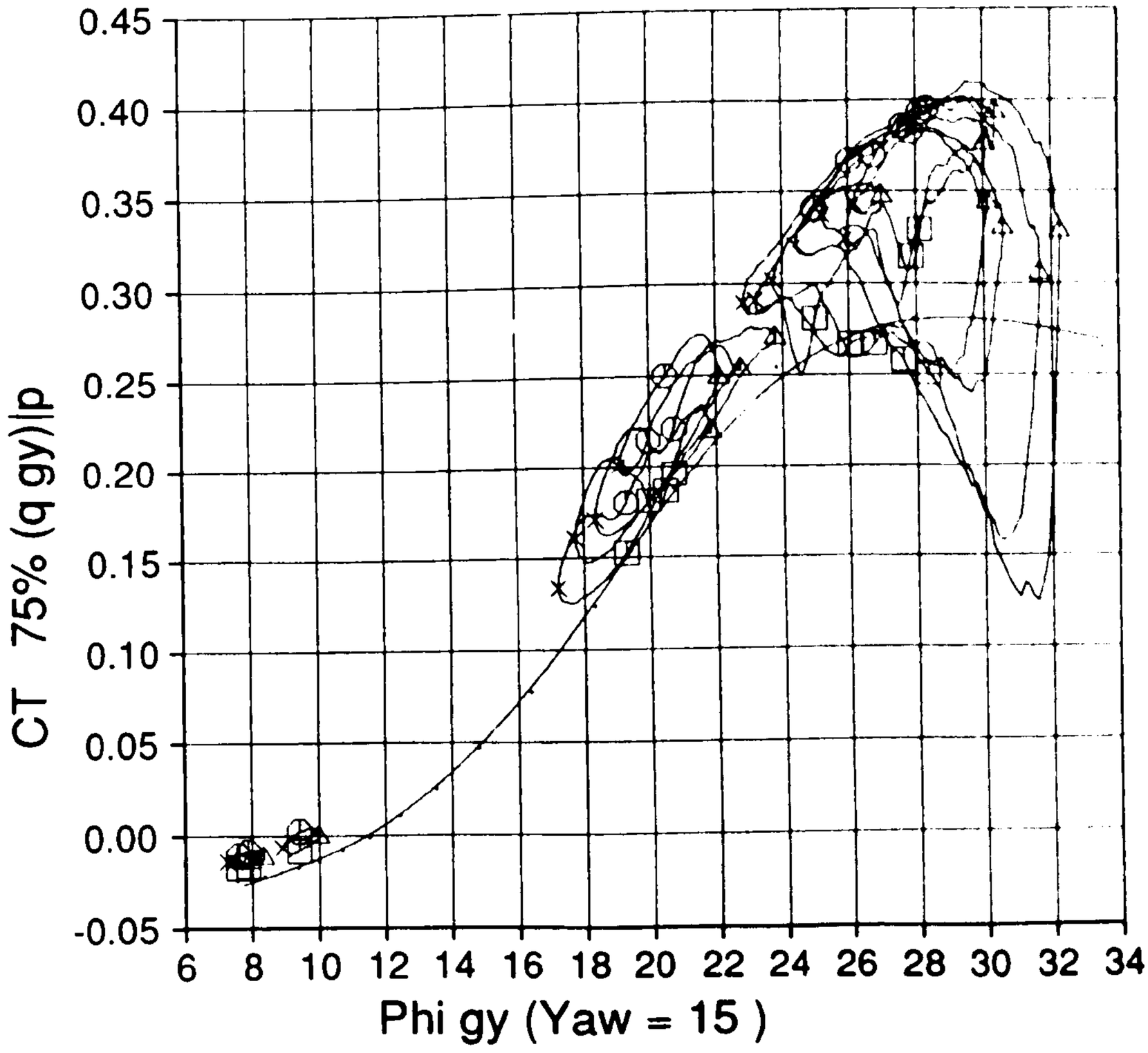

Cranfield

HAWT
Unsteady Aerodynamics
Experiment

Parametric Trends

Program V2.14

MARLEC Blades FI-1

14 sub-runs plotted
exactly 40 revs
in each sub run
Derived parameters from
PROFILES
TYPREV
z is Blade azimuth
× --- 90.0
○ --- 180.0
△ --- 270.0
□ --- 360.0

Figure 11.12

TREND.DAT;14

14-JUN-1990:10:08:53

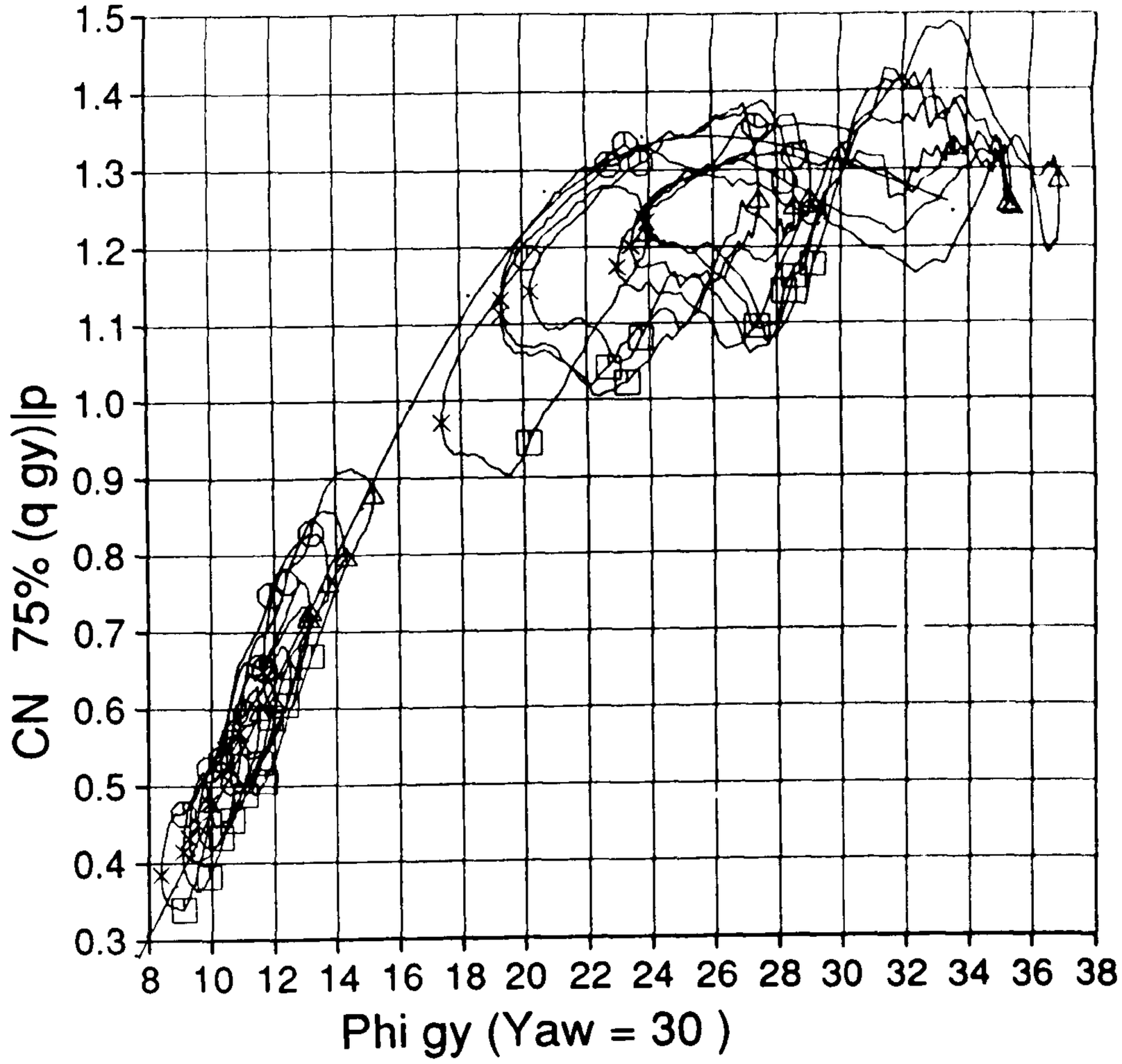

Cranfield

HAWT
Unsteady Aerodynamics
Experiment

Parametric Trends

Program V2.15

MARLEC Blades FI-1

18 sub-runs plotted
exactly 40 revs
in each sub run
Derived parameters from
PROFILES
TYPREV
z is Blade azimuth
× --- 90.0
◷ --- 180.0
△ --- 270.0
⊡ --- 360.0

Figure 11.13

TREND.DAT;15

14-JUN-1990:10:09:27

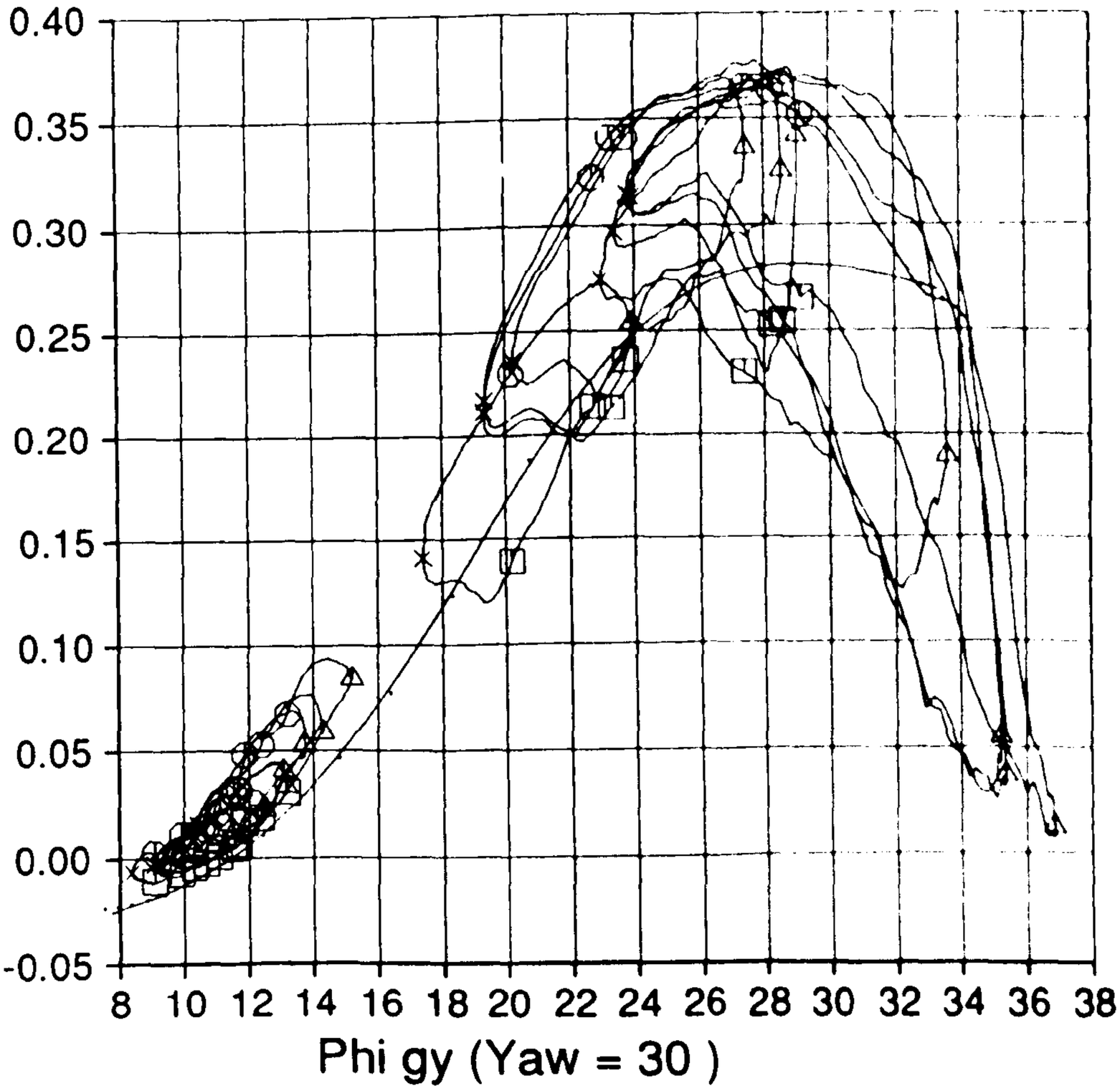

Cranfield

HAWT
Unsteady Aerodynamics
Experiment

Parametric Trends

Program V2.16

MARLEC Blades FI-1

18 sub-runs plotted
exactly 40 revs
in each sub run
Derived parameters from
PROFILES
TYPREV
z is Blade azimuth
× --- 90.0
◷ --- 180.0
△ --- 270.0
⊡ --- 360.0

Figure 11.14

TREND.DAT;16

14-JUN-1990:10:10:04

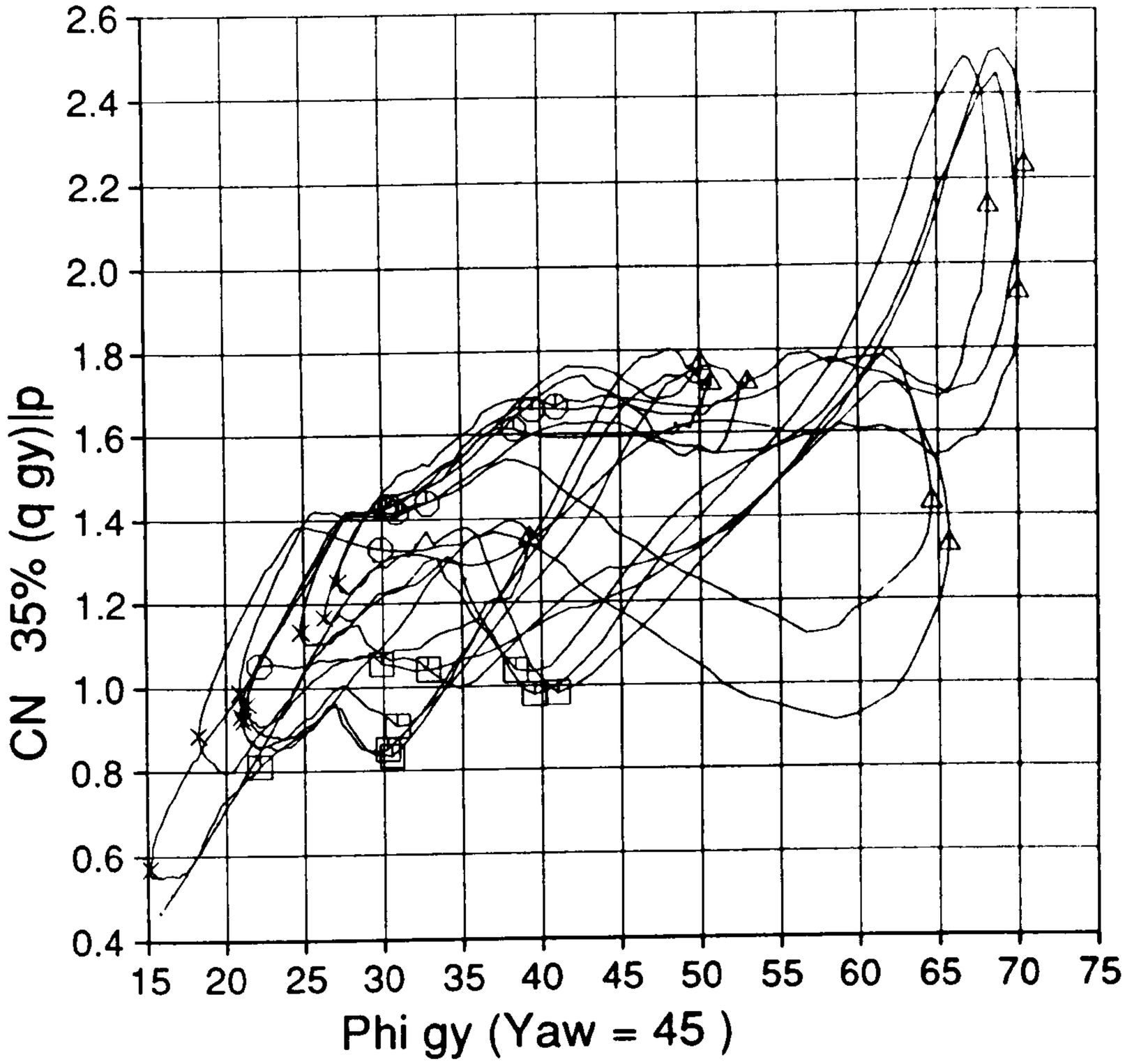

Cranfield

HAWT
Unsteady Aerodynamics
Experiment

Parametric Trends

Program V2.07

MARLEC Blades FI-1

9 sub-runs plotted
exactly 40 revs
in each sub run
Derived parameters from
PROFILES
TYPREV
z is Blade azimuth
× --- 90.0
○ --- 180.0
△ --- 270.0
□ --- 360.0

Figure 11.15

TREND.DAT;7

14-JUN-1990:10:05:20

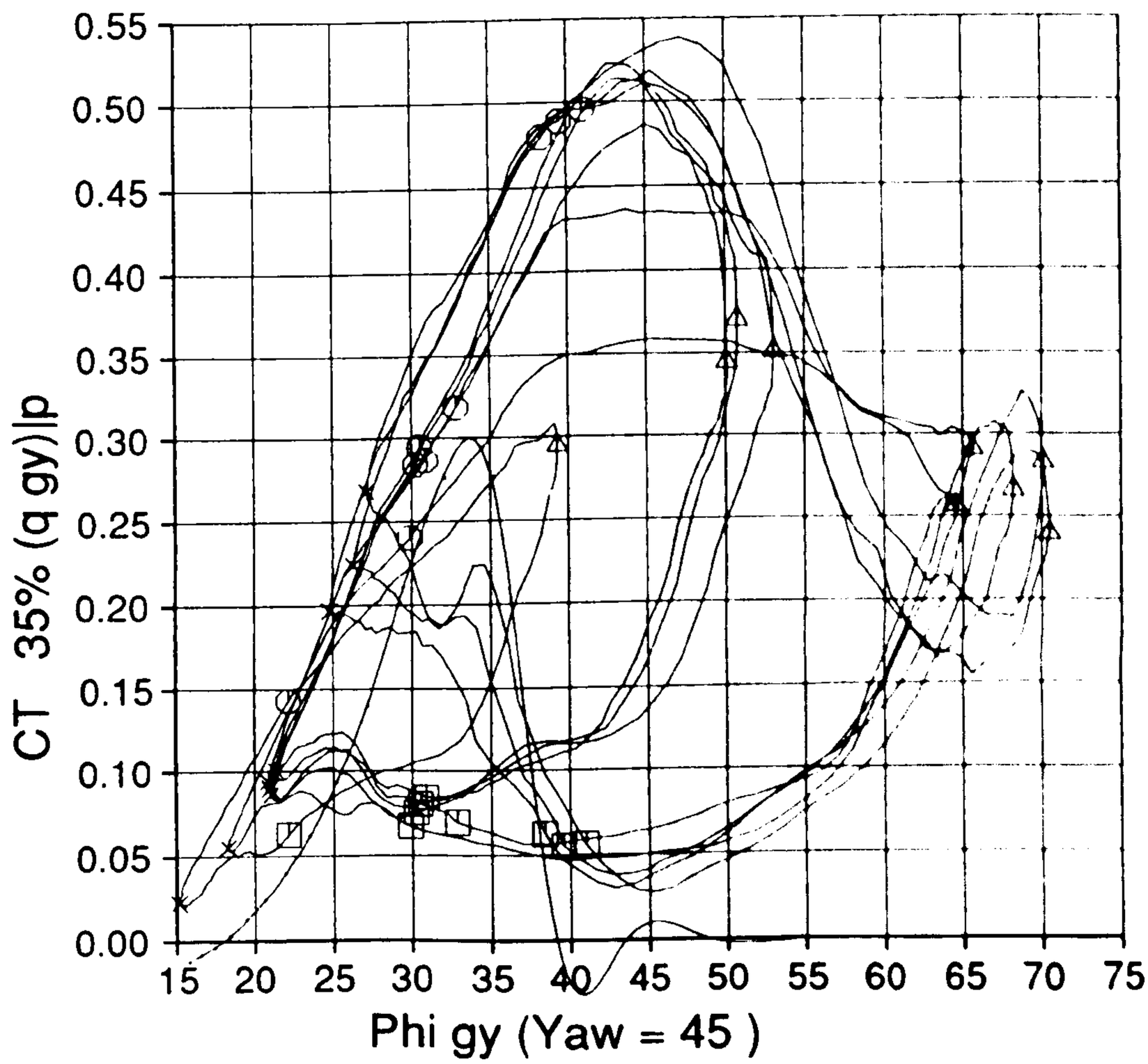

Cranfield

HAWT
Unsteady Aerodynamics
Experiment

Parametric Trends

Program V2.08

MARLEC Blades FI-1

9 sub-runs plotted
exactly 40 revs
in each sub run
Derived parameters from
PROFILES
TYPREV
z is Blade azimuth
× --- 90.0
○ --- 180.0
△ --- 270.0
□ --- 360.0

Figure 11.16

TREND.DAT;8

14-JUN-1990:10:05:54

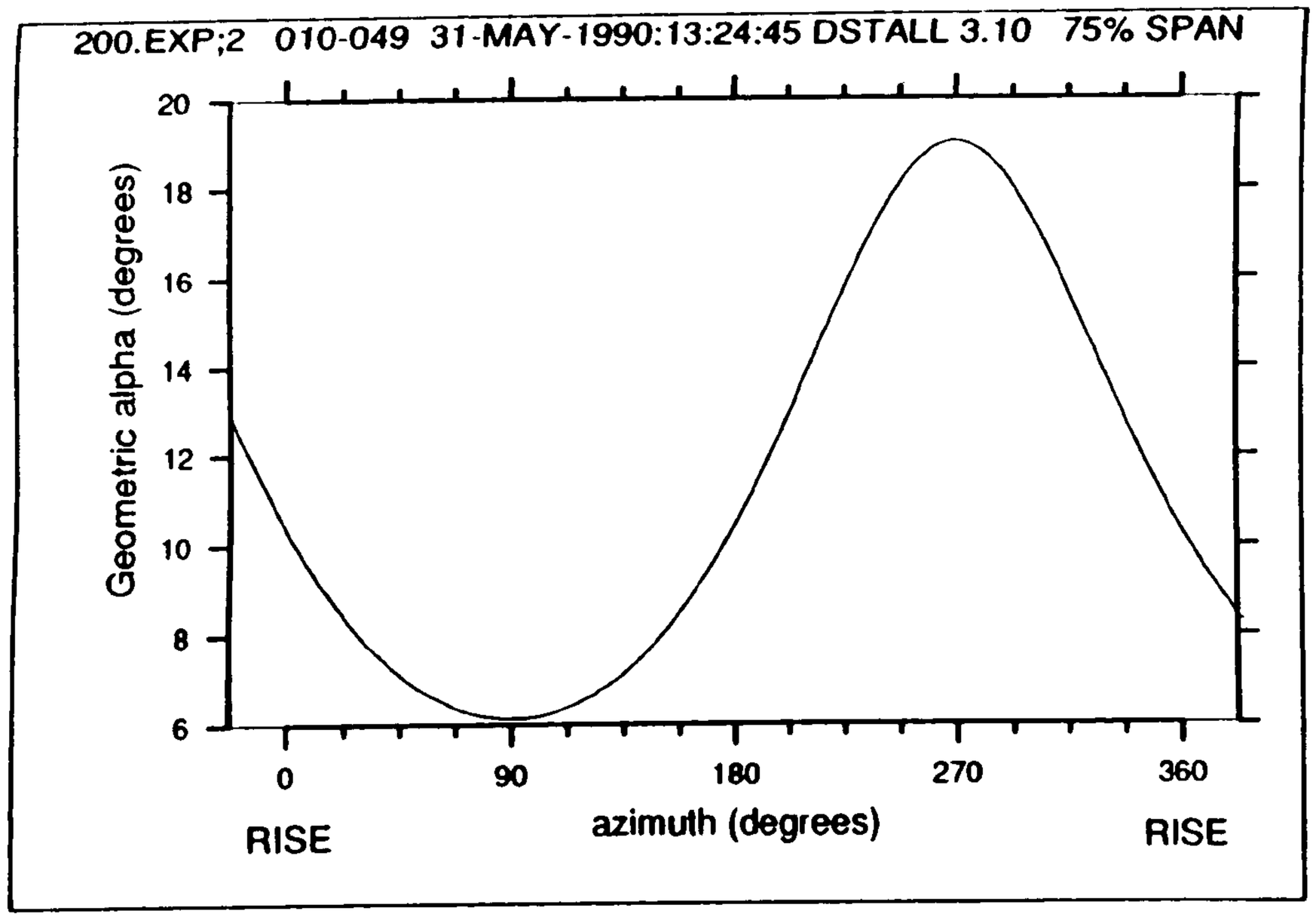
200.EXP;2 010-049 31-MAY-1990:13:24:45 DSTALL 3.10 75% SPAN
Geometric alpha (degrees)
azimuth (degrees)
RISE
RISE
0
90
180
270
360
6
8
10
12
14
16
18
20

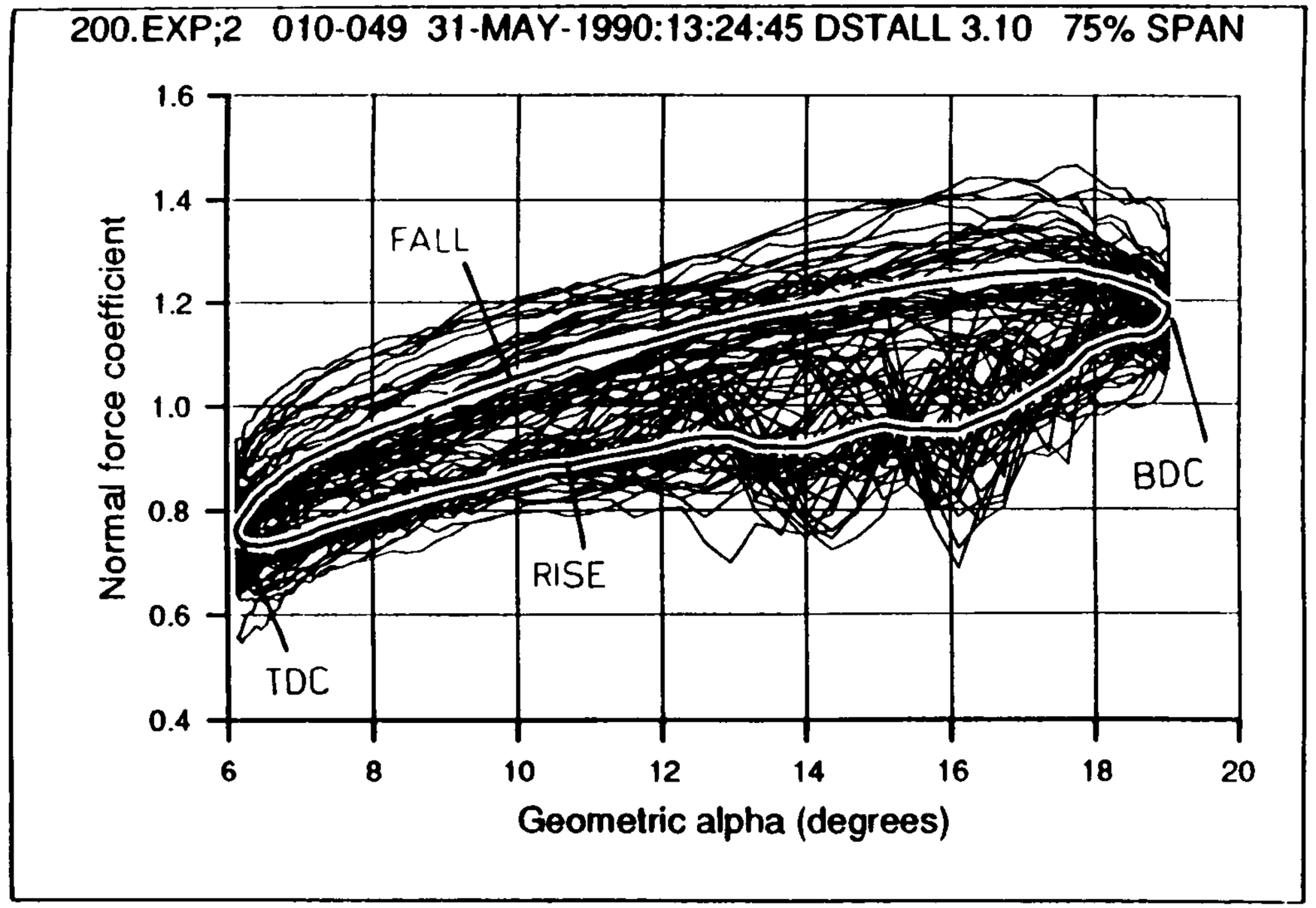
200.EXP;2 010-049 31-MAY-1990:13:24:45 DSTALL 3.10 75% SPAN
Normal force coefficient
Geometric alpha (degrees)
FALL
RISE
TDC
BDC
0.4
0.6
0.8
1.0
1.2
1.4
1.6
6
8
10
12
14
16
18
20

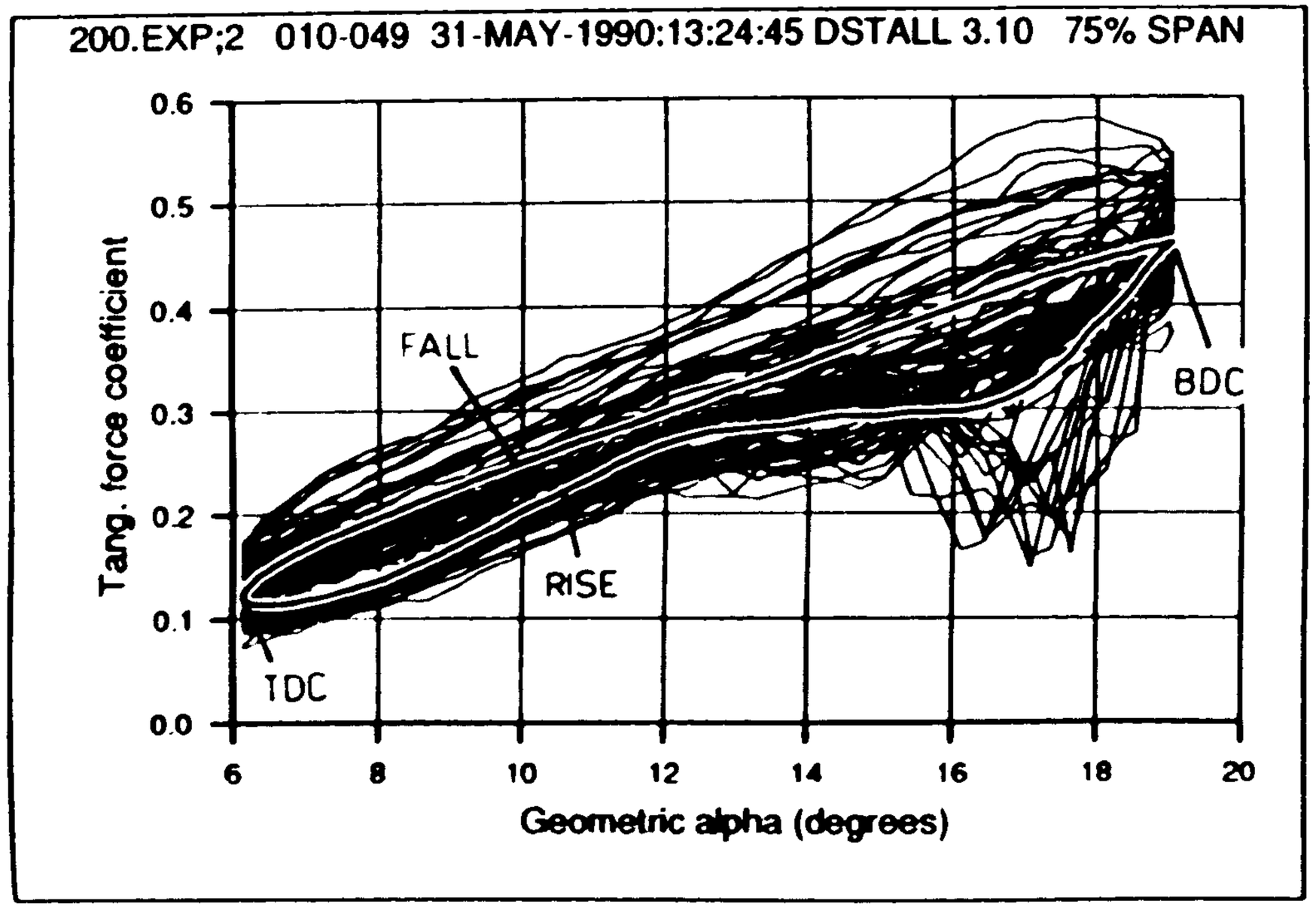
200.EXP;2 010-049 31-MAY-1990:13:24:45 DSTALL 3.10 75% SPAN
Tang. force coefficient
Geometric alpha (degrees)
FALL
RISE
TDC
BDC
0.0
0.1
0.2
0.3
0.4
0.5
0.6
6
8
10
12
14
16
18
20

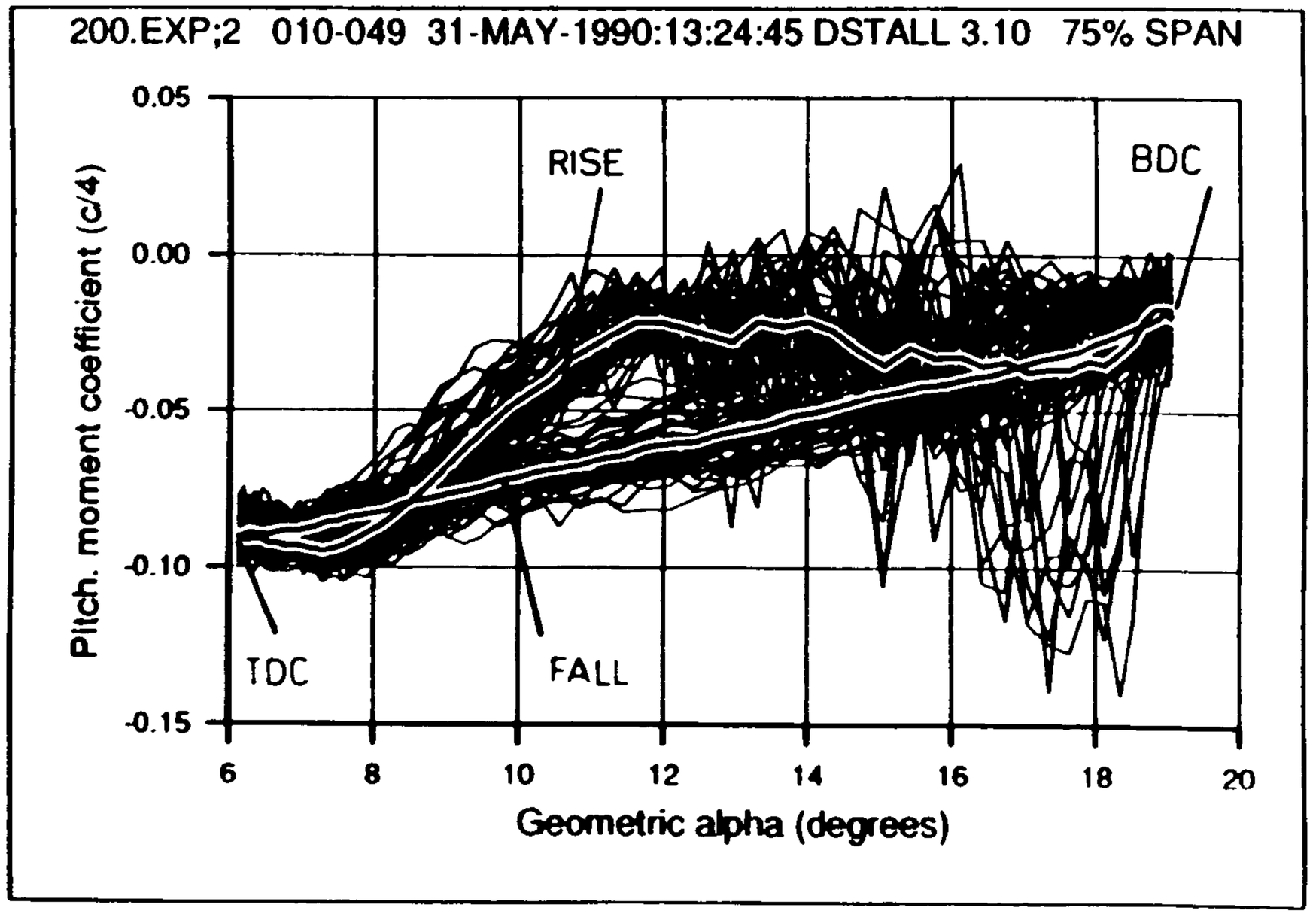
200.EXP;2 010-049 31-MAY-1990:13:24:45 DSTALL 3.10 75% SPAN
Pitch. moment coefficient (c/4)
Geometric alpha (degrees)
RISE
BDC
TDC
FALL
-0.15
-0.10
-0.05
0.00
0.05
6
8
10
12
14
16
18
20

Figure 11.17

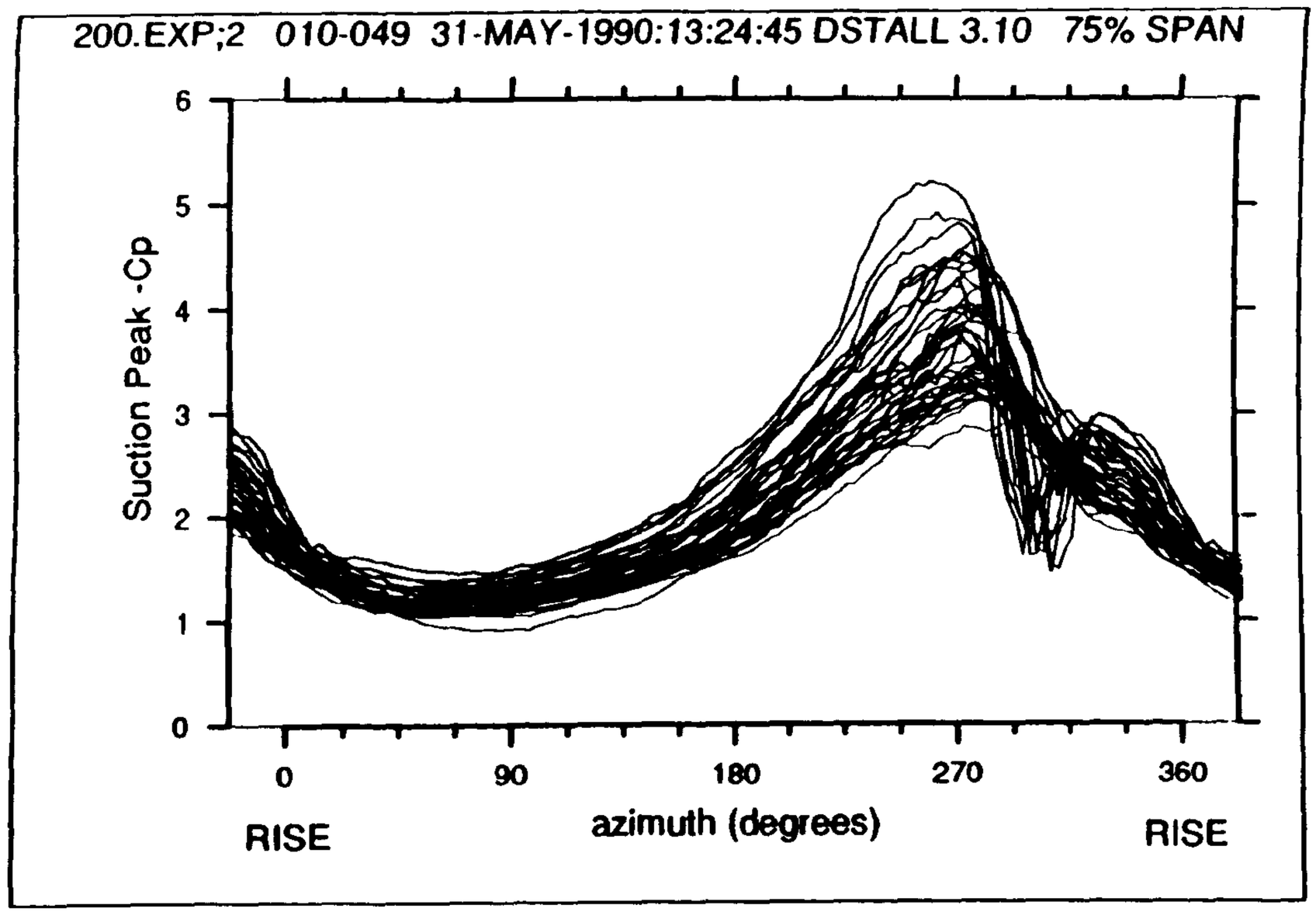
200.EXP;2 010-049 31-MAY-1990:13:24:45 DSTALL 3.10 75% SPAN
Suction Peak -Cp
azimuth (degrees)
RISE
RISE
0
90
180
270
360
0
1
2
3
4
5
6

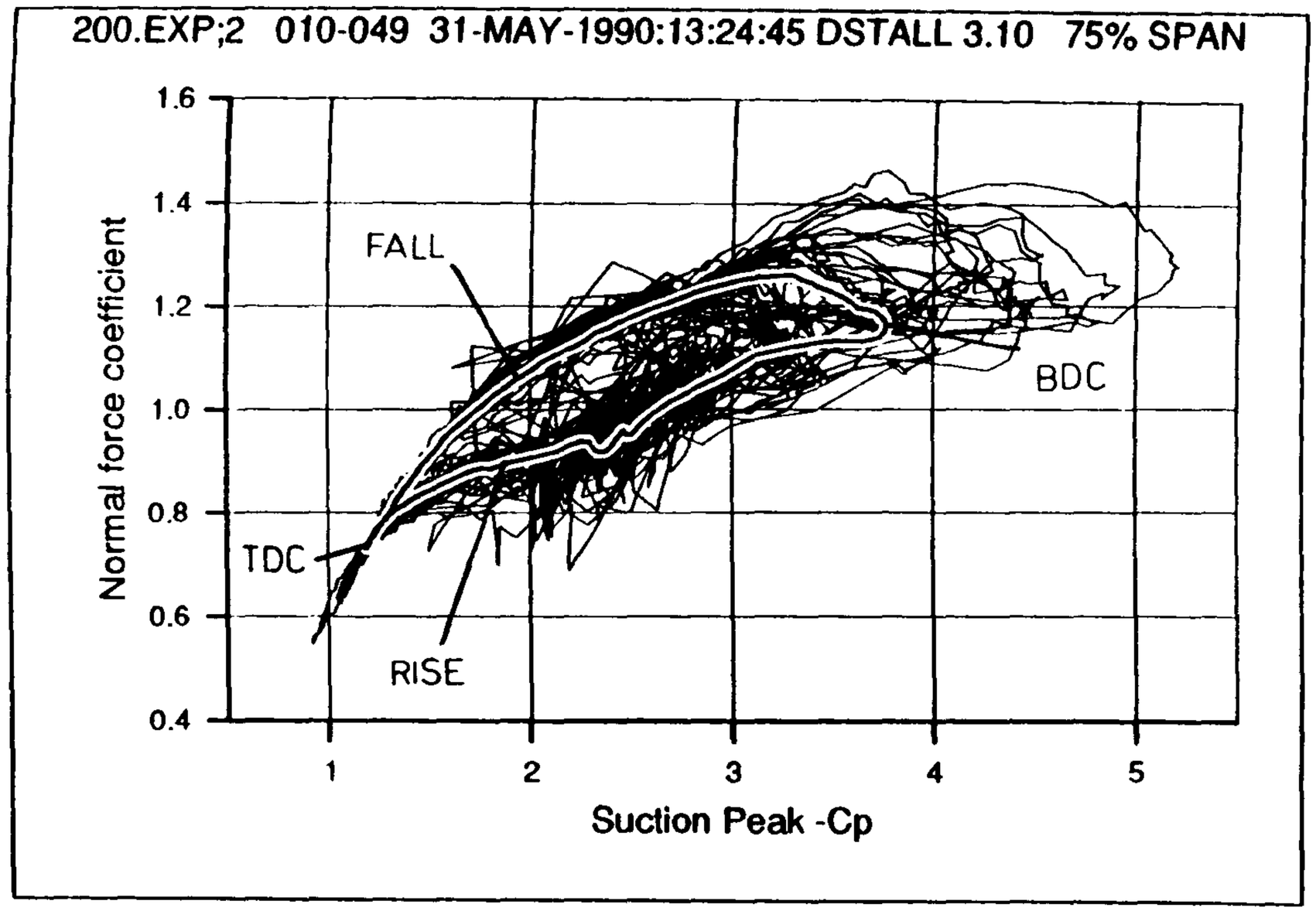
200.EXP;2 010-049 31-MAY-1990:13:24:45 DSTALL 3.10 75% SPAN
Normal force coefficient
Suction Peak -Cp
FALL
BDC
TDC
RISE
0.4
0.6
0.8
1.0
1.2
1.4
1.6
1
2
3
4
5

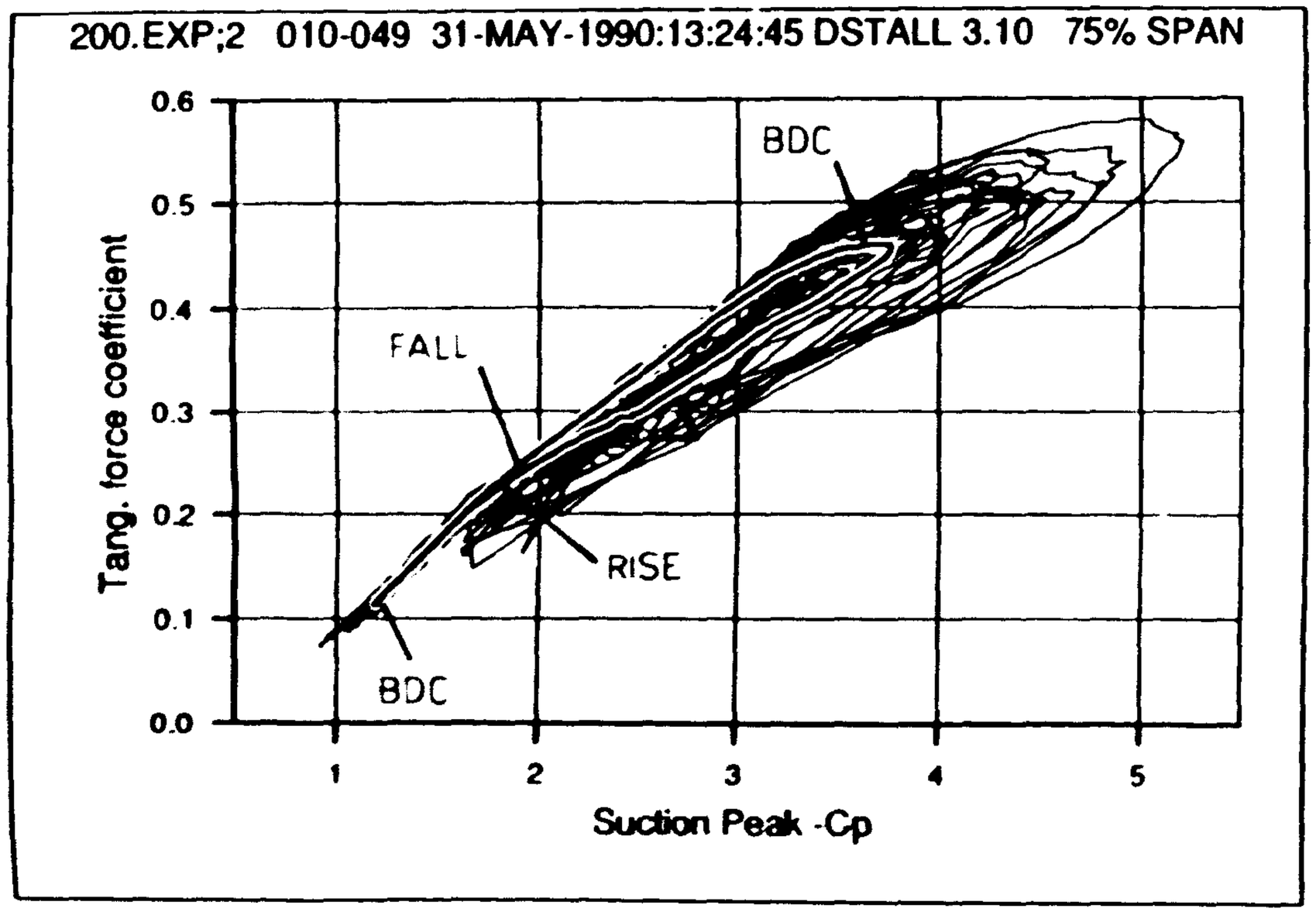
200.EXP;2 010-049 31-MAY-1990:13:24:45 DSTALL 3.10 75% SPAN
Tang. force coefficient
Suction Peak -Cp
BDC
FALL
RISE
BDC
0.0
0.1
0.2
0.3
0.4
0.5
0.6
1
2
3
4
5

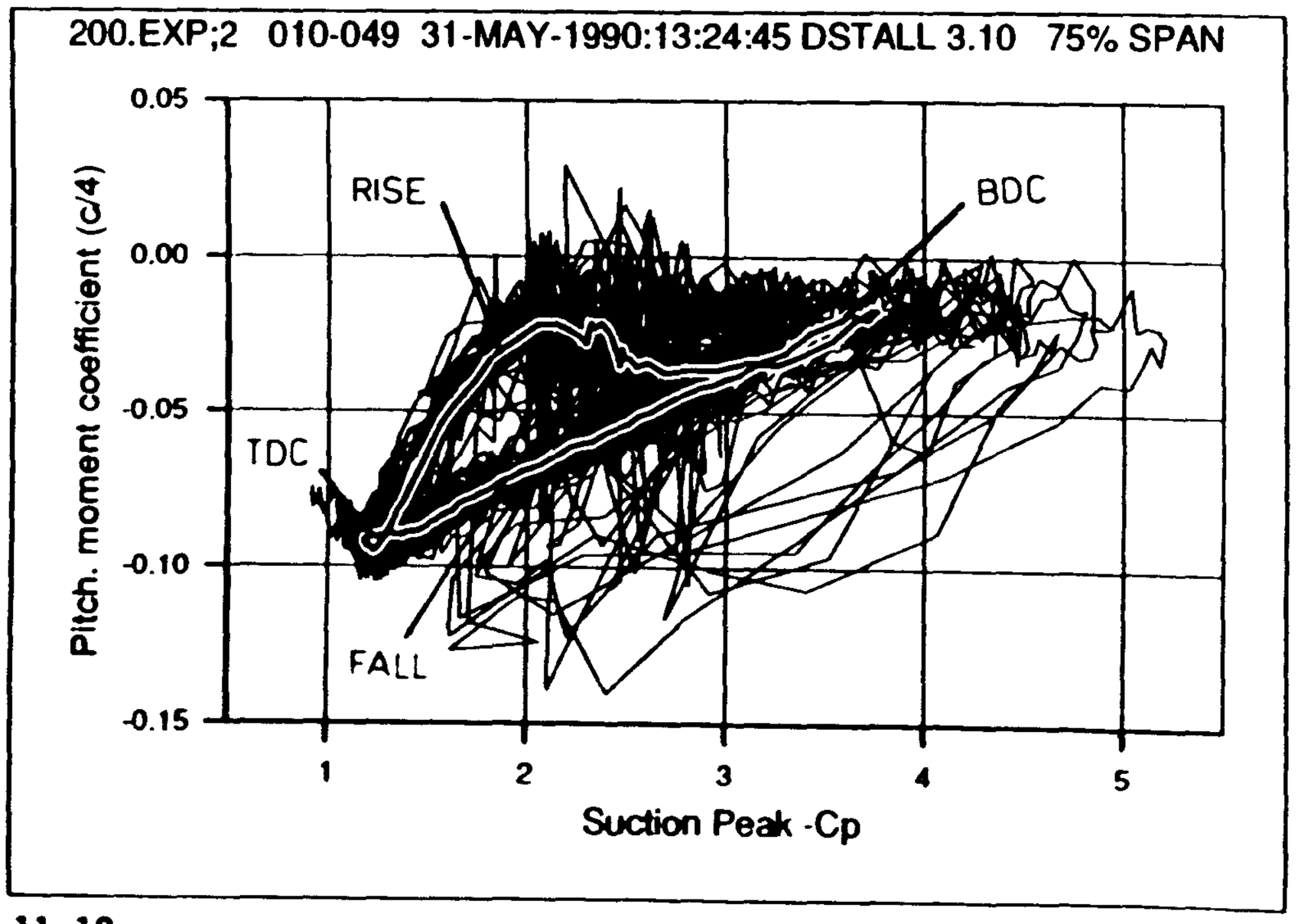
200.EXP;2 010-049 31-MAY-1990:13:24:45 DSTALL 3.10 75% SPAN
Pitch. moment coefficient (c/4)
Suction Peak -Cp
RISE
BDC
TDC
FALL
-0.15
-0.10
-0.05
0.00
0.05
1
2
3
4
5

Figure 11.18

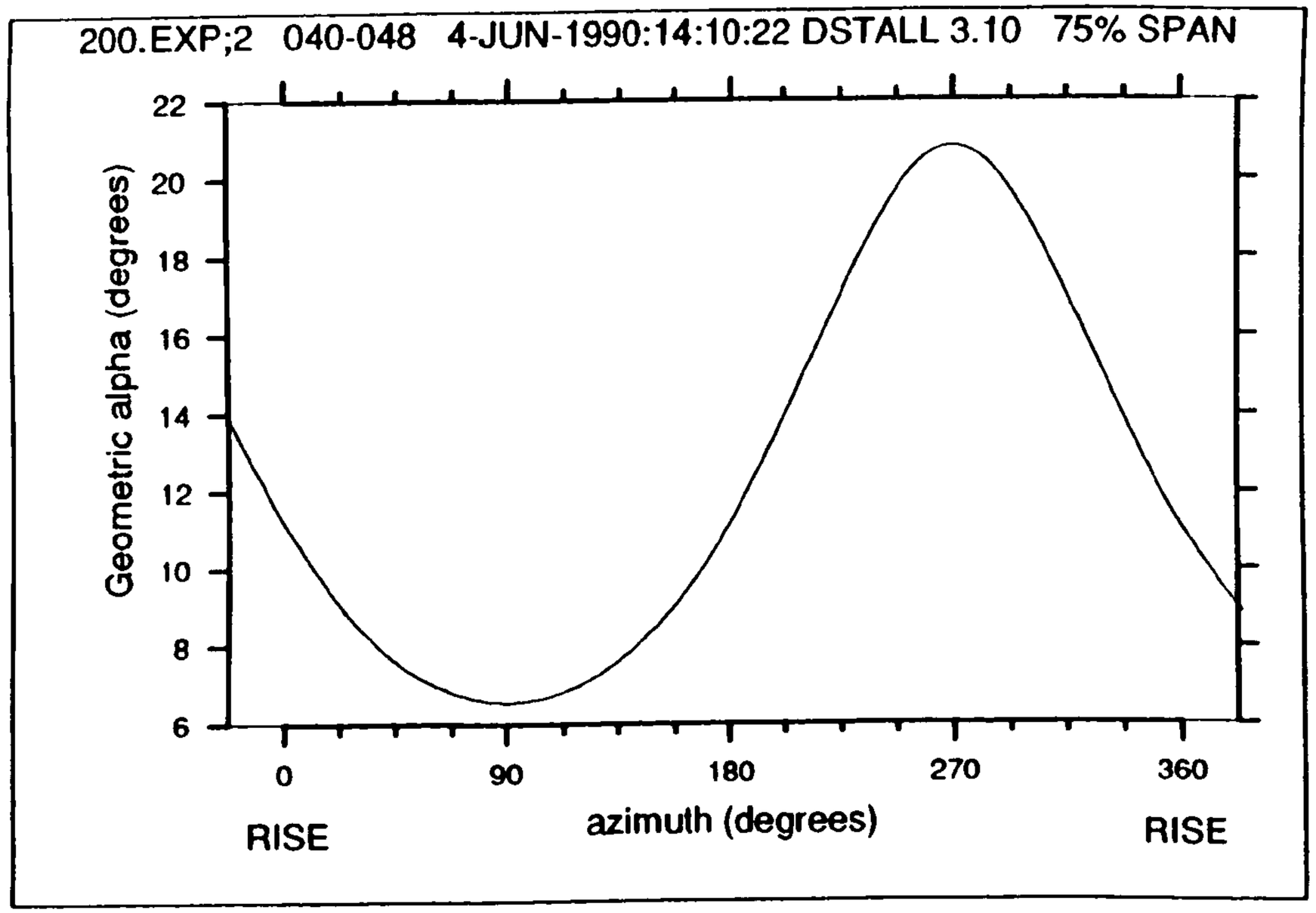
200.EXP;2 040-048 4-JUN-1990:14:10:22 DSTALL 3.10 75% SPAN
Geometric alpha (degrees)
22
20
18
16
14
12
10
8
6
0
90
180
270
360
RISE
azimuth (degrees)
RISE

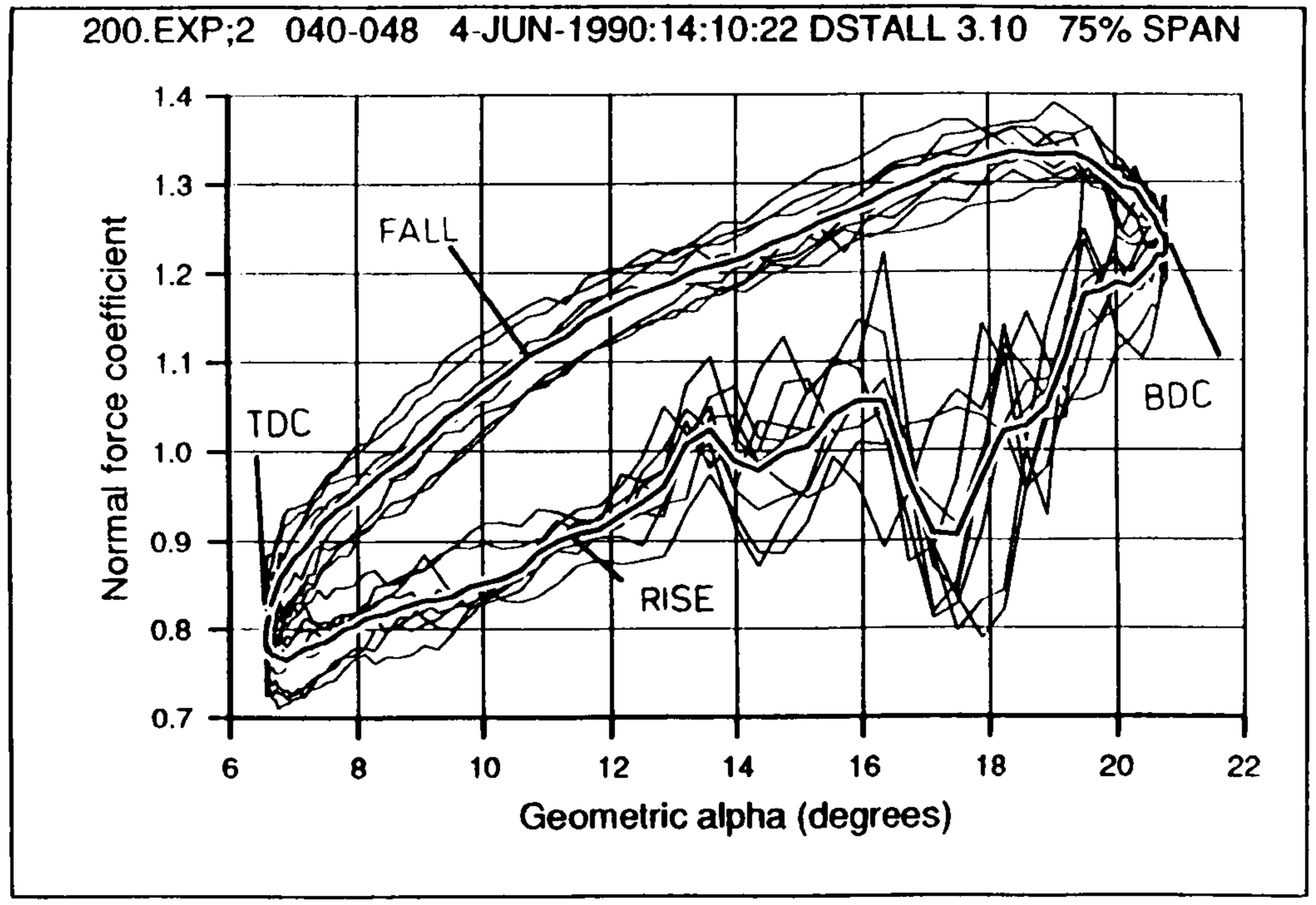
200.EXP;2 040-048 4-JUN-1990:14:10:22 DSTALL 3.10 75% SPAN
Normal force coefficient
1.4
1.3
1.2
1.1
1.0
0.9
0.8
0.7
FALL
TDC
BDC
RISE
6
8
10
12
14
16
18
20
22
Geometric alpha (degrees)

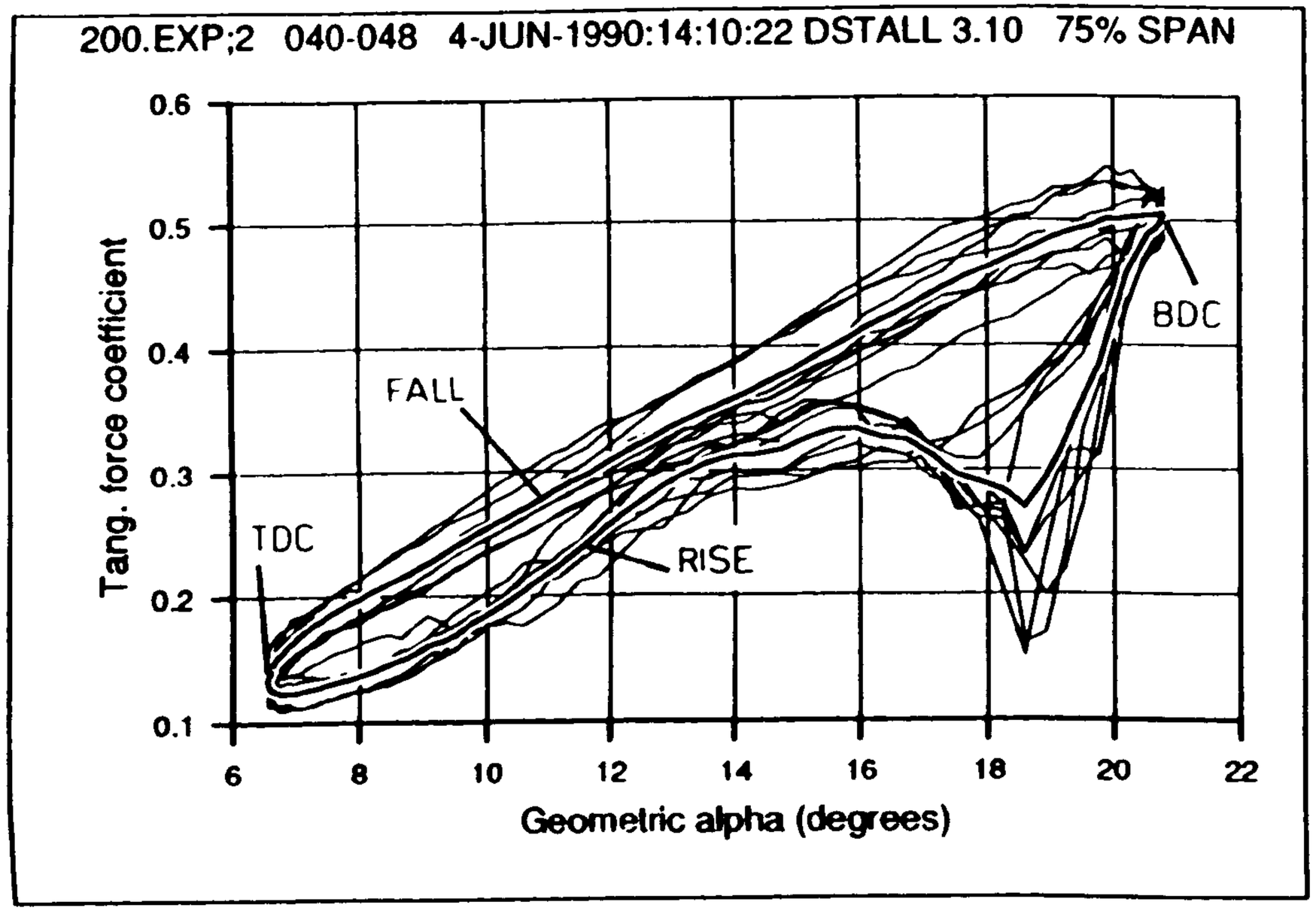
200.EXP;2 040-048 4-JUN-1990:14:10:22 DSTALL 3.10 75% SPAN
Tang. force coefficient
0.6
0.5
0.4
0.3
0.2
0.1
BDC
FALL
TDC
RISE
6
8
10
12
14
16
18
20
22
Geometric alpha (degrees)

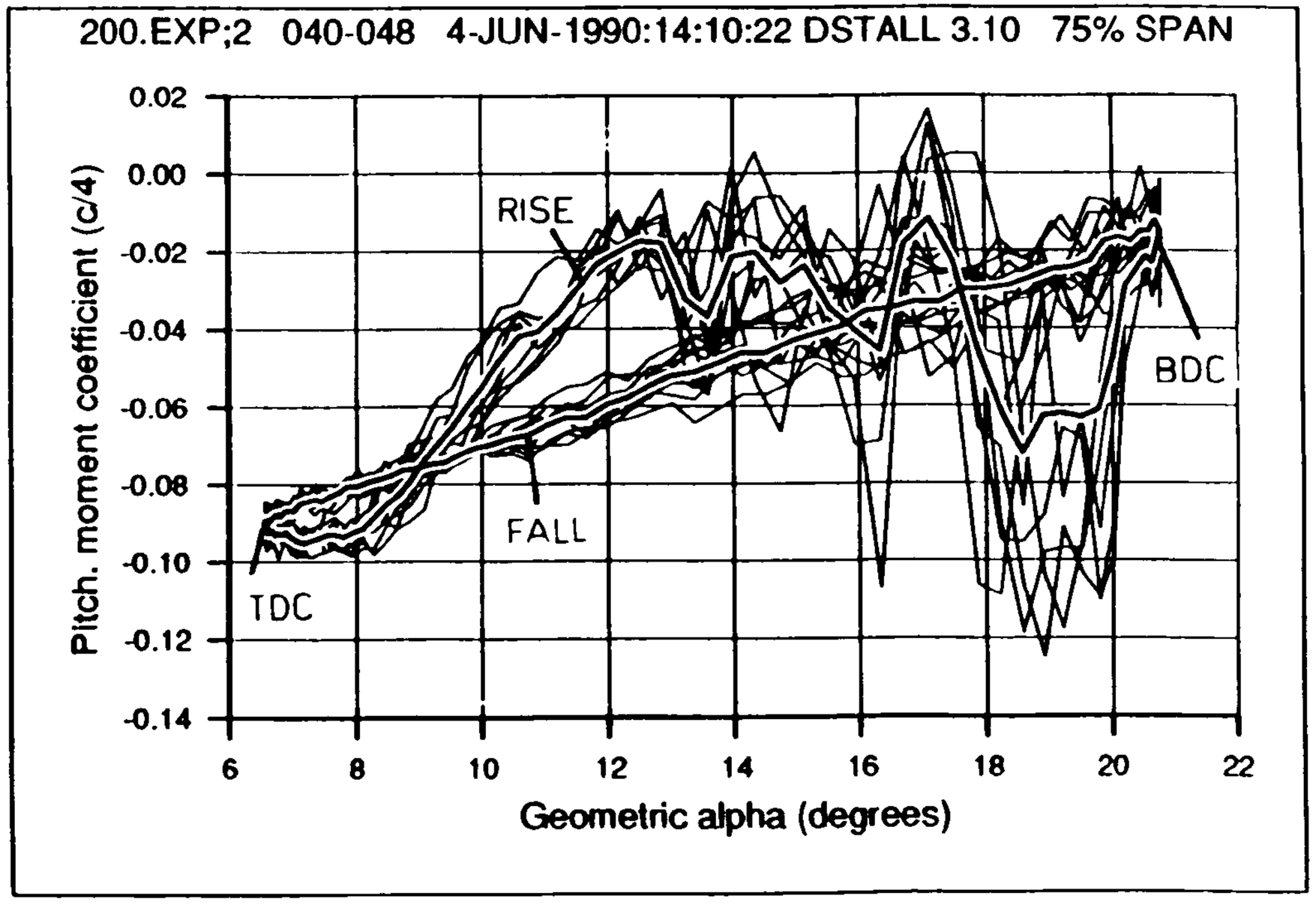
200.EXP;2 040-048 4-JUN-1990:14:10:22 DSTALL 3.10 75% SPAN
Pitch. moment coefficient (c/4)
0.02
0.00
-0.02
-0.04
-0.06
-0.08
-0.10
-0.12
-0.14
RISE
BDC
FALL
TDC
6
8
10
12
14
16
18
20
22
Geometric alpha (degrees)

Figure 11.19

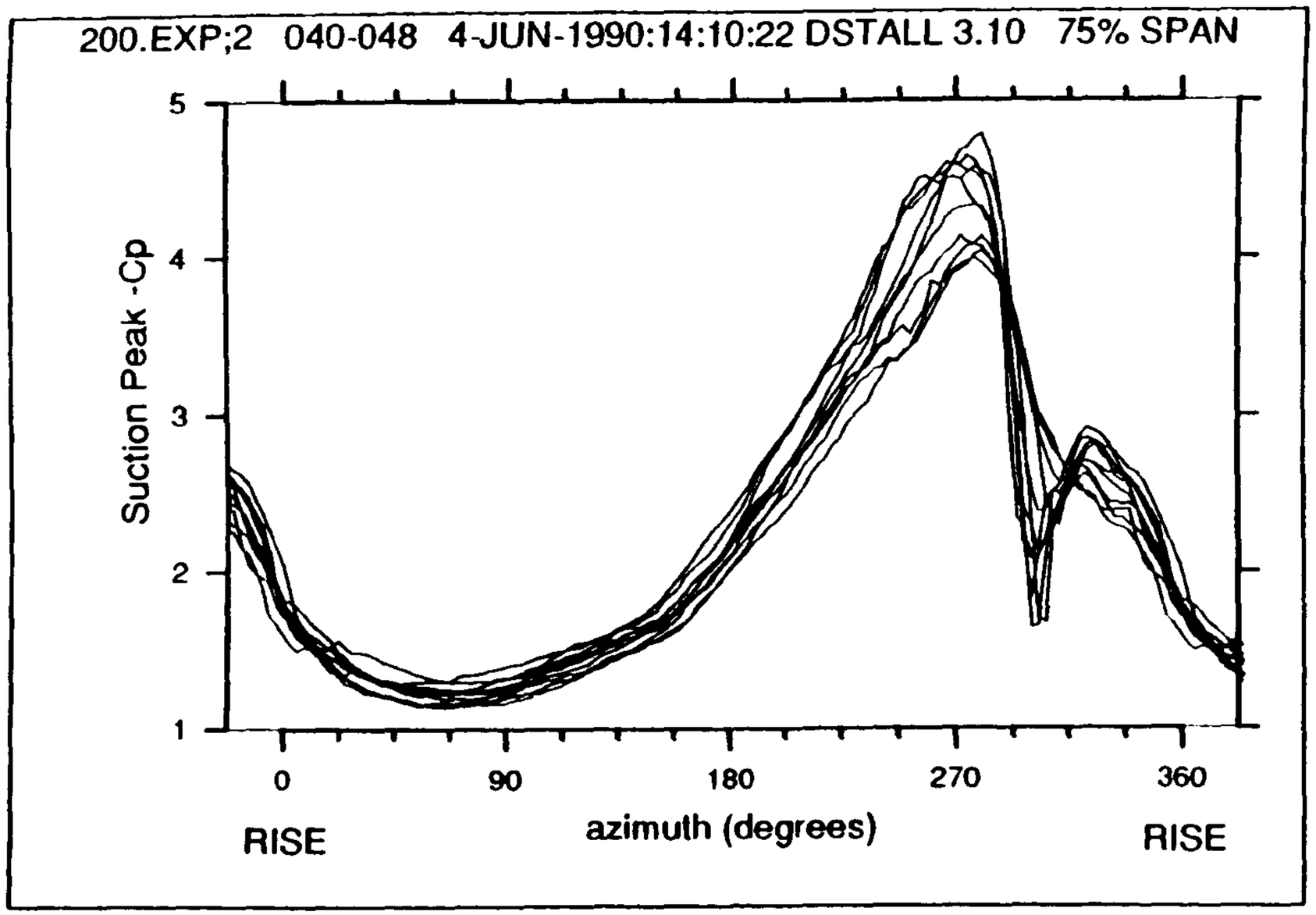
200.EXP;2 040-048 4-JUN-1990:14:10:22 DSTALL 3.10 75% SPAN
Suction Peak -Cp
azimuth (degrees)
RISE
RISE
0
90
180
270
360
1
2
3
4
5

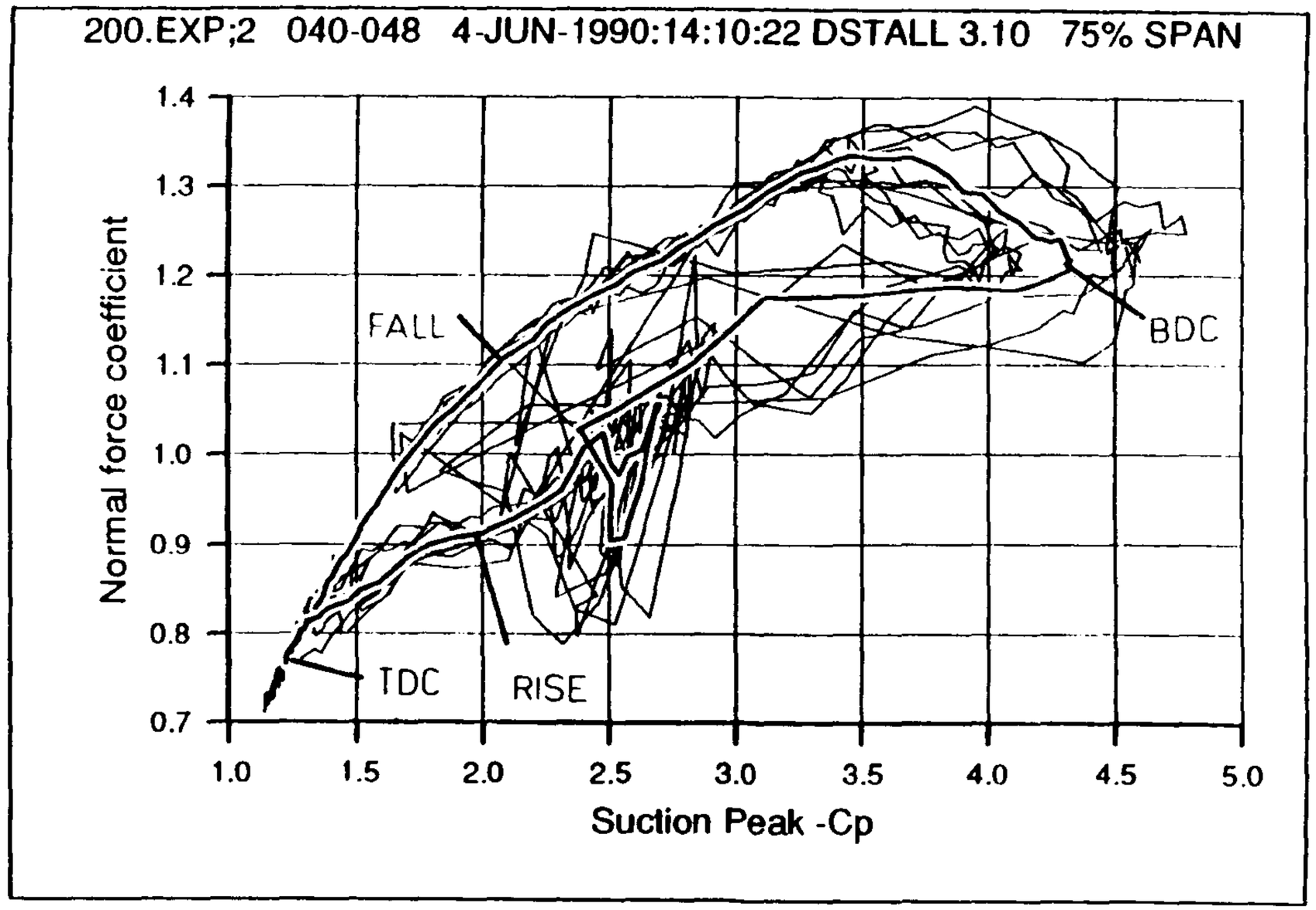
200.EXP;2 040-048 4-JUN-1990:14:10:22 DSTALL 3.10 75% SPAN
Normal force coefficient
Suction Peak -Cp
FALL
BDC
TDC
RISE
0.7
0.8
0.9
1.0
1.1
1.2
1.3
1.4
1.0
1.5
2.0
2.5
3.0
3.5
4.0
4.5
5.0

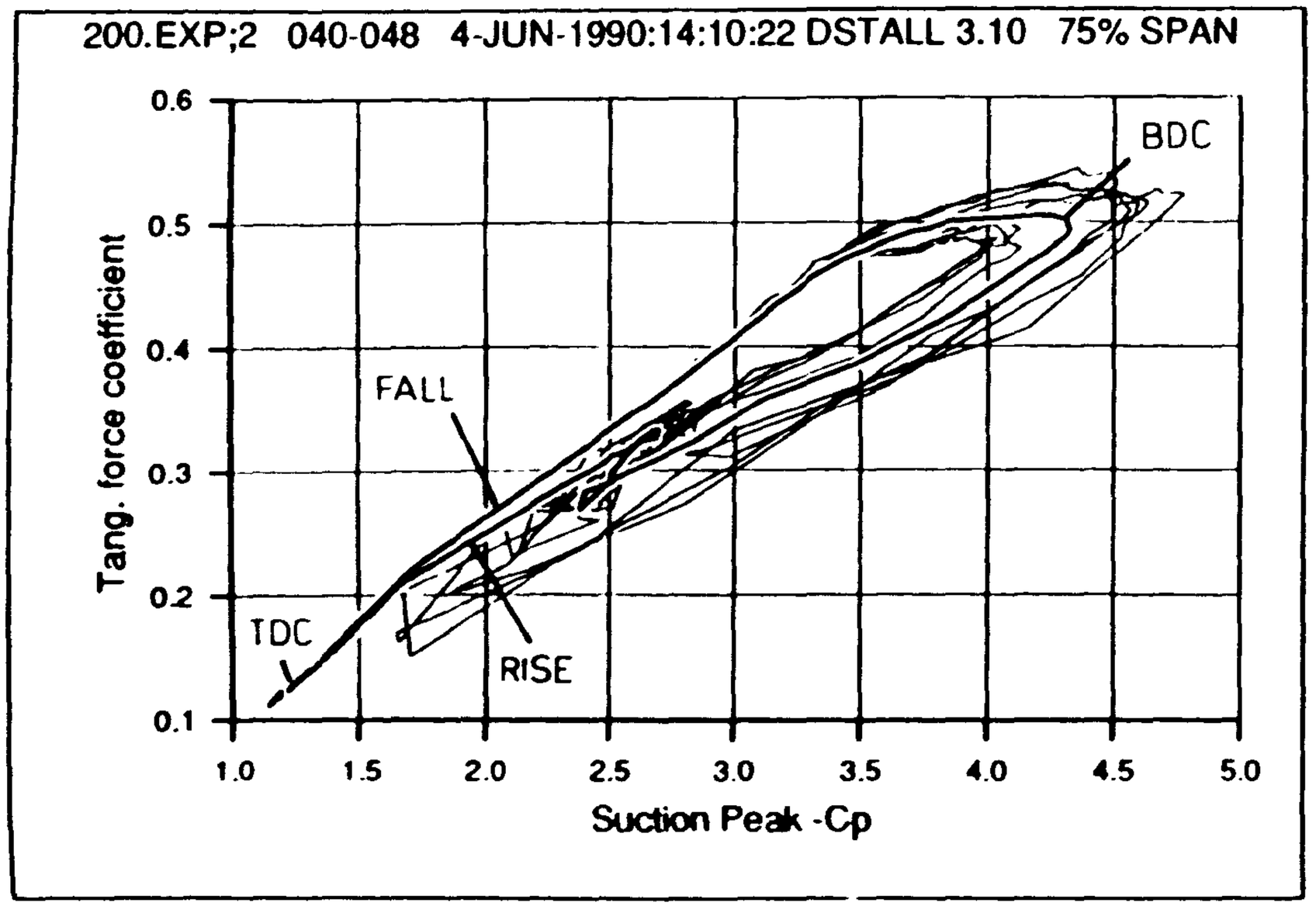
200.EXP;2 040-048 4-JUN-1990:14:10:22 DSTALL 3.10 75% SPAN
Tang. force coefficient
Suction Peak -Cp
BDC
FALL
TDC
RISE
0.1
0.2
0.3
0.4
0.5
0.6
1.0
1.5
2.0
2.5
3.0
3.5
4.0
4.5
5.0

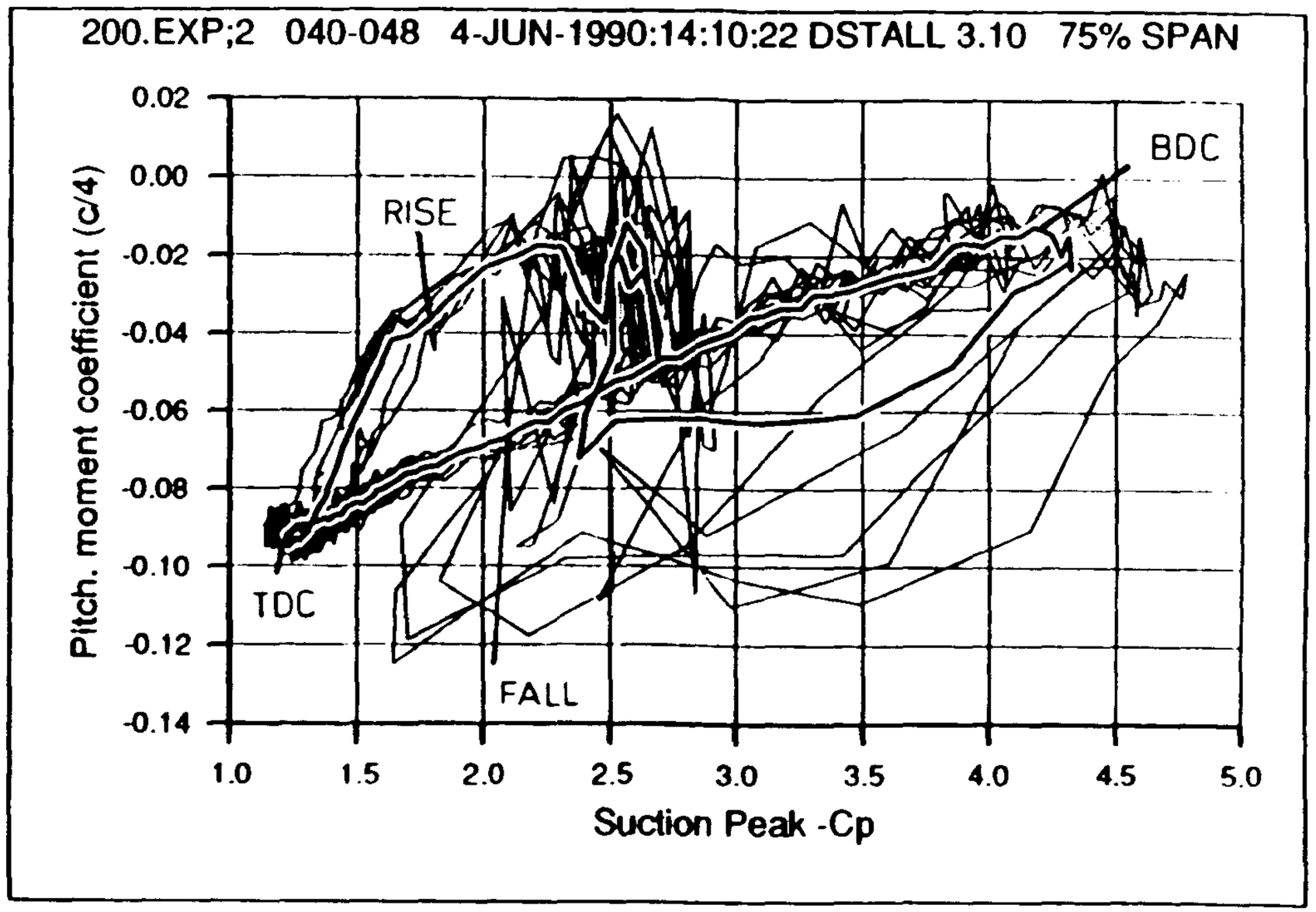
200.EXP;2 040-048 4-JUN-1990:14:10:22 DSTALL 3.10 75% SPAN
Pitch. moment coefficient (c/4)
Suction Peak -Cp
RISE
BDC
TDC
FALL
-0.14
-0.12
-0.10
-0.08
-0.06
-0.04
-0.02
0.00
0.02
1.0
1.5
2.0
2.5
3.0
3.5
4.0
4.5
5.0

Figure 11.20

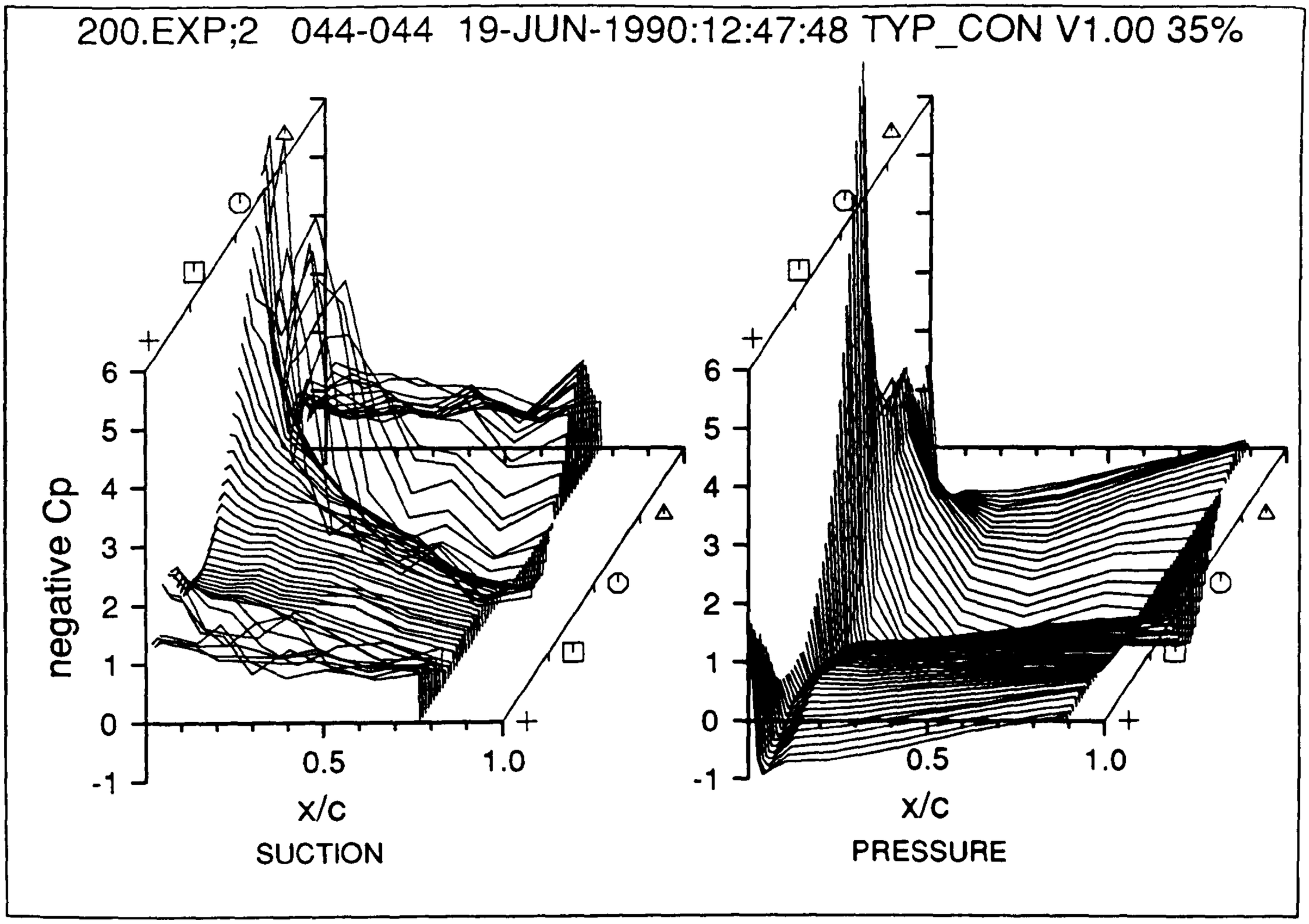
200.EXP;2 044-044 19-JUN-1990:12:47:48 TYP_CON V1.00 35%
negative Cp
6
5
4
3
2
1
0
-1
0.5
1.0
X/C
SUCTION
PRESSURE
200.EXP;2 044-044 19-JUN-1990:12:47:48 TYP_CON V1.00 75%
negative Cp
X/C
SUCTION
PRESSURE

Figure 11.21

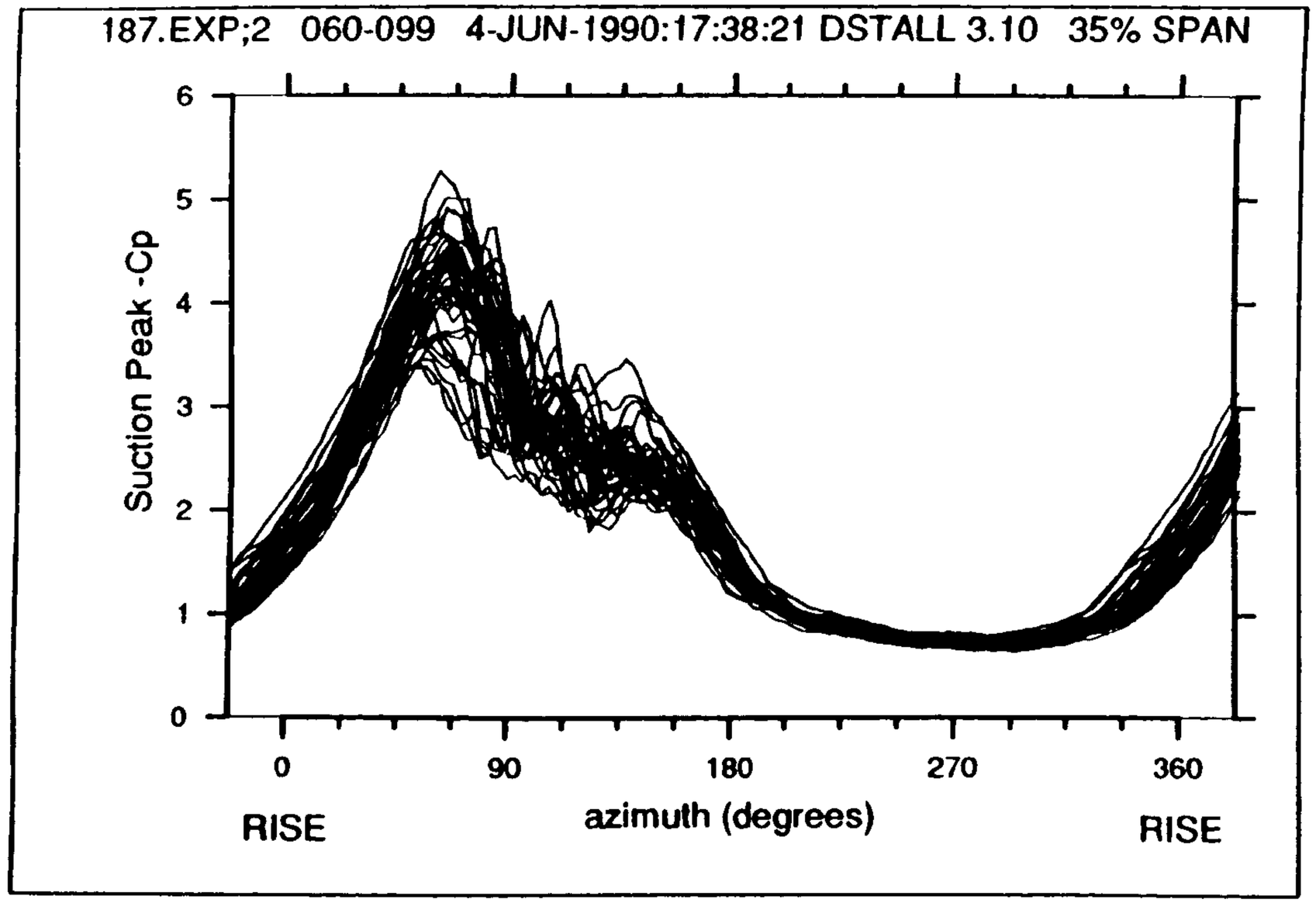
187.EXP;2 060-099 4-JUN-1990:17:38:21 DSTALL 3.10 35% SPAN
Suction Peak -Cp
azimuth (degrees)
RISE
RISE
0
90
180
270
360
0
1
2
3
4
5
6

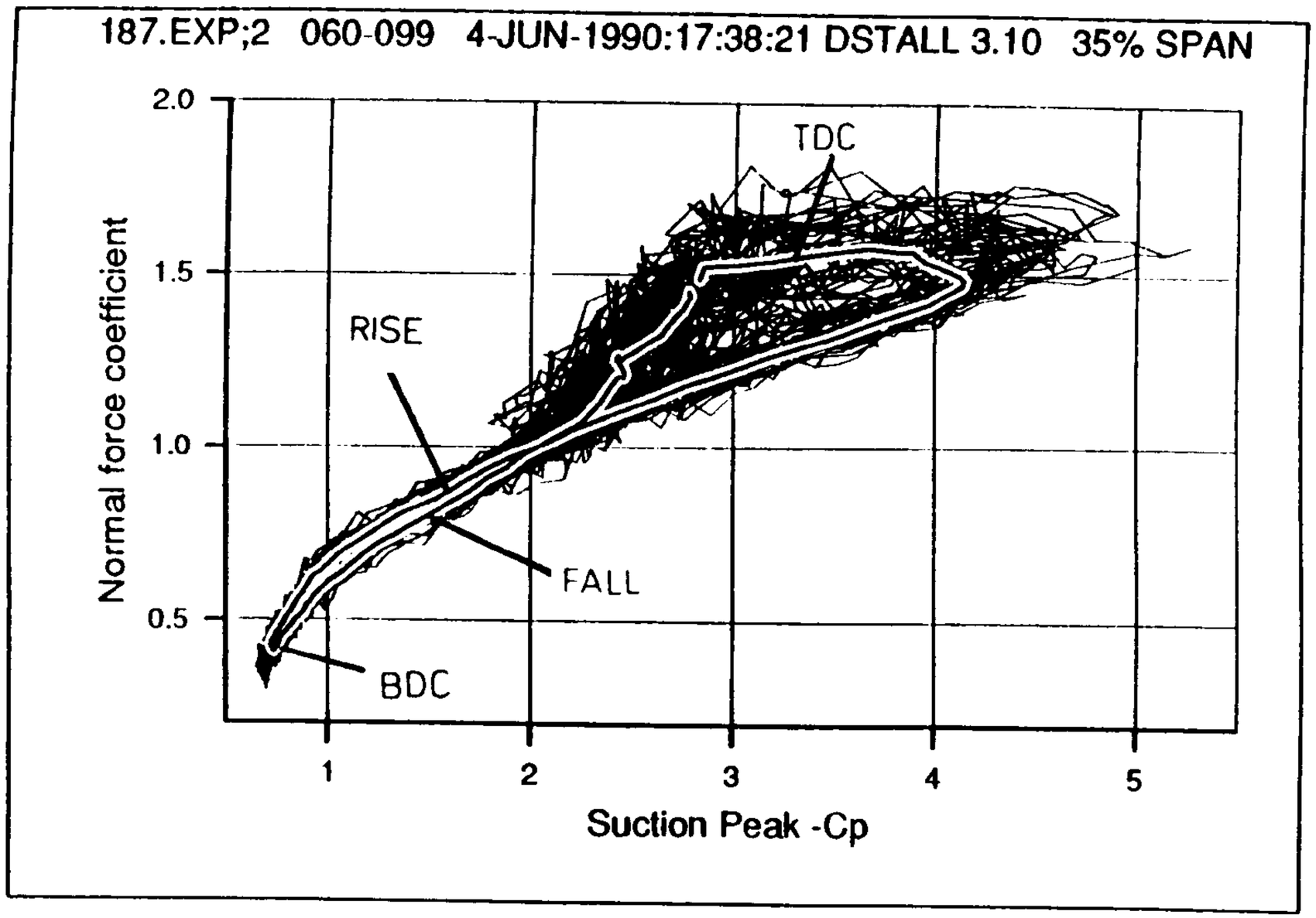
187.EXP;2 060-099 4-JUN-1990:17:38:21 DSTALL 3.10 35% SPAN
Normal force coefficient
Suction Peak -Cp
TDC
RISE
FALL
BDC
0.5
1.0
1.5
2.0
1
2
3
4
5

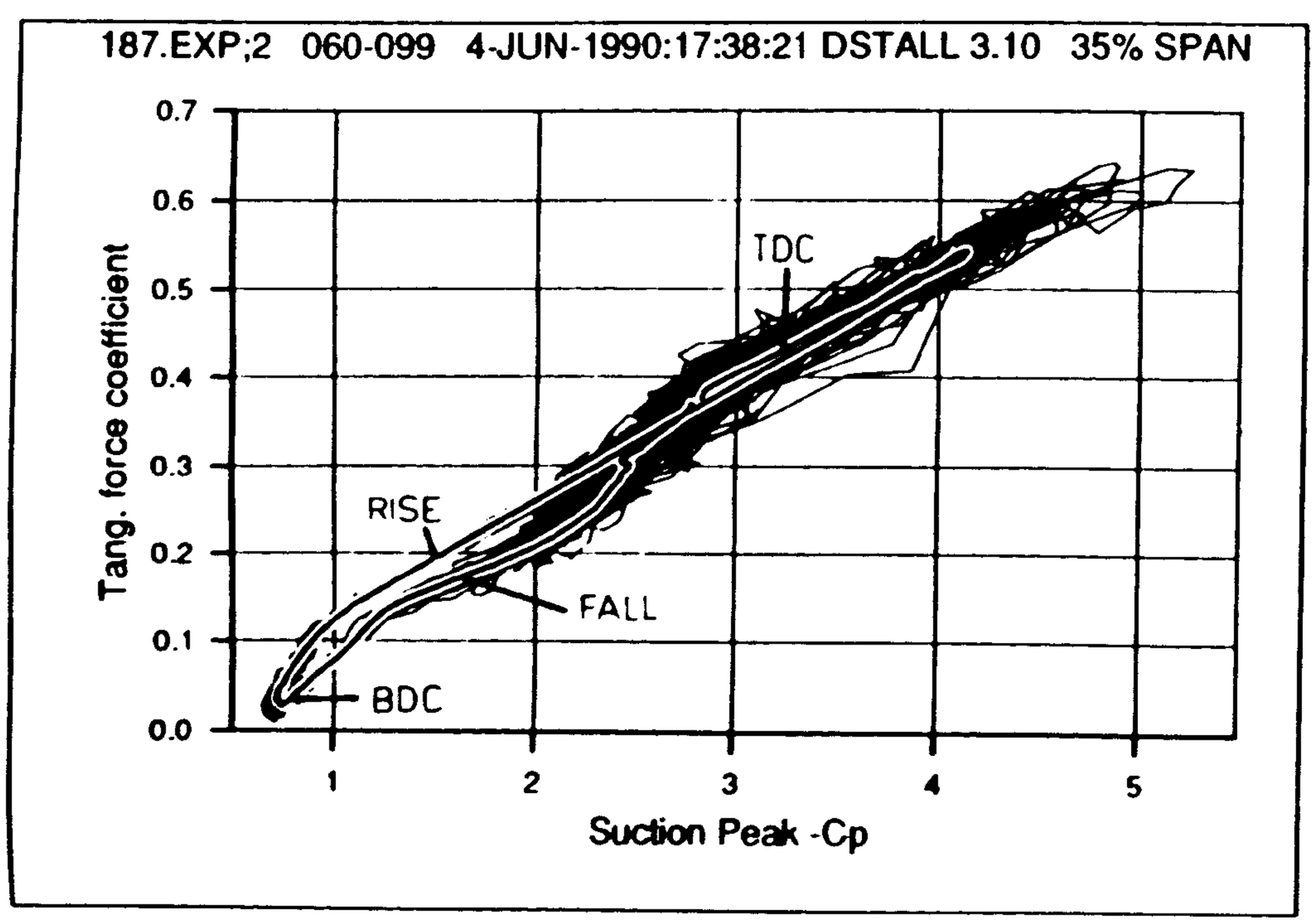
187.EXP;2 060-099 4-JUN-1990:17:38:21 DSTALL 3.10 35% SPAN
Tang. force coefficient
Suction Peak -Cp
TDC
RISE
FALL
BDC
0.0
0.1
0.2
0.3
0.4
0.5
0.6
0.7
1
2
3
4
5

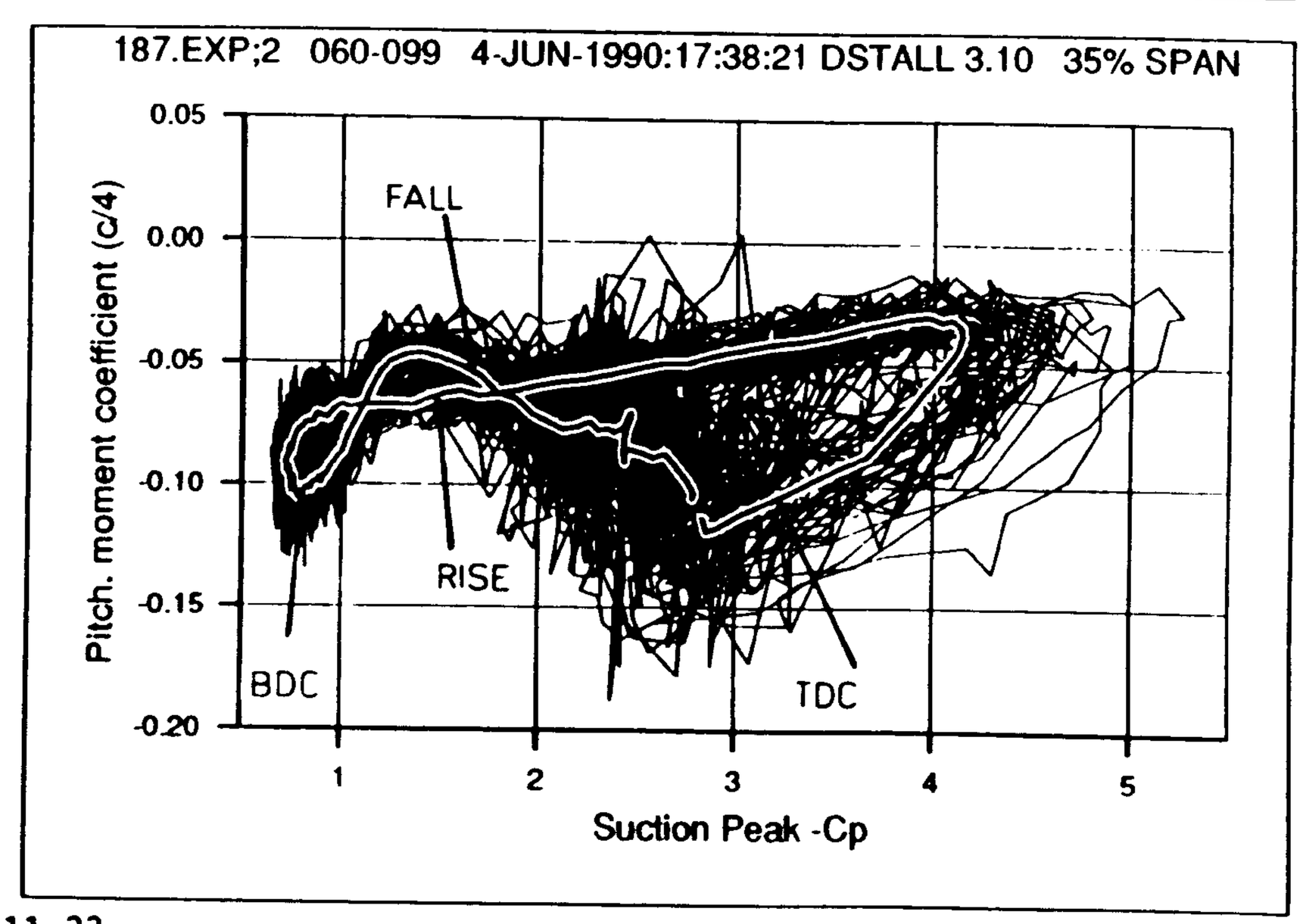
187.EXP;2 060-099 4-JUN-1990:17:38:21 DSTALL 3.10 35% SPAN
Pitch. moment coefficient (c/4)
Suction Peak -Cp
FALL
RISE
BDC
TDC
-0.20
-0.15
-0.10
-0.05
0.00
0.05
1
2
3
4
5

Figure 11.22

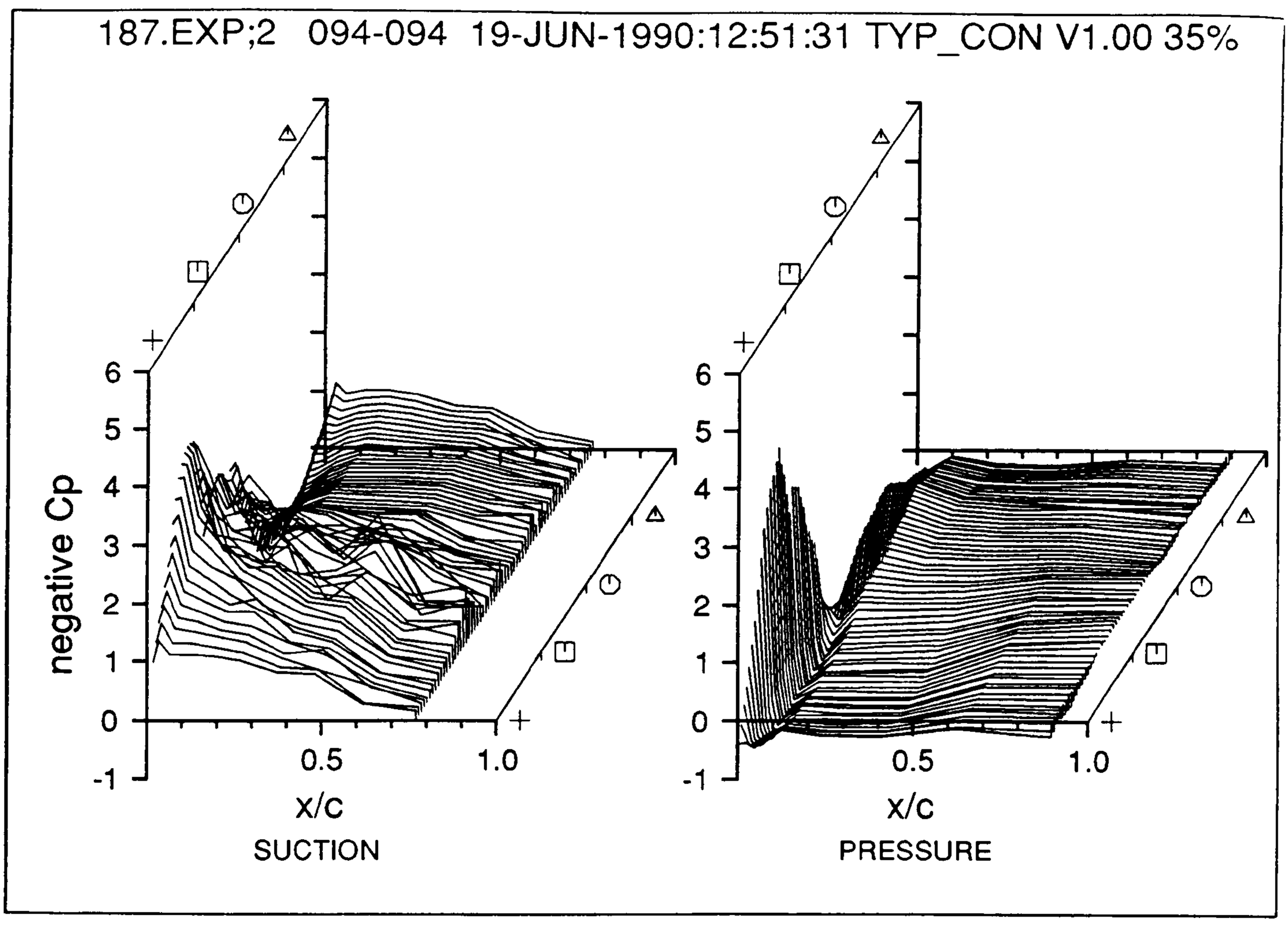
187.EXP;2 094-094 19-JUN-1990:12:51:31 TYP_CON V1.00 35%
negative Cp
6
5
4
3
2
1
0
-1
0.5
1.0
X/C
SUCTION
PRESSURE
187.EXP;2 094-094 19-JUN-1990:12:51:31 TYP_CON V1.00 75%

Figure 11.23

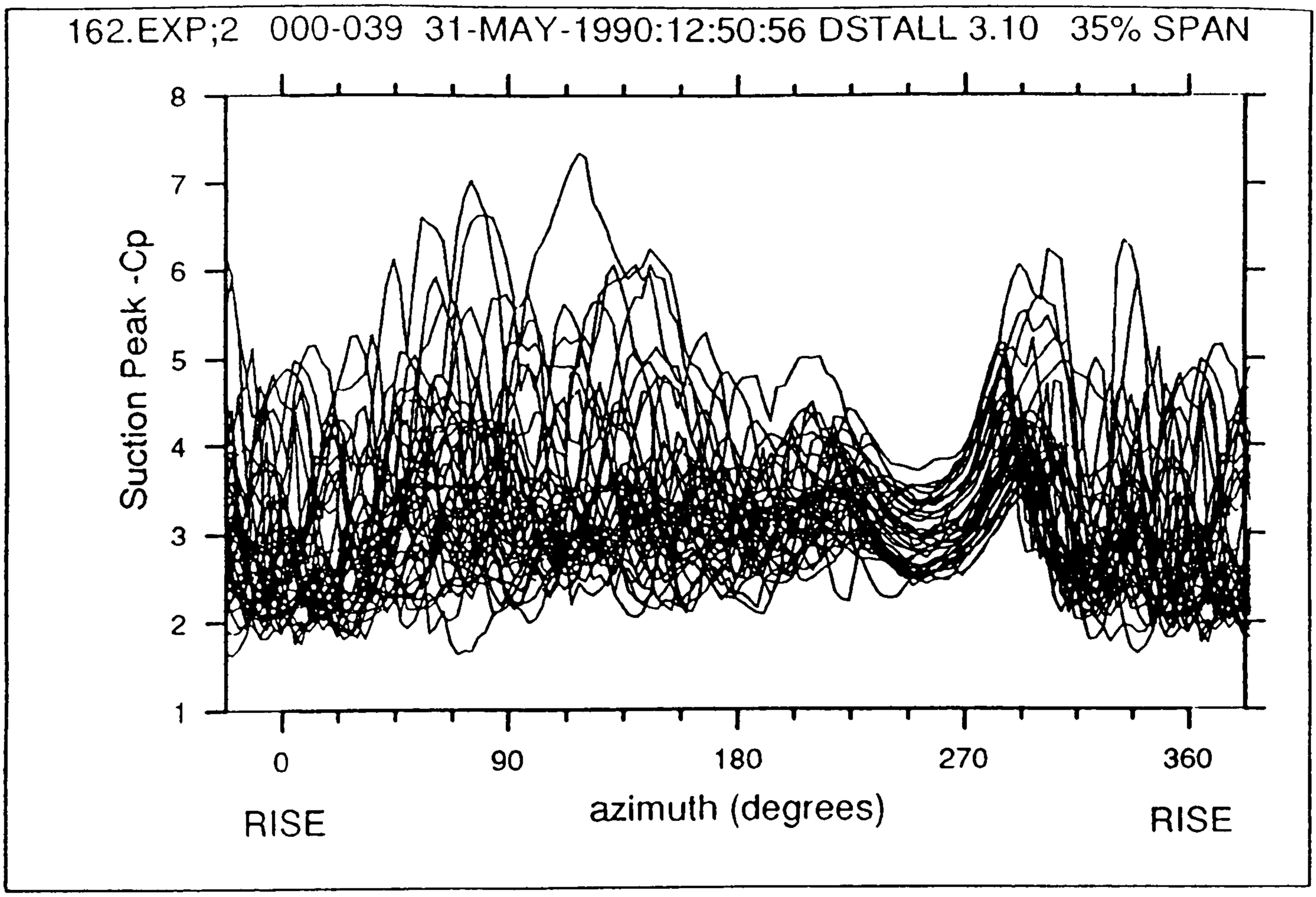
162.EXP;2 000-039 31-MAY-1990:12:50:56 DSTALL 3.10 35% SPAN
Suction Peak -Cp
8
7
6
5
4
3
2
1
0
90
180
270
360
RISE
azimuth (degrees)
RISE

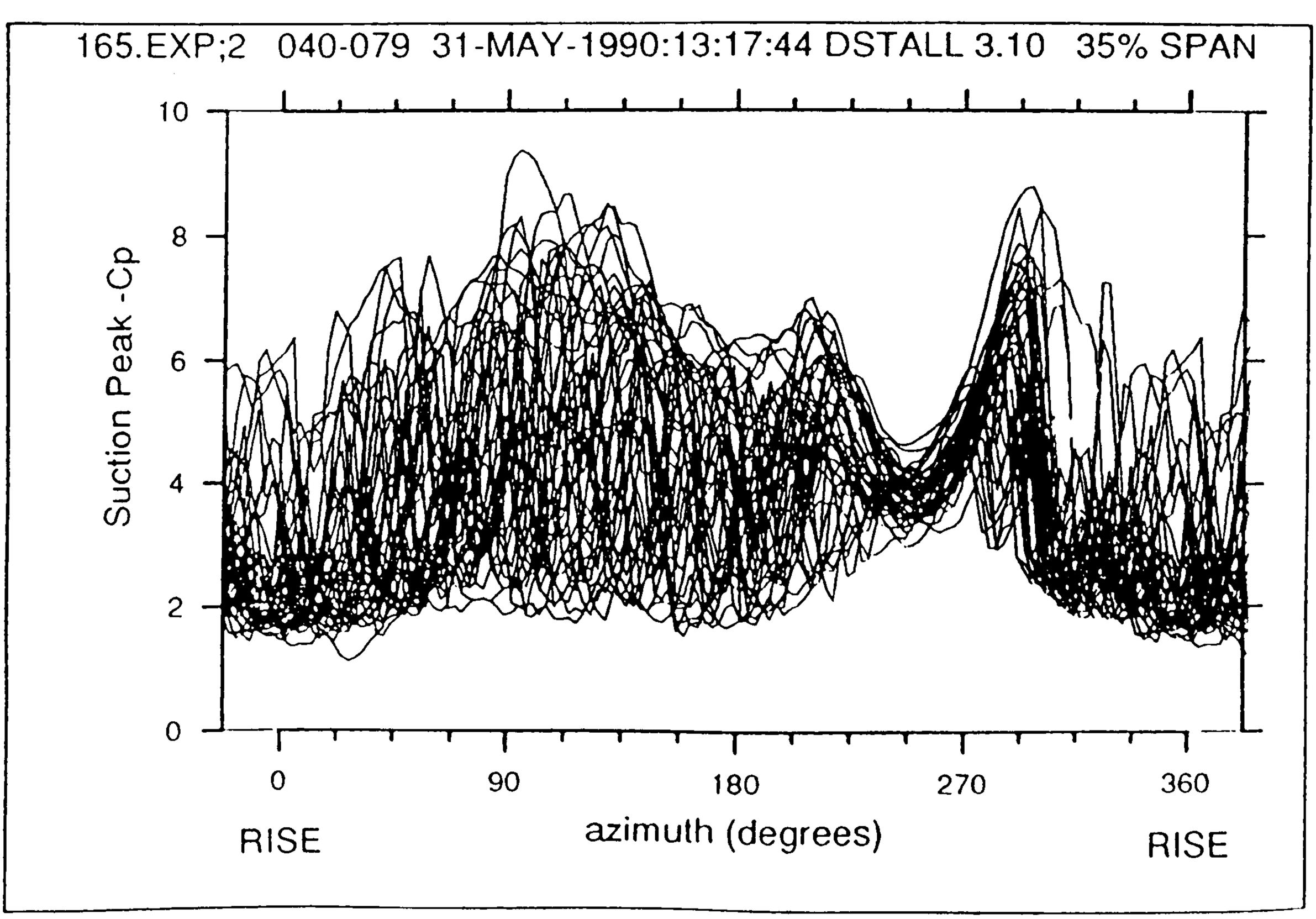
165.EXP;2 040-079 31-MAY-1990:13:17:44 DSTALL 3.10 35% SPAN
Suction Peak -Cp
10
8
6
4
2
0
0
90
180
270
360
RISE
azimuth (degrees)
RISE

Figure 11.24

a)

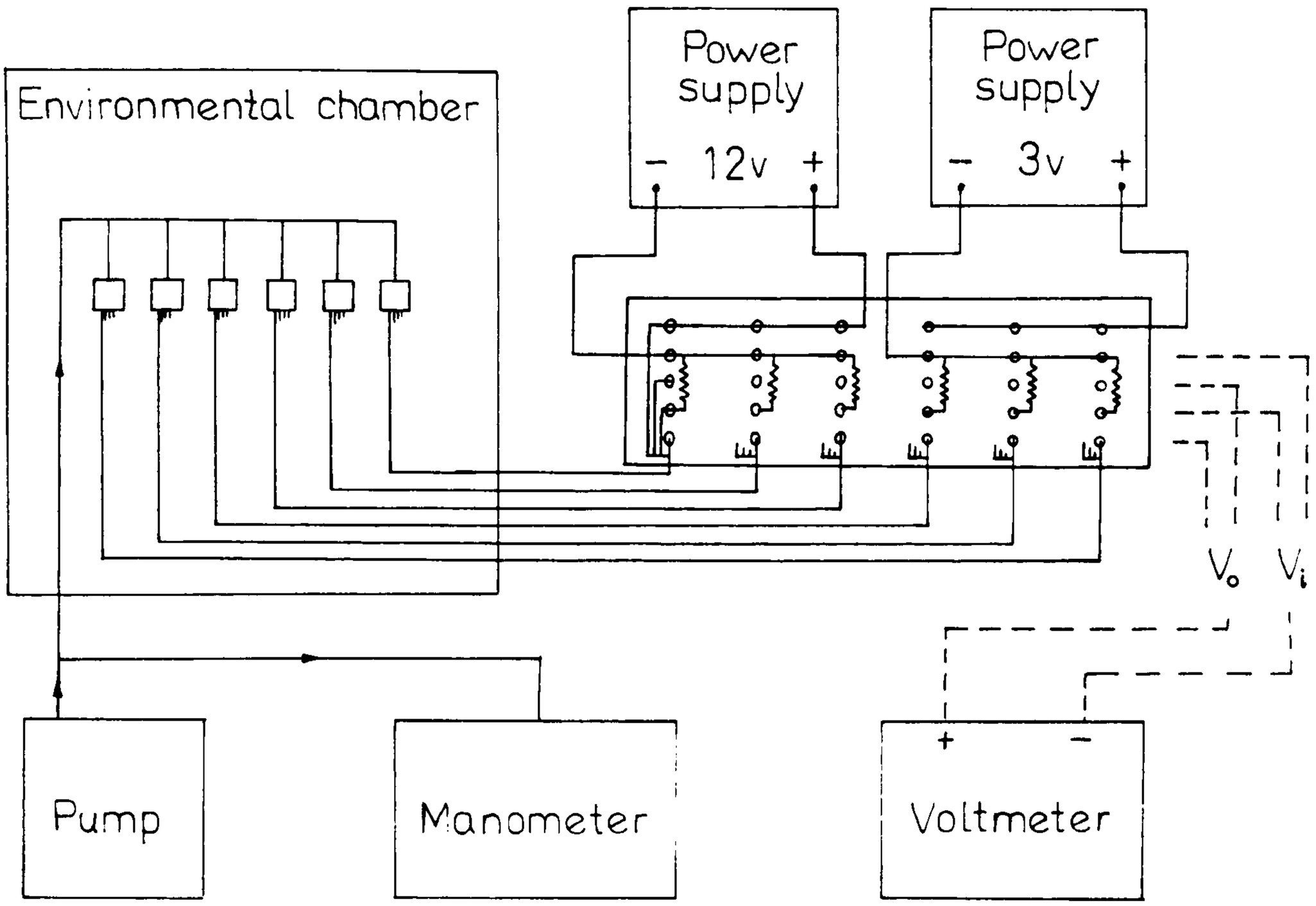

b)

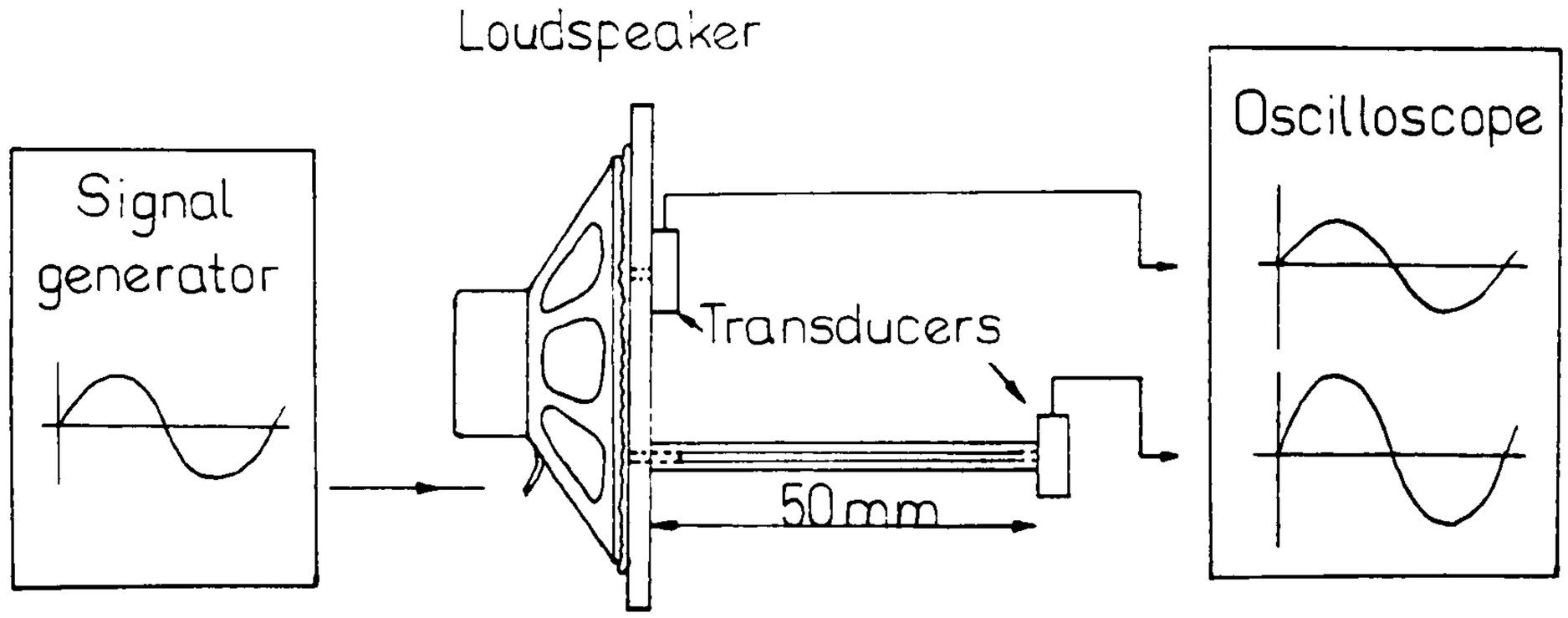

Figure AI.1 Pressure transducer choice experiments.

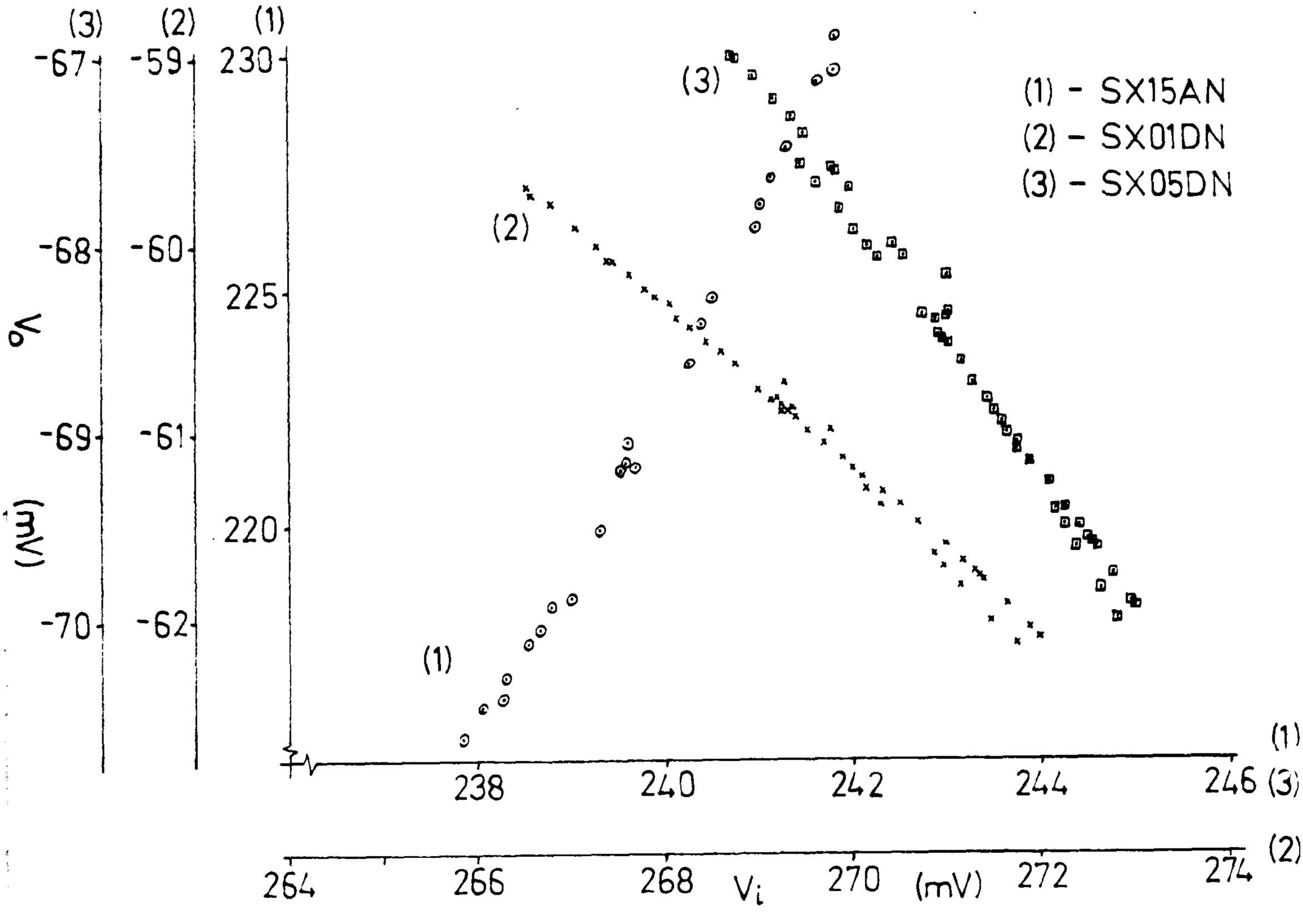

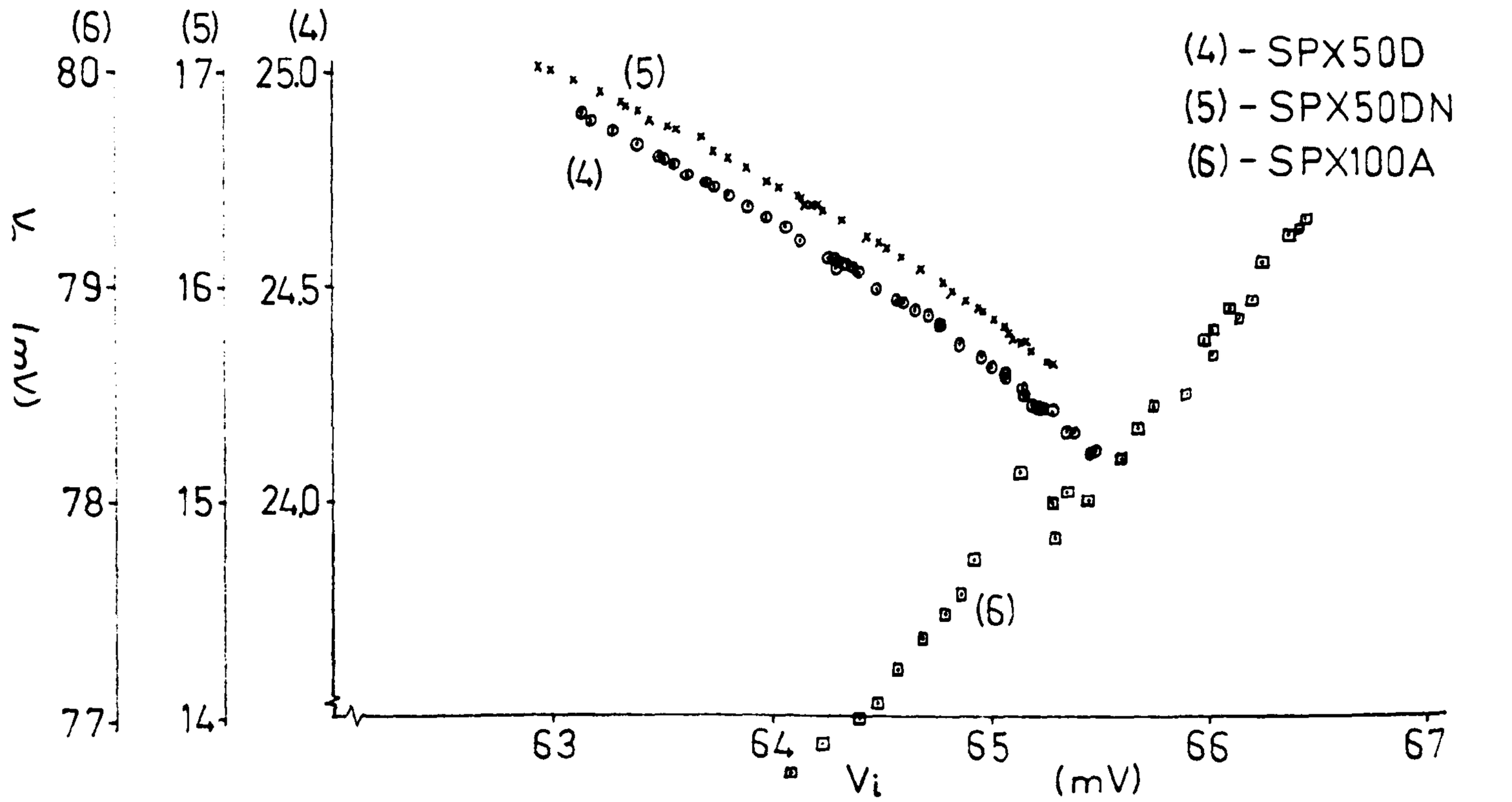

Figure AI.2 Temperature sensitivity for all six transducers tested.

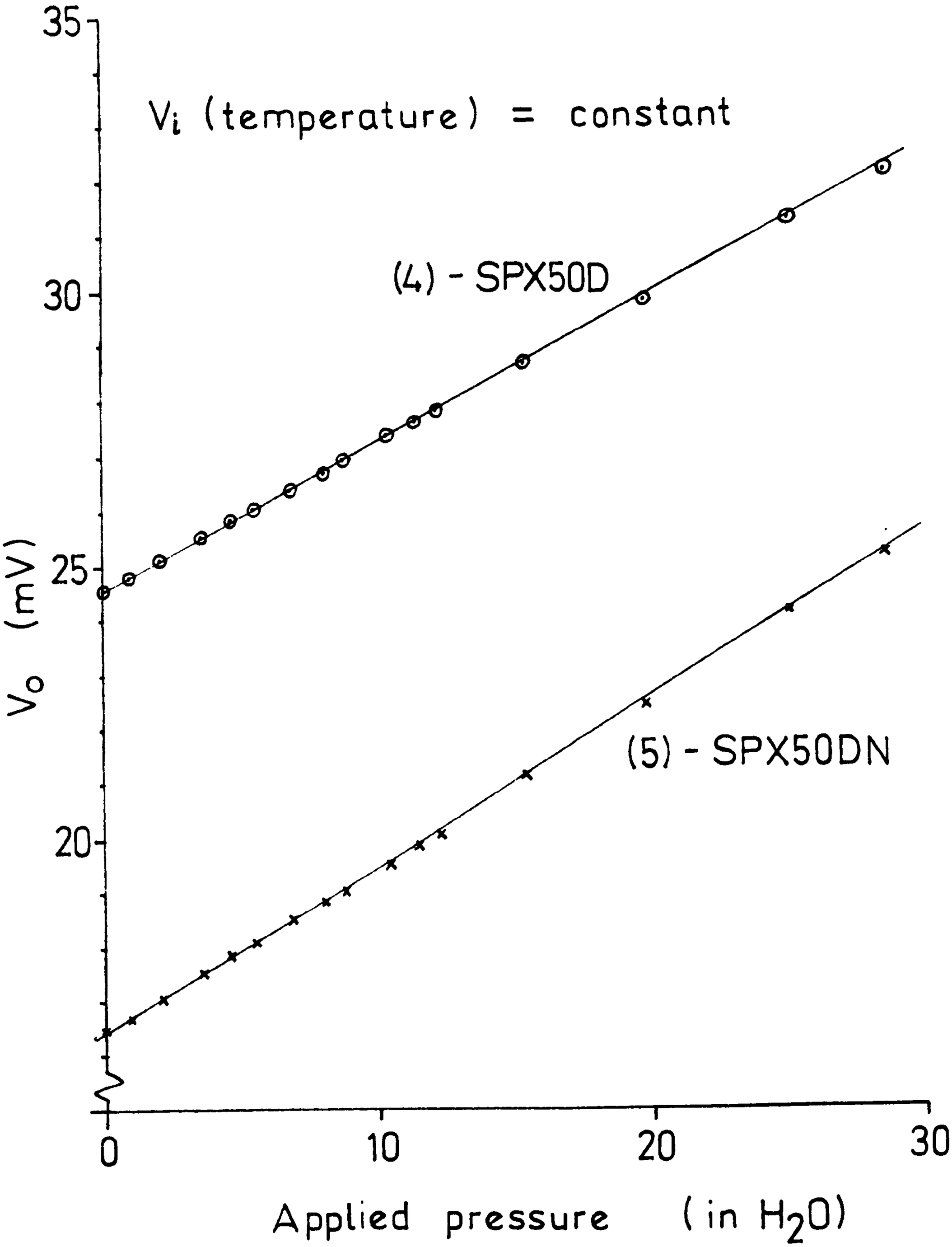

Figure AI.3 Pressure sensitivity of the SPX50D and SPX50DN transducers.

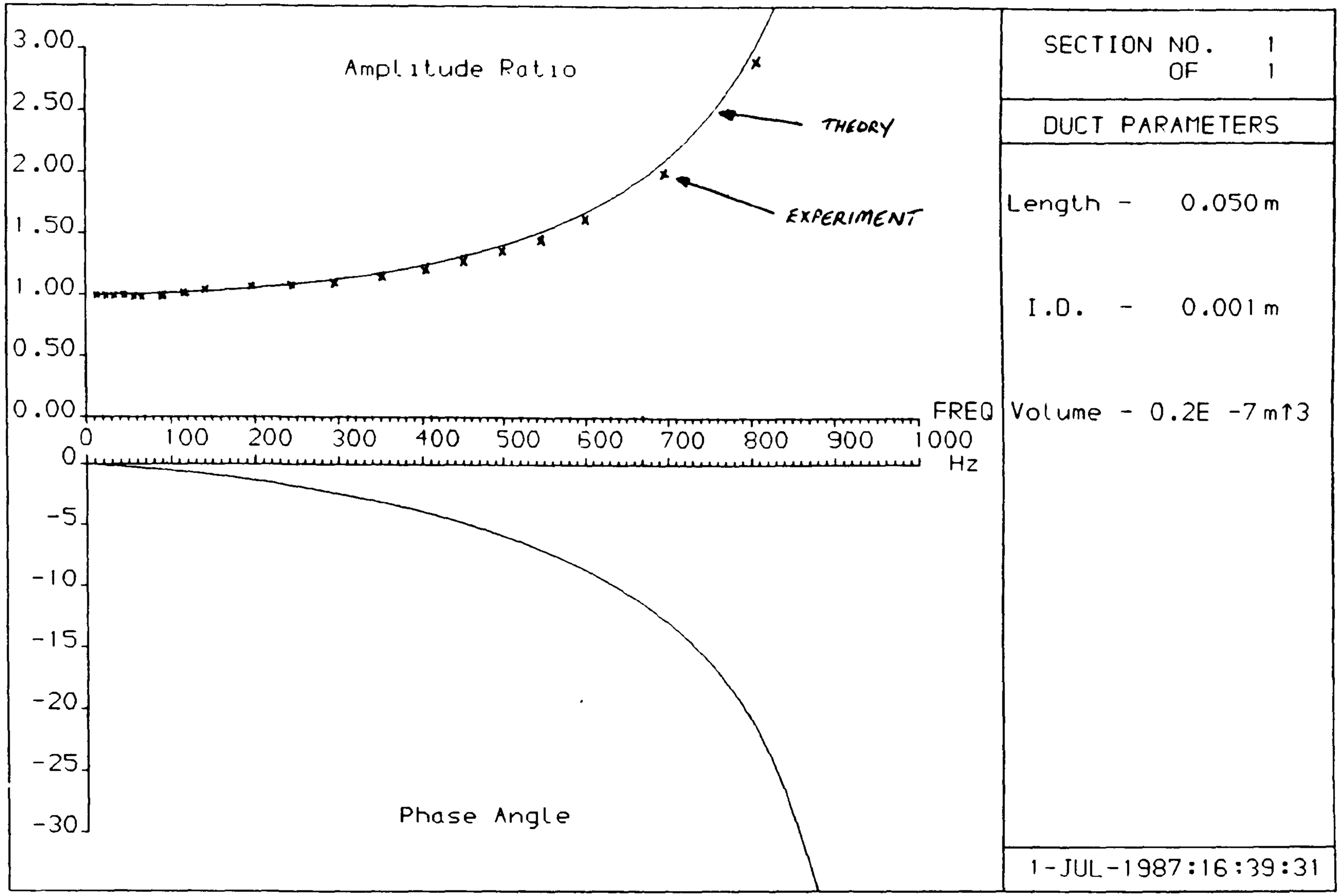

Figure AII.1 _ Frequency response of pressure transducer duct system; theory and experiment.